Design, Simulation, and Precision Manufacturing of Flexible-Backing, Morphing Composite Metamaterials that Lock Suddenly in Global Bending

by

Caleb Jordan Petersen

A dissertation submitted to the Graduate Faculty of
Auburn University
in partial fulfillment of the
requirements for the Degree of
Doctor of Philosophy

Auburn, Alabama
May 1, 2021

Keywords: Additive Manufacturing, Nonlinear Stiffness, Shell Buckling
Bending of Cylindrical Surfaces, Simulation of Woven Fabric in LS-Dyna, Metamaterials

Approved by

Dr. David Beale, Chair, Professor of Mechanical Engineering
Dr. Royall Broughton, Jr., Professor Emeritus of Polymer and Fiber Engineering
Dr. Peter Schwartz, Professor Emeritus of Mechanical Engineering and Polymer and Fiber Engineering
Dr. Maria Auad, Professor of Chemical Engineering

Abstract

Few composite structures, let alone single materials, are known that undergo sudden but reversible stiffening at a pre-engineered strain profile, especially in global bending. This research builds upon this author's previous disclosure of arrays of rigid tiles adhered to a flexible woven fabric substrate that elastically "lock up" (by increasing their effective bending stiffness by orders of magnitude) at a certain displacement profile, which is reviewed and contrasted with other shell-based metamaterials that stiffen with strain. The research then explores design constraints and the mathematics of tile shape and gaps for initially-planar tiled arrays that bend up to a singly-curved surface with a nearly-arbitrary curvature profile for the final lockup shape; these principles are then employed to create a 3D model of an array in Computer-Aided Design (CAD) software. This CAD geometry is then manufactured with additive manufacturing and tested, verifying that it does indeed lock up at an approximation of the target curvature profile. A simulation of the bending behavior of the initially-planar array is then undertaken in the LS-Dyna Finite Element Analysis (FEA) package to develop a general FEA approach for simulating such arrays. Next, an overview of cylinder-like closed surfaces surrounding a bending joint is undertaken with an eye to understanding what geometric features might enable such surfaces to tolerate large deflections of the joint without severe shell buckling that limits their bending stiffnesses, and what morphing pattern would be desirable for such a surface to enclose the ankle joint. In turn, the concept of using closed and doubly-curved surfaces for fabric-backed tiled arrays that might enclose the ankle joint and protect against excessive excursions is introduced and CAD geometry of such an array created, whereupon various approaches to simulating the array in LS-Dyna are undertaken. Some of these approaches reveal flaws in multiple LS-Dyna

material models for woven fabrics, so an alternative approach is implemented. Finally, several closed-surface arrays are manufactured using additive manufacturing with either a fabric or elastomeric backing, and qualitative testing indicates that such arrays can indeed tolerate some internal bending but require further modifications for satisfactory kinematic behavior for an ankle protector.

Acknowledgments

I am grateful to many people for their assistance in completing this dissertation. First of all, I would like to thank my major professor, Dr. Beale, for guiding me in my academic career since 2012 when I first had the pleasure of taking his machine design class. Dr. Beale has always given me helpful technical advice, helped me with journals and publishing, and generally been a source of encouragement. Thanks also to Dr. Broughton for his advice regarding polymer chemistry and reinforcement and fun, spirited discussions. Thanks to Dr. Auad for her assistance, great instruction in polymer properties, sharing 3D printing resources and lab space (tolerating occasional messiness on my part), and development of the Center for Advanced Polymers and Composites. Thanks to Dr. Schwartz for connecting me with the Gackstatter project and contributing his knowledge of fabric behavior and composite reinforcement in his excellent Mechanics of Composites class. All of my professors have been generous with their time, assistance, toleration of my pace of work, etc., and I am very appreciative of that.

Special thanks go to the Gackstatter Foundation for their generous support of my education and generously providing funds for materials and equipment.

Finally, I am grateful to my friends and family for encouraging me throughout the difficult process of performing my research and writing my dissertation. You know who you are.

Table of Contents

Contents

List of Tables

List of Figures

List of Graphs

List of Abbreviations

AM Additive Manufacturing

CAD Computer-Aided Design

DOF Degree(s) of Freedom

FDM Fused Deposition Modeling (an additive-manufacturing technology)

FEA Finite-Element Analysis

FOC "Frustrum-Of-Cone" (refers to a specific shape developed by this author that resembles a frustrum of a cone)

HDM "Hyperboloid-Derived Manifold" (refers to a specific shape developed by this author that resembles a hyperboloid of one sheet, discussed in greater detail in Chapter 8)

NURBS Non-Uniform Rational B-Spline

PETg Polyethylene Terephthalate, modified by glycol groups (a common additive-manufacturing feedstock)

ROM Range of Motion (i.e. in a kinematic sense)

TPE Thermoplastic Elastomer (used in the additive manufacturing of flexible materials)

TPU Thermoplastic PolyUrethane

Chapter 1. Overview and Introduction.

Shell structures that can be designed to exhibit sudden changes in their bending stiffness at specified bending strains could be beneficial in a variety of applications, including protective structures, morphing materials, and vibration isolation devices. Indeed, this researcher previously wrote a Master's thesis at Auburn University [1] that developed a preliminary approach to the solution of this problem, specifically targeting a protective composite for the human ankle joint that would allow the wearer to move his or her ankle within the safe range of motion (for his or her body) with almost no added stiffness from the protective device, but also see instantaneous and stiff lockup if the wearer came to exceed the safe range of motion of his or her ankle. At the conclusion of this researcher's Master's studies, he discovered that arrays of rigid tiles adhered to a thin fabric weave of a high-stiffness fiber (such as a para-aramid fiber like Kevlar or Twaron, which are additionally relatively abrasion-resistant for longer life in fully-reversed bending loadings) showed some promise for producing such a product, for he discovered that planar arrays of such a composite could be bent along various directions in uniaxial bending to produce sudden lockup after a target bending curvature was reached; of note, it was unclear how to precisely tailor the local geometry of the tiles in the array to achieve a specific lockup curvature, and at that point in the research, it was entirely conceptual, so the ability to achieve a specific bending lockup curvature was not then needed.

Additionally, most of the arrays disclosed in this Master's thesis were open, not closed (i.e. like cylinders), but open arrays would not provide the needed conformation to the human leg, nor (for various reasons) be well suited to tolerate the multiple degrees of freedom of the human ankle. That said, this researcher did attempt to modify the principle of planar arrays that lock up in bending by using a cylindrical manifold (i.e. a closed but singly-curved surface) for

the initial array; the results of this experiment were ambiguous, inasmuch as the resulting array had very limited initial freedom (corresponding to just a few degrees of protected-joint rotation) before lockup.

Thus, at the conclusion of the researcher's Master's studies, there were many fundamental questions remaining to be solved, both regarding the specific concept conceived of during his Master's research (the fabric-backed tiled array, in various shapes and embodiments), as well as regarding larger questions surrounding mechanical metamaterials and what patterns of morphing would be suitable for a cylinder-like surface enclosing a joint. As regards the fabric-backed tiled array concept, it was unclear whether closed-surface fabric-backed tiled arrays could effectively protect an ankle joint while conforming closely to it and allowing the full range of safe motion before locking up owing to the possibility of in-surface extension being required (which the fabric-backed arrays generally cannot bear, as discussed in detail during the review of this concept); additionally, it was entirely unknown how to design fabric-backed tiled arrays to control their pre-lockup and post-lockup shapes, especially for various array surface geometry classes (flat, singly-curved, positive-Gaussian-curvature, negative-Gaussian-curvature, or mixed-positive-and-negative-Gaussian-curvature surfaces; and open, singly-closed, or doubly-closed surfaces). As will be previewed in detail in the section in this chapter describing the overall thrust of this dissertation, it will address all of these questions surrounding the fabric-backed tiled array concept, as well as review recent advances in mechanical metamaterials (many of which occurred after the publication of this author's Master's thesis) and conduct an investigation into potential morphing transformations of a closed surface enclosing an ankle joint, none of which was undertaken in the Master's work.

Review of Desired Material/Metamaterial Properties.

The general qualities of a hypothetical strain-stiffening protective material should first be reviewed to illustrate how remarkably they differ from those of a typical material (even a moderately-nonlinear one). Ideally, a strain-stiffening material or structure would feel flexible to the point of having nearly zero bending stiffness within certain strain ranges (and, of course, this strain should be elastic, i.e. totally reversible), but at a specific bending strain, the structure should stiffen and resist further deformation with as little compliance as possible (though what strain there is after this "locking up" should also, ideally, be elastic). If the load is reversed or removed, the structure should recover and again feel flexible. The structure should also likely have constantly-high stiffness in uniaxial, uniform tension (instead of shell bending), though a similar regime of low tensile stiffness up to a specified tensile strain followed by rapid but reversible stiffening might also be desirable for some applications. Moreover, the strains at which lockup is initiated should be variable (by precision manufacturing, perhaps 3D printing) over the geometry of the shell, so that local curvatures at lockup can be set differently in different regions or even continuously to accurately represent a specific shape at lockup (e.g. an airfoil). However, so far, no single material, metamaterial structure, or composite (including composite metamaterial) is known that possesses such properties.

The overall geometry of the shell structure should be as thin as feasible. Depending on the application, the shell may need to be flat, singly-curved, or perhaps even doubly-curved (if bending of such a manifold is even feasible). Furthermore, the shell may need to be an open or closed surface, but for human protective applications, it will most likely need to be a closed surface, in order to practically surround the joint, and to control a joint with multiple degrees of freedom (e.g. an ankle or wrist). Significantly, closed surfaces entail further complications

owing to the significant offset between the neutral axis of bending and the furthermost cross-sectional areas of the surface in bending; whether by actually tensioning/compressing locally, or by [un]bending in such a way as to increase or decrease the effective overall length of the cross-sectional curve. Owing to the importance of making a protective manifold into a closed surface rather than an open one, but the considerable added difficulty of accommodating the length changes far from the neutral axis, this dissertation has been divided into two main parts following this chapter: the first part exclusively considers open surfaces that bend up to a prescribed curvature profile (subject to certain limitations) and then lock up reversibly against further bending in that direction thanks to the interrupted tiles with prescribed shapes and gap distances that are adhered to a thin fabric backing that is stiff in tension; the second part first investigates how to make a closed, cylinder-like surface bendable (namely in large-deflection bending), and then attempts to apply the interrupted-tile principle to make such a surface not only bendable but also lock up.

Preview of the Dissertation.

It would certainly be ideal if a simple, continuous material (rather than a difficult-to-manufacture metamaterial or composite) could be found that locks up in shell bending or at least tension or compression. Alas, there is no known single material that can produce a structure that can reversibly and elastically stiffen up rapidly by multiple orders of magnitude in bending at any strain, let alone one that can be tailored to stiffen up in bending at a specific, pre-engineered strain; a more detailed explanation of how all pre-existing single materials and most composite structures fail to produce this behavior is given in Chapter 2. Certainly, there are several classes of mechanical metamaterials that at least show stiffness increases with strain (sometimes significant enough to constitute lockup), although they have other flaws: these are discussed in

Chapter 2's extensive literature review on these strain-stiffening mechanical metamaterials, which is the first such literature review known.

As mentioned above, the author of this dissertation previously conceptualized [1] a composite material structure, consisting of an array of rigid tiles (with precisely-determined negative spaces between them in their initial configuration) bonded to a high-stiffness plain-weave fabric backing, that can significantly stiffen in bending when such deformation causes gaps between tiles to close, putting the tiles into compressive loading and the fabric substrate into tension. A review of this concept and an investigation into various tile geometries that have been investigated and manufactured with 3D printing is found in Chapter 3, along with any outside research that bears any similarity to this concept. Then, in Chapter 4, one particular set of tile geometries is used to first design in Computer-Aided Design (CAD) software and then manufacture an array that starts as a flat sheet but can be bent into a singly-curved surface with a specific curvature profile over the length of the surface; manufacturing considerations to precisely replicate this curvature are also discussed, and the experimental results of this process are disclosed. Next, in Chapter 5, a technique for modeling a composite fabric-tile array in the LS-Dyna Finite Element Analysis (FEA) code is developed in order to allow this researcher to simulate arrays to test their ability to bend freely before lockup but lock up at the desired bending strains; the technique is applied to the specific array described in Chapter 4, and simulation results are compared with experimental results. This work concludes Part I's investigation into open surfaces (i.e. surfaces that do not have seams; e.g. not cylinders) in bending; unfortunately, simple, developable, open surfaces (even if they can lock up in bending) are of limited utility for an ankle protector.

Next, Part II opens with Chapter 6's investigation into the large-deflection bending properties of closed (cylinder-like) surfaces and microstructures aligned on such surfaces, with an eye towards discovering principles to make such closed surfaces able to contain a joint that undergoes large rotational displacement without suffering catastrophic (stiffness-reducing) buckling under the applied strain field; after all, for a surface to lock up in bending, it must necessarily not lose its stiffness (though merely preserving initial bending stiffness is far from a sufficient condition for lockup). Outside research that is cited in this chapter inspired this author to pursue two different lines of original experimentation into buckling-resistant bending-capable closed surfaces, namely microstructured mesh arrays and bellows-like shells with normally-offset waviness. Both were found to have potential value, and a parallel between certain microstructures and the bias-compliance-enabling trellis mechanism of woven fabric was drawn, recommending insights for converting the planar-lockup tiled and fabric-backed arrays into cylindrical-lockup arrays with potentially-appropriate modifications.

In turn, Chapter 6 proposes a closed surface on which interrupted tiles should be arrayed, with a specific shape that is anticipated to be best suited as a practical ankle protector (when combined with other microstructure features). The surface's geometry is explored mathematically: it is a closed (like a cylinder or hyperboloid of one sheet, etc.) surface that additionally has negative Gaussian curvature (like a hyperboloid of one sheet and unlike a cylinder).

In turn, Chapter 7 undertakes to array interrupted tiles on the "hyperboloid-derived manifold" that first disclosed in the previous chapter. After CAD software is used to construct an array of tiles with gaps targeted at producing lockup from surface bending, the LS-Dyna FEA package is used to simulate the array in contact with a rotating leg with large deflection, though

the material model used, MAT_235, proves unreliable for these simulations owing to reasons discovered in Chapter 8, namely that the material model has unexpected instability when fabrics are subjected to significantly-biaxial tension stresses or strains (an error that did not come to light during the preliminary FEA work in Chapter 5 because the fabric was loaded only uniaxially there). Chapter 8 examines all the other micromechanics-based continuum models for fabric in LS-Dyna and conducts simple simulations with each, disclosing flaws that all of them have.

Fortunately, as discussed in Chapter 9, a newer formulation of MAT_034 allows for reasonably accurate and highly-robust simulation of woven fabrics in LS-Dyna even without tabulated data, including reduced-stiffness shearing, so the simulation is repeated with this formulation, which suggests that significant modifications to the kinematics of the concept may be required to properly control the ankle's range of motion.

Finally, Chapter 10 undertakes to manufacture the fabric-backed tiled array that was simulated in Chapters 7, 8, and 9, using either woven fabric or an elastomeric shell (created by multimaterial 3D printing) as the backing. The multimaterial 3D printing technique of manufacturing is found to be far faster with which to iterate, so several modifications of the structure are attempted therewith, and additionally one final tiled array on a bellows-like elastomeric shell (comparable to bellows-like shells studied in Chapter 6) is created and tested with promising results. Chapter 11 then summarizes all the conclusions and contributions of the dissertation and gives a framework for future research.

Part I. Lockup-Capable Open Surfaces.

Chapter 2. Previous and Outside Approaches to Shells that Lock Up in Bending, Tension, or Compression.

Abstract.

This chapter reviews existing (outside) research on materials, composites, and metamaterial structures that exhibit stiffness increases as a function of strain or displacement, with a special eye towards embodiments that have rapid, reversible, and elastic lockup at a tailorable strain profile. The chapter first gives a basic overview of the properties desired in a metamaterial that could solve this problem. With these in mind, the design space of known continuum materials is then surveyed for lockup potential and generally rejected, though the fact that elastomeric materials do tend to exhibit stiffness increases in tension is noted (unfortunately, the strains at which these occur are too high and the degree of change too low for practical use). Next, a review of the growing field of mechanical metamaterials is undertaken, first introducing the concept of a mechanical metamaterial and then focusing on those metamaterials with strain-stiffening properties; the review indicates that there are several microstructures that metamaterials may possess to enable elastic stiffening, including interrupted contacts that are closed up with displacement, microstructures that are initially subject to beam-bending that later experience mode-switching into tension-dominated modes (which are far stiffer than bending-dominated modes), and kinematic singularities. Many examples of stiffness-increasing metamaterials, both from outside literature and occasionally from this author's own work, are presented, though most prove deficient in their properties (especially in the magnitude of stiffness increases obtained). Finally, the special characteristics of fabrics are examined in light of the foregoing, indicating that fabrics are themselves relatively-simple metamaterials and

moreover may play a promising role in the development of the special composite metamaterial that stiffens in bending first described by this researcher in his earlier Master's thesis.

Introduction.

This dissertation considers a novel problem in material science: designing a material or composite whose stiffness (specifically shell-bending stiffness, rather than pure tensile stiffness) varies as a function of local strain, specifically producing a rapid and significant increase in bending stiffness after a certain strain is reached, while only exhibiting elastic deformation and not requiring any electronic control. The goal of this research was to produce a structure that can bend flexibly within a certain range of local curvatures, but that experiences local stiffening of its bending properties after a certain bending curvature is reached. More specifically, it would be desirable to be able to "program" (through passive design constraints) the structure to be able to bend or perhaps distort in a more complex way (e.g. potentially with shell extension or contraction, depending on the structure of the metamaterial) until it attains a specific shape (though there may be some potential limitations on this shape: for instance, some of the metamaterials described in this dissertation must morph from one singly-curved shape to another by a morphing that does not involve significant shearing or extension/contraction, only shell bending).

To add further complication to the geometry of a hypothetical protective device, it is desirable that the structure occupy a roughly-cylindrical shape in that it should fully wrap around a joint (such as the ankle) to a full, 360° extent; the material would need to exist in a suitable shape to allow for some morphing (potentially entailing shell bending, shell contraction, and/or shell extension) that would enable the structure to conform to the joint throughout its range of motion while acquiring the ability to lock up at certain displacements. Indeed, in order to

achieve high post-lockup global stiffness, creasing and shell buckling would at least need to be controlled (perhaps fully eliminated) in a hypothetical cylindrical ankle protector because shell buckling is often associated with a significant loss in the shell's stiffness against the bending load that produces it (though alternatively perhaps the magnitude of the lockup effect could be so strong as to overcome any stiffness losses from buckling). The constraints imposed by having a cylindrical shape enclosing the rotating joint are studied in greater detail in Part II (starting in Chapter 6) of this dissertation.

Additionally, the stiffness at lockup would ideally be multiple orders of magnitude larger than the pre-lockup stiffness, causing the stiffness of the protective device to go from great flexibility to maximum rigidity, in order to provide effective protection to the wearer in the lockup zone against excursions outside of the safe range of motion that could result in joint injury (potentially by resisting high dynamic loads that the wearer might be subjected to, perhaps on the order of a multiple of his or her bodyweight) while preventing energy waste and general alterations to the wearer's pattern of movement by limiting the pre-lockup stiffness. It is likely also desirable that the strain range for the transition from compliant to rigid be small, perhaps on the order of a few percent of the overall strain range (making the stiffness change rather sharp), although there would also likely be a lower limit on the magnitude of the transition strain range that would be tolerated, because in dynamic loading, an excessively-small strain range for lockup would translate to an excessively-short time interval during which lockup would occur, which could injure the wearer; that said, such properties (such as initial stiffness, transition range, etc.) could be fine-tuned later if a proof of concept is produced that has the properties that appear to be the most novel and hardest to achieve (namely significant increases at lockup and a

cylindrical embodiment). These properties are illustrated with a stress-strain graph of how the hypothetical material might ideally behave in Graph 1.

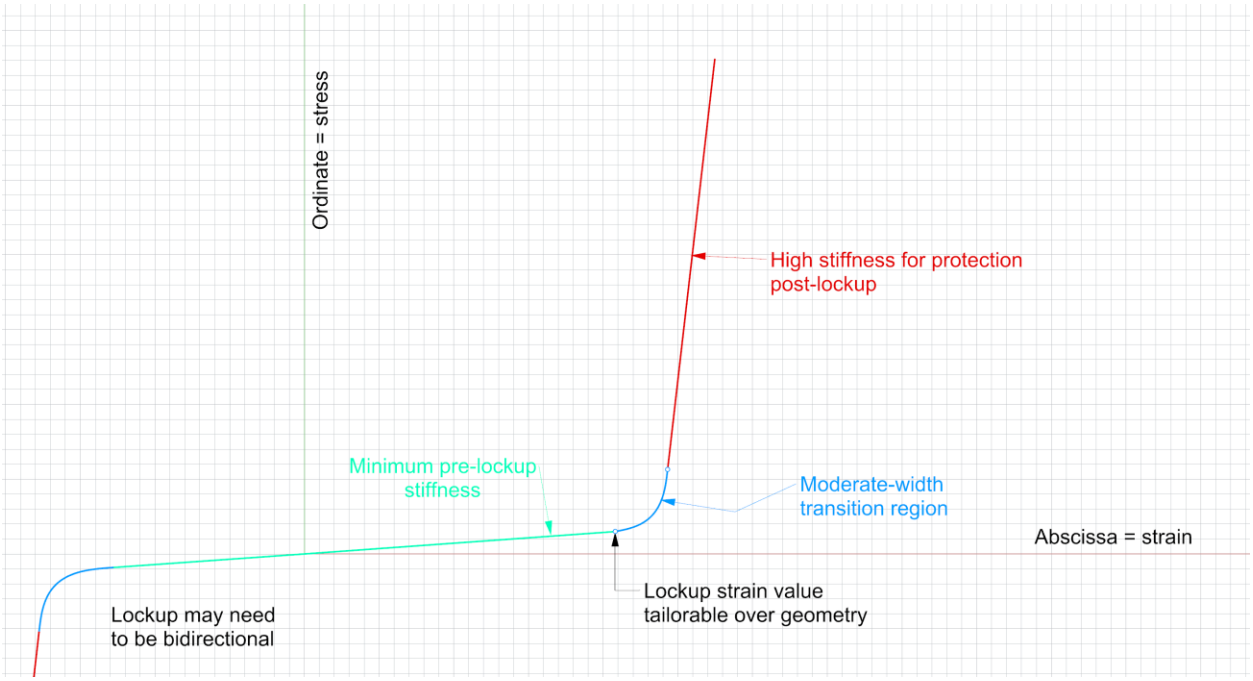

Graph 1: Conceptual graph illustrating the desired mechanical properties in terms of stress and strain for a hypothetical protective material.

Homogenous Materials that Stiffen in Compression or Tension.

The first approach to solving the variable-bending-stiffness problem was to investigate whether there was a homogenous material (or simple composite) known to exhibit the desired variation in stiffness. Specifically, the hypothetical material should exhibit a rapid but elastic stiffening (from very low stiffness, with a modulus on the order of kilopascals or megapascals, to very high stiffness, with a modulus on the order of gigapascals), either in uniaxial tension, uniaxial compression, or (in a more macro sense), shell bending (which combines tension in the region above the neutral axis/plane with compression in the region below the neutral axis), preferably with this stiffening-up effect occurring at moderate strains (on the order of 0.05, rather than at large strains, such as at 1.00 or greater). The hypothetical material would be especially

attractive if its precise lockup strain could be tailored (perhaps by locally varying its chemistry or the local weight proportion of composite additives), especially if it could be made anisotropic by tailoring its lockup strains in different bending directions of the shell; however, even if tailoring through chemistry or additive-density proved impossible, such a structure might still be tailored through geometric means (by changing the mesostructure, thickness, etc.), so this was not an essential requirement.

Perhaps surprisingly, an extensive survey of material science literature found no known continuous materials that exhibit rapid and large stiffening in tension or compression (or in bending, i.e. localized compression and tension increasing with offset from a neutral axis) within an elastic range, though some materials were found to meet some (not all) of these criteria. For instance, certain types of foams exhibit moderate stiffening in tension and somewhat more dramatic stiffening in compression (due to increasing self-contact between the walls of the foam cells during crushing), but in a large and inelastic strain regime (for instance, with strain on the order of 0.5) [2]; the stress-strain responses for a few such foams are graphed in Graph 2 (reprinted from [2]). Of note, the inelasticity of the strain regime for such foams would make bending irreversible even before the lockup shape is reached (and reversibility is desired even after the lockup shape has been reached and the material has stiffened up: if the load is removed, the material should be able to unbend back to its original shape). Additionally, the post-stiffening, maximum stiffness achievable of such foams is not as high as would be desired to minimize the volumetric footprint of a potential protective device.

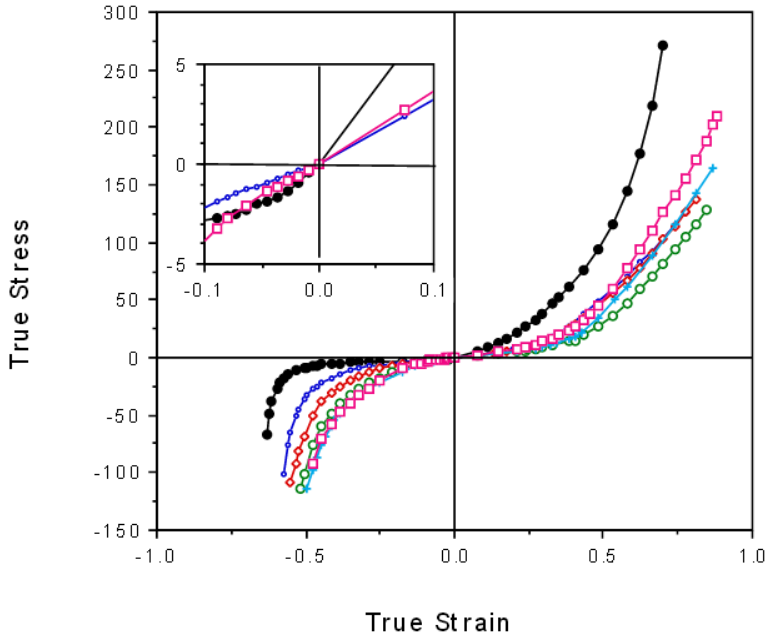

Graph 2: Compressive nonlinearity is quite significant for conventional, non-auxetic foams, as can be seen in this plot of stress vs. strain for several samples of foam. Unfortunately, the magnitude of strain required to achieve noticeable stiffening up is quite high, and moreover such strains are generally not recoverable (the source, [2], indicates that there is significant rib buckling and collapsing at higher global strains, which generally involves local plasticity within the foam ribs). The inset graph is simply a zoomed-in view of the stress and strain region near very low strain levels, indicating that the stiffness does change as the material transitions from tension to compression (though this finding is not especially relevant). The various line colors correspond to different volumetric compression ratios of Scott industrial foam, with black indicating 1.0, blue 2.0, red 2.6, green 3.2, cyan 3.7, and green 4.2. The stresses are in kPa, and the strains are dimensionless. This graph was taken from [2] with permission.

Similarly, hyperelastic elastomers sometimes demonstrate an increase in instantaneous-strain stiffness at high tensile strains (on the order of 1 strain or greater); while these may be superior to foams for this paper's application inasmuch as these high strains may still be elastic, their increase in stiffness is not large enough for the intended application, and moreover it is too gradual (and often characterized by complex nonlinearity, with multiple changes in the derivative of stiffness with respect to strain, i.e. a softening region, a roughly-linear region, and then a stiffening region). For instance, the Odgen hyperelastic material constitutive model used in FEA simulations of elastomers shows this behavior (elastic but weak stiffening up after high strains); the stress-strain responses of several characteristic actual materials that follow this model are depicted in Graph 3 (reprinted from [3]).

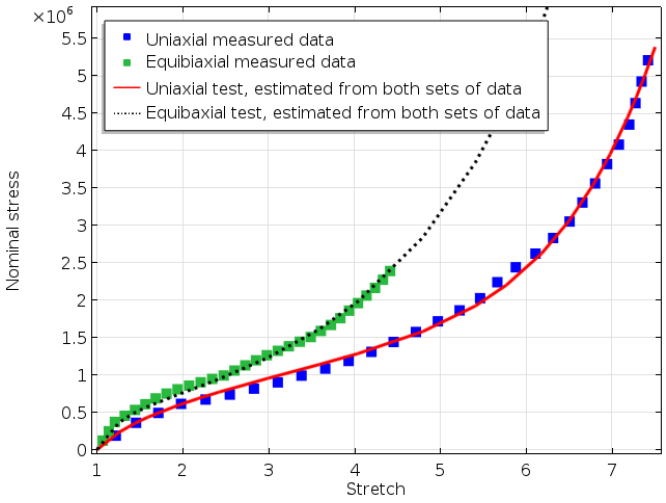

Graph 3: Stress-strain response in tension for two different elastomers, showing eventual stiffening up to a moderate extent (orders of magnitude less than desired for a joint-protecting kinematic structure), but at extreme strains, reprinted from [3] with permission.

Of note, some biological tissues, especially skin, behave like synthetic elastomers inasmuch as they do stiffen up somewhat in tension, but only with large strain and more weakly than needed for potential applications of this research [4]. For instance, the stress-strain responses of several strain-stiffening tissue samples (specifically, lung tissue from dogs) are shown in Graph 4; the large strains required to produce any stiffening-up effect, and the limited magnitude of the increase in stiffness, both prevent such materials from being practical for this application.

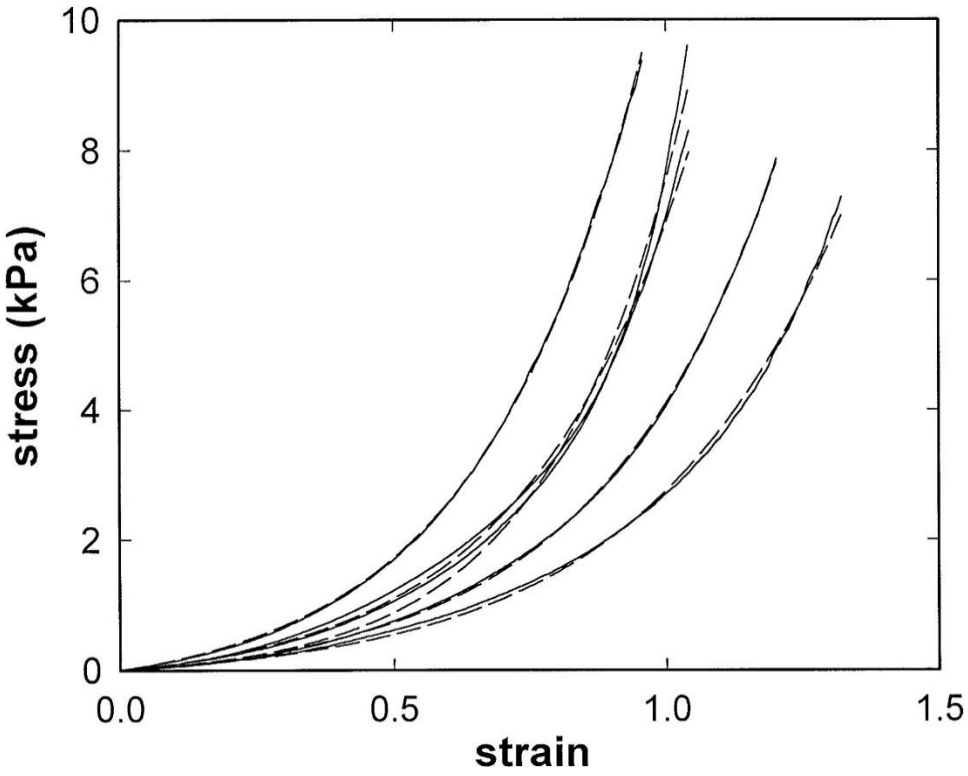

Graph 4: Stress-strain responses of several biological samples (specifically, lung tissue from dogs) that show J-curve behavior comparable to that of artificial elastomers. The different curves correspond to different samples, with the dashed lines corresponding to curve-fitting curves and the solid lines the raw data. Reprinted from [4] with permission.

Elastomers may also stiffen somewhat in compression, depending on the boundary conditions, due to their high Poisson's ratios and thus near-incompressibility; however, this effect tends to initiate near 0.3 compressive strain, and thus for an elastomeric structure to exhibit significant bending stiffness increases, it would at a minimum need to be made very thick to ensure high bending strains at least somewhere in the body (which might instead produce out-of-plane buckling, which would result in a further loss of stiffness). For instance, elastomers that follow the Yeoh constitutive model stiffen rather rapidly on the order of 4-5x after 0.3 compressive strain, which is at least superior to the larger strains required to activate the lower stiffening up magnitude for elastomers that stiffen in tension [5]. An example of the static stress-strain response of a material simulated with the Yeoh material model is shown in Graph 5.

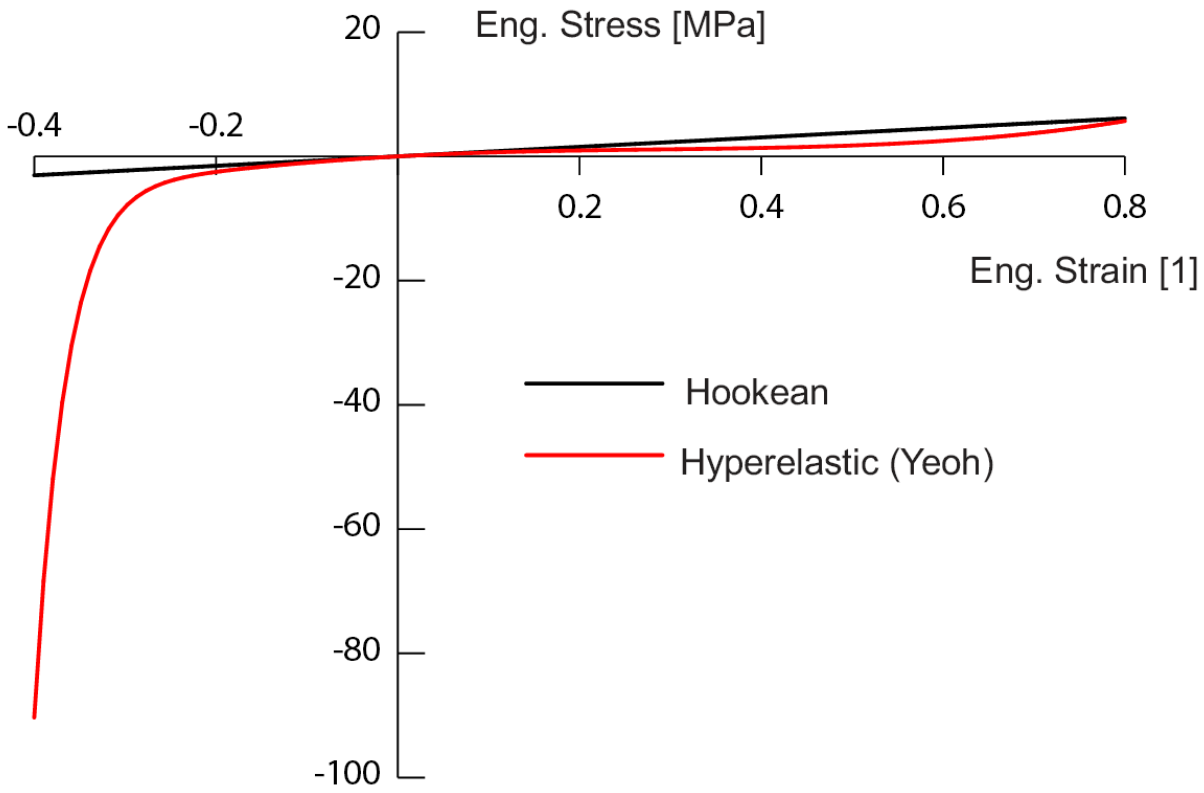

Graph 5: Compressive stiffening of an elastomer that follows the Yeoh model. Taken from [5] with permission.

Additionally, elastomers suffer from the Mullins Effect, whereby an elastomeric material becomes dramatically more compliant the second and subsequent times it reaches a certain stress level (i.e. in cyclic loading and unloading) [5], meaning any hypothetical protective product would need to be "broken in" with repeated loading and unloading before consistent behavior could be expected. Finally, solid elastomers have poor ventilation properties, which would be undesirable for a device to be worn for humans (though it might have mechanical applications).

Nonetheless, under the aegis of this researcher's previous Master's work, a basic FEA simulation was performed in ANSYS Workbench to evaluate whether a thick cylinder of an elastomer with some stiffening properties in both compression and tension at large strains would experience global stiffening when it enclosed a rotating inset cylinder jointed to the ground, with

the base of the rubber protector cantilevered to ground, and a symmetry plane established to reduce computation time [1]. The rubber protector conformed rather closely to the rotating cylinder (the initial offset between the two was small). The initial configuration of the cylindrical rubber shell and rigid rotating cylindrical "leg" is shown in Figure 1.

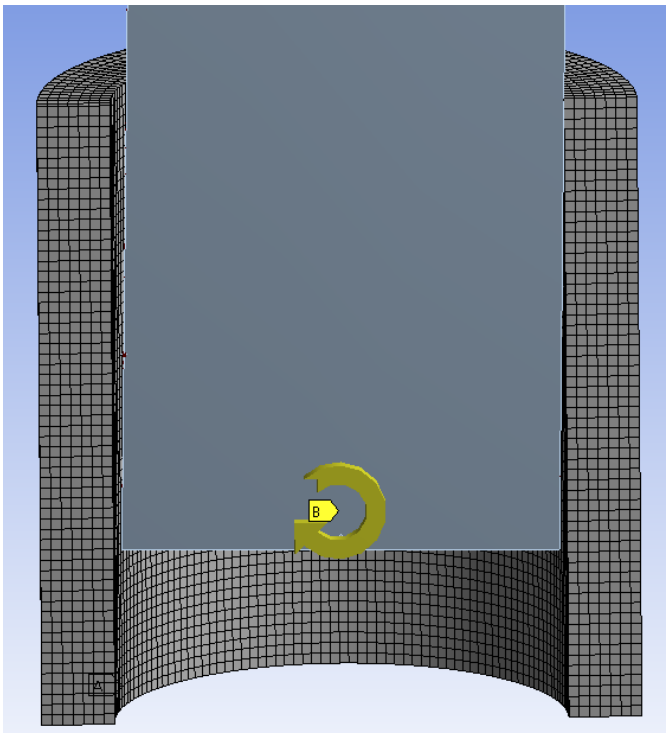

Figure 1: Boundary conditions for preliminary FEA of an elastomeric thick cylindrical shell, to evaluate whether it shows appropriate stiffening-up behavior. The center of rotation is indicated with a yellow point, "B", with rotation along the yellow arrow indicated.

As shown in Graph 6, there was indeed some stiffening-up behavior in the moment reaction required of the leg to rotate (although the data was surprisingly noisy, with a consistent tendency for individual points to jump towards zero moment reaction); however, it was not nearly as sudden as desired, nor indeed as sudden as the elastomer modelled stiffens in either uniaxial compression or tension. Despite the near incompressibility of the elastomer (from its high Poisson ratio), its very low shear stiffness likely allowed stresses to spread to areas of the sock not directly contacting the leg, thereby reducing the concentration of uniaxial tensile and

compressive stresses that could provoke stiffening; a contour plot of von Mises stress is shown in Figure 2. Moreover, the moment reaction at the center of rotation was indeed somewhat nonlinear, with the direction of concavity indicating some stiffening up. However, the magnitude of stiffening up was nowhere near what was desired, indicating that simple (non-microstructured) protectors, even of materials that intrinsically show some stiffening up, do not meet the goals of this research.

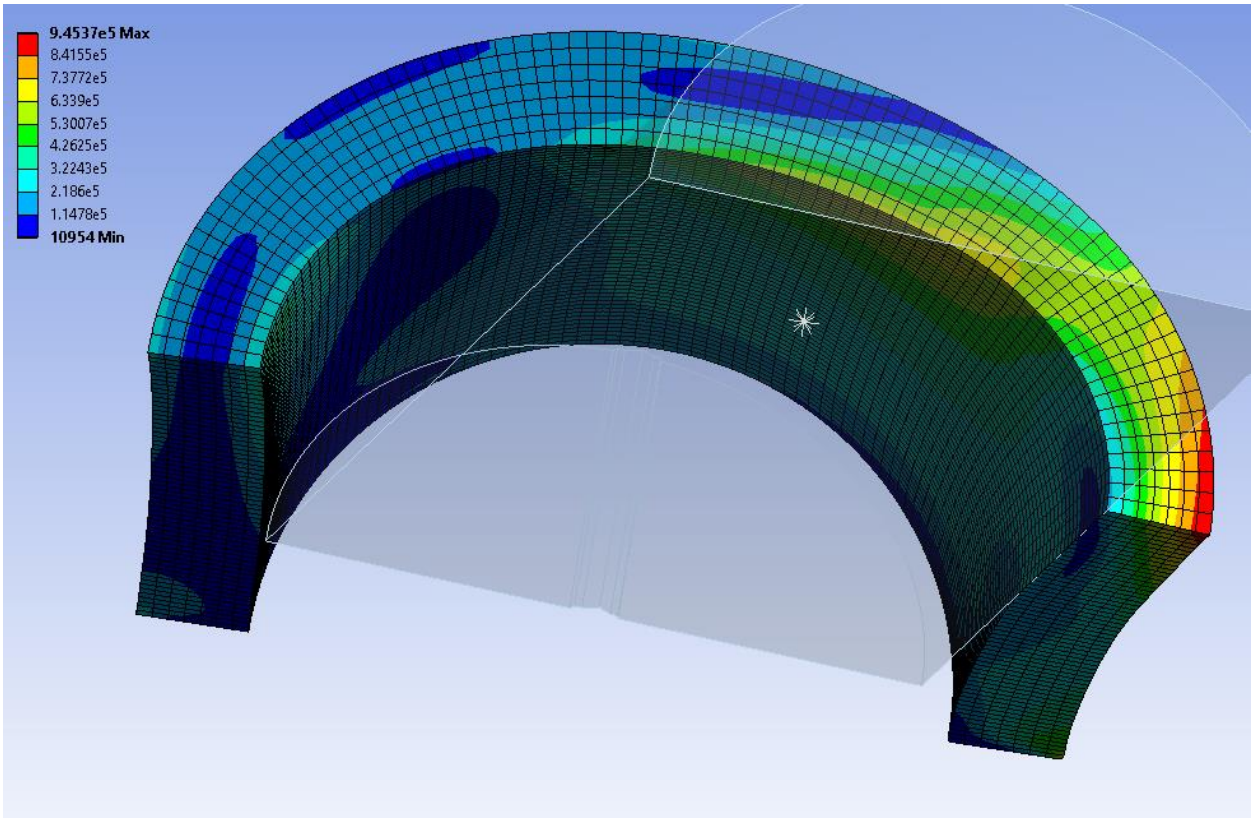

Figure 2: Contours of von-Mises stress in the rubber cylindrical protector after 12.5° of rotation of the "leg".

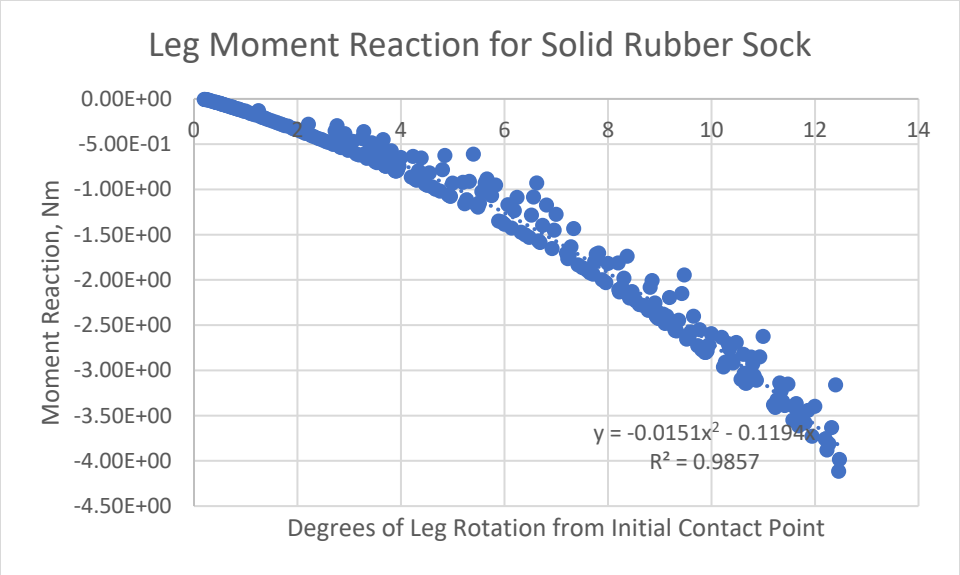

Graph 6: Moment reaction in FEA simulation of rubber cylindrical protector versus degrees of 'leg' rotation. Note the quadratic component that produces some concavity, i.e. stiffening up, but in practical terms, it is far from useful.

Biaxial-Braid Fabrics that Stiffen in Tension.

Fabrics (dry, without matrix) that are braided with a roughly 45° braid angle exhibit a non-trivial increase in the tensile stiffness of the braid (oriented along the cylindrical braid axis, i.e. at a 45° angle to the braided yarns themselves) after a certain amount of deformation. Specifically, the yarns reorient to follow the applied tension load more closely, eventually experiencing locking from compaction (since their radial stiffness is nonzero, if not always especially high). Moreover, the entire regime is elastic before and after lockup, which is desirable. Simbex, LLC patented a dynamic joint protector using this principle [6], although it does not appear to have been marketed. It should be noted that the material structure proposed by Simbex does not target bending, but rather tension; since fabric braids obviously buckle without bearing any appreciable amount of compressive load, to apply Simbex's principle to this research would require integrating the tensionable biaxial braids at an offset above the neutral plane of the bending shell, and a material that could bear compression without buckling at an equal distance offset from the neutral plane. Additionally, some added material would be needed

at the neutral plane that can resist tension and compression (to prevent uniaxial elongation or shortening of the material), perhaps a metal wire that is stiff enough not to buckle in compression. Since it is not clear what materials could provide the compressive lockup, this line of research was not pursued further by this researcher, just as Simbex, LLC appears to have abandoned its own research.

Existing Elastic Metamaterials as Potential Strain-Stiffening Structures.

Biaxially-braided fabrics or composite tubes and foams are strictly speaking not continuum materials at even the millimeter scale and could instead be said to be microstructured "metamaterials," a broad class of materials united by the fact that they possess special overall properties as a function of their microstructures that they would not have with a simple microstructure. Frequently, research into metamaterials concerns complex interactions with electromagnetic or acoustic waves, which is of course inapplicable to this research subject, but there is a growing class of mechanical metamaterials with special elastic properties resulting from their microstructures.

Introduction to Metamaterials.

Mechanical metamaterials are often engineered to have combinations of elastic moduli (Young's moduli), shear moduli, bulk moduli, or Poisson's ratios that are not achievable with simple, continuum materials, either anisotropically (in certain directions) or occasionally isotropically. The classic example of a mechanical metamaterial is an auxetic structure, i.e. a material that has a negative Poisson's ratio (at least in one direction; usually such metamaterials are anisotropic), even if the base material out of which it is structured (e.g. some ordinary, 3D printed polymer) lacks the auxetic property, as indeed nearly all known materials save for a few unusual crystals [7] and liquid-crystal polymers do [8], [9]. Indeed, multiple excellent review

papers have been written solely on the auxetic subset of mechanical metamaterials [10], [11]. However, it must be stressed that there are many other types of mechanical properties that can be achieved through metamaterial structures, as will be discussed below.

To appreciate the potential effect of microstructuring on elastic properties, a brief review of elastic theory is in order. For a linear-elastic and isotropic material, any two of the elastic parameters (choosing among the Young's modulus, shear modulus, bulk modulus, Poisson's ratio, or the rarely-used Lamé's first parameter and P-wave modulus) uniquely determine its static response properties [12]. For instance, and again only for an isotropic and linear-elastic material, if one takes the Young's modulus, *E*, and the Poisson's ratio, ν, as the unique determinants, the bulk modulus *K* and the shear modulus *G* can be determined from the following equations:

$$K = \frac{E}{3(1-2\nu)} \tag{2.1}$$

$$G = \frac{E}{2(1+\nu)} \tag{2.2}$$

In three-dimensional loading, an isotropic material's stress-strain response may be quantified by the isotropic form of Hooke's Law:

$$\begin{bmatrix} \epsilon_{xx} \\ \epsilon_{yy} \\ \epsilon_{zz} \\ 2\epsilon_{yz} \\ 2\epsilon_{zx} \\ 2\epsilon_{xy} \end{bmatrix} = \begin{bmatrix} \frac{1}{E} & -\frac{\nu}{E} & -\frac{\nu}{E} & 0 & 0 & 0 \\ -\frac{\nu}{E} & \frac{1}{E} & -\frac{\nu}{E} & 0 & 0 & 0 \\ -\frac{\nu}{E} & -\frac{\nu}{E} & \frac{1}{E} & 0 & 0 & 0 \\ 0 & 0 & 0 & \frac{1}{G} & 0 & 0 \\ 0 & 0 & 0 & 0 & \frac{1}{G} & 0 \\ 0 & 0 & 0 & 0 & 0 & \frac{1}{G} \end{bmatrix} \begin{bmatrix} \sigma_{xx} \\ \sigma_{yy} \\ \sigma_{zz} \\ \sigma_{yz} \\ \sigma_{zx} \\ \sigma_{xy} \end{bmatrix} \tag{2.3}$$

That said, since metamaterials are usually highly anisotropic, it is more helpful to review Hooke's Law for materials that are orthotropic (anisotropic along three orthogonal axes):

$$\begin{bmatrix} \epsilon_{xx} \\ \epsilon_{yy} \\ \epsilon_{zz} \\ 2\epsilon_{yz} \\ 2\epsilon_{zx} \\ 2\epsilon_{xy} \end{bmatrix} = \begin{bmatrix} \frac{1}{E_x} & -\frac{\nu_{yx}}{E_y} & -\frac{\nu_{zx}}{E_z} & 0 & 0 & 0 \\ -\frac{\nu_{xy}}{E_x} & \frac{1}{E_y} & -\frac{\nu_{zy}}{E_z} & 0 & 0 & 0 \\ -\frac{\nu_{xz}}{E_x} & -\frac{\nu_{yz}}{E_y} & \frac{1}{E_z} & 0 & 0 & 0 \\ 0 & 0 & 0 & \frac{1}{G_{yz}} & 0 & 0 \\ 0 & 0 & 0 & 0 & \frac{1}{G_{zx}} & 0 \\ 0 & 0 & 0 & 0 & 0 & \frac{1}{G_{xy}} \end{bmatrix} \begin{bmatrix} \sigma_{xx} \\ \sigma_{yy} \\ \sigma_{zz} \\ \sigma_{yz} \\ \sigma_{zx} \\ \sigma_{xy} \end{bmatrix} \tag{2.4}$$

In addition to anomalous Poisson's ratios, other unusual combinations of shear stiffness relative to Young's modulus, bulk modulus relative to elastic modulus, etc. can be achieved; for instance, the "pentamode" metamaterials studied by Muamer et. al. are nearly isotropic but have an effective bulk modulus that is far higher than the effective shear modulus, potentially on the order of 1000 times, resulting in the ability to shear easily but be very stiff under hydrostatic compression, much like a fluid (though it can only tolerate relatively low strains and deflections

before this behavior breaks down) [13]. Yu et. al. conducted an excellent review of the literature on mechanical metamaterials, noting that the literature has disclosed metamaterials having variously high, low and even transiently-negative Young's moduli, limited or exceptional ranges of motion (strain in the global sense); high or low shear and bulk moduli; and negative, zero, or positive Poisson's ratios [14].

Of note, even most auxetic metamaterials studied do not have constant Poisson's ratios with strain over their operating ranges, but rather see significant changes in the instantaneous Poisson's ratio with respect to strain: for instance, Tang and Yin studied auxetic structures with Poisson's ratios that varied from approximately -1 to slightly greater than 0.5 over their contraction-expansion range [15], and Zhang et. al. proposed a hierarchical (having unit cells inside unit cells) metamaterial with a Poisson's ratio varying from -3.5 to -1.5 over the deformation range [16]. This is not to suggest that there is a clear mechanism for converting negative (or variable) Poisson's ratio into stiffening per se, but merely that if one property can be made to be nonlinear with respect to strain, most likely Young's modulus or shear modulus could also be made nonlinear.

Indeed, beyond merely enabling relatively unusual ratios between tensile, shear, and bulk moduli, some metamaterials can even possess incremental negative stiffnesses in certain directions and within certain ranges, mainly by microstructures that are preloaded and multistable [17], [18]. While this is an interesting and counterintuitive property (most commonly employed in vibration dampeners), negative stiffness is certainly not the focus of this research; however, since negative-stiffness phases have been proposed to actually increase the overall stiffness of composite structures [19], and since (as will be explored below) the negative-stiffness properties of metamaterials that have them necessarily only exist within a region of

overall strains (else the material would violate the First Law of Thermodynamics), so the potential utility should not be dismissed out of hand. Moreover, if nothing else it highlights the fact that remarkable properties that can be achieved through tailored microstructures.

Despite the wide array of properties that may be targeted by metamaterials, there are a few "building blocks" from which nearly any mechanical metamaterial is built. Metamaterials that target high stiffness-to-weight ratios necessarily eschew kinematic freedom and generally consist of microscale truss structures with rigid joints; they generally have positive Poisson's ratios as well [20]. Some rigid metamaterials are compression-dominated at the unit cell level (resembling statically-determinate truss structures), and others bending-dominated (resembling cantilevered networks of beams); the former tend to be more rigid but more brittle [20]. Of course, metamaterials that are always rigid are of little relevance to this research.

In contrast, in their review of flexibility-optimized mechanical metamaterials, Bertoldi et. al. noticed that continuous (i.e. not composite or consisting of multiple materials) metamaterials all tend to use one of three principles for producing flexibility (not strictly speaking nonlinearity of force-displacement): slender elements/creases/tips that resemble flexures in compliant mechanisms (which, they observe, localize bending to a relatively specific region, and tend to have linear responses); long elastic beams (which frequently are made to buckle, but may also bend without axial compression); and finally, constrained (and preloaded) elastic beams that snap from one buckled configuration to the next (resulting in localized-negative stiffness regimes) [21]. In another review, Jia et. al. noted these principles and added interrupted contacts (of note, a principle that tends to result in stiffness increases with respect to deflection) as a principle that metamaterials can employ [22]. Crucially, they also summarized the nonlinearity of force-deflection response that such "building blocks" could impart in a helpful graphic that is

reprinted in Figure 3; that said, they did not specifically name or explore a metamaterial structure known to increase its stiffness in response to strains.

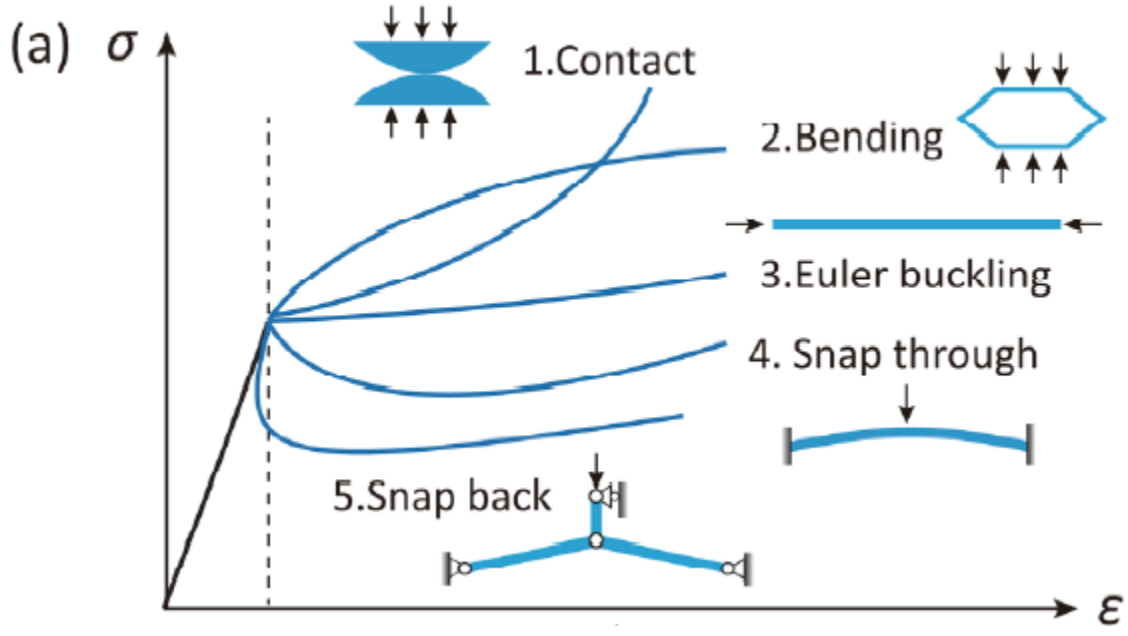

Figure 3: Graphic depicting the stress-strain responses of each of the five main "building blocks" for flexible mechanical metamaterials, reprinted from [22] with permission.

Mechanical Metamaterials with Strain-Stiffening Potential.

In principle, drawing from the following review of known displacement-stiffening metamaterials as well as this author's own experiments on the subject (described throughout the dissertation), there are several principles that can enable a metamaterial to become displacement-stiffening. The first is interrupted contact that produces stiffness from the contact force reaction once it is closed (closing being a function of displacement). Contact forces necessarily convey local compressive surface stresses (and occasionally shear stresses if friction is operative), although the use of interrupted chain rings could effectively produce stiffening-up in global tension displacement, as well as the more obvious stiffening in compressive displacement from non-interlocking elements. The second principle is mode-switching from bending to tension; all materials will naturally be stiffer in tension than in bending, with the most obvious example

being slack cables (themselves crude metamaterials, after a fashion, since the microstructures allow even more bending compliance than a solid cross-section of the same proportions would have), though wavy polymer beams have the effect to a lesser degree. The third principle is load reorientation and pertains to kinematic singularities in rigid body approximations of the mechanisms created by the metamaterial (though most metamaterials are effectively networks of compliant mechanisms rather than rigidly-jointed mechanisms). The following sections will illuminate each principle with examples.

Metamaterials that Stiffen from Self-Contact.

Theoretically, interrupted self-contact should be the most dramatic means of producing stiffening-up, yet it is the least apparent in what little literature there is on stiffening-up metamaterials. Although not strictly speaking made into a metamaterial, Tummala et. al. disclosed a compliant-mechanism joint with rotational stiffness with two modes, a low-stiffness mode for certain displacements, and a sudden increase in stiffness from self-contact at higher displacements [23]. An FEA simulation of the joint under deformation in the displacement range that gives low stiffness is reprinted in Figure 4; its bending stiffness is relatively low because only the small, secondary flexure is activated (the faces of the main beam are not in contact and thus cannot transmit compressive stress). A representative force-deflection curve for the joint is reprinted in Graph 7. The stiffening-up effect is certainly modest (owing to relatively-high stiffness from the flexure, even when the main segments are not in contact), and the structure would need to be oriented properly in a mesh network to create a metamaterial that stiffens under the appropriate load, but in principle this indicates that it is physically possible to create such a metamaterial.

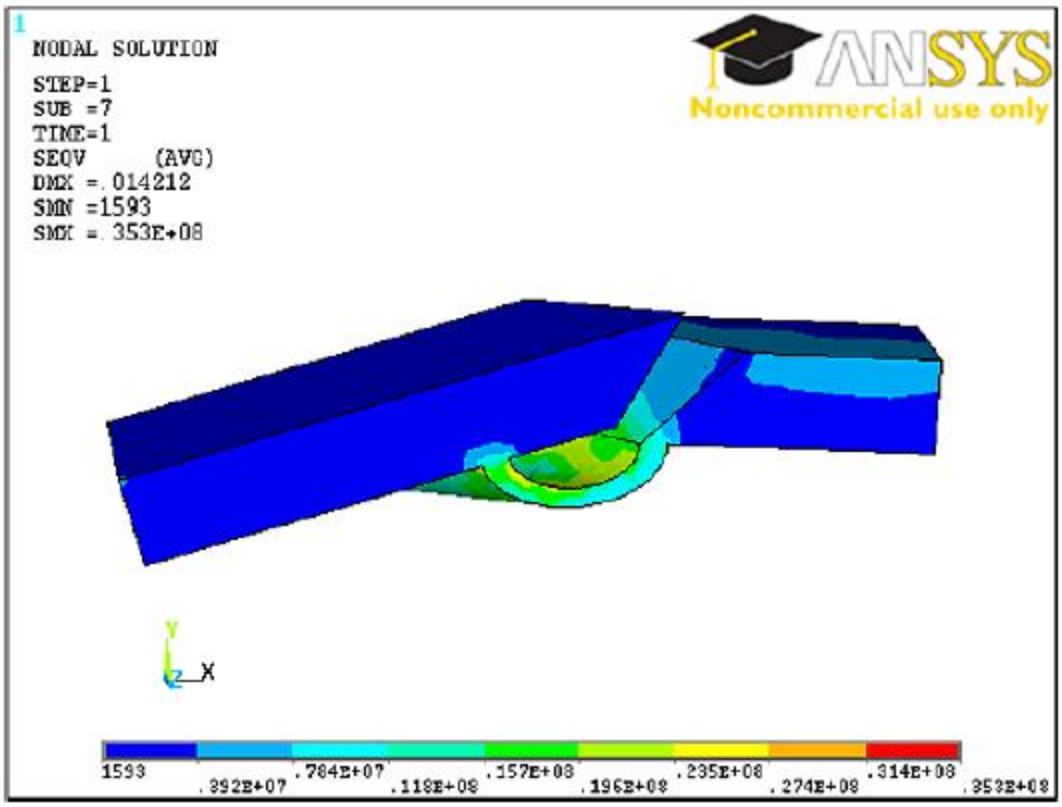

Figure 4: Two-stiffness joint, shown with the contact between the main joint bodies open, giving the structure low bending stiffness (as only the small flexure underneath is engaged). Reprinted from [23], with permission .

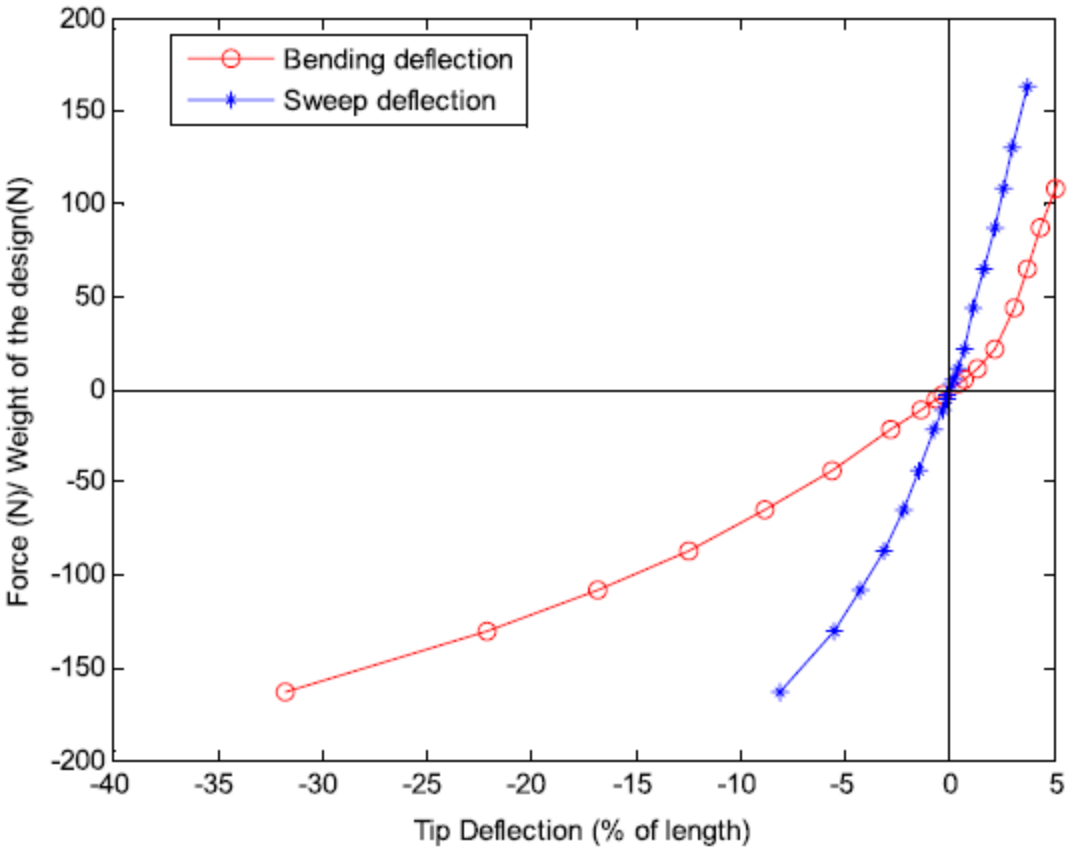

Graph 7: Force-deflection curve (shown in red) for the two-stiffness joint, with a stiffening-up factor on the order of 2x apparent after about 1% positive tip deflection. Reprinted from [23], with permission.

A frequently-studied class of metamaterials [24], [25], [26] that stiffens in compression from self-contact (at least if the material is thick enough to ensure proper self-contact) is the rotating-polygon class of auxetics (which are usually studied for their auxetic properties and not their compression-stiffening properties). These consist of squares or equilateral triangles jointed at their corners (either with rigid revolute joints or with compliant flexures that emulate revolute joints). Moreover, such a metamaterial's range of compression is limited by edge-to-edge contacts (save in the case of infinitely-thin sheets, for instance origami forms). The author of this dissertation created a structure consisting of rigid squares jointed by thin cables; its compressive-displacement behavior is illustrated in Figure 5. A compliant-mechanism version

of this structure was also patterned on a cylinder-like surface and studied in Chapter 6 (see Figure 219 in that chapter).

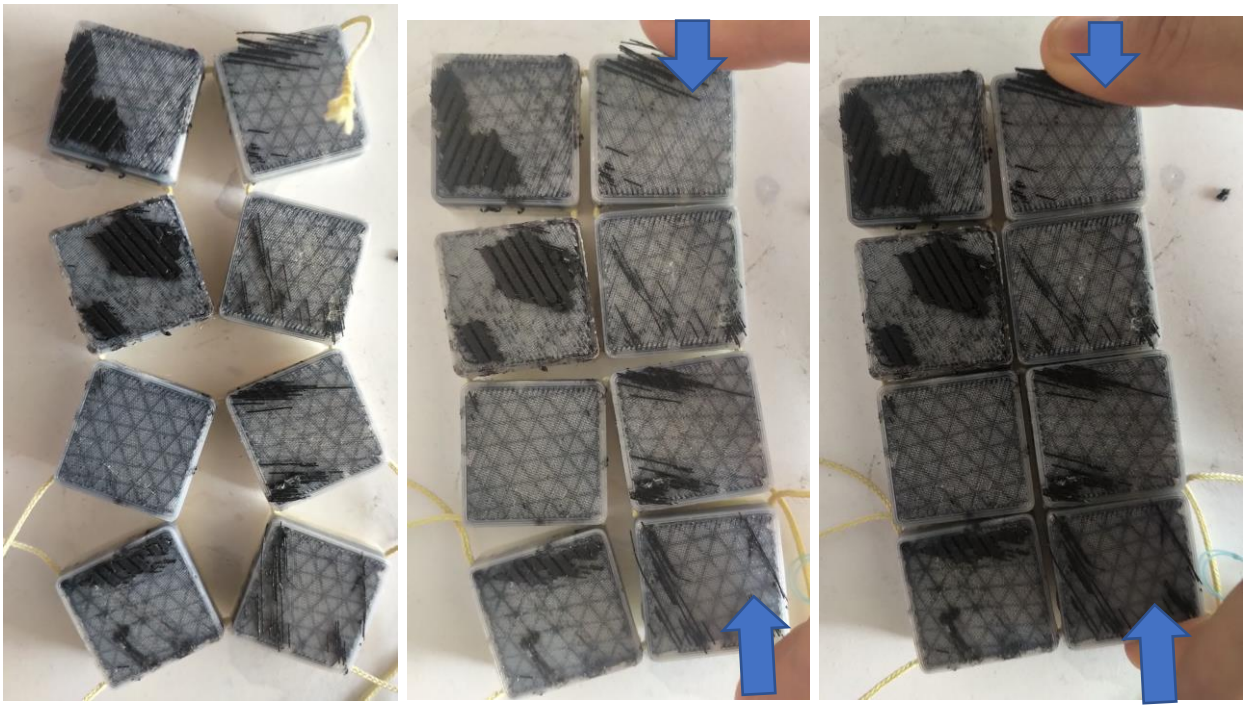

Figure 5: Progressive compressive deformation of a rotating-squares auxetic structure until edge-to-edge contact prevents further deformation.

There are various cylindrical metamaterials (i.e. having unit cells arrayed on a cylinder rather than a plane) that have initially-deactivated self contact modes that, when activated, at least moderately increase stiffness. The dart-auxetic cylindrical structure studied by Wang et. al. [27] that is explored more fully in Chapter 6 is an example of a self-contact-stiffening metamaterial as it stiffens in global compression from incremental contact between elastic shells. Additionally, the biaxially-oriented Cartesian mesh array developed by this author and patterned on a cylinder-like surface in Chapter 6 entails some self-contact between rigid links at their side faces after significant local extension or contraction; see Figure 198 and the surrounding discussion in Chapter 6.

Next, foam-like metamaterials with networks of beam-like structures see stiffness increases in large-deflection compression from self-contact between the beam elements, though often the strains required are prohibitively large and produce plastic deformation or even damage to the lattice structure that limits the maximum stiffening-up effect. For instance, Novak et. al. studied [28] foam-inspired 3D auxetic networks of beam-like structures with interstices that close up during high compressive strains; a series of images of the structure they studied at various degrees of compressive strain is reprinted in Figure 6, and its force-deflection curve reprinted in Graph 8.

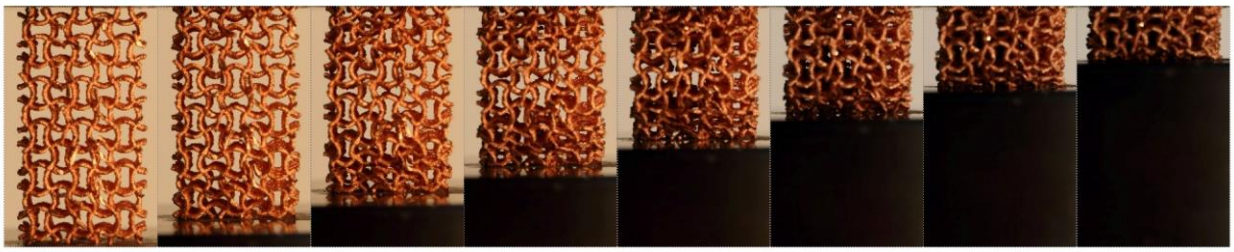

Figure 6: Foam-like metamaterial studied by Novak et. al. in various stages of compressive displacement, reprinted from [28] with permission.

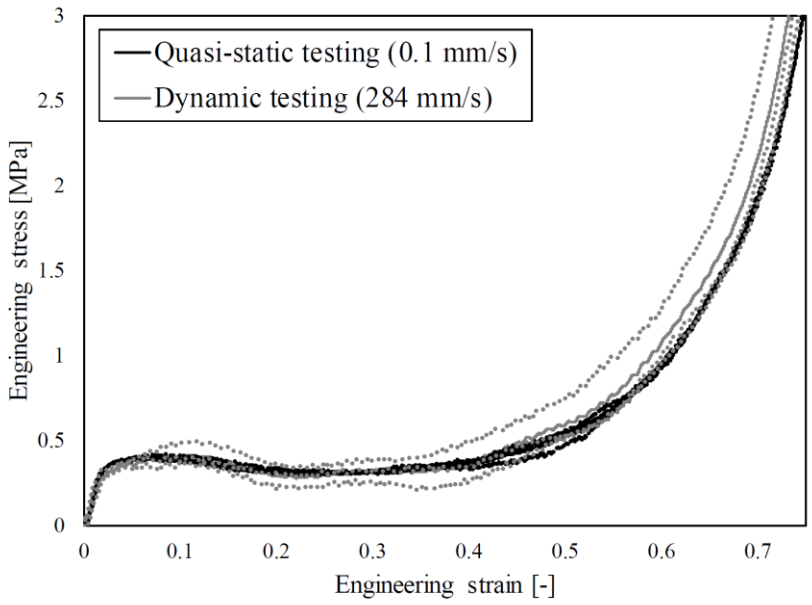

Graph 8: Force-deflection profile of the foam-like metamaterial studied by Novak et. al. in various stages of compressive displacement, reprinted from [28] with permission.

The final class of self-contact-driven stiffening metamaterials is chains and their 2D analogues, chainmail weaves; of note, they stiffen up when the overall structure is placed into overall tension (rather than from global compression, as with the other contact-locking materials described above) due to their interlocking rings coming into contact (though local contact stresses are of course compressive in nature). Occasionally, weaves are dense enough to produce lockup after compressive displacement as well, though curved rings are often unstable in this regard. Warner experimentally evaluated the extensional force-displacement properties of various traditional chainmail weaves, including the spiral weave, European four-in-one weave, and the simplest-possible chain weave; static stiffness was of course theoretically zero in the rigid-body modes until slack was taken up and contact initiated [29].

Surprisingly perhaps, there is no known research on chainmail weaves understood and quantified as mechanical metamaterials; the only known scholarly investigation into chainmail metamaterials explored an electromagnetic metamaterial having a reversed-sign Hall coefficient

[30], which is of no utility to this research. However, Ploszajski et. al. did propose a magneto-mechanical chainmail weave that might have altered bending stiffness under an external magnetic field; they even manufactured a rough prototype out of ferromagnetic steel by the Selective-Layer Sintering (SLS) additive process, showed the structure bending under gravity with and without an external magnetic field, and recommended further research to enable it to be made into a wrist-protective device, though they did not quantify their sample's mechanical properties in any way [31]. Ransley et. al. also explored chainmail structures with embedded NiTi shape memory actuators; the individual links can contract or expand when actuated, changing the shape of the entire weave [32].

It is likely that so little research into chainmail has been conducted owing to manufacturing difficulties. Most notably, chainmail weaves must have all links manufactured at once and together to make them interlock, which requires additive manufacturing, or else manufactured with holes that can be welded closed (which becomes somewhat more difficult for a 2D weave than a 1D chain owing to interferences). Additionally, rings would need complicated features to limit motion in various directions, which would present difficulties both with design and with manufacture. For instance, Figure 7 reprints a rendering of a proposed chainmail weave from this author's Master's thesis; note the complexity of the geometry (including significant overhangs), and the interlocking features (which additionally risk fusion of links together during additive manufacturing). This structure was never manufactured owing to its complexity.

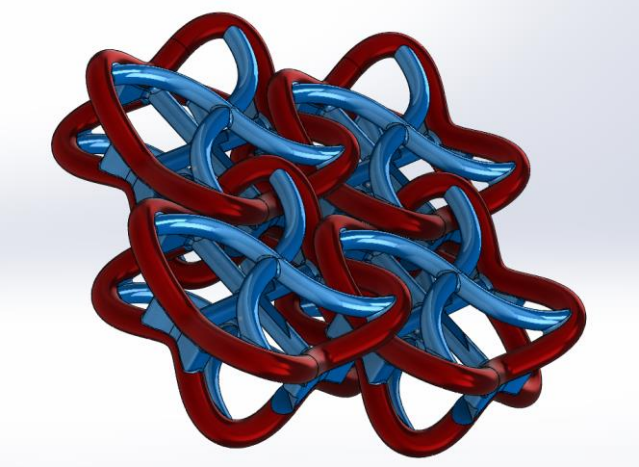

Figure 7: Proposed chainmail repeating unit (consisting of four links). The red and blue colorations do not have any mechanical significance; they are merely to highlight different types of features. This picture was taken from this author's Master's thesis [1].

Single-Collinear, Self-Contacting, Stiffening Origami.

Origami patterns have received considerable interest as a strategy for microstructuring metamaterials in ways that may additionally be relatively easy to manufacture since they can be carried out by folding of simple, flat sheets [33], [34], [35], though because folds are usually localized, this can be more difficult to accomplish than making non-repeating origami. (The related domain of kirigami structures adds the freedom to make selective cuts in the sheet as well as folds [36], [37]).

One outstanding example of an origami metamaterial capable of stiffening up over a displacement range is the "single-collinear" origami fold studied by Fang et. al., which they found demonstrated reversible and considerable elastic stiffening after a prescribed amount of linear compression [38], [39], specifically owing to facets (the faces, as distinct from the folds/creases) from adjacent unit cells coming into contact and being forced into facet bending, which is a stiff mode that tends to prevent further deformation. Additionally, from a kinematic

perspective, reorientation and flattening of the unit cell should also result in eventual tensile stiffening, although tension lockup was not explicitly studied by Fang et. al.

As such, the author of this dissertation created an origami metamaterial following the S-C paradigm developed by Fang et. al.: they specified that a unit cell must consist of four planar surfaces that are parallelograms, all with the same width and all with the same length, and additionally, their angles about the shared vertex must be subject to the equations:

$$A_1 + A_2 = A_3 + A_4 \tag{2.5}$$

$$A_1 + A_2 + A_3 + A_4 = 2\pi \text{ rad} \tag{2.6}$$

The former is a special requirement of the single-collinear cell (generating a collinear fold edge), and the second one is a universal requirement for all 4-vertex origami structures with shared folds (from basic geometry). In effect, there are four parameters to choose from: the length of a parallelogram *a*, the width of a parallelogram *b*, and two angles (either A_1 and A_4 or A_2 and A_3). The author of this dissertation selected $A_1 = 60°$ and $A_4 = 82°$, necessitating that $A_2 = 120°$ and $A_3 = 98°$ (plus $a = 30\text{mm}$ and $b = 20\text{mm}$), uniquely defining the unit cell shown in Figure 8, which is illustrated in slightly-folded configuration along with angles. Figure 9 shows two views from angles of the same unit cell in the same degree of actuation as Figure 8, and Figure 10 shows an array of many unit cells joined into a full metamaterial sheet.

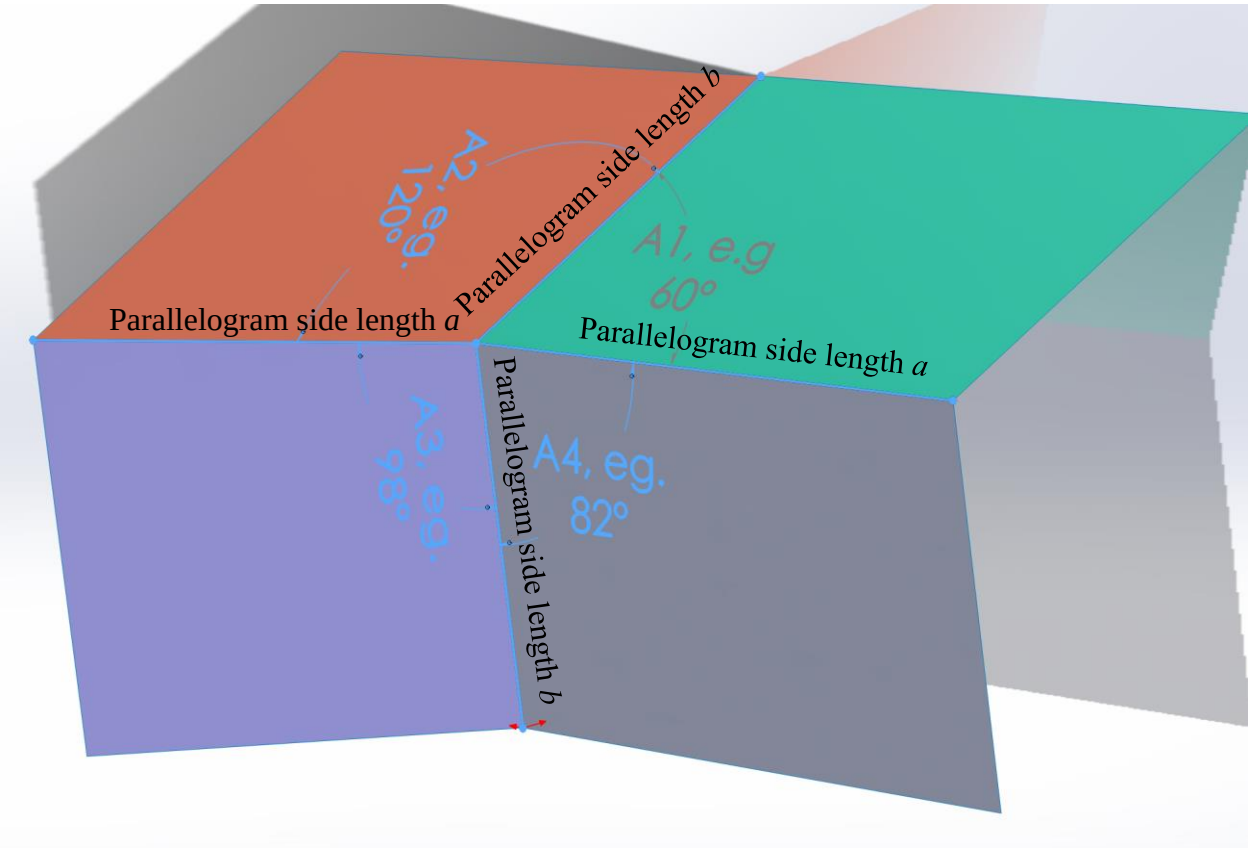

Figure 8: Four angles for one possible configuration of the S-C stiffening origami.

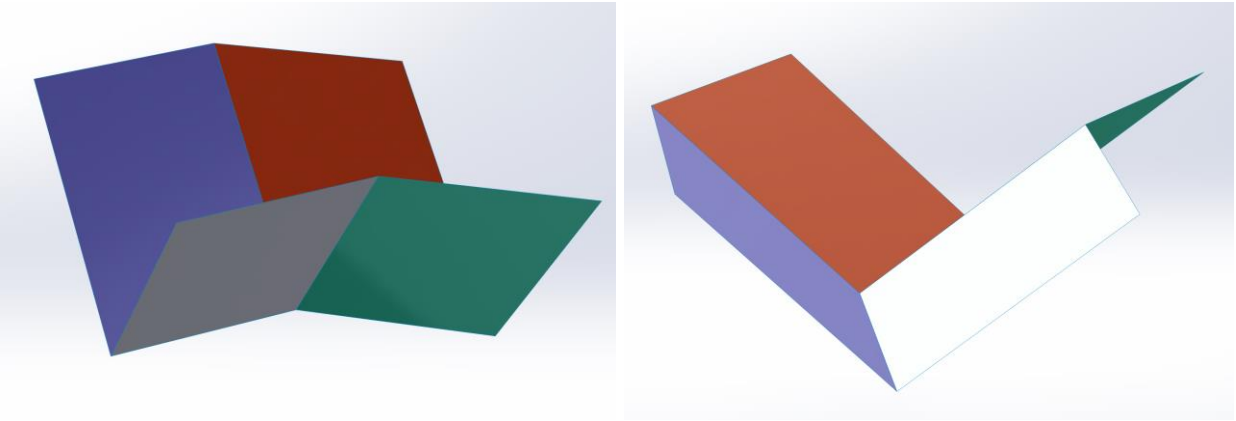

Figure 9: Two views of a Single-Collinear origami unit cell.

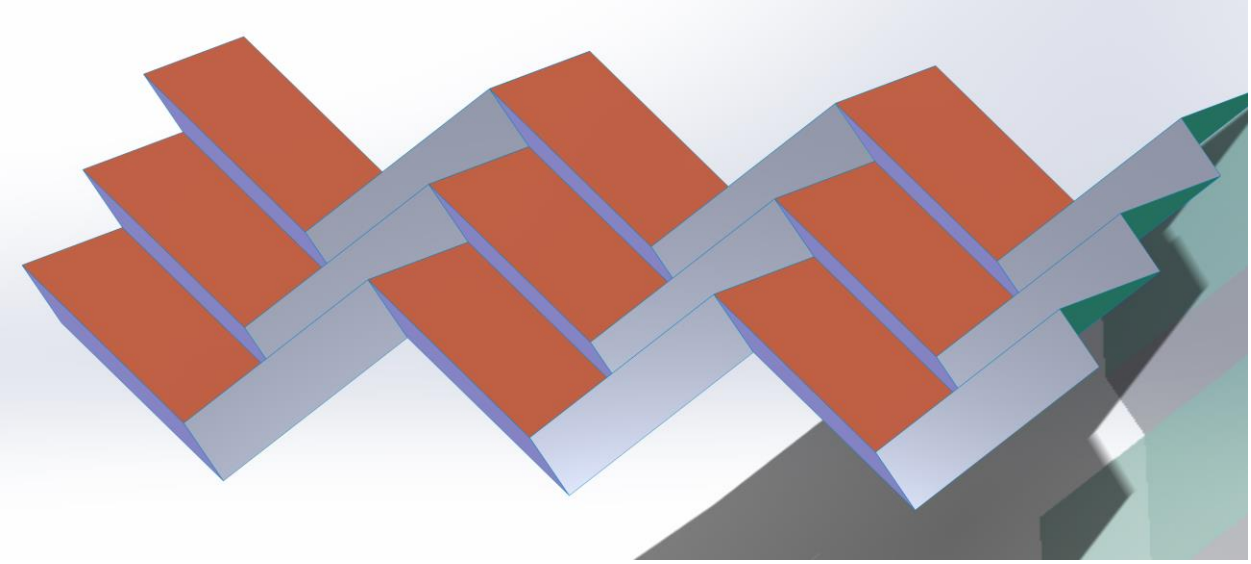

Figure 10: Multiple unit cells of Single-Collinear origami, arrayed and in partially-folded/actuated configuration.

It should be noted that Fang et. al. often vertically stacked and joined two unit cells with different angles but compatible overall lengths together, either in bulged-out or nested-in configurations, as shown in Figure 11; such stacked origami cannot be flattened. However, as seen in Figure 12, the non-stacked origami structure can be flattened to a plane (indeed, the reader may print this figure off, cut it out, fold along the lines, and create this origami metamaterial).

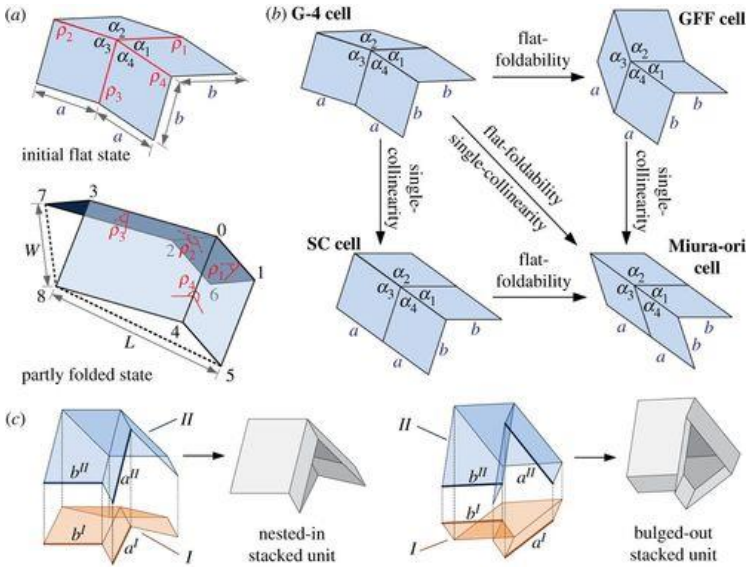

Figure 11: Combining multiple different origami patterns by stacking, as proposed by Fang et. al. Reprinted from [39] with permission.

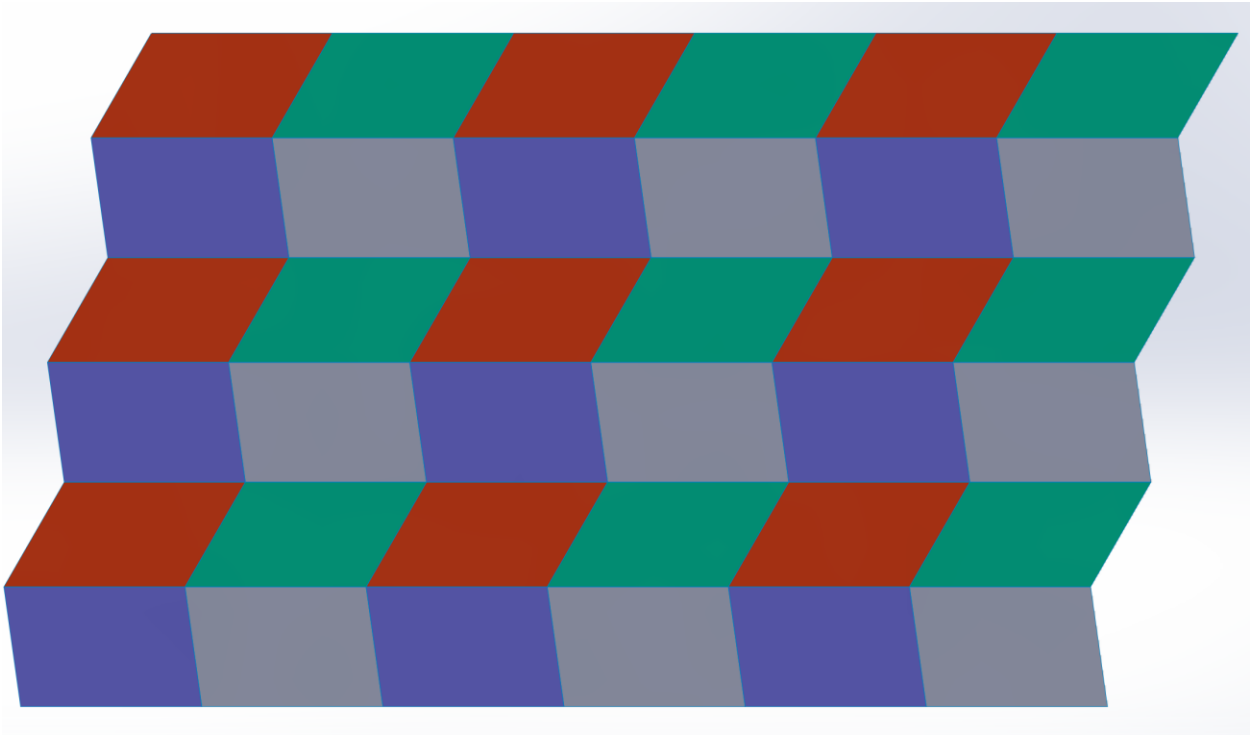

Figure 12: Flat pattern for one example single-collinear fold created by the dissertation author (there are infinitely many, based on the angles chosen, but the angles must adhere to certain rules).

Ultimately, the S-C origami pattern is essentially quite similar to the more-well-known Miura-Ori pattern, but with a crucial difference as regards the allowable angles in a unit cell, in

that the Miura-Ori configuration requires that angles 1 and 4 match, as must angles 1 and 2, thus reducing the number of independent sector angles to just one (whereas the S-C pattern has two independent sector angles) Alternately, this can be expressed in the form of the added constraint equation, on top of that expressed in Equations 2.5 and 2.6 above:

$$A_1 + A_3 = A_2 + A_4 \tag{2.7}$$

Interestingly, as Schenk and Guest discovered, two compatible Miura-Ori patterns can also be joined in layers to produce a structure in which some cells towards the middle of the structure lock after a certain amount of folding [40], which, owing to the kinematic limitations on the structure, produces global locking (though of note, not all cells experience the same deformation); an image of this locking Miura-Ori structure is reprinted in Figure 13.

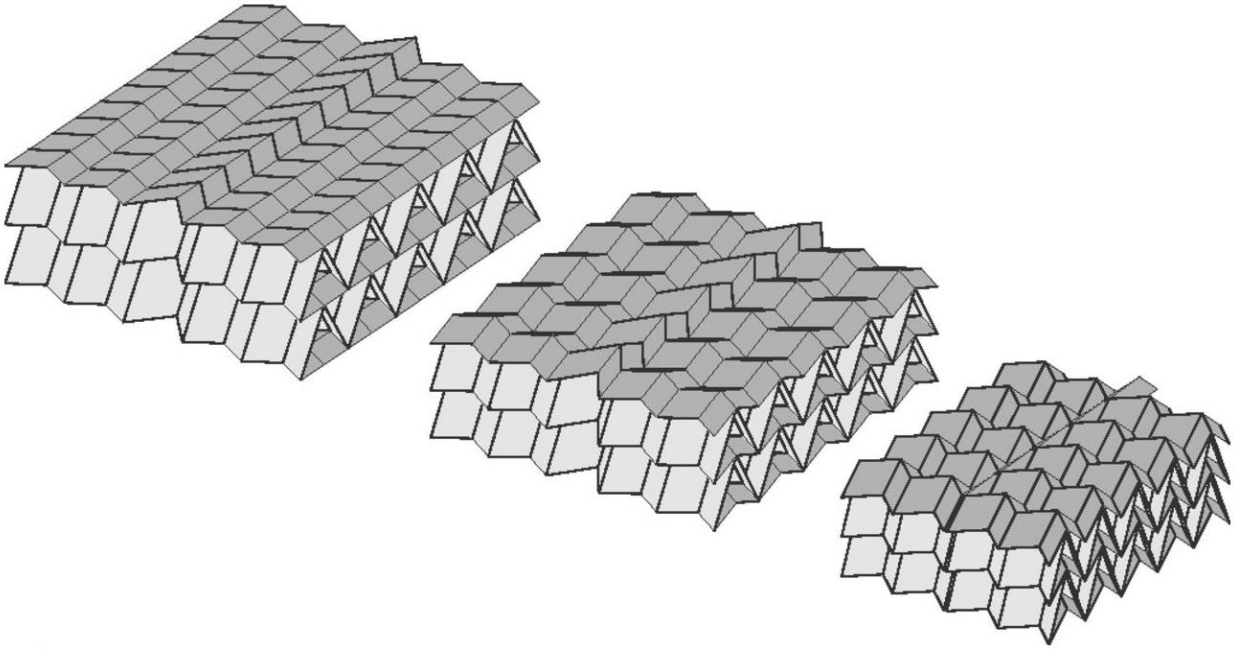

Figure 13: Self-locking transition in a complex structure of multiple Miura-Ori origami patterns (note the stacking of layers that each consist of two different but compatible patterns, one shown in dark grey, the other in light grey) discovered by Schenk and Guest. The left-most image shows the structure in its initial configuration; note that the unit cell shape is not constant, with the cells in the center having notably-different angles from other cells. The other two images show the deformation that brings the structure to locking (right-most image) from self-contact of faces. Reprinted with permission from [40].

In order to evaluate the lockup potential of S-C origami, a rigid-flexible composite structure was designed and manufactured using additive manufacturing, with the facets of the structure somewhat inset from their corners but thickened out-of-plane and then printed with a rigid polymer (PETg), and the folds turned into curved hinges and simultaneously printed out of thermoplastic elastomer. (Chapter 6 has a detailed discussion of simultaneous multimaterial 3D printing as applied to certain metamaterials). For comparison, Fang et. al. reported that the best embodiment of the origami structure from the standpoint of stiffness increase post-lockup was also a multimaterial, composite metamaterial, consisting of flexible polyethylene sheets connecting nearly-rigid steel facets, and that this material combination produced a stiffening-up factor of over 30x [39], whereas subsequent research with origami structures using only one material with thinned-out sections for folds produced a far lower stiffening-up factor of 2-4x depending on parameters. Figure 14 illustrates the composite structure of an assembly of two unit cells that Fang et. al. studied, as well as its force-deflection response to compression.

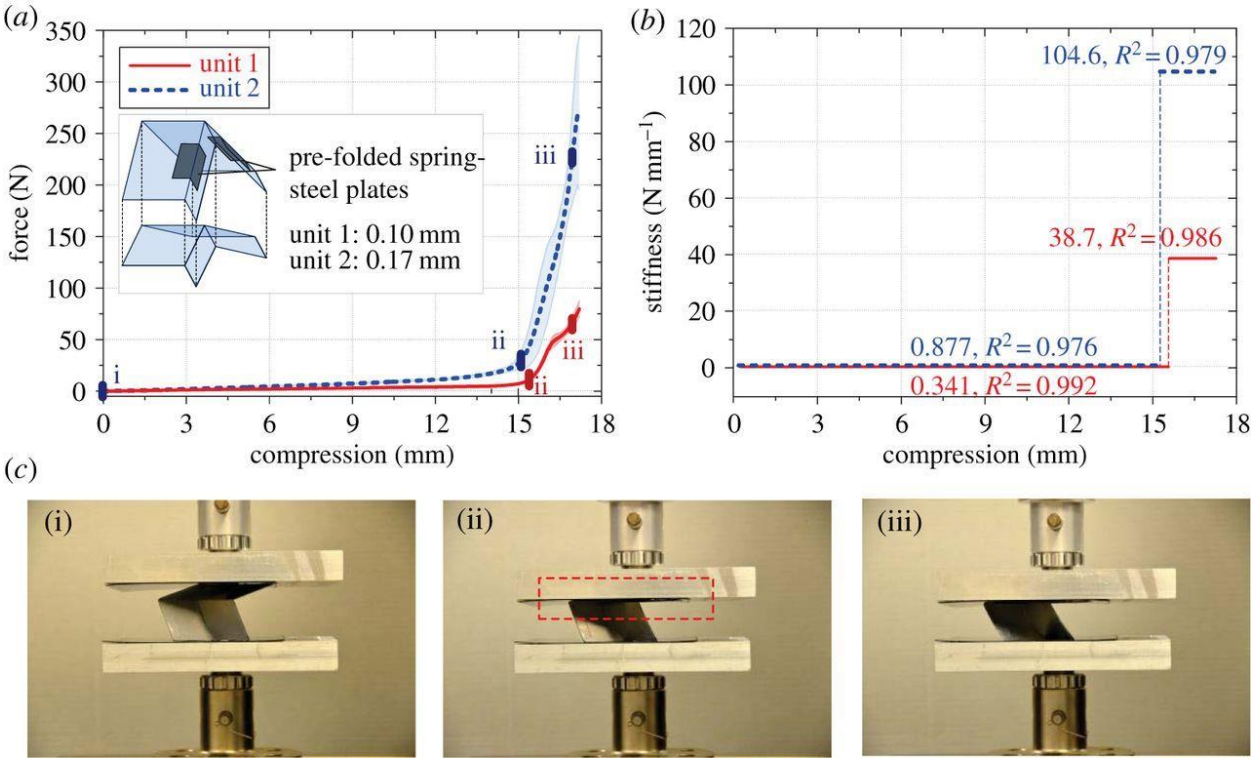

Figure 14: Composite structure (consisting of polyethylene joints and steel plates) and compression response (pre-lockup and post-lockup) from origami with two different parameters. Reprinted from [39] with permission.

In contrast, the author of this dissertation manufactured a sample structure of two unit cells, which is depicted in Figure 15 variously in its as-printed configuration (partially-actuated), compressed until the onset of contact between facets (which results in some stiffening up, though not to an exceptional degree), and then compressed further until lockup or potential joint failure.

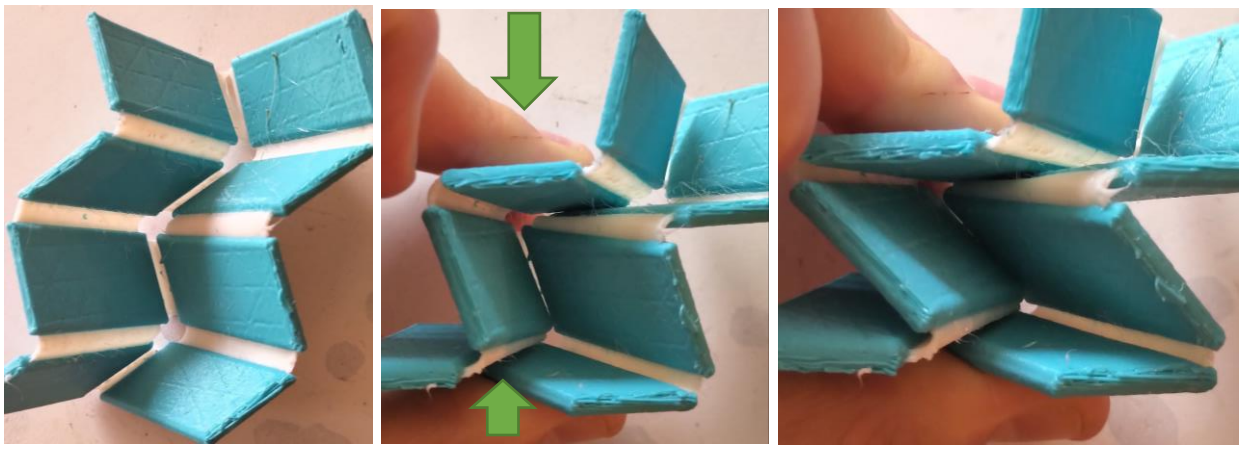

Figure 15: Two unit cells of this researcher's replication of S-C origami, modified with flexible elastomeric joints between rigid facets. Left: undeformed; middle: deformed until perceived onset of stiffening (from face-to-face contact between facets); right: deformed further, until interference between thick facets made further compression nearly impossible (it should be noted that, if the facets were infinitely thin, even if infinitely rigid, the structure could collapse entirely on its footprint; the interference here is entirely due to the facets not being infinitely thin).

Of note, the flexible shell-joints between the facets were easily damaged, and additionally loaded in torsion and tension (when ideally they would only be engaged in bending), as can be seen from a reverse view of the structure that is shown in Figure 16. Additionally, when placed into tension, the structure flattens (it only has one degree of freedom and thus displacements in one direction are coupled into complex kinematic behavior) until it is fully flattened, at which point it becomes considerably stiffer in tension since its joints can no longer bend (a relatively compliant mode) and are instead themselves tensioned (which is stiffer); this is the second main mode of stiffening (discussed in a subsequent subsection).

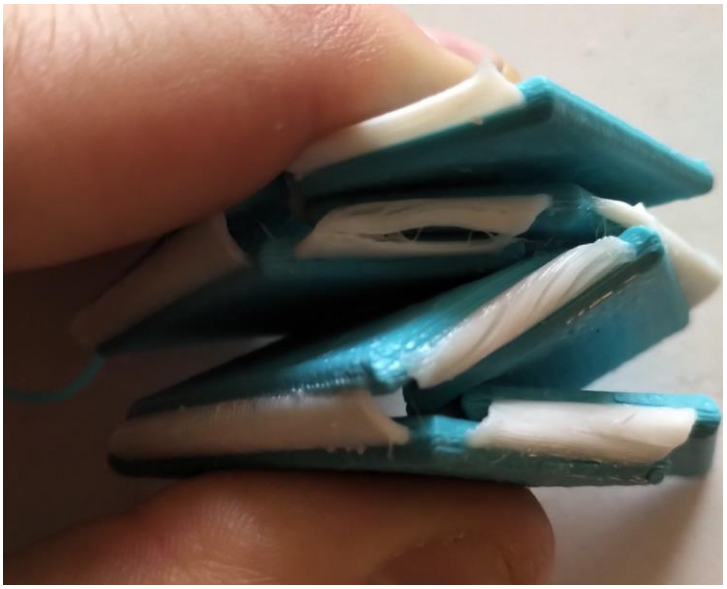

Figure 16: Applying a high compressive load to the S-C origami unit cell produces some kinematic distortions, including shearing and torsion in the joints (which are only supposed to bend about the fold axis), and even damage and tearing to the joints.

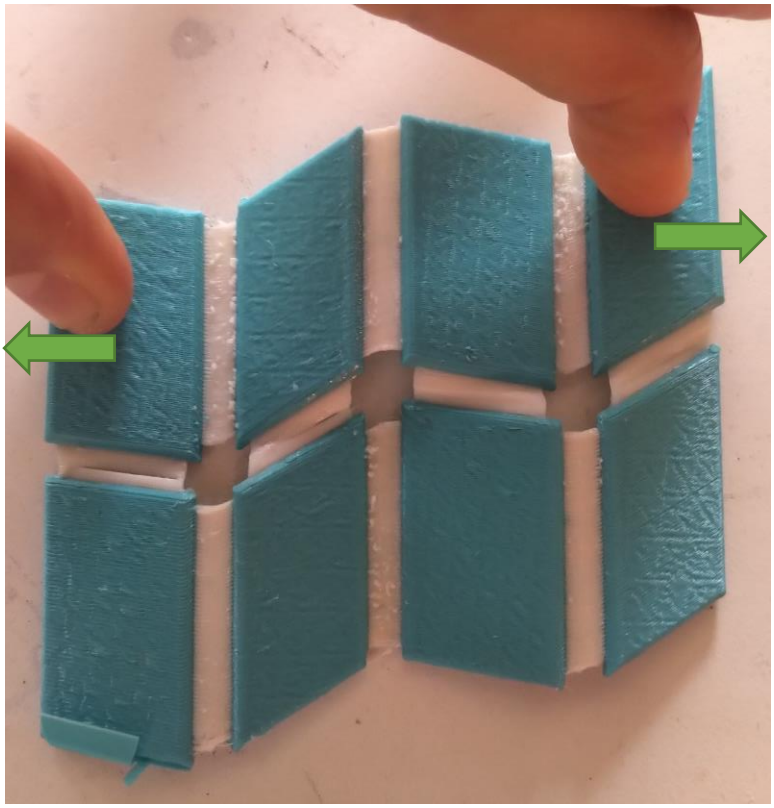

Figure 17: Flattening the origami pattern (compressing into the page from this view) and tensioning (along the green arrows) are coupled deformations. Additionally, once the structure is extended to this point, further tension loads can no longer be converted to bending of facets, meaning the structure should theoretically be stiffer in tension.

Other Stiffening and Self-Locking Origami Structures.

Kamrava et. al. reported a novel structure consisting of Miura-Ori origami folds being connected into closed loops that could then be tiled, a much more elaborate method of patterning than the simple sheets usually used in origami: in some sense, this may be thought of as a fractal or "hierarchical" metamaterial (in which the smallest repeating units are themselves joined not in a simple grid array but rather according to more complicated rules, often replicating the structure within the sub-array), and indeed fractal-hierarchical metamaterials are frequently preferred over simple metamaterials when greater elevation of properties (e.g. displacement tolerated) is needed [41]. Moreover, they reported that these structures stiffened considerably with progressive deformation [42]. An image of the basic structure that Kamrava et. al. produced is reprinted in Figure 18, and the force-deflection curves for various deformation modes are reprinted in Graph 9.

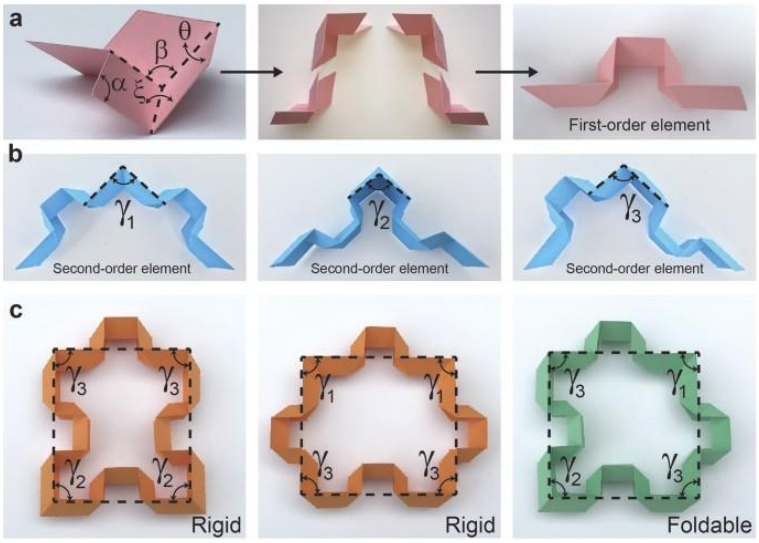

Figure 18: Fractal or hierarchical method of patterning a basic Miura-Ori unit cell (top-left, shown in pink) into higher-order elements. Reprinted from [42] with permission.

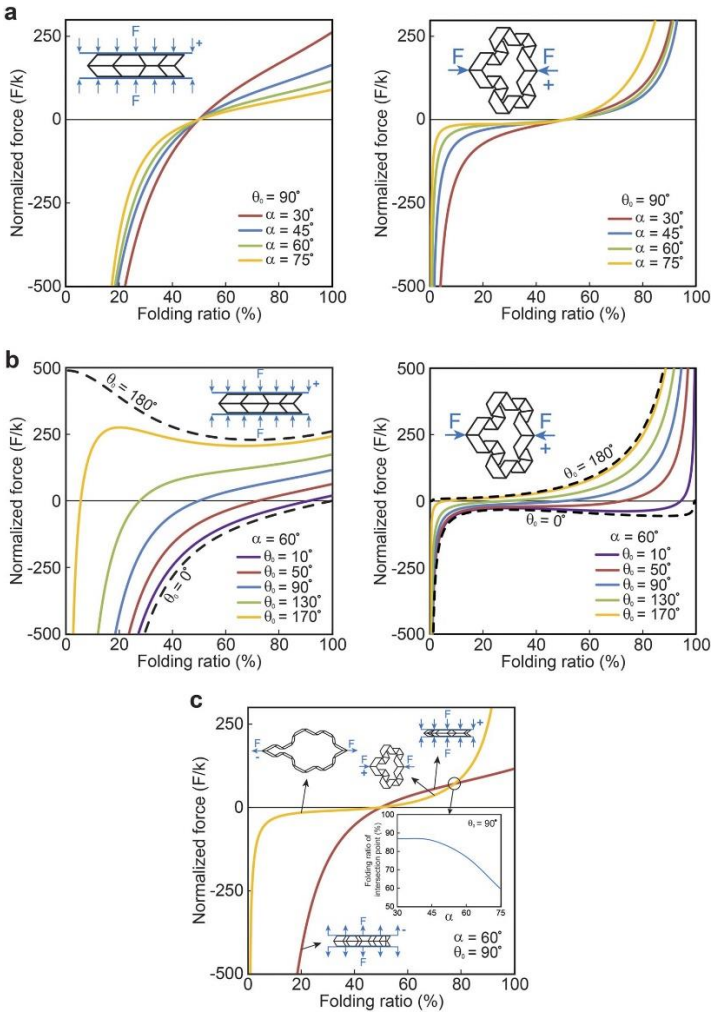

Graph 9: Force-deflection curves for various modes of the unit cells disclosed by Kamrava et. al. Reprinted from [42] with permission.

Additionally, Mukhopadhyay et. al. disclosed [43] that a "waterbomb" origami pattern arrayed on a cylinder that experienced moderate stiffening up (as well as radial contraction from an auxetic property) under compressive load; its undeformed shape, deformed shape, and force-deflection curve are all reprinted in Figure 19. Strictly speaking, they intended the structure to act as "distant actuators" producing complex shapes (such as inwards or outwards bulging) from local compression, certainly not as ankle-protectors or even strain-stiffening materials more broadly. Of note, the question of how to design a microstructure that can be tiled on cylinders

and enable the cylinder to contain a large-deflection-bending joint without shell buckling is a significant research problem in itself and is studied extensively in Chapter 6.

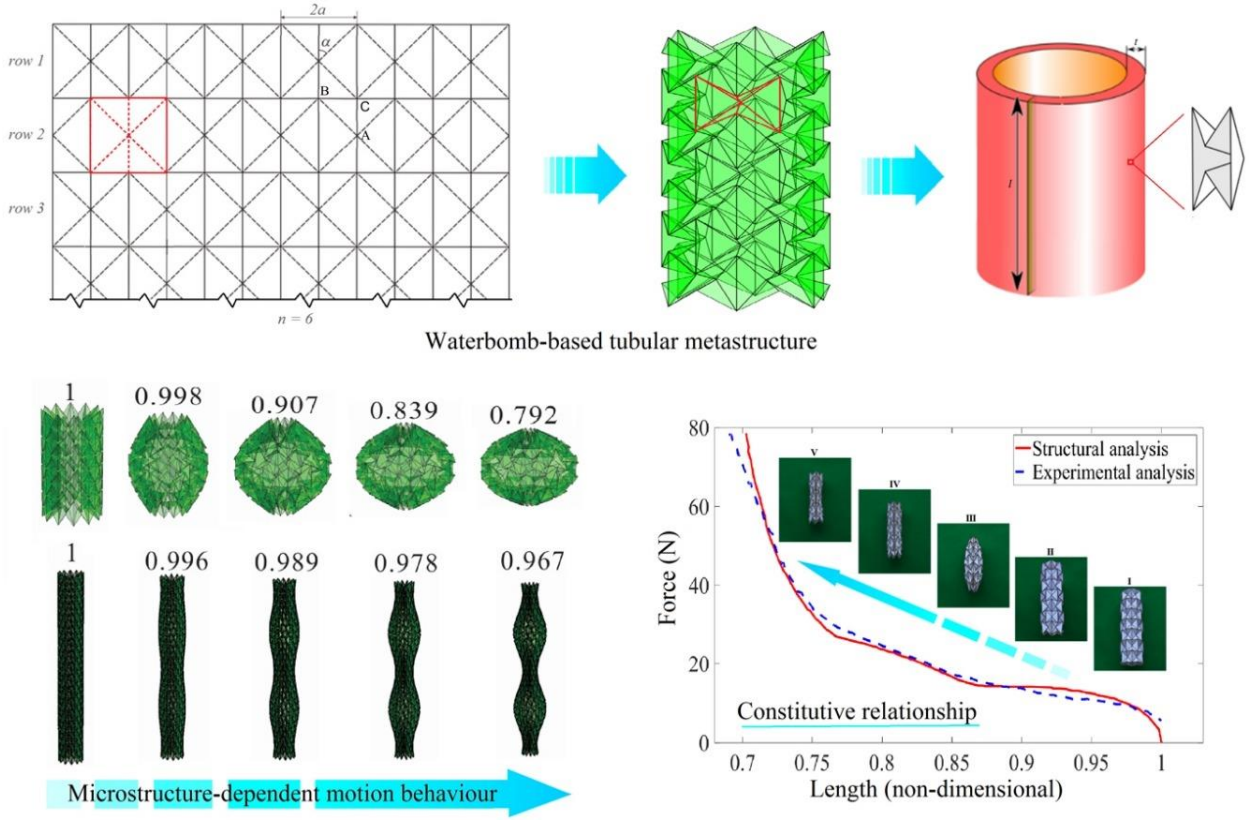

Figure 19: Undeformed and deformed shapes (expanding locally) and force-displacement curve of a waterbomb-origami tube. Reprinted from [43] with permission.

Finally, Li and Pellegrino proposed a morphing origami-inspired net whose maximum extents of deformation could be controlled by adding mechanical stops (faces on the origami facets that would come into contact at prescribed amounts of morphing) between joints [44]. The origami patterns they employed allowed their structures to conform to doubly-curved as well as singly-curved structures.

Metamaterials that Stiffen from Switching from Bending to Tension.

One has only to take a slack cable and pull on it until the slack is taken up to experience the extreme stiffening-up effect that is possible when a structure goes from bending-dominated

(as the slack cable initially is) to tension-dominated. While no known metamaterial structures specifically use initially-slack cables for any mechanical properties, owing probably to the lack of interest in stiffening structures and the difficulty of assembling slack cables to a metamaterial, an approximation may be found in curved beam-like structures that straighten in tension and thereby stiffen. For instance, Jang et. al. studied a class of metamaterials comprised of a network of thin, undulating beams that was explicitly engineered to replicate the stiffening-up property of natural biological materials such as skin [45]. When the "whorl" patterns are placed into tension, they eventually unbend until they are straight, whereupon further displacement results in tensioning the member rather than unbending it. Figure 20 is a reprint illustrating the initial and deformed shapes of such a metamaterial as well as its stress-strain response in tension.

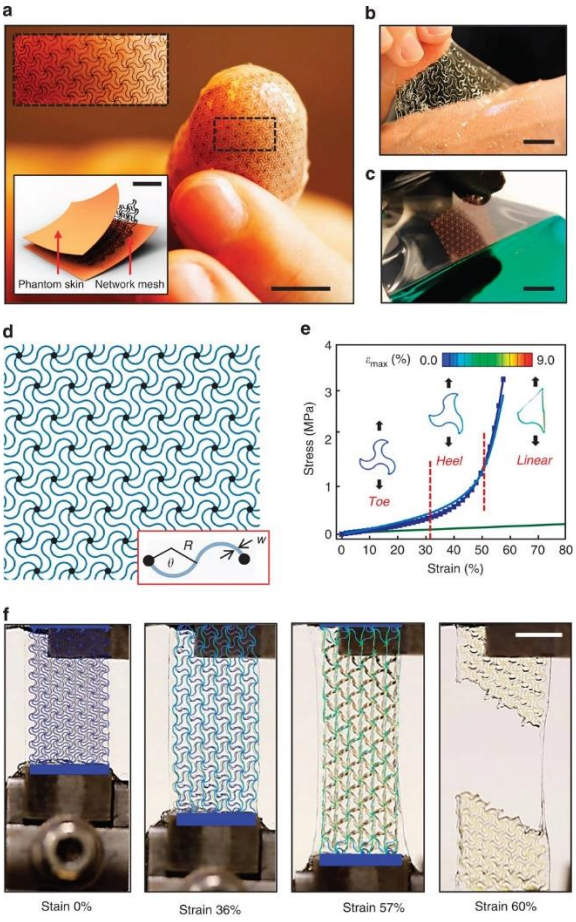

Figure 20: In-plane-undulating metamaterial with stiffening-up capability from the elongation of initially-whorled beam elements. Reprinted from [45] with permission.

In a similar vein, Li et. al. proposed a metamaterial comprised of flexible beams with out-of-plane undulations (rather than all undulations being confined to be in plane, as with the previous metamaterial discussed here) [46]. From a top-down view, the structure appears to be a simple Cartesian net of beams, but when viewed from the side or an angle, the undulation becomes apparent. Multiple views of this metamaterial are reprinted in Figure 21, and the stress-strain response of the structure under global tension is reprinted in Graph 10; note the continuous increase in tensile stiffness as the undulations are stretched out, with a larger initial amplitude of undulations predicting lower initial stiffness and greater stiffening-up capability.

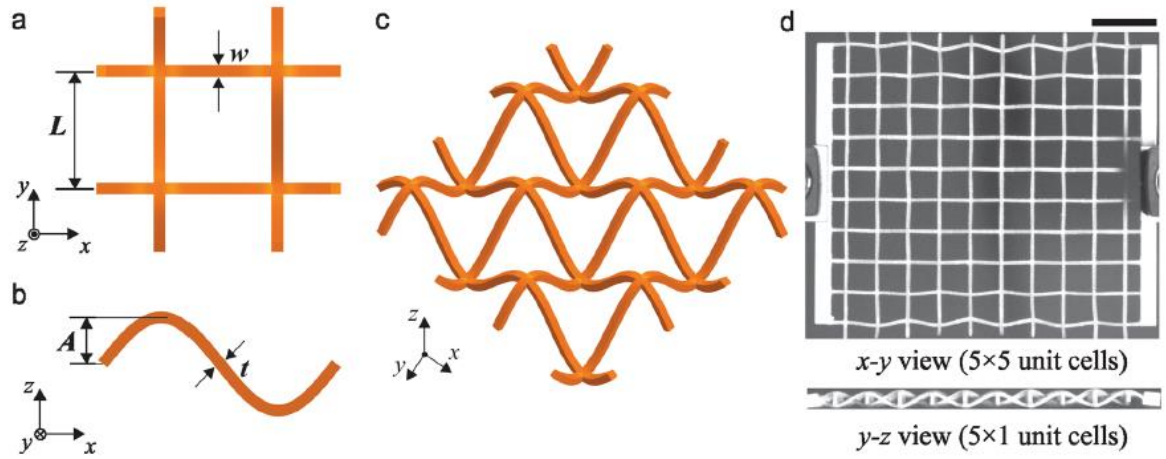

Figure 21: Overall structure of an out-of-plane undulating metamaterial. Reprinted from [46] with permission.

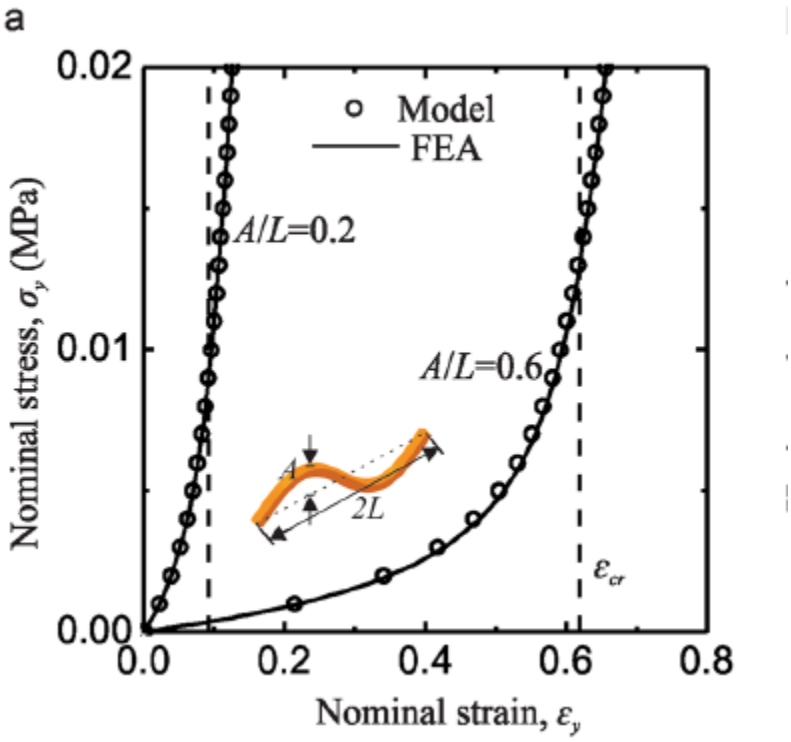

Graph 10: Stress-strain response of an out-of-plane-undulating metamaterial segment. Note the stiffening-up response, and that the magnitude of stiffness increase is greater when the ratio of the amplitude of the undulation to the wavelength is greater. Reprinted with permission from [46].

A complex snapping (bistable) metamaterial disclosed by Rafsanjani et. al. [47] additionally features moderate stiffening-up in extension when cantilevered slender beams are displaced at their centers to the point that tension becomes dominant, though strictly speaking the

beams are loaded in both bending and tension. Graph 11 shows the tensile response of the structure with images of the structure in various displacement states superimposed.

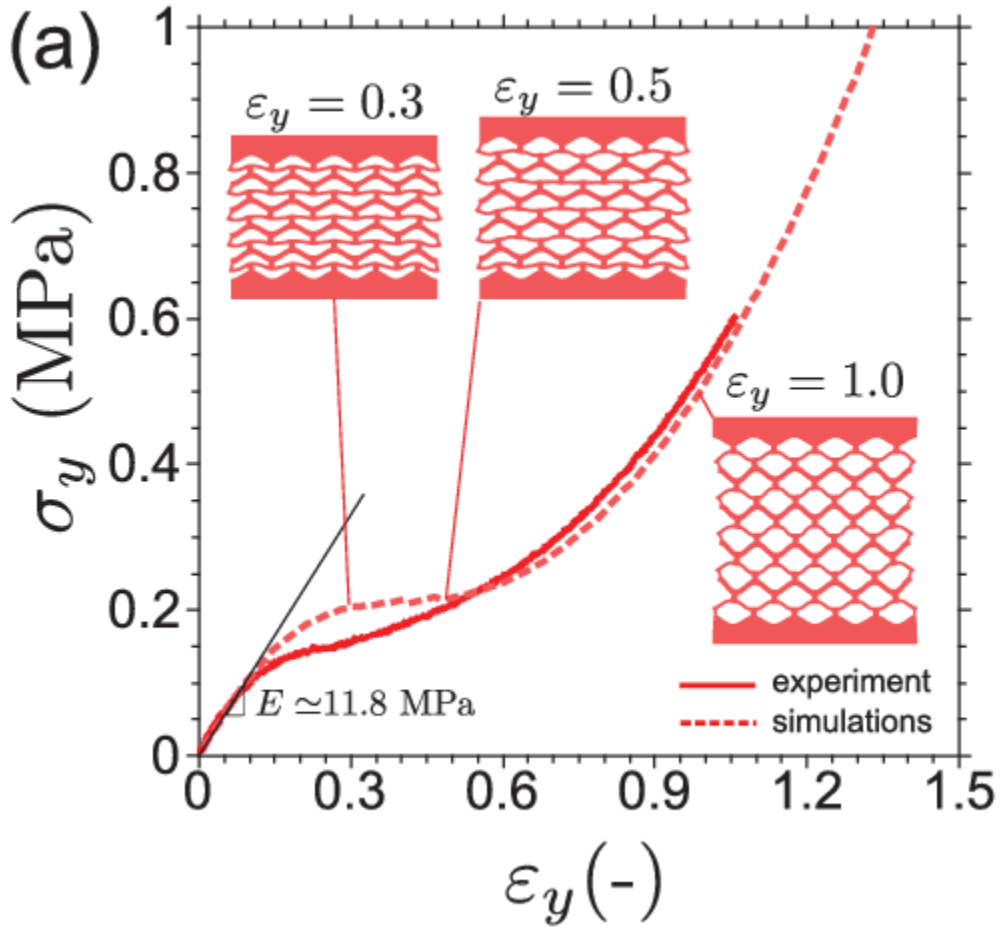

Graph 11: Tensile stress-strain response of one of the snapping (bistable) mechanical metamaterials studied by Rafsanjani et. al., with the deformed shape of the material superimposed on the graph. Reprinted from [47] with permission.

Metamaterials that Stiffen from Kinematic Singularities.

The final class of topology that can produce a stiffness increase after deformation pertains to the kinematics of rigid-body mechanisms and is only applicable to metamaterials that either closely approximate rigid-body mechanisms that have singularities (i.e. with nearly-ideal flexures that simulate revolute joints, etc.), or to micromechanism metamaterials that indeed have rigid joints (which are generally more difficult to manufacture and assemble than

compliant-mechanism-based metamaterials). For instance, suppose a metamaterial was constructed of perfectly-rigid links and revolute joints with the scissor linkage as the repeating unit; when the mechanism is fully lengthened in the *y* direction (collapsing onto its own footprint in the *x* direction), it encounters a kinematic singularity from which it cannot extend further; see Figure 22, and note that this is neglecting any interfering contacts between the links (which would also be a potential independent source of lockup).

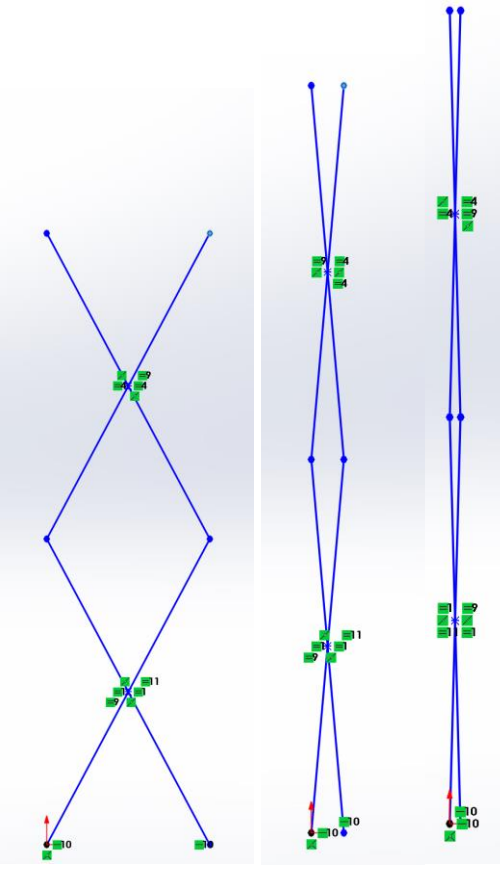

Figure 22: Kinematic singularity in a mechanism consisting of two scissor linkages with perfect revolute joints between the links.

A frequently-studied mechanical metamaterial, the rotating-squares auxetic metamaterial, has a kinematic singularity in tension that causes tensile lockup (see Figure 23), although as far as can be discerned from the literature, this property of the structure has never been exploited for stiffening purposes.

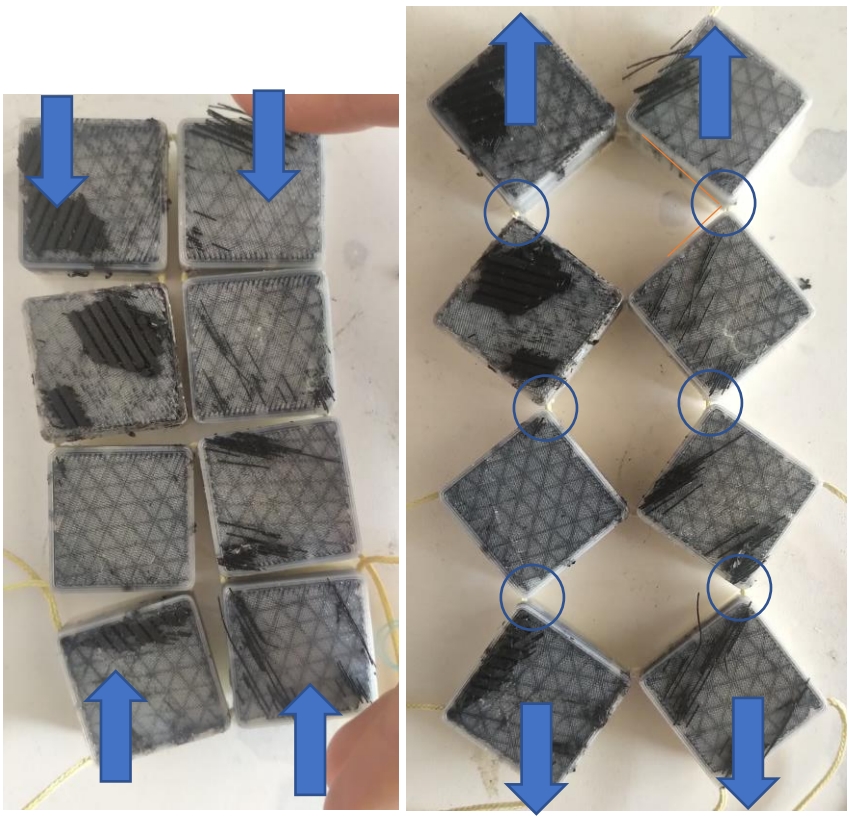

Figure 23: The rotating-square auxetic structure has a kinematic singularity when fully extended (with the rigid squares at exactly right angles relative to one another), as shown at right, whereas at left it is locked in compression. At full extension, the angle shown in orange would be a perfect right angle (it is difficult to photograph while applying tension). The cable-flexures simulate revolute joints that would occupy the positions circled in blue.

It must be stressed that it is not the auxetic property itself of the rotating-squares auxetic metamaterial that gives this stiffening-up potential, but rather the kinematics of the structure. In a similar vein, Cui and Ju studied [48] disparate rigid-body mechanisms (with torsional springs added to revolute joints to give the structure some initial stiffness) that could comprise the repeating units of a metamaterial, and then evaluated the structure's change in stiffness over displacement of ends, noting that the effective stiffness of the unit cells tended to increase towards infinity near singularities; Figure 24 reprints the force-deflection curves for several different structures in either mode around their singularities.

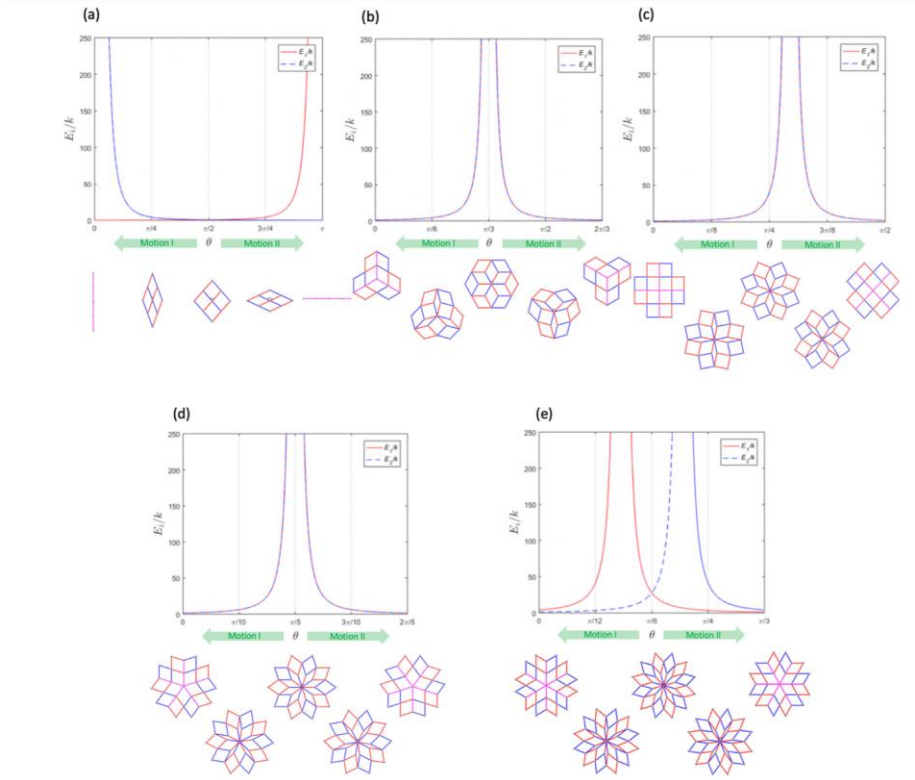

Fig. 7. Stiffness of MS-N in the principal directions and the corresponding configurations; (a) MS-4, (b) MS-6, (c) MS-8, (d) MS-10, (e) MS-12.

Figure 24: Effective stiffnesses for various pin-jointed kinematic structures with torsional springs between joints. Reprinted from [48] with permission.

While Cui and Ju only studied single unit cells theoretically, without manufacturing metamaterials consisting of multiple cells, Yang and Chen created a metamaterial-like assembly of rigid links following the pattern of the Bennett linkage in order to create a deployable structure (that incidentally mimics a Miura-Ori origami pattern) that has a kinematic singularity at full extent, though this aspect of the structure was not explicitly studied [49]. No doubt an arbitrary number of other kinematic linkages with kinematic singularities, having various degrees of freedom, can be designed and used as the basis of stiffening-capable metamaterials.

Multiphysics Metamaterials that are Stiffening-Capable.

Of note, many metamaterials are also "smart materials" that are capable of and indeed require some source of active control and actuation to achieve their properties. In the domain of stiffness-changing metamaterials, Harvard researchers Overvelde et. al. proposed a "reconfigurable origami" repeating unit that could be greatly expanded or contracted in multiple different directions and additionally stiffened and immobilized (relatively speaking) by the application of air pressure in different hoses [50]. Montgomery et. al. reviewed such actively-controlled metamaterials and their methods of manufacture in an excellent, recent article [51], noting that such active metamaterials may be controlled and powered through thermal, magnetic, swelling, fluidic, and other means. While active control may have its benefits, this dissertation's research is geared towards finding purely-passive structures, due to the potential unreliability, complications, etc. of any kind of active control. Thus, further research into this specific sub-domain of active metamaterials will be eschewed.

However, more in line with the goals of this research, Dudek et. al. found that an auxetic metamaterial modified by embedding small magnets into the beams comprising the metamaterial could produce either negative stiffness over a region, or high-magnitude stiffness increases, depending on the magnet polarity [52]; Slesarenko created a similar metamterial with a different structure and embedded magnets that also produced some stiffening effects [53]. Figure 25 depicts configurations of unit cells, either with repelling magnets or attracting magnets, embedded in some of the beams comprising the metamaterial studied by Dudek et. al. As can be seen in the picture, there are rigid revolute joints established between the rigid links, making this into a multimaterial composite metamaterial (with the magnets constituting a third material) that must be separately assembled; the revolute joints could be replaced by flexures (drawing from

compliant mechanism theory), or each rigid link could be replaced with a flexible beam with a cantilevered joint, to eliminate the assembly requirements for the mechanism (though assembly of magnets would still be required).

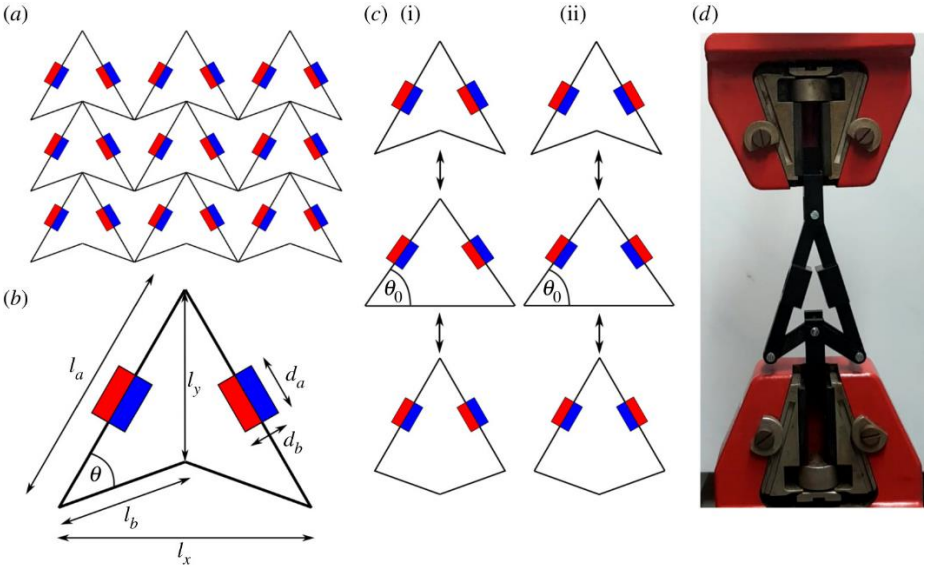

Figure 25: Dudek et. al.'s proposed magneto-mechanical metamaterial, with unit cells depicted, and multiple different potential magnet configurations, reprinted from [52] with permission.

Figure 26 depicts measures of the mechanical response of a unit cell to tension displacement, with graphs indicating that repelling magnets produced rapid stiffness increases as they approached contact (unsurprising since the repulsive force between same-polarity magnets tends to scale with the cube of distance), or rapid negative-stiffness if attracting magnets were used.

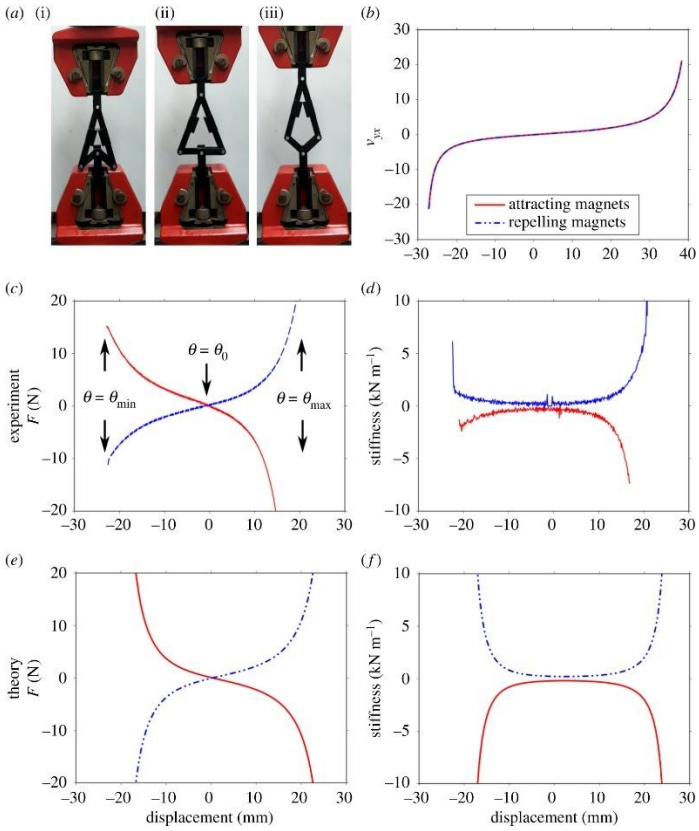

Figure 26: Graphs of the mechanical response of Dudek et. al.'s proposed magneto-mechanical metamaterial, featuring considerable stiffness increases with repelling magnets (and highly-negative stiffness with attracting magnets), reprinted from [52] with permission.

While this magneto-mechanical metamaterial that Dudek et. al. have proposed does indeed possess significant stiffening-up potential, the necessity of mounting magnets on many members is expected to greatly complicate both manufacturing and tailoring a complex structure to conform to the human ankle. Additionally, magnets tend to be dense and fragile, and might interfere with electronic devices or be attracted to ferromagnetic objects nearby, which would be undesirable for wear. Thus, this concept will not be explored further, other than to illustrate the potential that mechanical metamaterials may have as elastic stiffeners.

Metamaterials Relating to or Simulating Fabric.

In a sense, plain-weave fabrics are metamaterials (if perhaps the oldest and simplest known), because, if a thin shell could be made out of the solid, bulk material comprising each

filament, it would behave quite differently from the same thickness of fabric weave; thus, woven fabrics are metamaterials. Woven textiles have long been valued for clothing for the shear compliance they possess (facilitating conforming to doubly-curved surfaces without folds) as well as tension compliance along the bias (bisecting the warp and weft) from the trellis mechanism at each yarn intersection. Additionally, the capacity for microbuckling that individual yarns possess enables fabrics to buckle even more readily from an in-plane compressive load than could a shell of a continuous material with the same thickness and effective Young's modulus.

Indeed, there are fabric-like wavy metamaterials with structural elements engineered to enable non-woven structures to emulate these woven-fabric properties. For instance, Uysal and Stubbs designed a microstructure that could be 3D printed with an elastomer to create a structure to simulate woven fabrics inasmuch as the overall metamaterial was especially compliant in bending and readily microbuckled under in-plane compression (they also added thin, rigid tiles on top of the fabric-like elastomeric structure) [54]. That said, even the researchers involved in these fabric-simulating metamaterials do not give any practical reasons for which they should be preferred over true fabrics, and indeed they appear far more vulnerable to point loading, tearing, and uniaxial tensile failure than woven fabrics (even those of woven elastomeric fibers): their studies likely serve only to illustrate potential building blocks for metamaterials, though perhaps one day additively-manufactured, microstructured weaves will be created with high-strength fibers in many orientations (rather than the two orientations of warp and weft that plain weaves are limited to).

Caleb Petersen's Bending-Stiffening Fabric-Backed Tiled Array.

The question of the potential relationship between woven fabrics and mechanical metamaterials is not merely an academic exercise for understanding metamaterials more broadly: as mentioned in Chapter 1, this author's Master's thesis [1] disclosed one potential principle for creating a shell that stiffens after bending displacement that entails interrupted (self-)contacts that produce lockup in compression once the contacts between rigid faces are activated, along with a source of tensional stiffness to counterbalance it in the form of a woven fabric that is stiff in tension. Moreover, since the underlying fabric would be compliant in bending as long as the contacts between the rigid bodies adhered to it are inactive, the structure can have an excellent stiffening-up "figure of merit". Figure 27 illustrates the lockup behavior of this novel class of composite metamaterial.

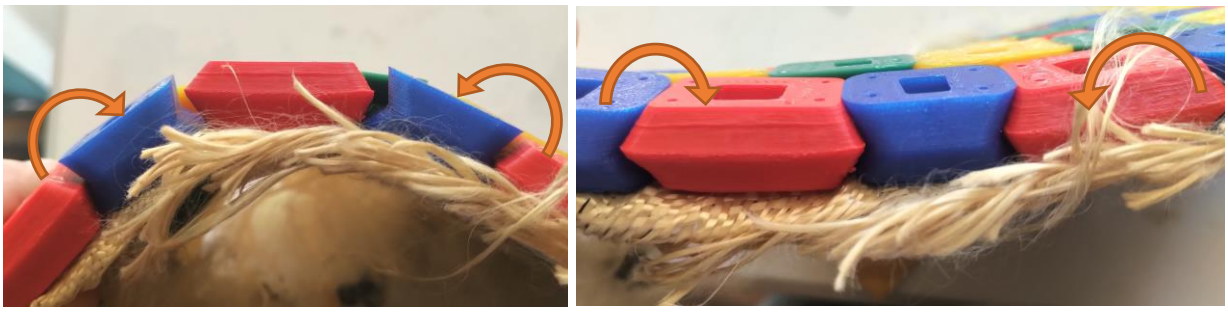

Figure 27: Fabric-backed tiled metamaterial in bending, in a low-stiffness region (left) and high-stiffness, locked-up region (right).

As an aside, the shear freedom afforded by the trellis mechanism of the underlying weave might be useful in kinematics that are more complicated than simple, single-curved bending, as might the compressive freedom from local microbuckling; the reasons for which these properties may be desired will be explored later.

Ultimately, this fabric-backed tiled composite metamaterial concept will be the dominant type studied in subsequent chapters of this dissertation, in embodiments variously targeted at

simple singly-curved shell bending and the more-complicated morphing of a cylinder-like structure fully enclosing a joint. In fact, the next chapter will introduce the concept of the fabric-backed tiled arrays as bend-stiffening metamaterials more rigorously and review any literature relevant to this concept.

Finally, strictly speaking it should be noted that woven fabrics tend to have an immediate low-stiffness region until "decrimping" is accomplished, owing to initial waviness in fibers that is somewhat straightened out in tension (straightening is limited by radial contacts between tows, and more straightening is possible in uniaxial than in biaxial tension), so to an extent, crimped fabrics are strain-stiffening materials [55]. Indeed, knitted fabrics (and composites containing them) are especially noteworthy for the magnitude of their stiffness changes (owing to the greater bending-dominance of knits relative to plain weaves) [56]. Even a non-woven fabric modified with auxetic-creating cuts demonstrated stiffening-up effects in tension, though whether from the kinematic-reorientation effects, decrimping of undulating if nonwoven fibers (likely limited for nonwovens as compared with wovens), or both was not made clear [57]. That said, the strain to decrimp the fabric is generally quite small (after which the material response is more or less linear up to failure), and the range for decrimping cannot really be increased without causing the structure to fall apart from excessive initial freedom unless the fibers are themselves stiffened in bending, which would increase the pre-lockup stiffness accordingly; thus, decrimping phenomena are unlikely to be the proper means of producing stiffening-up for an ankle protector.

Geometric Configurations for Ankle-Protecting Metamaterials.

Of the various stiffening-up-capable unit cells in metamaterials have been examined, most stiffen in in-plane displacement (whether extension, compression, or both). The selection

of a specific pattern or principle depends on the shape that the structure is intended to take throughout its range of motion and the corresponding stresses it might develop. In particular, there may be merits to structures that are dominated by shell bending and lock up from the structure having bending-lockup capability (entailing compressive lockup at the outer face and tensile stiffness/lockup on the inner face of the shell); these structures could act in pure bending and thus have no in-surface extensional or compressive strains. On the other hand, for an enclosure-surface (i.e. one that is closed like a cylinder around a joint), having same stress throughout the thickness (whether tension or compression) may be preferable, with less shell bending, and this mode would instead require significant elongations and contractions in different regions of the surface. Examples of surfaces morphing in either of these two opposing modes (either non-bending with extension and contraction, or constant-length bending without extension or contraction) are shown in Figure 28.

Alternatively, a hybrid loading and deformation pattern (entailing both shell bending and length changes in-surface) may be the appropriate mode; it is more complicated, however, and may require a commensurate amount of metamaterial tailoring to create one capable of morphing in this complex way, an arbitrary example of which is illustrated in Figure 29.

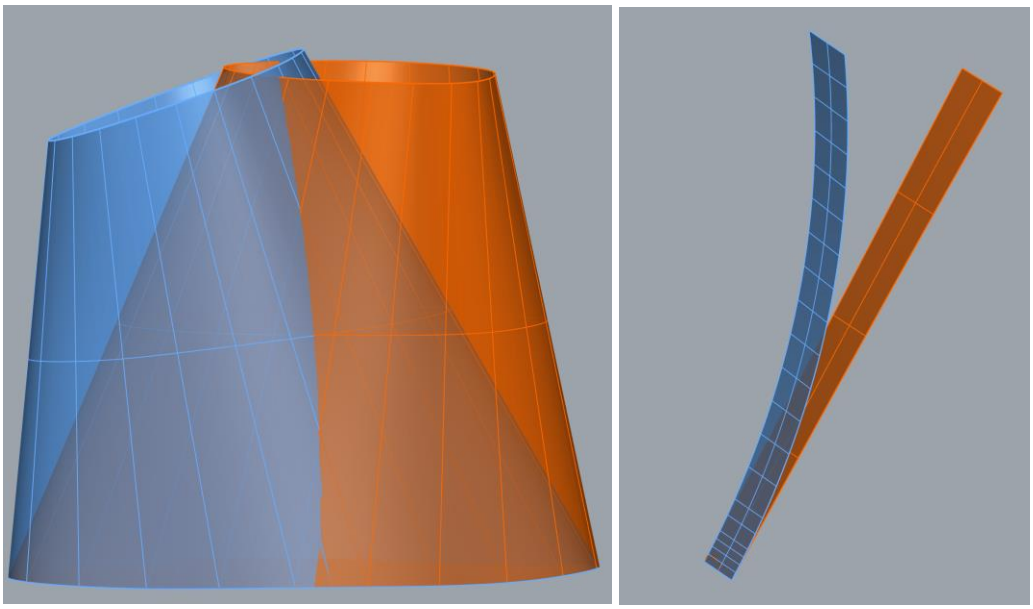

Figure 28: Hypothetical transformations illustrating potential metamaterial modes (in both cases, the orange shape is the initial shape, and the blue surface is the deformed shape). At left, the hypothetical metamaterial transitions from the orange shape to the blue shape with extension in some regions (e.g. those furthest to the right on the surface) and contraction in other regions (e.g. those furthest to the left on the surface), but with no bending to speak of. At right, the hypothetical metamaterial is transformed in pure bending, with no in-surface extension or compression (assuming a thin shell).

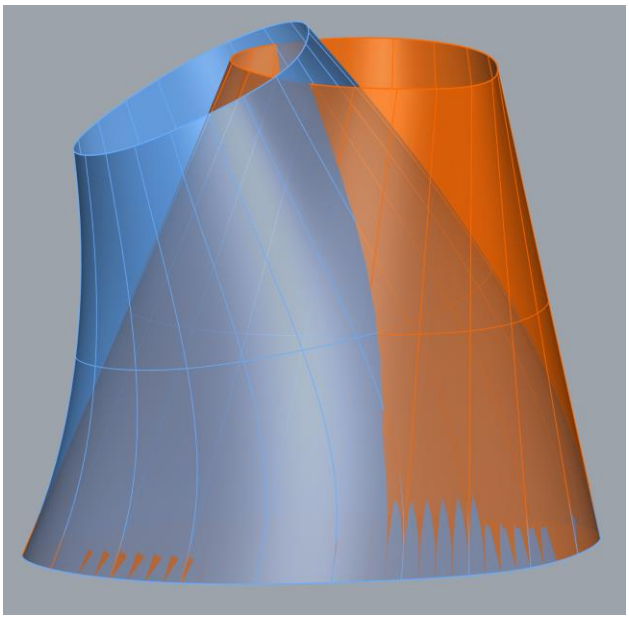

Figure 29: Hypothetical morphing transformation entailing both shell bending and extension/compression. In contrast to the previous figure, the morphing of the orange surface to the blue surface entails both shell bending and extension/compression in various regions and is thus a more complicated transition than either type in the previous figure.

This question will be explored in greater detail in Part II of this dissertation, starting in Chapter 6, which studies the behavior of closed (cylinder-like) surfaces and microstructures on

closed surfaces when subjected to bending moments. Indeed, the research of Part II indicates that contractile and expansive lockup in-surface alone is not sufficient for such cylinders, and they must have specific bending lockup capability as well (else shell buckling out-of-surface will tend to disengage compressive lockup). For now, it suffices to state that the fabric-backed rigid-tile array principle (mentioned briefly in this chapter and explored in greater detail in subsequent chapters, starting in Chapter 3) is bending-dominated in most embodiments, though it can be made tolerant of global compression owing to the ability of fabric to tolerate microbuckling.

As a final, cautionary note, metamaterial structures frequently have a characteristic scale transition region, below and above which properties can differ significantly; for instance, Coulais et. al. found that increasing the size of a certain metamaterial (that happened to be auxetic) that was loaded in compression actually increased the structure's extrinsic compressive stiffness (whereas a traditional, linear-elastic spring loses stiffness if another spring of equal stiffness is placed in series) within certain scale ranges, but outside this range (if the number of unit cells was made large), the effect was minor [58]. That said, some metamaterials, such as origami, are relatively scale-independent, with serious proposals for making origami on the nanoscale [59]. Ultimately, any study of a particular metamaterial in a particular application should involve varying the scale of the repeating unit greatly and evaluating the effect on the overall properties, in case a scale on the order of a certain intrinsic length is required. This scale-dependence of properties should ultimately not be surprising, considering it is the existence of subscale features that gives the metamaterial its unique properties in the first place.

Conclusion to Chapter 2.

The foregoing information should make it evident that there is no simple material science solution to this problem, though recent research into metamaterials has revealed the existence of

a wide range of complicated microstructures that can indeed produce stiffening in compression, tension, and/or shell bending to various degrees. In general, despite the great diversity of metamaterial structures, the mechanism of interrupted contacts being progressively engaged was what produced compressive stiffening, and mode-switching from bending (compliant) to tension (stiffer) or kinematic reorientations could produce tensile lockup. Of course, much more outside research towards protective structures has focused on the use of electronic controls and actuators (perhaps with shape-memory alloys [60], linear motor actuators [61], pneumatic actuators [62], etc.) rather than passive lockup, but active systems were deemed to be too unreliable, heavy, power-intensive, and slow to respond (as well as heat-producing, in the case of shape-memory alloy actuators) for this research.

Despite the richness of interesting metamaterials produced by the foregoing investigations, many proposed structures seemed impractical, owing to manufacturing and material constraints. However, the gradually-stiffening biaxial braids seemed a promising launching point for further research. In particular, the principle was slightly modified, as will be seen in the next chapter, by using a plain fabric weave rather than a biaxial braid, with fibers oriented in the 0° and 90° directions, and interrupted tiles rigidly attached to the fabric. The fabric is initially compliant in bending, but when the tiles contact on their edges at an offset from the neutral plane, they supply compressive stiffness and force the fabric into tension (a mode in which it is stiff).

Chapter 3. Introduction to Fabric-Backed Interrupted-Tile Arrays.

Abstract.

This chapter introduces a composite metamaterial that can lock up reversibly and elastically at a prescribed and tailorable profile of bending deformation and reviews any known outside literature of a comparable nature. The basic principles of the composite material are disclosed, with an eye towards requirements for the backing material and for the tiles.

Introduction.

While Chapter 2 revealed many metamaterials whose complex microstructures give them lockup ability after tensile and/or compressive strain, these metamaterials tended to have lockup only from in-plane compression or extension, rather than from out-of-plane bending, and it appeared that the ideal embodiment for an ankle protector would be dominated by out-of-plane bending. Of course, strictly speaking, out-of-plane shell bending entails compressive stresses on the inner face of the shell and tensile stresses on the outer face of the shell, as illustrated in Figure 30.

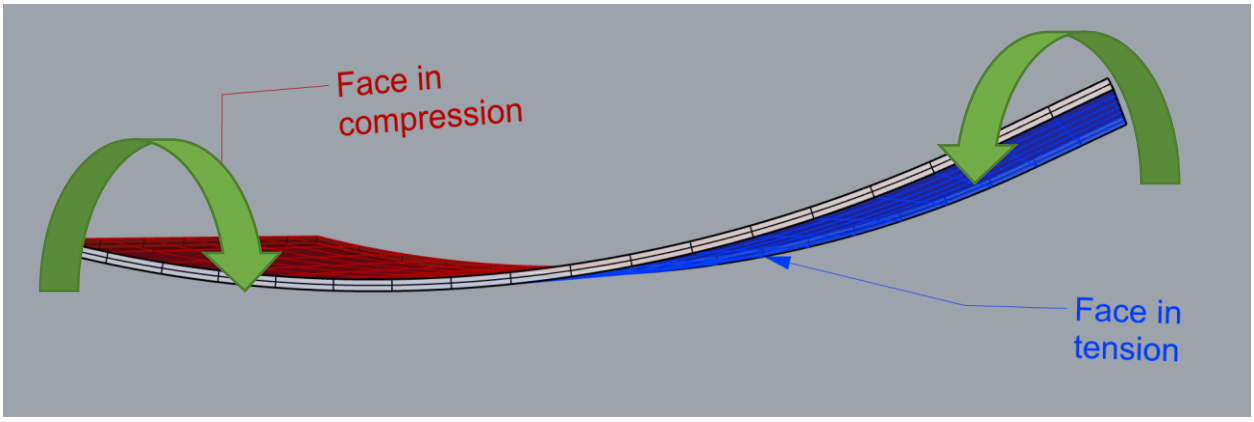

Figure 30: A moderate-thickness shell subject to bending will develop tensile stresses below the neutral axis/surface and compressive stresses above, with peak compression and tension at the top and bottom faces, respectively.

Theoretically, with infinite manufacturing precision, it might be possible to create a microstructured beam or shell with tiny stiffening features on the inner and outer faces, using one of the microstructures known from Chapter 2's investigations to stiffen up in both tension and compression. For instance, the rotating-squares auxetic structure (discussed in greater detail in Chapter 2 around Figure 23) has the added property of stiffening both in compression (from self-contact) and in tension (from a kinematic singularity) at prescribed strains, and Figure 31 shows what a thin, single-material shell having this type of cross section might look like in a neutral configuration. It must be stressed that this embodiment is a compliant-mechanism approximation of the perfect rotating-squares auxetic structure with rigid revolute joints; in the compliant-mechanism approximation, relatively-thin flexures replace revolute joints. In fact, this structure was scaled up and printed in thermoplastic polyurethane (TPU) elastomer and tested conceptually in bending, showing modes that should produce some stiffening up (by self-contact in the compressed region, and kinematic singularity/bending-to-tension mode switch in the tension region), as is shown in Figure 33.

However, it must be stressed that this is highly impractical to make a truly-thin shell with this microstructure for manufacturing reasons: it would entail shrinking the highly-detailed metamaterial microstructures that produce in-plane compressive and tensile lockup down to characteristic length scales that are a fraction of the shell thickness, which is simply impractical even with the most advanced additive manufacturing techniques presently available. For instance, for a shell thickness of 10mm (hardly "thin") and three unit cells through the thickness, the flexures would need to be 0.1mm thick, which is extremely delicate, as can be seen in Figure 32.

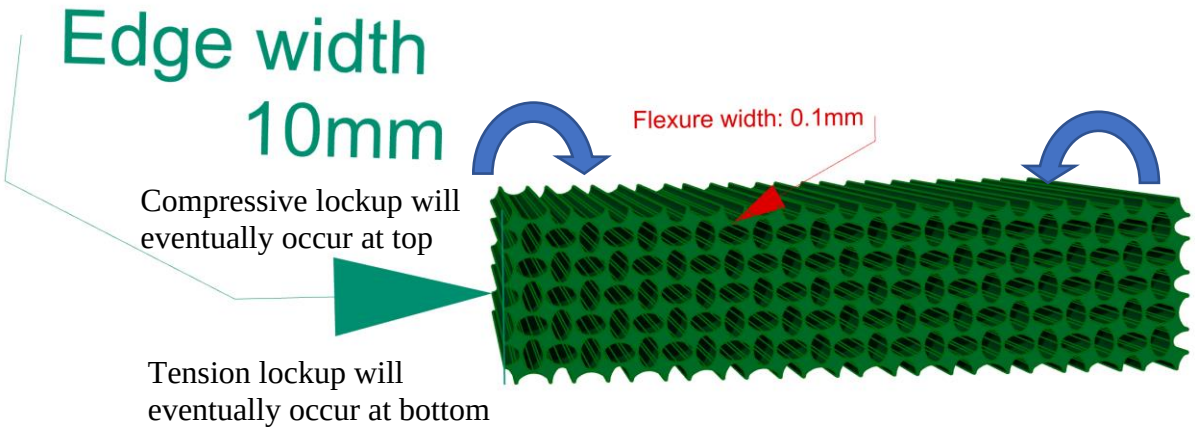

Figure 31: Hypothetical through-thickness-microstructured shell that uses the compressive lockup of self-contact and the tensile lockup mechanism of a kinematic singularity to produce lockup in global bending (as per the bending moments shown with blue arrows). Note that even if the entire structure is relatively thin (10mm thick), the flexure features must be miniscule at 0.1mm thick. Thus, this approach to creating a bending-locking metamaterial was abandoned owing to the incredibly-fine details required.

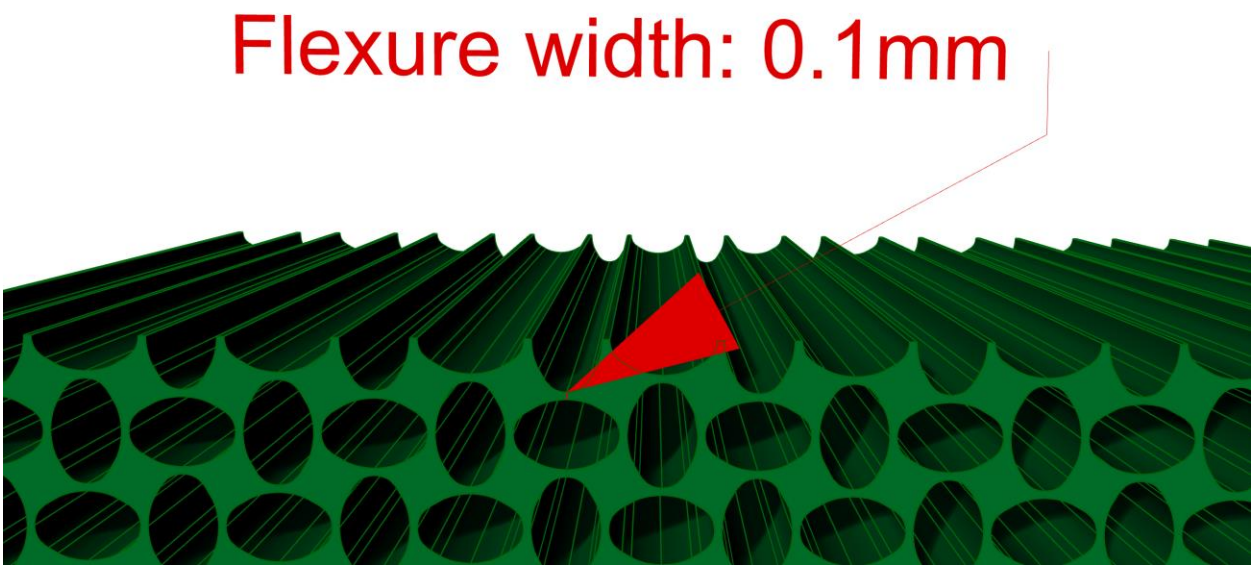

Figure 32: Closeup view of hypothetical through-thickness microstructured shell. Note the tiny flexure thickness required; it is not practical to create such a metamaterial with existing manufacturing techniques.

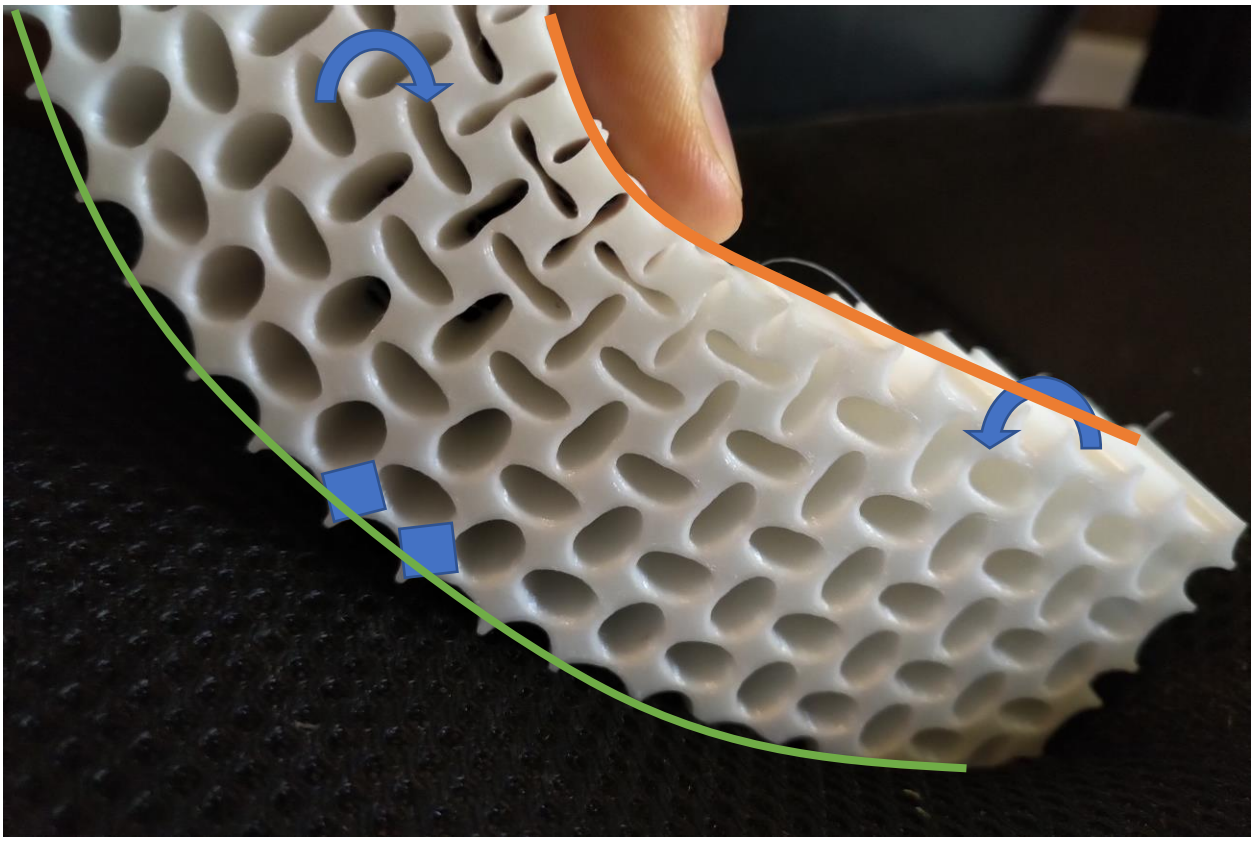

Figure 33: Magnifying the structure shown in the two previous figures, then printing in flexible TPU produces the following behavior. The region closest to the orange curve is subject to compression, which eventually causes the squares to engage in self-contact as the formerly-oval holes are closed up. In contrast, the opposite region (nearest to the green curve) is placed into tension, with the flexures themselves now tensioned (rather than subject to bending), with tension of flexures being a stiffer mode than bending. If the joints were perfect, rigid revolute joints, this would correspond to a kinematic singularity. The blue curved arrows indicate the bending moments applied, and the blue squares highlight how this compliant-mechanism metamaterial approximates squares that are rigidly jointed with revolute joints.

However, one composite concept involving rigid tiles on a flexible backing that is stiff in tension was quite promising for bending lockup, subject to certain design constraints on the unbent initial shape as well as the bent lockup shape. Mechanically speaking, the composite metamaterial combines thin fabrics (woven of fibers with very high tensile stiffness to give the overall fabric structure high tensile stiffness, but of low thickness to allow for flexibility in bending) with rigid tiles that are permanently adhered to the fabric (riveted, glued, and/or sewn). The rigid tiles have precisely-determined variable offsets between them in their initial position to ensure full contact between the tiles at lockup, and they have secondary geometric features to

handle small amounts of non-bending deformation (for instance, out-of-plane rotation or normal-to-surface displacement). In this composite material structure, local bending lockup occurs when the rigid tiles come into contact, not only exerting a compressive force on each other, but also placing the underlying fabric substrate into tension (which is a very rigid mode for fabrics of high-stiffness yarns), and global bending lockup results when all rigid tiles are in contact and the fabric tensioned everywhere. This principle can also be adapted with double-sided tiles (such that the fabric is in the center of the composite, and tiles are adhered to both faces of the fabric) to produce bending lockup in both directions. Figure 34 shows a diagram illustrating the principle features of a fabric-backed tiled composite bending-locking metamaterial.

Figure 34: Diagram of the basic components of the array. At left, a side profile view of the array is shown; at right, the underside of the array is shown (with rivets to lock the rigid tiles to the fabric, with the addition of glue).

Evolution of the Concept.

The concept of the fabric-backed tiled array for variable bending stiffness was first disclosed by this researcher in his Master's thesis [1]. One of the earliest arrays from that thesis is reprinted in Figure 35; note the 3D printed tiles with slight gaps between them that are adhered to a thin fabric backing (in this case, made of fine fiberglass, though obviously fiberglass would be a poor long-term choice due to its poor wear resistance).

Figure 35: Early fabric-backed array of rigid tiles, one of the simplest arrays created. The flaws this array possesses from lacking certain features are described in Chapter 4.

After discovering this principle, subsequent work (both in this author's Master's thesis and in Appendix III) investigated a number of potential shapes for the tiles when in planar arrays, including tiles designed to cam each other in various directions, tiles that contact around edges oriented in various directions (rather than the 0°/90° orientations of the array shown above), and tiles that are imbricated in various ways against sliding along an axis normal to the fabric [1]. Of note, no effort in the Master's thesis was made to target a specific lockup curvature profile (whether constant curvature, such as bending from a flat plane to an extruded arc, or variable curvature, such as bending from a flat plane to an airfoil profile); at the time of the Master's research, the focus was purely conceptual; however, in Chapter 4 of this dissertation, this problem is addressed mathematically.

Of note, some experimentation was also done with initially-curved arrays that are initially in either a sector-of-a-cylinder configuration (partial cylinder) or full cylinder (closed at a seam) to see how much the joint they enclose can bend before lockup, and it quickly became apparent

that full cylindrical arrays possessed much less freedom (or curvature) at lockup than did the flat versions (with the same vertical clearances between tiles) or than arc-segments that constitute only a portion of a full cylinder (compare Figure 36 to Figure 37). However, the question of how having the initial surface be closed (like a cylinder) impacts the structure's properties, and what modifications are necessary to allow the structure to tolerate large deflection on the part of the enclosed joint, is addressed in Part II of this dissertation, starting in Chapter 6.

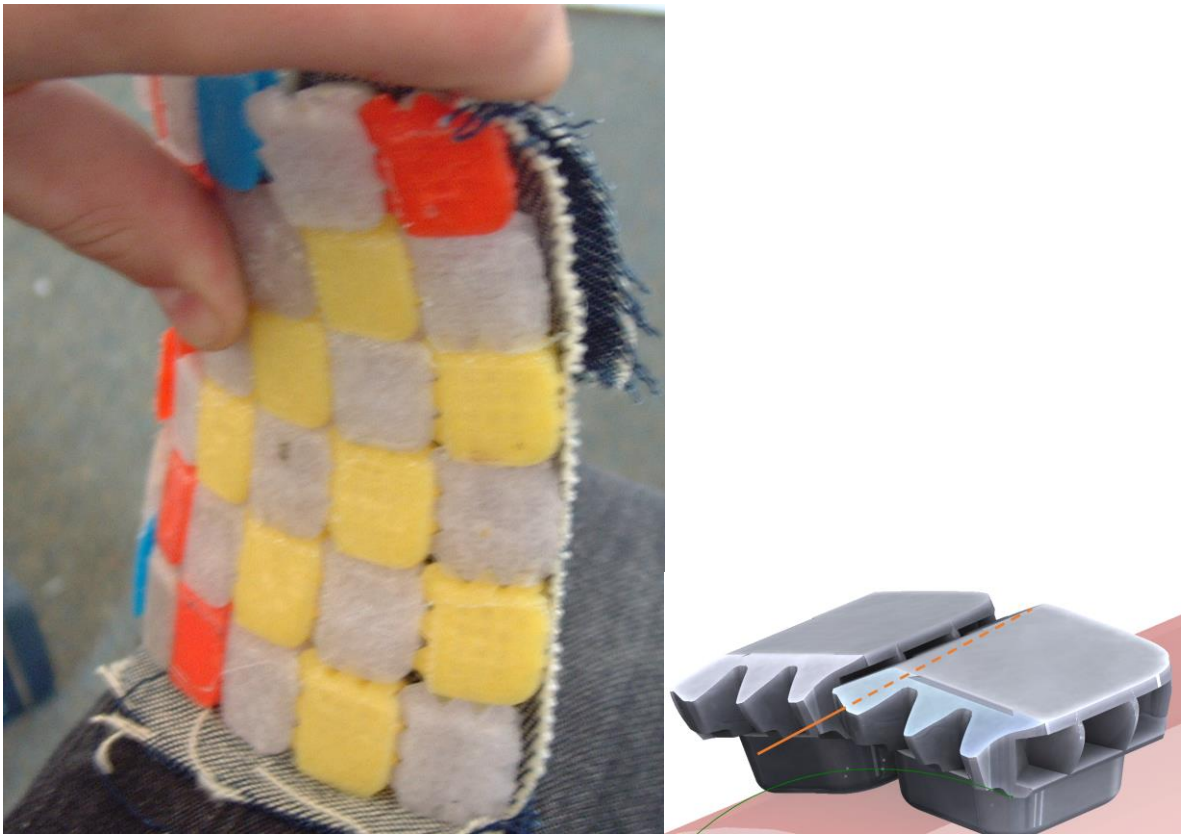

Figure 36: Lockup configuration of partial arc of a cylinder of "FTASF" ("Flared Teeth with Anti-Slide Features") array from this author's Master's thesis [1].

Figure 37: Lockup configuration of cylindrical wrapping of "FTASF" array from [1]. Note how small the deflection of the wrapped joint was.

Thus, at the conclusion of this author's Master's research, three areas for further research to be done in this PhD dissertation were identified. First, a desirable tile shape or set of shapes should be engineered to meet various practical criteria, including resistance to "jamming" (where tiles lock up in contact between faces that are not supposed to be the ones that produce lockup, i.e. misalignment), easy 3D printability, easy but precise assembly, strength, and sliding freedom in shear if needed. Of note, while many potential tile shapes were disclosed in the Master's thesis, there was little knowledge of what features were ideal, either for immediate lockup performance, or for long-term reliability, and additionally, manufacturing quality was poor. Second, research should be conducted into how to achieve a desired target lockup curvature profile, initially for singly-curved and open surfaces (in contrast to the Master's research, which did not systematically manipulate offset width and shape between tiles to achieve any specific post-lockup curvature, but at most merely varied the gaps between the tiles at their tips in a haphazard way), and then for closed surfaces in an appropriate bending mode as well. This might be achieved with a CAD algorithm or with an empirical correlation, but it might also

benefit from simulations in FEA. Third, a more in-depth investigation into the use of the fabric-backed tiled array principle for cylindrical (closed and singly-curved) or hyperboloidal (closed and negative-Gaussian-curvature) initial surfaces should be conducted, focusing on how to allow large deflection of an enclosed joint before lockup: if it is even possible at all, it would be useful to have some insight into why much larger gaps between tiles seem to be required for closed surfaces than for open and flat surfaces with the same target lockup curvature.

Outside Research of a Similar Nature.

Although the principle of fabric-backed interrupted-tile arrays was developed by the author of this dissertation independently, subsequent research into the patent literature disclosed a patent that was related. Specifically, researchers from MIT patented a flexible armor consisting of rigid tiles that have kinematic joints restricting their motion relative to one another on a flexible backing (whether fabric, foam, elastomer, etc.) [63]. However, that research focused on protecting objects from applied loads (such as point or knife-edge impacts, generally from contacting projectiles) while retaining some of the natural mobility of the wearer's joints, rather than controlling the kinematic behavior of a joint or producing a morphing surface, as the author of this dissertation is concerned with. Additionally, the MIT researchers imposed added kinematic restraints on their tiles, specifically that they might overlap in an imbricated fashion, or that they might be jointed with respect to each other (for instance, having pin joints); these conditions could be added to the shapes used by the author of this dissertation as well, but neither is necessary.

Finally, in a journal article corresponding to the patent, Ortiz et. al. implied that the backing of the array should be an elastomer, although they did not give any specifics and only specified that the "substrate" be "compliant" (which could imply compliant in bending or in

tension or perhaps both) [64], and indeed the patent drawings show a very thick substrate (see the patent drawing reprinted in Figure 38), which, if made of a high-stiffness fiber like Kevlar®, would produce significant bending stiffness before and after lockup. However, a low-stiffness backing (elastomer or soft foam) will produce very limited post-lockup stiffness once the tiles contact; for this research, it is essential to use a high-tensile-stiffness substrate (but make the substrate thin to reduce its pre-lockup bending stiffness). The importance of this difference cannot be overstated, although for a flexible armor to protect against point loads, the invention of Ortiz et. al. thick, soft, foam or elastomer backing is quite logical as it cushions the protected body and somewhat dissipates the pressure over a wider contact area. (Indeed, for some applications of this research, it might be wise to add some padding behind the fabric, on the opposite side of the tiles, but only for cushioning the wearer, not for lockup purposes, as low-tensile-stiffness foam will not contribute appreciably to post-lockup stiffness).

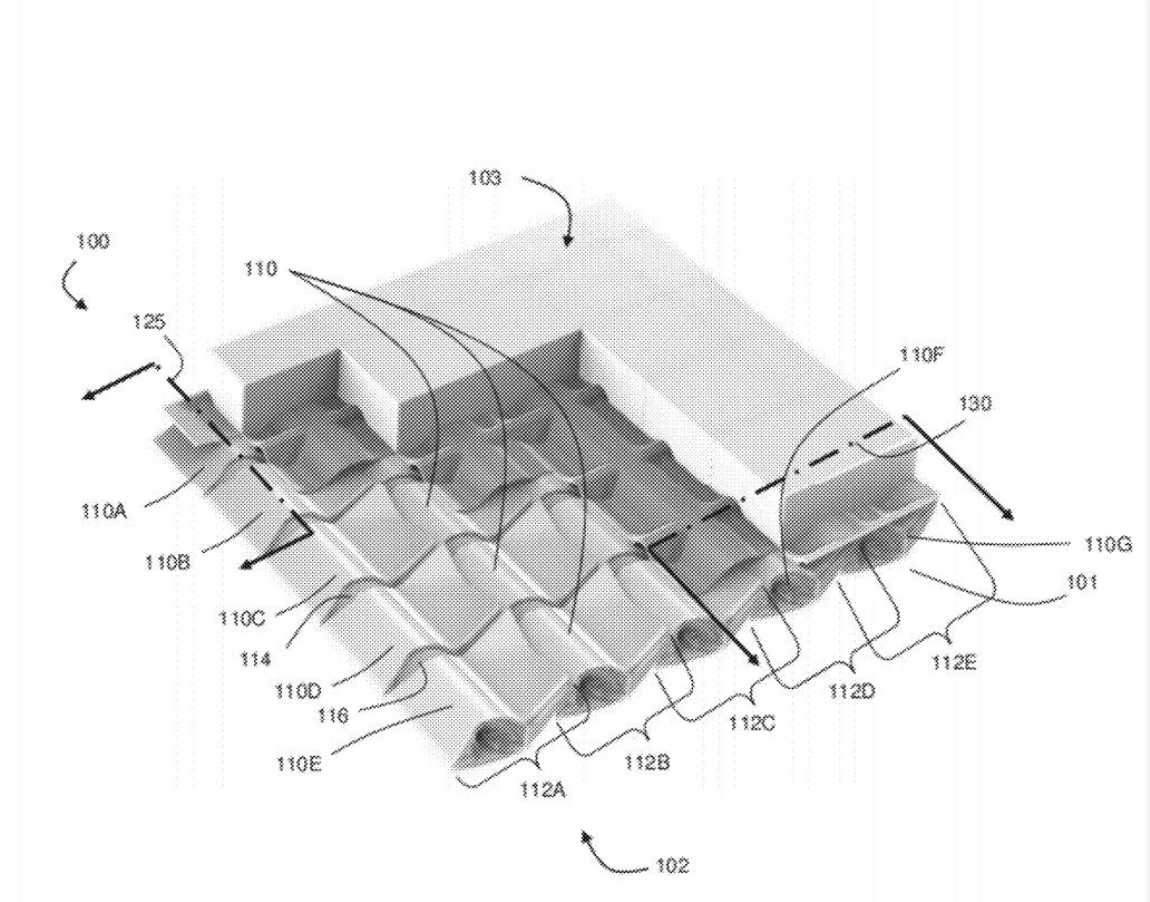

Figure 38: Patent drawing showing Ortiz et. al.'s proposed armor, reprinted from the patent [63]. Note the significant thickness of the flexible backing (indicated with number 103), which implies that it must be a soft elastomer or foam.

Additionally, as will be discussed in subsequent chapters, the tile design used by Ortiz et. al. in their invention is unsuitable to the purpose of this dissertation research. For one thing, Ortiz employs singly-imbricated, scale-like tiles, that overlap at an angle (crucial to ensuring that even the gaps between tiles are covered by rigid material and thus cannot allow projectiles to penetrate), whereas this dissertation instead finds that a doubly-imbricated geometry is preferable to prevent random tooth rotations and jamming. The singly-imbricated profile of the tiles can be observed in Figure 39.

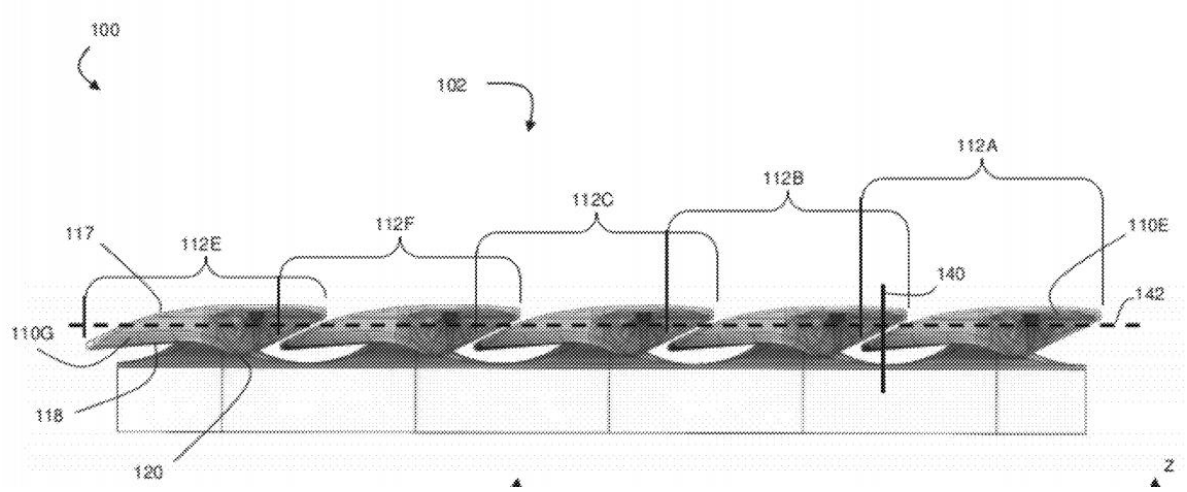

Figure 39: Profile view of the Ortiz et. al. armor, reprinted from the patent [63]. Note the imbricated structure of the rigid tiles (indicated with 112). This tile design proves to be less than ideal for the object of this dissertation's research.

Finally, an essential component of the Ortiz armor design is that each tile has at least one pin joint restricting its motion relative to an adjacent tile (with the pin conical in shape to facilitate reinsertion if the armor bends too much). While this is an interesting feature, it does not prove necessary for this dissertation's research. A top view of the Ortiz armor, focusing on the tiles and their pin joints, is reprinted from their patent in Figure 40.

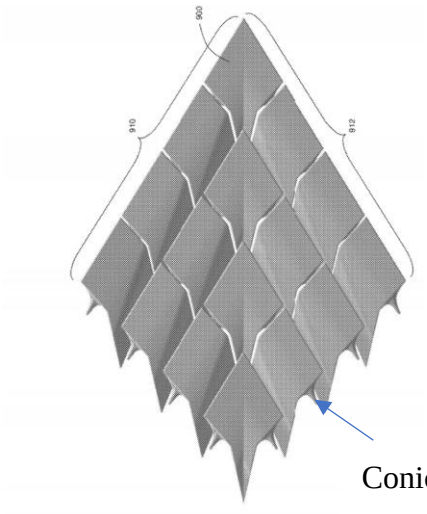

Conical protrusion that defines a revolute joint

Figure 40: Top view of Ortiz et. al.'s armor, illustrating the pin joints (with male elements given by conical protrusions, one of which is indicated with an arrow) between various tiles. Reprinted from the patent [63].

As an aside, it should also be noted that Ortiz's research group also investigated composites of angled rigid tiles embedded in an elastomeric matrix prior to developing their imbricated, scale-like armor array. Indeed, like the patented armor, the previous type of armor with angled tiles embedded in elastomer was intended to have some bending flexibility while resisting local indentation. However, there was never any design goal of having the stiffness of the composite in global bending vary as a function of deflection, and indeed there is no reason to believe that it would do so [65]. Ultimately, Rudykh, Ortiz, and Boyce were inspired by existing biological structures in nature, such as fish scale armor, but the force-deflection response of their rigid-tile-in-elastomeric-matrix armor is quite linear, and they make no mention of natural structures that might lock up in bending after a certain amount of deflection.

Aside from the patented concept of Ortiz et. al., little of relevance was found in the academic literature. Uysal and Stubbs disclosed [54] a glove-like metamaterial consisting of a microstructured elastomeric metamaterial backing and thin rigid tiles; however, there is no indication that the rigid tiles are intended to contact in shell bending (and indeed, they are poorly engineered to do so, being too thin and their gaps not designed properly). Moreover, although another source incorrectly cites [66] Uysal and Stubbs' work as being intended to limit the range of motion of the wrist, Uysal and Stubbs in fact make no claims in this regard.

However, it should be noted that there have been some non-academic creations of either private companies or individual hobbyists involving rigid tiles on fabric. Often, polymer tiles are 3D printed directly into fabric (which has some potential advantages as well as drawbacks that are discussed more fully in Chapter 4); for instance, 3D Systems experimented with printing various solid shapes onto fabric backing for fashion [67]. Hobbyists frequently recommend fabric meshes with low areal densities so that the polymer can surround the fabric both above

and below, and they often recommend printing the base of the tiles on the print bed (not on the fabric), pausing the print part-way through, and resuming it after placing the fabric on top of the partially-printed tiles (this reduces the likelihood of warpage and improves the bond between the fabric) [68].

Additionally, industrial designer Yael Akirav proposed a manufacturing method for creating origami patterns using a fabric substrate with some regions made relatively rigid against bending by 3D printing polymer borders enclosing the regions that were to be stiffened [69]. Strictly speaking, the added polymer layers were quite thin and not intended to contact with each other on their edges, but inasmuch as origami structures are metamaterials with interesting properties (as discussed earlier in Chapter 2, as well as later on in Chapter 6), this research may be tangentially relevant.

Finally, researchers at the industrial design studio Nervous System stretched flexible weaves of fabric with different strain fields and then 3D printed thin layers of rigid polymer onto the shell to cause the fabric to take on a different shape when the stress field was released (usually curving out-of-plane), primarily for aesthetic purposes [70]. While the ability to take on out-of-plane curvatures might facilitate conformity to a complex surface around a joint, the necessity of using fabric weaves that are soft in tension would likely limit their lockup potential.

Alternatives to Fabric Backing Considered.

The reader may be curious as to whether materials other than fabrics that have some bending compliance would make suitable backings for these lockup-capable arrays. As mentioned above, fabrics that are thin but of high-modulus fibers have the desirable combination of high tensile stiffness and low bending stiffness from the standpoint of minimizing pre-lockup

stiffness and maximizing post-lockup stiffness. In contrast, thick foams have the least desirable combination of low specific tensile stiffness (Young's modulus of the raw material) but higher general bending stiffness (i.e. the general bending stiffness of the entire structure or sample, as distinct from the specific stiffness property) because such foams will necessarily have to be thicker to develop even modest general tensile stiffness (a function of the cross-sectional area of the sample as well as the Young's modulus). Similarly, rubbers and other elastomers would be undesirable for their combination of high general bending stiffness and low specific tensile stiffness. Very thin sheets of metal might be acceptable from the standpoint of only looking at tensile and bending properties of the sample; however, the pre-lockup stiffness of a thin sheet of spring steel would still be far higher than that of a weave of Kevlar fabric with a thickness such that it has the same tensile stiffness as the steel (due to the crimp and microbuckling behavior of the yarns reducing bending stiffness further than one would expect from the Young's modulus of the individual fibers).

To demonstrate this numerically, it would be instructive to compare beams of various materials whose thickness is normalized to produce constant tensile stiffness. For instance, one could compare a woven fabric of Kevlar 49 (with fibers having a Young's modulus of 91GPa in the longitudinal direction [71]; assuming the transverse direction gives no contribution for stiffness and ignoring crimp effects, the effective stiffness might be said to be 45.5GPa) with a thicker sheet of elastomer (for instance, Hytrel 4100FL thermoplastic copolyester-ether polymer [72] having a Young's modulus of 130MPa in tension) and with a foam sheet (for instance, ethylene vinyl acetate foam with a density of 35kg/m^3 giving a durometer hardness of 48 on the OO scale [73], corresponding roughly to a Young's modulus of 100kPa [74]). Thus, ranked in terms of the stiffness of the Kevlar fabric, the elastomer is 1/350th as stiff in tension as the Kevlar

and the low-density foam is 1/455,000th as stiff, so the elastomer would need to be 350x as thick as the Kevlar and the foam 455,000x as thick (which already sounds quite impractical). Moreover, at such theoretical thicknesses, the bending modulus of the materials would show an even more drastic difference. Since the bending modulus *EI* is the product of the second moment of area of the cross-section in the direction of bending with the Young's modulus, and since the second moment of area scales with the cube of the thickness, the thickness-normalized elastomer would have a bending stiffness at least 42×10^6 times as high as that of the Kevlar weave, and the foam a bending stiffness that is 9×10^{16} times as high as that of the Kevlar weave. Granted, the tensile stiffness of even the thinnest possible Kevlar weave might be overengineered, even by a factor of 100x; even if this were so and the other materials were allowed to be only 1/100th as stiff as the Kevlar in tension, the elastomeric shell would have a bending stiffness of 42.9x that of the Kevlar, and the foam approximately 94,000,000 times as high. Ultimately, if figures-of-merit (lockup stiffness ratios) prove to be too low with a given backing material, it will generally be necessary to select one with a higher tensile stiffness but low bending stiffness.

Indeed, it should be noted that the foregoing analysis if anything understates the case in favor of dry woven fabrics, because their bending stiffness tends to be far lower than what their tensile modulus and cross-sectional thickness would predict, owing to fibers in the tows being unbonded and able to shear relative to one another. The ultimate stiffness post-lockup will also depend on the compressive stiffness of the tiles and their offset from the neutral axis, and with rigid tiles, the "figure of merit" (the ratio of the post-lockup bending stiffness to the initial stiffness) will just depend on the tile offset distance from the neutral axis, the backing's bending stiffness, and the backing's tensile stiffness.

Additionally, there are other ways in which fabric is superior to thin sheet metal of equal general tensile stiffness, namely in terms of the ease of manufacturing arrays by bonding the tiles to the backing (to be discussed in the next chapter) and fatigue life under repeated bending (whether or not lockup occurs). Finally, it is easier to manufacture arrays with initial (i.e. prior to lockup) curvature (instead of arrays that are initially flat) when the backing is fabric rather than a flat (if thin) sheet of steel, because the latter will tend to bend back to its original shape, whereas the fabric can drape without needing force to maintain it in a specific configuration. Consequently, the remainder of this dissertation will focus exclusively on fabric-backed arrays and not on other types of backing.

Chapter 4. Design and Manufacture of Planar Fabric-Backed Arrays with Optimized Structure that Lock up in Single-Curvature Bending.

Abstract.

The aim of this chapter is to design a composite metamaterial that can bend freely from its initial surface to a target surface. To this end, the mathematics of pure bending are reviewed to determine potential requirements for the initial and target surfaces for an array that can bend from a planar configuration to lockup into a surface of a specified curvature profile (with only one direction of curvature), using a repeating unit of tiles that has been found to meet certain practical constraints. After this, the next goal is to develop a method for manufacturing such an array (which will necessarily require high precision in the placement and variable offsets between the tiles, plus high strength in the bond between the tiles and the fabric) with a pre-selected target lockup shape in unidirectional and singly-curved bending. Once such an array is successfully produced, it should be tested experimentally, both to determine the magnitude of the stiffening up effect (or simply the final effective bending stiffness, given that the initial bending stiffness proves so low that it cannot resist the effects of gravity—such low initial stiffness is indeed desirable for most potential applications of this research), and to determine how accurately the final shape matches the targeted lockup shape. The structure should also be tested in bending in the perpendicular direction as well as in in-plane shear; ideally, it will have a high, constant stiffness (i.e. no initial freedom) in these directions, since the locked up surface is to be single-curvature only.

Introduction.

Generating the Initial and Target Manifolds.

To this end, the first step was to select an initial form-factor for the unbent membrane (i.e. a rectangular, planar surface), and then pick the target, bent shape that the composite material system is intended to be able to bend up to (but no further). For the initial base shape of the surface, a simple rectangle was deemed the most logical, and in particular the rectangle was chosen to have a long aspect ratio, with the long edges being the edges that are to bend (this ensures a large number of tiles will be present along the bending length, giving higher resolution with regards to attaining the target shape). The target shape was created rather arbitrarily, though one important constraint was that the length of its long edge must be the same as that for the unbent surface, and additionally it must be a singly-curved, developable surface, strictly speaking an extrusion of a planar curve (rather than the tangent developable of a non-planar space curve). Also, crucially, the defining curve (extruded to make the surface) of the target surface must be of the same length as the corresponding edge of the flat surface (as this length will be invariant in bending). The two surfaces are shown in Figure 41.

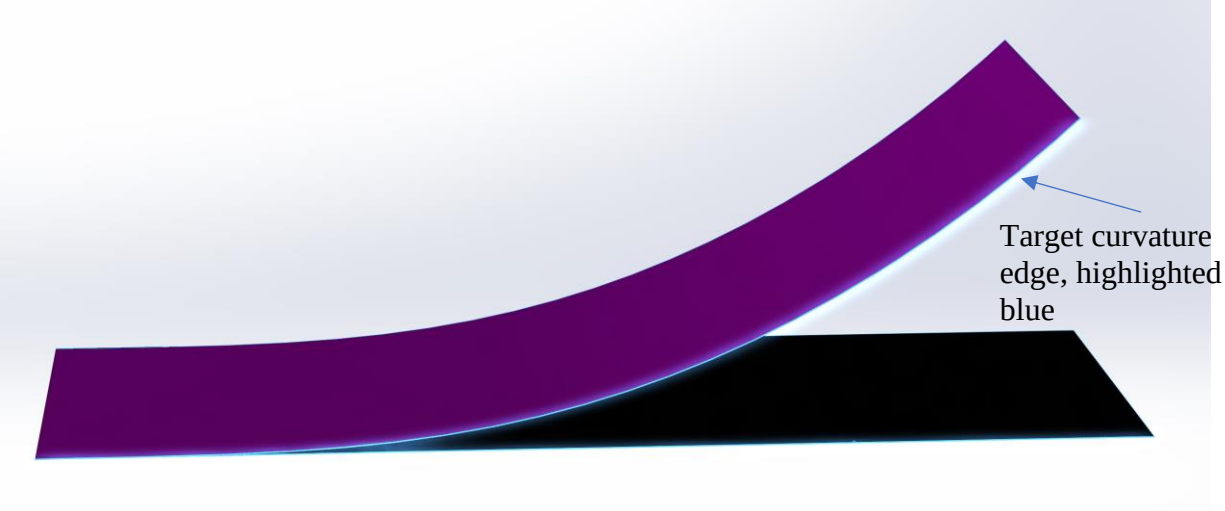

Figure 41: Initial planar-rectangular surface (shown in black) and target bending surface (shown in purple) for this chapter. Note that the purple surface was created by extruding the planar curve highlighted in blue along the short edge of the black surface).

General Requirements for Initial and Target Manifold Shapes.

It should be noted that only certain classes of initial and target surfaces can be used, owing to several constraints on bending surfaces that are best understood mathematically. The following section will review constraints on both the initial and target surfaces.

Insights from the Mathematics of Bending Surfaces.

The most important requirement on the two surfaces is that it should be possible to transform from the initial to the target surface by a pure bending operation. In differential geometry, a pure bending operation of an infinitely-thin surface (whether the surface is open or closed like a cylinder; and flat, singly-curved, or doubly-curved) must necessarily be an "isometry" operation, in that any curve drawn entirely on the surface has its length preserved. As corollaries, under such an isometry, the angles between any two tangent lines to arbitrary curves that are entirely on the surface must also be preserved; the areas of regions enclosed by closed curves on the surface must likewise be preserved; and finally, the shortest path (geodesic curve) between any two points on a surface must have its length preserved under bending [75].

Thus, this theoretical surface, in its bending mode(s), is infinitely stiff against tension or compression (which would change the lengths of curves on its surface) and likewise against shearing (which would change angles between tangent lines to curves on the surface). Clearly, in mechanical terms, this corresponds to the limiting case of a zero-thickness but infinite-elastic-modulus isotropic material; the infinite stiffness is sufficient to prevent all tension, compression, or shear inside the surface, while the zero-thickness gives a zero "moment of inertia" against bending, meaning zero bending stiffness.

This gives rise to the first formal requirement, stated mathematically by Treibergs [75]: for an isometric transformation mapping the initial surface onto the lockup/target surface (having been transformed by bending of the initial surface), the Riemannian metrics on the surface (such as angle of intersections of curves; areas; lengths of curves; etc.) are preserved. Practically, it suffices to ensure that the target surface can be created by one or more bending operations with the bending axis running through the initial manifold.

Introduction to the Gaussian Curvature of Surfaces.

As a consequence of the "isometry" that pure bending theoretically entails, the Gaussian curvature of the surface must also be everywhere preserved on the surface in a bending operation [76] (note that in most complex surfaces, the Gaussian curvature is not constant over the domain of the surface, so its distribution of potentially-unique values at every point is what must be preserved). This is intuitively understood by most people to be true as regards the bending of surfaces that are at most singly-curved (including flat planes), as such surfaces have a Gaussian curvature of zero everywhere; conversely, it is well known that a singly-curved surface can be flattened (going from zero Gaussian curvature to zero Gaussian curvature), but a doubly-curved

surface (having non-zero Gaussian curvature) cannot be flattened with a pure bending operation (i.e. without tensile/compressive/shear strain of the underlying material).

The Gaussian curvature of a surface is a local quantity (computed at every point on the surface), $K(x, y, z)$, defined as the product of the two principal curvatures (namely, the curvature in the direction of maximum curvature, and the curvature in the direction of minimum curvature, i.e. κ_1 and κ_2), at the given point (x, y, z) [77]:

$$K(x, y, z) = \kappa_1(x, y, z) \times \kappa_2(x, y, z)$$

When the Gaussian curvature of a surface is zero everywhere, the surface is either flat or at most singly curved (singly curved surfaces include extrusions of curves along a line, such as cylinders; cones and similar extrusions of curves up to a point-singularity; and an obscure class of surface known as the "tangent developable", created by sweeping a surface from the instantaneous tangent line of a space curve) [78]. Surfaces with Gaussian curvature everywhere are known as "developable" surfaces, because they can be bent flat out of ordinary shells without creating membrane stresses (or material tearing, or creasing to singularities), or a flat shell can be bent into their shape, again without creating membrane stresses. In contrast, doubly-curved surfaces have non-zero Gaussian curvature and are thus not developable; they cannot be bent flat without material crinkling, singularities, or significant in-membrane compression or tension, and they cannot be made from flat sheets without the same material crinkling, singularities, or significant in-membrane compression or tension. Due to the favorable economics of sheet metal manufacturing methods, in manufacturing it is often desirable to use developable surfaces wherever possible, or at most use surfaces that have very weak double curvature (that can be accommodated by the material undergoing elastic deformation during forming).

As mentioned in the remarks on the mathematics of a pure bending transformation, the distribution of Gaussian curvature on the initial and target surfaces must be identical: this is the second formal requirement on the initial and target surfaces. In other words, if the initial and target surfaces can be parametrized by *u* and *v* coordinates on the surface, for every *u* and *v* on both surfaces (and they should have the same maximum *u* and *v* extents owing to the length-preservation requirement stipulated earlier),

$$K_{initial}(u, v) = K_{target}(u, v) \; \forall \; (u, v)$$

Gaussian Curvature and Initial/Target Manifolds.

In Part I of this dissertation, the stipulation that both the initial and target manifolds must have zero Gaussian curvature will be made. Strictly speaking, a pure bending operation can bend a surface of non-zero Gaussian curvature to another surface (Gaussian curvature needs only be preserved, not necessarily zero, for pure bending). However, the added requirement of zero Gaussian curvature everywhere is made in order to facilitate tiling the initial surface with tiles, because the process for creating gaps between tiles of the proper magnitude to allow the initial and target shapes only works in one direction and would produce spurious interpenetrations of tiles if used in an attempt to tile a doubly-curved surface (this is a problem that is encountered in Chapter 7, necessitating added Boolean difference operations to relieve the interferences). Thus, formally, for every *u* and *v* on the initial and target surface,

$$K_{initial}(u, v) = K_{target}(u, v) \equiv 0 \; \forall \; (u, v)$$

Fortunately, both the initial surface (as a flat plane) and the target surface (as a linear extrusion of a planar curve) very obviously have zero Gaussian curvature everywhere. Indeed, in addition to linear extrusions of curves, lofts of a single curve to a single point (cone-like, though

ideally open and not closed) have Gaussian curvature everywhere, as do tangent developables. The zero Gaussian curvature of the target surface can be confirmed by performing a Gaussian contour plot on both surfaces (note that, despite the color scheme, this is not a Finite-Element Analysis and indeed has no direct translation to stresses, strains, or other quantities commonly plotted in FEA); the contour plot of Gaussian curvature on the initial surface is shown in Figure 42, and that on the target surface in Figure 43. In both cases, the plots are light green everywhere, which, according to the included scales, corresponds to zero Gaussian curvature.

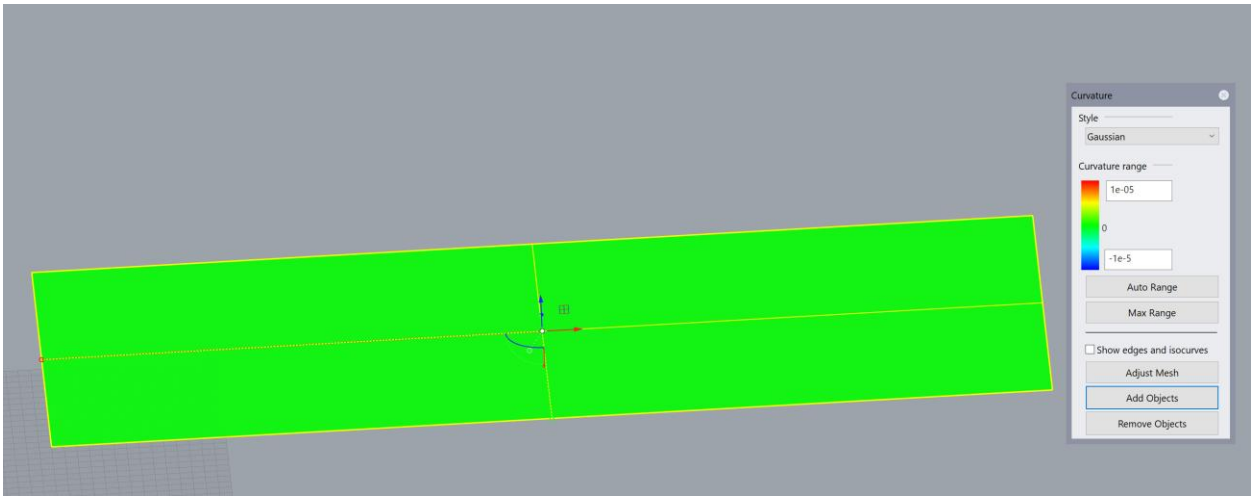

Figure 42: Contour plot of Gaussian curvature on the initial surface. It is zero everywhere.

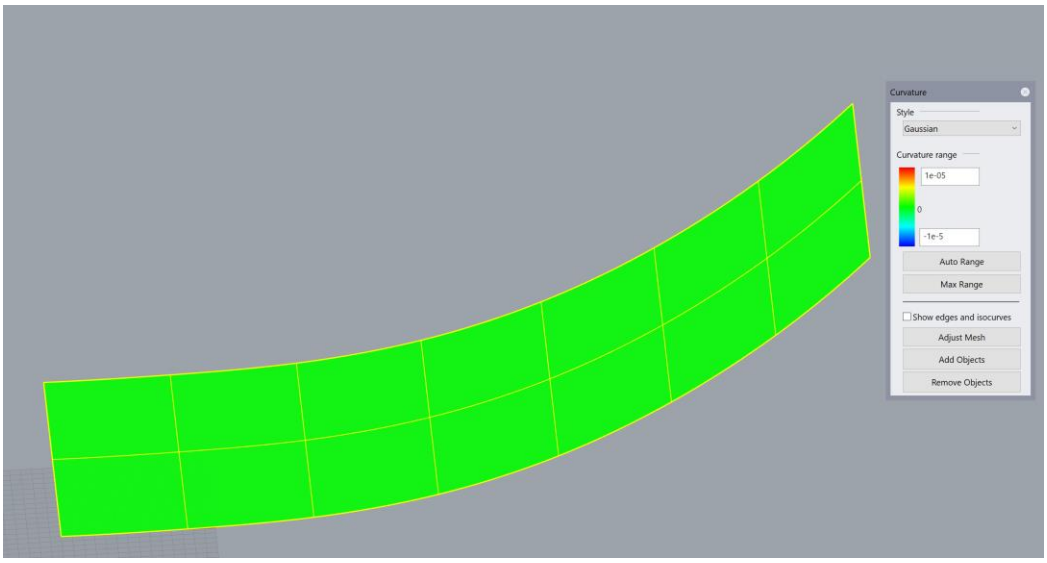

Figure 43: Contour plot of Gaussian curvature on the initial surface. It is also zero everywhere.

It must be stressed that Gaussian curvature and what one may think of intuitively as "curvature" are quite different; after all, the target surface clearly has "curvature" in one principal direction (κ_1), but the curvature in the other principal direction (κ_2) is everywhere zero. Plotting the "mean" curvature (the arithmetic average of the two, as opposed to the product of the two which is the Gaussian curvature) yields a contour plot that is more intuitively understandable, with significant variations over this singly-curved surface, as can be seen in Figure 44. As the target surface is a linear extrusion of a planar curve, the mean curvature gradients are aligned along the *y* axis.

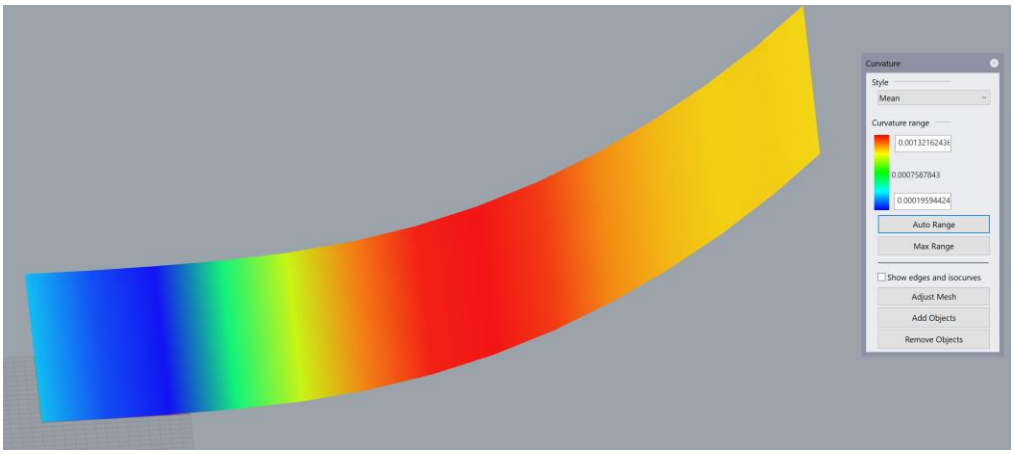

Figure 44: Contour plot of "mean" curvature (arithmetic mean of the principal curvatures at each point) on the target surface.

Inflection Points and Tiled Side(s)

The side(s) of the fabric on which tiles must be added depends on the direction of change of curvature from the initial to the target manifold. For a single-lockup (i.e. lockup only from positive bending, not negative bending) structure, tiles must be on the inside of the vector difference of the target surface minus the initial surface, i.e. in the opposite direction of the vector difference of the target surface's curvature combs minus those of the initial surface (if there are any; a flat surface has no curvature and thus its curvature combs are the zero vector). Figure 45 depicts the curvature comb on the target surface minus the initial surface (which is an extrusion of a horizontal line, so in this case the difference of the two is identical to the target surface); the combs point outwards and downwards, so the tiles must be generated upwards and inwards.

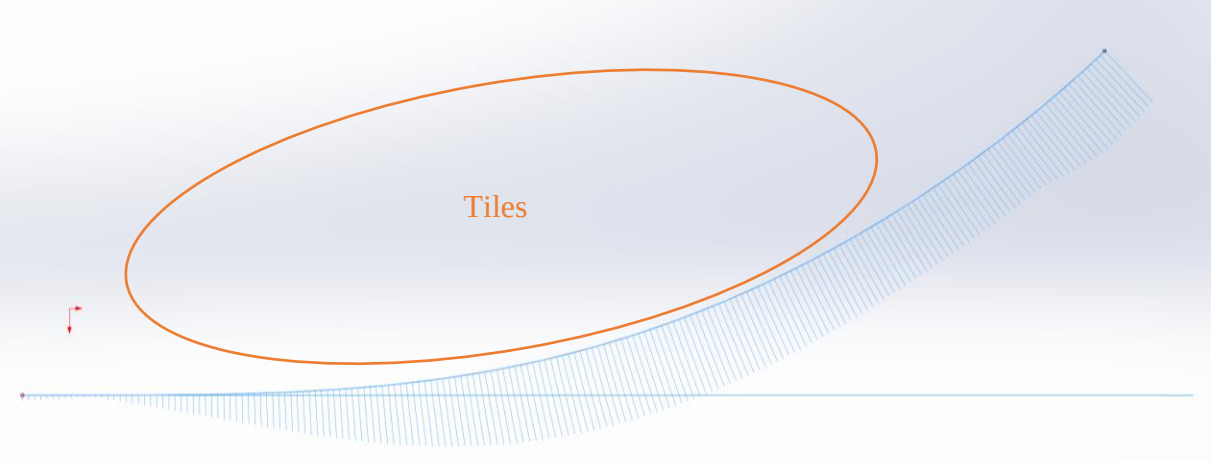

Figure 45: Curvature comb for the curve from which the singly-curved surface that is the target for bending lockup (purple in the previous figure) is extruded. The orange ellipse shows the region in which tiles must be generated. For those unfamiliar with the CAD concept of "curvature combs", a "comb" refers to a set of line segments that are normal to the curve at each point and whose length is proportionate to the curvature (longer comb segments in an area mean that, locally, the curvature is higher there) Note that there is no inflection point in this curve (i.e., the curvature combs do not change from pointing outward to inward or vice versa): otherwise, a double-sided array would be required.

Thus, if the array is to have tiles only on one side of the fabric (which is preferable from the standpoint of manufacturing complexity), there should be no inflection points in the curvature of the difference of the target surface's curve minus initial surface's curve. By looking at the curvature "comb" (shown above in Figure 45), it is apparent that there is no inflection point for the target manifold in this chapter minus the initial manifold (which, as a simple straight line with no curvature, makes the difference of target minus initial equal simply to the target curve), which can be verified by drawing a curve connecting the tips of the curvature combs.

If the secondary curve connecting the comb ends never intersects the base curve, then the base curve has no inflection point; otherwise, it has an inflection point at the location of each intersection (which is also the location at which the curvature combs have zero magnitude). For comparison, another curve was created with two inflection points (suppose this represents a target shape, to be bent up to from a flat surface of the same length, so the difference between the

two is equal to the target curve); the inflection points are circled and easily seen relatively easily with the addition of the curvature combs, as shown in Figure 46. If the target curve in Figure 46 (orange in color) is to be bent up to from a flat initial line (the black curve in this figure), then tiles will have to be generated on different sides of the fabric, with crossovers at the inflection points; the regions of the fabric where tiles must be placed for this combination of initial and target curves is shown in Figure 46.

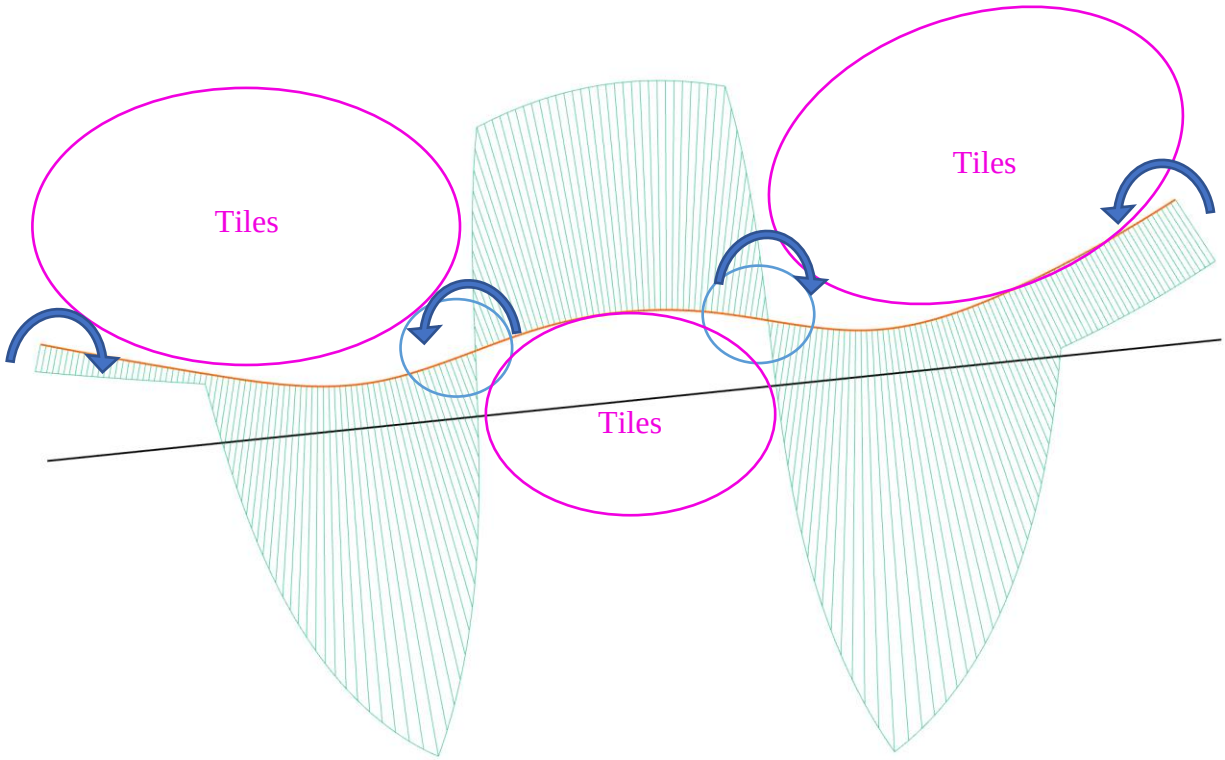

Figure 46: A curve (in orange) having two inflection points (circled in blue), with the curvature combs drawn in cyan. If the target curve is the orange curve and the initial curve the black line, then tiles will need to be generated on the sides of the fabric opposite the curvature combs on the target surface, i.e. in the regions circled with magenta ellipses. The directions of the bending moments required to bend the black curve to the orange curve are illustrated with blue arrows.

It must be stressed that the presence or absence of an inflection point in the target surface or initial surface alone does not indicate whether tiles need to change sides on the surface; it is the difference between the two surfaces that controls on which side tiles must be generated. For

instance, if the curve with inflection points shown in Figure 46 is extruded into the base surface, and the target surface is bent up further, then the vector difference between the two curves will be a simple arc without inflection points, and thus the side on which tiles to be generated will not vary over the surface—see Figure 47.

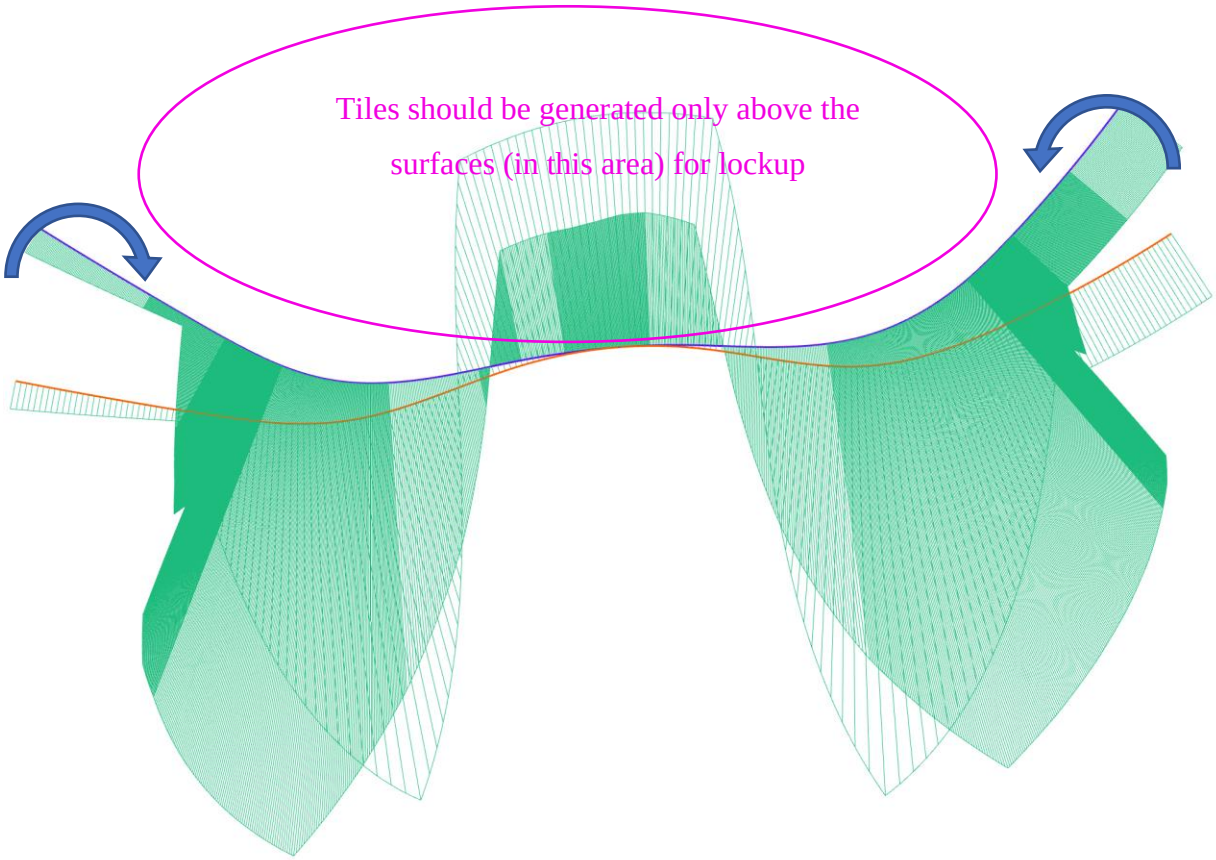

Figure 47: The orange curve defines the initial surface, and the purple curve defines the target/lockup surface. Although the two curves both have inflection points, the difference of purple minus orange is a simple arc, and thus tiles should only be generated on the top of the orange surface (indicated with the pink ellipse) to produce the purple lockup shape.

Fabric Weave Requirements.

It should also be noted that fabric weave imposes an added constraint on the shape required of the initial surface of the array: the surface must have its neutral axis parallel to one of the fiber directions (usually 0° or 90° in plain weaves, though one could shear the fabric), or in

other words the axis about which bending occurs must be orthogonal to one of the fiber directions. Otherwise, the fabric may experience excessive compliance along the bias (for instance, if the neutral axis of bending is at 45° relative to a plain weave, the unbonded parts of the fabric may contract along the bias with low stiffness and thus not give true stiffening up until shear locking occurs in enough regions to bear the load). Figure 48 shows an improper fabric orientation (with the warp and weft yarns oriented at nearly 45° to the axes along which the tiles are tiled and along which the structure is intended to be bent in lockup), and Figure 49 shows the correct weave orientation for instantaneous lockup.

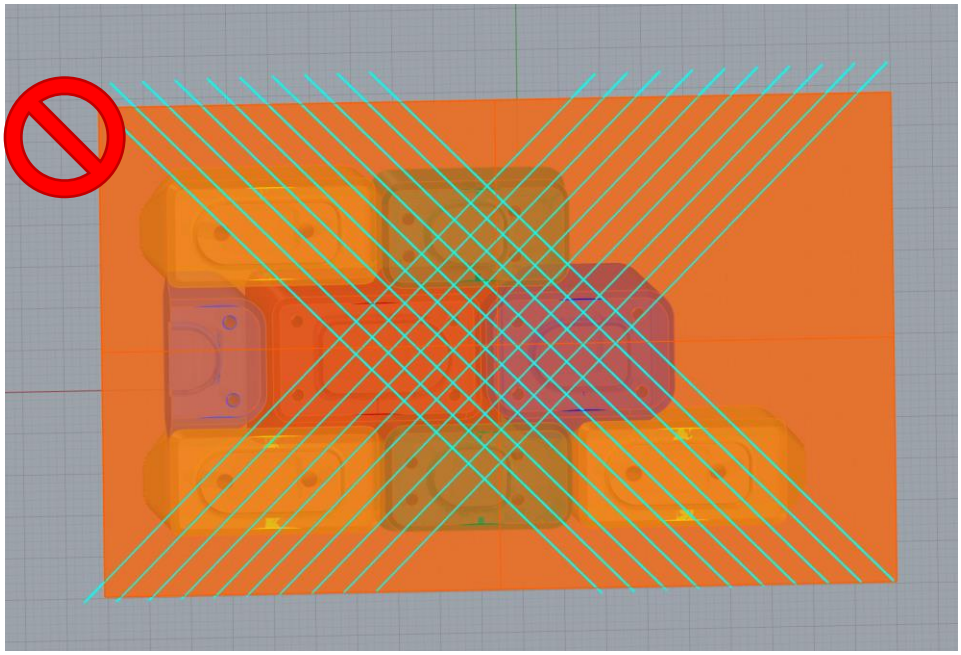

Figure 48: This is an undesirable configuration: the cyan lines indicate the direction of warp and weft in the fabric, indicating that the bias of the fabric is oriented on the x and y axes relative to the tiles. The structure will not stiffen up reliably with this fabric orientation.

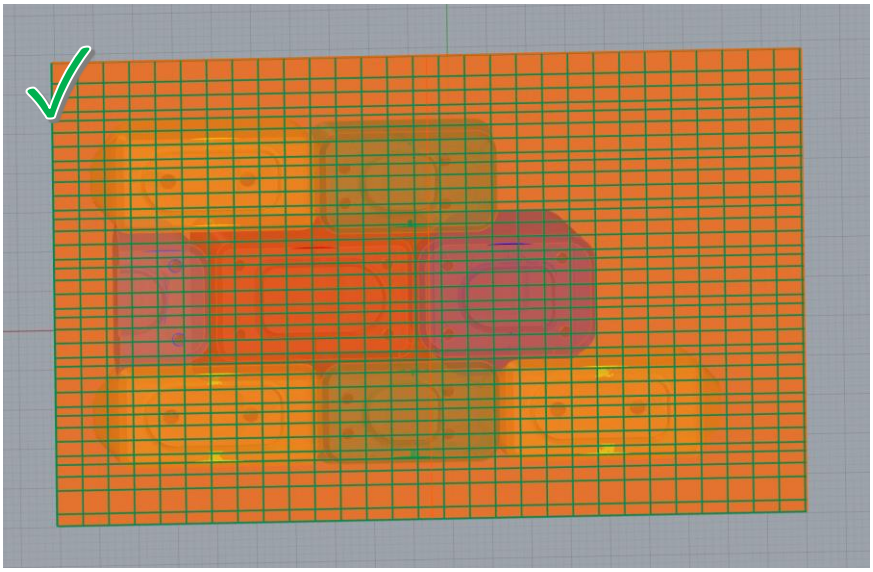

Figure 49: Correct orientation of warp and weft yarns (indicated with green lines) for instantaneous lockup after tiles contact each other.

In a similar vein, the axis of bending to generate the target surface from the initial surface should be parallel to either the warp or weft fibers, or else bias compliance effects will be engaged and the locked-up shape will not correspond to the engineered (target) shape. For instance, Figure 50 shows an initial and target surface where the target surface can be created by bending the initial surface about the bend axis shown; the fiber directions (warp and weft) for fabric that would conform to the two surfaces are shown, and it is clear that the bend axis parallels the warp axis, which is correct. In contrast, Figure 51 shows an incorrect orientation of the bending axis relative to the warp/weft lines that will produce excessive freedom owing to the bias compliance of the woven fabric (and the direction of bending having a non-zero trigonometric component relative to the bias).

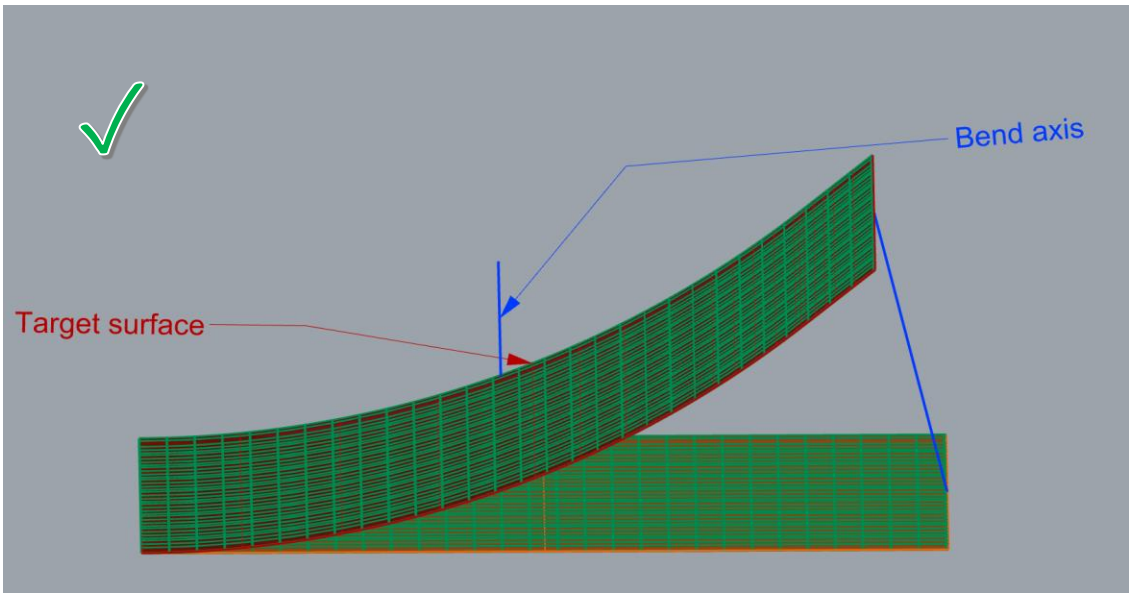

Figure 50: Correct orientation of the bend axis (shown in blue) relative to the fiber directions (it is parallel to the warp and orthogonal to the weft). Compare to an incorrect orientation depicted in three different views in the subsequent figures.

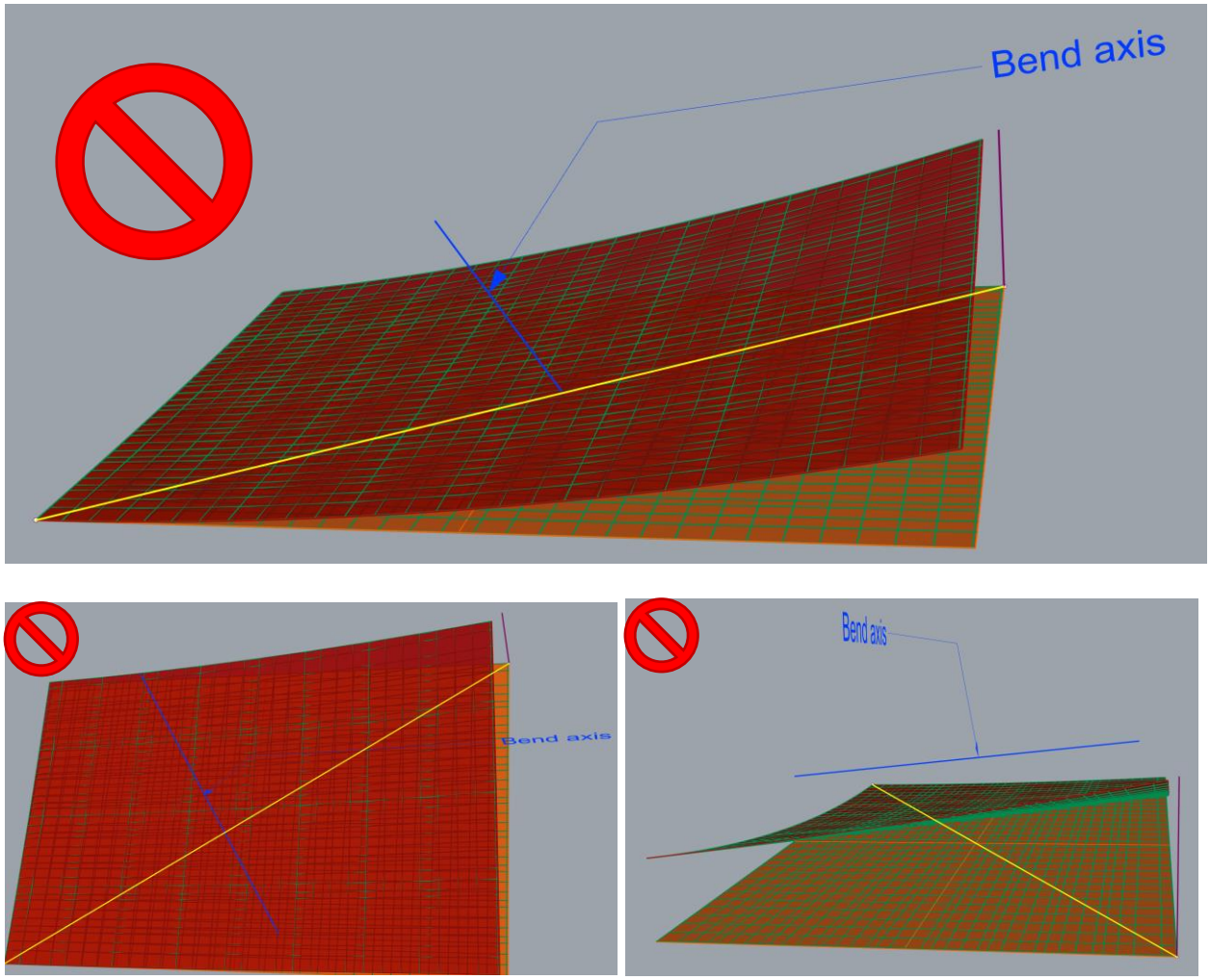

Figure 51: Three different views of an incorrect bending direction, involving bending about the axis shown in blue (effectively pulling the corner indicated by the yellow line up to modify the orange surface into the red surface). This direction of bending engages a component of the bias compliance of the weave (weave directions indicated by green lines) and will thus see extra freedom.

Granted, it might be possible to distort the fabric weave intentionally before gluing the tiles in order to ensure that fibers (rather than bias) lie along the intended load path, but this is undesirable. Additionally a quasi-isotropic (at least in plane) mat or laminate might be used instead of a plain-weave fabric to avoid bias-compliance issues, though the mat must be very thin to keep pre-lockup bending stiffness low and prevent fiber damage if large changes in curvature occur. Additionally, a triaxial fabric weave should not have bias compliance [79]; however, it should be noted that triaxial fabric weaves still have significant tensile anisotropy in-plane [80],

which is important if bending load paths do not correspond to any of the three fiber directions. While avoiding effects from bias compliance is important to ensuring lockup-surface fidelity in open surfaces, it may in fact be crucial to accommodating complex initial curvatures, such as doubly-curved surfaces and surfaces that are closed like cylinders, an issue that is discussed in Part II.

Moreover, even though a woven fabric itself may have considerable ability to shear (owing to the trellis mechanism of the weave), for the purpose of creating bending-lockup composite metamaterials with precise single-curvature lockup, the target surface should not require a shearing operation to create it from the initial surface, as shearing changes angles on the surface (making it a non-isometry), and additionally it changes the lengths of some curves (though not all). Regardless of what the fabric weave itself may tolerate, the addition of tiles tends to constrain the fabric against shear, and additionally it may bring tiles into premature contact if the magnitude of shear deformation is sufficiently large. Figure 52 depicts an example surface created by a forbidden shear operation, comparing it to an acceptable surface that is created only by bending the initial surface.

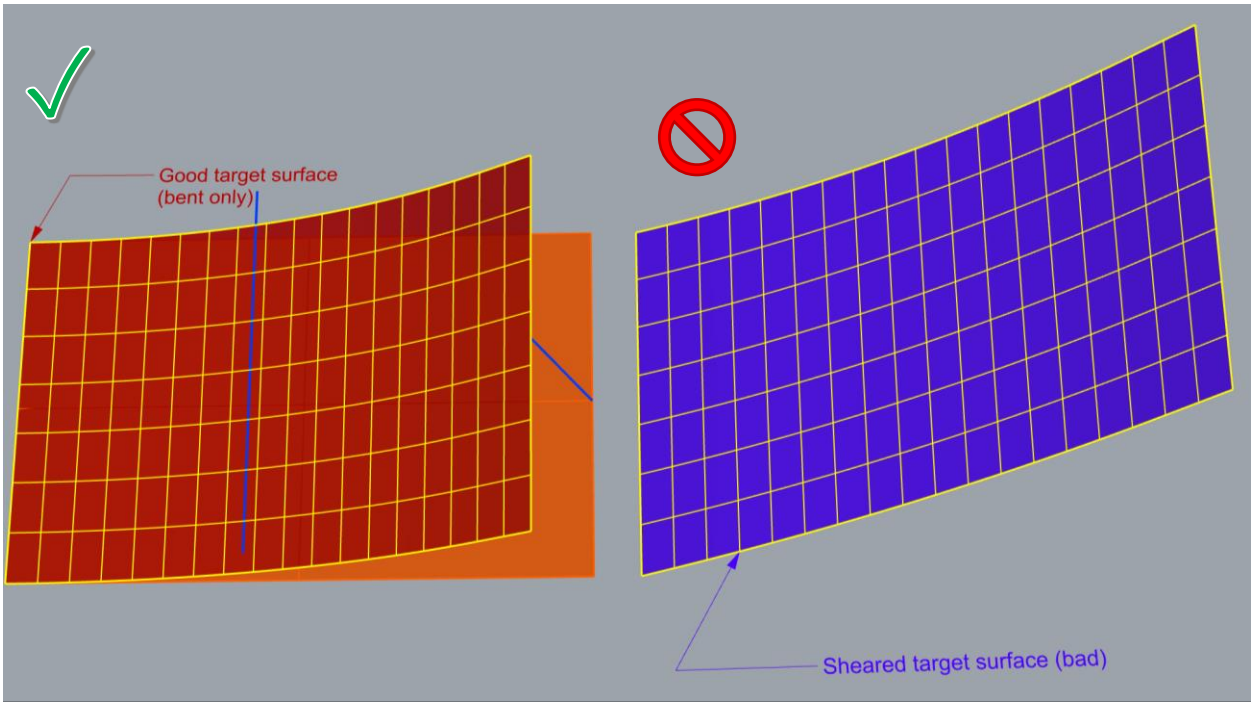

Figure 52: For an initial surface shown in orange, an acceptable target surface is shown in red (it only requires a bending operation, about the axis shown in blue, to create the red surface from the orange surface). In contrast, the surface shown in violet is the result of subsequently shearing the red surface, which makes it an unacceptable surface type (additionally, the warp and weft are no longer orthogonal on this surface, though a trimmed surface with warp and weft orthogonal could be created).

Magnitude and Scale Constraints.

Practically speaking, the radius of curvature of the target surface must not be so small as to require a gap between tips of tiles that is more than the width of a tile, or else so much of the tile will be cut away that it will have a sharp edge (the reader is referred to the subsequent section of this chapter on calculating the needed offsets between tiles).

Trivially, the surface must also not interpenetrate itself (e.g. Figure 53). For the purposes of this chapter, even a shared seam edge is discouraged though possible if all bending isometry requirements are met: note that closed surfaces tend to require changes in Gaussian curvature (evidence of a non-isometry) to enclose a bending joint even with sliding (as will be discussed extensively in Part II of this dissertation).

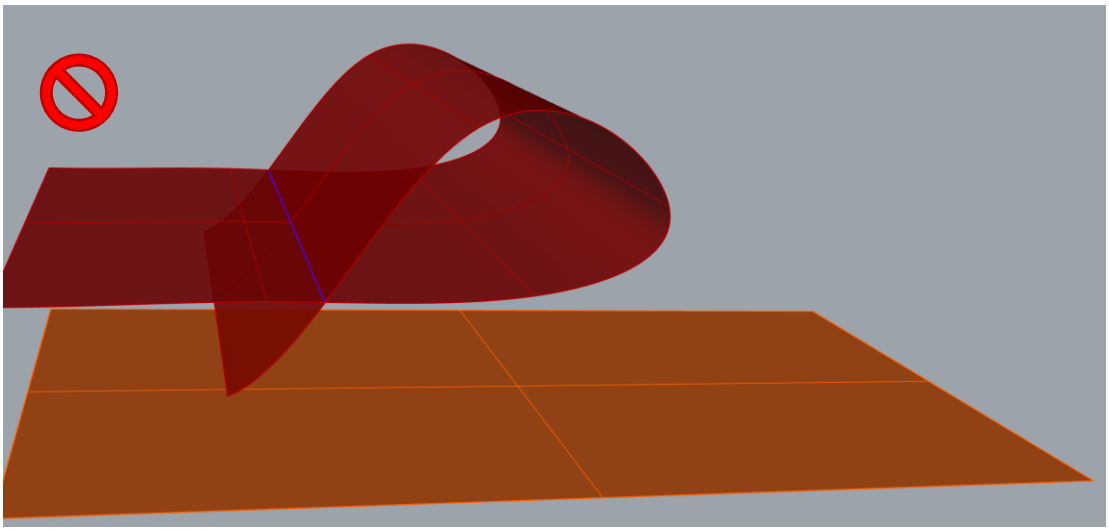

Figure 53: Forbidden target surface type shown in red. Note the self-intersection, which is shown with a blue line.

Similarly, even if the target surface does not interpenetrate itself, if regions come too close to other regions of the surface, tiles that are generated at an offset may end up interpenetrating, so clearance of at least twice the desired tile thickness between regions of the surface that loop back are necessary; Figure 54 illustrates the pitfall when there is insufficient clearance for tiles of a certain thickness.

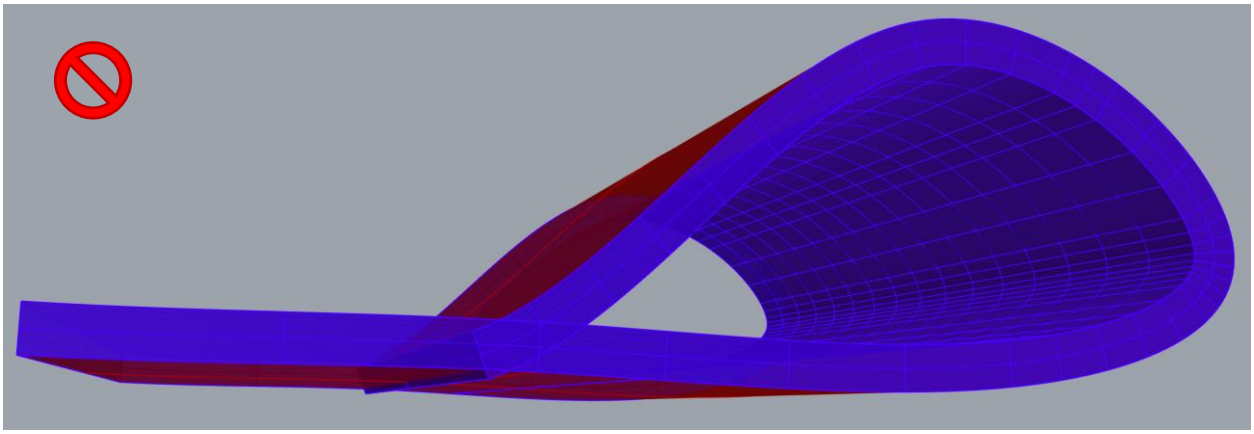

Figure 54: Even though the target surface itself (shown in red) does not intersect itself, the offset region shown in violet (representing the domain that tiles may occupy) does, indicating that either a thinner offset region for tiles must be used, or alternately the red surface must be adjusted to increase the distance between close loop-back regions.

Designing the Repeating Unit of Rigid Tiles, Prior to Offsets.

The next step in generating the array was to develop the basic geometry of the repeating unit of tiles, with parameters for offsets on the tiles' edge faces that can be varied according to the curvature at lockup that is desired (the calculation of the offsets will be discussed in greater detail below). The geometry chosen for this chapter was the result of considerable trial and error as to specific geometric features that tiles should possess for this application (with some previous tile geometries that were tried and rejected shown in Appendix III). The first relevant feature needed is a chamfer at the base of the tile for increased free fabric area between tiles (shown in Figure 55 and Figure 56) to ensure that the pre-lockup stiffness is low by ensuring that the free fabric area is not so short as to be excessively stiff in bending. Indeed, if glue fully coats fabric (which becomes increasingly likely due to gluing errors and glue spreading via surface tension), the substrate would become very stiff indeed, comparable to a single-layer fabric layup of Kevlar-reinforced polymer (unless the fibers break in the polymer matrix from the bending, in which case post-lockup stiffness would be lost). Using tiles without chamfers at the base would result in low unbonded fabric area (even without any seepage of glue into areas not directly in contact with the tiles), and it is easy to imagine that excessive glue could totally cover some areas of the fabric due to operator error during gluing.

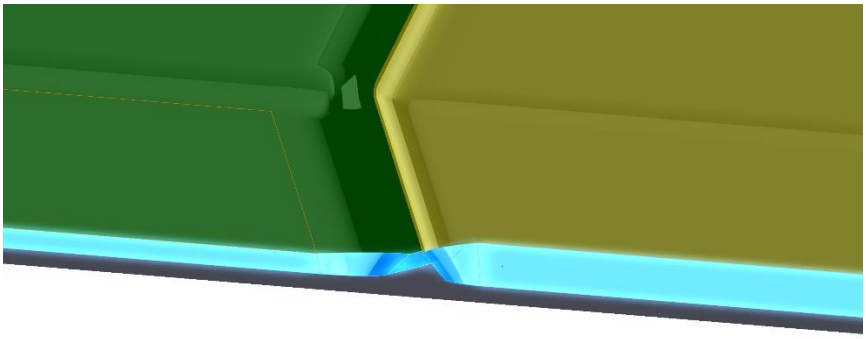

Figure 55: Side view of two tiles highlighting the chamfer feature added (highlighted in light blue) to the bases of the tiles to reduce the area of the fabric that is bonded to the tiles, thus increasing the amount of free fabric that can bend prior to lockup. See the next image for a zoomed-out view.

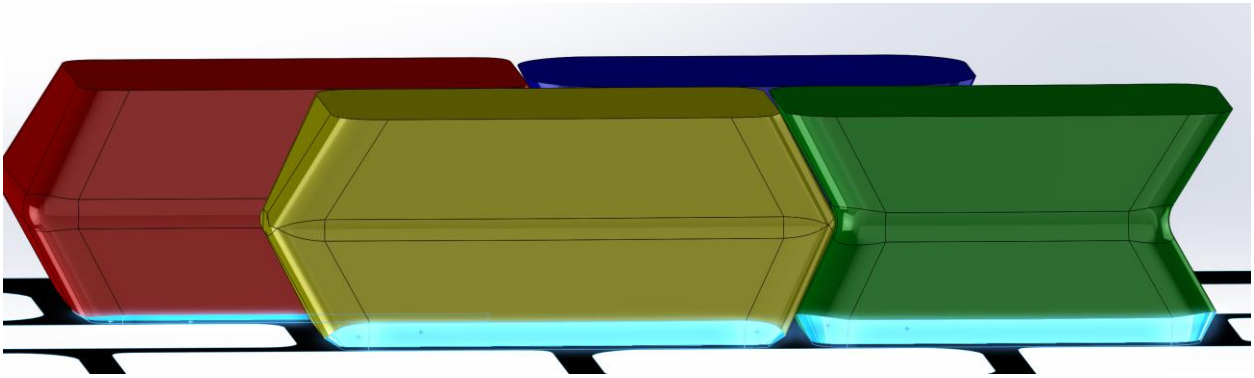

Figure 56: Zoomed-out, side view of all four tiles in the repeating unit, with the chamfer feature highlighted in light blue on the yellow, green, and red tiles; the region of fabric that is not bonded to the tiles is also shown in black (the larger the chamfer, the larger the unbonded fabric region as shown in black).

Additionally, the tiles should have interlocking features such that a given tile cannot be displaced normal to the surface (at least without inducing local bending that will in turn increase the restoring force), thus making the tiles "self-centering". One way to achieve this was with a repeating unit consisting of four unique tiles, with each tile having a surface that is either concave inward or outwards on its *x* and *y* edges: the tiles are color-coded to distinguish them, and the red tile is convex outwards in both the *x* and *y* directions; the blue tile is concave outwards in the *y* direction but concave inwards in the *x* direction (mating with the convexity of the red tile that is alternated in the *x* direction with the blue tile); the yellow tile is concave in the *y* direction (mating with the *y*-direction convexity of the red and blue tiles) and convex in the *x*

direction; and the green tile is concave in both *x* and *y* directions (so that it mates with the convexity of the yellow tile in the *x* direction and the convexity of the red and blue tiles that are tiled in the *y* direction). The "doubly-imbricated" concept is illustrated with several renderings for clarity, first with a top-down view in Figure 57 (with the *x* and *y* axes also drawn); then in a view normal to the *y* axis in Figure 58 (with the *x* and *z* axes also drawn); and finally in a view normal to the *x* axis in Figure 59 (with the *y* and *z* axes also drawn).

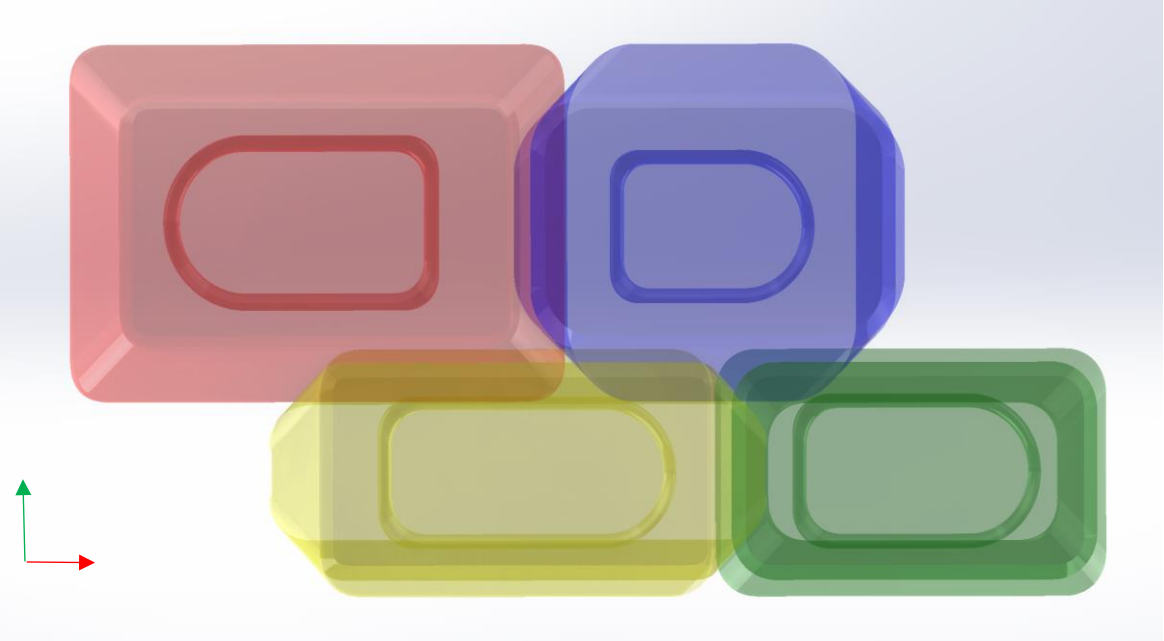

Figure 57: Top-down view (with tiles made transparent) showing interlocking features, specifically a pattern of concavity or convexity in the vertical and horizontal directions (red is convex in both, blue is convex in the vertical direction but concave in the horizontal, yellow convex in the horizontal but concave in the vertical, and green concave in both). The "D"-shaped embossed cuts at the bottom of each tile will be explained later. The x-axis is drawn in red, and the y-axis is drawn in green.

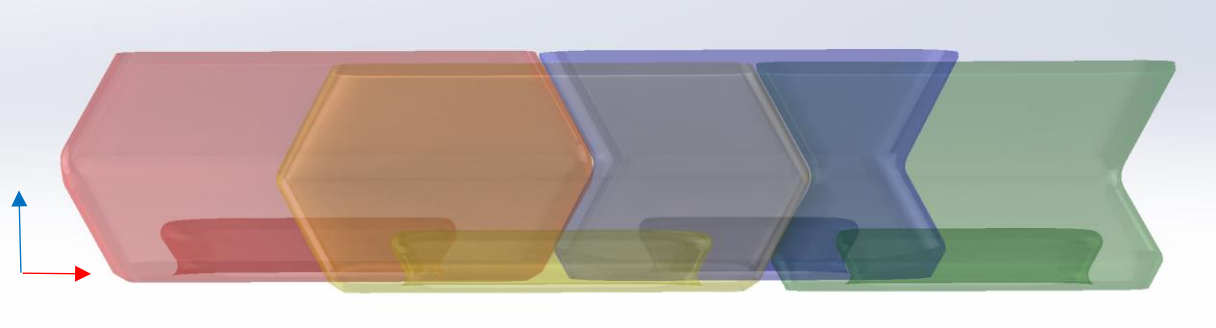

Figure 58: Front view of the repeating unit, with the view normal to the y-axis, with x axis drawn in red, and z-axis drawn in blue.

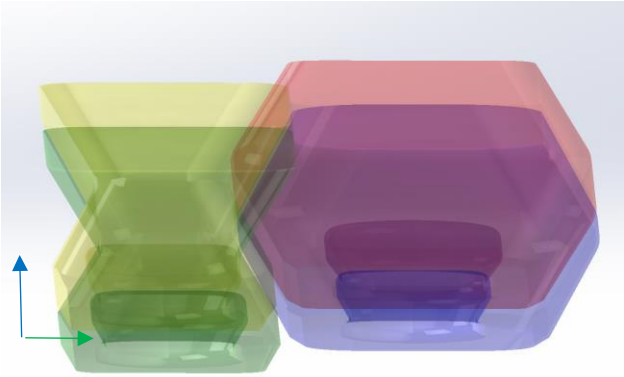

Figure 59: Side view of the repeating unit, with the view normal to the x-axis, with y axis drawn in green, and z-axis drawn in blue.

Additionally, four tiles should not meet at a shared corner, but rather one row of tiles should be offset horizontally from the previous row, much as bricks are generally laid in a wall. (In this researcher's experience, having four tiles share a corner results in spurious added shearing freedom or added bending freedom along the line of curvature defined by the diagonals, since corners can never be perfectly sharp, and indeed there are reasons to prefer rounded/filleted corners, such as avoiding stress concentrations and reducing warpage during 3D printing). An improper, non-offset unit cell is shown in to contrast with the proper, offset unit cell shown in Figure 57-Figure 59.

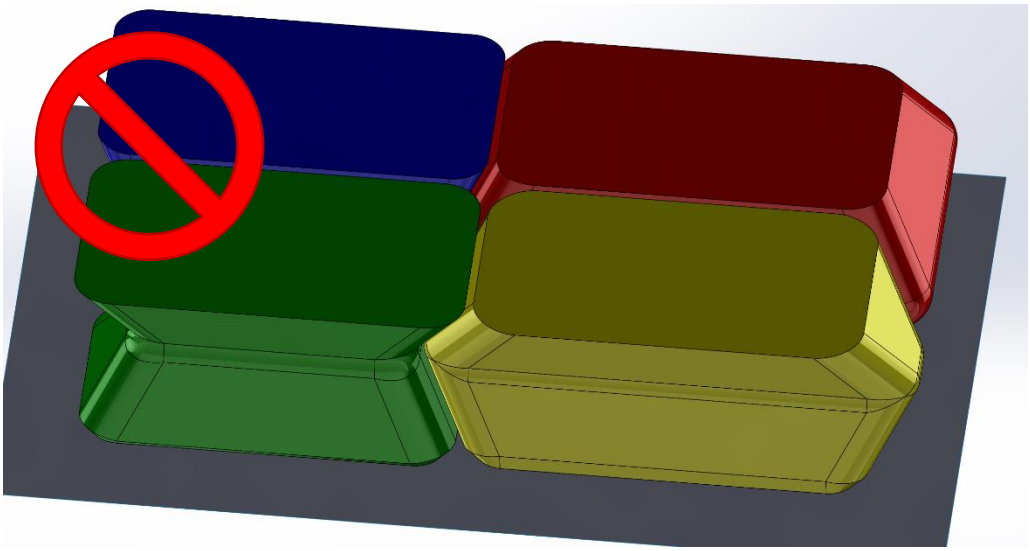

Figure 60: Improper unit cell: no horizontal offset between the row with red and blue tiles and that with yellow and green tiles. Note the shared corner in this unit cell, which can be a locus for added (undesirable) freedom along the diagonals.

Analyzing the Curvature of the Underlying Surface in Preparation for Calculating Tile Gaps.

In order to precisely calculate the *x*-direction offsets for each tile, it was first necessary to calculate the instantaneous curvature on the underlying curve (that is, the curve that was extruded to give the target surface) at the midpoint between the two non-offset tiles. This can be accomplished in several different ways. The most analytic approach is to represent the curve with an interpolating function and to calculate its curvature algebraically; in fact, there are many ways to represent spline curves: simple curves with no inflection points can be represented with Hermite or Bezier curves, whereas more complicated curves (with more control points, inflection points, knots, etc.) may require higher-order B-splines or NURBS curves to represent them accurately. Since this curve does not have a single inflection point, it may be reasonably accurately represented as a single cubic Bezier curve; the approximating single cubic Bezier curve is shown highlighted in yellow (along with its control points), with the true curve shown in pink, in Figure 61. Of course, there is some slight deviation between the single cubic Bezier

curve and the ideal curve; for greater accuracy, one could construct a piecewise spline to fit the original curve exactly.

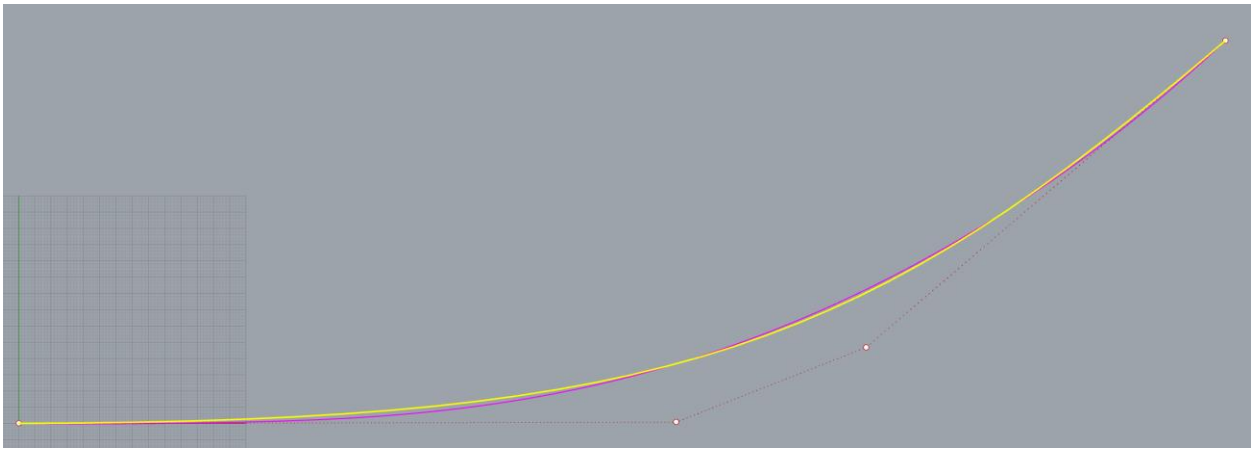

Figure 61: An approximating single cubic Bezier curve is shown highlighted in yellow (along with its control points), with the true curve shown in pink.

The underlying equation for any cubic Bezier curve can be generated from a knowledge of the four control points' *x*, *y*, and *z* coordinates, plus the basis functions required for a cubic Bezier curve (these prescribe how the curve interpolates between the points and are also known as Bernstein polynomials of order 4 and degree 3); this will return a set of three functions that give *x*, *y*, and *z* for the curve in terms of a single length parameter (here denoted *u*; in some other texts, it may be denoted *t* or *s*). The following matrix equation gives $x(u)$, $y(u)$, and $z(u)$ [81]:

$$[x\ y\ z] = [u^3\ u^2\ u\ 1]\begin{bmatrix} -1 & 3 & -3 & 1 \\ 3 & -6 & 3 & 0 \\ -3 & 3 & 0 & 0 \\ 1 & 0 & 0 & 0 \end{bmatrix}\begin{bmatrix} x_1 & y_1 & z_1 \\ x_2 & y_2 & z_2 \\ x_3 & y_3 & z_3 \\ x_4 & y_4 & z_4 \end{bmatrix} \tag{4.1}$$

For the specific Bezier curve shown in Figure 61, the four control points have the following *x*, *y*, and *z* coordinates, shown in Table 1. Note that the *y* coordinates of each control point are all 0, which means that the curve is planar (specifically, on the *xz* plane). In general, for this process, the extruding curve that defines the target manifold should be a planar curve and extruded along the weft direction; otherwise, the fabric will have to shear to follow the manifold.

Table 1: Control point coordinates for the single approximating cubic Bezier curve shown in Figure 61.

Control Point Number	x-coordinate (mm)	y-coordinate (mm)	z-coordinate (mm)
1	0	0	0
2	202.583	0	0.358
3	261.126	0	23.368
4	371.802	0	117.762

Consequently, by using the coordinates and basis functions for a Bezier curve, we may obtain cubic functions parametrized with respect to *u* (where *u* varies, by convention, from 0 to 1 and corresponds to the length traveled from the first control point to the last control point; note that the first and last control points of a Bezier curve are on the curve, whereas the intermediate two are not on the curve but bound the curve. If a Bezier cubic spline does not have an inflection point, it will not cross the control "open polygon" that is defined by drawing lies from the first to the second, second to third, and third to fourth point). This gives the following parametric functions for this curve:

$$x(u) = 196.2u^3 - 432.1u^2 + 607.7u, 0 \leq u \leq 1 \tag{4.2}$$

$$y(u) \equiv 0 \tag{4.3}$$

$$z(u) = 48.73u^3 + 67.96u^2 + 1.074u, 0 \leq u \leq 1 \tag{4.4}$$

From these equations, an equation relating the instantaneous curvature at any parameter *u* on the curve (between 0 and 1 inclusive) can be developed from the basic equation for the curvature of a space curve:

$$\kappa(u) = \frac{\|\vec{r}'(u) \times \vec{r}''(u)\|}{\|\vec{r}'(u)\|^3} \tag{4.5}$$

where the vector function $\vec{r}(u)$ is simply the sum of the $x(u)$ parametric equation times the x-direction unit vector with the corresponding equations and unit vectors for y and z. Performing the needed algebra first gives the following intermediate derivatives:

$$\vec{r}'(u) = (588.5u^2 - 864.2u + 607.7)\vec{\imath} + 0\vec{\jmath} + (146.2u^2 + 135.9u + 1.074)\vec{k} \tag{4.6}$$

$$\vec{r}''(u) = (1177u - 864.2)\vec{\imath} + 0\vec{\jmath} + (292.4u + 135.9)\vec{k} \tag{4.7}$$

Next, the cross product of the two vector functions in the numerator is calculated with the determinant method as follows:

$$\vec{r}'(u) \times \vec{r}''(u) = \begin{vmatrix} \vec{\imath} & \vec{\jmath} & \vec{k} \\ (588.5u^2 - 864.2u + 607.7) & 0 & (146.2u^2 + 135.9u + 1.074) \\ (1177u - 864.2) & 0 & (292.4u + 135.9) \end{vmatrix} \tag{4.8}$$

$$\vec{r}'(u) \times \vec{r}''(u) = (-10.26u^3 + 206350u^2 - 176400u - 83522)\,\vec{\jmath}$$

Clearly, the magnitude of the vector cross product shown above does not even require the usual square root of the sum of the squares of the x, y, and z components, since this particular cross-product only has a y component. However, the magnitude of the vector on the denominator of the curvature expression must be evaluated with square roots:

$$\|\vec{r}'(u)\| = \sqrt{(588.5u^2 - 864.2u + 607.7)^2 + 0^2 + (146.2u^2 + 135.9u + 1.074)^2} \tag{4.9}$$

$$\|\vec{r}'(u)\| = \sqrt{367700u^4 - 977400u^3 + 1481000u^2 - 1050000u + 369300}$$

Finally, the full expression for the curvature of the curve over the parameter u can be obtained by combining the above expressions as follows:

$$\kappa(u) = \frac{|-10.26u^3 + 206350u^2 - 176400u - 83522|}{\sqrt{367700u^4 - 977400u^3 + 1481000u^2 - 1050000u + 369300}^3} \tag{4.10}$$

This relation allows the curvature over the entire range of the curve to be plotted against the parameter u, as done in Graph 12. The radius of curvature, ρ, which is the numerical reciprocal of the curvature ($\rho = \frac{1}{\kappa}$), is plotted in Graph 13. Clearly, the curvature of this particular curve is numerically most intense at a point slightly past the midpoint of the curve (the midpoint being where u=0.5), which corresponds with the appearance of the curve. Certainly, the curvature is not constant (a circular arc, by contrast, would have constant curvature, though other conic sections would not).

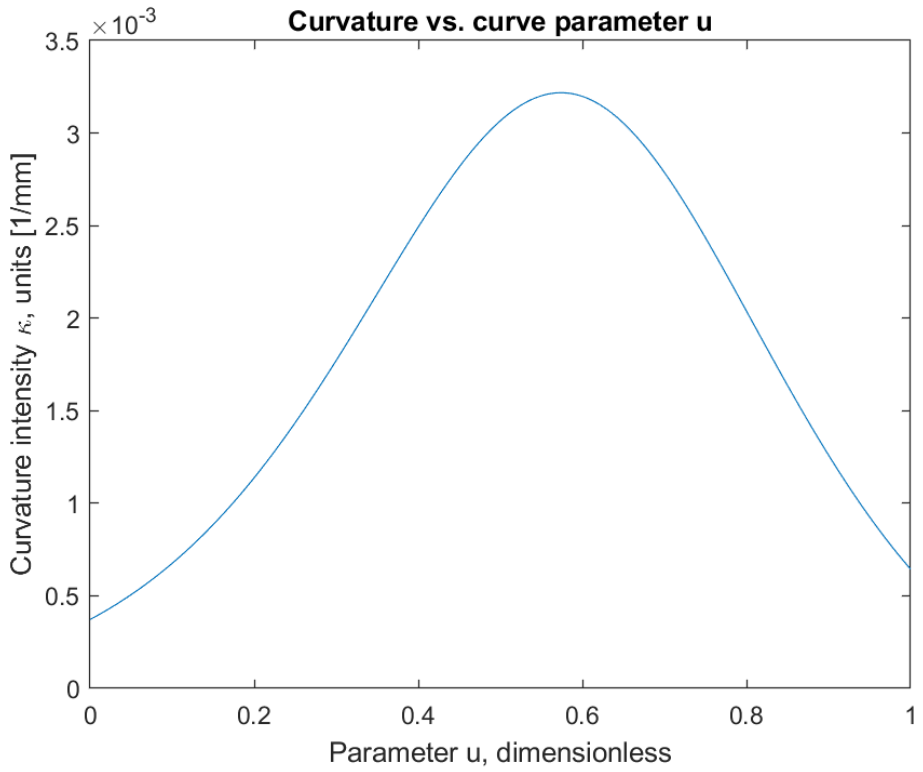

Graph 12: Variation of curvature intensity over the parameter u, *relating the fraction of the length of the curve travelled from the start to the end. Note that the dimensionless parameter* u *does not exactly correspond to the x-coordinate (it would only correspond to the* x*-coordinate if the curve was a flat, horizontal line, which would have no curvature of course).*

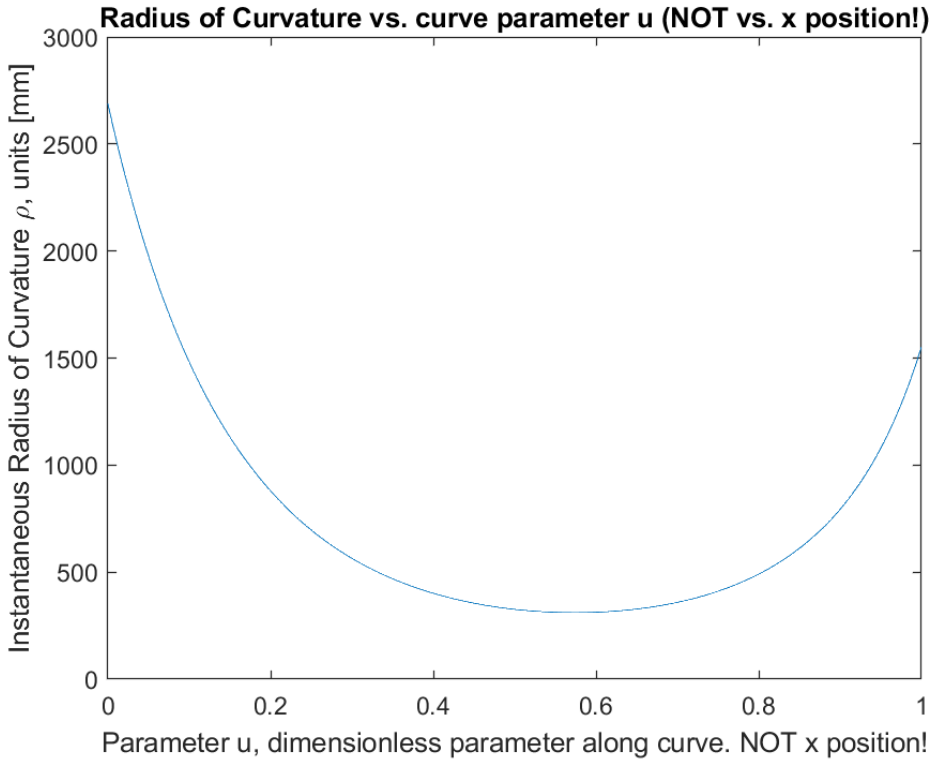

Graph 13: Variation of radius of curvature over the parameter u*, relating the fraction of the length of the curve travelled from the start to the end. It is stressed that this is not the x-position of a coordinate on the curved target surface (u is proportional only to the x-coordinate of the initial, flat surface, not the curved-up, target surface, in this case).*

Alternatively, it might make sense to plot the *z*-coordinates vs. *x*-coordinates of this (*xz*-planar) curve with one ordinate axis (thereby showing the overall shape of the curve) and plot the curvature vs. *x*-position of the curve with the other ordinate axis, as done in Graph 14. This graph was in fact scaled to ensure that the plot of the curve's *z*-coordinates vs. *x*-coordinates had a 1:1 scale, showing the true shape of the curve without distortion. This allows for easy visual comparison of the curve's shape with its varying magnitude of curvature.

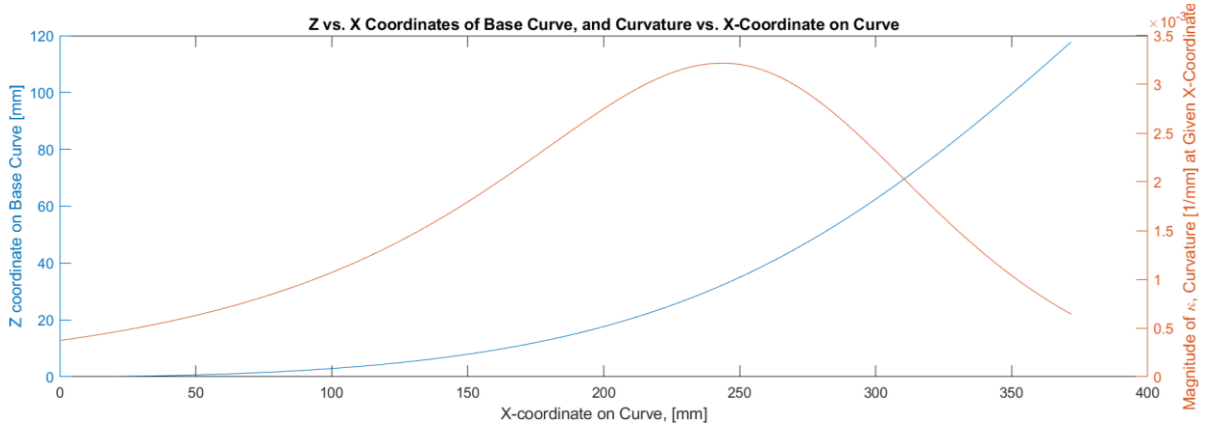

Graph 14: Plotting the shape of the curve in blue (z-coordinates vs. x-coordinates, since this curve lies in the xz plane), and the magnitude of curvature vs. the x-coordinate position in orange.

Armed with the numerical magnitude of the curvature of the curve over its length (whether measured by the *x*-coordinate, or by the dimensionless parameter *u*), it was then possible to compute the magnitude of the gap that should exist between each set of tiles to bring about lockup at the intended shape.

Tiling the Array and Adding Variable Offsets.

Once the unit cell was prepared, it was tiled over the rectangular flat surface, and then, crucially, variable offsets were added between the surfaces of each tile and those to the right and left (i.e. in the *x* direction as indicated with red arrows when axes are shown) as a function of the instantaneous curvature desired at that *x*-distance along the lockup-defining spline from the origin. Additionally, the offset for a given pair of tiles varies linearly as a function of distance from the neutral axis, i.e. with the height (in the *z* direction) from the base rectangular surface. Note that the offset in the *y* direction (the axis indicated with a green arrow) was very small and constant with respect to *x* and *y* coordinates (ideally it would be zero, but because of manufacturing constraints that will be discussed later, some small offset is required to prevent tiles from interfering in this direction when assembled, even though they are printed separately).

The final array, with offsets varying with respect to *x* and *z* but not *y* position, is shown in Figure 62; additionally, Figure 63 and Figure 64 contain closeup views of comparatively small and large offset gaps between teeth in the horizontal direction. The next subsection of this chapter will explain multiple methods of constructing the offsets.

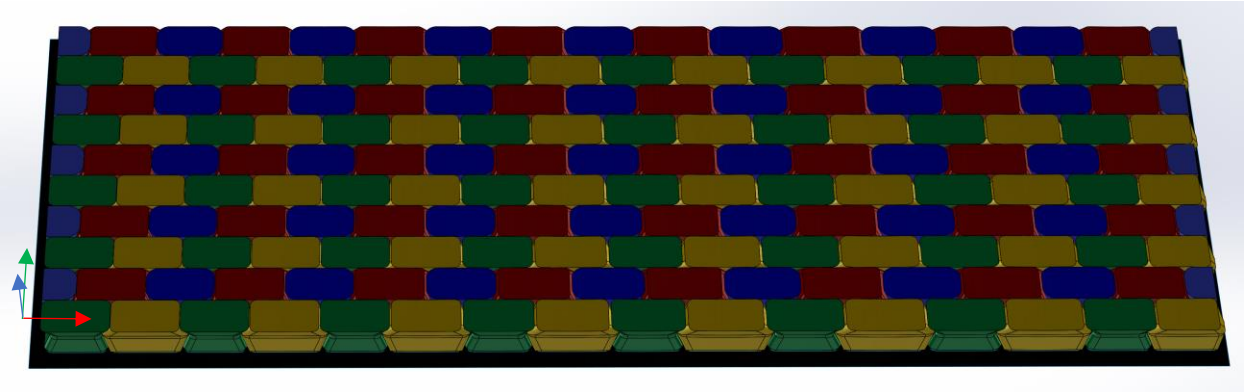

Figure 62: Overall view of array generated by tiling the repeating unit and after adding variable offsets with respect to x *and* z *coordinate and desired post-lockup curvature.*

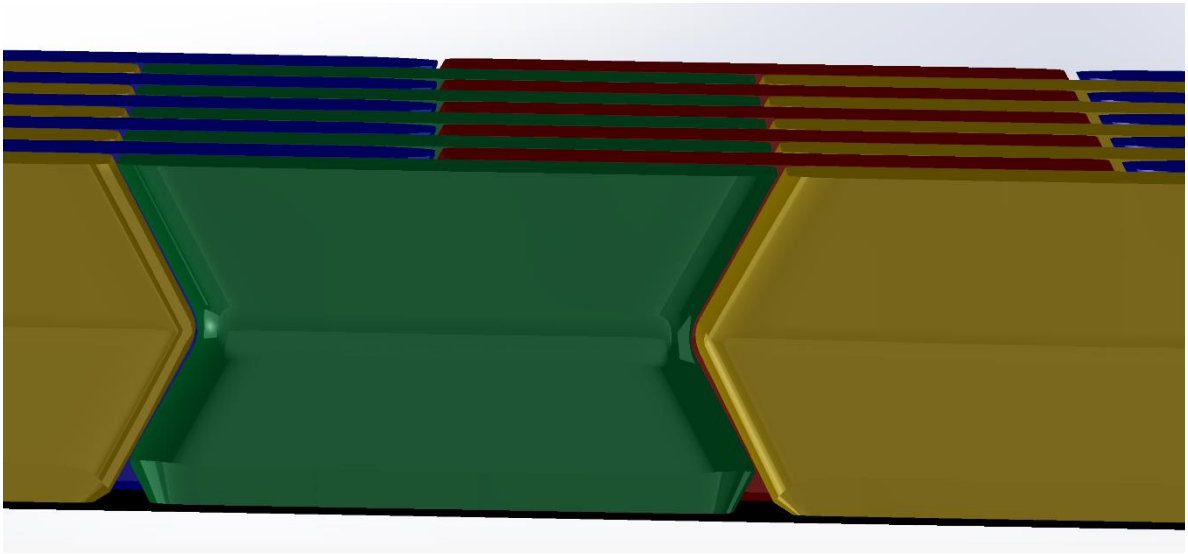

Figure 63: These teeth have small offsets between each other in the x *direction, because the average curvature of the target lockup surface is relatively low at the* x*-coordinate of the centroids of the green tile and adjacent yellow tiles.*

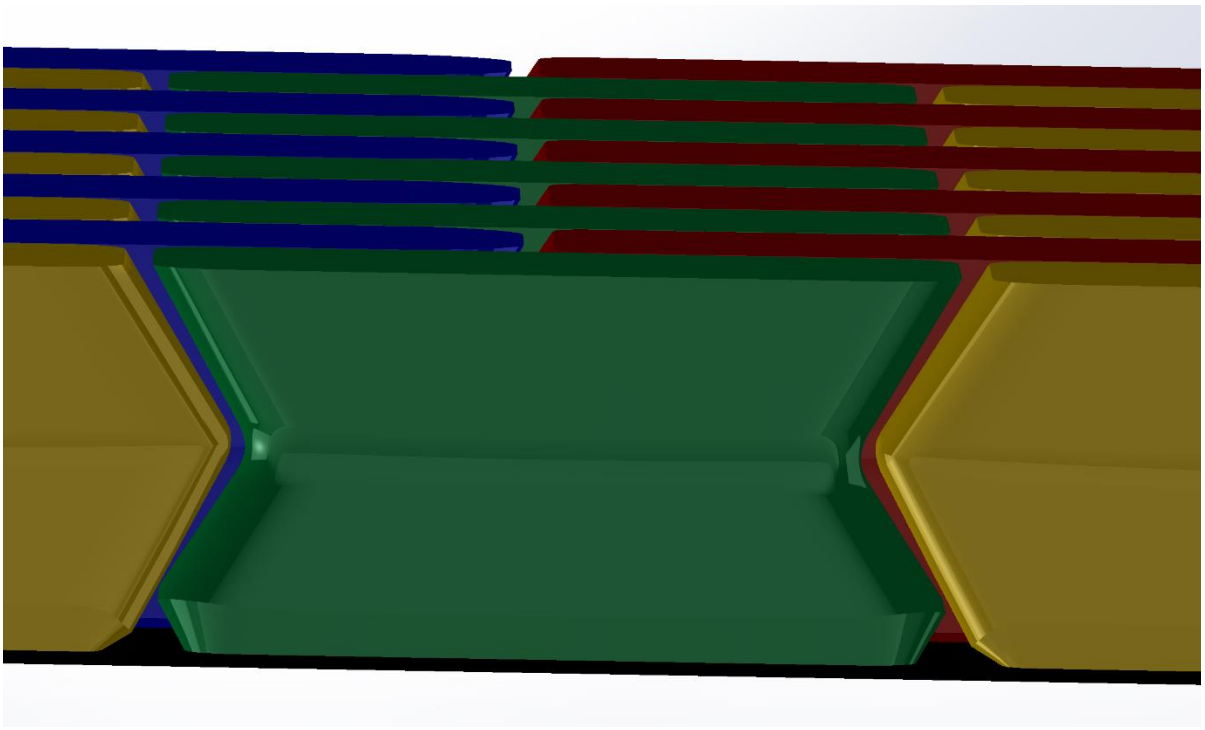

Figure 64: These teeth have larger offsets (as compared with the teeth in the previous figure) between each other in the x direction, because the average curvature of the target lockup surface is relatively high there.

Calculating Tile Offsets: Locally-Constant Curvature Method.

The simplest method for calculating the shape and relative positioning of the tiles required to produce lockup at the target curvature entails locally distorting each tile with an arc having a radius equal to the local radius of curvature of the lockup-target curve at the centroid of the tile.

This is a slight approximation, inasmuch as the curvature of the lockup-target curve in fact varies continuously (including over the length of each tile), but, if the tiles are sufficiently short (and generally small in all dimensions) with respect to the rate of change of the curvature of the curve with respect to travel along the curve (i.e. parameter u), it should be acceptable. For instance, using the example of this chapter, the longest tiles are the yellow tiles, having a bounding-box length of 30.71mm; the largest change in the radius of curvature of the lockup-

target curve (which occurs at the inflection points of the graph of curvature vs. parameter *u* as shown in Graph 12, i.e. where parameter *u* is 0.31 from the left end, corresponding to a length of 124.69mm from the left end) produces a radius of curvature of 470.133mm at the left end and 613.558mm at the right end of a hypothetical yellow tile placed there, and a radius of curvature of 515.716mm at the center, which differs somewhat from the geometric mean of the left and right-end local radii of curvature (537.08mm) as well as the arithmetic mean of the left-end and right-end local radii of curvature (541.84mm), but the difference is within 10%. Errors are necessarily smaller at other points on the curve where the curvature changes less rapidly. Graph 15 shows the average radii of curvature at each centroid-point for a tile at lockup on this array, plotted against the *x*-position of that tile's centroid when flat (not when locked up).

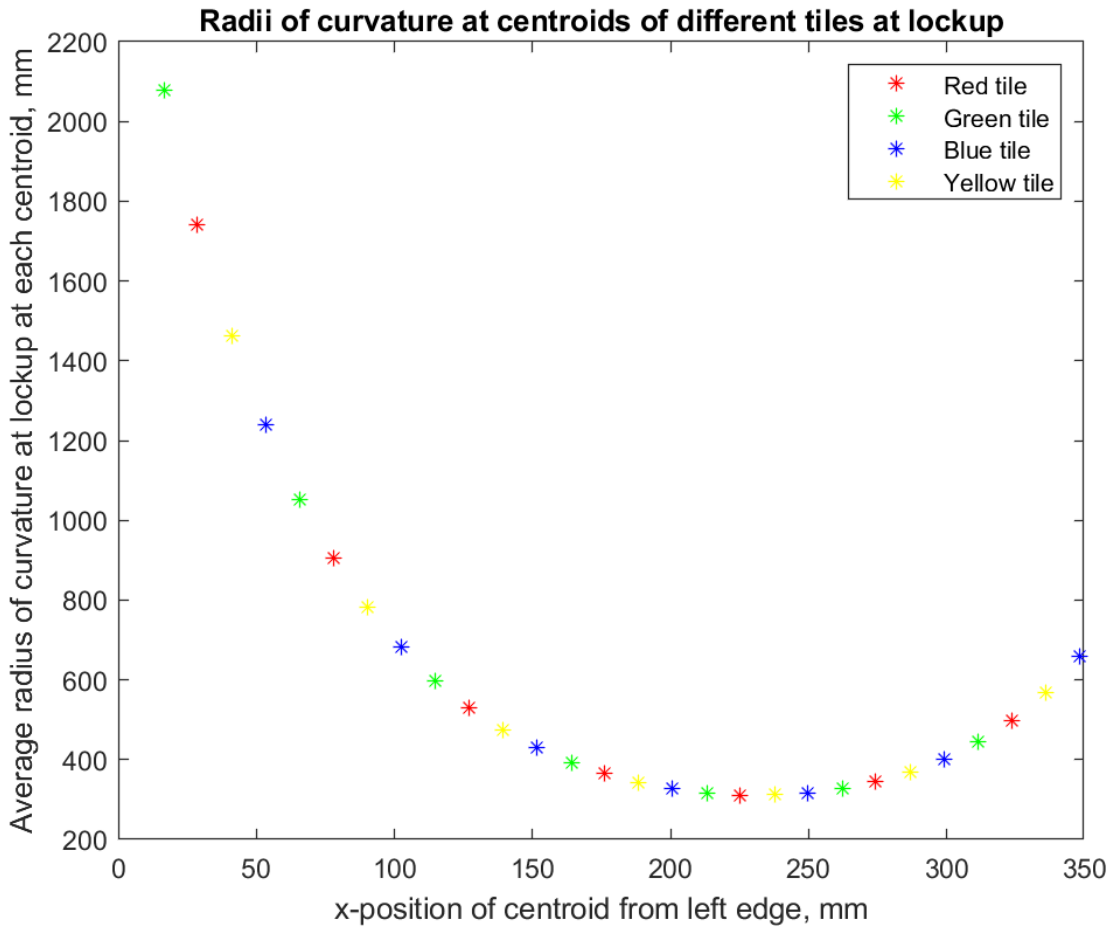

Graph 15: Average radius of curvature at lockup at each tile's centroid, plotted against the tile's x-position when flat.

Once the local radius of curvature is determined, the gap profile must be constructed. First, it should be noted that the added distance between a pair of tiles should vary linearly from 0 at the bottom to the full gap distance at the top surface. The full gap distance at the top surface is a function of the average radius of curvature at lockup at the centroid of the tile: using geometry and the Law of Cosines, the shape that a generic square must be bent into to result in lengthwise contact at a certain radius of curvature may be calculated as follows. First, the sector angle θ_{sector} must be found based on the quantity w_{old} (the width of the tile at its base) and the local radius of curvature ρ_{target} of the target surface:

$$\theta_{sector} = \frac{w_{old}}{\rho_{target}} \tag{4.11}$$

Next, an isosceles triangle on a bent version of the tile (the top and bottom surfaces do not matter when the curvature is small, but it is ideal to make them match the radius when the curvature is high) is constructed, from the center of the sector to the top of the tile (distance $\rho_{target} - h_{tile}$, where h_{tile} is the height of the tile); the Law of Cosines then enables the calculation of the width of the line at the top of the bent tiles (not to be confused with the length of the arc at the top of the bent tile, which is moderately different), giving the relation:

$$w_{top}^{new} = \sqrt{2\left(\rho_{target} - h_{tile}\right)^2 (1 - \cos\theta)} \tag{4.12}$$

Finally, the total linear distance between two tiles, Δ , can be calculated as follows:

$$\Delta = w_{top}^{new} - w_{old} \tag{4.13}$$

Armed with this quantity, the designer can either taper (in a trapezoidal deformation pattern, contracting towards the top) or bend the tile (e.g. with a cage transformation) about a point on the base surface that shares the *x*-coordinate of the centroid until the linear gap is achieved, or alternatively s/he may use extruded cuts with an initial offset of 0 at the base, ramping linearly up to the maximum width $\Delta/2$. An illustration of these quantities are shown for a generic tile (with rather tight target radius of curvature, it must be added) in Figure 65.

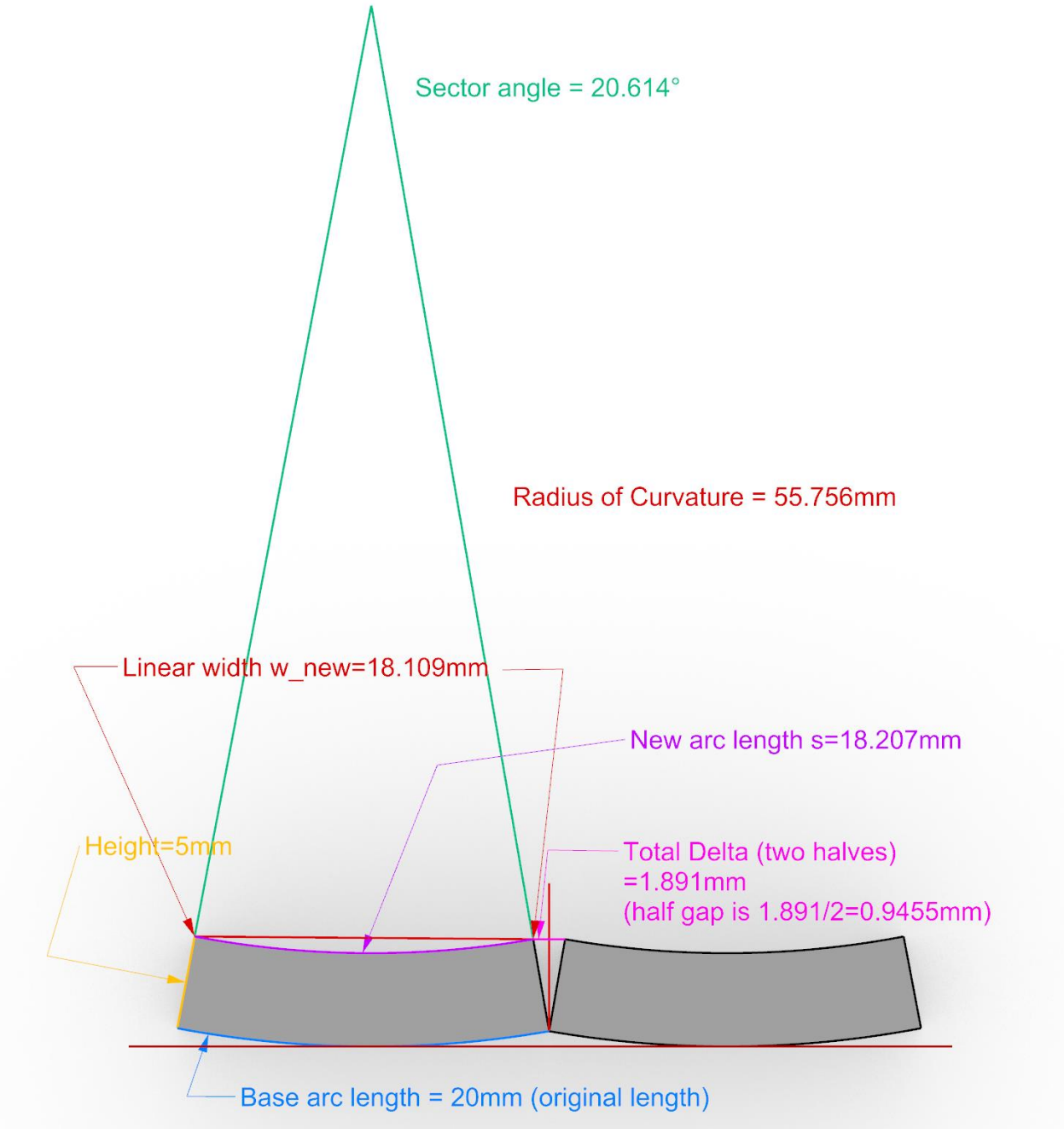

Figure 65: Schematic of the quantities used in calculating the gap between tiles that lock up in bending at this radius of curvature.

It should be noted that the foregoing analysis is for an initial surface that is totally flat; however, it is indeed possible to create a fabric-backed tiled array that initially conforms to a singly-curved rather than flat surface; the designer must follow the "bending" operations (or,

equivalently, make extruded cuts with the without then to make the tiles conform to the initial surface) to create tiles with the appropriate shape, then tile them on the initial surface, and then repeat the process on these already-modified tiles with the lockup surface profile to calculate the lockup shape.

Using the above methodology, the gap profiles for each tile on the example array in this chapter were calculated and sorted by color and plotted in three-dimensional surface plots. All calculations were in MATLAB, and MATLAB code is included in Appendix I. The x-axis of each plot corresponds the x-axis coordinate of the centroid of each tile; the y-axis to distance from the base surface (going from 0 up to the maximum height of all tiles, in this case 11.86mm for all tiles), and the *z*-axis corresponds to the half of the total distance between two tiles (i.e. $\Delta/2$, the distance from the edge of one tile to the centerline between the two tiles). Each graph is color-coded based on the color of tiles involved (which corresponds to their shape in terms of concavity and convexity in *x* and *y* directions), and, to aid visualization, the surfaces graphed are shaded with a gradient that makes them darker as *z* (representing the quantity $\Delta/2$) increases. The graphs are shown with the quantities plotted separately for the four different colors/classes of tiles in Graph 16 through Graph 19 below, and together in Graph 20 for comparison (the main comparison being that the red and yellow tiles are longer than the blue and green tiles, and consequently produce greater gaps for the same radius of curvature).

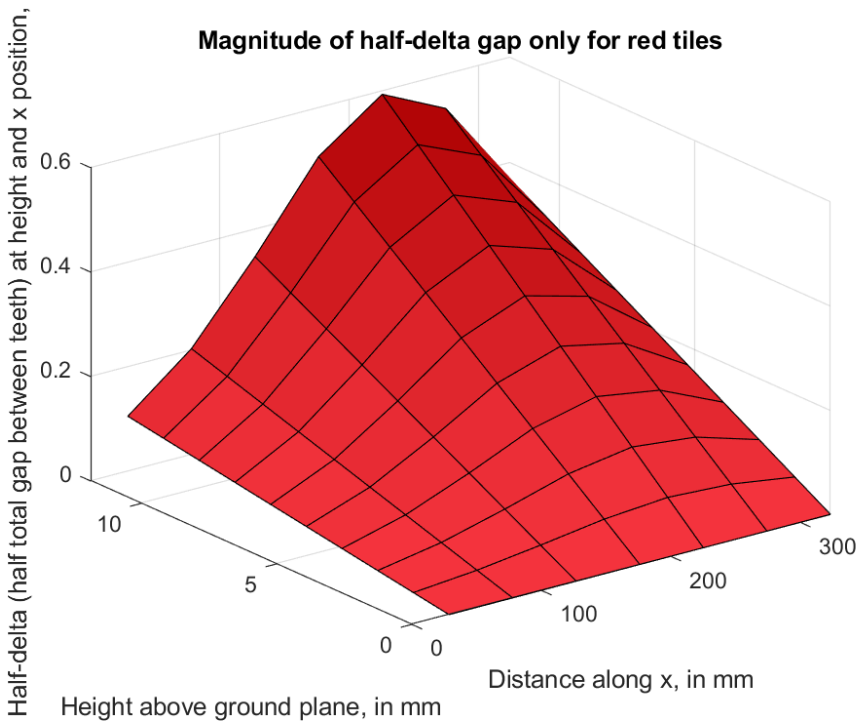

Graph 16: Plotting on the z-axis the quantity half the gap distance (i.e. $\Delta/2$) between two tiles at the instantaneous radius of curvature for the red tiles with centroids at the given x-positions (also plotted on the x-axis) and for varying distance from the bottom of the tiles to the top (which is plotted on the y-axis).

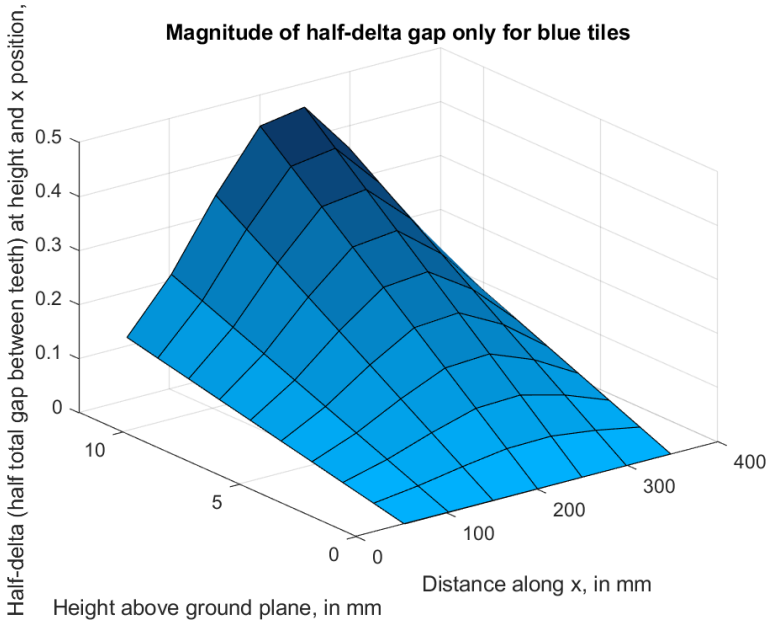

Graph 17: Plotting on the z-axis the quantity half the gap distance (i.e. $\Delta/2$) between two tiles at the instantaneous radius of curvature for the blue tiles with centroids at the given x-positions (also plotted on the x-axis) and for varying distance from the bottom of the tiles to the top (which is plotted on the y-axis).

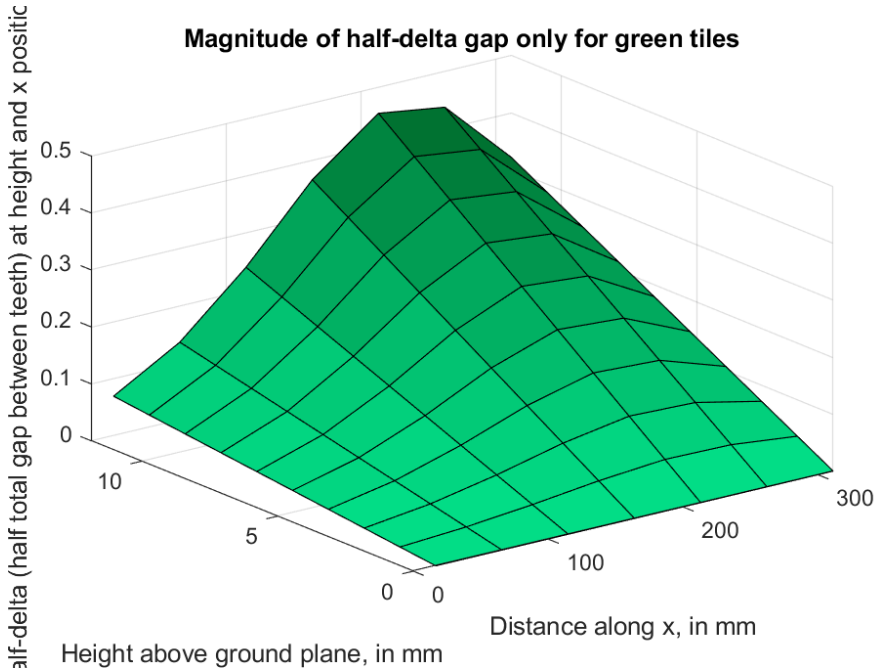

Graph 18: Plotting on the z-axis the quantity half the gap distance (i.e. $\Delta/2$) between two tiles at the instantaneous radius of curvature for the green tiles with centroids at the given x-positions (also plotted on the x-axis) and for varying distance from the bottom of the tiles to the top (which is plotted on the y-axis).

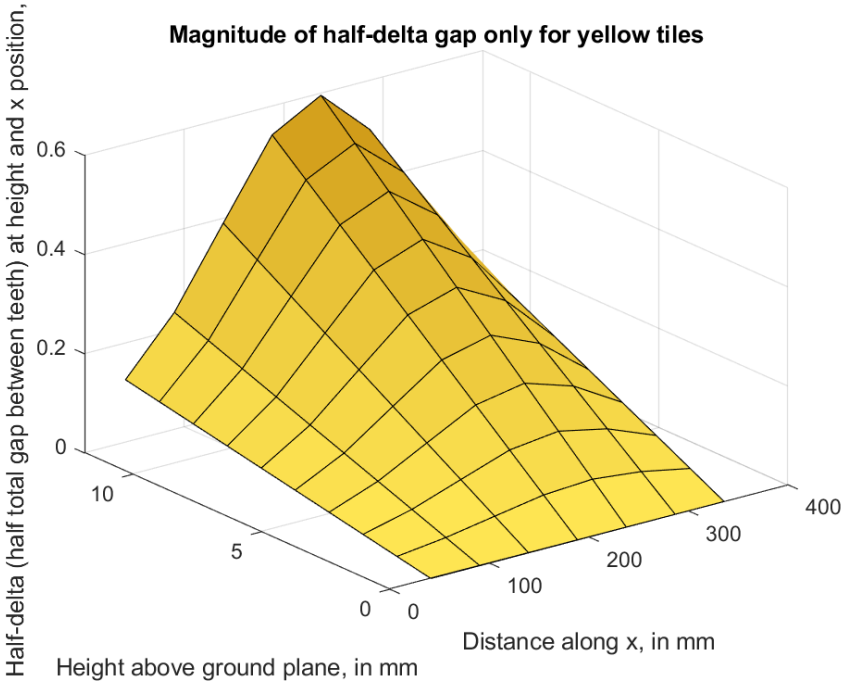

Graph 19: Plotting on the z-axis the quantity half the gap distance (i.e. $\Delta/2$) between two tiles at the instantaneous radius of curvature for the yellow tiles with centroids at the given x-positions (also plotted on the x-axis) and for varying distance from the bottom of the tiles to the top (which is plotted on the y-axis).

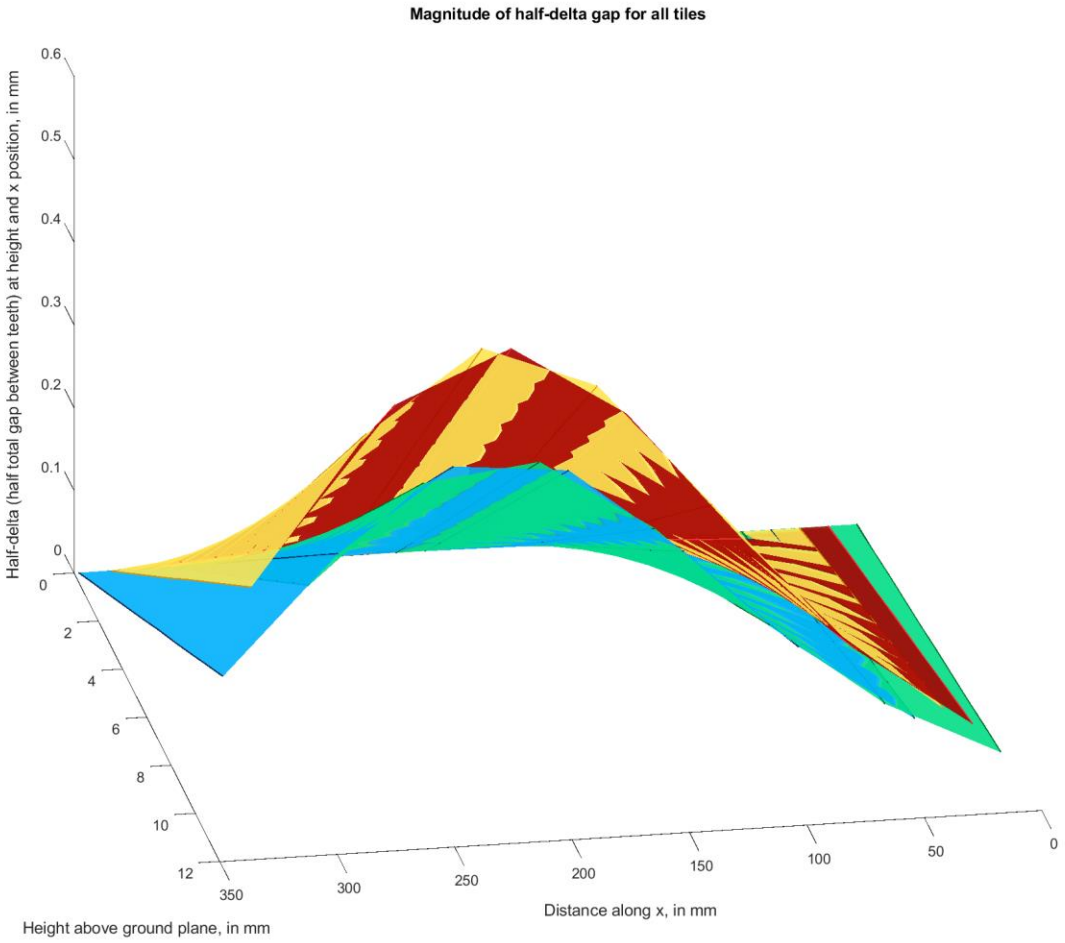

Graph 20: Plotting on the z-axis the quantity half the gap distance (i.e. $\Delta/2$) between two tiles at the instantaneous radius of curvature for the red tiles with centroids at the given x-positions (also plotted on the x-axis) and for varying distance from the bottom of the tiles to the top (which is plotted on the y-axis), with each surface colored by tile type. Note that the gaps are somewhat greater for the red and yellow tiles as they are longer than the blue and green tiles.

Constructing Offset Tiles: Other Methods

Another method for calculating tile gaps could be to use a CAD package to construct a constant-offset-distance surface from the target surface, offset by the height of the tiles, where the offset represents the top surface that the tiles are to take on (and the original, non-offset curved surface the bottom surfaces of the tiles, which are in contact with the fabric). The *u*-coordinate (parametrized with respect to length) of the right and left edges of each tile on the

base surface could be mapped to the same *u*-coordinate on the offset surface, and vertical lines drawn between the two points to illustrate the target shape.

A final method could make use of cage transformations or similar, requiring the matching of control points on the control object to corresponding control points on the target surface. This method is the most general method and allows one to conform to doubly-curved surfaces.

Manufacturing of the Array.

The ideal method for manufacturing a single array of this type is with additive manufacturing, partly because it is a one-off production, but additionally because there are many different parts to be made (specifically, because of the variable offset required in the *x* direction between tiles, there are eight sets of different tiles, and in each set, there are four unique tiles). Additionally, because three out of the four unique shapes in each unit cell have undercuts that would require extra machining axes to produce, they cannot be produced on a 3-axis mill, requiring at least 4 axes even with specialized workholding devices and preferably 5 to obviate the workholding devices. Fortunately, modern fused deposition modeling (FDM) 3D printers are easy to use and can rapidly produce the needed parts with acceptable quality, although end-use applications might benefit from better precision and smaller tile sizes (best achieved with injection molding, which has the added benefit of higher manufacturing volume, although other 3D printing processes, like SLA, can also achieve excellent resolution).

However, there are many important manufacturing considerations that must be taken into account; it would not be wise to simply export the CAD model shown in Figure 62 as a single STL and print it directly. First, the tiles need to be totally separated mechanically (rather than fused together), yet positioned very precisely relative to each other; as can be seen in Graph 16

through Graph 20, many tiles have horizontal gaps on the order of less than 0.4mm, and the *y*-direction gaps are always nominally zero; note that FDM printers generally cannot resolve gaps between parts that are not a large fraction of the nozzle width (though printing parameters and printer quality affect this).

As such, the tiles will need to be printed separately to prevent them from fusing together, yet with features that enable them to be precisely indexed with as small a gap as possible in the *y* direction, and the appropriate gaps (ranging from 0.1mm to 0.95mm) in the *x* direction; additionally, the tiles will ideally be non-interchangeable in the *x* direction, in order to guard against manufacturing error. The tiles could be precisely positioned and temporarily held with a separate workholding device that could also be 3D printed, with features that allow the tiles to be slid onto the fixture from the right side in a direction tangential to the surface; once all of the tiles have been bonded to the fabric, the entire assembly can be lifted off the workholding device. Figure 66 shows the cut features added to the tiles to allow them to be held by the workholding device, Figure 67 shows a rendering of the tiles positioned on the workholding device, and Figure 69 uses a section view to illustrate how the extruded features on the workholding device hold and position the tiles.

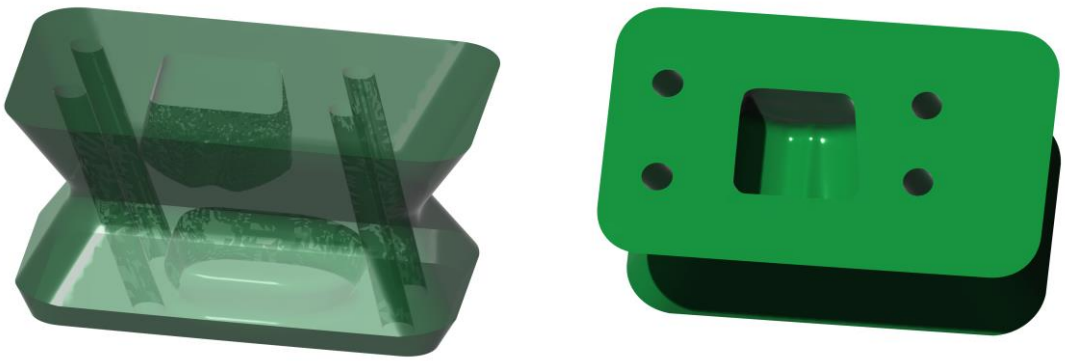

Figure 66: Extruded cut (asymmetric trapezoid in cross-section, with added rotary features allowing for some rotation to wiggle the tile onto the mating extruded surface) feature into one tile, allowing it to be placed onto the corresponding feature in the

workholding device, then slid in one direction to temporarily prevent the tile from moving vertically away from the workholder. The transparent view on the left illustrates the depth of the hole.

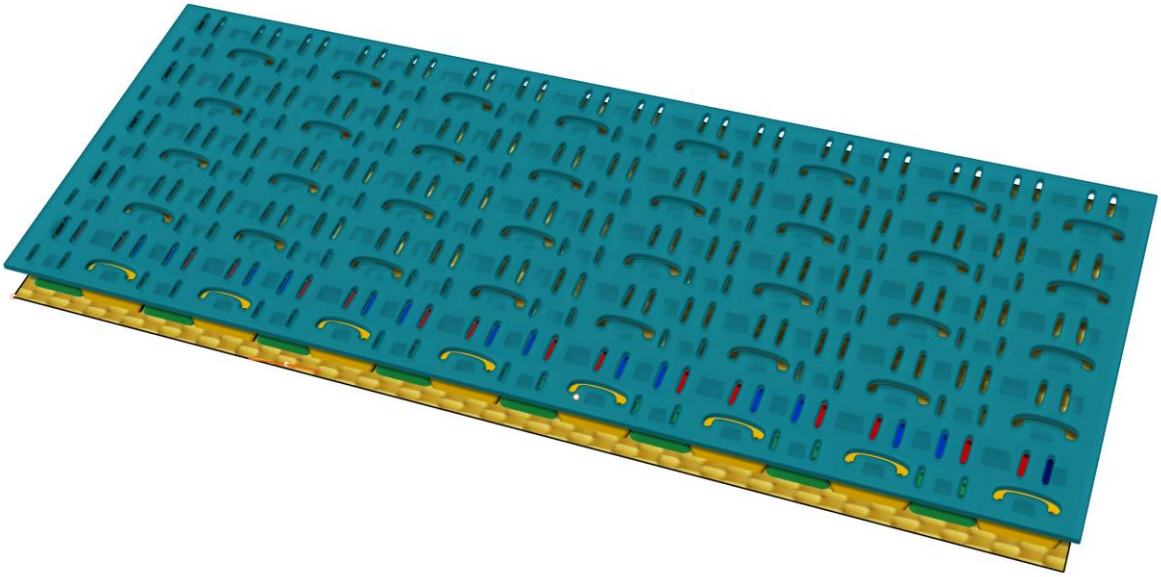

Figure 67: Overall underside view of the workholding device, positioning tiles.

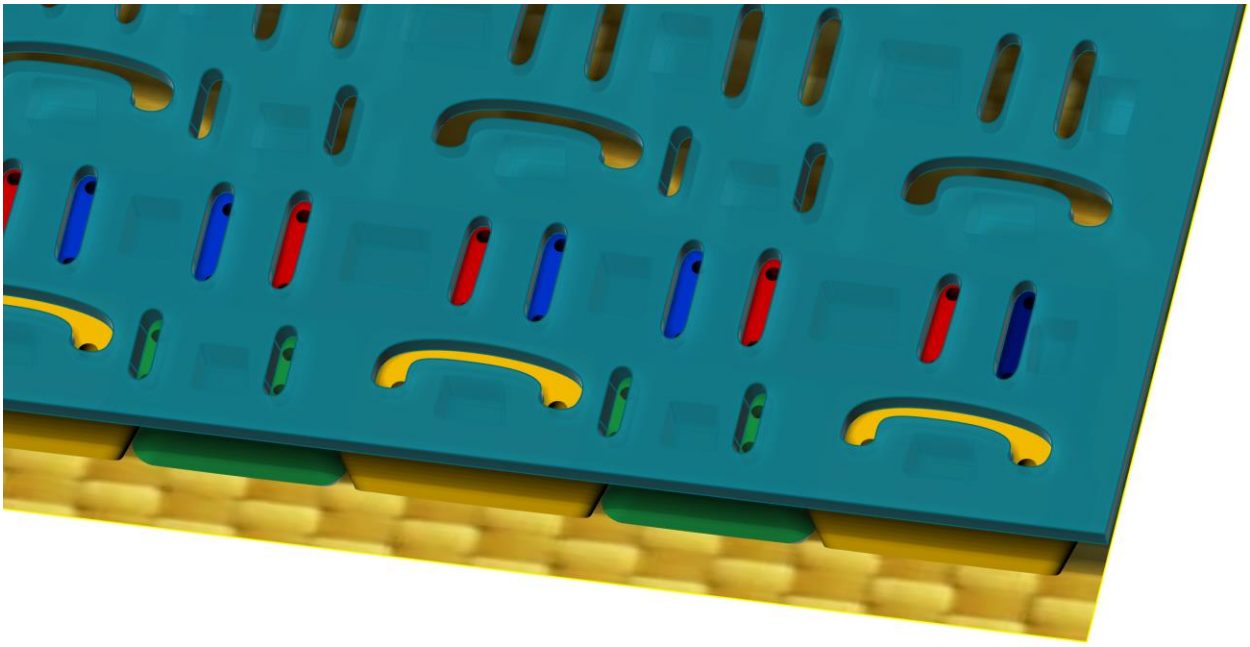

Figure 68: Closeup view of a row of tiles assembled on the workholding device.

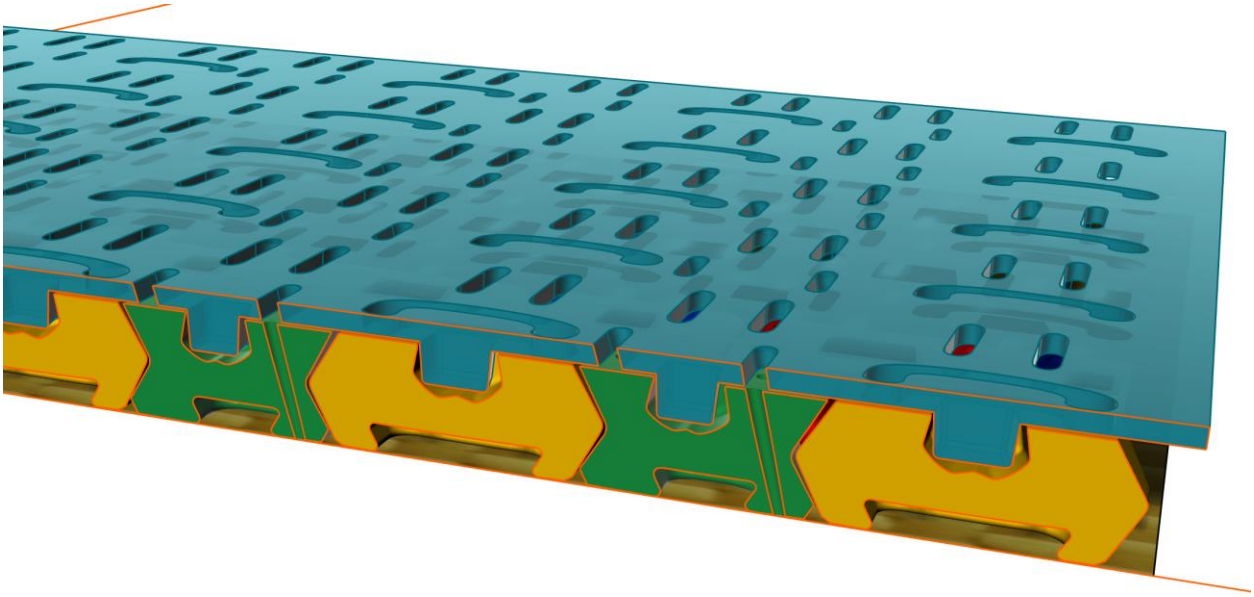

Figure 69: Section view (with sectioning curves shown in orange) of assembled tiles on the workholding device and fabric underneath.

The tiles also had cylindrical holes through which to pass a threaded needle to allow sewing of the tiles to the fabric, and the workholding device had corresponding features cut into it (shaped like the letter C) to ensure that the thread would not bind the tiles to the workholding device (which would prevent them from coming off unless the thread was cut, which would defeat the purpose of sewing). However, sewing proved unnecessary as the cyanoacrylate bond between tiles and fabric was quite reliable, so the extra work of sewing was generally not undertaken, though one tile was sewn to the fabric just to test the methodology, with the result shown in Figure 70. Figure 71 shows the entire workholding device as printed. The cut in the corner indicates where to start applying the tiles.

Figure 70: One tile and its corresponding button were sewn to the fabric with Kevlar braided rope to test the feasibility of sewing. The left image shows the top of the tile and the right image shows the underside of the button/rivet.

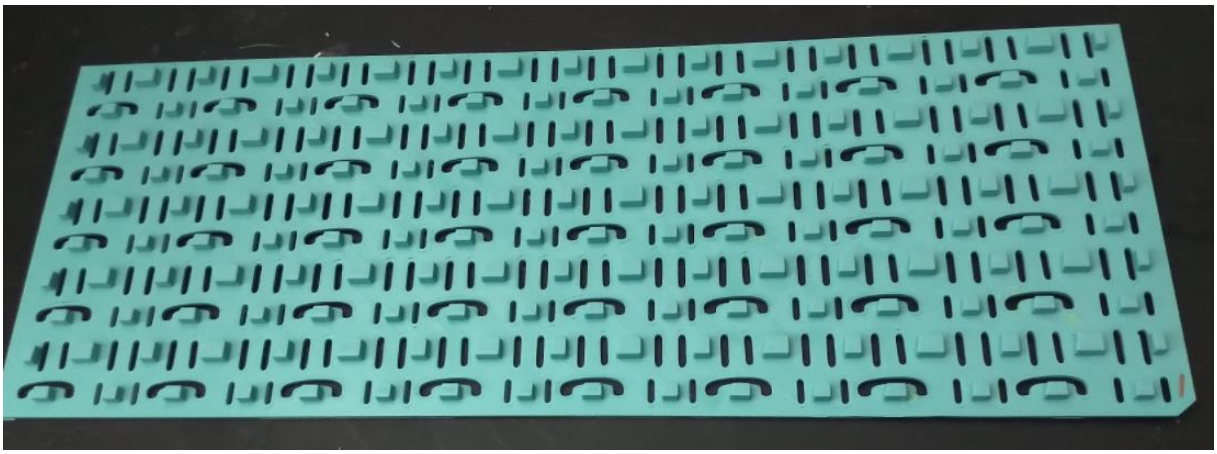

Figure 71: Overall view of workholding device for the precise positioning of tiles, as printed on an FDM 3D printer.

Once the tiles are precisely positioned relative to each other, it is necessary to permanently affix them to the fabric. In this researcher's experience, it is not effective to glue woven fabrics to flat faces as the bond tends to be weak against peeling forces; instead, each tile should have a cup-like depression with an inward draft in part of what will become the bottom face (facing the fabric), and a precise amount of adhesive used to coat this cup; then, a plastic part that must be printed separately called a "button" or "rivet" will be forced over the fabric with a press-fit, thereby not only coating the fabric with adhesive, but itself providing some resistance to the fabric being removed. A rendering of the tile and button with some offset

between them (to allow for a press-fit that sandwiches a fabric of thickness of around 0.6mm) is shown in Figure 73, and a rendering of the tile attached to the fabric with this method is shown in Figure 73.

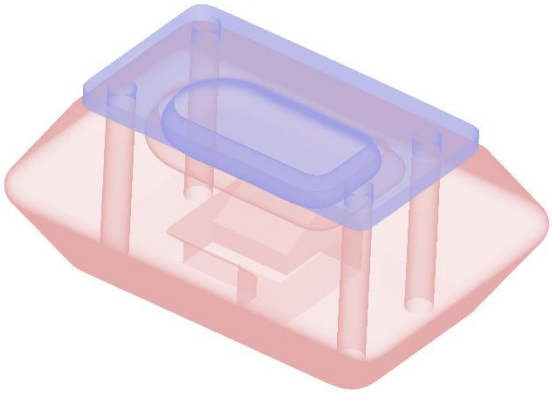

Figure 72: Button (shown in purple) and tile (shown in pink), transparent view to show the glue-holding cup in the tile and inset anvil on the button that presses the fabric into the cup on the tile.

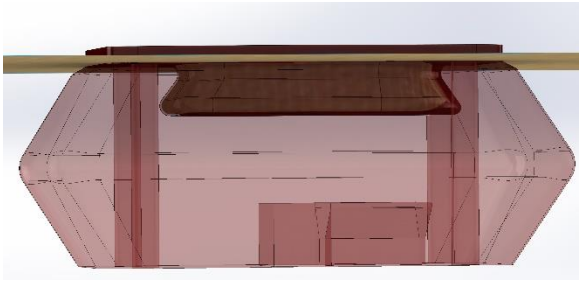

Figure 73: Tile attached to fabric by forcing a button into the inward-drafted cup (previously filled with glue). Note that there is an offset between the tile and button that is not visible once the fabric contours around the button—otherwise it would be too difficult to press the button in.

Experimental Evaluation of Manufactured Array for Post-Lockup Curvature.

Once designed, the tiles were printed individually (rather than in array) in PLA (polylactic acid), a stiff if somewhat brittle thermoplastic that is well regarded for ease of printing without warping, which additionally makes it one of the best FDM feedstocks for dimensional accuracy. The pieces were printed with the "cups" (for glue) facing down; thus, the features that index on the workholding piece were facing up, not requiring any support material

(which might otherwise reduce the precision and smoothness of these features and thus make it difficult to slide the part on and off). The tiles were printed with modest infill, several perimeters and top/bottom layers, and a 0.4mm nozzle (0.48mm line width for most features). Even on printers of modest quality and cost like the FlashForge Creator Pro [82], surface quality and resolution of details was more than acceptable, although precision and accuracy are hardly synonymous (i.e. it remains to be seen how accurately tolerances were met, which will be determined by the bending deflection of the array). Figure 74 shows a view of an individual tile after printing and removing support material but prior to assembly (note that tiles were kept separately, in numbered containers based on their position from the origin, as even tiles of the same color are not interchangeable; there was little space on the surface of the tile to emboss or engrave a number, though subsequent chapters that used larger tiles do involve such physical numbering to avoid confusing tiles).

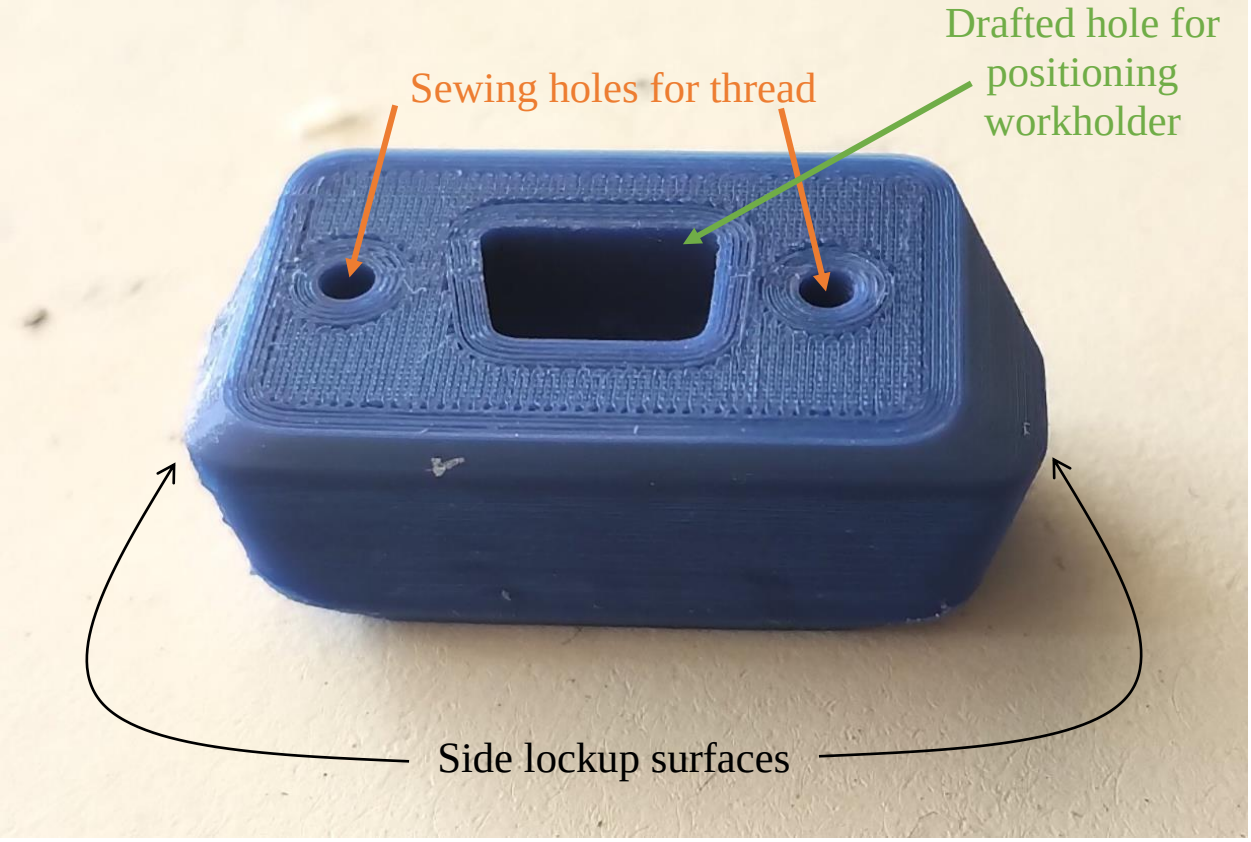

Figure 74: This tile corresponds to yellow tile #5 from the left (it was printed in blue PLA owing to a shortage of yellow PLA). Compare to the underside view in the next Figure.

Figure 75: Underside view of a single tile.

After all tiles were printed, they were assembled on the workholding device by number, then cyanoacrylate glue was poured into the exposed cups on the tiles, the fabric placed over the tile with uniform tension, and the button forced into the cup (with a hammer if necessary). Figure 76 shows the fully-assembled array. Of note, while the entire width was tiled (because the curvature varies over the width, i.e. in the *x*-axis direction), the full depth was only tiled in some areas, and in others a depth of four tiles was glued, in order to save time gluing (as it is a labor-intensive process, and the goal of this chapter was merely to test the lockup curvature and general manufacturing process). Figure 76 shows the structure as manufactured in the initial configuration.

Figure 76: Array as manufactured, in a flat configuration. The weave is somewhat distorted; the fringed edge should follow the blue line, but in fact deviates ever more notably from it.

It was noted during the assembly of the array that the fabric weave becomes highly distorted by the buttons when they are being pressed in, both locally and globally. Local distortion is due to the depth of the projections on the buttons, and it is likely that the local distortions add up to produce global distortion. The local distortion around the fabric weave after riveting is shown with a closeup image in Figure 77, and Figure 78 shows how the weave conforms to the extruded boss of the rivet/button after gluing with a rivet that has been removed (this rivet was glued with hot glue so it could easily be removed; the others were glued with cyanoacrylate, which created a very tenacious bond that could not be manually torn even with pliers, though no precise quantification of the bond strength was made).

The global distortion is evident in Figure 76 (shown above), where the difference between the actual edge shape of the fabric and the correct edge shape indicates that the fabric was accidentally sheared during the manufacturing process, resulting in the warp and weft not being exactly orthogonal to the tiles (or to each other). To combat this, it might be wise to

construct guides for the fabric in the future, to ensure that it is always properly aligned relative to the tiles.

Much of the problem stems from the fact that extra length and width of fabric is consumed by the "riveting" of the tiles to the fabric than the footprint area would indicate, owing to the undulation of the fabric around the rivet boss (i.e. the starting sheet of fabric must be both wider and longer than the final array owing to the undulations); these undulations can be seen around the extruded boss feature on one button/rivet in Figure 78, and the local distortion resulting in nearby areas of the weave is shown in the underside view of the array that is printed in Figure 77. To reduce the distorting impact of these undulations, the tiles must be "riveted" in monotonic order in the *y* direction (i.e. starting at the bottom and working to the top, or vice versa, rather than riveting both top and bottom, then working inwards), because and riveting both ends first would leave insufficient fabric for other tiles (preventing the button from being pressed in, as the Kevlar fabric is very stiff in tension).

Figure 77: Underside of the assembly, showing rivets and the distortion in the weave that resulted from riveting.

Figure 78: Distortion in the weave from the extruded boss on the face of each rivet (top side view, not underside view). One tile was glued with hot glue and ripped off to illustrate the weave distortion from the rivet.

It is unclear what the practical effects of fabric distortion are, given that the array was successfully manufactured. It is unlikely that it significantly impacts the curvature at lockup, but if the fabric is locally reoriented by a significant rotation (on the order of 45°), bias compliance might come into play along the load path, resulting in the membrane being able to deform significantly in tension, at least until shear locking, and thus some spurious freedom being added. (However, it might be localized enough that the redundancy of having several rows of identical tiles would prevent any noticeable excessive freedom).

Finally, a sheet having the target curvature profile (to which the array is supposed to bend up and then lock up) was also 3D printed, with cup-shaped depressions for the rivets, to evaluate the accuracy of the manufacturing method and design method used to create the tiles. This thin shell structure is shown by itself in Figure 79.

Figure 79: Two views of the thin shell with the lockup profile for testing the lockup curvature of the manufactured array.

The fabric-backed tiled array was then clamped to one end of the lockup-testing shell, and the other end raised until lockup was felt, and the tip displacement measured at 38.44mm with calipers, as illustrated in Figure 80 and Figure 81. Admittedly, this quantity would ideally be 0mm.

Figure 80: After manufacturing and assembling the array and testing it on the 3D printed curvature-testing manifold, there was some undesirable further deflection of the tip possible. This was measured with calipers to be 38.44mm, and elastica theory was later used to estimate how much inaccuracy in the average achieved radius of curvature there was.

Figure 81: Closeup view of the persistent tip offset between the target curvature and the achieved curvature.

Numerical Approximation of the Actual Deformed Shape and Comparison with Ideal Shape.

While any deviation from the target curvature is evidence of imprecision, 38.44mm of deviation is not as meaningful as it may first appear, because it is the deflection of a cantilevered

beam of considerable length (approximately 400mm), and because a beam's tip displacement is based on the integration of its slope (related to its curvature, assuming small displacement), modest slope errors will be integrated over distance to produce larger displacement errors, especially at the tip of a long beam. A more accurate measure would be the root-mean-square deviation of the instantaneous curvature of the actual surface vs. the target surface, sampled at several points. To calculate this, an elastic curve was first estimated from the tip deflection, as shown in Figure 82.

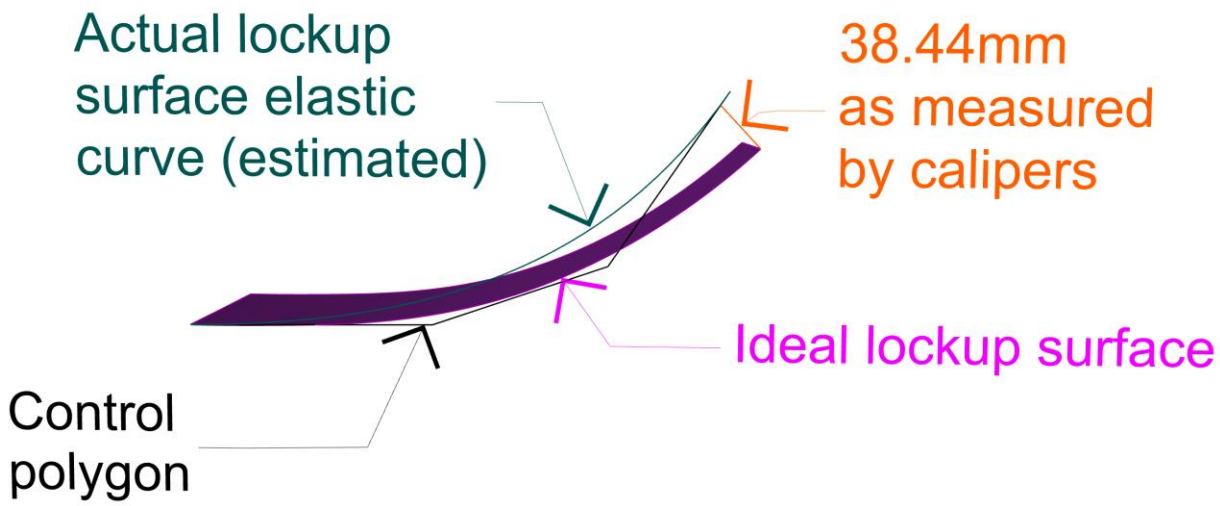

Figure 82: Estimated elastic curve of the actual lockup surface (teal), compared with the ideal lockup surface (purple), from the tip offset (orange).

This elastic curve was rebuilt so that it would be a cubic Bezier curve with four control points. The control points were then determined and reprinted in Table 2.

Table 2: Control point coordinates for the cubic Bezier curve approximating the elastic curve of the actual lockup surface (as distinct from the ideal lockup surface).

Control Point Number	x-coordinate (mm)	y-coordinate (mm)	z-coordinate (mm)
1	0	0	0
2	159.454	0	1.463

3	273.828	0	40.745
4	351.846	0	154.684

Using the Bezier basis equation, the elastica spline was found to have the following parametric form:

$$x(u) = 8.72u^3 - 135.24u^2 + 478.36u, 0 \leq u \leq 1 \quad (4.13)$$

$$y(u) \equiv 0 \quad (4.14)$$

$$z(u) = 36.84u^3 + 113.46u^2 + 4.39u, 0 \leq u \leq 1 \quad (4.15)$$

In turn, the curvature intensity and instantaneous radius of curvature were plotted for both the engineered target curve and the elastic curve approximating the shape with an extra 38.44mm of tip deflection in Graph 21 and Graph 22, respectively.

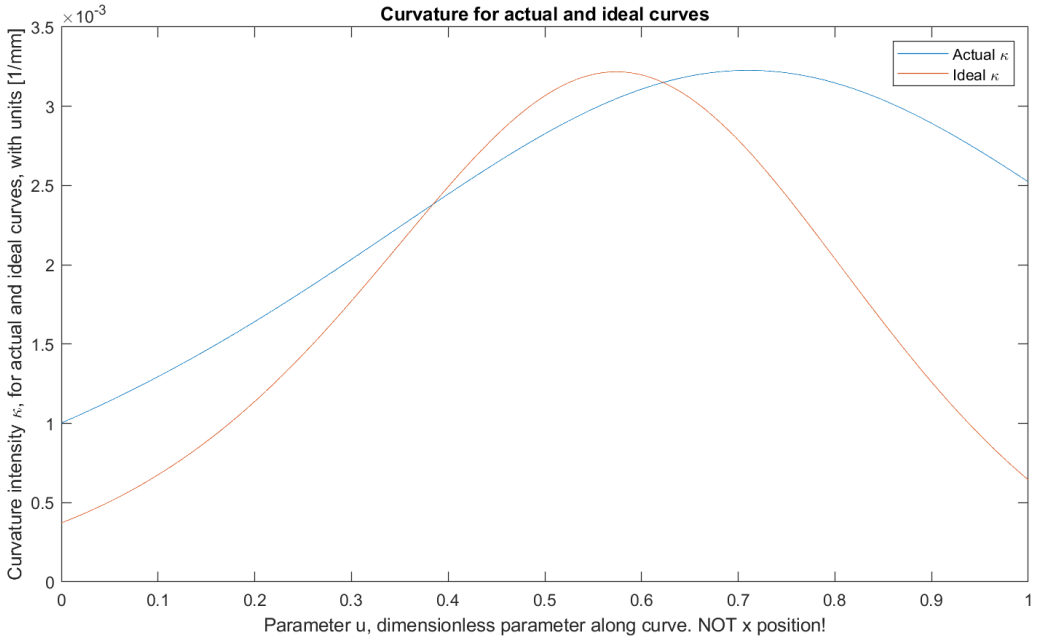

Graph 21: Curvature intensity for the elastic curve corresponding to tip deflection of 38.44mm above what is desired ("actual") vs. ideal target curve's curvature.

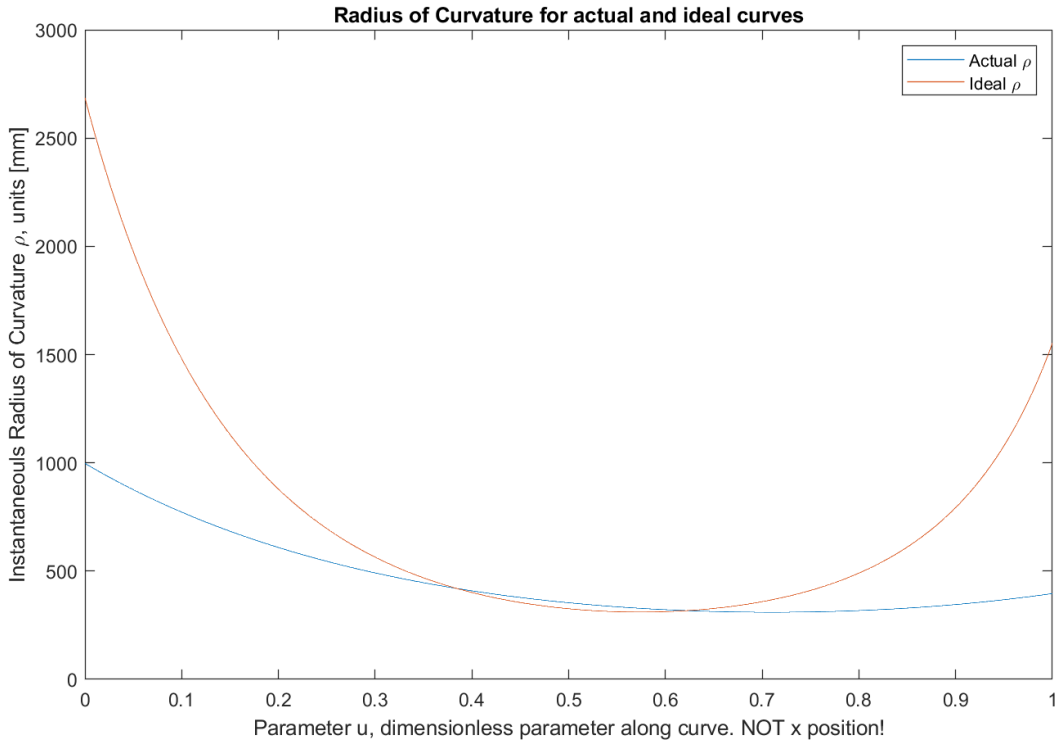

Graph 22: Radius of curvature for the elastic curve corresponding to tip deflection of 38.44mm above what is desired ("actual") vs. ideal target curve's curvature.

Finally, the curvature intensity values for the two curves (real and ideal) were compared with a root-mean-square formula (in MATLAB; code is in Appendix II), giving an RMS error for curvature intensity of $0.0261mm^{-1}$, corresponding to a radius of curvature error of 38.31mm. Thus, the error in the array's bending configuration may not be as dramatic as it initially appears.

Sources of Manufacturing Error.

The probable sources of this error of excessive freedom before lockup are quite diverse. The most obvious is imprecise replication of the CAD geometry by 3D printing; the printers used were uncalibrated and not necessarily accurate even to 0.2mm when uncalibrated, so both tiles and the workholder may have been out-of-spec: if the tiles were overextruded or scaled over 100%, less curvature at lockup than engineered would be the result, and if they were

underextruded or scaled under 100%, more curvature lockup than desired would be the result. If the workholder were out of spec, it might position the tiles further apart than desired (which would create excessive freedom before lockup), or too close together (which would result in less freedom than desired before lockup). Additionally, it should be noted that there were small added offsets (0.05mm everywhere) added between the tiles for FEA purposes (discussed in the next chapter), in order to prevent interpenetration of mesh elements in FEA; this may have contributed to the excessive freedom shown by this sample.

A more-complicated but significant source of error is the fabric weave being distorted significantly by the rivets and general manufacturing errors, both locally (see Figure 77) and moreover globally (from additive effects of local distortion plus large misalignment of the fabric relative to the tiles, as shown earlier in Figure 76 and immediately below in Figure 83): sufficient distortion in the weave could cause local reorientation of the fabric bias, introducing undesired added compliance in the fabric itself and delaying the full tensile stiffness of the fabric until the added freedom of the local reorientations of the trellis mechanism was entirely taken up. If an application is identified for these arrays, future research should investigate the amount of precision needed in manufacturing to achieve the target precision in lockup shape and tip deflection, as well as propose modifications to the design of the rivets/buttons so that they do not introduce so much distortion (pure sewing may be a preferable means of attaching the tiles, albeit more time-consuming).

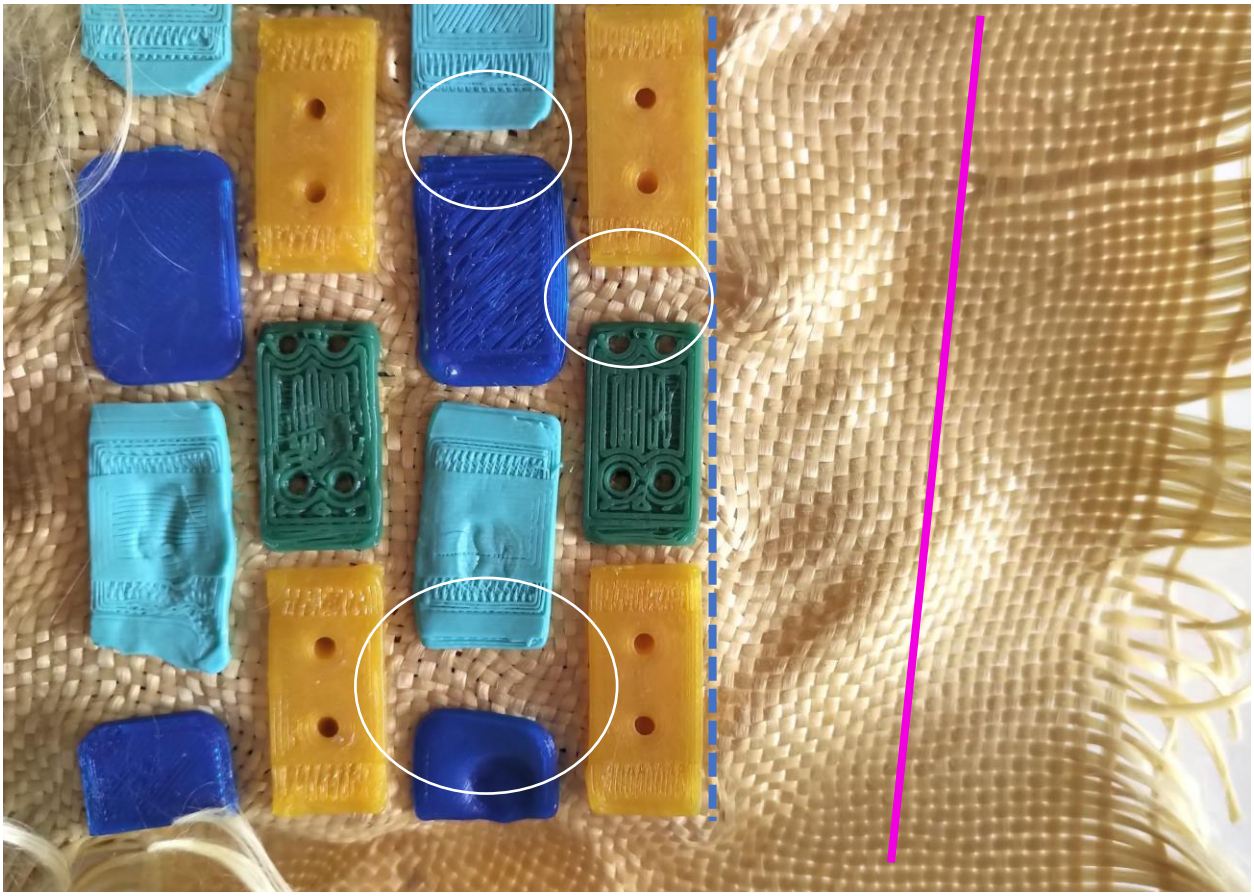

Figure 83: Comparison of local and global distortion in the weave from rivets and manufacturing errors, respectively. A few regions of local distortion between rivets are circled in white; note the "whorled" pattern of the weave there. In contrast, the global distortion consists of the tiles being misaligned with the warp yarns; the actual warp yarn orientation is indicated in pink, whereas it should instead follow the dotted blue line.

Of note, the only direction that was engineered for lockup was upwards bending. It would be possible to limit the maximum curvature (and program a shape) for bending in the opposite direction if, instead of rivets, full tiles were used on the reverse. Currently, with simple rivets, the structure is able to roll up reasonably tightly in the direction opposite that of lockup; Figure 84 illustrates the behavior of the array when bent in the opposite direction. Note that while the structure can be curved quite tightly and rolled up on itself, there is eventually interference (partly between rivets) that limits the radius of curvature to which it can be rolled up. Note that no engineering or design of its unbending properties was undertaken as this was not deemed important; if the designer wished to create an array that could be rolled up even more

tightly, modifications to the rivets (reducing their width and thickness) or replacing rivets entirely with sewn threads only would be logical.

Figure 84: Unbending (i.e. bending in the opposite direction of the one towards which lockup was engineered) entails much greater freedom, though the array was not explicitly designed either for lockup or freedom,

Conclusions to Chapter 4.

Ultimately, this chapter demonstrates the successful engineering of a fabric-backed tiled array that can bend from a flat (planar) manifold to a singly-curved manifold with reasonable accuracy in the replication of curvature and reasonable strength. Certainly, future research could advance the concept by increasing the precision of manufacturing such arrays.

The easiest potential future research could focus on producing double-sided arrays that can start bending from a flat surface and then bend upwards or downwards towards different target surfaces—effectively, the buttons on the bottom of the fabric should be replaced with

other tiles. Potential applications of this research (such as tank treads) might require bidirectional lockup.

Further research might also focus on how to produce arrays that would be thinner, which would require the tiles to be scaled down not just in the thickness direction, but also likely in the other two directions (otherwise, the angles of the convex-concave features that ensure self-centering behavior in response to a minor disturbance in the position of one tooth along a line normal to the surface might become too sharp). Additionally, making the tiles smaller in all dimensions would improve the fidelity of lockup curvature and general array smoothness. However, the FDM printers employed in this research may make manufacturing of smaller tiles difficult, specifically because of the extruded-cut features required to precisely index the tiles in space before gluing (the overall tile shape could easily be reduced in size without fidelity issues, but if the tabs are made much smaller, the offsets may not be proper and thus the tiles may not slide on and off properly; additionally, the tabs may simply prove too weak).

Using a higher-resolution process like SLA could allow smaller features (e.g. to accommodate the tabs on the workholding piece) to be made sufficiently precisely. The large workholding device might itself need to be produced on SLA though (either as one piece or a rigid assembly of sub-pieces if a large-enough printer is not available).

Future research should also examine the fatigue life of the entire assembly in reversed bending; while the Kevlar yarns used in the fabric are wear-resistant, repeated fabric bending may eventually wear them down, causing the fabric to fail. Because the tiles are rigidly attached to the fabric and negligible deformation is seen at the tile level, it seems unlikely that they would be at risk of fatigue failure.

Finally, future research could also investigate the feasibility of producing surfaces (either initial or target) that are not “simple” in the sense of being open and flat or singly curved. Surfaces that are closed and/or doubly-curved might be more desirable for certain applications; however, complex reorientation of the fabric (along the bias) or of the tiles may be required to achieve this, and additionally, microstructuring of the fabric, cutting holes into it, or using different types of weaves (possibly including 3D weaves) might prove necessary.

Chapter 5. LS-Dyna Model for Numerical Simulation of Singly-Curved Fabric-Backed Arrays in Bending and Lockup.

Abstract.

This chapter employs the LS-Dyna finite element code to simulate the array from the previous chapter as it bends upwards from a flat shape until lockup is initiated by interrupted tile contacts and the fabric's inherent tensile stiffness. The simulation assumes perfectly rigid tiles and a perfect connection between tiles and fabric (established by sharing nodes between mesh elements for the tiles and fabric), and simulates the fabric using MAT_235, a special micromechanics continuum material model intended for modeling woven fabrics; it is assumed that the fabric weave is not distorted or otherwise disturbed during the manufacturing process. The deformed result at lockup is compared with the desired lockup shape. The post-lockup stiffness is not evaluated, because the primary goal of FEA is simply to ascertain the lockup shape of any arbitrary array, and various second-order phenomena would make the predicted stiffness inaccurate in any case (3D printed tiles have complex internal microstructures that are difficult to accurately simulate; fabric weaves are somewhat distorted during manufacturing; treating the tiles as elastic rather than rigid greatly increases computational time). The simulation is a dynamic simulation because MAT_235 is not supported by the LS-Dyna solver for use with implicit analyses (including static implicit). The results indicate that the simulation methodology confirms the accuracy of the design of the gap profiles for producing the desired target lockup curvature, at least for unidirectional bending of developable surfaces.

Introduction.

The goal of this chapter is to develop a technique for accurately simulating the mechanical behavior of fabric-backed arrays under various loading conditions (including point loading and contact with a moving body). This technique should take initial manifold and tile geometries and predict the lockup shape to save the designer time by allowing the evaluation of CAD geometry without having to manufacture and assemble all the tiles (as described in the previous chapter, manufacturing such arrays is quite time-consuming owing to the necessity of printing the individual tiles separately, arranging them on a workholding device, adhering them to the fabric, etc.). The ability to simulate the arrays will prove especially beneficial for analyzing arrays based on singly-closed (hyperboloidal) surfaces, to be discussed in the next chapter, because they are especially difficult to manufacture, and given that it is unclear if they will work for the intended application, it is wise to begin with a computer simulation.

The simulation requires a Finite Element Method (FEM) solver, such as LS-Dyna, rather than a simpler rigid-body dynamics solver, because the complex behavior of the dry fabric (in particular, its bias compliance, low stiffness in bending, and high stiffness in tension) does not lend itself to being modeled with kinematic joints. LS-Dyna's explicit solver is a particularly suitable solver for this problem thanks to its robust handling of interrupted contacts, large deflection, and material models for dry fabrics [83].

Generating the Simulation Geometry.

In order to create a FEA model of the array, preliminary work revealed difficulties meshing the original solid geometry, necessitating the replacement of individual trimmed surfaces with continuous, untrimmed surfaces [with the exception of the planar top surfaces, whose trim curves were redone] having Bezier splines for their U and V curves (rather than the

piecewise splines of limited continuity more commonly used in NURBS modelling). Additionally, regenerating the surfaces produced some interpenetrations between tiles (illustrated in Figure 85), requiring manual sculpting of the tiles by moving their control points manually to ensure proper clearances. (Performing Boolean subtraction operations would have been easier and more accurate but would have produced trimmed surfaces that could have presented meshing difficulties).

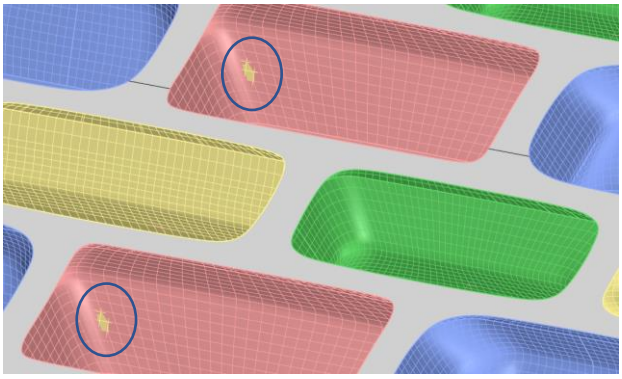

Figure 85: Regenerated surfaces with the UV curves being exclusively Bezier curves with their infinite continuity; unfortunately, there were some minor areas of interpenetration between tiles (e.g. red and yellow). Areas of spurious interpenetration are shown circled in blue.

Once the geometry was successfully regenerated to the point that it could be meshed correctly in ANSYS Workbench, further operations had to be performed to make the tiles and fabric one continuous, manifold surface without overlaps. First, the bottom surfaces of the tiles were removed (turning them from closed solid bodies into open shell/surface bodies). Then, the initial surface was modeled as a thin surface rather than a solid, and the areas of the fabric that would be bonded to the tiles were trimmed out of the fabric surface, resulting in the fabric surface and the now-hollow and open tile surfaces sharing edges, as can be seen in Figure 86. These steps to ensure node sharing between tiles and fabric (rather than merely establishing bonded contacts) were necessary because the LS-Dyna solver exhibits a bug that causes it to spuriously delete elements of fabric modeled with MAT_234 and MAT_235 that are in bonded

contact to other bodies (causing the fabric to instantly disappear). Figure 87 shows a closeup view of meshed regions of the fabric and tiles, with the node-sharing between tiles and fabric evident.

Since the tiles are to be modeled as rigid bodies, the fact that they are modeled with shell surfaces rather than solid bodies will not produce spurious compliance or buckling modes, and additionally, their nominal shell thickness does not matter as it is neglected in the contact algorithm. (However, if they were not treated as rigid bodies, this approach could cause the tile surfaces to deform greatly under contact loads, depending on the stiffness and shell thickness used). Additionally, the holes in the fabric in place of fabric regions that would be glued to the tile do not matter as those regions that are glued effectively become rigid. Also note that, for this first simulation investigating lockup shape, it was sufficient to model one row of unit cells, since the rows are repeated in the *y* direction (though, as mentioned above, there are differences in the *x* direction, so simply modeling one unit cell would not be correct).

Using a soft element size constraint of 0.5mm, a quad-dominant surface mesh of 203,958 elements was generated, as shown in Figure 86 and Figure 87. This sizing was chosen intuitively, as it seems wise to have at least four elements on the fabric between tiles. Considering that many of those elements are rigid, solution time should not be excessive.

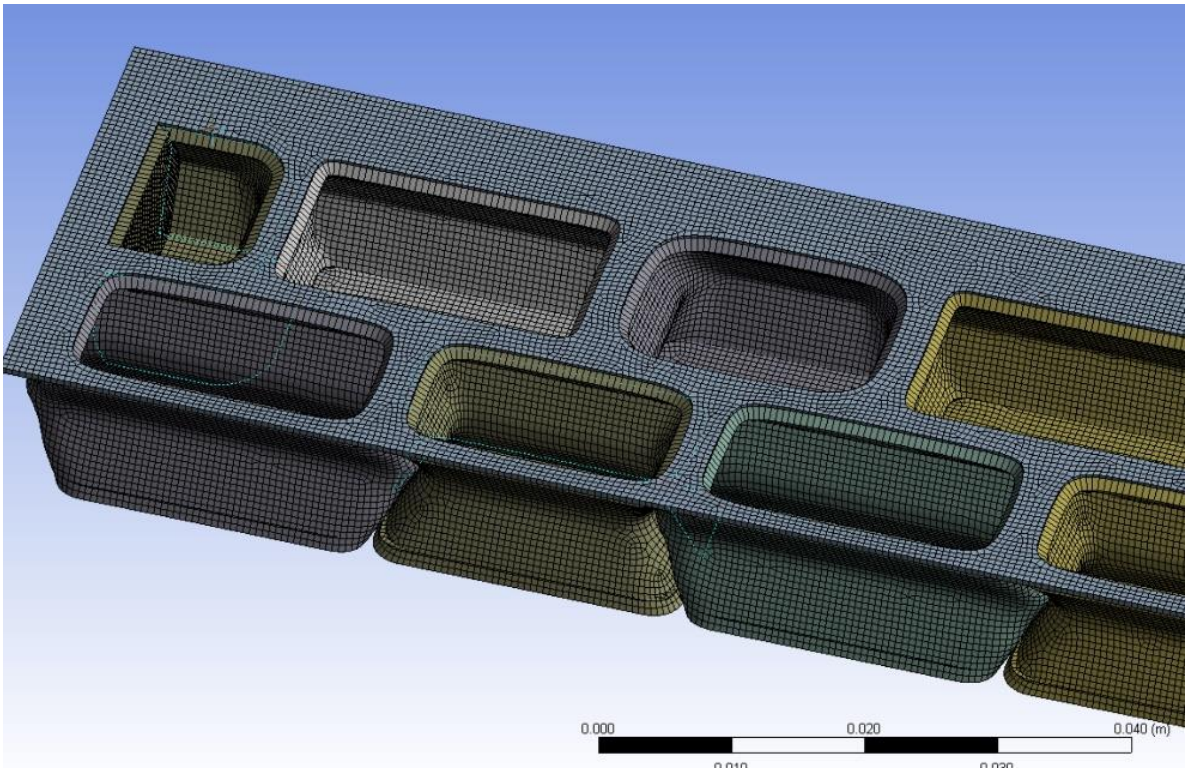

Figure 86: Overview of the mesh used to model the system. Note the open bottoms of the tiles.

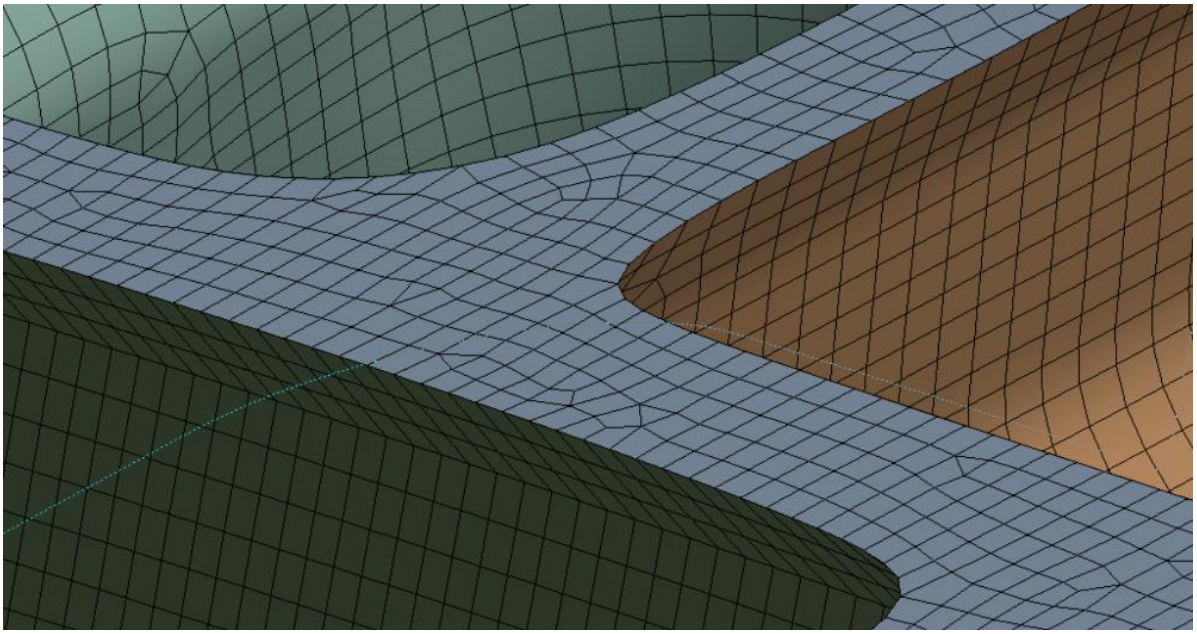

Figure 87: Closeup view of the mesh used to model the system. Note node sharing between tile surface bodies and the fabric surface.

Material Models for Dry Fabric

After successful meshing in ANSYS Workbench, the model was exported to a .k file to be edited in LS-Dyna's LS-PrePost. In particular, it was first necessary to apply appropriate material and shell-thickness parameters to the fabric, in order to accurately simulate the low bending stiffness relative to high tensile stiffness that these weaves have. It would be ideal if second-order effects like yarn reorientation from shear and even shear-lockup effects could be accurately captured by the material model as well. One of the many advantages of LS-Dyna is the multiplicity of different material models it offers (over 250, not counting user-generated materials).

It should be noted that all material models that LS-Dyna offers for woven fabrics are examined in depth in Chapter 8. However, it will be briefly noted here that LS-Dyna has several continuum material models that allow an entire fabric body to be modelled with a low-density mesh of shell elements (rather than individually modelling yarns, as bundles of anisotropic beams, which would greatly increase both design time and simulation time). MAT_034, the first continuum dry fabric model for LS-Dyna, can simulate dry fabrics in tension, shear, and bending (if a 'coating' is added) [84]. MAT_034 was modified [85] to create MAT_034M, with accurate coupling between fiber stresses in the fabric membrane and nonlinear Poisson effects. Neither version of MAT_034 treats bias compliance or yarn reorientation (and locking) in shear unless user-supplied curves relating shear stress to strain are supplied (which were not available to this author, nor was the needed equipment to test them available), however, so neither is suitable for fabric drape or multiaxial-loading simulations.

However, LS-Dyna does boast several dry fabric models that are able to capture microscale behaviors of woven fabrics. First, MAT_234 (VISCOELASTIC LOOSE FABRIC)

[86] and the similar material model MAT_235 (MICROMECHANICS DRY FABRIC) [87] both treat reorientation of yarns; MAT_235 adds compaction and shear locking, and MAT_234 treats failure with strain-rate dependence (which is not relevant to this simulation, since failure criteria and strength are not yet of interest). MAT_214 was developed for ballistic impacts with strain-rate dependence and crimp behavior but does not explicitly treat the trellis mechanism behavior [88].

For the purposes of this research, MAT_235 and MAT_234 seem to be the most attractive for the accurate simulation of dry fabrics with bias compliance, even though bias compliance is not expected to be of great importance for planar surfaces in bending (it is, however, of great importance for cylinder-like fabric-backed arrays, simulation of which is conducted in Chapter 7 on the basis of the preliminary techniques developed in this chapter, Chapter 5). As will be discussed below, attempts to use MAT_234 resulted in a fatal error (likely due to a software bug), leaving MAT_235 as the only remaining option. Material parameters for a plain-weave Kevlar 29 fabric modelled with MAT_235 were taken from [71] with some modifications (although the most important parameters are those pertaining to the fabric's shear locking and bias behavior; the fabric thickness was of less importance to lockup shape, although the thickness value used in the simulation was measured from the fabric sample rather than obtained from the source); the parameters are reprinted below in Figure 90.

Of note, because this material model correctly treats bias compliance (which will prove especially important in the next chapter), it is necessary to indicate to the solver how the fabric is oriented (i.e. where the bias is); specifically, for anisotropic materials, each element can have a principal orientation vector (allowing complicated composite layups to be represented), or, if the

fiber orientation profile is relatively simple, most materials allow a global definition of the element orientation.

Introduction to MAT_235.

The MAT_235 model is technically for an infinite-diameter biaxial braid instead of a flat fabric, so the vector of symmetry for this infinite braid must be specified. This has two implications: first, it can model fabrics that are not woven orthogonally (i.e. fibers need not be at 0°/90° relative to each other, but at some other constant angle, e.g. 0°/60° for a skewed fabric). Secondly, to represent a 0°/90° fabric (as desired here), the vector given for the global orthotropic specification should itself be a 45° angle when the 0° (warp) yarns lie along the global *x* axis and the 90° (weft) yarns lie along the global *y* axis. Consequently, to enable the global orthotropic specification of anisotropy (rather than having to manually specify each element's orientation), AOPT was set to 2, and then the vector defining the material's principal axis of anisotropy was given as ⟨1,1,0⟩. Similarly, the THI variable on the card was set to 45 (establishing 45° as the bisecting angle of symmetry, i.e. establishing a 0°/90° weave).

Other, more-traditional, mechanical parameters of note are the bulk stiffness and density of Kevlar (card entries RO, E1, E2, G12, G23, V12, and V23, which respectively correspond to the density, longitudinal fiber stiffness, transverse fiber stiffness, 12-direction and 23-direction shear moduli, and 12-direction and 23-direction Poisson's ratios). Values for these quantities appropriate for simulating Kevlar fabric were copied from the doctoral dissertation of Hill, who studied Kevlar 49 woven fabrics used in inflatable aerodynamic decelerators [71], and the material properties "card" for LS-Dyna to use this model is shown in Figure 90.

An astute observer will note that the MAT_235 card does not have any parameters pertaining to the coverage factor (woven density) of the fabric, yarn thickness, or other properties

(which are indeed to be specified in MAT_234); this is because MAT_235 assumes a rather tightly-woven fabric (which is reasonable for this simulation) whose thickness is given by the shell thickness of the part. Additionally, on line 2, the card has an entry for ultimate tensile strength at failure, denoted Xt; the documentation indicates [84] it is not yet implemented, but it was seen as wise to put in a large number regardless (especially considering the fact that LS-Dyna's fabric material models sometimes experience spurious failure and element deletion, even when the material model does not specify element erosion). Because viscoelastic effects were ignored, VMB and VME (viscous moduli for normal and shear strain rates, respectively) were both set to zero. TRS, the transverse shear modulus of the fabric layer, was assigned a small measure of 100MPa for accurate shear behavior, following the example of Kilimtzidis et. al., who indicate the factor can be scaled up by an order of 10 if necessary to accurately capture shear behavior [89].

Next, the variable THL specifies the locking angle of the weave/braid; it does not matter very much for a simulation of unidirectional bending when the projected neutral axis lies on the warp (or weft) 0°/90° direction, as bias effects should not be visible globally (at most, they might appear locally near the tiles), but it will matter greatly in Part II of this dissertation (where bias effects will become more prominent during the bending of a closed, cylinder-like surface). Ultimately, the eventual locking of a fabric or braid that is sheared (or tensioned along the bias) is governed by the trellis mechanism of the fibers rotating relative to each other about their overlap points and eventually closing up the gaps between them. The way this is simulated for a 45° braid (i.e. 0°/90° fabric) is illustrated in Tabiei and Ivanov's original paper outlining the development of the MAT_235 material model [90] as reprinted below in Figure 88:

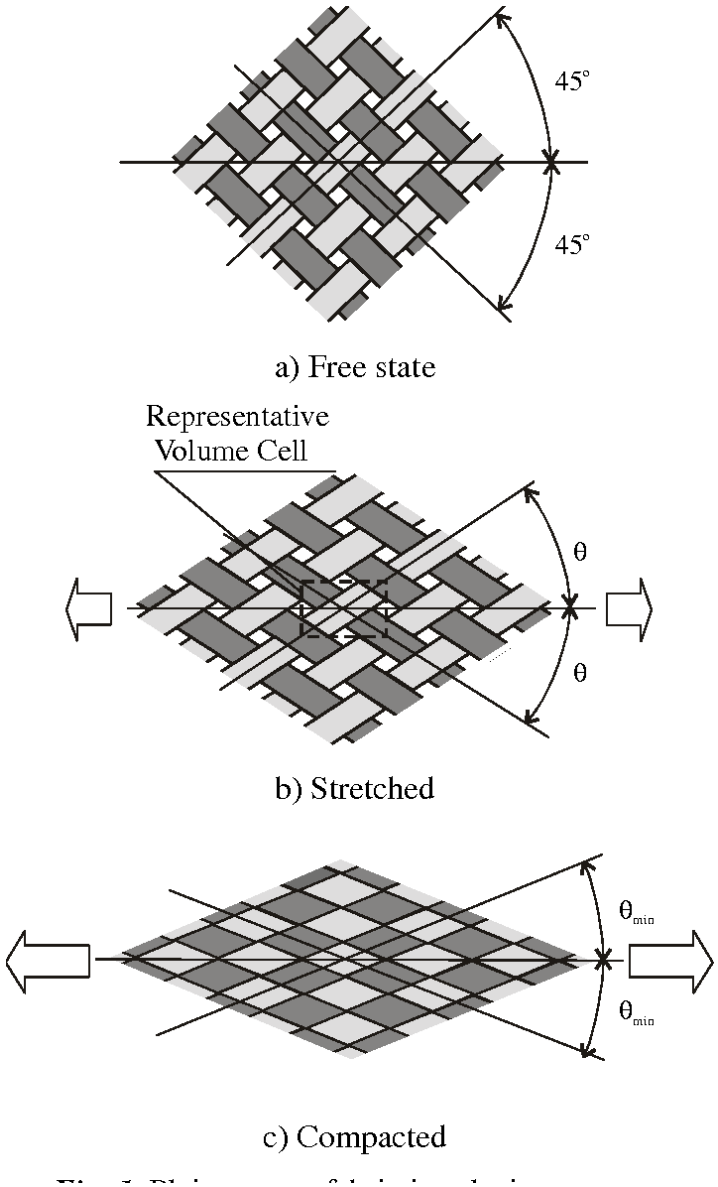

Figure 88: Interlacing mechanism of MAT_235, reprinted from [87] with permission. While this image shows a 0°/90° fabric tensioned along the bias (i.e. at 45°, equivalent to a +45°/-45° braid of infinite diameter tensioned along the braid axis), the material model can treat other braid angles.

Additionally, the undulation behavior (prior to crimping) of the yarns is taken into consideration by the values BWI and BFI (initial warp and fill undulation, respectively), which in this simulation were each set to 5° following the example of [71]. The MAT_235 model itself treats the yarns as beams that are angled above each other at the cross-over point, which is given

its own stiffness; a schematic of how the model simulates the crossovers is reprinted in Figure 89.

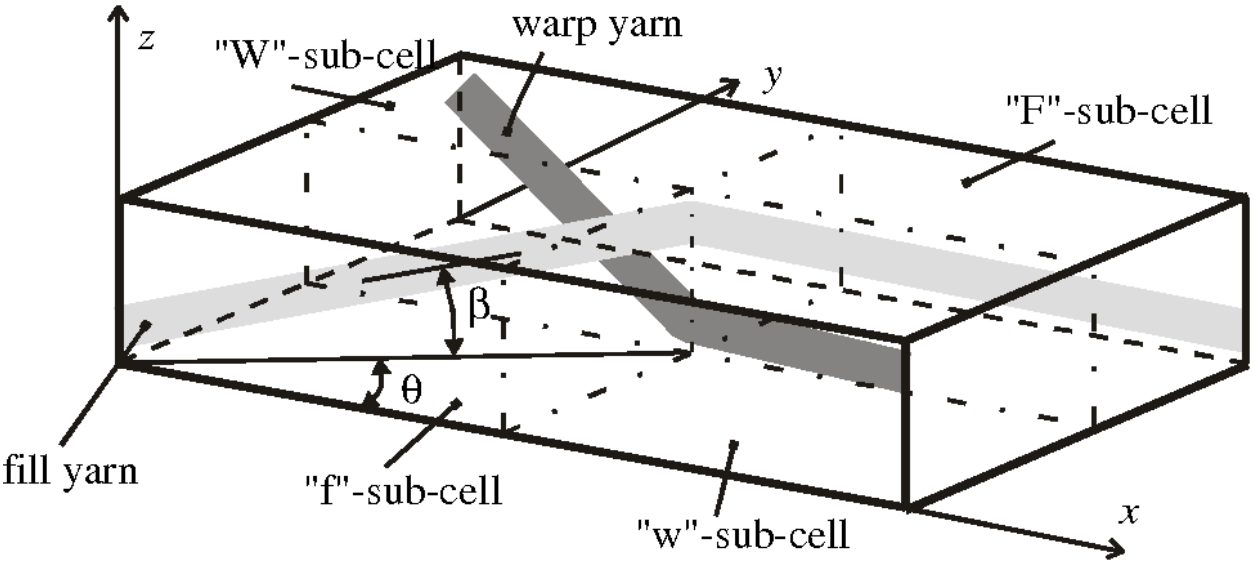

Figure 89: Illustrating the crossover effect of the warp and fill yarns as simulated by the continuum mechanics model of MAT_235, reprinted from [86] with permission.

*MAT_MICROMECHANICS_DRY_FABRIC_(TITLE) (1)

	TITLE							
	KevlrFab							
1	MID	RO	E1	E2	G12	G23	V12	V23
	35	1440.0000	9.900e+10	7.400e+09	2.500e+09	5.000e+09	0.2000000	0.2000000
2	Xt	THI	THL	BFI	BWI	DSCF	CNST	ATLR
	1.000e+10	45.000000	7.5000000	1.0000000	1.0000000	1.000e-05	1000.00000	5.0000000
3	VMB	VME	TRS	FFLG	AOPT			
	0.0	0.0	0.0	0.0	2.0000000			
4	Xp	Yp	Zp	A1	A2	A3		
	0.0	0.0	0.0	1.0000000	1.0000000	0.0		
5	V1	V2	V3	D1	D2	D3		
	0.0	0.0	0.0	0.0	0.0	0.0		

*Figure 90: Material properties used in this simulation for *MAT_MICROMECHANICS_DRY_FABRIC (235) with the kg-m-s consistent unit system (for easy appreciation of a reader who might be used to the kg-m-s unit system). Note that in fact a different unit system was generally used in actual simulations.*

Of note, constants for a plain-woven Kevlar fabric were also found for MAT_234 in Fein's Master's thesis [91], prompting this researcher to attempt a simulation with MAT_234 as

well; the constants for the MAT_234 card are shown in Figure 91. Interestingly, as will be explored in greater detail in Chapter 7, MAT_234 appears to have a bug that causes its elements to instantly erode when they share nodes with other materials (such as MAT_001_ELASTIC or MAT_020_RIGID), since the solver rapidly printed errors about failed warp and weft yarns and eroded most elements at the very beginning of the simulation. Because MAT_235 produced acceptable results, no further exploration of how to make MAT_234 work as well was deemed necessary.

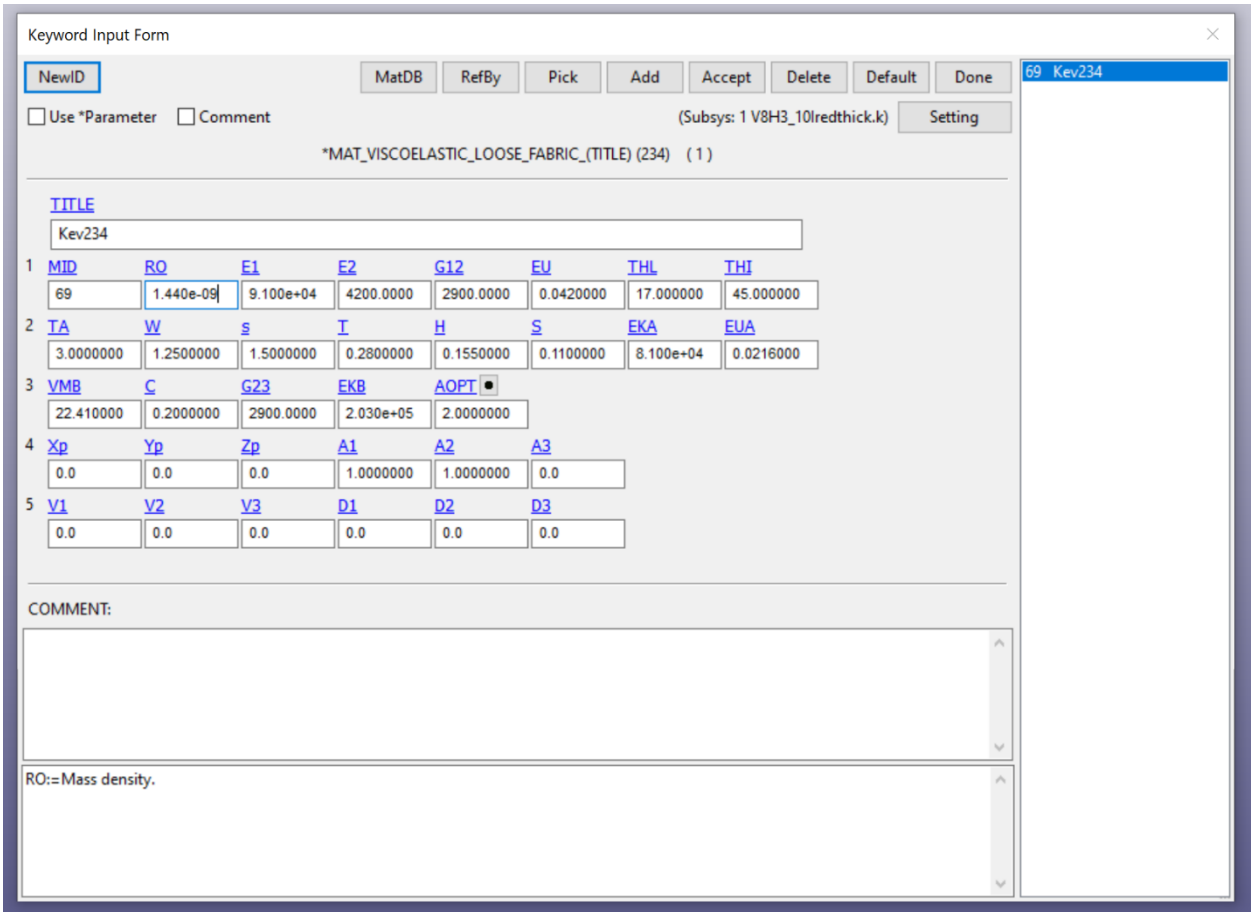

Figure 91: Constants for MAT_234 woven Kevlar fabric, expressed in consistent N-mm-s units. Unfortunately, the solver exhibited a fatal error of spurious element erosion with MAT_234, prompting this researcher to discontinue its use in this application.

Specifying Element Orientations.

Additionally, because MAT_235 is an anisotropic material model inasmuch as it treats bias compliance in a biaxial braid or 0°-90° plain-weave fabric, it is necessary to specify the orientation of a vector that bisects the angle made by the warps and wefts (or bisects the braid in the case of a biaxial braid). In general, this vector can be assigned either globally (either explicitly defining this vector in terms of the global coordinate system, or alternatively defining it in terms of the cross product of a global, user-specified vector and the normal vector of each element) or uniquely for each element by defining the "principal material direction vector" (a feature of each element commonly ignored save when anisotropic and composite material models are used), either manually or with composites-oriented preprocessing software, such as ANSYS ACP. Manual methods are needed usually only when complex layups are involved, especially with fabric draping over highly-curved surfaces that may distort the fabric. In this chapter, the global, vector method is sufficient since the fabric shape starts out flat.

Boundary Conditions and Loads.

To determine the curvature at lockup of an array in bending, boundary conditions were chosen to replicate cantilevered bending, with one end fixed (both in displacement and in slope in *xyz*) and the other end loaded by a moment about the *y*-axis and additionally constrained against displacement in the *y* direction and rotation in the *x* and *z* directions. The force was a constant-magnitude (100N), constant-direction force (rather than one that reorients to stay perpendicular to the edge of the fabric as it curves), although the distinction matters little considering how stiff in tension the fabric backing is. The displacement and force were both applied over a large number of nodes, with the nodes used shown in Figure 92.

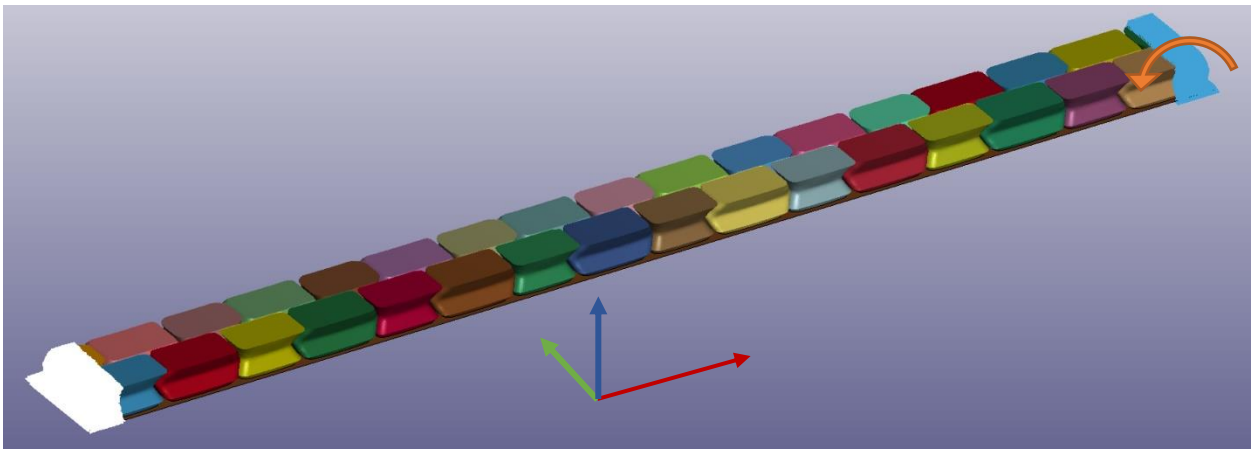

Figure 92: Location of fixed boundary condition (nodes highlighted in white) and applied force and additional constraints against displacement in the y direction and rotation in the x and z directions (nodes highlighted in sky blue) in LS-Dyna PrePost. Note that the colors used for the bodies in LS-PrePost do not correspond to the red/green/blue/yellow color scheme used in CAD. The x direction is shown with a red vector, the y direction with a green vector, and the z direction with a blue vector.

Contact Specifications.

Additionally, contacts were established between all the shells of the tiles with *CONTACT_AUTOMATIC_SINGLE_SURFACE with the SOFT=2 pinball-segment-based contact, warped-segment checking and sliding (SBOPT=5.0), shell thickness not considered (THKOPT=2) and Coulomb friction (with static coefficient 0.5 and dynamic coefficient 0.3—these numbers are of course wild approximations, inasmuch as friction coefficients vary greatly based on material and surface finish, but the PLA used in the manufacturing in the previous chapter will have a relatively high friction coefficient, especially with the surface roughness inherent in the layer-based FDM process). It was also found that adding a miniscule extra thickness (SLDTHK=1.004e-4 mm, SLDSTF=2000MPa) was necessary to prevent shell interpenetration. The entire contact card is reprinted below in Figure 93.

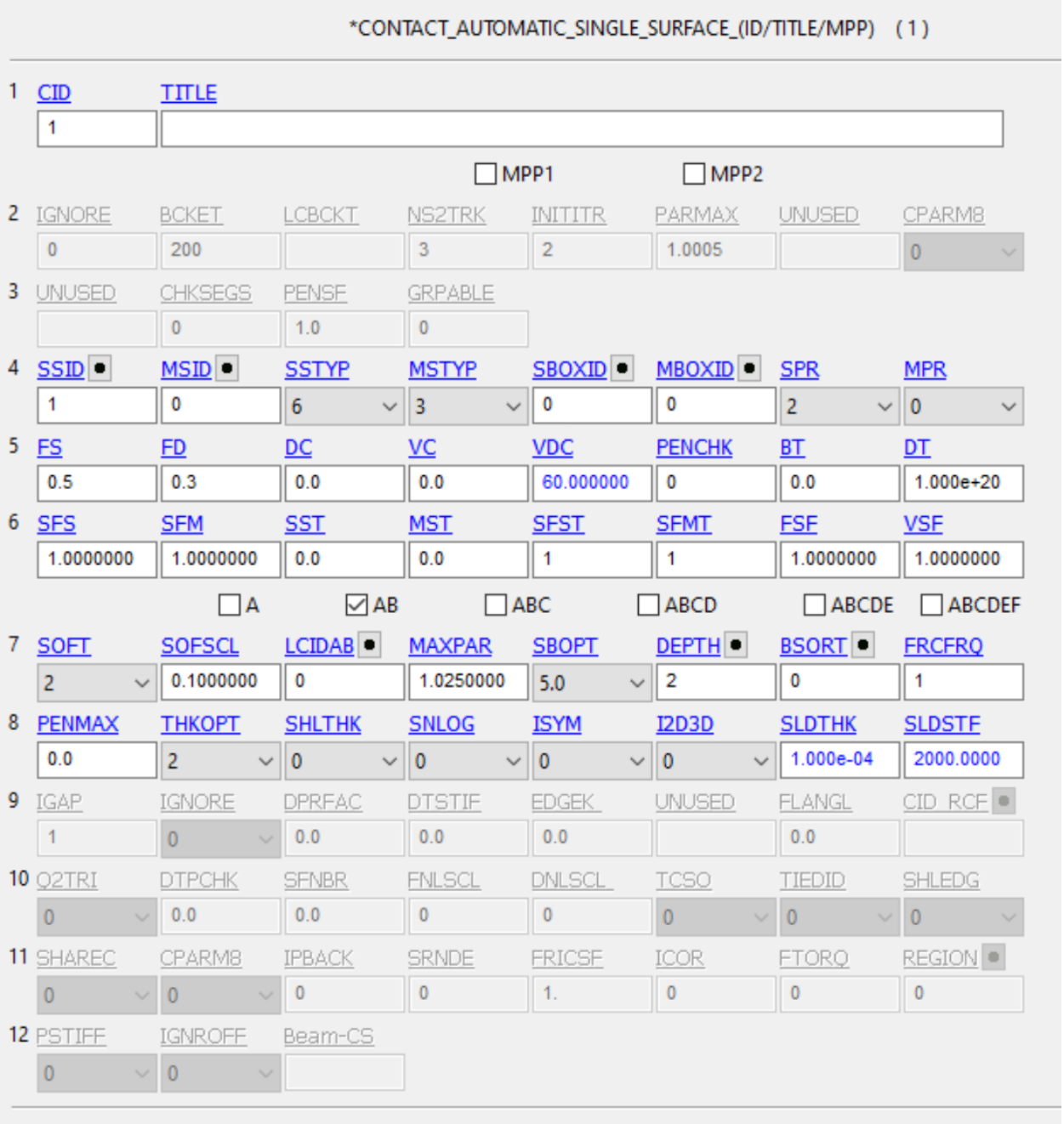

*Figure 93: All settings in the *CONTACT_AUTOMATIC_SINGLE_SURFACE card.*

It should be noted that failing to use the SHLTHK, SLDTHK and SLDSTF parameters above in a preliminary simulation caused the solver to predict premature contact between tiles (i.e. contacts were activated when there was a significant gap between tiles, as shown in Figure

94) and thus stiffen up too early, producing maximum lockup curvature that was lower than desired, as can be seen in Figure 95.

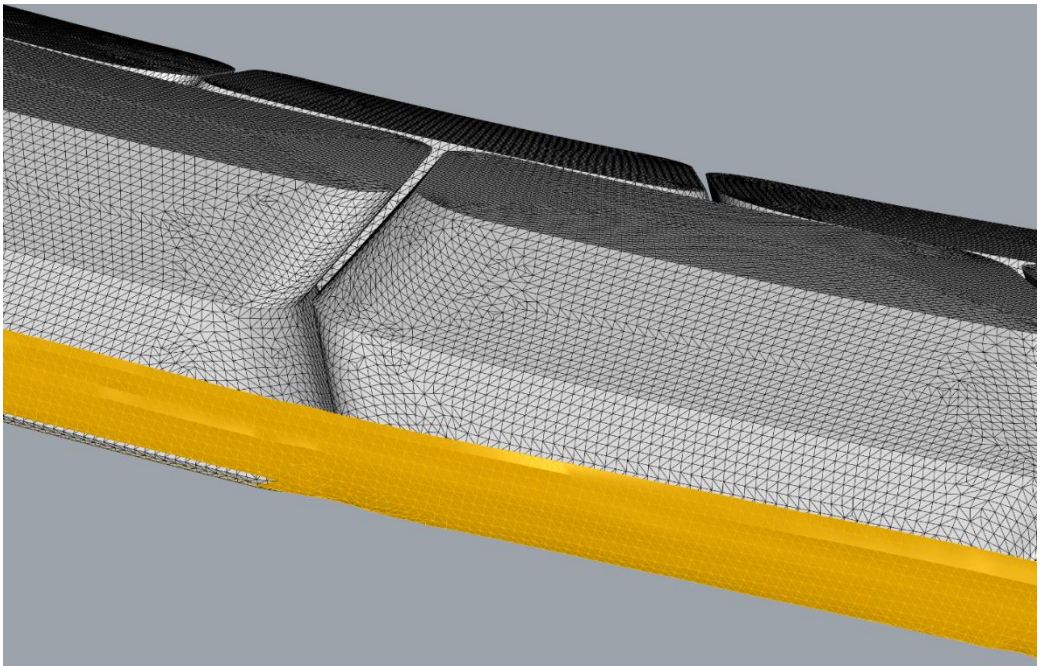

Figure 94: When the necessary parameters were not used for the contact model, spurious "contact" was registered when elements were in fact not in contact and large gaps existed between them.

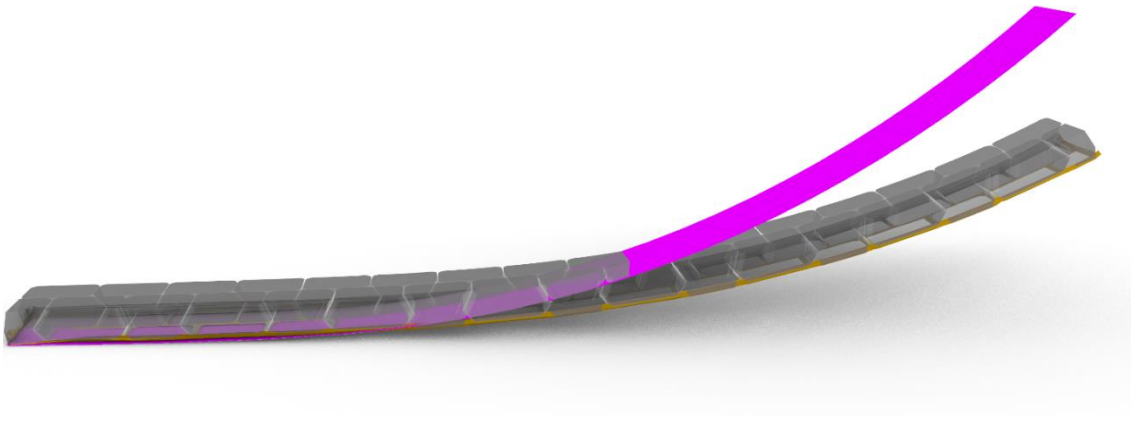

Figure 95: The premature contact shown in the previous figure resulted in the entire array (shown in grey and yellow) not reaching its full curvature (shown in purple), prompting an investigation into the needed settings for accurate contact.

Finally, as mentioned above, the connection between the rigid shells representing the tiles and the flexible, trimmed shell representing the fabric was established by node sharing rather than bonded contacts (due to an apparent bug in LS-Dyna that causes the fabric elements to erode when placed into bonded contact). There was no need to establish additional contacts between unbonded fabric elements and tiles, because the tiles are close enough to each other that they will contact each other before contacting the fabric (at least when bent up; when bent down, the tiles might contact the fabric first). Node sharing was ensured during the meshing stage in ANSYS Workbench, when the edge connectivity was highlighted in different colors, showing connections between the fabric and tiles; additionally, it can be observed in the fact that the grid elements of the fabric and tiles always appear to coincide (prior to establishing node sharing, they rarely coincided).

Ensuring Rapid Solve Time.

LS-Dyna's explicit mode was required, since woven fabric material models like MAT_234 and MAT_235 do not support the implicit solver—this is unfortunate, as in many cases the implicit solver takes less wall time of simulation to perform. Occasionally implicit solves fail to converge, though even then LS-Dyna can switch intelligently into explicit mode rather than simply failing the simulation. It was performed on Auburn University's Hopper high-performance cluster [92], with the optimum number of cores for minimizing overall wall time found to be 10 cores (the number of cores in a single processor): of note, the simulation was actually slower (had negative speedup) with 20 cores (the number of cores in an entire node, which consists of two processors connected by a 9.6GT/s QPI Link bus), indicating that the bus between processors was the rate-limiting factor. (Larger simulations might still benefit from more processors and even supercomputer nodes).

Since the aim of this simulation was more or less “kinematic” in nature (determining lockup shapes), rather than more-accurate dynamics (e.g. determining forces/stresses/loads), it was seen as justifiable to use a form of mass scaling to increase the minimum timestep allowable (while still ensuring convergence under the Courant-Friedrichs-Lewy condition for hyperbolic differential equations’ convergence [93]). Specifically, the density of the individual Kevlar yarns in the fabric was increased from 1440kg/m^3 (their actual value) to 144,000kg/m^3, thereby significantly increasing the minimum timestep by reducing the soundspeed in the Kevlar fabric. (There was no sense in attempting mass scaling on the tiles, because they were modelled with a rigid material and thus do not have individual strain waves).

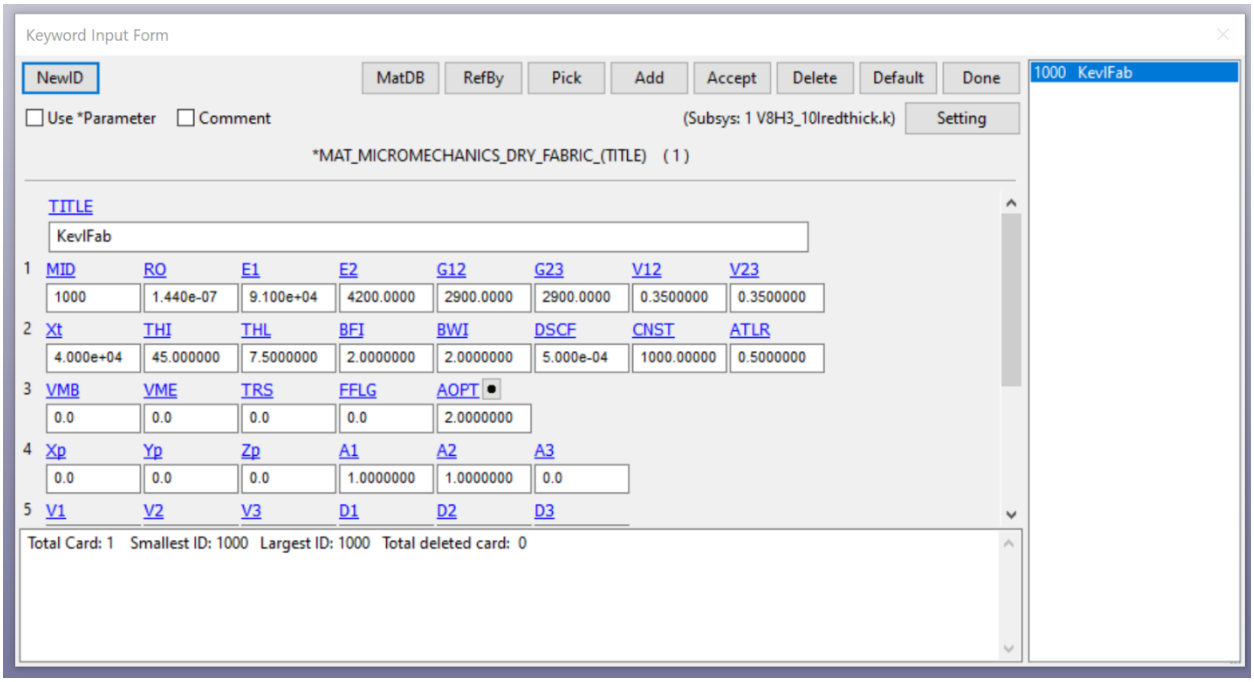

Figure 96: Mass-scaled material model for Kevlar fabric. Note that the density was increased artificially from the correct 1.44e-09 (in N-mm-s consistent units) to 1.44e-07, a mass-scaling factor of 100.

The moment to bend the array of tiles at the far end of the cantilevered boundary condition was increased proportionately (necessary since the inertia/mass of the system was increased so much), since it was indeed a moment rather than a prescribed displacement over

time. It was discovered that an 500Nmm peak moment (rapidly ramped up) was sufficient to accelerate the free end of the cantilevered system at a "reasonable" speed in simulation terms (fast enough that the simulation did not require too many time cycles to complete, but slow enough to be physically reasonable and not cause excessive contact interpenetrations). The force curve used is shown in Figure 97.

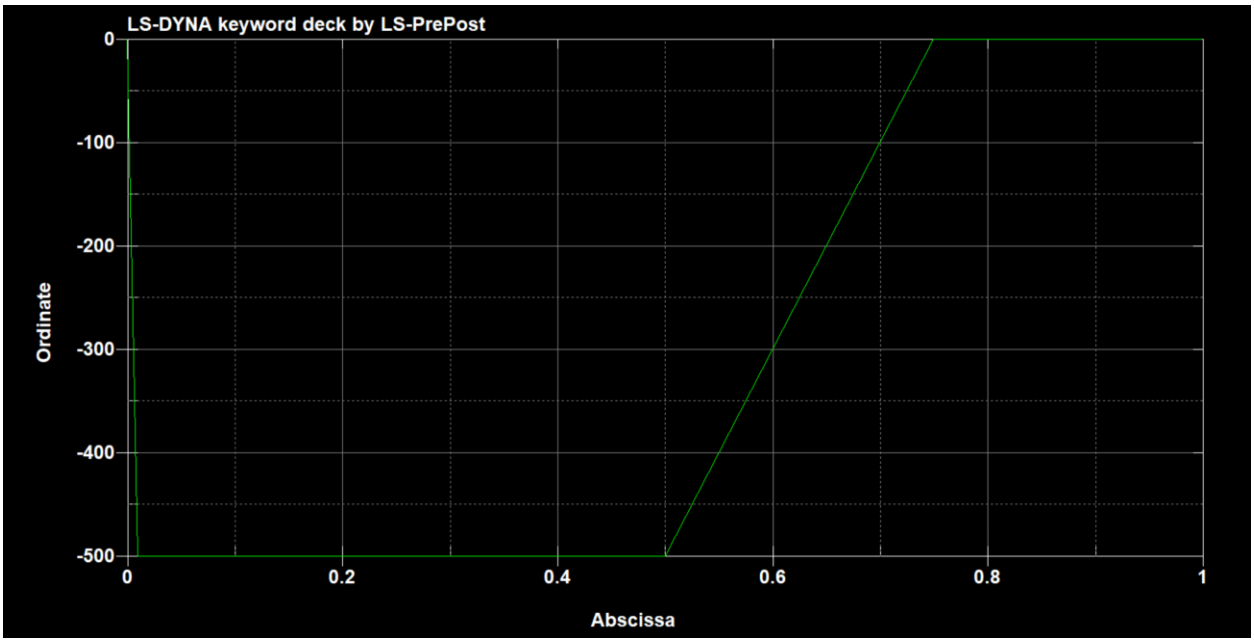

Figure 97: Moment-vs-time profile (ordinate measured in Nmm, time in sec) used in the simulation.

Simulation Results.

The simulation took approximately 5 days of wall time, with d3plot files output at regular intervals in order to show graphically how the composite structure deformed over time. The d3plot files were examined in LS-PrePost, and the frame with peak deformation had its deformed result was exported as an STL in order to compare the deformed fabric surface to the target curvature shape.

It should be noted that there were two different states of interest in the simulation: the state at which the tiles were fully contacting at their tips, and the state of maximum displacement

before the structure bounced back. Ideally, the two states would be nearly identical (as the fabric should be quite stiff in tension and moreover the tiles are themselves rigid, so once the tiles were fully contacted it should barely displace further). Unfortunately, perhaps due to the mass scaling and the high rate at which the load was applied (in order to make the simulation finish in a reasonable timeframe as regards wall time), there was a significant disconnect between the two states, as illustrated in Figure 98. In particular, the maximum extent of bending resulted in a further 64.198mm of displacement from the tip of the target surface, whereas the first state at which all tiles were fully contacted only had an extra 32.963mm of extra displacement.

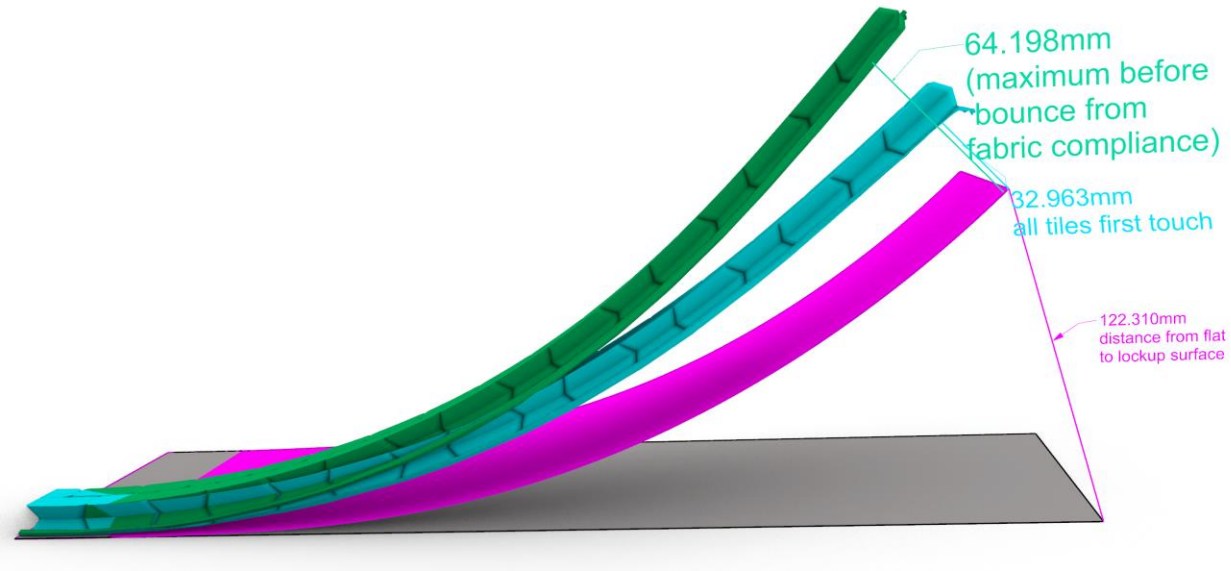

Figure 98: Overall view of the deformed result from the first simulation at the maximum extent of bending (shown in green) and at the point at which all tiles were manually verified to have locked up (shown in grey/yellow/blue). The pink surface shows the desired lockup profile; ideally, the FEA results would lie exactly on this surface.

It is likely that a significant contributor to the excessive displacement at the state just when tiles are fully contacted (shown in cyan in Figure 98 above) is primarily a function of extra insets of 0.05mm that were applied between tiles to prevent near-interpenetration at the start of the simulation. While there are contact algorithms that can fix initial interpenetrations in LS-

Dyna, they do not work with rigid bodies without moving the entire bodies (which would have instantly created significant stresses in the fabric), so, owing to meshing imprecisions and the like, this universal offset was seen as necessary. Considering that this is not a small fraction of the smallest initial gap, which was on the order of 0.12mm, it is perhaps not surprising that this affected the curvature at full tile contact. Indeed, this is very similar to the reported 38.44mm of excess deflection reported in the experimental evaluation of the array conducted in Chapter 4. Additionally,

In contrast, the further increase in curvature before true bounce-back was likely a function of the dynamic loading as well as certain parameters used in the material model causing the fabric to be too compliant in tension. As shown in Figure 99 and Figure 100, the fabric between the tiles developed significant stresses and strains (respectively) in the *x*-direction

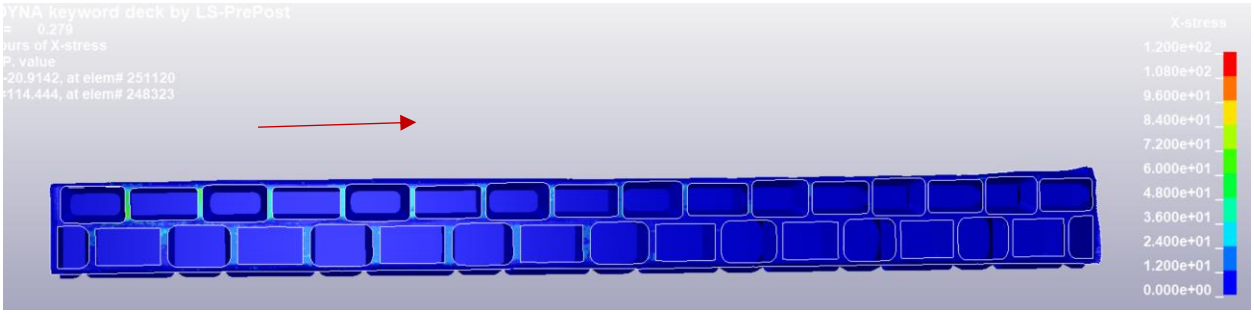

Figure 99: Contours of x-stress at the timestep of maximum simulated deflection (t=0.27s) in the fabric between tiles show considerable stresses in the fabric (max of 120MPa), as well as noteworthy asymmetry between the two rows of tiles (though they do have different shapes, so perhaps this is not entirely unexpected. The red arrow indicates the x-direction.

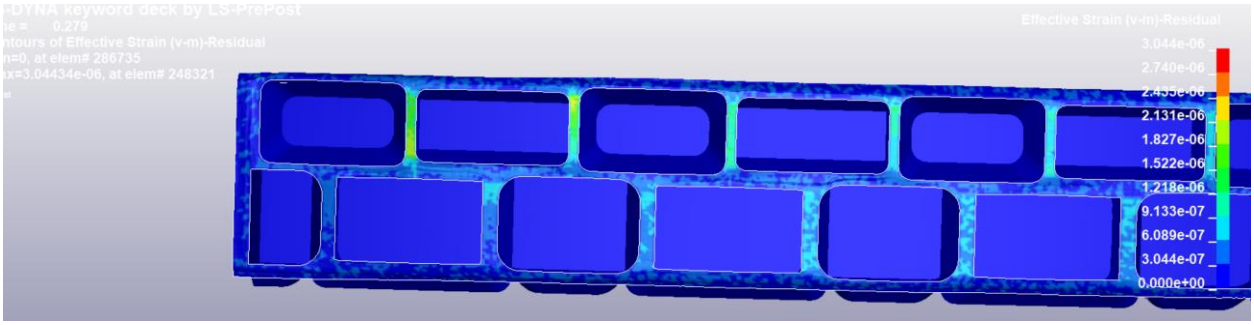

Figure 100: Contours of x-strain at the time of maximum simulated deflection (t=0.27s) show overall small strains in the fabric even at full decrimping, as well as noteworthy asymmetry between the two rows of tiles (though they do have different shapes, so perhaps this is not entirely unexpected.

In his dissertation (the source of the material parameters for this simulation), Hill himself noted [71] that it was wise to conduct a sensitivity analysis to the effect of changing the crimp/undulation angle in the warp and weft directions in LS-Dyna's MAT_235 by comparing simulation results to experimental results to find the ideal level; he did propose using a crimp angle of only 1° for his application (involving relatively-unconstrained weaves, quite different from this application), but experimented with values as high as 10°. Geometrically speaking, it should be noted that this is quite a low crimp angle for an actual woven fabric. In fact, when a unit cell of the weave used in this dissertation was modelled in the open-source textile modelling software TexGen [94] and then exported to Rhinoceros3D for measurement of the predicted crimp angles, it was found that the true tangent angle was 11.12°, as shown in

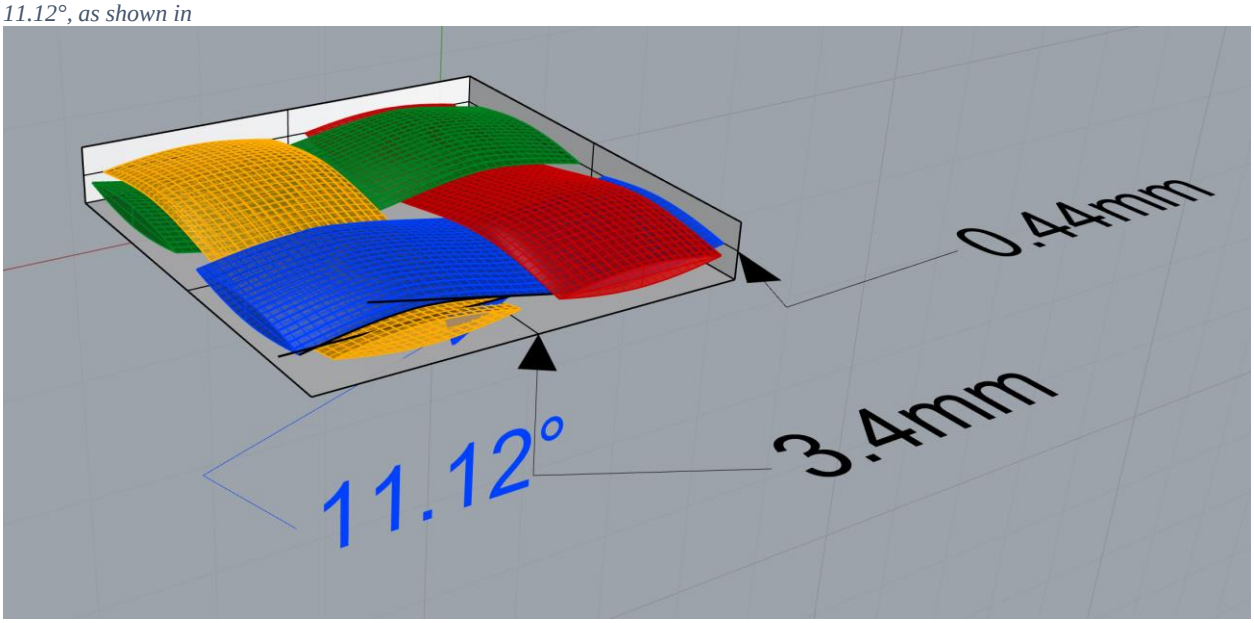

Figure 101.

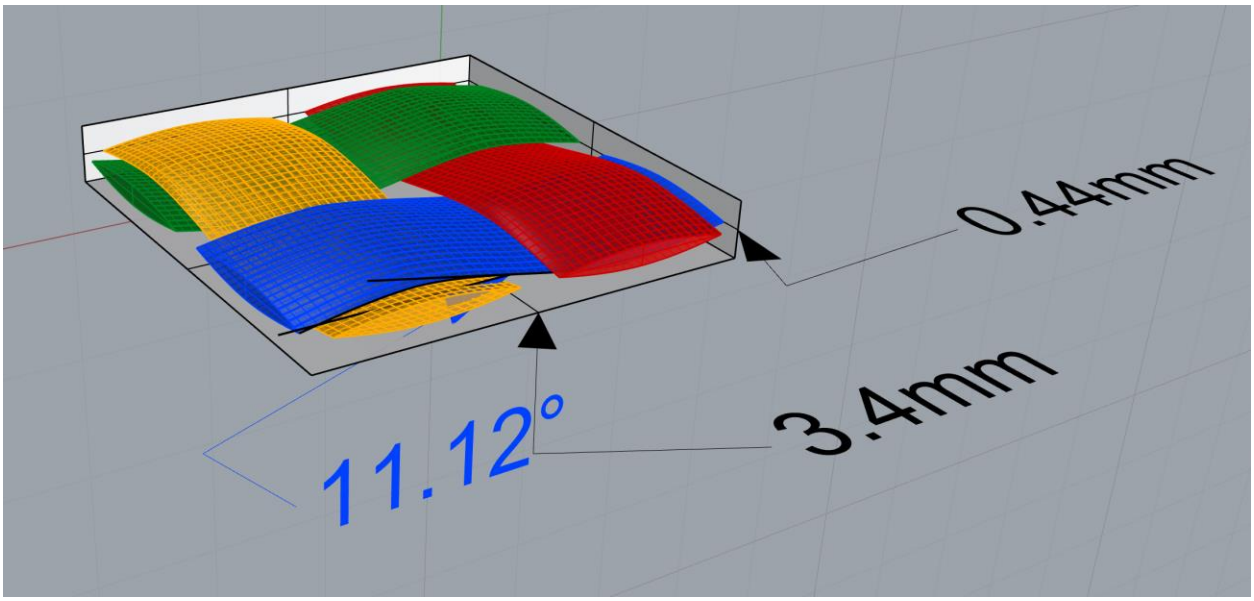

Figure 101: Unit cell of the actual weave used, modeled in TexGen, with the crimp angle measured.

Fortunately, the contact between the tiles was accurately simulated, with no spurious offsets between contacts developed (which plagued the preliminary simulations, underpredicting the curvature at lockup), and additionally that there were no interpenetrations or inactive contacts between tiles (which would overpredict the curvature at lockup or perhaps not even result in lockup at all). Figure 102 shows that the contact behavior between tiles was correct and devoid of spurious offsets, and Figure 103 shows that there was no overpenetration between tiles. Thus, at the very least, there were no problems with contact between the tiles that would have underpredicted or overpredicted lockup curvature.

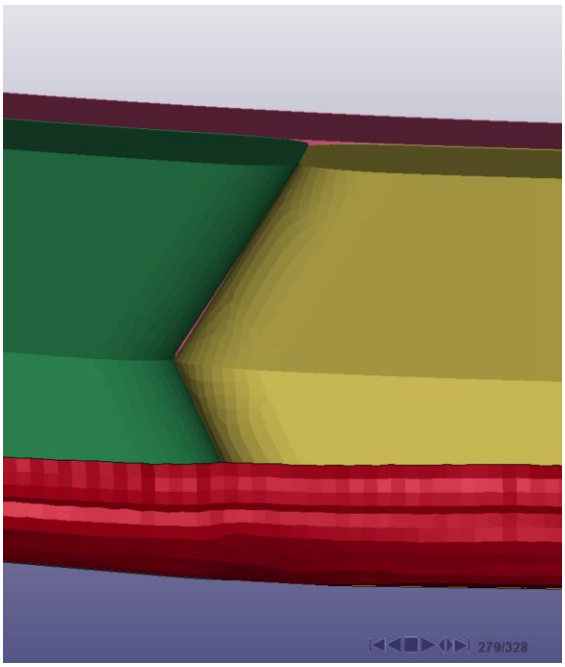

Figure 102: Side view of two fully-contacting tiles at lockup.

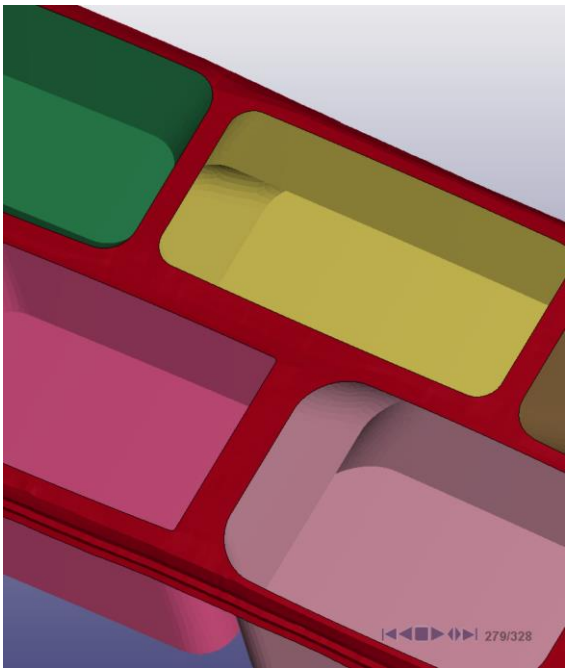

Figure 103: Underside view of fully-contacting but not-interpenetrating tiles, showing correct behavior.

Due to the rigidity of the tiles, the constant nature of the force, and the dynamic nature of the simulation (because there was not enough computing time available to simulate a slower

loading), the simulation exhibited considerable “bounce-back” and “springiness” (e.g. see Figure 104 and Graph 23, which plots the displacement of a node at the very tip of the array over the time of the simulation) that one can intuitively recognize is not present when one bends a physical sample of the composite in real life at a rate of deformation that is orders of magnitude slower than what was simulated (and with the applied force decreasing because the human mind anticipates lockup, rather than remaining constant). However, this was not a problem from the standpoint of determining the maximum deflection at lockup.

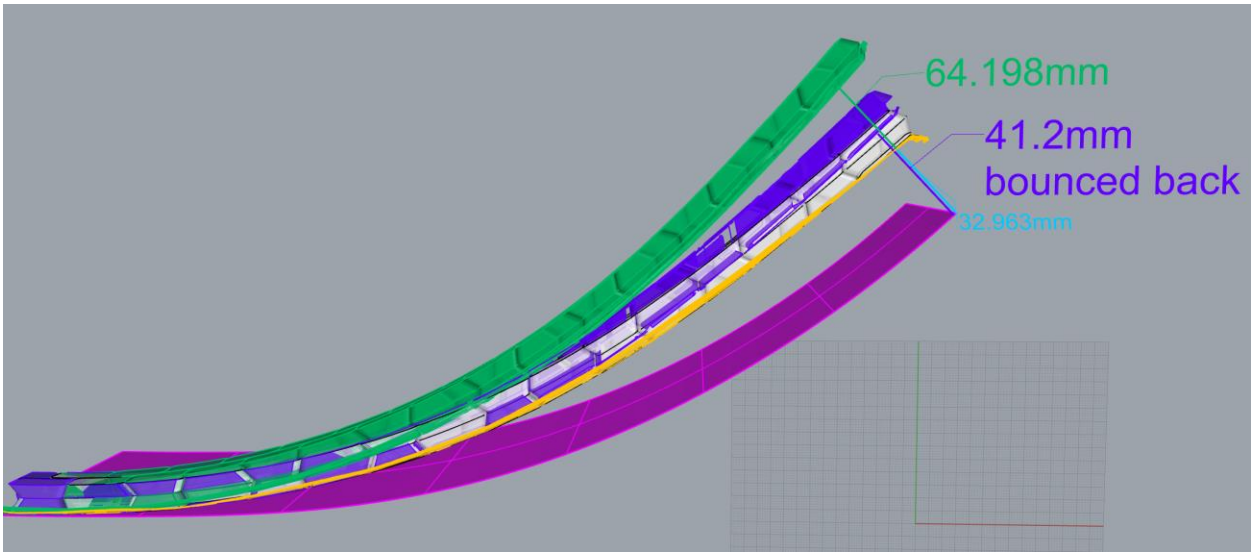

Figure 104: After the frame shown in the previous figure, the simulation saw the deflection oscillating/“bouncing” somewhat, with the state shown in violet being one position that was reached when the tiles were fully contacting. The state shown in green corresponds to extra deflection from tensile compliance in the fabric.

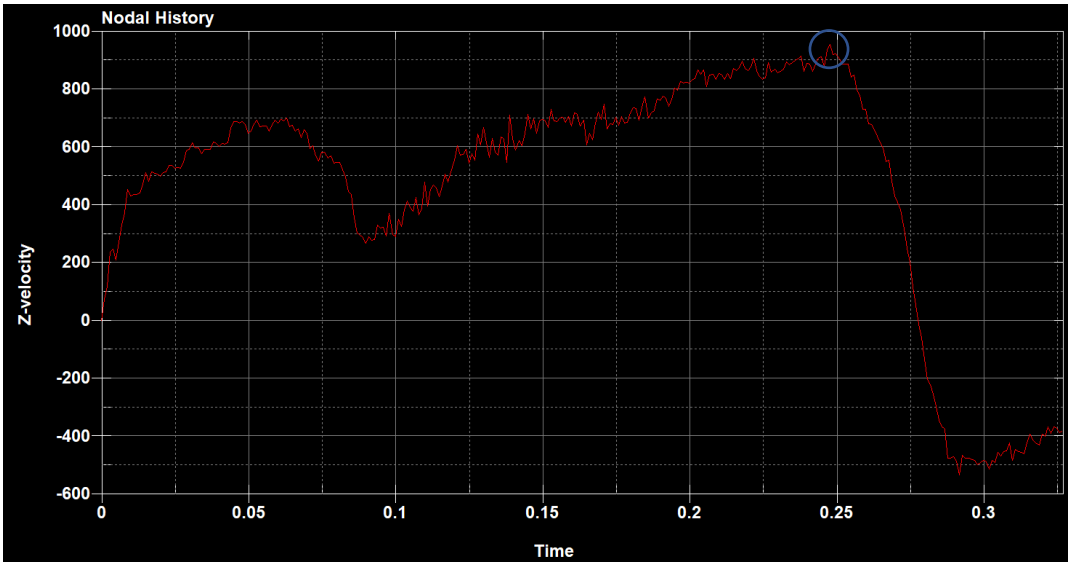

Graph 23: The z-deflection of a node at the very tip of the array was plotted over time, illustrating the "bouncing" after it reached its peak value (circled in blue).

One minor feature of note is that, due to the significant mass-scaling applied to the fabric material model, free areas of the cloth (i.e. mesh elements not near tiles that constrain their motion somewhat) appeared to billow and followed the tiles with significant lag, as shown in Figure 105. This did not have any obvious detrimental effects on accurately modeling the lockup properties, however, because the fabric was properly constrained and tensioned between tiles (as can be seen in Figure 106).

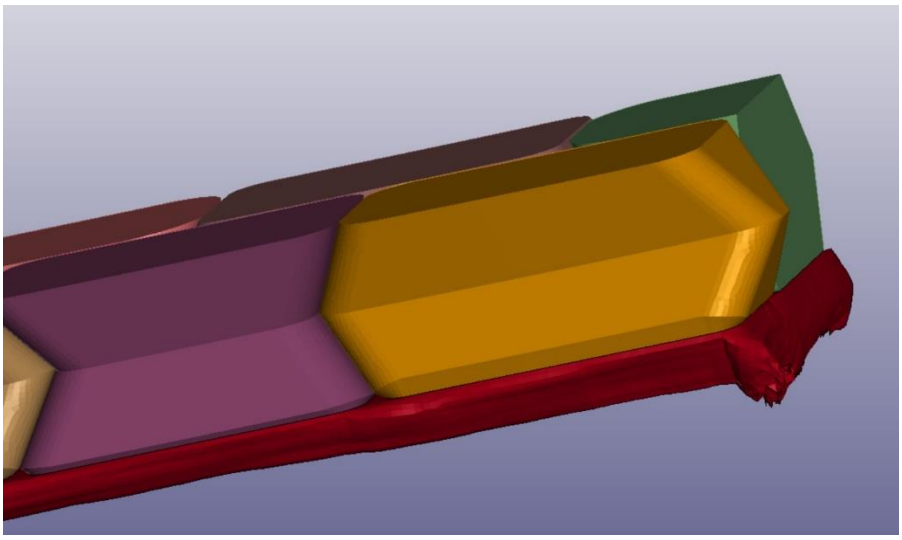

Figure 105: Billowing fabric (due to elevated inertia) at the free ends of the composite. It is not indicative of concern relative to the scope of the simulation.

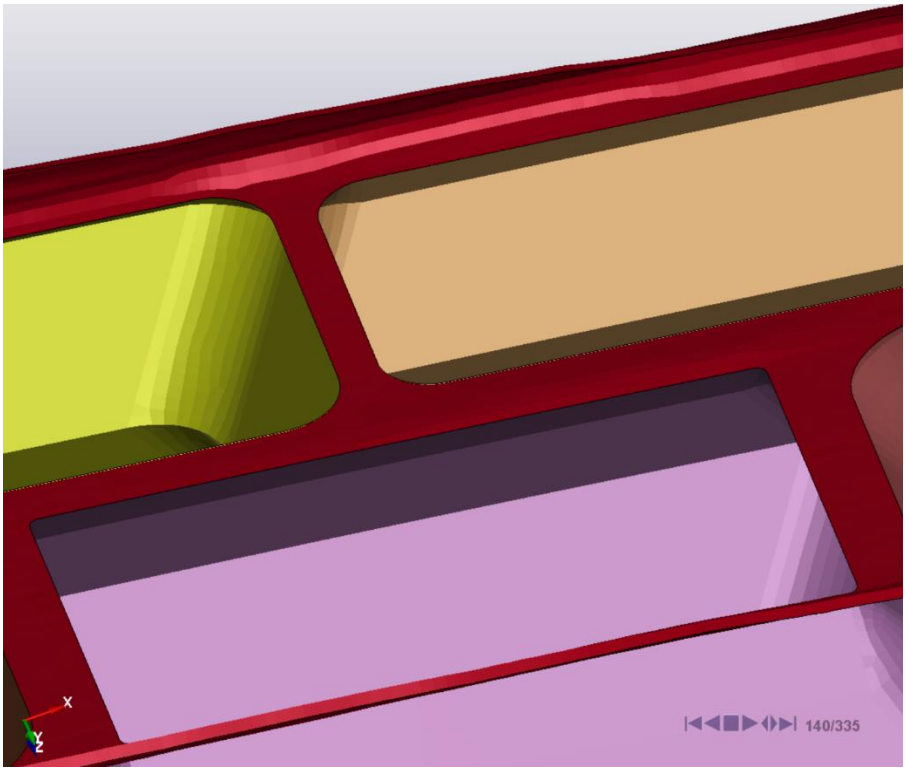

Figure 106: Fabric tensioned and constrained between tiles, not billowing freely as at the edges (shown in the previous figure). This behavior is correctly simulated.

Limitations of this FEA Approach.

In addition to only being able to simulate existing arrays (rather than generate arrays to conform to a complex shell bending strain pattern), this approach has another flaw: it only predicts the shape immediately after lockup, assuming that the tiles are perfectly rigid and do not display any elastic or plastic strain (let alone failure) themselves, and likewise assuming that the bond between tiles and fabric never fails. Most real-world applications will require the array to take a significant amount of load after lockup, rather than merely achieving a target shape with very little load. Consequently, the designer must be able to predict the plastic deformation and ultimate strengths for complex loading patterns.

Unfortunately, using FEA as described in this chapter seems unwise for determining the ultimate strength of the assembly, and instead this author proposes using simple experiments of arrays loaded in three-point or four-point bending, which is done in Chapter 5. There are several reasons that justify eschewing FEA analysis of the assembly for determining strength. First, tiles may be made by additive manufacturing methods that often produce complex microstructures based on the orientation of print rasters, infill density, raster and layer thickness, etc.; certainly, the strength of such a part printed by FDM would be at least somewhat inferior to the hypothetical strength of a part made in the same resin by injection molding, and additionally the strength would exhibit considerable isotropy, generally being weakest between layers (as discussed in Chapter 5) but also depending on the quality of bonds between in-plane rasters. Likewise though to a lesser extent, the stiffnesses of such additively-manufactured parts in bending, contact loading, etc. may differ modestly from as-injection-molded parts' stiffnesses and would likely exhibit some anisotropy. As such, FEA would likely give erroneous predictions of tile and button behavior. A section view of a render of the individual lines to be

printed on an Ultimaker 3 printer with a 0.5mm-diameter nozzle printing layers of 0.18mm height is shown in Figure 107; it is not difficult to see that poor bonds either in the *xy* plane between rasters or especially in the *z* direction could produce a part that is far weaker than the bulk strength of the raw resin would predict; additionally, the orientations of perimeter and infill lines can affect how loaded the *x*, *y*, and *z* bonds between different rasters end up being.

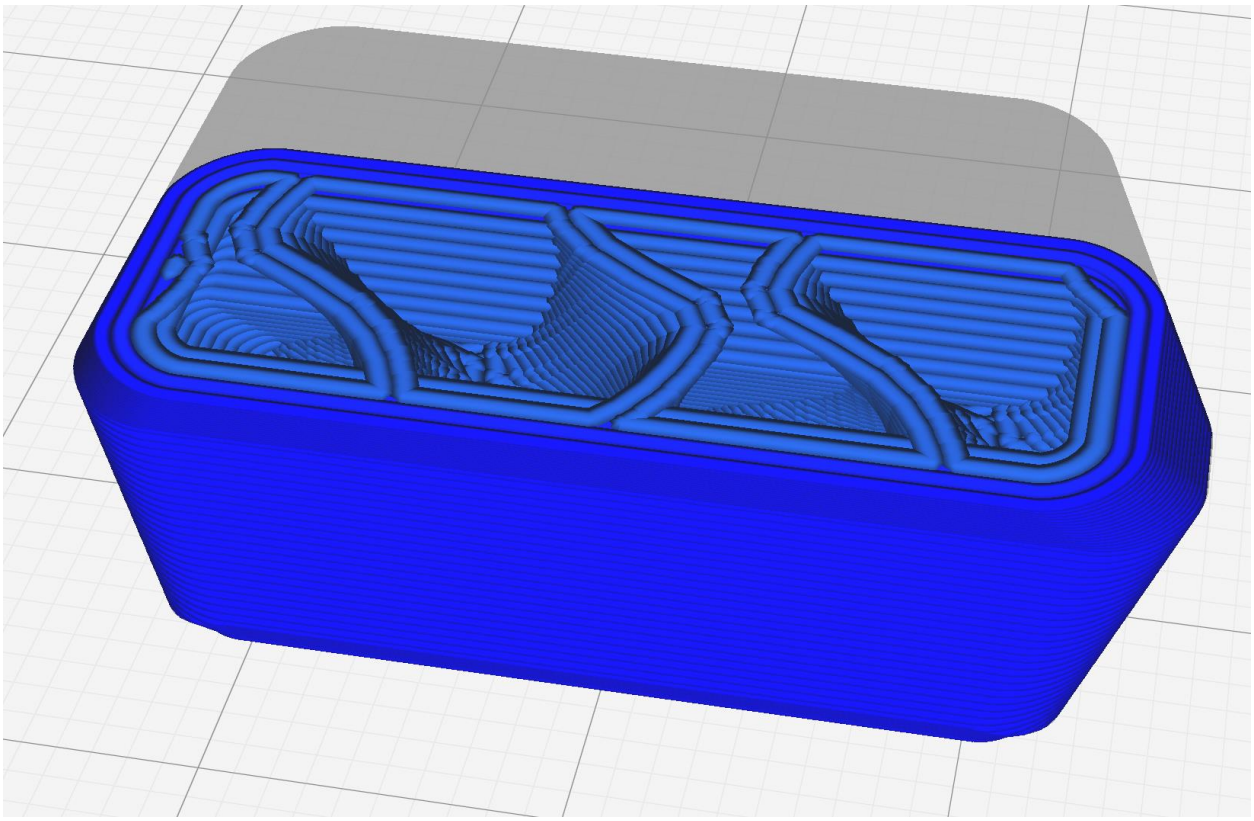

Figure 107: Sectioned view of rendering of G-code to produce one tile on an Ultimaker 3 3D printer. Note that the dimensions of the individual rasters (layer height and line width within plane) have noticeable effects on local stiffnesses and strengths in various anisotropic directions.

Moreover, of even greater concern from a failure standpoint is failure in the bond between tile and fabric (as augmented by the button, which may itself break or merely separate from the fabric, thus ceasing to exert a press-fit effect to adhere the tile to the fabric), and this can scarcely be predicted from simple geometric models treating the fabric as a shelled surface and the tiles as flat surfaces without at least performing experiments to measure the bond

strength in shear, peel, and tension between “typical” buttons, tiles, and fabric. The problem is confounded further when one considers the complex contours of the button and tile surfaces and how the fabric “drapes” to conform to them.

Finally, in the event that neither the tiles, nor the buttons, nor the bonds between tiles, buttons, and fabric, are the weak links, and instead the fabric itself fails, FEA might be somewhat more suited to predict failure loads, given that LS-Dyna has excellent micromechanics models for predicting both deformation and failure of woven fabrics. That said, it should be noted that the user interface of LS-Dyna PrePost 4.7 (the latest version as of this writing) states that the entry nominally giving the ultimate strength at failure is not actually used by the solver (presumably a future edition will implement failure by element erosion or some damage formula), as shown in a screen capture in Figure 108. Even if this were implemented, usually failure in micromechanical models is simulated merely by deleting elements that exceed some stress or strain value, rather than simply generating a crack between elements; thus, the post-erosion behavior of the entire part depends on how large of an element that is deleted, meaning the failure analysis needs to be calibrated to a certain mesh size with considerable experimentation.

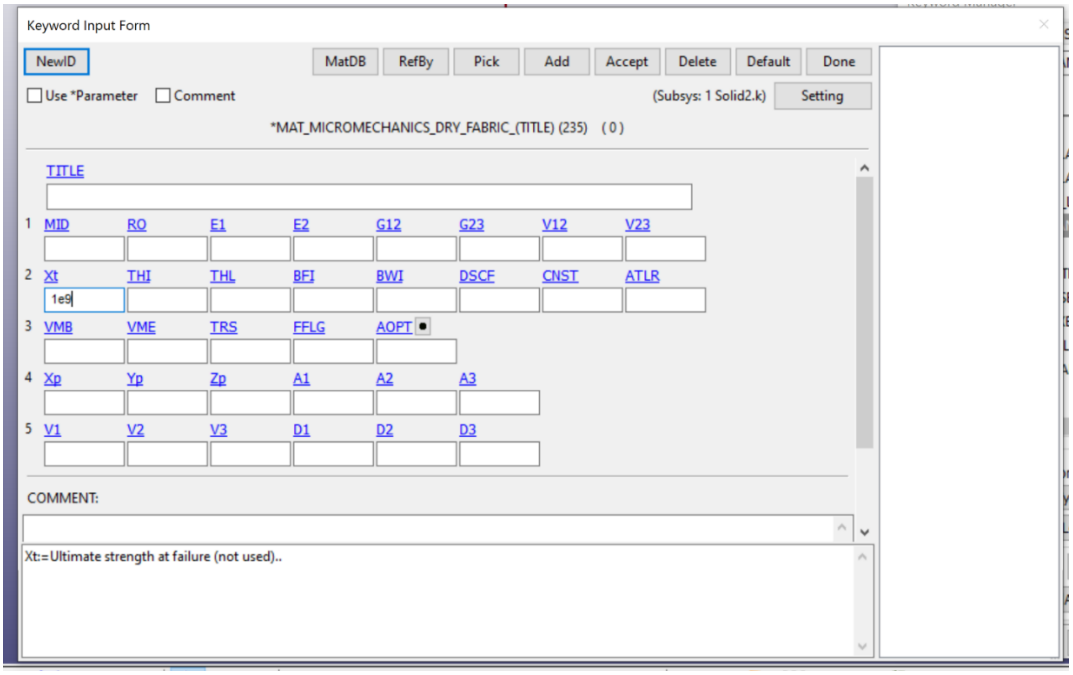

Figure 108: The latest version of LS-PrePost (as of this writing), 4.7, states that failing elements after they reach their ultimate strength has not yet been implemented in MAT_235.

Thus, this author recommends only using FEA to confirm the predicted behavior of arrays that bend towards singly-curved target manifolds (though, as can be seen in this chapter and in Chapter 4 and in this chapter, the formula developed to calculate the needed tile gap length for a given target curvature is sufficiently accurate to generally not need FEA validation), or perhaps to investigate more complex behaviors, such as arrays that exist on closed surfaces or surfaces that are doubly-curved. The next chapter in particular will discuss one such array whose mechanical behavior (and indeed manufacture) is significantly complicated by being on an initial surface that is both doubly-curved and closed. This array is expected to benefit significantly from being simulated without the designer needing to painstakingly manufacture it, and, furthermore, the simulation will hopefully give some insight into what the target shape of the manifold should be to accommodate a joint inside that is rotating to a certain position before lockup.

Conclusions.

The foregoing results indicate that this is a valid technique for simulating arrays in various loading conditions as compared with the experimental results of the previous chapter, though further work should be done to perfect the algorithm for computing gaps between tiles for a desired lockup profile. Certainly, for accurate simulation, this technique requires that the fabric weave is not distorted excessively from the material orientations used in LS-Dyna and if the user is willing to manually determine where contacts are closed, or alternatively engage in some experimentation to evaluate the proper parameters for correct tensile behavior from the fabric material model. Unfortunately, it is only a forward computation method, meaning that once the array is generated its performance can be verified, but the solver gives no direct information on how to generate an array for a desired lockup shape given an input shape. This is unfortunate, as Part II of this dissertation will treat initial arrays that have topologies that differ greatly from that of the initial surface used in this and the previous chapter, and it is unclear how to calculate the tile offsets, or even what a desirable target shape for the arrays might be.

Part II. Lockup-Capable Closed Surfaces.

Chapter 6. Introduction to and Literature Survey of Closed (Cylinder-Like) Surfaces that Tolerate Large-Deflection Bending.

Abstract.

This chapter examines the behavior of geometries that are closed like cylinders and enclose a joint that is undergoing bending. The chapter introduces the basic geometric constraints on an ideal ankle protector, and then proposes a specific manifold shape (to later be tiled with rigid tiles that should produce lockup when the enclosed joint bends to a certain degree). Next, the geometry of this shape is quantified with an eye towards its Gaussian curvature and the continuity of its *uv* curves. The behavior of a linear-elastic shell made in this shape is examined and found deficient in terms of tolerating large-deflection bending without severe shell buckling that reduces its stiffness. This illustrates the importance of a literature review of closed surfaces in large-deflection bending, which is conducted with special attention towards bellows-like surfaces since sinusoidal mesostructures allow cylinder-like surfaces to tolerate more global deformation without buckling. Indeed, several bellows geometries are applied to the hyperboloid-like manifold chosen for an ankle protector, with the behavior of such shapes qualified by 3D printing thin shells out of elastomer in those shapes with favorable results as regards bending tolerance, but no obvious way to produce rapid ~~r~~and rigid lockup. A literature review of other strategies focusing on complex microstructures (consisting primarily of tiny beams that can undergo large amounts of local bending, into which global tension and compression are translated depending on the geometry of the surface) is then performed with reference to Chapter 2's discussion of strain-stiffening metamaterials, with recommendations for the creation of a lockup-capable ankle protector with the fabric-backed tiled array principle. Finally, original metamaterial structures in hyperboloid form designed by this researcher are

tested in various modes and the most effective microstructures chosen, with potential implications for the deformation modes that fabric-backed tiled composite metamaterial arrays should undergo to conform to an ankle joint while being capable of eventual lockup.

Closed-Initial-Manifold Fabric-Backed Array as a Potential Ankle Protector.

The research in this chapter was specifically targeted at extending the original principle (of flat arrays that lock up in single-curvature bending) to protecting a human ankle joint with a pre-curved, closed surface: in fact, the problem of protecting the ankle joint with a suddenly-locking material or structure was the motivation for this author's Master's thesis [1]. While the open and initially-flat arrays studied in previous chapters of this dissertation show an interesting physical principle, they were not seen as the ultimate solution to the ankle-protection problem (but might have relevance to other problems not researched here), both for mechanical reasons and for product-design reasons. As regards mechanical concerns, the 2D arrays studied in the previous chapters are only intended to bend in one direction, and generally have limited to no freedom in other directions. While this is fine for joints that are approximately revolute joints (e.g. the joints between the bones of the fingers), attempting to use several thin strips of these 2D arrays (oriented cylindrically about the ankle) would overall greatly stiffen the protector due to strips being quite stiff in the direction of bending for which they were not designed to have initial compliance. Figure 109 illustrates what such an arrangement of several disjointed strips would look like, but Figure 110 indicates why this would not be functional for creating a device to protect a multi-DoF joint such as the ankle while still giving initial freedom, as certain strips would be unable to bend side-to-side (as this would result in a length change); see Chapter 4 for a thorough discussion on the allowable bending mode for singly-curved and open fabric-backed tiled arrays.

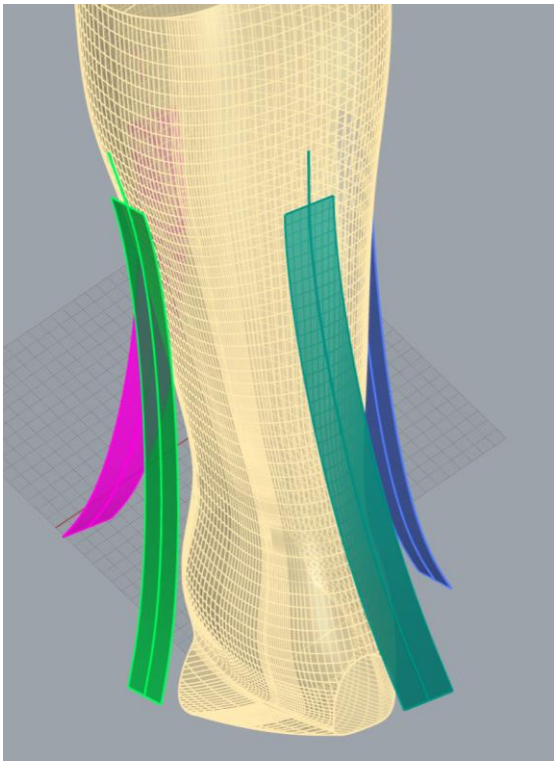

Figure 109: Depicts the flawed concept of using multiple disjointed singly-curved strips to protect the ankle—as noted in the text, this concept is not likely to work, and the point of this illustration is only to show what the concept even looks like. The next figure explains why it would not work.

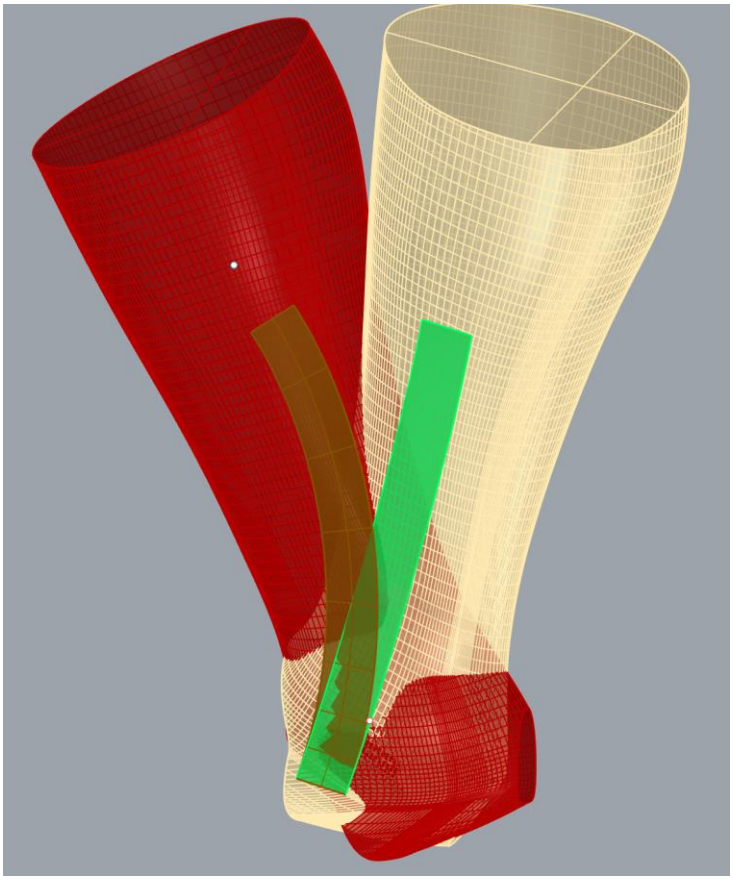

Figure 110: Looking at the left-side view of the disjoint-strip failed concept (the other three strips that were shown in the previous picture are hidden in this one for clarity). If the leg were to rotate forward (from the initial position in yellow, to the final position in red), the strip on the side would have to bend side-to-side, from green to brown, which is not allowed for fabric-backed arrays as the axis of bending has a component that is normal to the surface (see Chapter 4 on the geometric requirements for arrays) and this results in the forward edge of the brown strip being shorter than the corresponding edge of the green strip, and the rearward edge of the brown strip being longer than that of the green strip—an illegal length change that a stiff fabric cannot accommodate. Instead, the green strip would only be allowed to further intensify its existing single-direction curvature, or alternately flatten.

Additionally, if the strips were wide rather than relatively narrow, they would not conform well to the joint and thus occupy more volume (especially distant from the lower leg, which has a greater effect on increasing the mass moment of inertia of the lower leg) than desired. Finally, disconnected strips have the potential to "flop" when the wearer runs or otherwise accelerates the lower leg, which would distract the wearer and have the potential to catch on obstacles. Thus, it seems wise to target a unitary, conformal, and continuous topology for the protective device.

The Practical Importance of Close Geometric Conformity to the Protected Joint.

Indeed, as a digression, it should be noted that closely conforming to the joint to be protected (when it is deflected at every possible position) is essential to minimize the footprint of the protective device; after all, if the footprint of the device were of no concern, it would be trivial to merely put some physical stops on projections attached to the shoe that impact the wearer's shin, but obviously such a solution would be large, inelegant, prone to catching on obstacles in the wearer's environment, of excessive mass-moment of inertia (resisting changes in the orientation of the lower leg and thus hindering athletic performance), and generally uncomfortable. A depiction of such a trivial and undesirable approach is shown in Figure 111; note how large the footprint is, especially at the top of the device (imperfect conformity to the ankle is more tolerable lower down on the leg, e.g. near the ball of the ankle itself, just as pants and shoes do have some offset from this part of the body as well, but not from the calf or higher).

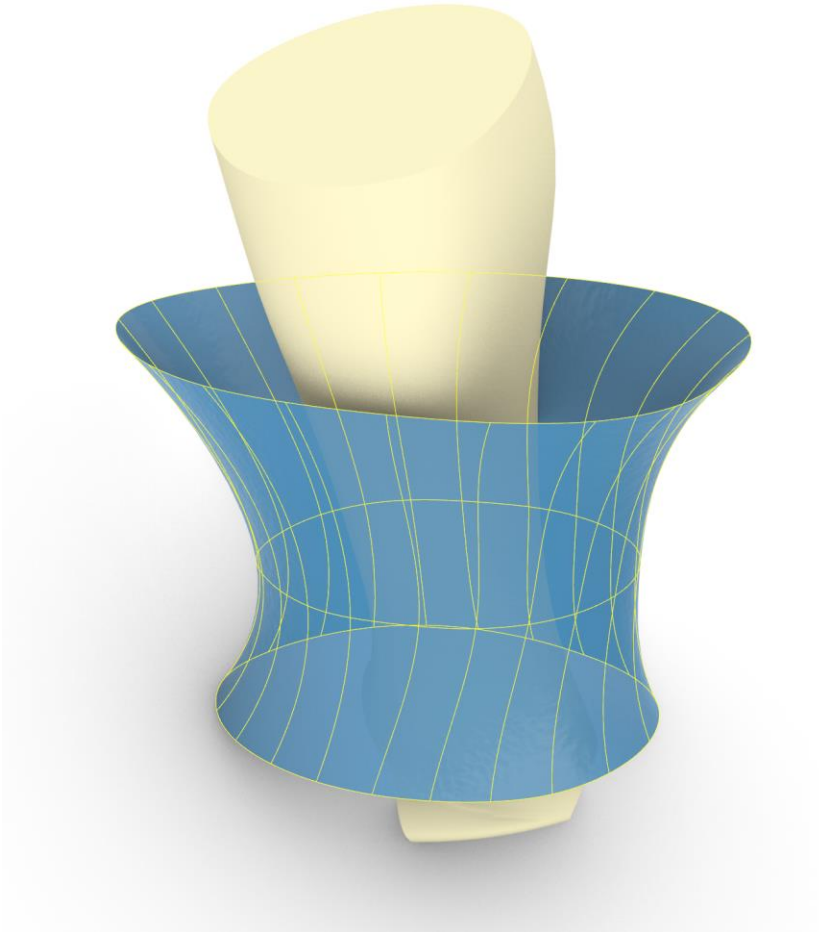

Figure 111: Trivial and undesirable approach for making a simple, rigid protective device for the ankle (protective device shown in blue with yellow lines depicting the uv *curves). This is not the approach to be used in this dissertation because its volumetric footprint is overly large at the top, rather than conforming closely to the leg.*

Rejecting Non-Enclosed Protective Approaches.

It should be admitted that the few known outside attempts at producing a device to limit the range of motion of a joint like the ankle or wrist do not use cylindrical enclosures at all, but rather use disjoint strips of fabric-like material that stiffens gradually when loaded in tension (but buckles and is flexible in bending), connected to the joint by cables. For instance, Pattinson et. al. at MIT designed a 3D printable metamaterial with initially-slack steel cables embedded that produced modest increases in the overall structure's tensile stiffness once the slack was taken up [95]. The researchers then attached this material with cables to a point on the lower leg and to

another on the wearer's shoe and measured the effective stiffness of the wearer's ankle joint with and without the added structure, noting that the joint's stiffness nearly doubled in the direction they chose to protect, while remaining nearly constant in other directions. However, since the strips are interrupted and do not enclose the leg closely at all, but rather can "flop" around to the side of the leg or catch on protruding obstacles, it is clear that this approach is not suitable for dynamic movements (or perhaps even for sedentary users unless properly enclosed without limiting the strip's ability to deform somewhat in tension). Similarly, Simbex LLC's patent [6] discloses a fabric weave that stiffens in tension due to the trellis mechanism locking up; this tensionable member is also to be connected to a joint (like the wrist) by cables, and thus has the same flaws as the MIT team's approach, which probably explains why Simbex's patent was apparently never commercialized.

Designing the Shape of the Undeformed Surface: Surface Geometry Considerations.

The initial manifold used in this chapter will differ notably from the planar initial manifold used in the previous two chapters. First, to enclose the ankle like an uncapped cylinder, the surface must have a single seam at which its cylindrical face is closed and continuous. The surface will be modelled as a Non-Uniform, Rational B-Spline (NURBS) surface, so it is useful to think of it in terms of the qualities of the curves in the *u* and *v* directions that comprise it: i.e. the curves in the *u* direction are all closed ("periodic") curves, and thus, one of the *v* curves acts as a seam for the surface. However, the *v*-direction curves will necessarily be open, not closed. Because it was sculpted from a hyperboloid of one sheet, it will be referred to as the Hyperboloid-Derived Manifold (HDM) and used extensively in Part II of this dissertation. The surface is rendered (with the *u* and *v* curves drawn) in Figure 112. This view also shows the current position of the surface seam, the edge along which the surface joins to

itself to become a closed surface (note that the seam can be shifted to any *v* curve without changing the geometry or topology of the surface in any way, since the surface is of degree 3 and continuous in *uv*). A half-section of the surface was also 3D printed and tested on the author's lower leg to ensure conformity (the shell was rigid and not expected to have any kinematic properties), as can be seen in Figure 113.

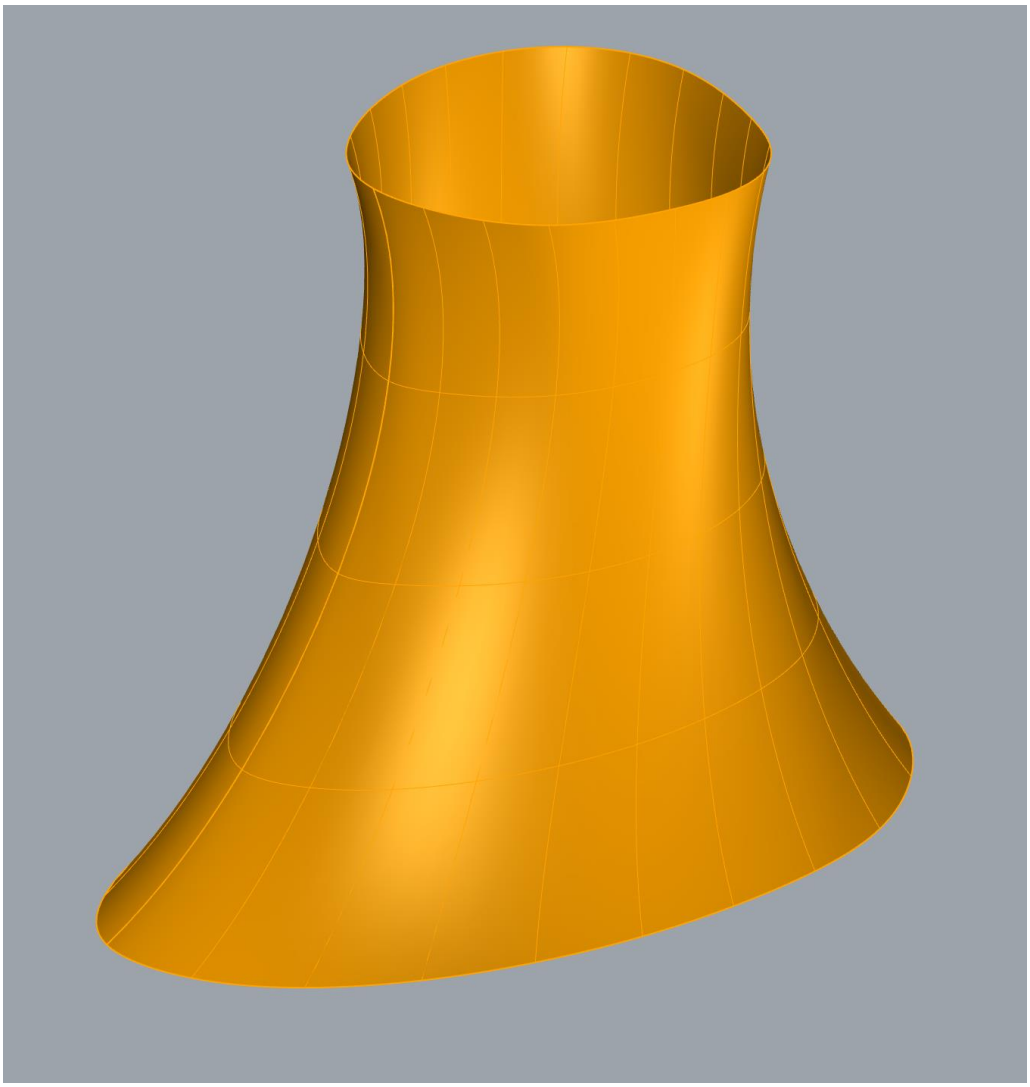

Figure 112: Potential undeformed shape for an ankle protector. It was derived from a hyperboloid of one sheet but sculpted by moving surface control points. The surface is a singly-closed surface (like a cylinder) with no point singularities. Additionally, it is doubly-curved, due to the curves in both the u *and* v *directions being curved; specifically, it has mostly negative Gaussian curvature, though some regions have positive curvature. The* u *and* v *NURBS curves that define the NURBS surface are drawn in lighter yellow. The surface seam is the quasi-vertical curve that is drawn slightly thicker than others at the very front of the manifold (towards the left of this image).*

Figure 113: A half-section of the hyperboloid-derived manifold was printed at 100% scale and then placed over the author's lower leg to verify that the shape is an appropriate one.

Clearly, the simple, planar surface used in the previous chapters for the initial manifold was not periodic and did not have seam curves as it was entirely open (since it did not have seam curves, it also did not have any singularity points). The same is true of the target manifold, to which the array of tiles on fabric in the previous chapters was to be bent until it locked up.

In contrast, from the standpoint of surface modeling with NURBS, this quasi-cylindrical/hyperboloidal surface (as shown in Figure 112) has a seam curve and no singularity point and thus will be denoted in this author's parlance as a "singly-closed" surface. Of note, the hyperboloidal is not watertight and does not enclose a volume (as one would expect, for a jointed limb could not go through such a surface), and thus it is important to distinguish it from a surface with spherical topology that is entirely closed and watertight (such a surface could be called "doubly-closed"). In NURBS geometry, a spherical surface or surface of similar "doubly-closed" (in this author's parlance) topology is formed by revolving an arc about an axis, generating singularities at the ends of the arc as well as a single seam; indeed, a doubly-closed single surface cannot be made without singularities (although, to use surface geometry

nomenclature, a closed polysurface of multiple surfaces that share edges and perhaps some higher degree of continuity could be constructed without any pointwise singularities). On the other hand, open surfaces could also have singularities (though they certainly do not need to); for instance, the surface of revolution shown in Figure 114 is an open surface in topological terms since it is not watertight, but in NURBS modeling it is a periodic surface of revolution with a singularity point at the axis of rotation and a single seam at which it is closed (of note, there are trimmed NURBS approximations of this surface without a tip singularity). Thus, to recapitulate, the surface used in this chapter should be singly-closed like a cylinder (with closed curves in the *u* direction but not in the *v* direction) and not have any singularities.

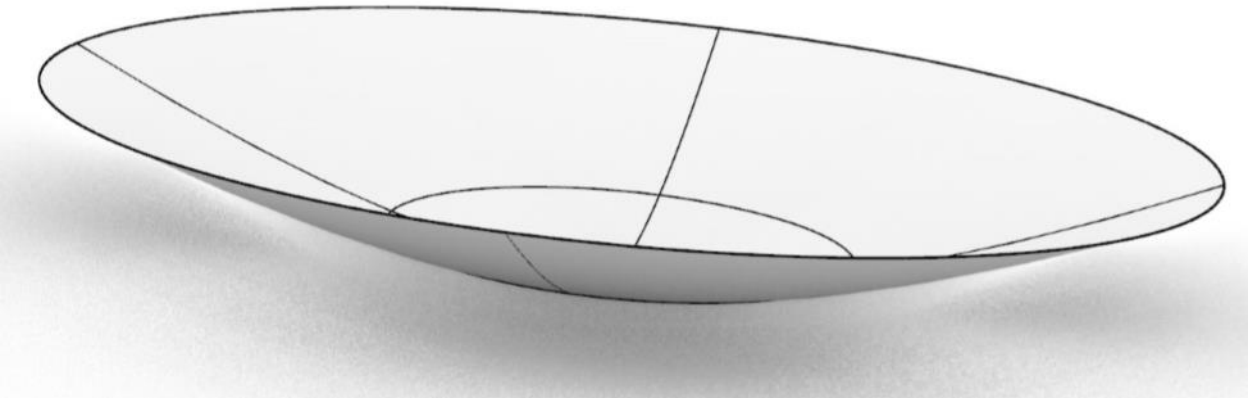

Figure 114: A periodic surface with a single seam but also a singularity at the ends, meaning that it looks "open". It is not closed like a cylinder, but strictly speaking its NURBS representation is closed in the sense of the surface having a seam, but it is not cylinder-like (does not encircle a joint) because that seam has a singularity point.

Characterizing the Gaussian Curvature of the Undeformed Surface.

Another important distinction between the initial surface used in this chapter and the surfaces used in previous chapters lies in the nature of the dimensionality of the curvature of these surfaces. The initial and target surfaces used in Chapters 4 through 7 were singly-curved surfaces, also known as developable surfaces, the meaning of which will be explored immediately below. In contrast, nearly all surfaces studied in Part II, including the HDM surface

that is used most widely, are doubly-curved surfaces, meaning that both the *u* and *v* curves that generate the surface have curvature, or, more formally, that Gaussian curvature is nonzero, at least at most regions on the surface citation (the Gaussian curvature could be zero at specific points or along specific curves on the surface, or at entire regions on a polysurface).

The simple surfaces used as initial and target manifold shapes in Part I of this dissertation had Gaussian curvature that was constant at zero everywhere on every surface. However, not only will the more-complex surfaces in Part II have non-zero Gaussian curvatures, but their distributions of Gaussian curvature will generally be complex and vary over the surface (perhaps the Gaussian curvature is negative or positive everywhere on the domain, or perhaps there are regions of positive Gaussian curvature and regions of negative Gaussian curvature). Where Gaussian curvature is positive, the surface's two principal curvature directions point in the same direction (both outward or both inward, depending on the surface normal)—for instance, a sphere, an ellipsoid, and a paraboloid have positive Gaussian curvature everywhere. In contrast, where Gaussian curvature is negative, the surface's two principal curvature directions point in opposite directions (one outward, one inward), sometimes referred to colloquially as a "saddle point". Similarly, if a surface has a saddle point, its Gaussian curvature will be negative at least at that point and in its vicinity (though not necessarily elsewhere on the surface). Moreover, surfaces like the hyperbolic paraboloid [96] and hyperboloid of one sheet [97] have negative Gaussian curvature everywhere, while still-more-complex surfaces could have regions of positive Gaussian curvature and regions of negative Gaussian curvature, with points or curves on the surface at which the Gaussian curvature is locally zero (however, in NURBS modeling, a unitary surface could not have nonzero areas, rather than zero-thickness lines or points, on which the Gaussian curvature is exactly zero if it also has regions of non-zero curvature, because of the

continuity required of NURBS single surfaces; however, polysurfaces could indeed be formed of zero-Gaussian-curvature surfaces connected with some degree of continuity to non-zero-Gaussian-curvature surfaces [98]).

The surface that was first introduced in Figure 112 and that is to be the basis of the potential ankle protector in this and subsequent chapters has its Gaussian curvature distribution shown in Figure 115. Note that Gaussian curvature is depicted by coloring the surface; in this software package, blue regions indicate areas of the most strongly-negative Gaussian curvature on the surface, green areas indicate areas of near-zero Gaussian curvature, and red areas (not present on this surface) would be areas of the most strongly-positive Gaussian curvature. Note that at most of the area on the surface, the Gaussian curvature is negative (hyperboloid-like), though some areas are very close to zero (nearly cylinder-like). Clearly, this surface is doubly-curved, not developable.

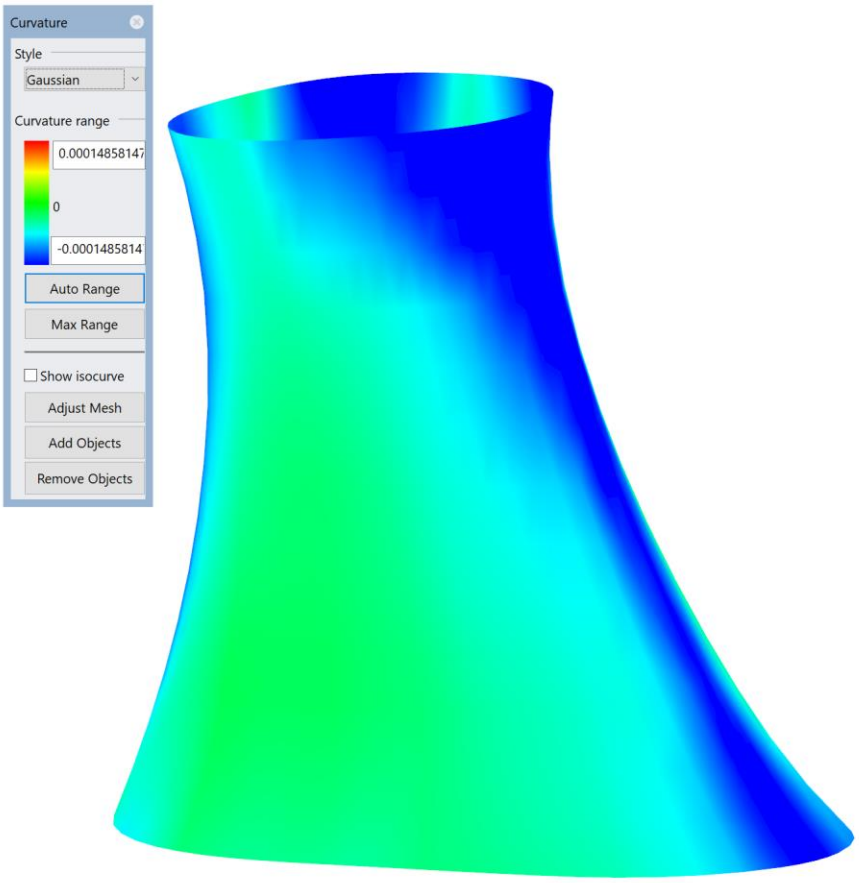

Figure 115: Contours of Gaussian curvature plotted on the surface. Areas that are green in color have approximately zero Gaussian curvature (cylinder or sheet-like), whereas those in blue have the most strongly-negative Gaussian curvature (hyperboloid-like). There are no areas on this surface with positive Gaussian curvature (sphere-like). A scale is shown to the left. Units are derived from mm, although relative magnitudes over the surface are more important than absolute.

The question whether or not a surface is "developable" should not be confused with the question of whether or not it is "ruled". In general, a ruled surface is defined as one on which, for every point on the surface, there lies at least one line segment through that point that also lies entirely on the surface. As a consequence of this property, ruled surfaces can be generated by sweeping a line through space along guide curves (that may be open or closed curves) [99]. While many ruled surfaces are indeed also developable (i.e. singly-curved), there also exist some ruled surfaces that are doubly-curved. For instance, both the elliptic hyperboloid of one sheet and the hyperbolic paraboloid are ruled surfaces (more specifically, doubly-ruled surfaces

inasmuch as not one but two distinct line segments on those surfaces pass through each point on those surfaces) that also have double curvature (nonzero Gaussian curvature) instead of single curvature (zero Gaussian curvature, i.e. developable) [99].

In general, the "standard" geometric surface that the surface that is to be tiled in this chapter (shown in Figure 112 and Figure 115, among others later on) most closely approximates is the hyperboloid of one sheet (also known as the elliptic hyperboloid, and not to be confused with the hyperboloid of two sheets): not only does the hyperboloid of one sheet have negative Gaussian curvature everywhere, but it is a periodic surface with a surface seam with no point singularities. Of course, this is merely a resemblance (and indeed, the custom surface for this chapter, henceforth to be referred to as the hyperboloid-derived surface, was created by sculpting the control points of a true hyperboloid of one sheet). For comparison, an example hyperboloid of one sheet in NURBS representation is shown in Figure 116, with the surface seam highlighted in yellow. Effectively, a hyperboloid of one sheet is a surface of revolution formed by rotating a hyperbola about an axis that the hyperbola does not intersect. (It should not be confused with a hyperboloid of two sheets, which consists of two surfaces of positive Gaussian curvature, not negative Gaussian curvature as with the hyperboloid of one sheet; the two surfaces comprising the hyperboloid of two sheets are formed by revolving both branches of a hyperboloid about an axis that intersects the hyperboloid).

Figure 116: Hyperboloid of one sheet (a surface of revolution), with the seam of the surface (i.e. the hyperboloid that generates the surface by revolution about the central axis) highlighted in yellow. Note that it has fundamentally similar topology to the "hyperboloid-derived surface" that will be used in an attempt to create an ankle protector.

In addition to revolving a hyperboloid to generate the surface in NURBS geometry, a hyperboloid of one sheet can be generated from the zero set of a polynomial of second degree in three variables, according to the equation [97]:

$$\frac{x^2}{a^2} + \frac{y^2}{b^2} - \frac{z^2}{c^2} = 1 \tag{6.1}$$

However, equation-driven surfaces are not used in exact form in NURBS geometry (approximations exist with patching topology). Of note, if the coefficients *a* and *b* in the above equation are unequal, the resulting hyperboloid will not be a surface of revolution (i.e. not have circular cross-sections when sectioned by a plane normal to the *z* axis), but rather be a "rail-revolved" surface (specifically, with ellipsoidal cross-sections when sectioned by a plane normal

to the *z* axis). An example of the latter type of hyperboloid, a rail-revolved surface with ellipsoidal cross-sections when sectioned normal to the *z*-axis, is shown in Figure 117.

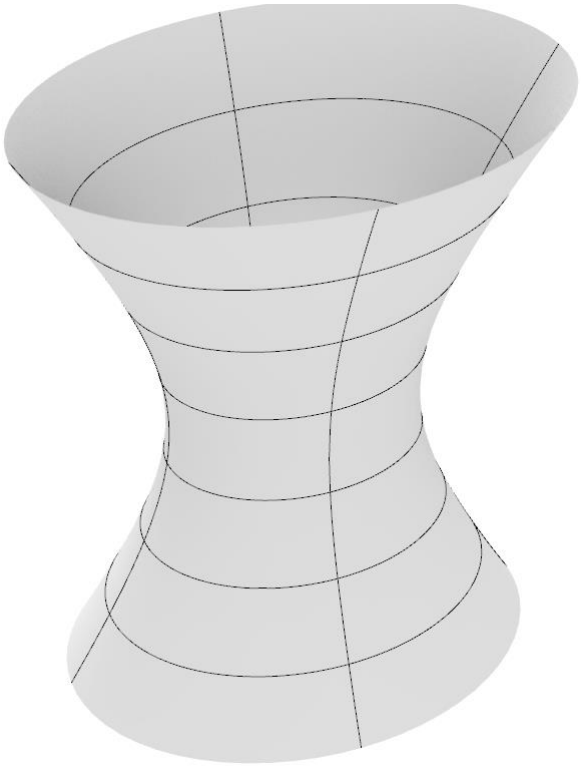

Figure 117: Hyperboloid of one sheet with ellipsoidal z cross sections, created by scaling parameters in the equation or by scaling the surface along an axis.

Ultimately, the "hyperboloid-derived surface" that will be the initial manifold created for this chapter was generated by first creating a hyperboloid of one sheet (around a 3D model of a human lower leg and a tennis shoe for sizing). Then, this surface was rebuilt with many control points, which were then moved manually to "sculpt" a surface that more or less conforms to the leg around the ankle, with some outward flare at the top and bottom. The surface was rebuilt as necessary according to the conventions of surface modeling. The reason that a hyperboloid of one sheet was chosen for the starting geometry, instead of a simpler cylinder, was that the inward curvature in the *v* direction was intuitively felt to be better able to resist the shell buckling that might greatly reduce the surface's post-lockup bending stiffness. Additionally, the hyperboloid-

style surface conforms better to the geometry of an ankle than a cylinder, because it flares inwards near the middle, which is beneficial from the standpoint of reducing the surface area and thus mass (since the mass of the system would be roughly directly proportional to the surface area, given that the tiles are offset by a constant thickness from the underlying manifold), and additionally it would reduce the mass moment of inertia that a hypothetical ankle protector would add (which increases with the square of the offsetting distance from the ankle, even with constant mass).

Characterizing the UV Curvature of the Manifold.

A more-detailed investigation of the curvature of the surface can be performed using curvature "combs" (also referred to as "wires", depending on the CAD package), which follow the *u* and *v* curves and indicate the magnitude and direction of the curvature locally at a set number of points on each *u* or *v* curve. When these "combs" are plotted at a fairly high number of intervals on the surface, as done in Figure 118, the direction of curvature for the *u* and for the *v* curves becomes readily apparent. The curves that go more or less "vertically" (*v* curves by convention) have their curvature combs plotted in cyan; note that the curvature on these *v* curves is always outwards (away from the closed surface), but since (at least in this CAD package) the curvature comb is plotted in the opposite direction of the radii of curvature, the cyan curves point towards the inside of the closed surface. In contrast, the "horizontal" curves, *u* by convention, have their curvatures oriented inwards (but combs pointing outwards, again due to the behavior of this CAD package). In general, it is desirable for the *u* and *v* curves in the surface to not have excessive changes in their curvatures at any point. For those unfamiliar with *uv* surface mappings, a brief explanation is shown in Figure 119. (It is analogous to mapping a space curve with the parameter *s*: $x = f_1(s), y = f_2(s), z = f_3(s)$).

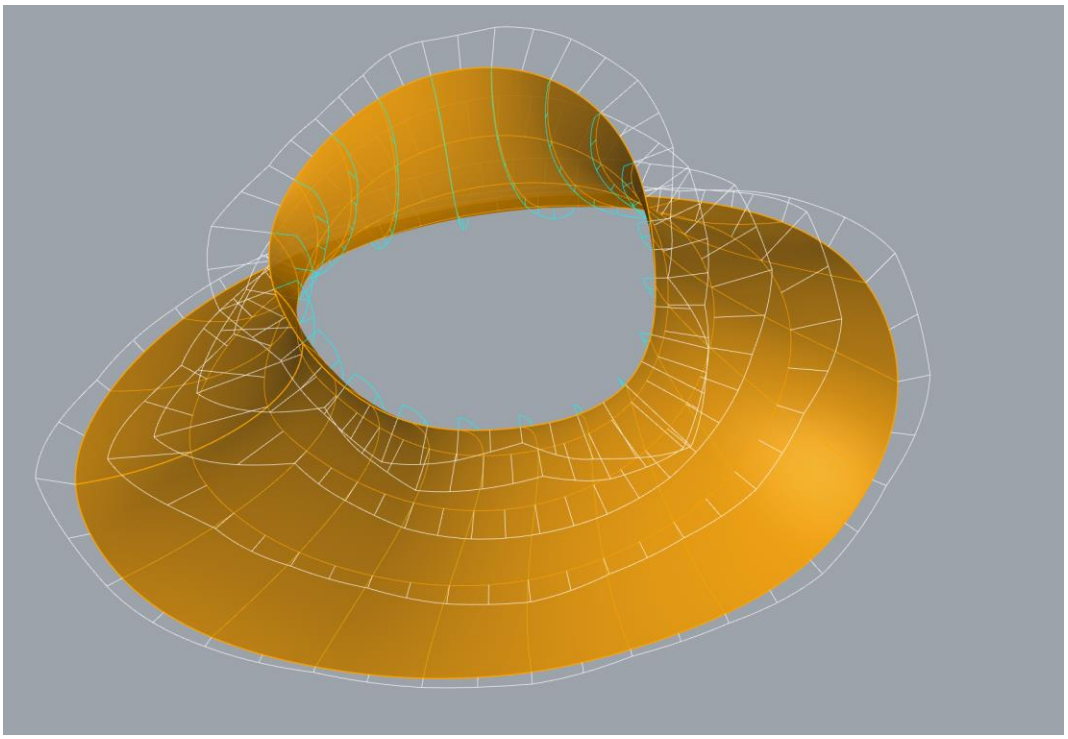

Figure 118: This underside view shows the curvature profiles of the curves in both the u *and* v *directions of the surface by showing "wires" or "combs". The "combs" that are white in color are in the* u *direction, and those of cyan color are lie in the* v *direction, which is roughly vertical.*

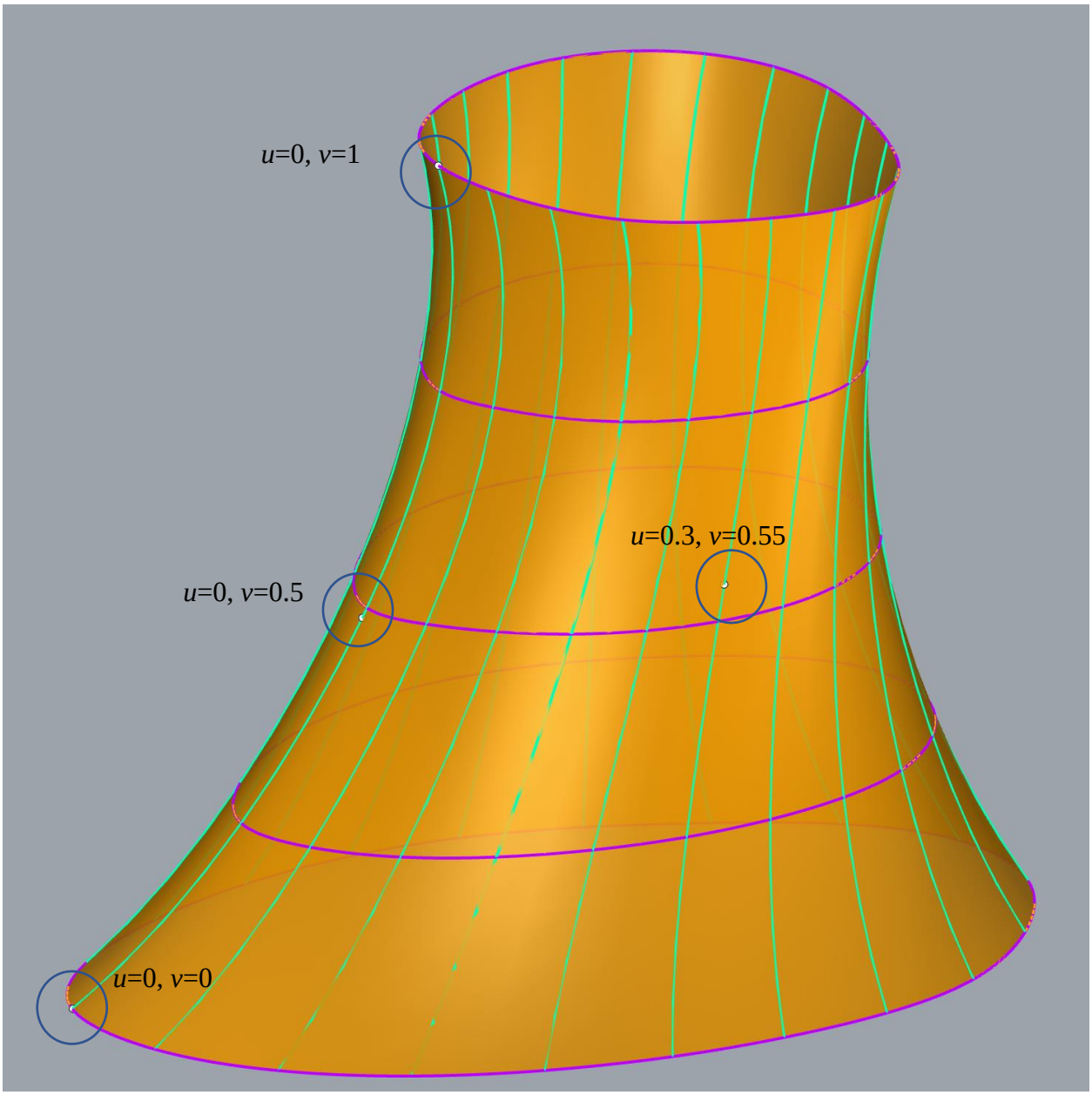

Figure 119: Illustrating the concept of uv *mappings of surfaces. The sea-green curves are in the* v *direction, and the pink curves define the* u *direction (the pink curves are closed, the sea-green curves open). Some example (*u,v*) coordinates of points on the surface are shown; note that the parameters range from 0 to 1 for both* u *and* v*. Additionally, the parameter* w *is used to refer to displacement normal to and not on the surface.*

Testing the Hyperboloid-Derived Surface in Shell Bending.

For preliminary information, a thin-walled but solid version of this hyperboloid-derived manifold was 3D printed in a soft, thermoplastic elastomer to evaluate its behavior in bending. Certainly it was not anticipated that a fabric structure of the same geometry would have

comparable properties, for many reasons, principally because fabrics microbuckle in compression at the yarn level. Other factors that would make the mechanical response of a fabric manifold categorically different from that of an elastomeric shell are the disparity between tensile and bending stiffness being far higher for fabrics than for elastomeric shells and the lack of a bias-compliance "trellis" mechanism in the 3D printed elastomer (versus its presence in fabric). Moreover, the final structure that this chapter is to generate, an array of rigid tiles on a flexible fabric backing, would have even more pronounced differences in properties once the tiles are added. However, it was intuitively plausible that, for the tiled structure to effectively generate significant lockup stiffness, it should not experience excessive deflection during shell buckling (though some is likely unavoidable in large-deflection bending), and additionally it should not see shear "kinking" if the top is tied to the rotating leg (as discussed below).

The undeformed shell structure is shown as-printed and deformed in Figure 120. Note how the structure does crease near its center when made to bend; at this point, the structure becomes far less stiff against further bending, which may not bode well for the success of this manifold. Interestingly, if a rigid tube is placed inside the surface (better approximating a human leg) and rotated forwards, the structure cannot buckle inwards near the center and thus becomes much stiffer; shell buckling instead occurs very near the bottom of the shell, as can be observed in Figure 122. Of course, a fabric structure would not be stiff in this mode due to the compression it entails resulting in fabric microbuckling at the yarn level, so this seems to improve the chances that this manifold shape will be successful when translated into a fabric-backed tiled array.

Figure 120: Left: undeformed 3D print of hyperboloid-derived manifold. Center and right: two different views of the shell being bent forward. Note the significant creasing inwards near the middle of the shape.

Figure 121: Top view of the hyperboloid-derived manifold in point loading approximating bending. (Left: undeformed, right: deformed). Note the moderate change in the cross-section, especially in the middle of the manifold (where it creases inwards significantly) but also near the top (where it ovalizes somewhat).

Figure 122: If a rigid object is placed inside the manifold to prevent it from buckling inwards, the next shell-buckling mode concentrates deformation near the bottom of the shape (circled in blue), and the structure becomes considerably stiffened.

In any event, it is reasonable to assume that a fabric-backed array would behave quite differently, mainly because fabric can easily compress thanks to local microbuckling of the yarns. Additionally, rigid tiles would constrain larger-scale shell buckling somewhat, and moreover, this manifold is the most pleasing to the eye and parsimonious with material and mass-moment of inertia, so it was the one chosen for the simulations that follow. However, for the sake of completeness, the other manifold geometries that were considered are disclosed and investigated somewhat below.

Alternatives to the Hyperboloid-Derived Manifold.

Straight Cylindrical Manifold.

In terms of singly-closed surfaces with constant tangent directions at their tops and bottoms, there were four alternatives to the modified hyperboloid of one sheet that were rejected: a singly-curved but closed cylinder, a doubly-curved and closed surface with positive Gaussian curvature (like a truncated sphere or Chinese lampshade), and two classes of surfaces with

variable Gaussian curvature (vase-like). In the first case, such a cylinder would be produced by performing a linear extrusion of a curve encircling the leg. This is quite simple to create CAD geometry of (for instance, such a surface is shown in Figure 123: it is a "cylinder" in the most general sense, with a closed curve as its extrusion profile: of course, it is not a "right circular cylinder" inasmuch as the generating curve is not circular, and the curve is not extruded normal to the plane it lies in).

However, the lack of flaring inward at the top and bottom of a cylindrical surface was intuitively felt to result in more buckling and crinkling to conform to a rotating joint, especially if the top edge is tied to the leg due to global shear as well as length changes. Additionally, a flared surface like the hyperboloid-like manifold selected in this chapter has superior initial linear bending stiffness as compared with a cylinder, simply due to the greater distance of the material from the central axis.

Finally, such a cylindrical surface would experience extreme shell buckling by creasing with large underlying rotation of the leg (which would be both difficult to predict, and likely reduce the stiffness of the array, which might counteract the lockup effect). The reader can easily verify this by simply bending a cardboard tube and observing its shell buckling after a brief period of elastic bending. Admittedly, at this stage in the research it was far from clear that this hyperboloidal manifold shape would be much better in terms of resistance to buckling during bending; furthermore, even if the resistance to buckling of a plain manifold (without tiles) proves to be poor, the addition of tiles might constrain shell buckling in the circumferential direction and thus allow the array to maintain its stiffness against buckling once lockup is desired.

Figure 123: Alternative initial manifold: it is singly curved (thus, its Gaussian curvature is zero everywhere). However, it is intuitively felt to be inferior to the manifold preferred in this chapter (shown in Figure 112) because its single curvature gives less resistance to buckling.

Positive-Gaussian-Curvature, Truncated-Sphere Manifold.

The second potential alternative to the hyperboloid-like manifold would have mostly positive Gaussian curvature everywhere and resemble a Chinese lampshade or truncated sphere. Specifically, it could be generated by lofting with tangent or curvature continuity between two truncated-conical surfaces that flare outward rather than inward (as with the hyperboloid-of-one-sheet-inspired surface, which could be generated by lofting with tangency continuity between truncated-conical surfaces that flare inward). Strictly speaking, in terms of NURBS modeling, the surface was not spherical at all, nor truncated in any way, as it is not advisable to use trimmed surfaces for some of the operations required further on. This manifold is shown in

Figure 124, and a contour plot of its Gaussian curvature is shown in Figure 125. The manifold would understandably be expected to crease (shell-buckle) inwards when the joint it encloses bends, perhaps slightly above its centerline. Clearly, the manifold does not conform closely to the leg, producing excessive area (ergo mass) and excessive offset (ergo excessive mass-moment of inertia), and generally appears unsightly and comical.

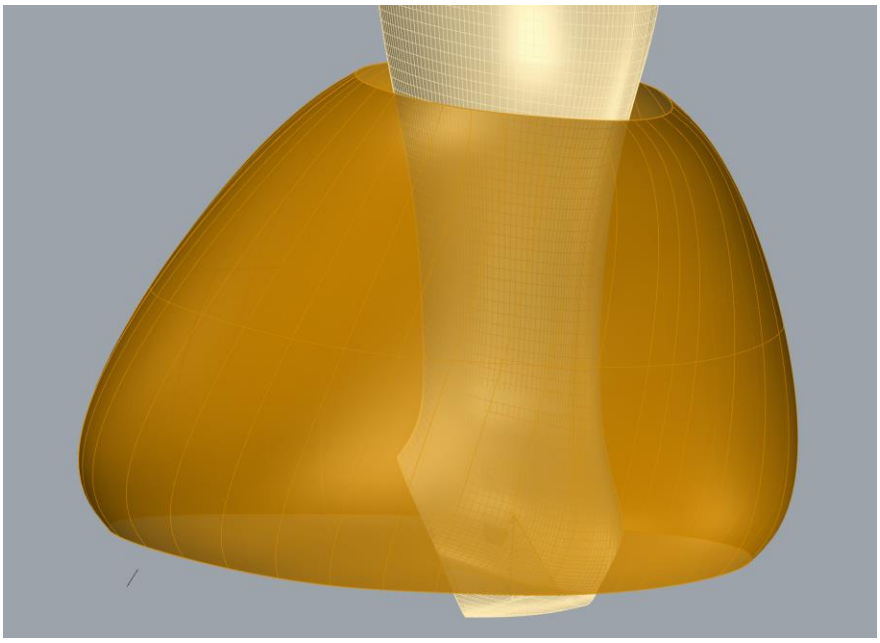

Figure 124: Hypothetical alternative to the hyperboloid-derived manifold; this one instead has positive Gaussian curvature and resembles a Chinese lampshade. The surface curves outwards at both the top and bottom, producing positive Gaussian curvature nearly everywhere).

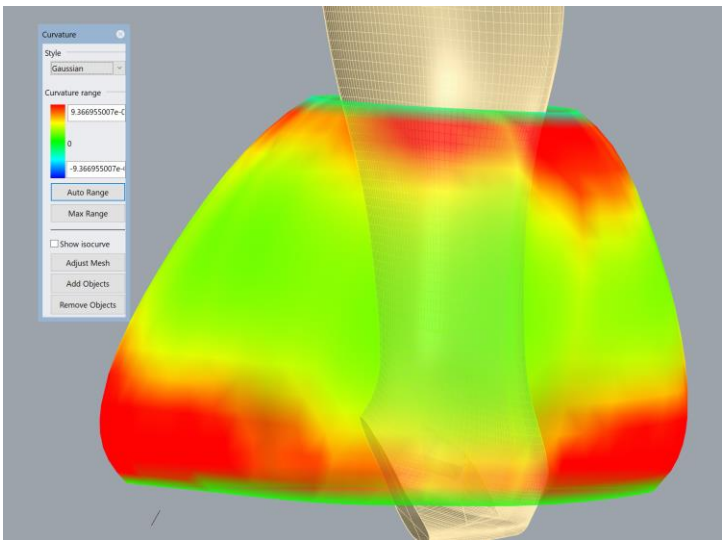

Figure 125: The Gaussian curvature over the "Chinese lampshade" surface is positive everywhere, as evidenced by the fact that no cyan or blue is visible on this contour plot save there. However, the intensity of the Gaussian curvature does vary over the geometry, from nearly-flat in the middle to more sharply doubly-curved at the top and bottom.

S-Shaped "Carafe" Manifold with Alternating Tangent Directions.

Alternatives to the foregoing manifolds could be generated by reversing the direction of the flare of the conical surface that generates the loft at either the top or the bottom, creating a surface that resembles a "carafe" for serving beverages. For instance, the following surface flares outward at the top (near the calf) but inward at the bottom (near the shoe), as depicted in Figure 126. A contour plot of its Gaussian curvature distribution is shown in Figure 127; note that it has regions of both negative and positive Gaussian curvature, as well as a transitional region in the center.

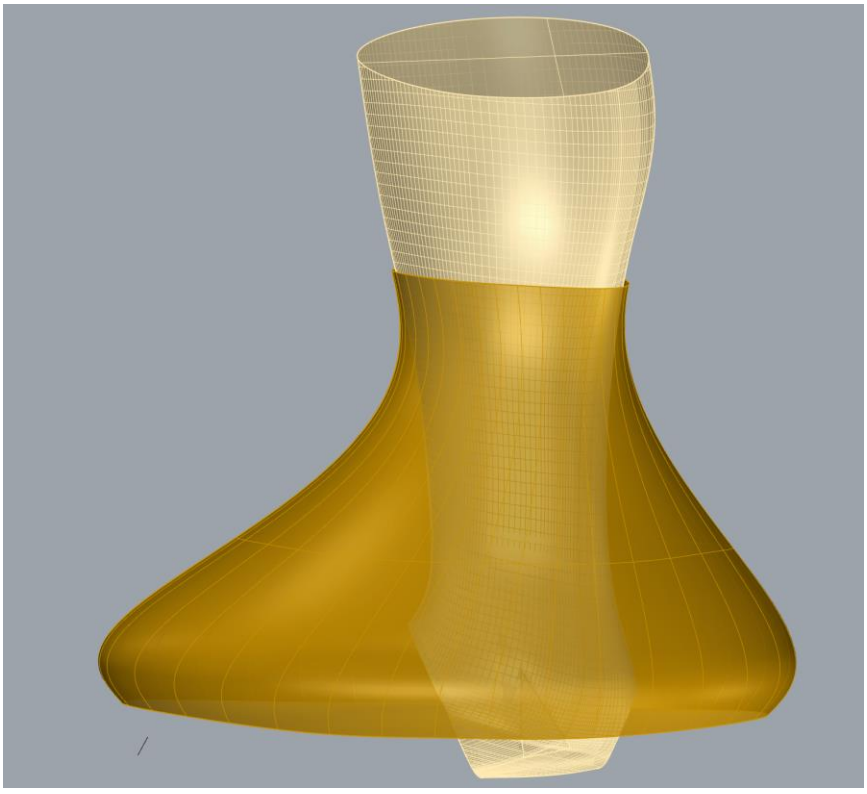

Figure 126: "S-shaped" manifold bulging outwards at the base and inwards towards the top of the leg.

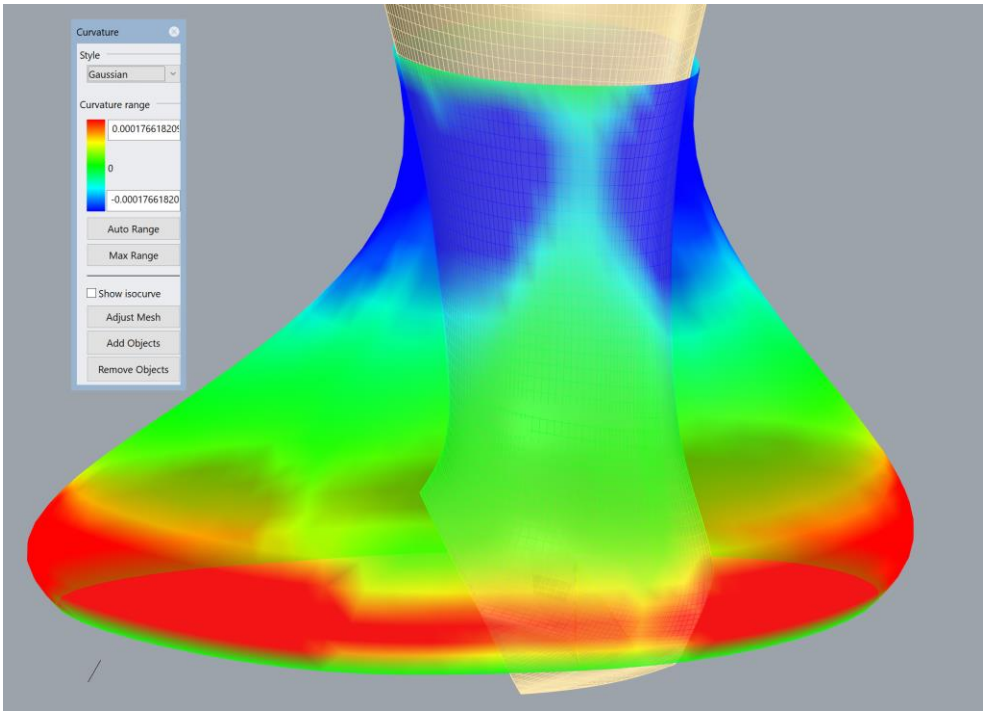

Figure 127: Contours of Gaussian curvature on the "carafe" surface. The green regions have nearly zero Gaussian curvature; i.e. the surface is roughly singly-curved there. Blue areas have the most negative Gaussian curvature (i.e. those regions have a saddle-shaped curvature profile), and red areas have the most positive Gaussian curvature (i.e. those areas have synclastic curvature, like a bowl). Note that this is purely for visualization and is not a form of finite-element analysis, nor does it directly correspond with mechanical properties.

While it is not especially economical with space, the "carafe surface" is at least superior to the "Chinese lampshade" in terms of conformity to the leg. Additionally, when a thin-shelled version was additively manufactured out of soft thermoplastic elastomer and subjected to bending, it proved more successful in containing a joint with large bending deflection. Intriguingly, this was accomplished by localizing its shell buckling to the central strip of the surface, as shown in Figure 128. This was probably the result of the fact that the area of near-zero Gaussian curvature (which is the most amenable to bending) coincides with the center of the surface (as shown in Figure 127). Unfortunately, this severe creasing was too concentrated in this region (it would be desirable to distribute the deformation over a larger area), and additionally, there was some ovalization (inward bending in one direction, outward bending in another) of the top region, as can be seen from the top-down view in Figure 129.

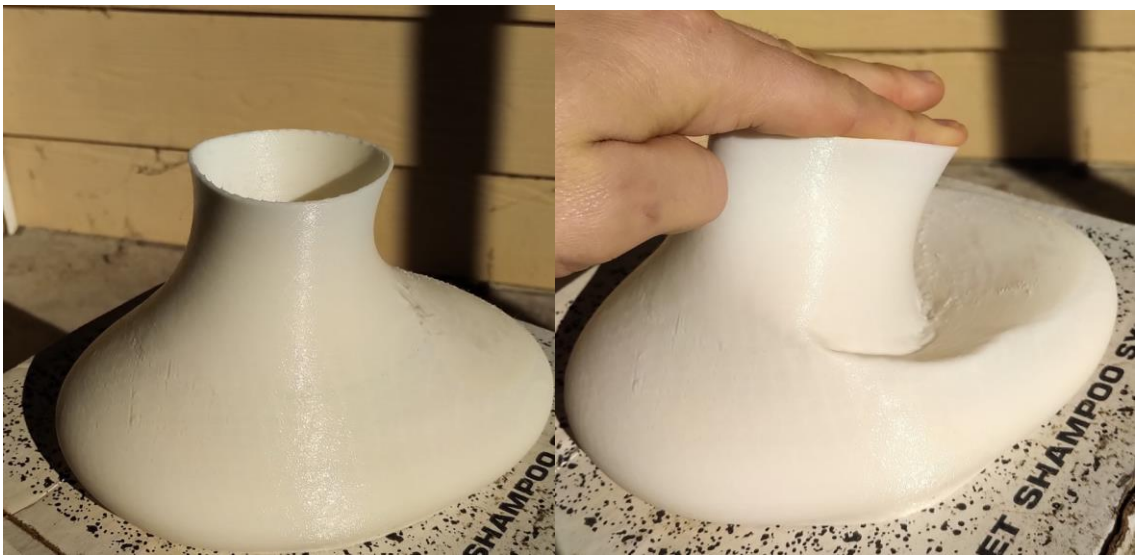

Figure 128: The S-shaped, "carafe" manifold in global bending. Like the hyperboloidal manifold, it does witness significant shell buckling during bending, but it results in far less loss of cross-sectional area about the middle region, and consequently far less catastrophic loss of bending stiffness.

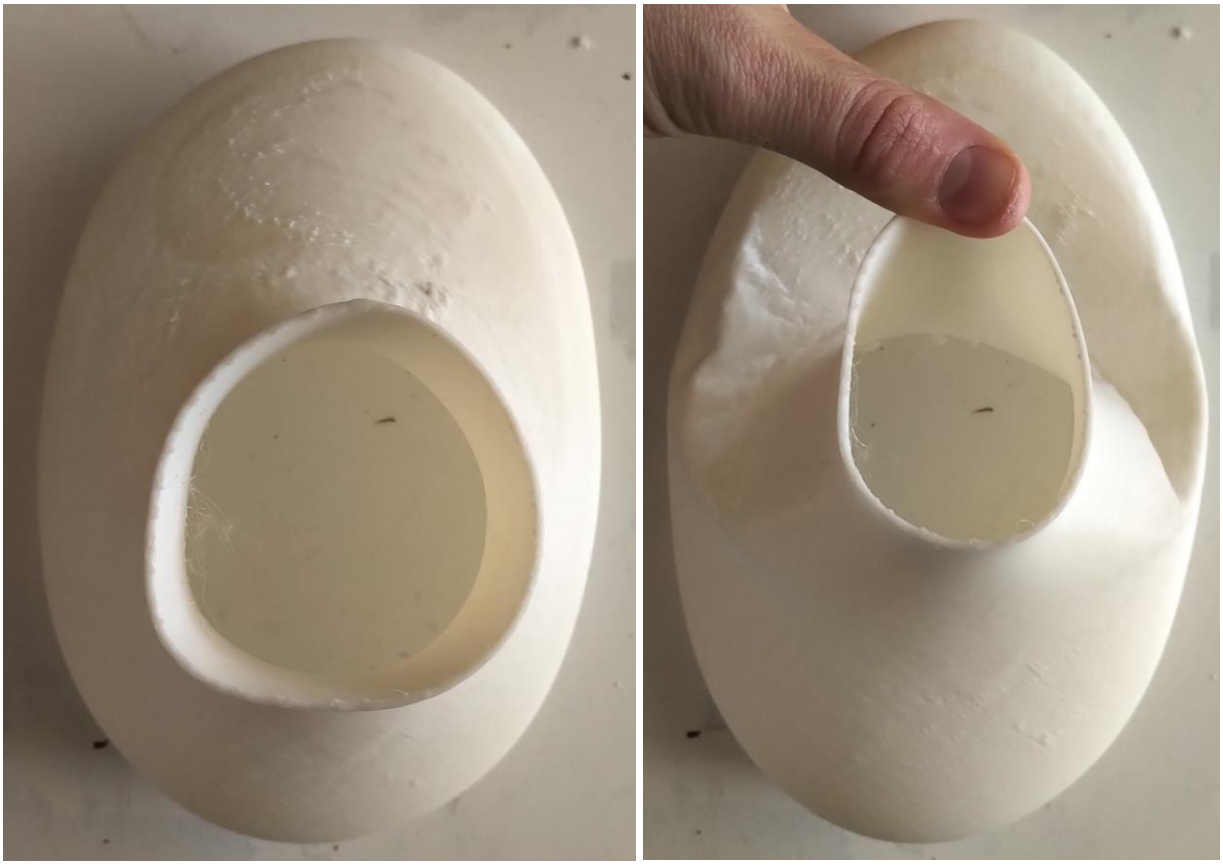

Figure 129: Top-down view of the "carafe"-shaped manifold in point loading to simulate bending. Note the ovalization of the cross-section (especially near the top), as well as the creasing evident in the middle section of the manifold.

S-Shaped "Bell" Manifold with Reversed Tangent Directions.

The final combination of tangent directions for the loft could produce a bell-shaped surface that flares outward at the top and inward at the bottom, as depicted in Figure 130. This surface also appears unsightly and ponderous due to its outward flare at the top and would not likely be ideal. A contour plot of its Gaussian curvatures is shown in Figure 131; note that the region near the top has positive Gaussian curvature (sphere-like), and the area near the base has negative Gaussian curvature (saddle-like), with the central region having low-magnitude Gaussian curvature and thus being nearly developable (as with the previous S-shaped surface, the "carafe").

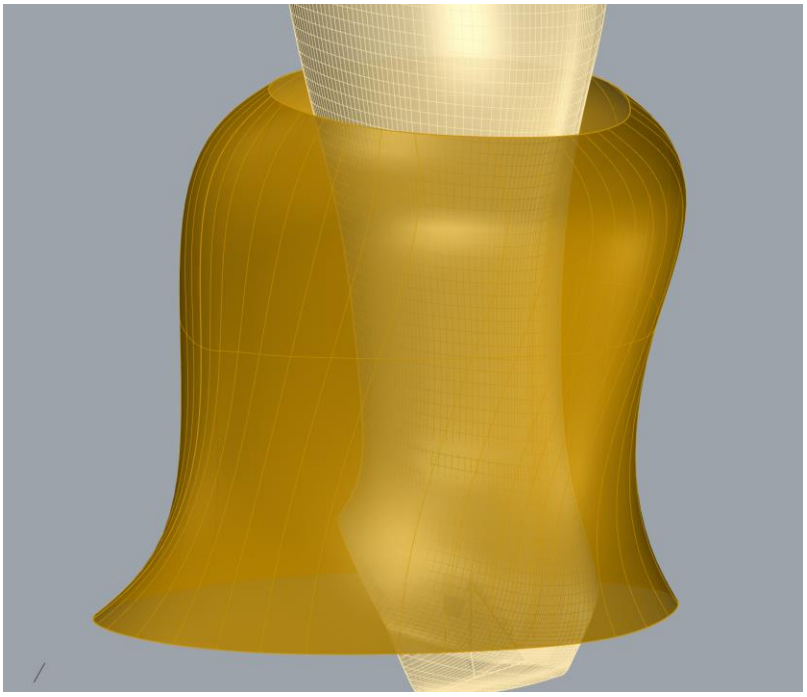

Figure 130: CAD geometry of the S-shaped "bell" surface.

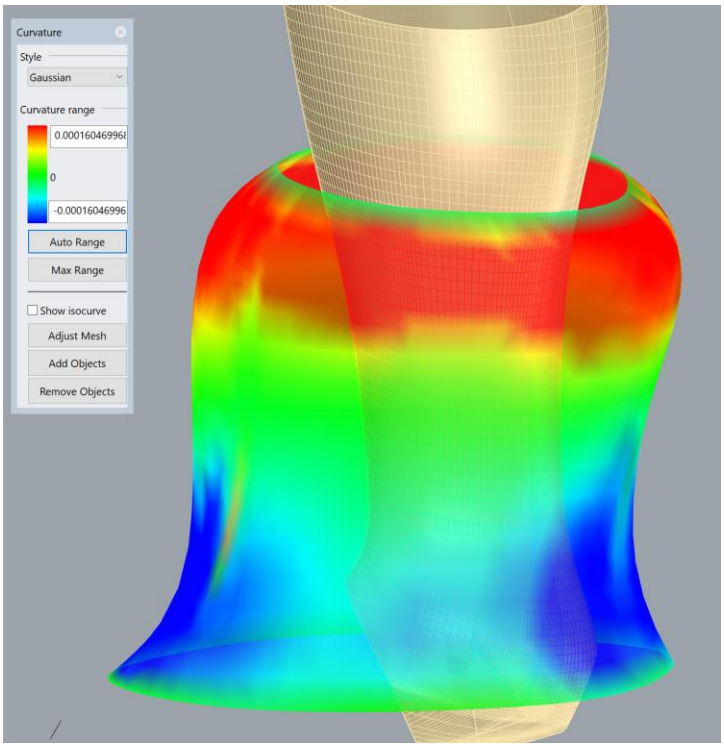

Figure 131: Contour plot of Gaussian curvature over the "bell" surface. Note that it has synclastic and anticlastic areas. Additionally, note that this is purely for visualization and is not a form of finite-element analysis, nor does it directly correspond with mechanical properties.

Application of Mathematical Theory of Bending to Cylinders.

Thus, in the case of a perfect cylinder (closed along its lengthwise seam, but, as a single surface, not capped), the only bending modes it can have are from loading along vertical lines in a radial direction. For instance, a right circular cylinder could be bent into an elliptical cylinder (a linear extrusion of an ellipse), which is also a singly-curved surface (with zero Gaussian curvature), as shown in Figure 132. Indeed, theoretically it could be smashed totally flat (neglecting the thickness of the surface itself, which is assumed to be zero). Additionally, many more-complicated loadings could be applied while still avoiding the introduction of double-curvature (i.e. avoiding any change in the Gaussian curvature distribution over the face of the surface, which in the case of a cylinder must be zero everywhere). For instance, the same surface could be bent inwards along some lines and outwards among others, as shown in Figure

133; crucially, as the contour plot of Gaussian curvature shows (also in Figure 133), the Gaussian curvature on the bent surface remains everywhere zero. This can be verified with a cardboard tube, which one can easily flatten or bend into other cross sections, though of course, in a real, physical material (with finite tensile stiffness and non-zero thickness, thus non-zero bending modulus), all of these loadings have low-stiffness but not zero-stiffness responses, owing to the nature of real materials.

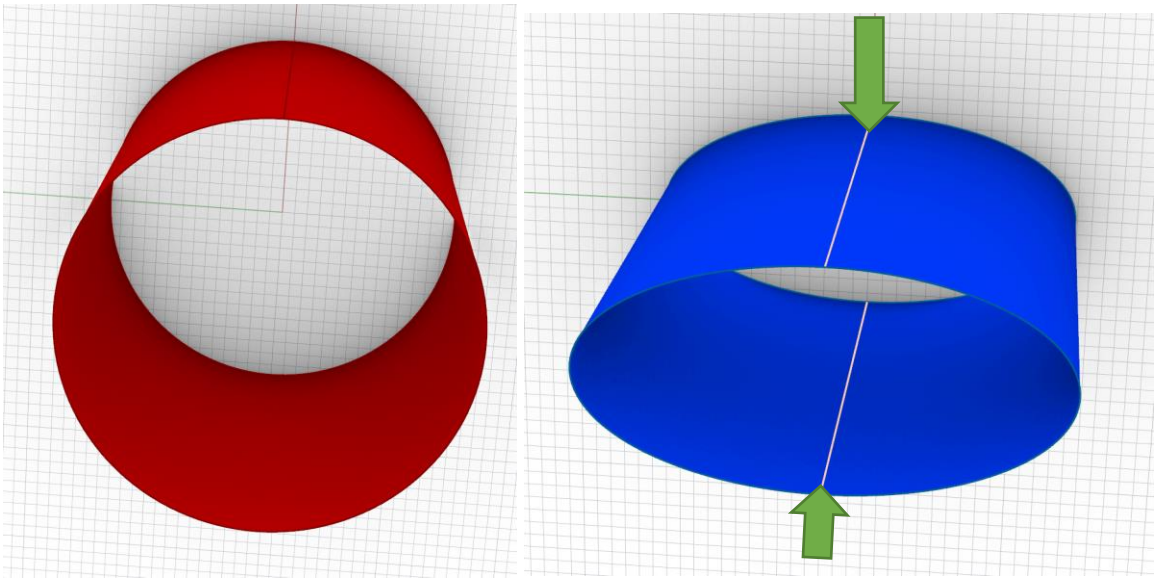

Figure 132: A right circular cylinder (left: unbent), a singly-curved but closed surface, can be bent by loading along lines in radial directions, e.g. as shown on the right, a loading that converts it into an elliptical cylinder, and indeed this elliptical cylinder is still singly-curved (and closed along its seam).

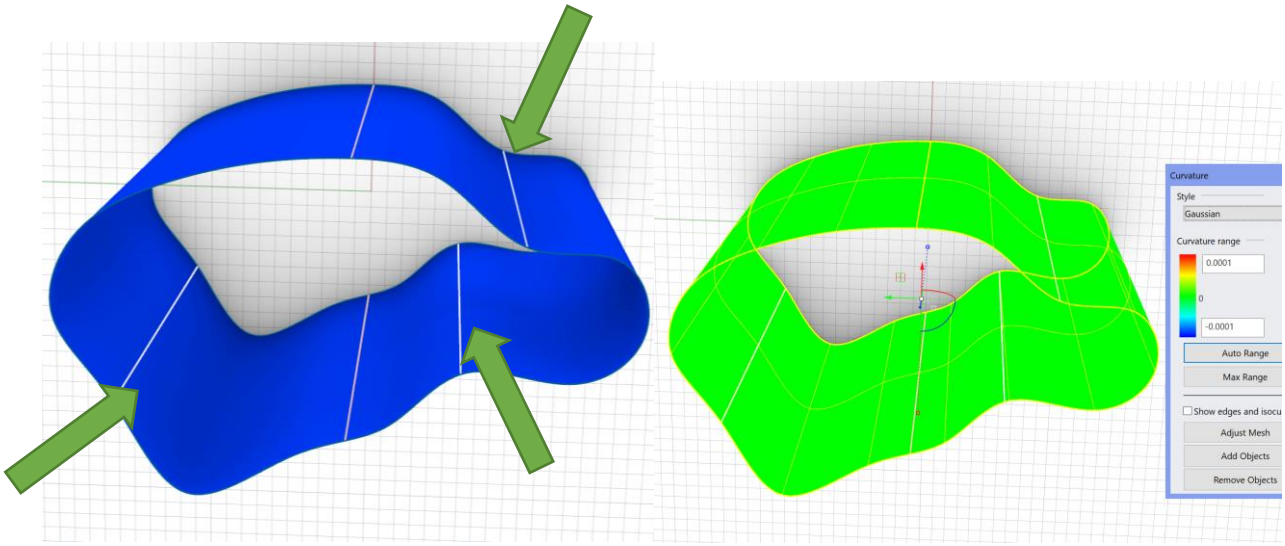

Figure 133: Any arbitrary radial loading that preserves the Gaussian curvature distribution but may alter the cross section is mathematically considered a pure bending of the right circular cylinder.

Of note, however, the cylindrical surface cannot be bent (in the differential-geometry sense of an isometry) like a thin beam along its long axis into, for instance, a sweep of a circle along an arc (i.e. a section of a torus); this hypothetical transformation, which is not pure bending, is illustrated in Figure 134 as an example of a surface transformation that cannot be accomplished by pure surface bending in the mathematical sense, as it would entail lengthening some curves and shortening others, and thus would not be an isometry. Equivalently, this hypothetical transformation would result in the target surface having double curvature regions (non-zero Gaussian curvature), as illustrated in Figure 134. The fact that a beam of infinitesimal thickness could be bent along the neutral axis into this shape is irrelevant to the question of whether it is a surface-bending operation (it is not), since mathematically, zero-stiffness bending of surfaces must preserve the distribution of Gaussian curvatures on the surface (in the case of a cylinder, keeping them zero everywhere). Indeed, the transformed surface acquires regions of positive Gaussian curvature and regions of negative Gaussian curvature, as the contour plot in Figure 135 illustrates.

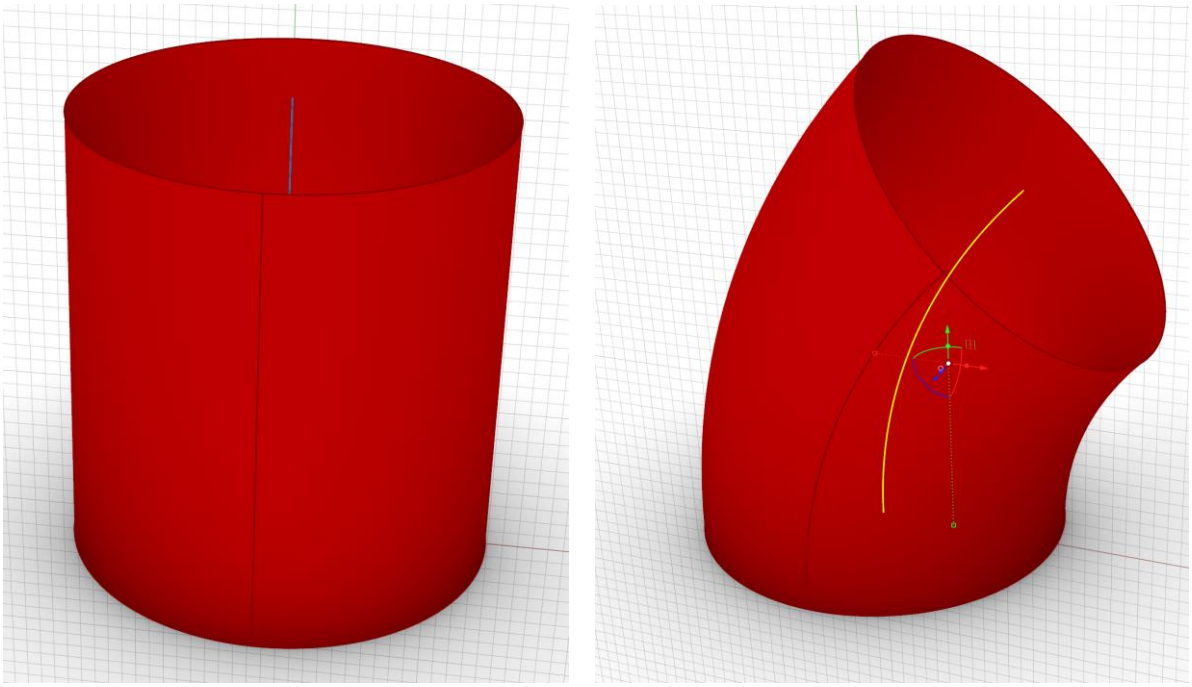

Figure 134: It must be stressed that the transformation shown from left to right is not a surface-bending operation, owing to the fact that it is not an isometry (i.e. the lengths of curves on the left side of the cylinder are increased; those of curves on the right side of the cylinder are decreased), and additionally it changes the Gaussian curvature map of the surface (see next Figure). The neutral axis of this transformation is highlighted in yellow in the image on the right.

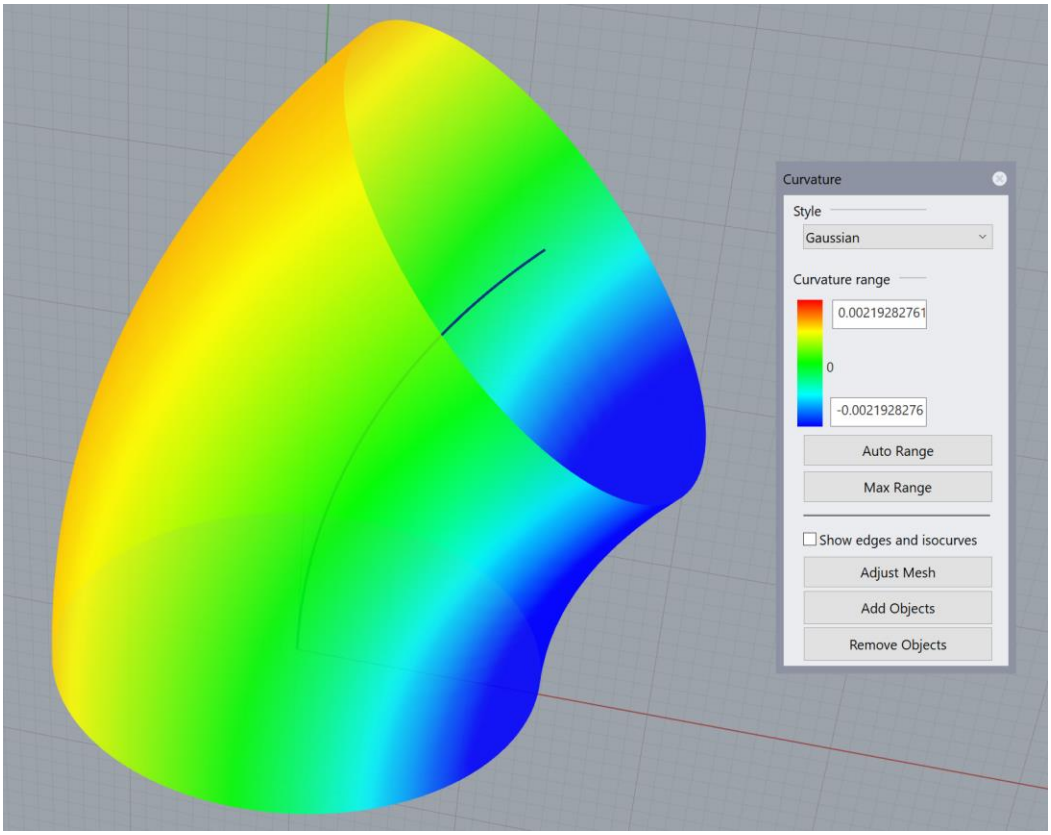

Figure 135: Contour plot of Gaussian curvatures on the hypothetical transformation described in the previous Figure. Note that the untransformed right cylinder has zero Gaussian curvature everywhere, whereas this transformed cylinder has regions of non-zero Gaussian curvature.

Thus, it is evidently no simple matter to create an enclosing surface around a linkage bending at a joint (e.g. the human leg rotating relative to the foot about the ankle joint); mathematically, a cylinder is stiffened against such a rotational transformation (it must not be called bending in the strict, mathematical sense). Of course, if one subjects a thin-walled cylinder to bending moments at both ends, it will not be infinitely stiff, but will rather rapidly crease (technically after a brief region of elastic stiffness) and then lose most stiffness entirely. This may seem like a contradiction of the previous observation regarding the fact that a cylindrical surface cannot be smoothly bent into the surface in Figure 135 above, but it is not because theoretically the creases of the buckled shell are curves/points of singularity in the Gaussian curvature (though, as curves/points, infinitely thin, and thus not full regions)

In another vein that is also relevant to this research, this formal understanding reveals that doubly-curved surfaces can also have true bending modes, but this must theoretically entail continuous transformation of the surface that preserves the Gaussian curvature at every point (and preserves the lengths of all curves drawn on the surface, etc.) [100], save for creases (which become singularities) as will be discussed below. For instance, in a manner similar to the cylinder being bent inwards by inwards-directed radial loadings, the hyperboloid-derived surface can be easily squeezed inwards, though

For instance, consider the thin elastomeric shell based on the hyperboloid-derived manifold that was manufactured and forced to enclose a rotating cylindrical body. What was imprecisely termed "bending" of the shell in that previous section was not a pure bending isometry. Instead, potentially-desirable modes for an ankle protector likely entail shearing, in-surface compression, and perhaps in-surface extension in addition to true bending (see Figure 28 and Figure 29 in Chapter 2 and Figure 142 and Figure 143 in this chapter).

In contrast, the true bending modes that entail pure isometries (preserving Gaussian curvature profiles, angles on the surface, and lengths of curves on the surface) for the HDM surface are just radially-directed and shown in Figure 136. Unfortunately, these are not useful modes for an ankle protector. (Strictly speaking, this is an imperfect approximation of bending in the sense of differential geometry: after all, the elastomeric shell certainly does not have infinite tensile/compressive/shear stiffness, and on the other hand, its thickness is large enough that it has greater-than-zero bending stiffness. However, a researcher can intuitively feel what is a low-stiffness mode corresponding to the theoretically-zero-stiffness mode of pure, mathematical bending, and what loading entails significant stretching or shearing to the shell, as this has a palpably-far-stiffer response).

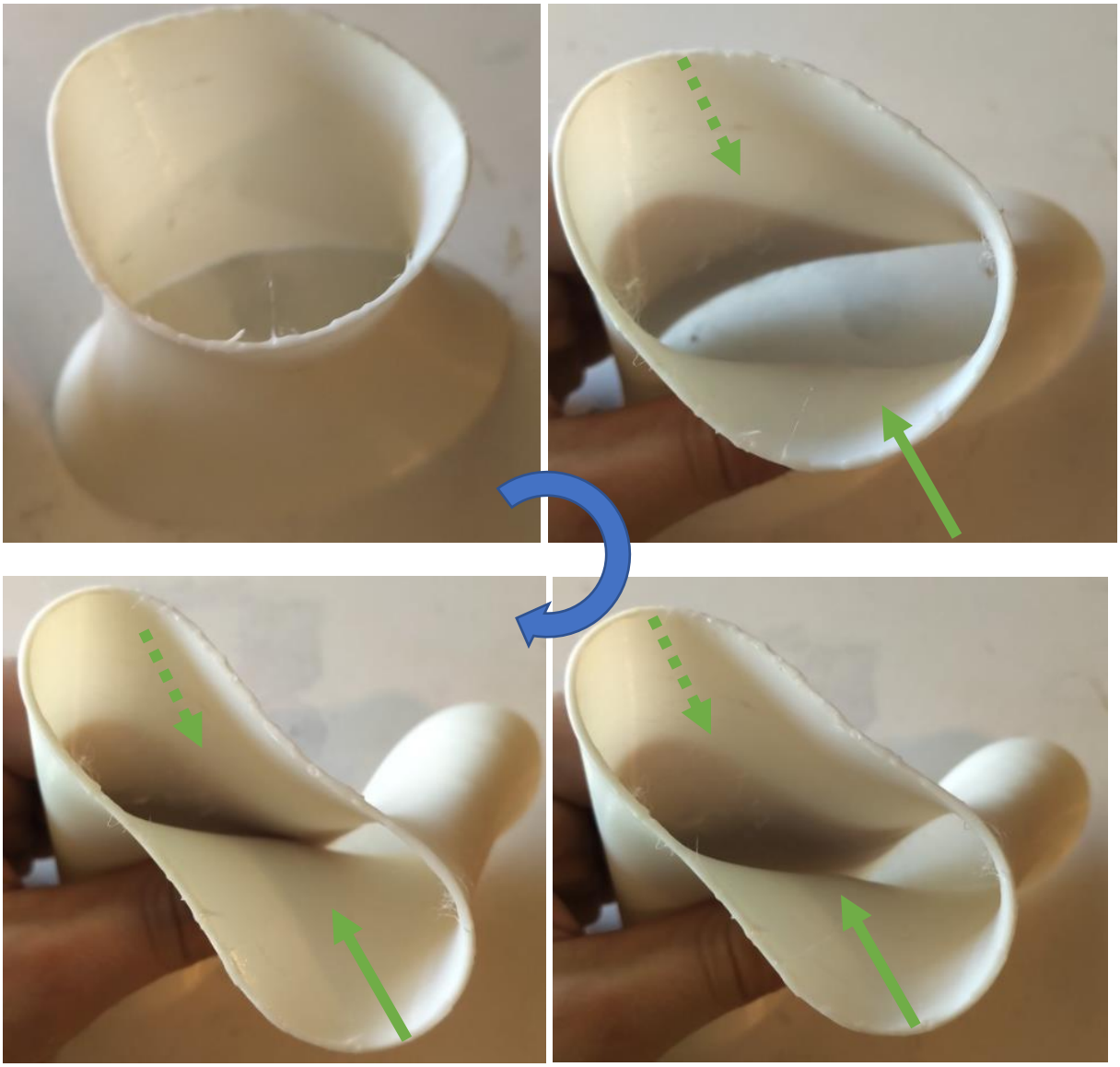

Figure 136: One example bending mode of the HDM surface (which has generally negative Gaussian curvature), with increasing deformation clockwise from top left (as indicated by the blue clockwise arrow in the center). The green arrows show the directions of point loading to produce this bending transformation. Note that the surface is never flattened at all, but rather comes to approach a saddle-shaped surface-precisely what is expected, since bending transformations must preserve the Gaussian curvature profile over the surface.

Similarly, some isometry modes (pure bending modes) for a paraboloid dish, which has positive Gaussian curvature everywhere, are shown in Figure 137 and Figure 138. Certainly, a paraboloidal shell can "bend" in some modes, but only those that preserve Gaussian curvature and do not entail flattening.

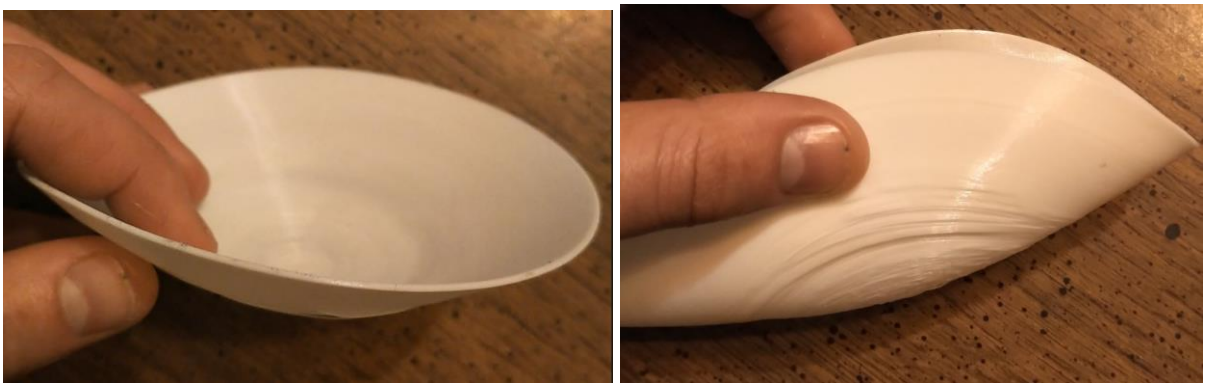

Figure 137: Side view of a bending mode that a paraboloid shell possesses. Note that the Gaussian curvature of the surface is preserved under true bending, though the principal curvatures are certainly not preserved.

Figure 138: Alternate views of the same paraboloidal shell as in the previous figure under one of its (infinitely-many) bending modes.

Creasing of Surfaces in Bending.

Surfaces that crease in bending may appear to violate the previously-stated rule that thin elastic shells do not change their Gaussian curvature distributions under bending, so the role of creases in the bending responses of all surfaces, including open and closed, singly-curved and doubly-curved, should be addressed. Theoretically, a perfectly-sharp crease interrupts the mathematical continuity of the surface: it preserves positional continuity (the lowest order of

continuity), but violates all higher orders (tangency, continuity, "G3" which responds to a continuously-differentiable curvature, "G4" which corresponds to a continuously-differentiable gradient of curvature, etc.). Surface continuity is commonly evaluated in CAD packages with the use of "zebra stripes"; where the zebra stripes are disjointed, the surface only has positional continuity and lacks tangency continuity. (Likewise, where the zebra stripes change angle suddenly, the surface has tangency continuity, but there is a break in curvature continuity; the continuity of the zebra stripes is effectively one order lower than that of the surface). For instance, Figure 139 illustrates a crease on a surface and its corresponding zebra stripe pattern.

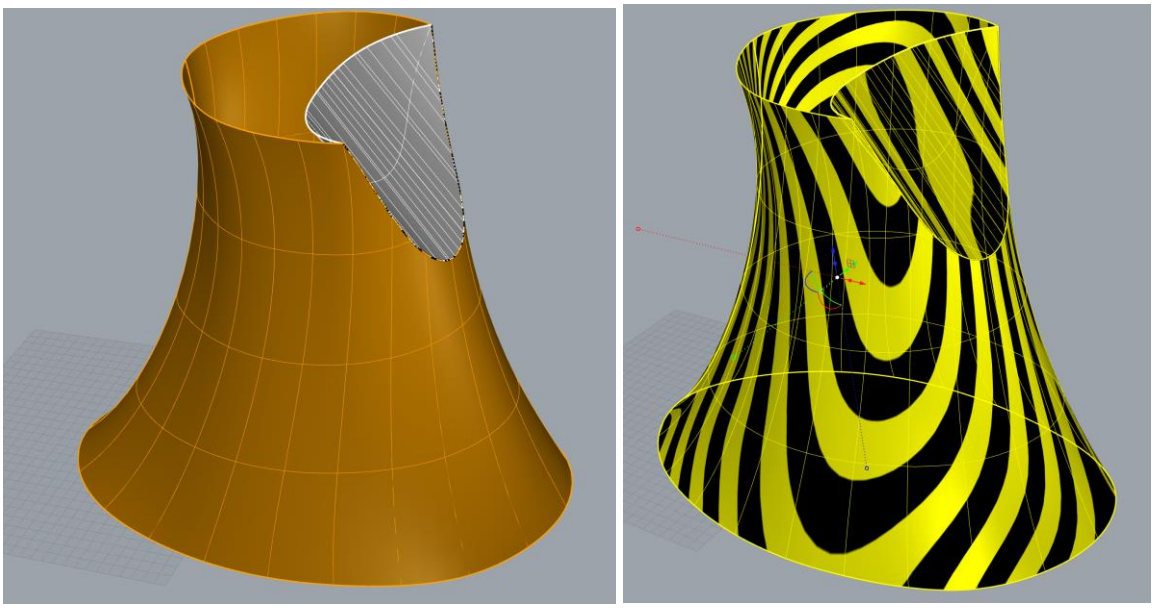

Figure 139: A crease shown on the HDM surface, with the interior of the crease colored white in the left view, and the entire polysurface shaded with zebra stripes illustrating the tangency discontinuity at the crease in the right view. This is not necessarily the exact shape that the inward crease would take and is made purely for concept-demonstration purposes.

Thus, since creases are curvature and even tangency discontinuities, the Gaussian curvature cannot be defined strictly on the crease curve, at least if it is perfectly sharp (as with a theoretical surface that is infinitely thin) [101]. However, on both sides of the crease, the Gaussian curvature profile that existed prior to the introduction of the crease must be preserved: indeed, Bende et. al. designed shells of various topologies (open or closed; positive, zero, or

negative Gaussian curvature) with crease lines along which the shell had bistable, snapping-mechanism-like deformations. Additionally, they found that the creased region had the highest strain energy density (from tensile strains), though the interior regions bounded by the crease (and the edge of the shell as applicable) often had high strain energies as well [102].

In a similar vein, if the paraboloid surface (shown earlier in bending modes that preserve Gaussian curvature in Figure 137 and Figure 138) is creased by indentation inwards (producing a bistable "snapping" effect), for instance, the Gaussian curvature will nonetheless be preserved both inside and outside the crease (the indented region is still dome-like in its curvature and indeed unchanged in shape other than being inverted: see Figure 140.

Figure 140: Introducing a crease line, which theoretically entails a singularity of Gaussian curvature. Both inside and outside the crease, the Gaussian curvature is positive (dome-like), though the direction of principal curvature does indeed change. The crease line produces high stress in the shell and thus has already resulted in damage to the 3D-printed part.

Thus, creases enable a surface to take on a shape that appears different from its uncreased form and to allow greater displacement; in effect, creases tend to act as hinges. For instance, it was noted in the testing of a thin elastic shell in the shape of the HDM that the structure exhibited creasing about its midsection when the leg was bent forwards, and the bending stiffness of the structure decreased commensurately. The crease (a region of near-singularity in Gaussian curvature) acts as a hinge around which the surrounding regions of the shell tend to rotate, and with low stiffness as well due to the reduced distance away from the neutral axis of bending that the crease causes. However, strategically-placed creases (in the form of origami) may give desired kinematic properties, as will be discussed below.

Interface between Hypothetical Closed-Surface Array and Leg: Sliding or Tied?

In selecting a manifold shape as well as when designing the properties of a metamterial, it is essential to consider the ideal boundary condition at the top of the hypothetical, cylinder-shaped protective device, namely whether the leg should slide inside the device or whether the device should be wrapped tightly enough around the calf muscle that it cannot slide appreciably relative to the leg. The boundary conditions will be intimately related to the shapes that the structure should take on in various joint configurations. (It is assumed that the boundary condition at the bottom will be somehow rigidly fixed to the wearer's shoe.) The reader will recall that this question was initially broached at the end of Chapter 2's discussion of metamaterials, which revealed some in outside literature that can lock up after extensional or compressive strains, as well as introducing this author's own metamaterial that locks up in bending.

The latter approach of constraining the top edge of the manifold to the same position on the leg seems more difficult to design a metamaterial for, because the amount of global

shortening (or buckling) of curves on the manifold in the area around where the leg moves towards would be greater than with the former approach, as would the amount of global lengthening on the opposite side: this length-changing approach is illustrated in Figure 141 with a hypothetical manifold enclosing a bending leg, and it is in principle similar to Figure 29 at the end of Chapter 2, which also showed a complicated morphing involving both shell bending and in-surface extension/compression. Clearly, this type of transformation requires severe length changes in various areas of the manifold (on top of shell bending) and thus is not easily accomplished, especially since the fabric-backed tiled arrays are specified not to have curves on their surfaces change length under bending. Granted, this obstacle might be overcome by allowing the fabric to locally experience shell buckling in areas where global compression is required, and to construct the array with fabric in a pre-buckled configuration in areas where global extensibility is required, but this is expected to add considerable complication to the design process and thus will not be undertaken unless the basic principle of a cylindrical protective array proves to be a sound one.

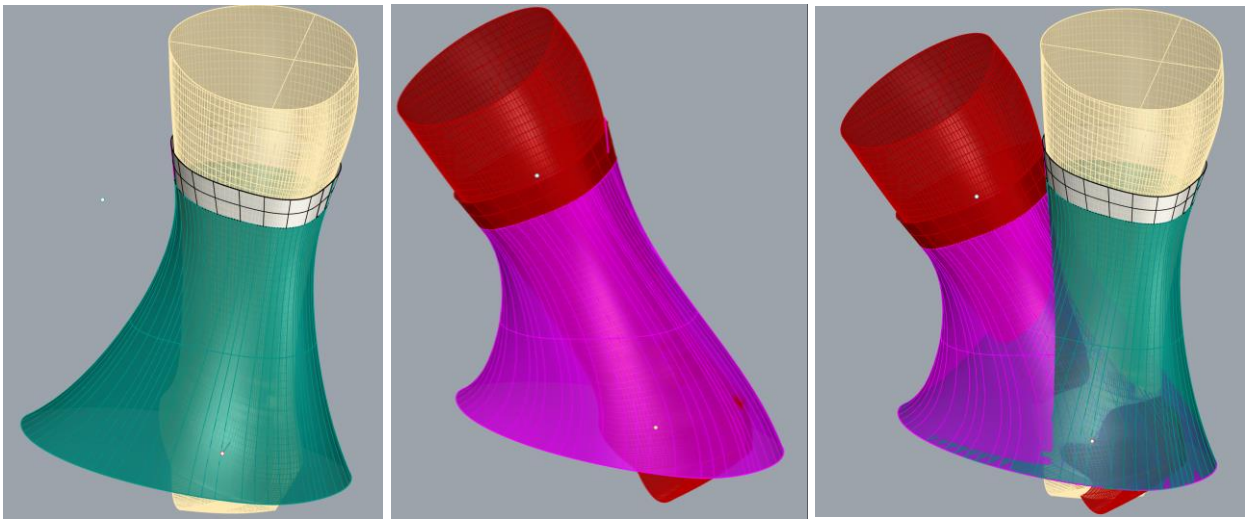

Figure 141: Depicting the concept of fixing the top edge of the manifold with a hypothetical material that can strain in such a way as to stay constrained at the top and bottom and yet accommodate a rotating leg. As this is a hypothetical material, an object of research would be to replicate this behavior, if it is seen as desirable and feasible; it must be stressed that this is not

normal behavior for linear elastic shells. Left: hypothetical manifold shown in green, constrained top and bottom, but with leg in neutral position. Middle: hypothetical manifold shown in pink, with leg dorsiflexed (bent forwards) and manifold still constrained to the top and bottom. Note how the curves on the front of the pink manifold are shorter than the corresponding curves on the front of the green manifold, and how the curves on the back of the pink manifold are longer than the corresponding ones on the back of the green manifold. Right: just shows the two manifolds together for easy comparison.

Since the behavior depicted in Figure 141 is unlikely to be achievable even with a highly-advanced metamaterial, the alternative boundary condition, in which the leg slides relative to the top edge of the manifold, will likely be employed instead. This boundary condition would presumably be compatible with a cylindrical structure in bending with the potential addition of global compression (which will produce microbuckling of the fabric) but not tensional strain (in which the fabric would be quite stiff). Shear of the structure might also be tolerable if sufficient areas of the fabric could be unbonded without sacrificing lockup ability at the needed strain (i.e. it might prove necessary to make the tiles flare outwards considerably but from a small footprint on the fabric). It is hoped that the work in this chapter may elucidate the potential behavior of surfaces that can be achieved.

Two hypothetical non-extensional morphing modes were conceived of specifically for a fabric-backed tiled metamaterial: one that allowed bending, shear, and in-surface compression, and one that only allowed bending and shear; both forbid tension. (Other metamaterials that are not composites involving woven fabrics may also tolerate tension; such metamaterials are also explored in cylindrical form in this chapter, as well as conceptually in Chapter 2). The HDM surface was manually modified by sculpting and cage transformations in an attempt to estimate what it might look like after the leg rotated forwards with either morphing and its attendant set of constraints, and the resulting area change was noted: if both compressive and tensile strain are to be avoided, it was intuitively felt that area changes should be small, though of note shear deformation can also change area; however, if contraction of the overall shape is permitted, then the area might also decrease.

If subject to the former set of constraints (shear, bending, and contraction permitted), the morphed surface (created manually and intuitively, not through any explicit algorithm) had an area reduction from 64,250mm^2 to 54,933mm^2, a decrease of 14.5% (of course, in practice the area would not really decrease, and at best the fabric would not exactly conform to this shape, but rather display areas of wavy local buckling; at worst, this might not be a possible morphing). An image of this hypothetical morphing is shown in Figure 142.

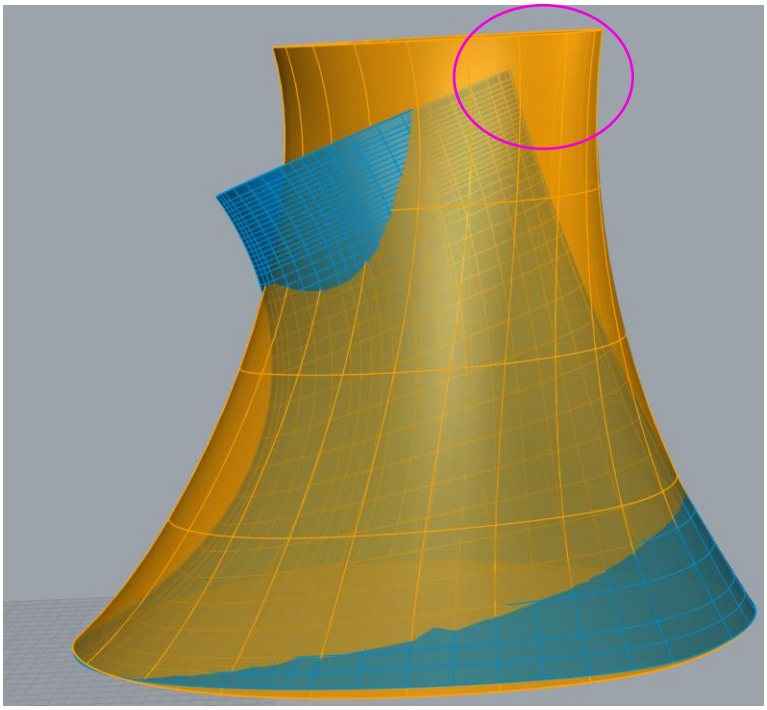

Figure 142: Of note, even if a real fabric shape could follow this general deformation pattern, it would not compress continuously in-surface but would rather have considerable waviness from microbuckling (outwards-directed and perhaps additionally inwards-directed). There is also necessarily sliding between the leg and manifold, especially at the rear edge (as circled in pink) where tensile strains cannot develop in the fabric.

In contrast, if contraction (reduction in area) is not permitted, the manifold's morphing under forward rotation of the leg might resemble what is shown in Figure 143. Note that the cross-section was expected to "ovalize" somewhat inwards in order to compensate for extensional strains elsewhere to keep the area change to a minimum. In fact, the initial manifold has a surface area of 64,250mm^2, and the proposed target manifold shown in Figure 143 has an

area of 64,493mm^2, a change of 0.4% which is at least promising, though this is only a conceptual and preliminary test of possible morphings. The real tests can only be made once a metamaterial is fully designed and either simulated numerically (as in Chapters 7, 8, and 9) or manufactured and tested experimentally (as in Chapter 10), as the morphing-response of the structure will be heavily dependent on the nonlinear properties of the metamaterial that composes it.

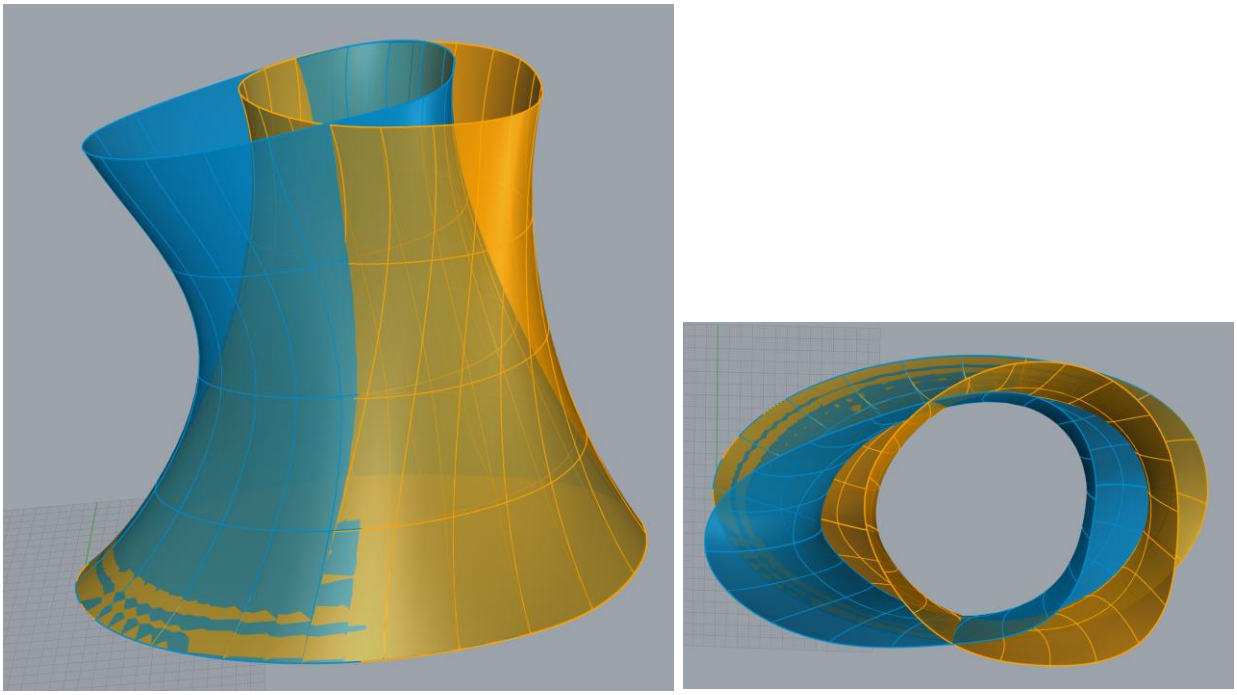

Figure 143: Potential morphing that seeks to avoid contraction and extension but permits shell bending and shear. Note that this is not the result of any numerical simulation, and thus it is not clear that contraction and extension are everywhere successfully avoided; the only indication is that area is nearly unchanged.

Preliminary and Outside Research on Cylindrical Shells in Large-Deflection Bending.

The problem of protecting a joint with a closed-surface (quasi-cylindrical) manifold is clearly related to the problem of how much a closed surface can bend without large-scale and uncontrolled "kinking" (experiencing shell buckling), which greatly softens its bending response (for this reason, shell buckling tends to be an instability phenomenon, with exceptions for

localized buckling regimes that are soon arrested, some of which will be discussed in subsequent sections of this chapter).

Interestingly, there is little scientific literature that explicitly addresses cylinders specifically in large deflection, perhaps because tailored materials that have a hope of being able to bend with large deflections as closed surfaces are relatively new and often proceed from advances in additive manufacturing (which allow their physical creation) and computer simulation and design capabilities. Decades ago in 1927, Braizer investigated the buckling curvature for a homogenous and "long" (relative to the radius) tube of cylindrical cross-section subjected to pure bending; he also investigated the way the cross-section of the tube deforms before buckling [103]. Unfortunately, this research reflects what is intuitively obvious, that thin cylindrical shells cannot tolerate large-deflection bending without shell buckling. Yao built upon this research to investigate the effects of the thickness ratio on the mode of shell buckling (localized waviness versus a global degeneration in the cross section from circular to oval) of cylindrical tubes in large deflection [104]. Cimpoeru also investigated the imposed bending curvature required to buckle a square-cross-section tube with a certain thickness and yield strength, and then investigate the post-buckling behavior of such tubes (given that the material used could tolerate a large amount of further plastic deformation before failure), though the investigation offers little insight into how to prevent shell buckling [105]. More recently, Houliara and Karamanos studied [106] the bending response of long, thin cylindrical shells subjected to pure bending moments, quantifying how the cross-section of such a tube first "ovalizes" (i.e. becomes distorted so as to reduce the second moment of area locally and thus reduce the bending stiffness according to the direction of bending), and then studying how shell buckling follows with FEA. Certainly their research is valuable for avoiding buckling or

predicting post-buckling behavior in small to moderate-deformation regimes, but it offers limited insight in how to make a relatively-short cylinder tolerate large-displacement bending without "excessive" shell buckling (defined in the sense of producing a feedback loop of softening or similar unstable response).

Bellows in Large-Deflection Bending.

The most prominent example from everyday life of a cylinder-like shape that tolerates large deflection bending is a shape created by adding sinusoid-like waviness radially: in short, a bellows shape, found in vacuum hoses, plastic straws that can bend with tight curvature, etc. In pure mechanical engineering, such bellows are generally valued more for their axial compliance (and ability to generate airflow) than for their bending ability; for instance, a review by Wilson [107] of the literature on the design of metal-shell bellows found only one archaic article on the bending properties of such structures, specifically toroidal-shell expansion bellows (sometimes referred to as "Omega-shaped" bellows) which the author studied in only a small-deflection, linear regime [108], making it of limited utility to this discussion. Global bending should not be confused with local shell bending, as it is understood that, even in a linear regime, global pressure loads place regions of the bellows (or indeed any structure consisting of toroidal shells) into local shell bending [109]. The only known qualitative study of a shape specifically identified as a bellows that was indeed subjected to large-displacement bending is the work of Park et. al., which did not compare its bending properties (especially how much it could bend before collapsing) quantitatively with a comparable cylinder but merely proposed such a bellows as a tracheal graft [110], though certainly many other works have explored bioprinted tracheal grafts with various geometric properties (such works generally do not connect the concept of a mechanical bellows with their proposed trachea grafts).

Modifying the Hyperboloid-Derived Manifold with Bellows Features.

However, the foregoing information, as well as intuitive experience with vacuum hoses, was enough to inspire a quick test of how the hyperboloid-of-one-sheet-derived surface would perform if modified into a bellows with waviness normal to the surface. Certainly, such waviness could vary in amplitude, wavelength, and specific shape (e.g. sinusoidal, or with greater curvature, perhaps from reentrant curves).

Hyperboloid-Derived Manifold with Standard Sinusoidal Waviness.

The most logical method of creating geometry based on the hyperboloid-derived manifold chosen above that has superior bending tolerance would be to rail-revolve a sinusoidally-displaced edge around the base curve of the original surface. The sinusoidal displacement should only add offset to the original manifold, not inset (else it might penetrate into the leg). The geometry generated by this process is shown in Figure 144.

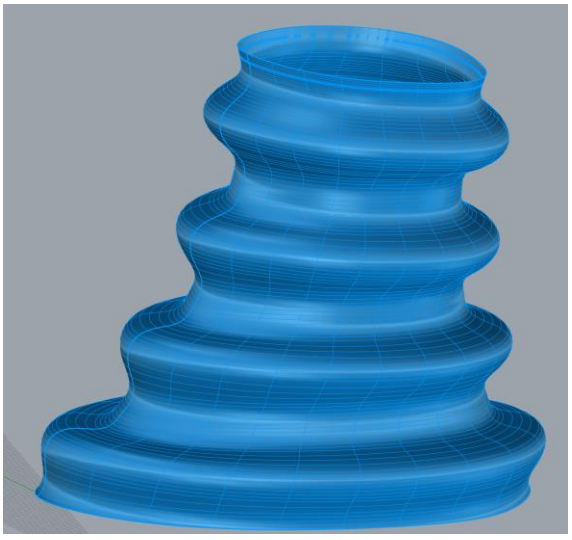

Figure 144: Hyperboloid-derived manifold, modified with selective offsets in the form of sinusoidal waviness.

As can be seen in a plot of Gaussian curvature contours shown in Figure 145, the surface is strongly doubly-curved (with relatively high Gaussian curvature magnitude), and moreover

areas of synclastic Gaussian curvature (positive Gaussian curvature; sphere-like) alternate with areas of anticlastic Gaussian curvature (negative Gaussian curvature; saddle-like). This adds considerable complexity to the surface, and in particular, it is unclear how the positive Gaussian curvature areas of the surface could be tiled successfully. Additionally, the waviness adds further distance away from the leg (worsening the quality of conformation to the leg).

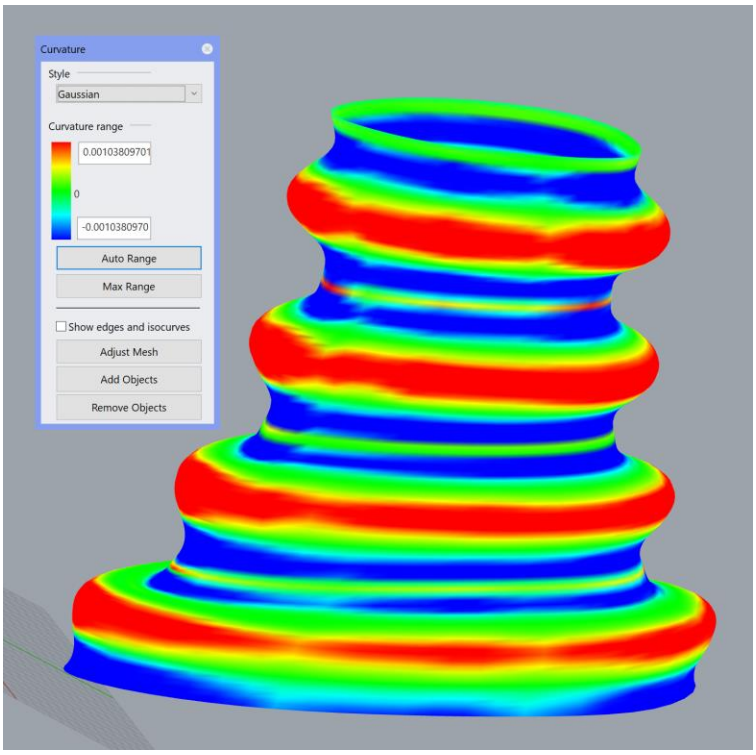

Figure 145: Contour plot of Gaussian curvature over the hyperboloid-of-one-sheet-derived manifold that was then modified with sinusoidal waviness. Note that this is purely for visualization and is not a form of finite-element analysis, nor does it directly correspond with mechanical properties.

When this surface was offset to produce a thin solid and the solid was 3D printed out of thermoplastic elastomer, it had significant ability to undergo global compression and bending (though was relatively stiff in global tension), as can be seen in Figure 144. Due to its stiffness in tension, the leg would have to slide inside the structure; it could not be tied to the top of the leg due to length changes (in the direction of tensioning) being required to accommodate that

boundary condition. Additionally, the structure no obvious lockup, nor is it clear how to make it lock up.

Figure 146: Left: undeformed wavy manifold; right: wavy manifold accommodating large forward bending from compression. Note that some breakaway support remains adhered to the model, but it did not significantly impact its mechanical behavior.

Figure 147: Top view of the wavy hyperboloid-derived-manifold in bending (left: undeformed, right: bent forwards).

Upon closer inspection, the waviness appeared to function in two ways. First, the sinusoidally-offset areas gave increased shell-bending stiffness in the circumferential direction (more precisely, stiffening the circumferential *u*-direction curves from reducing their curvature by bending about a vertical axis—see Figure 148 for more detail). This stiffens locally against

bending and thus shell buckling inwards in that direction (compare to the plain, hyperboloid-derived manifold, which creases and buckles sharply inwards during such bending, as shown previously in Figure 120).

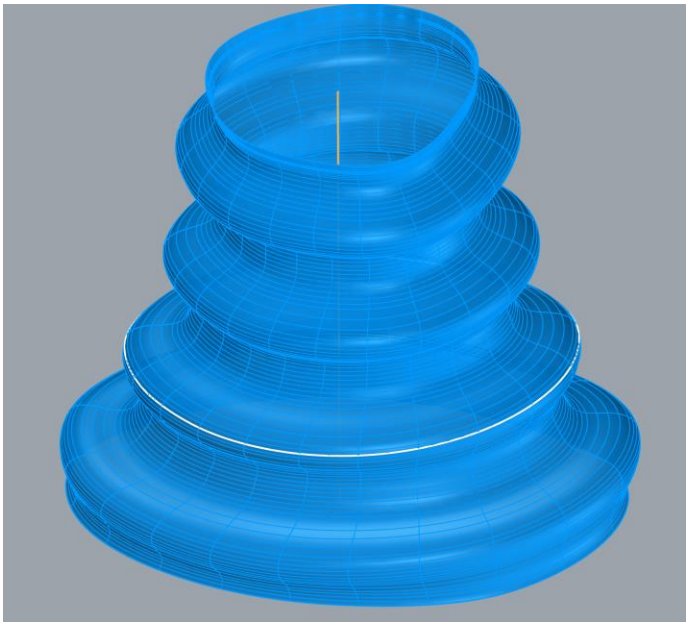

Figure 148: The peaks of the sinusoidal waves (one of which is highlighted with a white curve) are relatively stiff in circumferential bending (i.e. bending about an axis roughly parallel to the orange vertical line); in effect, the structure is stiffened against shell buckling inwards that the simple manifold rapidly undergoes without added stiffness.

Instead, the global bending of the "leg" going forward appears to cause local shell bending in the wavy direction, potentially resulting in local creasing at the root of the wave. This is illustrated with a close-up view in Figure 149. There is a perceptible amount of bistability and snap-through when bending and especially when compressing the structure vertically (see Figure 150 for the view of the structure when compressed vertically, and note the localized shell buckling with creases forming in entire circumferential bands), likely due to this very localized shell buckling phenomenon. Note that the surface is fairly stiff in global tension, perhaps because no shell buckling modes can be engaged.

Figure 149: Closeup of the sinusoidally-offset-hyperboloid manifold, globally bending forwards. Note the local creasing in certain areas, as denoted with the blue arrows.

Figure 150: The structure is compliant in global compression. Note that circumferential bands of shell buckling form between the waves.

Unsurprisingly, this capability of enclosing large-deflection bending without catastrophic creasing applied in any direction, including side-to-side bending (see Figure 151), again due to global compression resulting from local shell bending and even local shell buckling (see Figure 151). No attempt was made during this preliminary design to alter the manifold's behavior in side-to-side versus front-to-back bending, though such modifications would be wise in a final product.

Figure 151: View from the "rear" (if the flexible object were to be worn around the ankle) showing the ability to bend side-to-side.

Hyperboloid-Derived Manifold with Reentrant Waviness.

It seemed logical that the success of the previous shape could be expanded by increasing the curvature of the curve that is rail-revolved to add waviness. In particular, the repeating unit of this curve could have two inflection points and thus there could be added waviness all over the manifold. This geometry is shown in Figure 152 and Figure 153, with the generating curve highlighted in yellow to emphasize the reentrant character of its curvature (note that some of the inward folds are hidden and would not be perceptible if this curve were not highlighted).

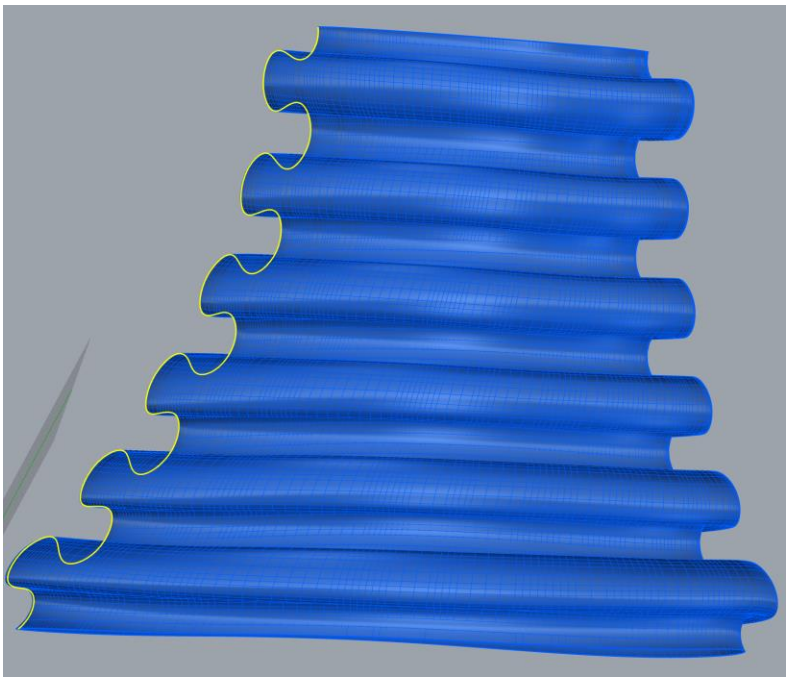

Figure 152: Reentrant waviness profile added to the hyperboloid of one sheet for increased "bellows-like" characteristics. The generating curve is highlighted in yellow to emphasize the reentrant character of its curvature (note that some of the inward folds are hidden and would not be perceptible if this curve were not highlighted).

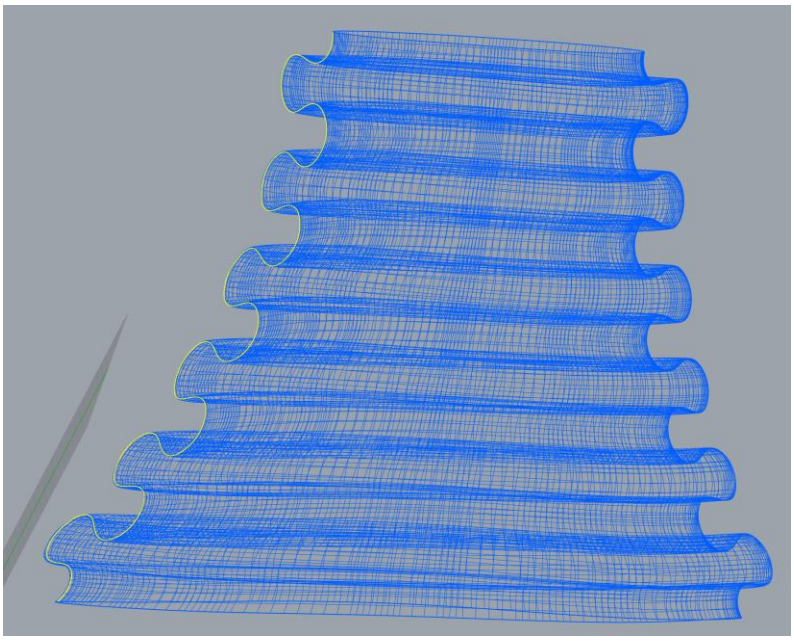

Figure 153: Wireframe view of the reentrant-waviness hyperboloid-derived shape. Again, the generating curve is highlighted in yellow.

As a contour plot of Gaussian curvature over the surface reveals (see Figure 154), the surface is very complicated, with each "ring" having an outer region of positive Gaussian

curvature (sphere-like), followed by a small area of negative Gaussian curvature, then another positive Gaussian curvature area, then the main inwards-curved region having negative Gaussian curvature, etc.

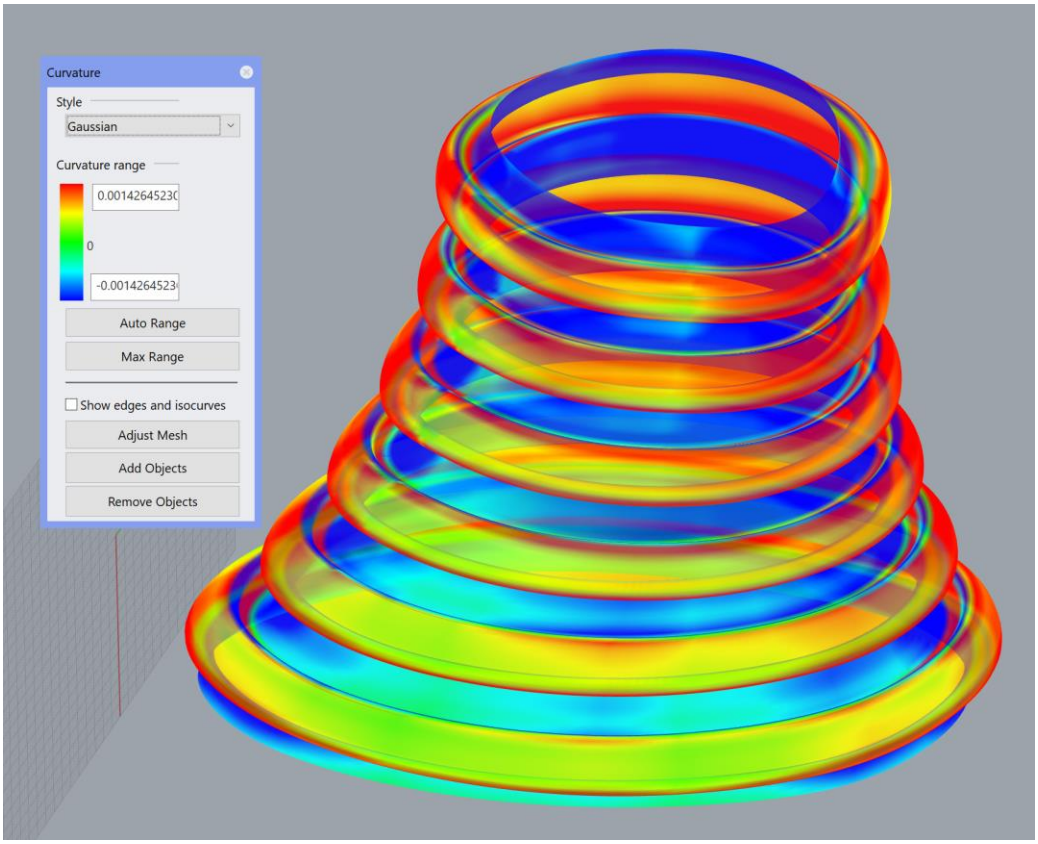

Figure 154: Plot of Gaussian curvature contours on the surface, with red indicating strongly positive Gaussian curvature, blue indicating strongly negative, and green roughly zero. Note that this is purely for visualization and is not a form of finite-element analysis, nor does it directly correspond with mechanical properties.

The surface is the most tolerant yet of bending, and it can be bent until the main regions of positive Gaussian curvature in each repeating unit touch, whereupon its stiffness increases modestly (not enough to allow for lockup, however, and of note the pre-lockup stiffness is significant). Its bending behavior is shown in Figure 155.

Figure 155: Reentrant-bellows pattern imposed on the hyperboloid-manifold, printed in the form of a thin, elastomeric shell. Left: undeformed structure. Center: structure bent forwards. Right: structure bent rearwards.

Figure 156: Top view of the reentrant-bellows hyperboloid-derived manifold structure in bending (left: undeformed; right: bent to the right). The cross-section shape is roughly unchanged, with little ovalization to speak of.

As with the previous structure, it is fairly compliant in global compression; additionally and unlike the previous structure, it is also compliant in tension. This behavior no doubt is the driver of its bending compliance, since bending produces local regions of compressive stress, and other regions of tensile stress. It is depicted in Figure 157.

Figure 157: Left: behavior of structure in global compression. Right: behavior of structure in tension. Note that the roughness of the surface is due to breakaway support material from the 3D printing process.

Hyperboloid-Derived Manifold with "Egg Carton", Alternating Sinusoidal Waviness.

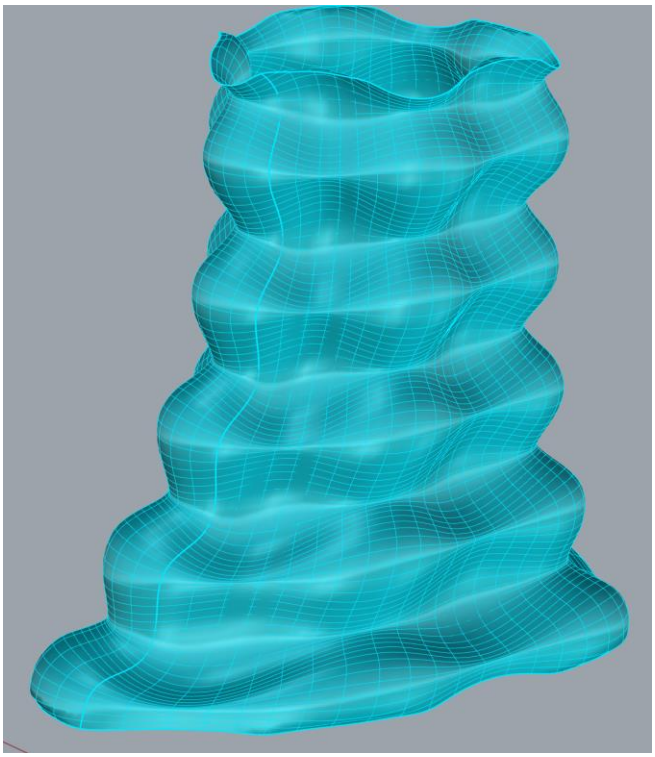

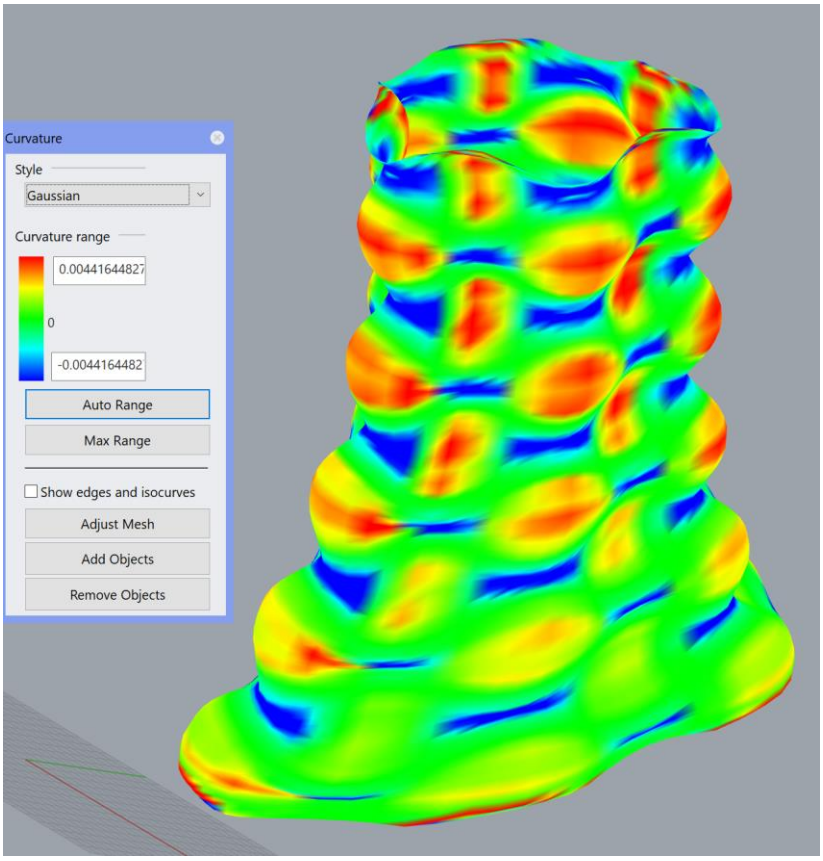

Figure 158: Contours of Gaussian curvature on the "egg-carton"-textured, hyperboloid-derived manifold. Note that this is purely for visualization and is not a form of finite-element analysis, nor does it directly correspond with mechanical properties.

Figure 159: Side view of the "Egg-carton"-textured, hyperboloid-derived manifold surface in bending.

Figure 160: Top view of the "egg-carton"-textured, hyperboloid-derived manifold surface in bending. Note that the cross-section is not changed much (little ovalization).

Hyperboloid-Derived Manifold with Contoured-Normal-Displacement Waviness.

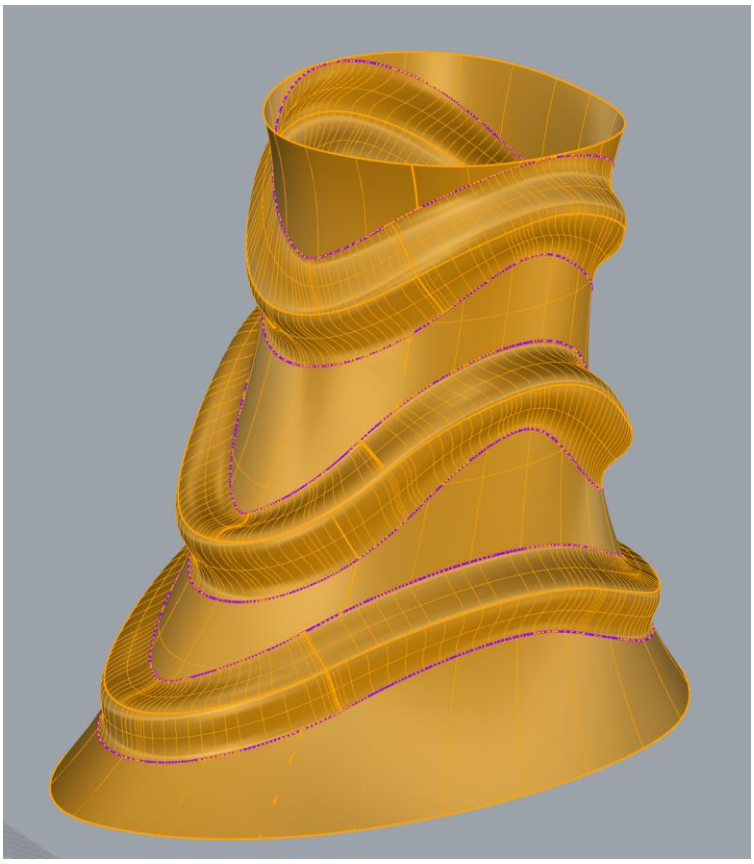

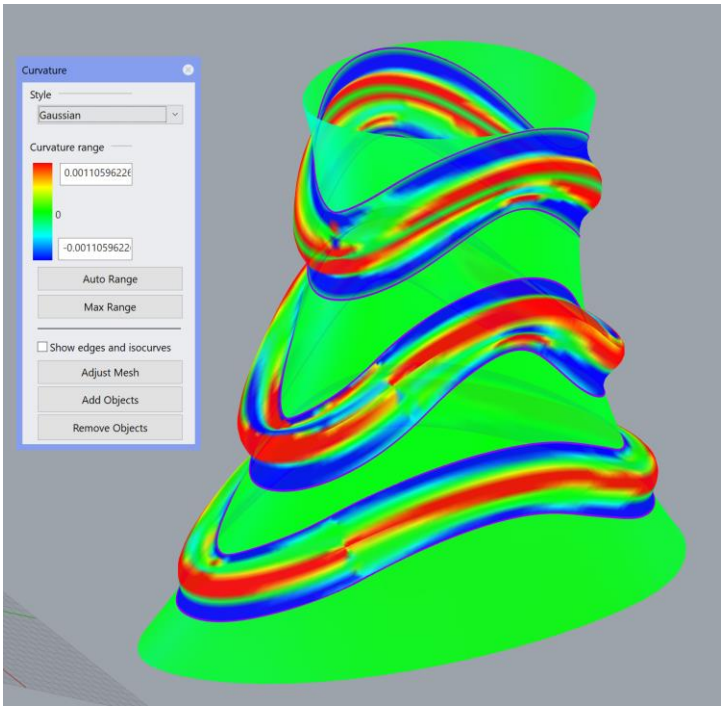
Curvature
Style
Gaussian
Curvature range
0.0011059622
0
-0.0011059622
Auto Range
Max Range
Show edges and isocurves
Adjust Mesh
Add Objects
Remove Objects

Figure 161: Vertical compression of the structure results in some regions buckling inwards.

"Carafe" Manifold with Reentrant Waviness.

To conclude this investigation into the effect of adding bellows-like reentrant (or sinusoidal) waviness, the "carafe"-shaped manifold discussed in a previous section was modified accordingly with reentrant waviness and then a thin shell with this surface printed, as shown in Figure 162.

Figure 162: "Carafe" manifold with reentrant waviness, 3D printed in thermoplastic elastomer.

The structure had considerable bending freedom, as well as compressive freedom, as can be seen in Figure 163. This is unsurprising, considering that the simple (i.e. without added waviness) "carafe" surface had a buckled shape in bending that was if anything far more conducive to tolerating a bending joint inside, and this wavy texture was shown repeatedly above to give compressive, bending, and sometimes tensile compliance by transforming global shell buckling into localized buckling and bending.

Figure 163: Left: bending compliance of the structure. Right: vertical-compression compliance of the structure.

Origami-Based Approaches to Cylinder Bending.

Folding strategies (including origami and kirigami) sit at the intersection between the two aforementioned strategies for making a closed cylinder-like or hyperboloid-like surface that can tolerate large-deflection bending: bellows-like surfaces with waviness, and microstructured metamaterials. Folding can allow flat sheets to be conformed at the macro level to complex surfaces, including doubly-curved surfaces and closed surfaces. For instance, Dudte et. al. developed a process using the Miura-Ori collapsible origami pattern to replicate the overall shape of an arbitrary continuous surface (whether closed or open, doubly-curved or developable/singly-curved); however, the researchers made no claims as to the ability of such folded surfaces to tolerate large-deflection global bending when closed (cylinder/hyperboloid-like), let alone to maintain stiffness or much less radically increase their tensile (and indirectly bending) stiffness at a prescribed amount of deflection [111]. An approximation of a hyperboloid structure created by this research is reprinted in Figure 164.

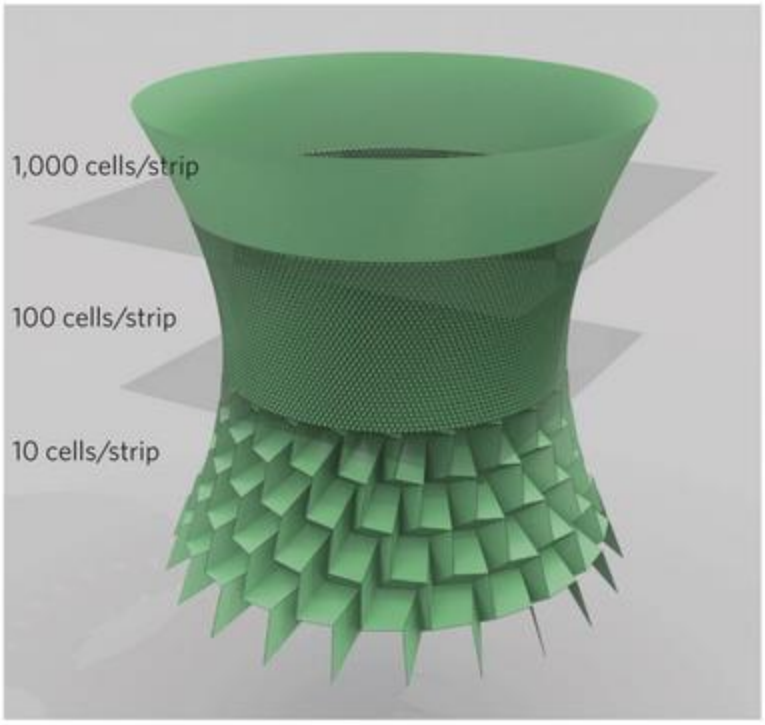

Figure 164: Dudte et. al. proposed an algorithm for conforming an origami metamaterial to a hyperboloid of one sheet. Reprinted from [111] with permission.

That said, other sources indicate that open surfaces produced by other folding patterns (such as the "waterbomb" fold) have low-energy modes that they can morph along, effectively conferring large-deflection freedom to doubly-curved surfaces, not just in the sense of true bending (which must preserve Gaussian curvature), but more-complex morphings that do not preserve Gaussian curvature [112] (this is noteworthy considering that, without the "metamaterial" quality conferred by the origami, a doubly-curved surface out of a homogenous material would tend either to be stiff or at most to buckle in bending, rather than morphing continuously); however, these are open surfaces, not closed surfaces like cylinders and hyperboloids.

A considerable fraction of the research into origami for mechanical engineering applications in fact produces structures that loosely approximate closed surfaces like cylinders.

However, these cylinders are intended to shorten or lengthen as their primary mechanism, and indeed they can often collapse to nearly flat onto their own footprints ("flat-foldable") or be designed to have some curvature when extending [113] (generating a revolved/swept path, rather than a straight extrusion). However, these structures are not intended to tolerate macroscopic large-deflection bending, and most of the research on them does not even consider how the structures would behave when subjected to bending loads. This does not mean that they would precisely be rigid in bending, simply because (as mentioned above) the structures are simply not particularly rigid (even in modes other than their lowest-energy kinematic mechanism) because the underlying paper isn't; for instance, research by Wei-Hsi Chen et. al. into the use of origami bellows as actuators for soft robots entailed the bellows being subject to low but non-trivial global bending curvatures with no remarks as to shell buckling or other effects from this bending load [114]. Similarly, Yan Chen et. al. reported an entire class of rigidly-foldable origami tubes that might follow curved patterns rather than straight, but are (like other classes of origami tubes) specified to only have one degree of freedom [115], and thus would not be suitable even for unidirectional bending (since some regions of the structure must be extended and others compressed), much less bending in different directions (as required for a multi-DOF joint like the human ankle).

Kirigami structures, which combine the folding of origami with the added freedom to cut into the underlying material, could supply greater design freedom and indeed allow closer conformity to a target surface or the simulation of auxetic properties [112]; additionally, some research concerns how to produce cylinders (potentially with auxetic properties—this being desirable for certain applications, though not likely for the joint-protection application), though extensional properties rather than bending tolerance is what is targeted . However, as with

origami, it is unclear how to make them selectively stiffen after a certain amount of deflection with enough magnitude to prevent injury to a human athlete.

Even if some origami fold would allow the creation of structures that loosely follow closed surfaces and can undergo large bending deflections by morphing rather than buckling in unexpected modes, they would be unable to lockup at a desired bending deflection, since origami pieces are nearly produced by plastically deforming a substrate that is usually quite soft (e.g. common cellulose paper). Thus, the very method of manufacturing at least standard origami pieces seems to limit it to making flexible pieces with low stiffness potential, although some research has focused on creating origami-like structures with relatively-rigid members and flexibility relatively localized at specific joint areas [116] (much like how compliant mechanisms use thin beam-like areas to give local flexibility but then thicken other parts of the mechanism into relatively-rigid, rod-like structures). Even still, it is unclear how lockup could be achieved with this paradigm.

A subtler problem is that origami pieces tend to have a mechanism with only one degree of freedom. Thus, even if a fold pattern capable of large-deflection bending as its primary mechanism were discovered, it would probably only tolerate bending in one direction, and be highly stressed (until plastic deformation and joint tearing) in the other; however, a joint protector for a joint with multiple degrees of freedom, such as the ankle or wrist, must itself have multiple global effective degrees of freedom. Granted, some research has investigated creating origami-based mechanisms with multiple DOF [117], but these in reality have little in common with the origami tessellations discussed earlier to approximate surfaces; these multiple-DOF origami mechanisms use simple folds approximating revolute joints and are little different in

practical kinematics from simple linkages; there is no obvious way of tessellating them to create closed-surface enclosures for a joint.

Existing Fabric-Backed Approaches to Large-Deflection Cylinder Bending.

It is no accident that existing products that tightly conform to the human ankle yet tolerate bending (e.g. boots, socks) are made of low-bending-stiffness materials, whether leather or textiles. Since all thin weaves of fabric are especially compliant in compression (regardless of whether they are stiff or stretchy in tension) owing to the microbuckling modes that fibers will experience, this should come as no surprise. Of note, however, most textiles used for socks and gloves are additionally compliant in tension, either because knits are used (which gain added compliance from the looping structures, combined with the natural bending compliance of yarns and tows), or because elastomeric fibers with intrinsic stretch are employed. There are relatively few known high-tech attempts at protecting the ankle joint with fabrics, however, namely because merely conforming to the joint is necessary but insufficient to also offer protection against excessive kinematic displacement.

For instance, Ahrendt et. al. disclosed [118] a knee protector constructed by bonding relatively rigid polymer beams jointed by a revolute joint whose axis passes through the knee onto a compliant textile blend of polyamide and elastane. Indeed, the textile conforms closely to the knee regardless of its angle of deflection, and the two sets of rods that are jointed by a revolute joint can stiffen the knee joint against side-to-side loading (and could likely be modified to cause the joint to lock up after a certain amount of knee dorsiflexion/plantarflexion, if so desired). However, unfortunately this is of limited value to a joint like the ankle that has multiple degrees of freedom, as imposing a revolute joint over the ankle joint (which is more accurately approximated by a Hooke/universal joint) would totally constrain one direction of

necessary motion. Likewise, because of the intrinsic offset of the rigid rods from the ankle joint itself, merely using a ball joint in place of a revolute joint on the bracing mechanism would not be efficacious in restoring the ankle joint's natural freedom: the offset necessitates a length change in curves on the bending surface enclosing the joint, yet rigid links with ball joints cannot tolerate that. Additionally, because of the elastane content of the textile, it offers little tensile stiffness itself and thus can contribute little to hypothetical lockup; its main purpose appears to be locating the rigid elements around the knee. Finally, Ahrendt et. al.'s work is concerned primarily with their novel manufacturing method (FDM 3D printing directly onto the fabric) and thus does not even disclose how much stiffness the structure contributes to stabilizing the knee joint. One wonders if the method of attachment (solely using slightly-tensioned elastomeric fabric) is sufficient to stabilize against severe loads, or if the structure would simply slip or break in that case.

Another work of research that at least attempts to enclose a multiple-degree-of-freedom joint is the glove disclosed by Uysal and Stubbs [54], which another source incorrectly cites [66] as being intended to limit the range of motion of the wrist (though in fact Uysal and Stubbs make no claims in this regard). Uysal and Stubbs's work uses additive manufacturing of two polymers, one soft (LAY-FOMM 40) and further microstructured into a fabric-like weave, and the other comparably rigid (PLA) and formed into thin tiles on top of the fabric-like elastomeric structure. This description may conjure up images of the fabric-backed tile arrays disclosed in Chapter 3 and studied throughout this dissertation; however, Uysal and Stubbs' structures are not intended to lock up in bending in any direction; their focus is only on how different patterns of tiles and pseudo-weaves of the elastomeric substrate affect the drapability of the fabric structures and on which structures are most aesthetically pleasing. At the end they disclose an image of a

structure enclosing the wrist, with no engineering data nor images of how the structure tolerates deformation of the wrist joint, etc. In fact, while the tiles do have gaps between them that should allow for some bending before the gaps are closed, the authors do not even show the fabric being bent in this direction (rather, it is bent in the opposite direction, trending towards further opening up of gaps between tiles). Moreover, both the tile designs and the fabric design are lacking if the goal is to produce lockup in bending (even in simple bending towards developable/singly-curved surfaces): the tiles are too short and have no anti-sliding features on their sides, and the fabric is no doubt very compliant in tension and thus incapable of producing much lockup even if the tiles do not slide.

Literature Survey of Cylinders of Metamaterials Capable of Large-Deflection Bending.

While Uysal and Stubbs's research employed a type of microstructured shape to simulate woven fabric with a structure that could be easily manufactured additively, there may be other applications of microstructured metamaterials of relevance to this problem. As mentioned in Chapter 2, "metamaterials" are microstructured materials that possess unique properties lacking in the bulk material, potentially including elastic properties (such as unusually high or low bulk, shear, or elastic moduli or Poisson's ratio), damping properties, mechano-thermal properties (e.g. novel thermal expansion coefficients), optical properties, etc. Chapter 2 focused on the applicability of any known metamaterials for producing simple tensile, compressive, or bending stiffening and lockup (primarily in open shells), whereas this chapter also considers the potential utility of mechanical metamaterials for solving the more general problem of preventing a closed-surface shell from experiencing catastrophic shell buckling when containing a bending joint, with special attention given to those metamaterials that are also capable of stiffening up and locking after prescribed deflection.

Auxetic-Mesh Tubes in Bending.

Much of the research into mechanical metamaterials, especially those patterns on cylindrical surfaces, concerns specifically auxetic metamaterials. Interestingly, Karnessis et. al. found that microstructured cylindrical tubes made of a "bowtie/reentrant hexagon" auxetic lattice demonstrated improved resistance to kinking under pure bending as compared with a non-auxetic hexagonal lattice tube (specifically one in "zig-zag" configuration rather than "armchair configuration", to borrow terms from the study of carbon nanotubes; the issue of hexagonal configurations will be explored in greater detail later in this chapter), with the maximum curvature the structure can tolerate before shell buckling dependent on the parameters used to generate the bowtie hexagons [119]. However, even the optimal configuration of these auxetic tubes resulted in far less curvature before kinking than would be desired for this application, as can be seen in the reprint in Figure 165, likely because the cantilevered joints were too stiff to allow much deformation.

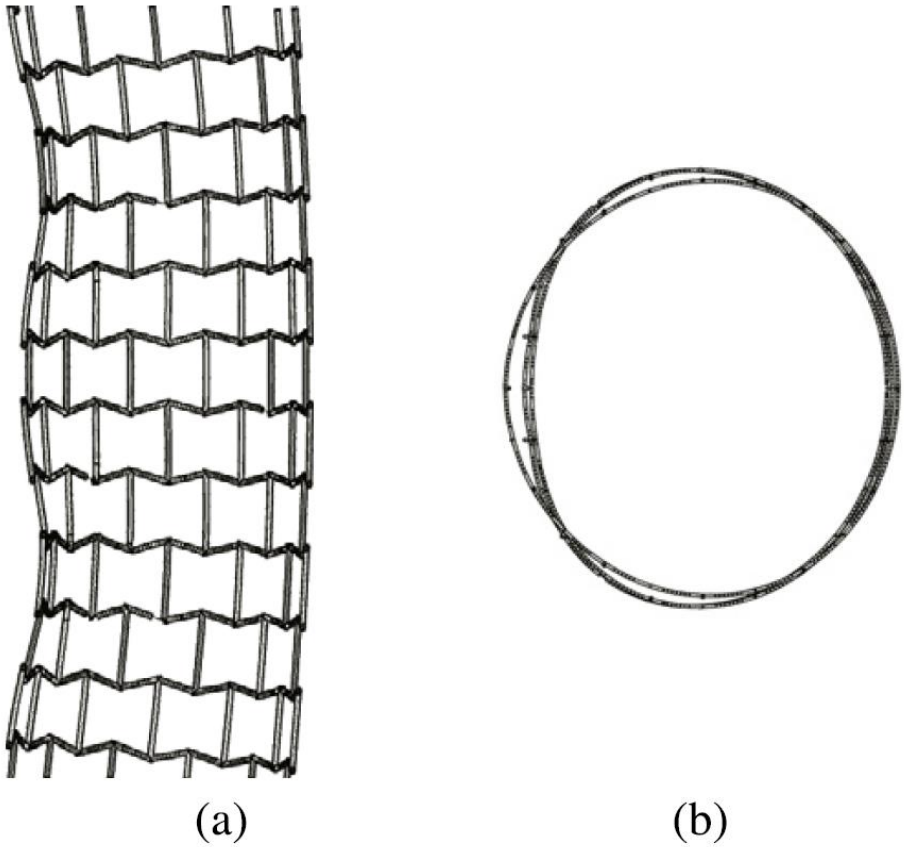

Figure 165: Reentrant/bowtie-hexagon auxetic cylindrical tube subjected to a bending moment, reprinted from [119] with permission.

Sedal et. al. also found [120] that tiling an auxetic bowtie pattern on a cylinder with a polymer that is fairly compliant produces a structure that is somewhat resistant to shell buckling in global bending and can even be used as a bending actuator, although this auxetic cylinder also enclosed a pressurized tube that would inherently resist shell buckling to an extent.

Another closed surface with an auxetic pattern that is intended to tolerate significant deflection in multiple directions on the part of the joint it encloses is a 3D printed neck brace with a complex beam-based auxetic microstructure, disclosed by Panico et. al. [121]. Unlike the cylinders researched by Karnessis et. al., Panico et. al.'s work employs a different auxetic pattern, one derived from the Koch fractal curve that can be modified over the surface of the

neck protector according to the desired stiffness. While the researchers show the device being worn while the wearer's neck tilts in different directions to moderate degrees, they do not conduct any kind of investigation into the maximum deflection that the joint protector can tolerate, nor do they disclose any quantitative mechanical data on how (if at all) the structure indeed protects or stiffens the joint at any amount of deflection. Finally, while the visible views of the brace (reprinted in Figure 166) suggest that it is closed like a cylinder (indeed, a hyperboloid of one sheet, because the surface flares inwards at both the top and bottom), the researchers do not indicate how the structure can be taken off or put on the body while being so closed (if indeed it is), so perhaps it has a slit the back and is thus discontinuous there.

Figure 166: Auxetic mesh neck protector, in various bending modes, disclosed by Panico et. al. Reprinted with permission from [121].

Ultimately, the dearth of mechanical information as regards the neck protector of Panico et. al. is compounded by the fact that the researchers do not give a convincing rationale for picking an auxetic pattern for the mesostructure; early parts of the paper discuss the fact that auxetic lattices tend to contract towards point loads, but there is little obvious reason to value this property for a neck protector engaged in global bending, and the researchers do not construct a similar mesh with a non-auxetic pattern for comparison. Indeed, one's intuition is that the

capacity of a microstructure to tolerate in-plane compression and tension is more important to the apparent resilience against shell buckling that this neck protector offers, a hypothesis that will be explored in detail in subsequent sections of this chapter, where original, microstructured mesh arrays are manufactured and tested. Unfortunately, this in-surface compliance in tension and compression presents a potential conflict with the goal for a structure to lock up in bending after a prescribed amount of deflection, unless of course the underlying structure can be made to stiffen in tension (or compression) rapidly at a desired deflection.

Another widely-studied auxetic pattern for a shell geometry entails cutting circular holes into a solid sheet, creating a geometry that approximates the auxetic mesh pattern having square (relatively-rigid) bodies jointed by revolute joints (in this case, compliant beam joints). Strictly speaking, the auxetic mechanism comes about from post-buckling of the structure at the joints, which causes the formerly-circular holes to become oblong; in practice, the solid regions (formerly solid squares at the diagonals formed by the circular holes) rotate relative to one another in the same way that corner-jointed squares in a rigid square auxetic rotate, as can be seen in Figure 167.

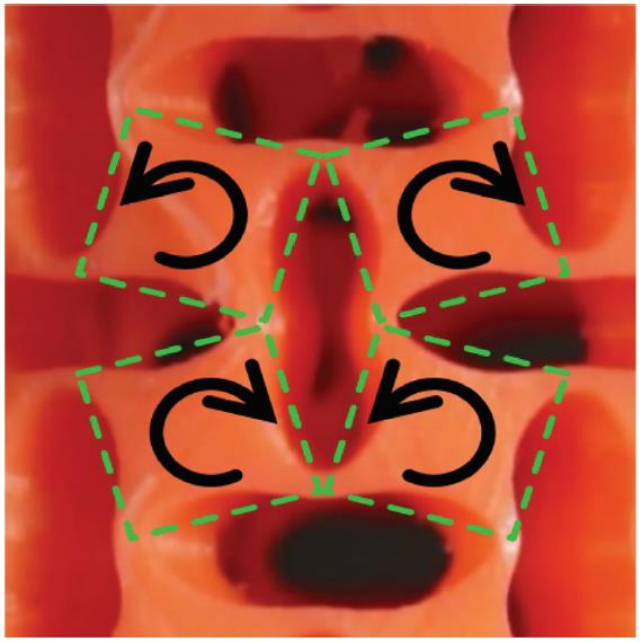

Figure 167: Auxetic mechanism of an auxetic metamaterial created by cutting circular holes into a solid sheet. Compare to the undeformed unit cell that can be seen in Figure 168. Reprinted with permission from [122].

For instance, Broeren et. al. studied such circular-hole auxetic cylinders in global compression, finding that they tolerated vertical compressive strains on the order of 12% [122]; a figure of such a cylindrical shell is reprinted in Figure 168. That said, they did not study the structures in tension or in bending at all. Additionally, Lazarus and Reis proposed a modification to a circular-hole auxetic cylinder in which most of the holes were filled; if the tubular auxetic structure was pressurized internally, the tube would be made to bend to a moderate degree, albeit with some inwards shell buckling [123]; an image of this structure in various stages of bending from internal pressurization is reprinted in Figure 169.

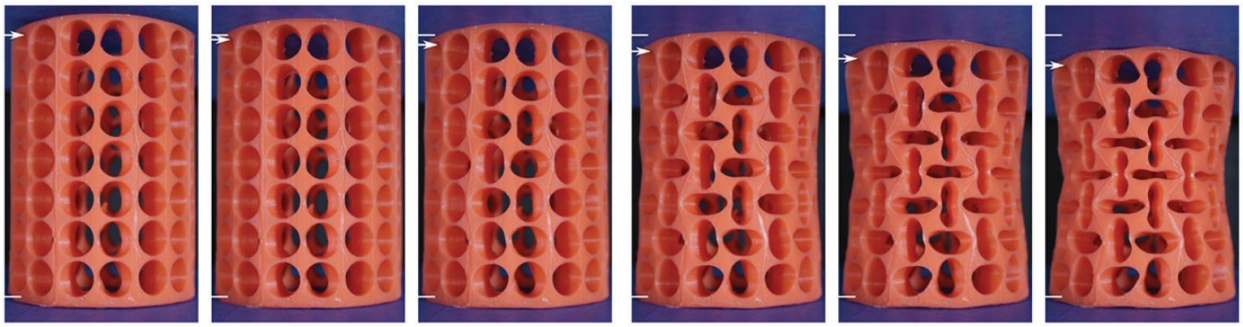

Figure 168: Circular-hole auxetic cylinder in global compression, reprinted with permission from [122].

Figure 169: Modified-circular-hole auxetic cylinder (with many circular holes plugged), experiencing sympathetic bending from increasing applied inflation pressure (the parameter η is a dimensionless parameter referring to the added pumped volume). Reprinted with permission from [123].

Lei et. al. studied [124] auxetic meshes consisting of sinusoids in both the *u* and *v* directions (intersecting at swastika-like shapes), patterned on a cylinder, primarily in tension and compression (wherein the structures were compliant and resistant to global shell buckling) and incidentally in low-deflection bending as well, even comparing this sinusoid-based auxetic structure to a Cartesian net (having vertically-oriented and tangentially-oriented members).

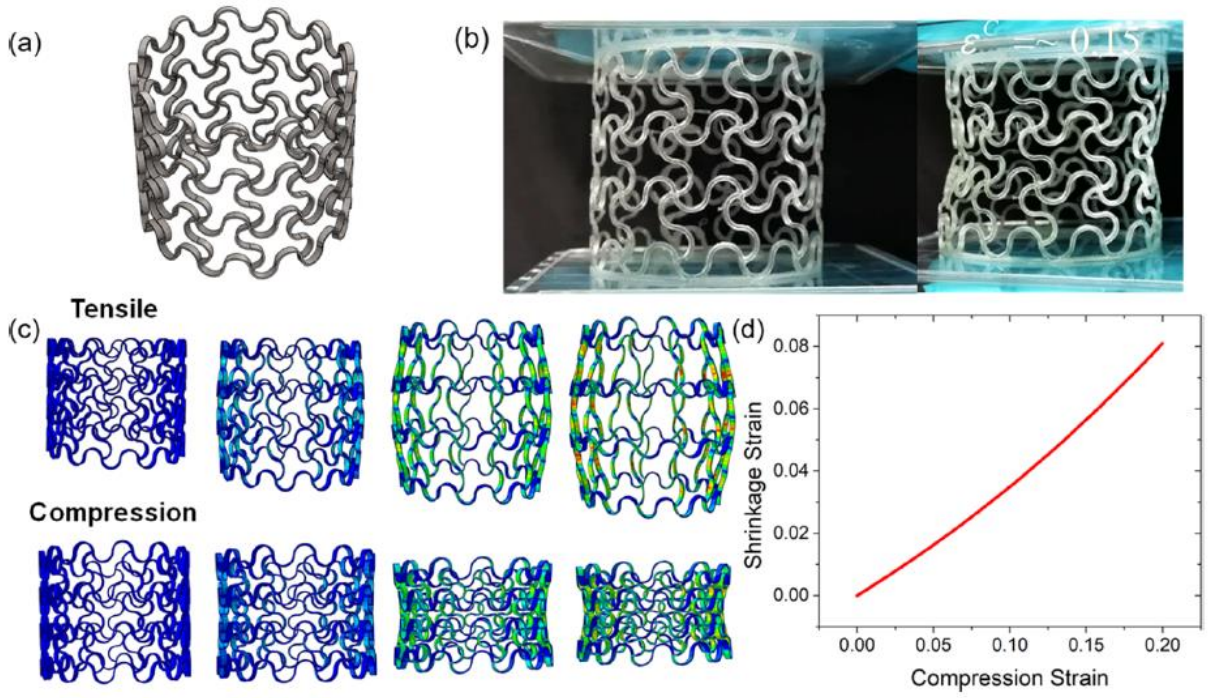

Figure 170: Reprinted with permission from [124]. Copyright 2019 American Chemical Society

Finally, Wang et. al. studied [27] a cylinder with an "arrowhead"/reentrant-dart auxetic structure, consisting of bendable closed-circle shells that were stacked to create the reentrant dart shape on the face of a cylinder. The structure was studied only in vertical compression, not in bending (nor in tension), but at least the authors did discover that it was able to tolerate large compressive strains without shell buckling, and additionally, once members came into vertical contact, the structure stiffened rapidly (with secant compressive stiffness increasing from 133kN/m from strains of 0% to 22.2% to 2,250kN/m for strains from 22.2% to 35.6%). A set of images of FEA simulations of two configurations of these structures under various compressive displacements is reprinted in Figure 171. Owing to the initial compressive compliance and lack of any features that would inhibit bending, the structure is expected to tolerate moderate bending (ideally followed by stiffening-up). The work of Wang et. al. should not be confused with the work of Yang and Ma concerning auxetic quasi-solid cylinders of revolution (where the curve

that was revolved to generate the cylinder was a plane reentrant-dart auxetic pattern) as this work studied a solid structure and did not locate auxetic features on the outer surface but rather on the interior of the solid cylinder [125], whereas Wang et. al. studied hollow shell structures that would be amenable to enclosing a joint.

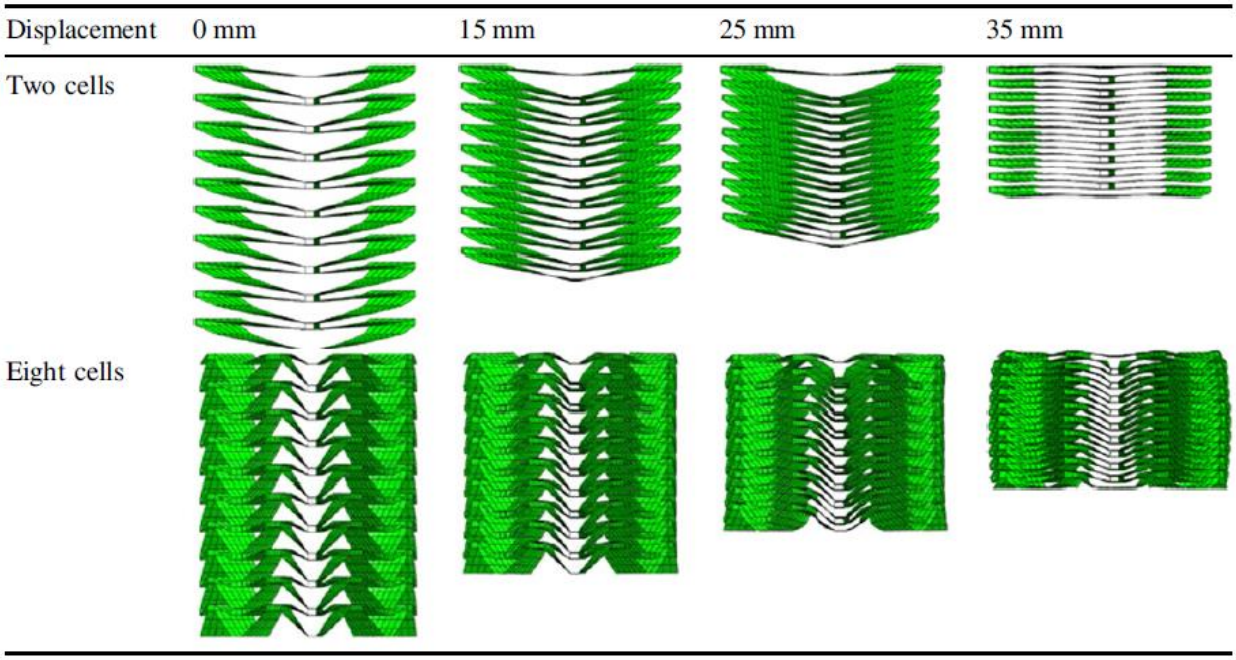

Figure 171: FEA results of two different cylindrical reentrant-dart auxetic structures under various compressive displacements. Reprinted from [27].

It should be noted that none of the aforementioned works pursued auxetic cylinders merely for the sake of resisting shell buckling in bending; rather, their auxetic properties were genuinely desired, indeed usually for compressive rather than bending properties. Thus, although all the microstructures surveyed in this section were auxetic, this is not to imply that the auxetic property itself is necessarily beneficial for avoiding shell buckling in a cylinder-like microstructured surface. Indeed, in the section in this chapter on the author of this dissertation's original microstructured mesh arrays, some non-auxetic closed-surface structures will be tested in bending and indeed found to be resistant to shell buckling.

Biaxial Braids in Bending and Compression.

Perhaps the simplest possible microstructure that nonetheless imparts novel compressive, tensile, or bending properties when tiled on a cylinder is the (non-auxetic!) biaxial braid. A biaxial braid is essentially a cylindrical wrapping of a plain fabric weave, with the vertical axis at an angle to the fibers; also, in a true-biaxial braid, the wrapping has planar symmetry groups, so it is not chiral. A biaxial braid may also be considered to be a wrapping of helices with opposing directions that undulate with respect to each other. For instance, one variation of Auburn University's Open-Architecture Composite Structures (O-ACS) was notably compliant in bending and compression (unlike most O-ACSs, which were engineered to have maximally-high stiffness-to-weight ratios). This variation entailed braiding the composite yarns biaxially without any added axial yarns, and additionally any adhesive bonds (from curing the prepreg) between yarns were subsequently broken in order to allow the yarns to rotate and even slide relatively freely with respect to one another. In effect, it was as if the structure consisted of tiny beams jointed by ball joints at X-shaped overlaps. Owing to the rotational freedom of the overlapping yarns as well as the innate bending compliance at the beam level, the structures were fairly compliant in both bending and compression, and moreover, they were exceptionally resistant to buckling, with axial compression coupled positively to radial expansion (with an effective positive Poisson's ratio). That said, such biaxial braids were far stiffer in bending and axial loads than single-helix springs of the same carbon-fiber cured yarn, owing to the added constraint and radial interference from those helices in the biaxial braid in the opposite direction.

Biaxially-Braided Open-Architecture Composite Structures from Auburn University.

The Open-Architecture Composite Structures (O-ACS) were developed at Auburn University. To manufacture them, prepreg and carbon-fiber yarns are braided around a mandrel,

and once braided, the yarns are then cured in an oven, solidifying not only the matrix around the carbon fibers, but also usually bonding yarns to each other. Generally, the design goal for such braided tubes is to inexpensively produce spars with higher bending, torsion, or tensile stiffness than that offered either by metal tubes, or even by solid tubes manufactured by solid carbon fiber layup techniques [126]. However, it is possible to change the braiding regime to produce structures that are flexible in bending, tension, and compression, specifically by braiding without axial elements, and manually breaking the bonds that naturally form between the yarns after the prepreg is cured. An O-ACS tube designed for rigidity in bending and other modes is shown in Figure 172, whereas a biaxial-only braid with low bending stiffness is shown in Figure 173 for comparison.

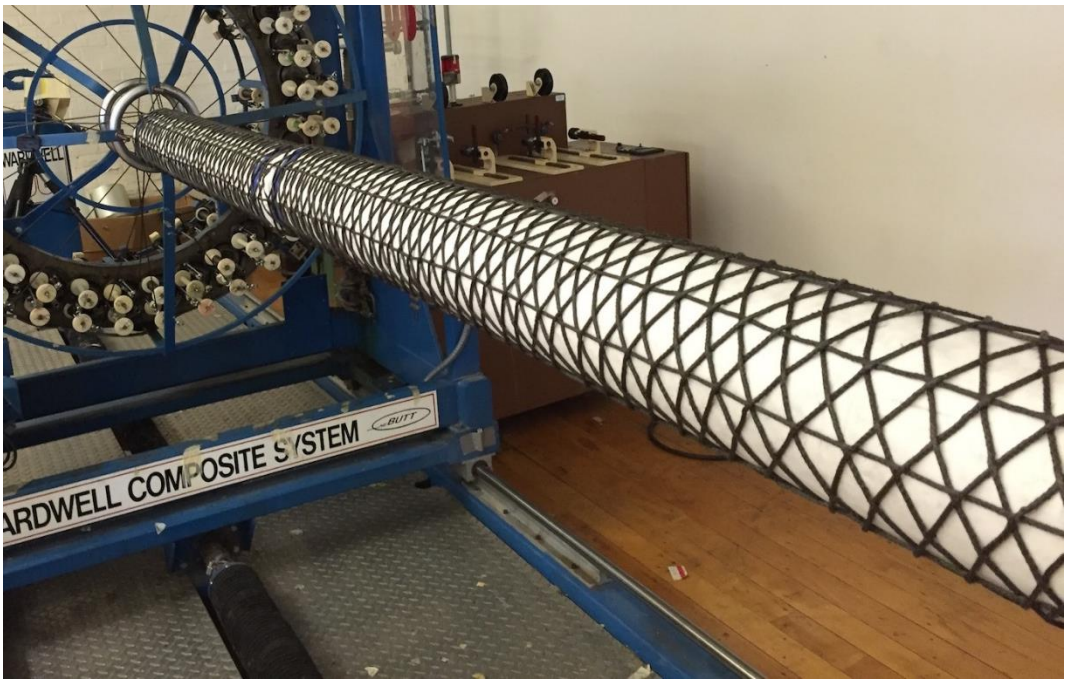

Figure 172: Braiding a high-stiffness braid. Note the axial yarns that go along the length of the tube and contribute greatly to the stiffness of the structure.

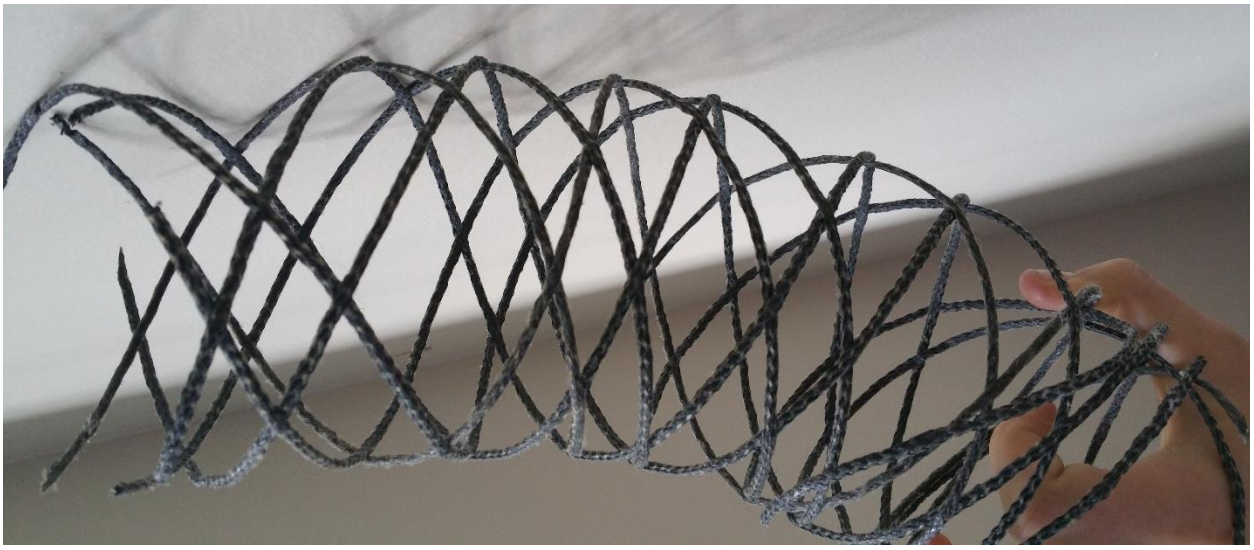

Figure 173: Biaxial-braid O-ACS tube showing low bending stiffness, and considerable resistance to shell buckling in bending.

While the low bending stiffness of O-ACS tubes might make them a useful component of a composite that can be tailored to lock up in bending, strictly speaking the tubes by themselves do not exhibit the desired bending stiffness lockup properties at all, though they were tested qualitatively in case any particular braid profiles offered native lockup potential (without added microstructural features). A wide variety of braid angles and configurations was investigated during this researcher's Master's research, to no avail [1]. For instance, Figure 174 shows the force-deflection curve for one representative sample subjected to three-point bending; while the graph is, strictly speaking, concave-up as desired, the magnitude of the stiffness increase is miniscule. Additionally, there are many other issues with using O-ACS for these intended applications, including high initial stiffness (tending to result in excessive work on the part of the athlete even when his/her joint is in the safe zone), poor bending fatigue life on the part of individual yarns, and poor repeatability of mechanical response.

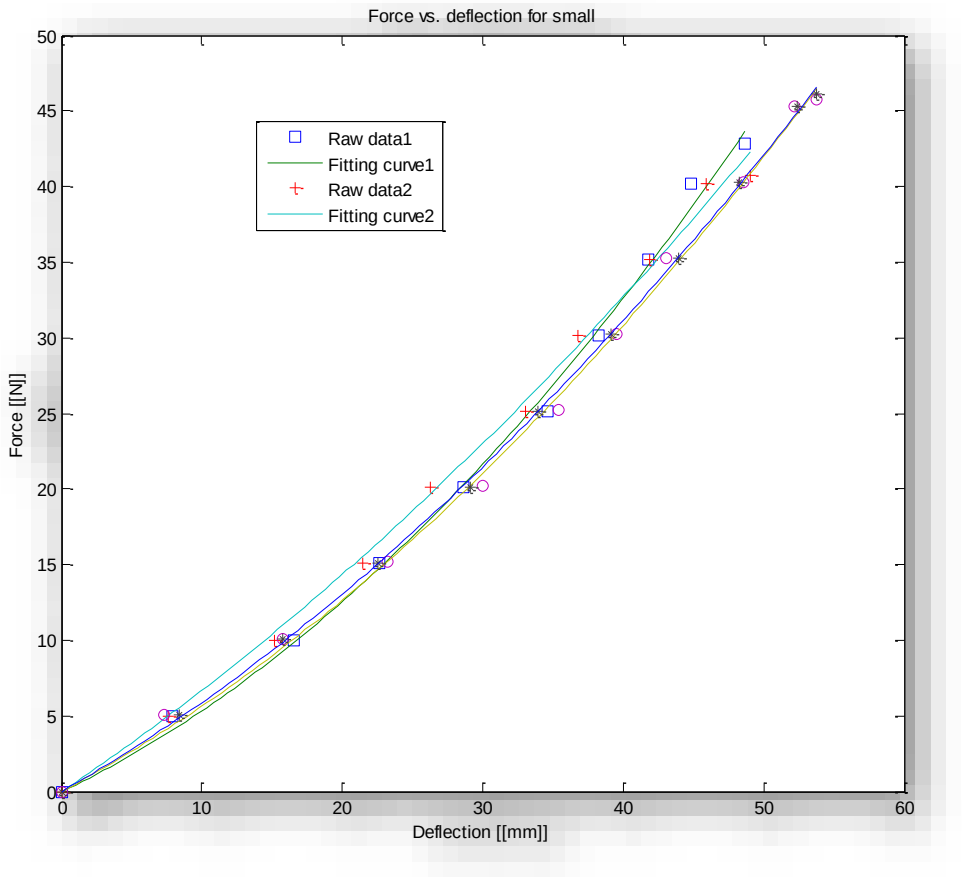

Figure 174: Representative force-deflection curve for four-point bending of O-ACS biaxial braids (in this case, a high-braid-angle tube with 3" diameter). While the curves are technically concave-up, they do not demonstrate multiple-order-of-magnitude changes in stiffness, especially with a small transition region. Thus, these structures were abandoned in the search for lockup-capable geometries.

Ultimately, though this chapter is concerned with avoiding shell buckling rather than producing bending lockup per se, it should be noted that the trellis mechanism of a biaxial braid can sometimes even produce tensile stiffening if the radial stiffness of the individual yarns is engaged by "jamming" the mechanism (however, this requires a high weave density to limit the gap size between yarns in order to make this feasible, and in experiments disclosed in this researcher's Master's thesis [1] on this subject, strong lockup proved elusive, and indeed the structures had undesirably-high initial bending stiffness (though orders of magnitude less than triaxial weaves). This occurs even in biaxial braids of dry, flexible yarns (i.e. as distinct from

braids cured, prepreg yarns): as discussed in Chapter 2, putting biaxial braids of dry fabric into tension an additionally produce some modest increases in tensile stiffness, on the order of 50%.

Thus, if aforementioned issues with biaxial braids (such as excessive initial stiffness and poor fatigue life) could be surmounted, future research might focus on adding rigid tiles to the wires of the open structure (or perhaps use a biaxial braid of another material, such as a low-diameter high-strength metal wire). On the other hand, since the biaxial braids feature a trellis mechanism that is comparable to that of a plain-weave fabric that allows local compression or tension (albeit with other sympathetic stresses developing in other directions), the effectiveness of biaxial braids in tolerating compression may recommend the use of woven or braided fabrics with rigid tiles attached, perhaps with the bias (i.e. a vector bisecting the warp and weft lines) oriented vertically as with the biaxial braids. This issue will be explored in greater detail in subsequent chapters.

Chiral Pseudo-Biaxial Cylinders in Bending, Tension, and Compression.

Lipton et. al. investigated [127] a novel class of structures consisting of compliant beams patterned on cylinders with helical trajectories that effectively constituted quasi-biaxial structures (quasi-biaxial rather than true-biaxial because they were chiral, i.e. did not have planar symmetry and in effect had different helix angles in the clockwise and counterclockwise directions). The beams were not necessarily undulating over-under each other (as in a biaxial braid), but were either intersecting (but made of compliant material, e.g. laser-cut PTFE cylinders) or were jointed at revolute joints (whose axes intersect with the long axis of the cylinder). Additionally, the differing helix angles chosen for clockwise and counterclockwise helices gave the structures auxetic properties (though true biaxial braids are not auxetic). The researchers found that such structures could tolerate significant compressive and tensile length changes (often on the order of

30%) without shell buckling and can be designed to collapse on their own footprint (in compression) or expand radially (in tension). Additionally, like the true-biaxial braids described above, the chiral structures were capable of bending to moderate degrees without apparent shell buckling, though the researchers did not quantify the bending range, peak curvature, or bending stiffness of the structures. An example of a bending-tolerant cylindrical structure from this research is reprinted in Figure 175.

Figure 175: Chiral-biaxial structure in combined bending and torsion, reprinted from [127] with permission.

Ultimately, Lipton et. al. intended the structures to act as actuators that produced sympathetic deformations (bending, vertical compression, or vertical tension) when torqued at the base, which explains their choice of chiral geometries (as chiral geometries couple torsion to other mechanical modes, whereas plane-symmetric, non-chiral geometries do not); the authors had no interest in merely producing buckling-resistant shell structures, let alone lockup-capable protective structures. The authors even investigated combining multiple cylinders concentrically (giving each different handedness and other properties), or placing multiple cylinders side-by-

side (in a 1x2 or 2x2 array) to allow the entire structure of two or four cylinders to extend, compress, or bend side-to-side or front-to-back depending on the torque load applied to each cylinder. The concepts of placing cylinders side-by-side is not applicable to the problem of protecting an ankle joint, but a metamaterial capable of either bending or tension/compression may be.

Miscellaneous Bending-Tolerant Microstructures.

Similarly, biomechanical engineers have created a variety of stent designs (including but hardly limited to biaxial braids) that allow tubular structures to bend somewhat with limited creasing, in this case in order to accommodate the natural curvature of blood vessels and to be delivered to the target location without tearing the blood vessel. For instance, Hemmler et. al. proposed a stent consisting of "stacked sinusoids" (wires with sinusoidal waviness stacked vertically and composing a cylinder), with the peaks and troughs of sinusoids joined to one another [128]. Unsurprisingly, they found such structures were quite tolerant of all manner of deformations, including bending, point loads, pressure loads, etc.; of course, there was no desire for eventual lockup after a prescribed amount of bending, nor did the structure have that capability. A variety of other microstructures have been successfully used to create tubular stents that can bend sharply without catastrophic shell buckling, including triaxial braids in which the wires can slide relative to one another to accommodate bending [129]; reentrant star auxetic patterns [130]; a novel structure known as the "modified ring-and-link" structure [131]; and tetrachiral auxetic patterns [130]. Additionally, researchers have proposed other patterns without indication of whether or not they successfully sustain large-deflection bending without catastrophic shell buckling, including hierarchical (i.e. multi-level, fractal-like) auxetic structures from jointed rigid squares [132]; auxetic structures from crisscrossing sinusoids [133]; and no

doubt others. Significantly, many of these proposed structures are only simulated in FEA and never manufactured, for their geometric complexity greatly complicates practical manufacture, even with cutting-edge AM techniques. If a means of suddenly stiffening these metamaterials after a certain amount of underlying-joint deflection could be discovered, they might be suitable for the ankle-protector problem; otherwise, they at most can provide some clues as to how to prevent shell buckling. Of note, most of these microstructures translate global compression (and often tension) into local bending of the individual beams that make up the microstructure, and in fact the bending beams roughly stay on the imaginary simple surface manifold that the metamaterial exists on. This is not directly applicable to this dissertation's approach with fabric-backed arrays, though certainly plain-weave fabrics are microstructured materials with considerable tolerance for localized compression.

In a related vein, Jennett's PhD thesis from MIT explored bending-capable morphing tube-like structures consisting of beam-like elements (having a wavy structure that allows their ends to be compressed because the wavy areas bend easily) joined in a truss-like configuration and offset from the neutral axis [134]. Since the overall structure can tolerate moderate bending curvatures and has a considerable offset from the neutral axis, it may be relevant to this research; it indicates that mesostructures that successfully tolerate large bending deflections generally require in-surface compressive (and perhaps tensile) compliance, at least up to a point. Unfortunately, the bending structure he proposed is capable of bending only in one direction and is relatively rigid in the orthogonal direction, limiting its applicability to protecting a multiple-DOF joint like the ankle or wrist. Moreover, none of the samples shown in Jennett's research were capable of locking up in bending deformation, even in the direction in which they were able to bend. As an aside, Jennett's work focused on morphing, bending-dominated structures (shells

and solids) that are either static and as rigid as possible, or compliant and actively controlled by tensionable cables: although the main thrust of this author's dissertation is passive metamaterials rather than actively-actuated structures as in Jensen's work, actively-morphing structures might also profit from the concepts discovered in this dissertation.

Finally, a complicated truss microstructure consisting of biaxial weaves braced by triangular truss elements and manufactured out of an elastomer was found in the literature and shown to be capable of enclosing a bending joint (in this case, a finger) [135]. The researchers' stated goal, however, was not to optimize towards bending properties, but rather produce a structure capable of extremely large global tensile strain (on the order of 400%), by combining a method of manufacturing with high-strain elastomer along with a microstructure that augmented the global tolerance for tensile displacement (before tearing of the underlying material) by converting global tensile loads into some bending components of individual truss elements. That said, the researchers did choose to graduate the density of the beams comprising the structure, making it highest in the center, which is relevant for bending properties but not for tensile properties. Ultimately, the researchers did not quantify the bending properties of their would-be finger protector in any way, and certainly made no claims of variable bending stiffness. In the image of the structure enclosing a bending finger, the shell still started to develop a wave-like pattern reminiscent of shell buckling in the outline of the outer surface of the structure, but it was far more controlled than one would see with a monolithic structure. This is no doubt in part thanks to the ability of individual beams to buckle and rotate at the overlaps, but also a function of the low-stiffness elastomer that was used.

Original Microstructured-Mesh Cylinder-Like Surfaces in Bending.

The auxetic neck brace described by Panico et. al. [121] is allegedly able to enclose a multi-DOF joint (in this case, the human neck) and tolerate large deflections in the underlying joint. Granted, these researchers offer very little information on their creation, including why they preferred a specifically auxetic microstructure (as compared with, for instance, a microstructure having an overall Poisson's ratio that is positive), in addition to giving no indication of how they remove it from the wearer's neck or the range of motion that it permits. Consequently, it seemed worthwhile to explore this concept further.

To this end, the author of this dissertation created several multimaterial composite mesh arrays. Each array consisted of two materials, one a flexible polyether-ester thermoplastic elastomer (trade name: Hytrel 4100FL), and the other comparatively rigid, namely polyethylene terephthalate (glycol-modified to reduce hygroscopicity). Note that multimaterial 3D prints are discussed in far greater detail in Chapter 10, where the technique is used for tiled arrays on elastomeric shells that not only tolerate bending deflection but even stiffen up at a prescribed displacement. In the case of this chapter, however, the elastomeric parts created compliant joints that resembled ball joints in rigid bodies in that they were relatively compliant in both bending and torsion, but relatively stiff in tension, compression, and shear; the joints were then linked by rigid members that would be comparatively stiff in all possible modes (bending, torsion, shear, and axial tension/compression). A view of one such multimaterial compliant approximation of a ball joint, specifically one connecting three relatively-rigid beams at a common point, is shown in Figure 176.

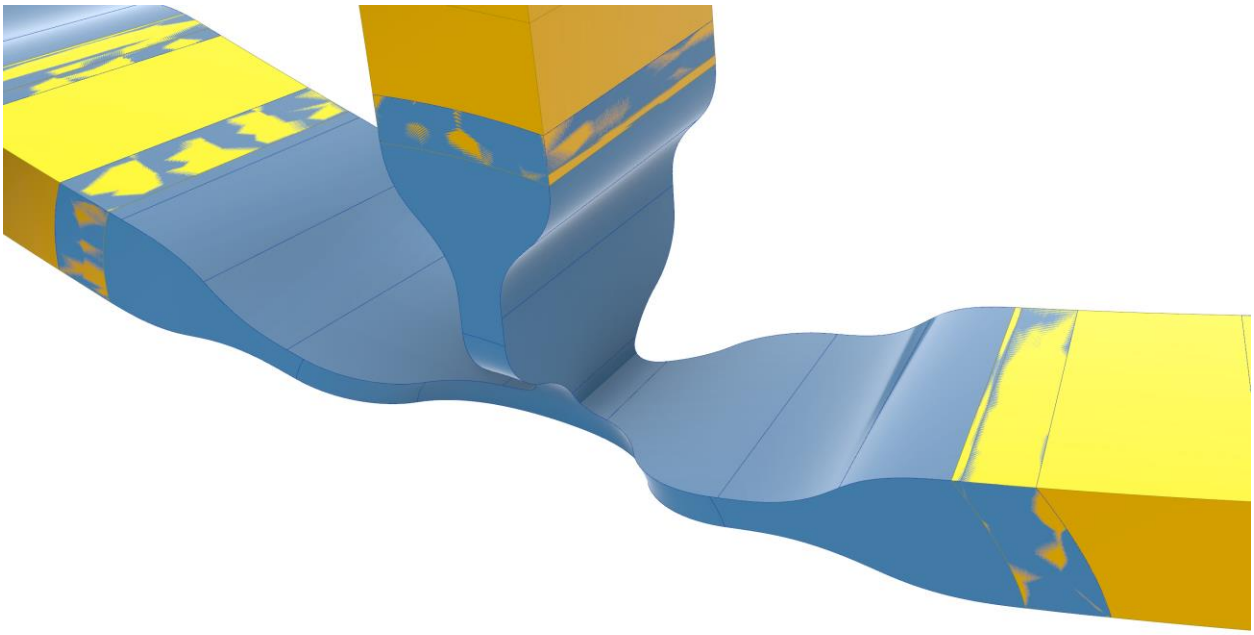

Figure 176: Closeup view of a single complaint joint (colored cerulean) that resembles a ball/spherical joint due to its compliance in both bending and torsion but relative stiffness against tension, compression, and shear. The joint is between three rigid elements (colored in gold).

Note that this type of composite structure differs greatly from the auxetic meshes studied by researchers like Karnessis and Panico; the composite attempts to localize bending deformation to the thermoplastic elastomer component (in the limiting case, as the TPE component becomes infinitely small, it trends towards a ball joint), whereas the outside researchers' works use beams that bend along their entire length, rather than simply at specific loci. The principle of designing a multimaterial composite with both compliant and rigid regions to simulate traditional kinematic joints was most akin to the principle used in the work of Ou et. al. at MIT in developing the so-called "KinetiX" deformable structures [136]. However, the "KinetiX" structures use joints that are far less sophisticated geometrically than those of this researcher's own invention: the joints in the "KinetiX" structures are simple beams (though thinner in one direction than the orthogonal direction, in order to give a definite bias to bend in that specific direction) of elastomeric material connected to relatively-rigid polymer bars. Thus,

the joints in the “KinetiX” structures most closely approximate revolute joints, with one degree of freedom (rotation along one axis).

As an aside, it should be mentioned that the “KinetiX” research itself was focused on creating metamaterial-like structures that changed shape in some regions in response to localized deformation in other regions: for instance, one prototype, if pinched inward in one region, would induce bending along the entire length of the structure. Indeed, the “KinetiX” prototypes all effectively had one quasi-kinematic mode (which could be designed to entail bending, scaling, shearing, twisting, or some combination of the above, by employing links and joints with the proper relative orientations); this would be unsuitable for a protector for a multiple-DOF joint. At the very least, some “KinetiX” structures disclosed were capable of bending and otherwise morphing to approximate surfaces of varied Gaussian curvatures depending on the degree of actuation (for instance, a roughly-flat metamaterial could bend into a doubly-curved surface with bowl-like, positive, Gaussian curvature), though this is not necessarily germane to the issues studied in this dissertation (merely unique relative to ordinary shells, which must be notably strained to change their Gaussian curvature, e.g. to go from doubly-curved to singly-curved). Ultimately, however, no mention was made of designing any “KinetiX” structure to rapidly increase its stiffness in a formerly-low-stiffness kinematic mode after a prescribed amount of deflection, and none of the “KinetiX” structures disclosed were tiled on closed (cylinder-like) surfaces, only on open surfaces or along space curves. Thus, the “KinetiX” principle was not likely to directly solve either the main problem of creating a lockup-capable closed surface, or the preliminary problem of creating a closed surface that can enclose a joint with significant rotation without buckling. However, modifying the “KinetiX” concept with a joint design that gives added degrees of freedom (approximating a ball joint rather than a revolute joint) and using

different layouts of links from those used by the "KinetiX" researchers might enable the construction of closed surfaces that can indeed tolerate significant bending deflection without shell buckling, and might even give insight into potential lockup behavior.

Original Microstructured Auxetic Reentrant-Hexagon Cylinder-Like Mesh.

A reentrant-hexagon "bowtie" auxetic array was used as the basic geometric pattern for the first mesh; note that this array is different from the auxetic array picked by Panico et. al. in many ways, including in terms of its anisotropy, but it is the most basic and well-studied auxetic array. Indeed, this pattern is often studied for its ability to produce synclastic curvature (i.e. positive/bowl-like Gaussian curvature) [137]; certainly, the target surface for this research (the hyperboloid-derived manifold) is not a positive-Gaussian-curvature (synclastically-curved) surface but rather a negative-Gaussian-curvature surface (anticlastically-curved), which may prove problematic for its kinematic properties. It corresponds to Kade Chan's "Magic Ball" origami pattern, which is likewise able to conform to synclastically-curved surfaces (like spheres) [138]; indeed, there are correspondences between other auxetic structures and origami patterns as well: for instance, the square and triangular "waterbomb" origami patterns correspond to auxetic, jointed arrays of rigid squares and triangles, respectively [139].

Of note, this "bowtie" array is the same pattern as that used by Karnessis et. al. in their aforementioned study of how to make microstructured cylindrical tubes that are more resistant to shell buckling when subjected to bending [49]; thus, testing this mesh pattern may give some insight into the mechanisms behind the findings disclosed by Karnessis et. al. Note that, in this case, the auxetic structure was patterned on the HDM proposed earlier in this chapter, and it is certainly not a true cylinder; it is closed like a cylinder, but curves inward somewhat like a hyperboloid of one sheet. The CAD geometry of the overall mesh array is depicted in Figure

177, differentiating the rigid and flexible members by different colors, and a closeup view of one joint between three rigid members is shown in Figure 176.

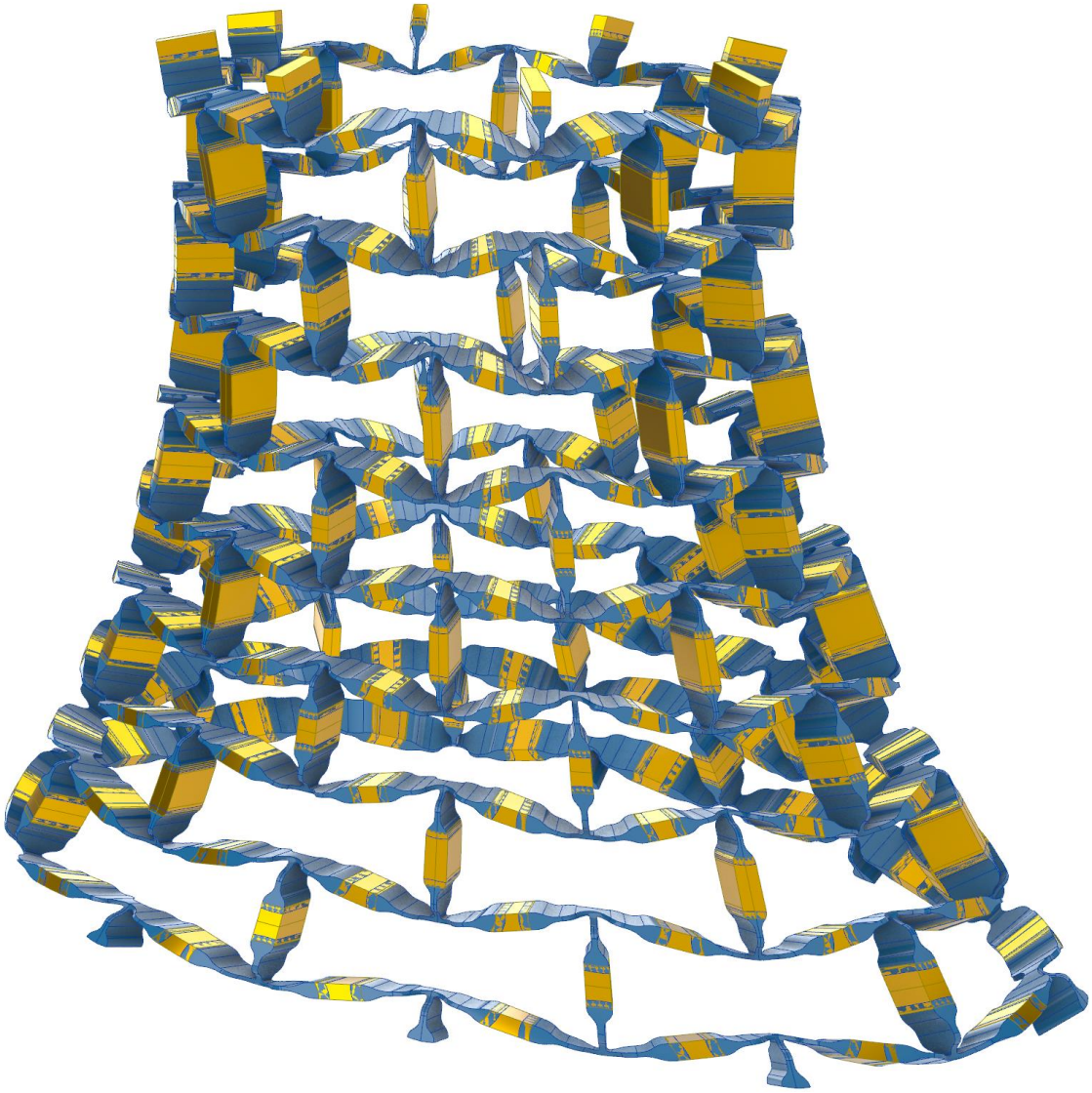

Figure 177: Overall view of the reentrant-hexagon "bowtie" auxetic array on a cylinder-like surface discussed in greater detail in the next chapter. The rigid components are colored gold, the flexible components cerulean.

Since the 3D printer used (the Ultimaker S5) to manufacture this mesh-array only allowed the use of two materials at a time, not three, it was necessary to support overhangs with one of the two structural materials (it was not possible to support them with a third material that might either dissolve in water or simply break away more easily at low temperatures than at high

temperatures); PETg was chosen over TPE owing to the relative brittleness of the former, and since the joints of the mesh (printed in TPE) are more fragile than the rigid beams (printed in PETg) and it was presumed that the affinity between TPE and PETg would at least be lower than that between layers of TPE. Since dissolvable support material was not an option with this print, the support material had to be broken away by hand after the print, a painstaking process that occasionally resulted in the breakage of joints (which had to be repaired by hot-melt adhesive). The mesh array is shown as printed once the support material was successfully removed in Figure 178, which also illustrates how the mesh structure was compliant in many possible loadings, including vertical compression.

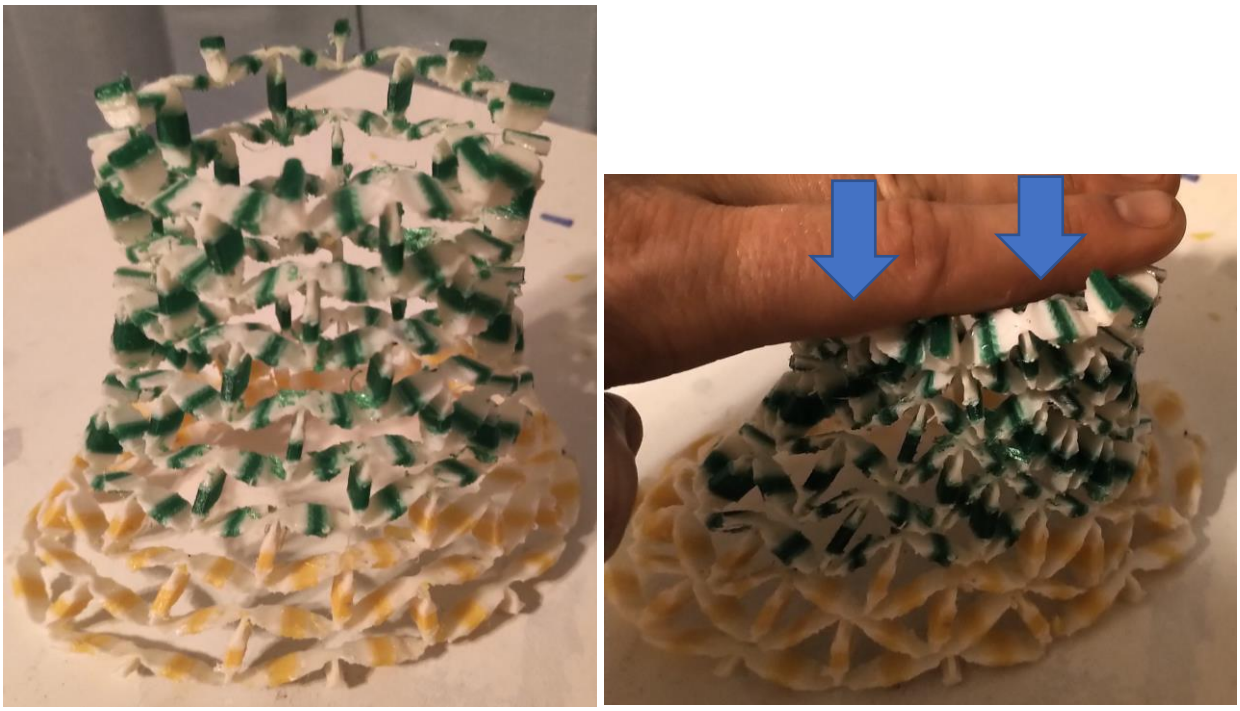

Figure 178: Microstructured, auxetic, cylinder-like array after manufacturing by multimaterial 3D printing and manually breaking away support material. Note that the rigid material changes color from yellow to green at a certain height; this is due to the material running out of yellow PETg and being switched over to green PETg mid-print; it does not correspond to any significant mechanical gradient. Left: structure in neutral, unloaded position. Right: structure compressed vertically (resulting in sympathetic inwards compression due to the negative Poisson's ratio of the structure).

In accordance with the findings of Karnessis et. al. regarding the resistance of auxetic microstructured tubes to shell buckling when loaded in global bending, it was likewise found that

this auxetic mesh array could tolerate significant bending (resulting from the rotation of an enclosed revolute joint) without obvious shell buckling or creasing. This finding was discovered by placing the mesh array on a test fixture for ankle-enclosing manifolds consisting of a rigid rotating "leg" and a base with a revolute joint, which is discussed in greater detail in Chapter 9 (see Figure 328 through Figure 330 for more information on this fixture). The auxetic mesh array's mechanical response to the rotation of the simulated leg is depicted in Figure 179; note that the mesh array does not evince any creasing or shell buckling until the reentrant hexagonal "bowtie" shapes have fully contracted to the point that different joints begin to touch each other (this state is illustrated in Figure 180); this is vastly superior resistance to shell buckling as compared with a thin shell of the same underlying shape (e.g. see Figure 120 earlier in this chapter). That said, the elastic response of the auxetic mesh was very soft indeed, and it is not apparent how to cause such an auxetic mesh structure to stiffen by several orders of magnitude after a certain amount of leg rotation.

Figure 179: Placing the microstructured, auxetic, cylinder-like mesh array on a test fixture to simulate the leg (discussed in greater detail in a subsequent chapter) and rotating the simulated leg forwards. Note that the mesh array was quite tolerant of the large rotation of the leg joint it enclosed, at least from the standpoint of avoiding shell buckling.

Figure 180: Once the auxetic mesh array has been deformed to the point that different flexible joints begin to touch each other, the array does become vulnerable to mild shell buckling when the enclosed joint undergoes further rotation.

Original Microstructured Non-Auxetic "Zig-zag" Hexagonal Mesh Array in Bending.

For purposes of comparison, a similar microstructured metamaterial unit cell was tiled over the same surface as the previous one, but it was given a convex-hexagonal unit cell instead of the reentrant, "bowtie" hexagonal unit cell used in the previous section: the convex-hexagonal unit cell should not have auxetic properties (at least until significantly deformed). The goal of this experiment was to qualitatively evaluate whether it was specifically the auxetic properties of the microstructure that made the previous mesh array so resistant to shell buckling in bending, or whether it was simply the microstructured nature that allows significant in-plane tensile and compressive strains. The CAD geometry of the non-auxetic mesh array is shown in Figure 181; like the auxetic mesh array of the previous section, this non-auxetic mesh array uses compliant

joints of thermoplastic elastomer between relatively rigid bars, and must be manufactured using multimaterial 3D printing. The joints are comparable to those used in the previous mesh array, and a closeup is shown in Figure 182.

Figure 181: Non-auxetic mesh array, based on non-reentrant convex hexagons. Compare to the auxetic mesh array of the previous section, shown in Figure 177 among others.

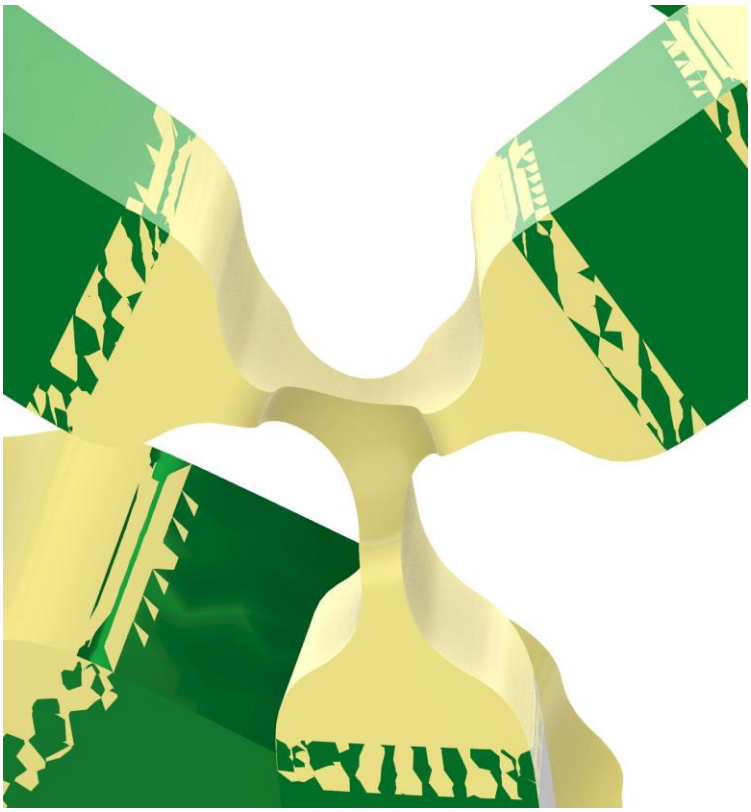

Figure 182: Closeup view of one compliant joint between three rigid beams. As with the auxetic mesh array, the non-auxetic mesh array uses joints that simulate ball joints, having low bending and torsional stiffness but relatively high tensile and shear stiffness.

As with the previous mesh array, this array was printed on an Ultimaker S5 using Hytrel 4100FL thermoplastic elastomer for the flexible joints, and standard PETg for the rigid bodies. Unlike the previous mesh array, which used standard "zig-zag"-pattern breakaway support generated in Cura, this print was assigned tree-like support instead, owing to the great difficulty of breaking away the zig-zag lines from the previous print without damaging it; a picture of the multi-material print in the middle of the print, featuring tree support, is shown in Figure 183. After the print was finished, the tree-like support structures were manually removed, which was easier to do without damaging the joints than it was to remove the "zig-zag" support used in the auxetic microstructured mesh array, though still painstaking (thus, the tree-like support structure would be recommended for future such microstructured mesh arrays).

Figure 183: Mid-print picture of the non-auxetic mesh array, featuring tree-like support out of PETg (green color). The pale white material is Hytrel 4100FL thermoplastic elastomer.

The non-auxetic array displayed significantly different properties as compared with the auxetic array, giving preliminary credence to Karnessis et. al.'s hypothesis that cylinders or other closed surfaces with auxetic microstructures have superior resistance to shell buckling and kinking than do non-auxetic microstructures of comparable coverage factors. When subjected to a bending moment (unfortunately, the structure was printed at too small of a scale to fit on the

simulated “leg” test fixture, owing to print time and material constraints, so this researcher had to approximate this loading by hand), the tensioned region (i.e. rear part of the mesh when the structure is being bent forwards) saw relatively little strain (certainly no kinking) owing to the fact that the beams that were initially nearly-vertical in orientation prior to loading were aligned fully in the vertical direction after just a small amount of deformation and thus this region became quite stiff. In contrast, the compressed region developed local surface kinks (tending to produce waviness normal to the original surface profile) reminiscent of buckling in continuous surfaces (though of note, the elastomeric shells displayed much simpler buckling behavior, creasing inwards at just one crease rather than featuring both outwards and inwards creases as this non-auxetic mesh array does). Additionally, other cells in the compressed region compressed so significantly that they became distorted into rectangular or even reentrant/bowtie hexagonal cells. Figure 184 and Figure 185 depict the structure in bending from two different views, noting areas of out-of-surface buckling as well as cell compression.

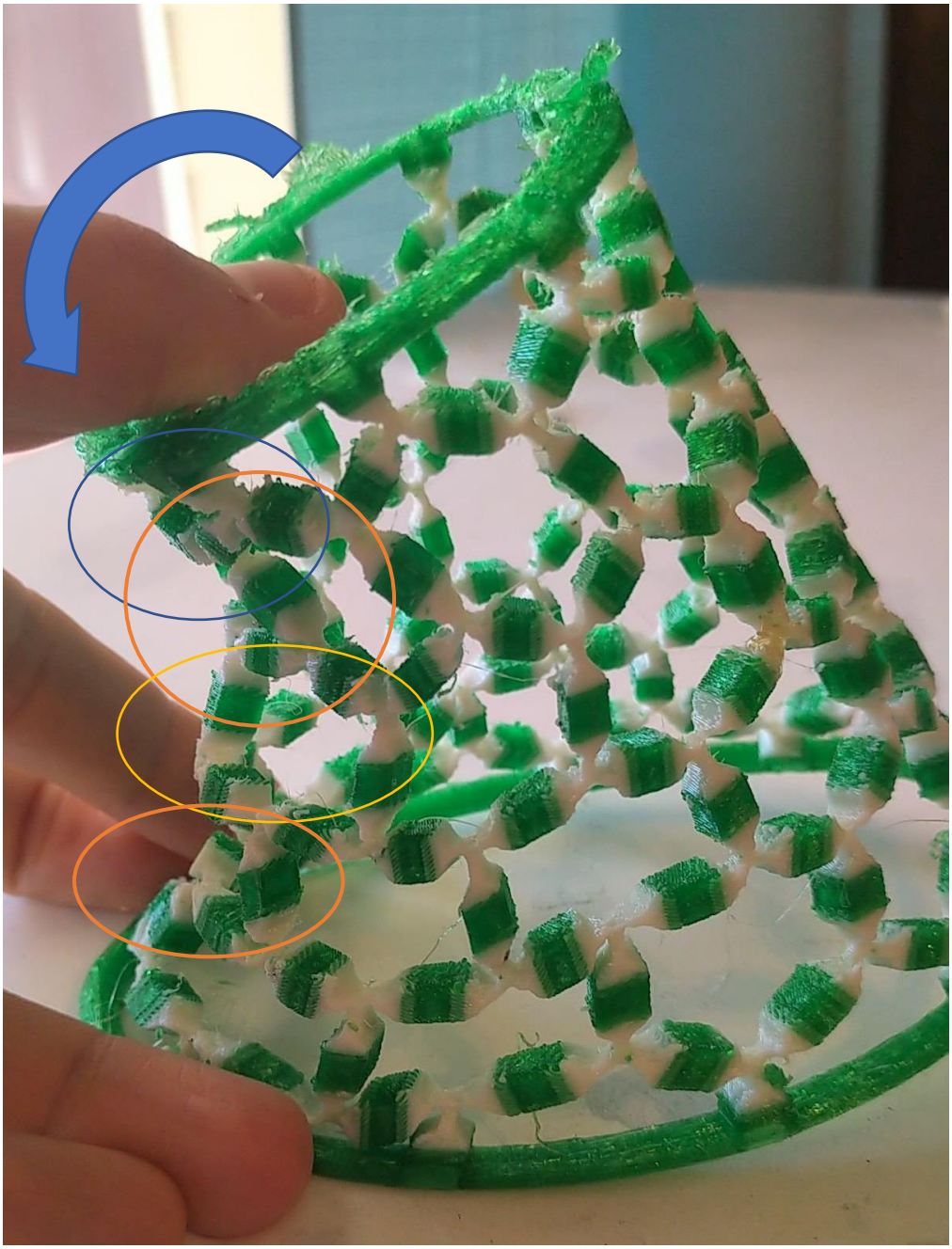

Figure 184: The non-auxetic microstructured mesh array tended to be far more compliant in local compression than in local tension, so applying a bending moment to the top rigid ring tended to lift up the rear and additionally resulted in more compressive strain in the front than tensile strain in the rear. Some cells were greatly compressed, even nearly collapsed by this compression (e.g. the one circled in blue). Note the significant local kinking in certain mesh elements, namely those circled in orange, which feature both significant compression of the unit cell in-surface as well as out-of-surface inwards-directed bending/creasing. On the other hand, the cell circled in yellow is somewhat bowed outwards rather than inwards: the curvature of the surface does not vary monotonically.

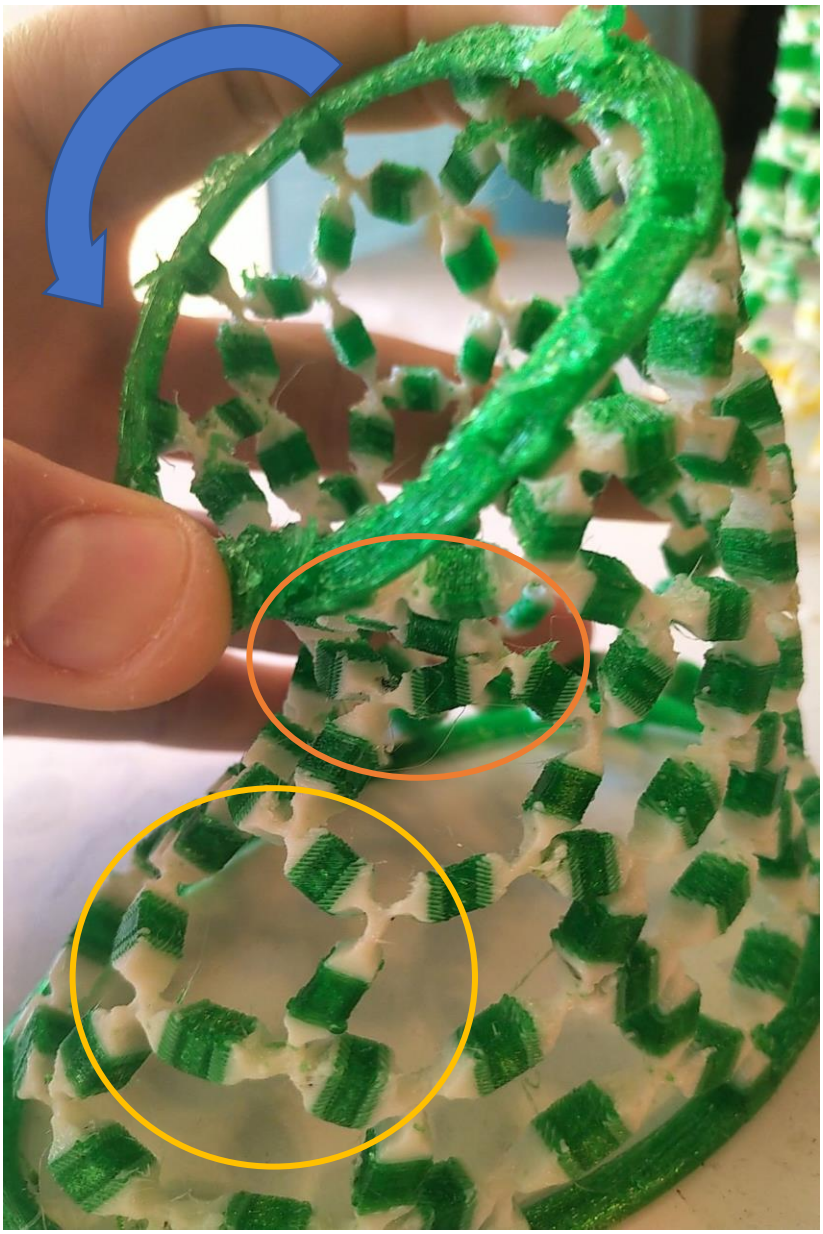

Figure 185: View of the non-auxetic mesh array in global bending from the front. Note the significant local kinking in certain mesh elements, namely those circled in orange, which feature both significant compression of the unit cell in-surface as well as out-of-surface inwards-directed bending/creasing. On the other hand, the cells below (circled in yellow) are somewhat bowed outwards rather than inwards: the curvature of the surface does not vary monotonically.

The surface was moderately compliant in global compression, albeit less so than the reentrant auxetic mesh array studied in the previous section. Some cells (generally those in the highest and lowest ranks, i.e. closest to the top and bottom of the array) distorted so much that they became concave reentrant hexagons; indeed, once the cells had started to become concave,

the structure demonstrated bistability, in that it tended to compress further of its own accord, and the user had to exert some force (miniscule in overall magnitude owing to the compliance of the structure, but noteworthy nonetheless) to overcome this bistable mode and return the structure to its original shape. Additionally, global vertical compression resulted in some shell buckling and kinking (namely towards the front of the surface, where its Gaussian curvature was most negative), and additionally it produced some shearing in cells on the sides. All these phenomena are depicted in Figure 186, and additionally, Figure 187 shows a closeup of the bottom-most rank of cells having been made concave by significant compression and thereby activating their second bistable mode.

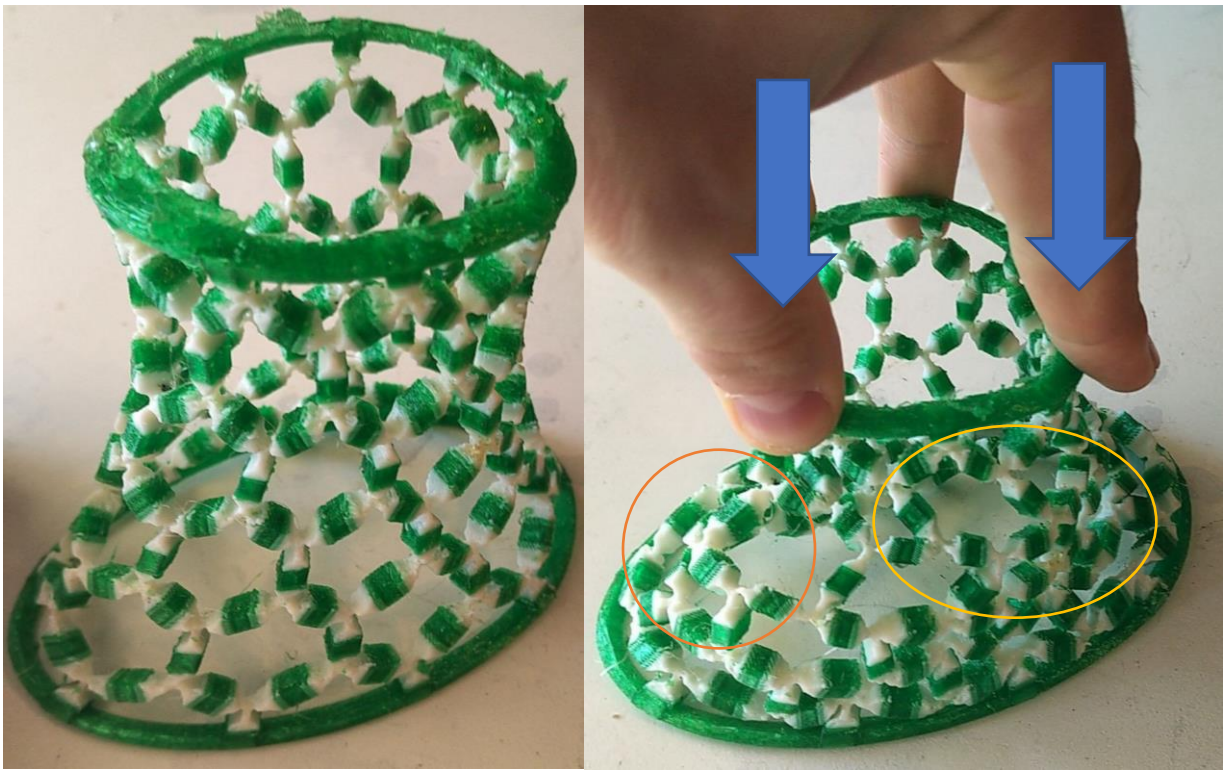

Figure 186: The non-auxetic hexagonal mesh responds less "gracefully" to vertical compression than does the auxetic mesh array; the non-auxetic mesh effectively undergoes shell buckling outwards (or rather, an imaginary surface through the links does) in the region circled in orange, whereas other regions see strange shearing and rotational deformations (e.g. as circled in yellow). Finally, the regions toward the bottom compressed so significantly that the cells become auxetic-like reentrant bowtie hexagons from severe distortion, although they tend to snap back when the compressive load is released (see the next Figure for a closeup). Indeed, this was a bistable mode, as, if compressed to this point, these cells would stay in their concave configuration unless some tensile force was exerted to return them to their original configuration.

Figure 187: Bistability phenomenon when the array is subject to global vertical compression (as per the previous figure); the hexagons that were previously convex become compressed into "bowtie" reentrant hexagons (as in the auxetic pattern used for the mesh array in the previous section).

Comparison between the Non-Auxetic Hexagonal Mesh Array and Carbon Nanotubes.

Clearly, the non-auxetic "zig-zag" hexagonal array was indeed less suited to non-buckled deformation under bending loads than the auxetic array. Indeed, the non-auxetic "zig-zag" hexagonal array brings to mind the structure of a carbon nanotube (or other nanotube, e.g. boron nitride), which consists of carbon atoms arrayed in hexagons on the face of a cylinder (thus a

closed surface) with electrical bonds between atoms. Of note, carbon nanotubes are exceptionally stiff and strong in axial loading, in both tension and bending [140], although notably they are relatively compliant against radial deformation (though still on the order of GPa) [141]; when subjected to bending (or compression in long form), they do tend to undergo shell buckling, though they are quite resilient against failure in such loadings and tend to spring back though eventually experience plastic deformation [142].

Carbon nanotubes have three primary classes of configurations, based on the orientation of the hexagons (formed by carbon-carbon bonds) in the arrays on the tube surface. The "zig-zag" configuration entails the vertically-oriented lines (bonds between carbon atoms) being discontinuous but sharing axes and additionally has no lines oriented fully circumferentially/horizontally (rather, it has zig-zagging lines roughly circumferentially); in contrast, the "armchair" configuration has no lines oriented truly vertically and instead only has zig-zag lines that are nearly vertical. Finally, the "chiral" configuration does not have rotational axis-symmetry and instead has some intrinsic twist (how much is determined by the basis vector). Figure 188 depicts the three types of nanotubes. Clearly, the mesh array studied in the previous section most closely resembles the zig-zag configuration, though of course it is not tiled on a true cylinder but rather the hyperboloid-derived manifold developed in this dissertation.

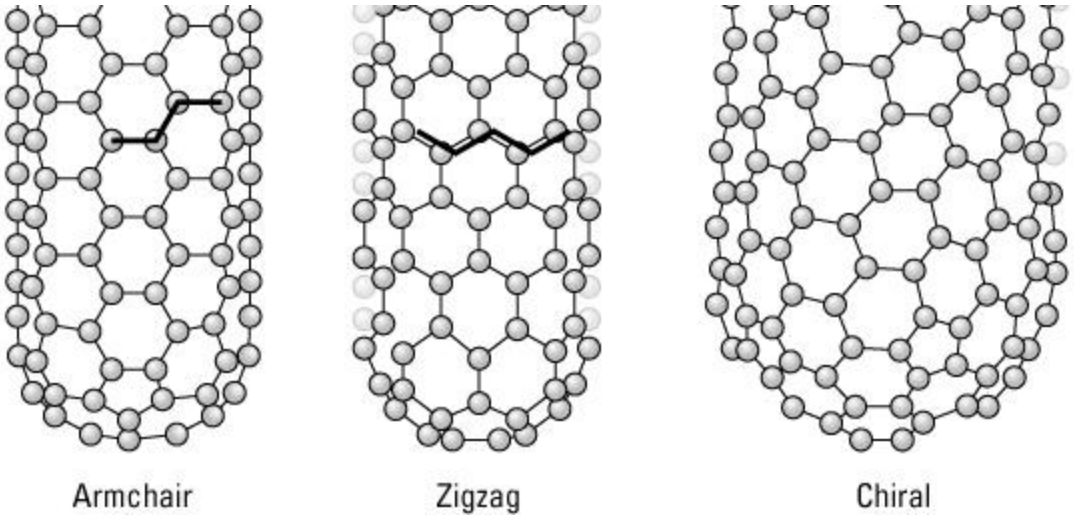

Figure 188: Schematics of the three types of configurations of carbon nanotubes, taken from [143].

Original Microstructured Non-Auxetic "Armchair" Hexagonal Mesh Array in Bending.

As described in the previous section, the non-auxetic mesh array that tiled hexagons in the "zig-zag" configuration was rather prone to shell buckling in bending, certainly more so than the reentrant-bowtie mesh array, which was in agreement with Karnessis et. al.'s findings regarding cylindrical tubes [119] (though of course, Karnessis et. al. studied true cylinders, namely with a longer aspect ratio, whereas this dissertation's original work in this domain used the hyperboloid-derived manifold instead of a cylinder). However, it was conceivable that the "armchair" hexagonal configuration could prove far more suitable for the application, since it does not have any members that are oriented fully vertically (instead, many members are slightly at an angle from the vertical orientation, whereas other members are purely circumferential/horizontal in orientation). Additionally, Karnessis et. al. did not even study "armchair"-configuration hexagonal arrays in their work, which would seem to necessitate studying this question in this dissertation.

Of note, neither Karnessis et. al. nor this researcher chose to study chiral hexagonal tilings on closed surfaces, because chiral structures tend to couple vertical compressive or tensile

properties with torsion [134], and tolerating significant torsional displacement is not necessary in this application (after all, the lower leg of a healthy human can scarcely permit much transverse rotation about the long axis of the leg without serious ankle or knee injury). Additionally, spurious torsional displacement of the protective structure could result in misaligning load paths (e.g. the loading direction originally corresponding to forwards-and-backwards movement, i.e. plantarflexion/dorsiflexion, might under significant rotation be reoriented to the side-to-side or inversion/eversion direction, which tolerates far less foot rotation before injury); thus, it seems wise to avoid chiral structures or other structures that can see large torsional displacements.

Thus, it seemed wise to construct a multimaterial, non-auxetic hexagonal mesh array with hexagons oriented in the "armchair" configuration but otherwise sharing the same joint design and rigid member design as previous arrays (especially the previous non-auxetic hexagonal array). Effectively, before tiling, the array was rotated 90° from the configuration used by the "zig-zag" array in order to create the "armchair" array. A rendering of the resulting multimaterial mesh array is shown in Figure 189; note that none of the members are oriented precisely in the vertical direction, though the non-horizontal ones have a significant vertical component.

Figure 189: CAD rendering of the "armchair" hexagonal mesh array, with flexible elements colored in yellow and rigid elements in green.

The array was manufactured with the multimaterial printing methodology and Ultimaker S5 printer used for other arrays, although in this case, owing to material availability, natural-color ABS was used in place of PETg (DuPont indicated that ABS is also expected to blend well with its Hytrel 4100FL thermoplastic elastomer [144], as indeed it did). After printing and manually breaking away the tree-like support, the structure was tested, first in bending, where it was considerably more resistant to shell buckling than the "zig-zag" hexagonal mesh array, as can be seen by comparing Figure 190 (showing the newer "armchair" array in bending) with Figure 184 (showing the "zig-zag" array with evident shell creasing and distortion).

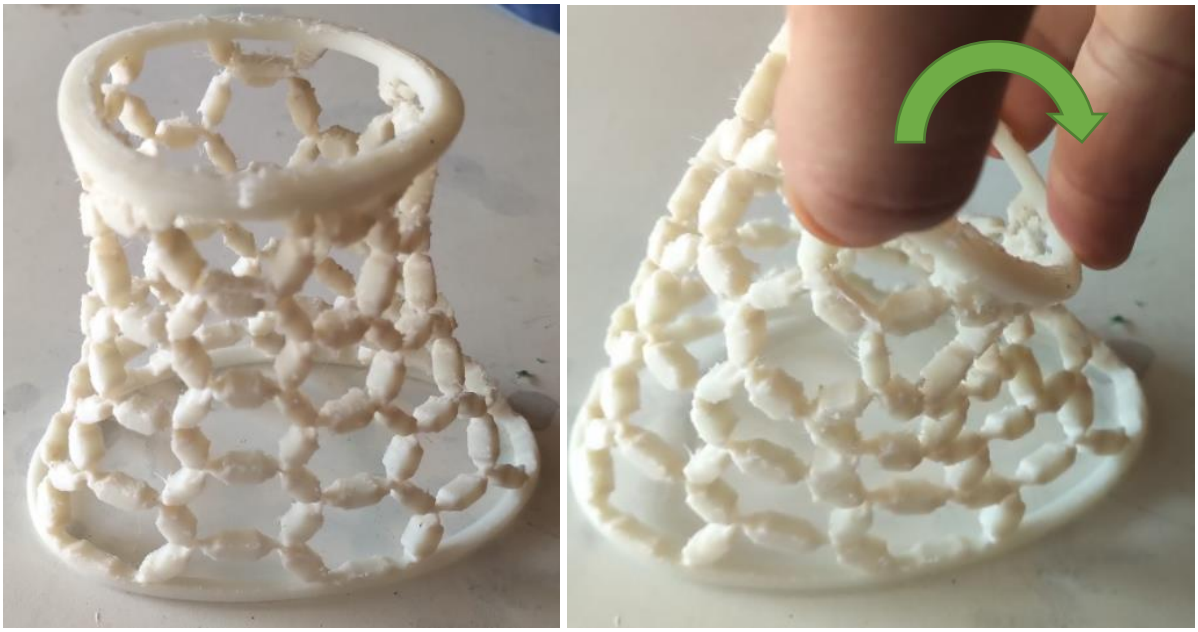

Figure 190: Side view of the "armchair" hexagonal mesh array in bending (left: undeformed; right: bent forwards). Note that the "armchair" hexagonal mesh array is far more graceful in bending than the "zig-zag" hexagonal mesh array, tolerating considerable local compression in the front without shell creasing.

The "armchair" hexagonal mesh array's superior resistance to shell buckling and creasing is likely due to Certainly, this gives the "armchair" array considerable compressive freedom without buckling (ending once the hexagons are distorted into parallelograms or even reentrant/bowtie hexagons), as can be seen in Figure 191. Of note, true to the non-auxetic nature of the hexagonal mesh arrays, vertical compression results in some slight radial expansion (whereas the auxetic array experienced some inwards radial contraction when compressed vertically).

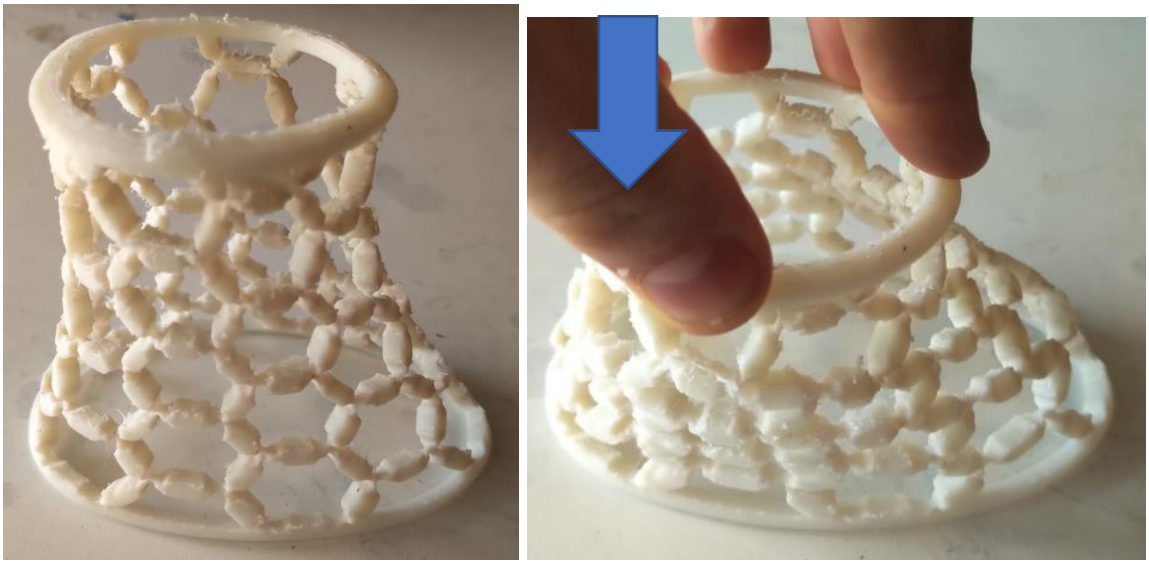

Figure 191: Side view of the "armchair" hexagonal mesh array in vertical compression (left: uncompressed; right: compressed vertically).

Specifically, it appears that the large proportion of rigid members that are oriented somewhat at an angle to the vertical, rather than directly aligned in the vertical as with the "zig-zag" array, is what allows global compressive loads to translate into a flattening mode of the individual hexagons (tending to squeeze the horizontally/circumferentially-oriented members towards each other), which is a low-stiffness mode. Indeed, as a fraction of the overall length, the vertical component of the length of the four angled (i.e. not fully vertically-oriented) members is higher in the "armchair" array than is the vertical length of the four angled (i.e. not fully horizontally-oriented) elements in the "zig-zag" array; since the elements of the arrays themselves cannot directly compress, but rather only take up compression by rotating, those at an angle to the vertical that nonetheless have a vertical component to their orientations can see the vertical components of their length decreased by rotating at the flexible joint. Thus, the "armchair" array would be expected to have better compressive tolerance (and presumably tolerance of tension as well) than the "zig-zag" array, precisely what is borne out by this qualitative comparison.

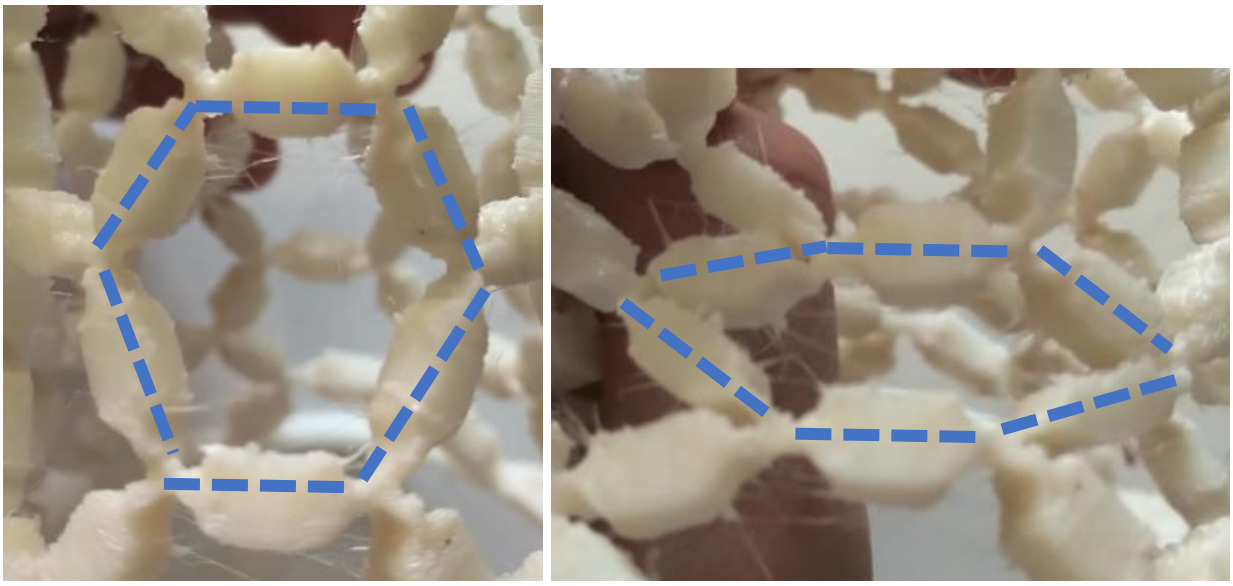

Figure 192: Closeup view of a single hexagon in the "armchair" hexagonal mesh. Left: neutral position; right: four side angled elements closing up, allowing the top and bottom horizontal elements to get closer and compress vertically.

Indeed, one important finding of this section is that the earlier finding of Karnessis et. al. regarding the superiority of the reentrant-hexagon auxetic mesh structure over the "zig-zag" non-auxetic hexagonal mesh structure is incomplete in that it does not study the "armchair" configuration and presumes that the greater buckling resistance of the structure is due to the auxetic nature of the reentrant hexagonal mesh rather than the increased vertical component of length of non-vertically-oriented members that both the auxetic reentrant/bowtie-hexagon and the non-auxetic "armchair" hexagon configurations have relative to the "zig-zag" hexagonal array, so most likely it is this property that explains their qualitatively superior bending/buckling-resistance performance, and not auxetic or negative Poisson-ratio effects, though certainly this should be explored in future research into other arrays with different Poisson ratios and other configurations.

Original Microstructured Non-Auxetic Vertically-Oriented Cartesian Mesh Array in Bending.

To conclude the investigation into the properties of microstructured mesh arrays in global bending, it seemed wise to explore Cartesian arrays (i.e. mesh elements in "X" configurations relative to one another, especially at right angles), as those most closely approximate woven fabrics, and woven fabrics have thus far been an integral component of planar-lockup-capable tiled arrays. Without resorting to chiral structures (which, as mentioned previously, tend to couple torsion with bending/compression/tension), there are two possible configurations for Cartesian arrays with right angles between mesh elements: mesh elements oriented vertically and circumferentially/horizontally, and mesh elements oriented such that vertical vectors bisect the right angle between elements. The former (which will be referred to as the "vertically-oriented Cartesian mesh array" for relative simplicity) is depicted in Figure 193 and would approximate woven fabric with the weft oriented vertically and the warp oriented circumferentially (with the seam sewn closed). As in all previous original mesh arrays discussed in this chapter, it was a multimaterial composite with flexible joints connecting rigid members.

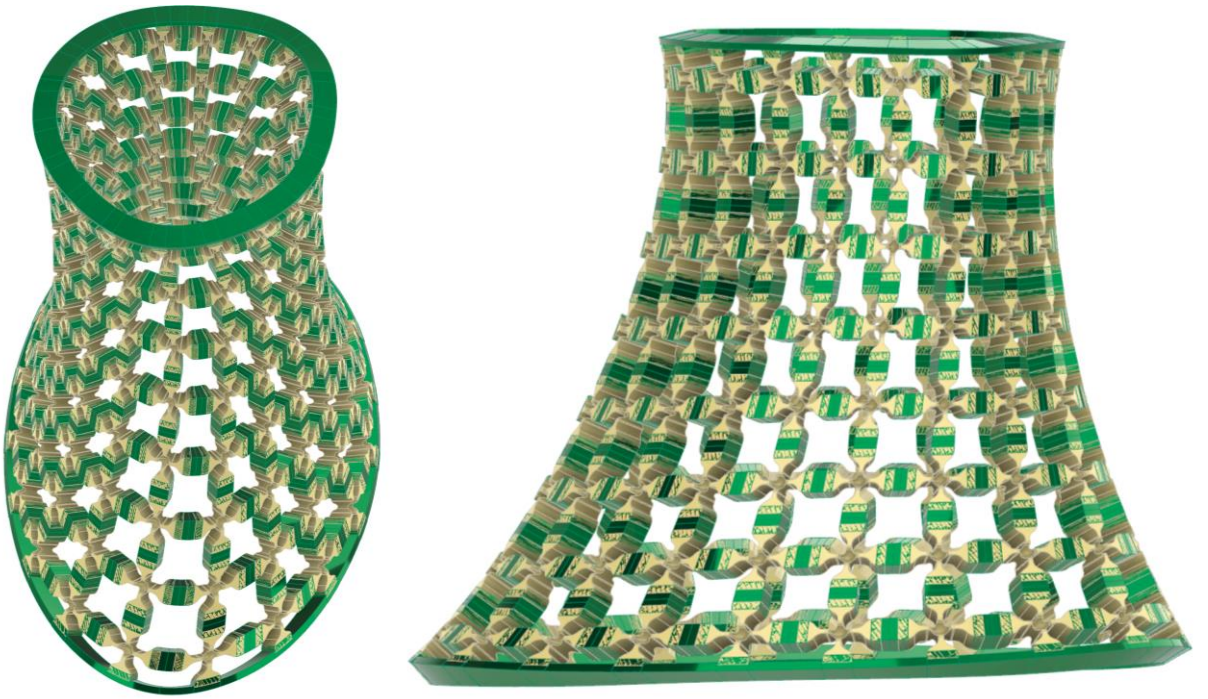

Figure 193: CAD rendering of the vertically-oriented Cartesian mesh array in two views. Note that the elements meet at right angles.

Once manufactured, the vertically-oriented Cartesian array displayed unique behavior distinguishing it from the other mesh arrays studied so far. The near-vertical orientation of half of its members forced the structure to crease inwards when a bending moment was applied at the top ring (as seen in Figure 194), and indeed it was quite stiff throughout this mode; however, when subjected to a pure horizontal shearing force at the top ring instead, the structure was far more compliant and required far more deflection to produce inwards-directed shell creasing, owing to the shear freedom of the elements (especially on the sides of the structure), as can be seen in Figure 195.

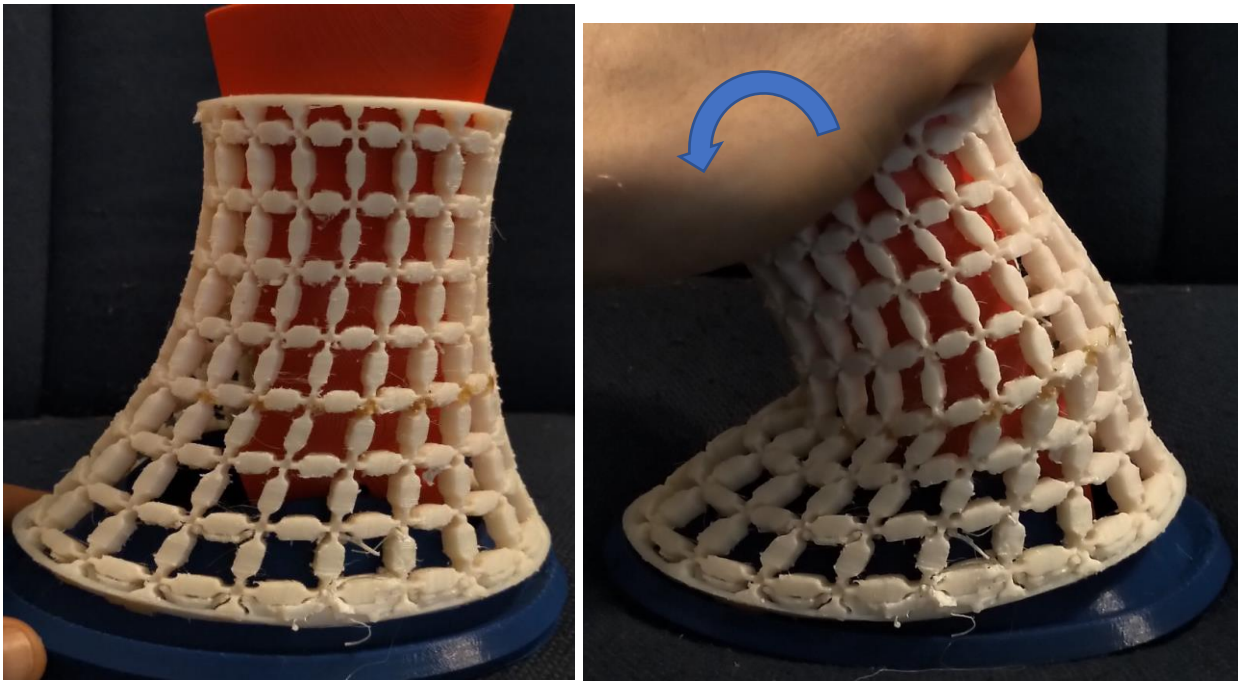

Figure 194: Side view of the vertically-oriented Cartesian mesh array in bending (right: test fixture torqued; left: unloaded). The structure tends to crease inwards in this loading, and indeed it is far stiffer than other mesh arrays tested so far, no doubt owing to the near-vertical orientation of half of the members.

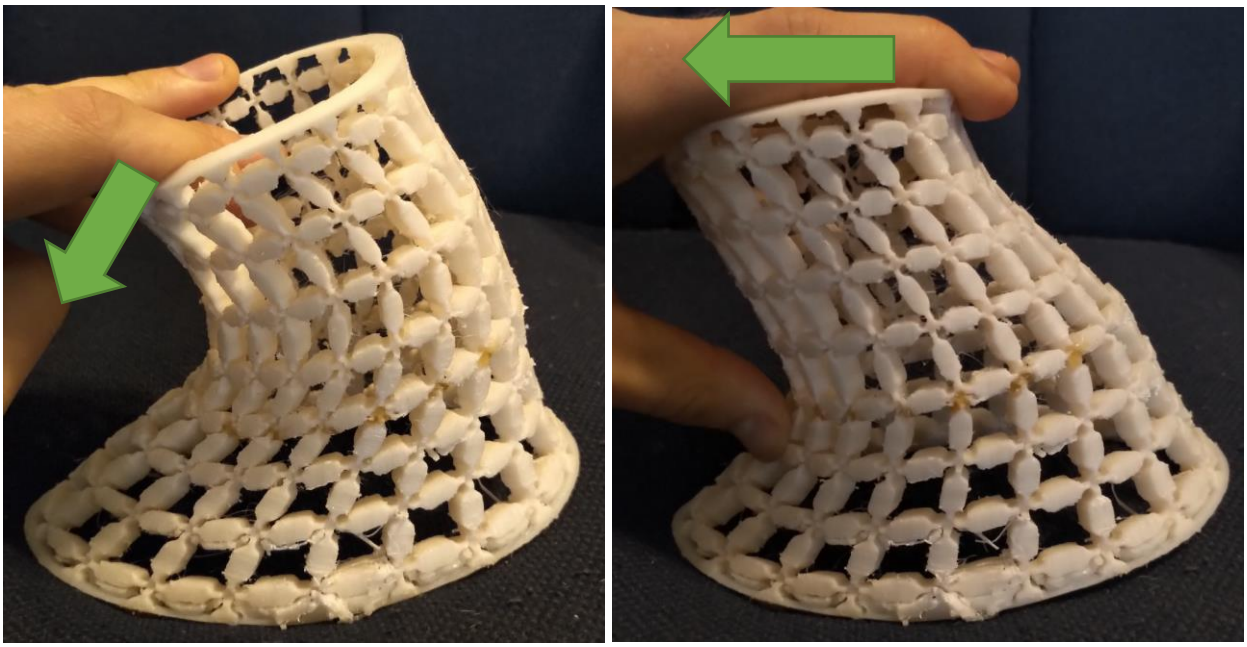

Figure 195: The vertically-oriented Cartesian mesh displays a slightly different response when given a point load oriented forwards and down (as shown in the left image) versus merely forwards (as shown in the right image), since shearing of the individual cells of 4 mesh elements each is the softest mode, and the loading in the right image (pure horizontal force) produces more shearing whereas the loading in the left image (force with a significant downwards component) attempts to compress vertically-oriented members, against which the structure is much stiffer.

Finally, the trellis mechanism of the underlying mesh made the global mode in which the structure is most compliant global torsion rather than compression, bending, etc. as for other structures. On a true cylinder, an applied torsion will be converted entirely into shear stresses within the surface; although the hyperboloid-derived manifold is not a perfect cylinder, it was evident that global torsion was mostly converted into local shearing of mesh elements, which additionally produced some coupled contraction in the vertical direction, as can be seen in Figure 196.

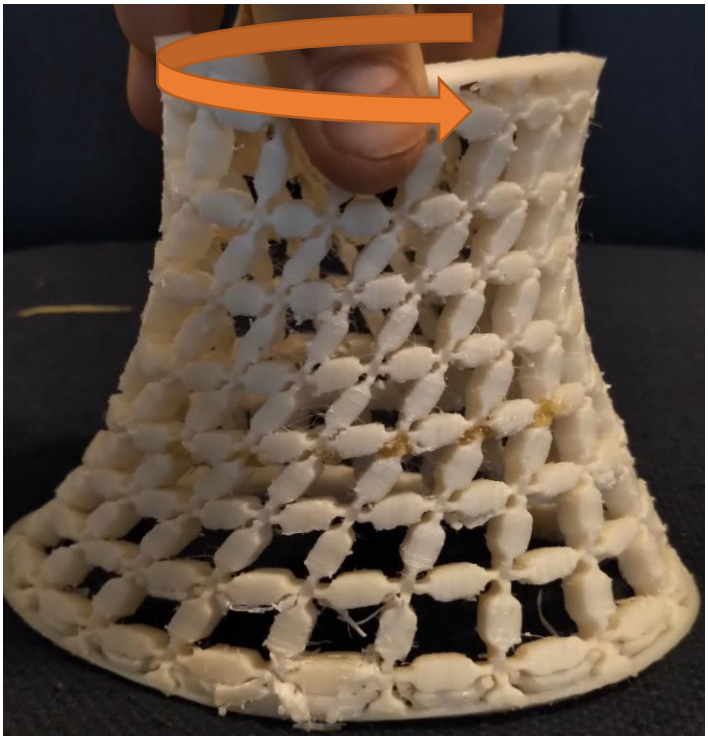

Figure 196: The vertically-oriented Cartesian mesh array was quite compliant in torsion about a vertical axis—this is not desirable for an ankle protector.

Ultimately, the response of this particular mesh structure in simulated leg rotation and similar bending loadings was rather unfavorable, but the reader should be cautioned against drawing conclusions as to the suitability of woven fabrics (oriented such that either warp or weft is in the vertical direction), since thin woven fabrics have negligible effective compressive

stiffness owing to microbuckling of filaments and shell buckling of the shell (enabled by fabrics' very low bending stiffness), whereas this vertically-oriented Cartesian mesh array was for some reason somewhat constrained against out-of-surface bending of individual links (required to enable local shell buckling to relieve compressive stress owing to the inability of in-surface rotations to accommodate it, in contrast with other mesh arrays such as the "armchair" hexagon and biaxially-oriented Cartesian mesh, both of which were laid out in such a way that their repeating units could convert applied vertical compression into link rotation to shorten the overall unit cell), despite the ball-joint-like freedom that all joints had. Certainly, if a mesh structure like one of the ones described in this chapter were to be used as the basis of an ankle protector (with some other added mechanism for stiffening up), the vertically-oriented Cartesian array would be a poor choice of mesh structure, but its poor performance does not necessarily contraindicate the use of a vertically-oriented fabric weave for a cylinder-like fabric-backed array; the primary point of this section was to expand on the work of teams like Karnessis et. al. and Panico et. al. in exploring what enables cylinder-like structures to be more tolerant of bending.

Original Microstructured Non-Auxetic Biaxially-Oriented Cartesian Mesh Array in Bending.

In contrast to the previous mesh array, the other potential non-chiral configuration of a Cartesian array approximates a biaxial braid (or just a single piece of fabric cut along the bias and with the bias oriented vertically), with the roughly-vertically-oriented *v* curves that define the surface bisecting the right-angled joints. The structure might also be compared with the biaxially-braided O-ACS tubes mentioned earlier in this chapter. A rendering of this geometry is shown in Figure 197.

Figure 197: CAD rendering of the biaxially-oriented Cartesian mesh array in two views. Note that the elements meet at nearly right angles; there has been a small amount of distortion, but it should not affect the overall mechanical response of the mesh.

When printed, the biaxially-oriented Cartesian mesh array showed excellent bending tolerance, owing to the ability of the X-shaped joints to change the height of their individual bounding boxes (effectively tolerating moderate amounts of compression or elongation), with a side view of the array in forwards-directed bending shown in Figure 198, a front view in Figure 199, and a rear view in Figure 200.

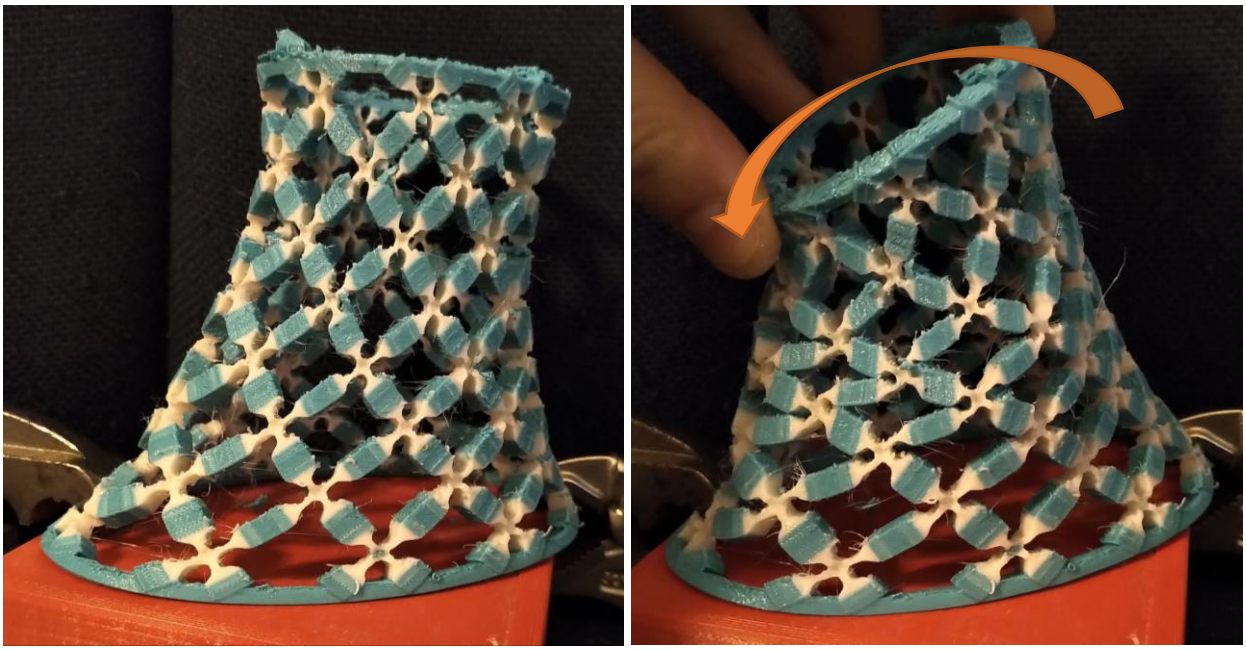

Figure 198: Side view of the biaxially-oriented Cartesian mesh with bending moment applied to the top ring (right), causing compression in the front region of the manifold (in the right picture, the front region of the manifold as worn on the leg corresponds to the left half in this picture) and tension in the rear-most members. See the next Figure for a front view instead of this side view.

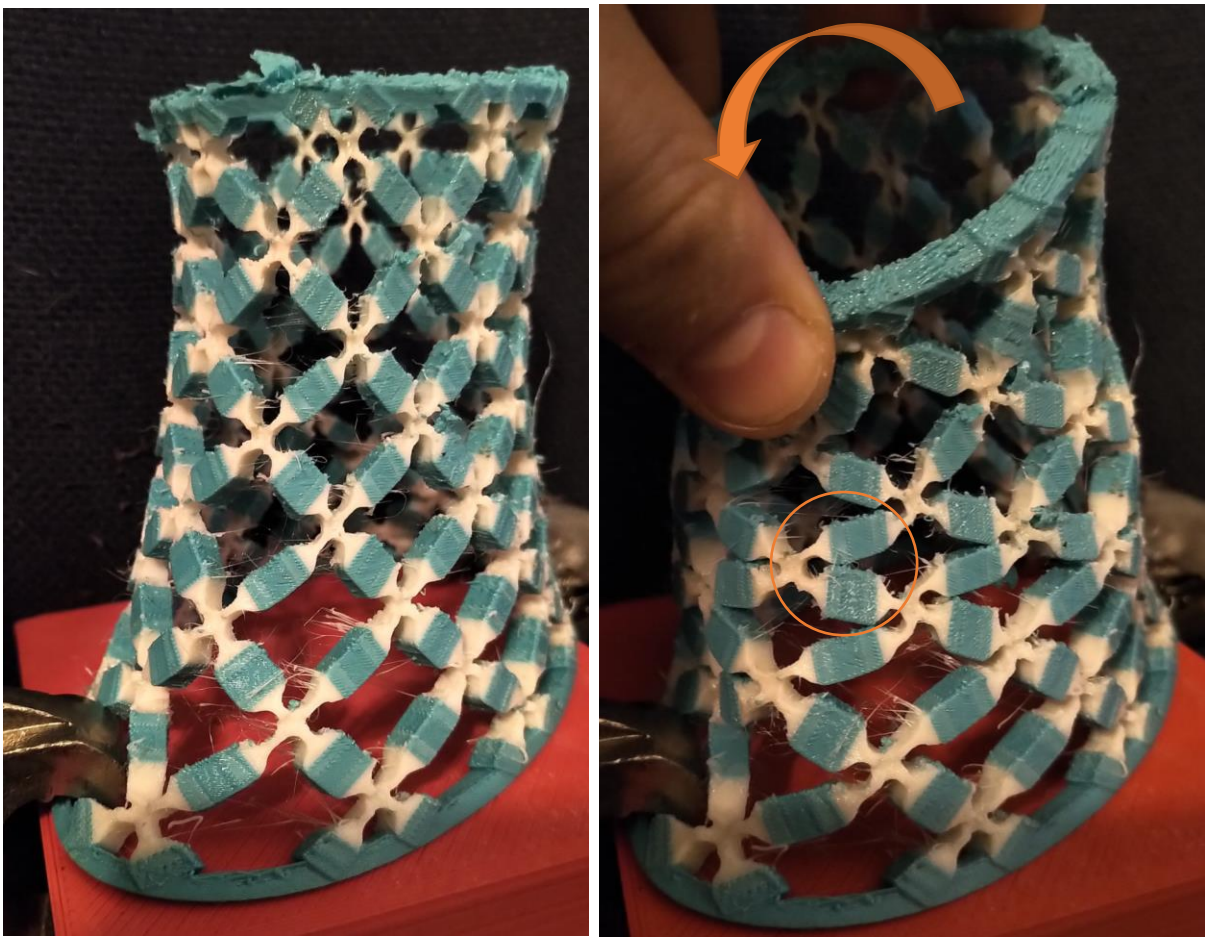

Figure 199: Front view of the biaxially-oriented mesh array bent forwards (right). Note that some rigid elements came into contact with each other (e.g. two contacting elements are circled with orange), preventing them from rotating further, though any stiffening-up effect from this was mild because other modes of deformation (e.g. normal to the surface) were still available to the structure. Compare to the side view in the previous Figure. Also see the rear view in the next figure.

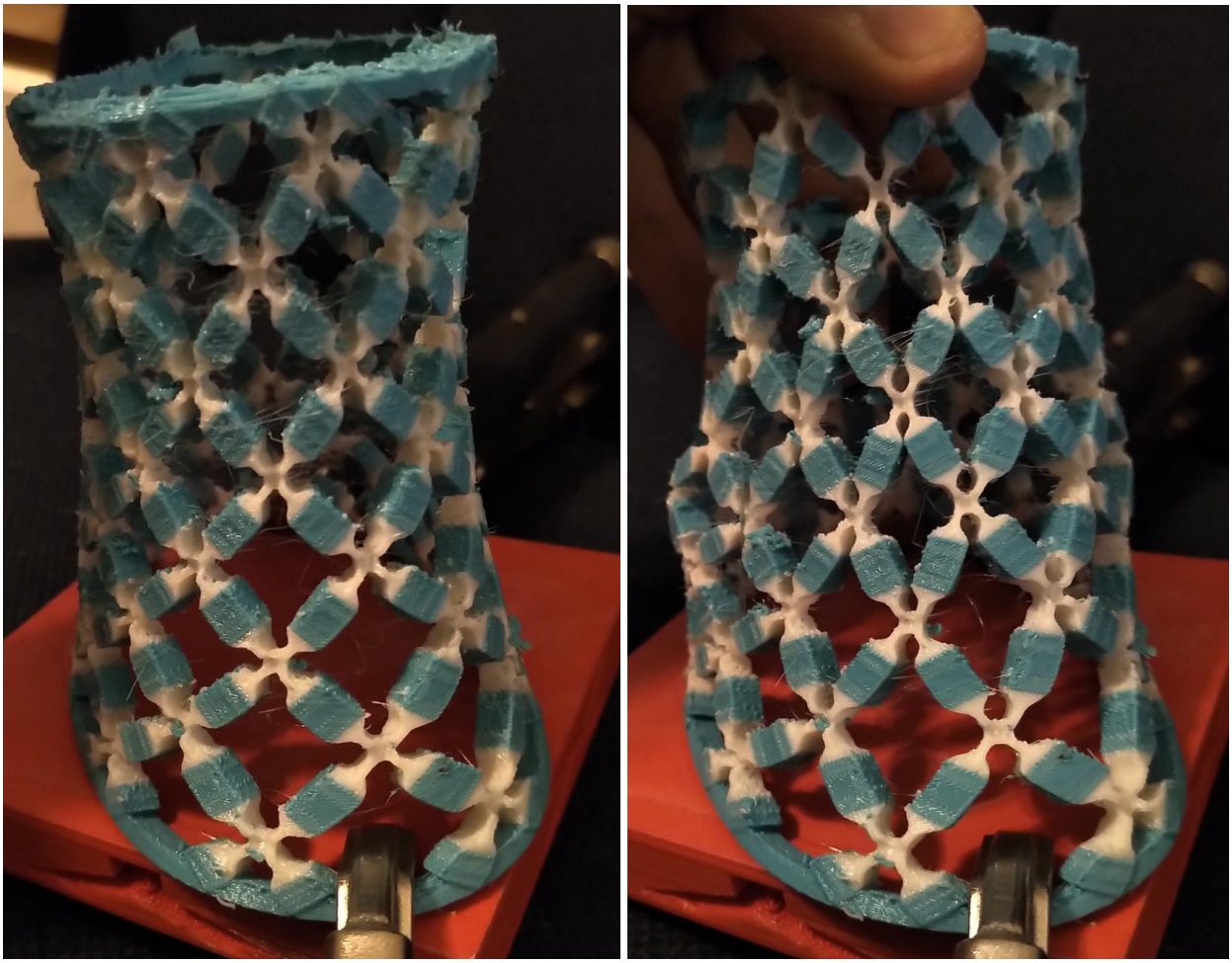

Figure 200: View from the rear of the biaxially-oriented Cartesian mesh array, bending the array forwards (i.e. into the page) and subjecting the rear mesh elements to tension, rotating them vertically. Once the rigid members begin to contact at their sides, the structure does stiffen somewhat in tension, though this structure is not likely to be suited for lockup purposes without significant additions to the microstructure.

. One may compare the response of the individual repeating units in this array to the links of a scissor linkage, which has considerable ability to shorten or lengthen at the distal ends; indeed, some research into metamaterial structures has explicitly employed scissor linkages (often with compliant joints) for 2D purposes [145], though no known research has used the linkage for a metamaterial in a cylindrical or other closed-surface configuration, and all known previous uses of the scissor linkage for metamaterials use joints approximating revolute joints rather than ball joints (it is the latter innovation that allows the cylinder-like structure to tolerate different directions of deformation). Additionally, whereas planar scissor linkages with revolute

joints are generally limited in their motion by collisions between joints and rigid links, this biaxially-oriented mesh array was limited in its freedom by incipient contacts between the side faces of the rigid bodies (one such contact is highlighted in Figure 199). It should be noted that, once these contacts engaged, they did not produce lockup in the sense of limiting further motion with a multiple-order-of-magnitude stiffness increase; in fact, the structure did become vulnerable to shell buckling once it could no longer convert compressive displacements into rotation of mesh elements (owing to their inability to rotate further due to side-to-side contacts); two views of the post-buckled configuration of the mesh array are shown in Figure 200. Of course, the primary focus of this section was merely to produce bending capable closed manifolds, rather than actually seeking to add lockup capability to such structures, and certainly this array is more resistant to shell buckling than solid shells (other than bellows-structured shells), which at least represents an improvement.

Figure 201: Two views of the biaxially-oriented Cartesian mesh array in post-buckling configuration, demonstrating that the structure is not impervious to shell buckling once the rigid members begin to touch, and as a corollary, it does not stiffen up appreciably once rigid members touch, owing to other low-stiffness modes it has.

In addition to tolerating far more global bending before shell buckling than solid shells, the structure readily tolerates global vertical compression, at least until the rigid elements begin to contact each other along their side faces, as can be seen in Figure 202. (Side contact between rigid elements was not the only limiting factor for compressive freedom; a second-order effect was the rotation of the center of the flexible joints relative to all four rigid elements, generally alternating in clockwise and counter-clockwise directions; this appears to be due to the distance between the rigid members and the length of the compliant regions. The effect is also pointed out in Figure 202). There was significant radial expansion as a sympathetic deformation from the vertical compression, indicating that the effective Poisson's ratio is positive and quite possibly locally greater than 0.5 in the "bias" direction (woven fabrics often have elevated Poisson's ratios along their bias directions as well, frequently greater than the 0.5 theoretical maximum of incompressibility for a continuous material, though they usually are not constant with respect to amount of strain [146]).

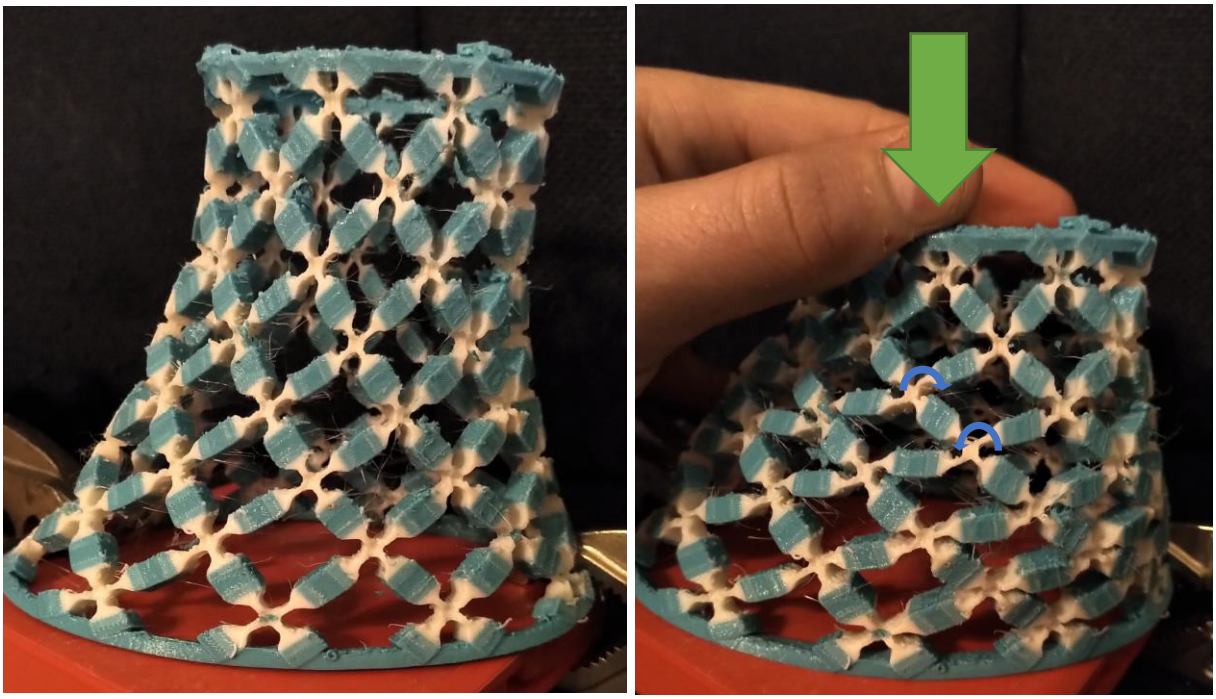

Figure 202: The structure is compliant in vertical compression, at least until the rigid members begin to contact at their sides. Additionally, under global vertical compression, the central regions of each joint tended to rotate slightly relative to the surface normal (or to the four rigid members they were joined to), as illustrated for a couple of joints with blue arrows. The rotations generally alternated between clockwise and counter-clockwise.

Finally, as a direct inverse to the vertically-oriented Cartesian array, the biaxially-oriented Cartesian array was remarkably stiff against pure shear; trying to force the top ring forwards while fixing the base and not allowing the top ring to rotate was one of the stiffest possible modes for the structure, and eventually caused a novel pattern of inwards-directed

buckling, as can be seen in

Figure 203. This is a phenomenon that could not be detected with the O-ACS biaxially-braided structures, perhaps because their members are orders of magnitude stiffer than the compliant-jointed meshes, thereby reducing the perceived differences between shearing and bending modes' stiffnesses.

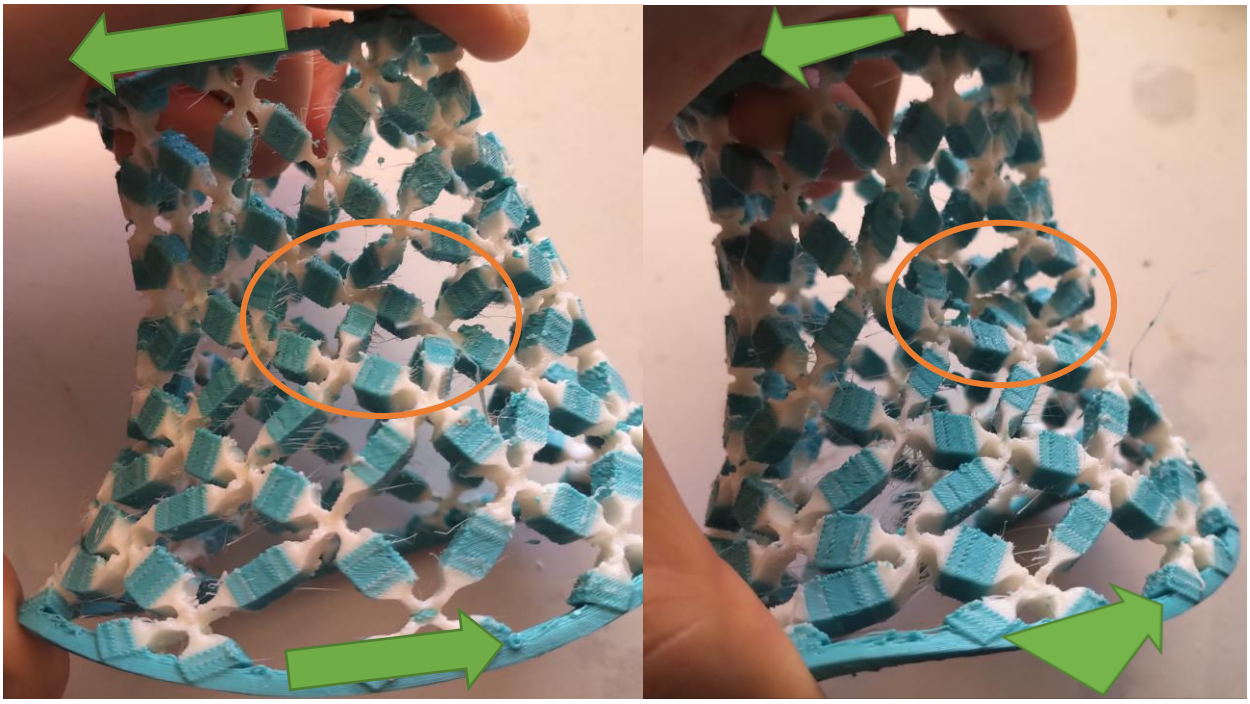

Figure 203: Attempting to shear the structure by forcing the top ring directly forwards relative to the bottom ring (with the green arrows indicating the direction of shear) produced a very stiff response and eventually shell buckling in regions, e.g. as circled above in orange.

Biaxial Mesh Array on Different Manifold Shapes.

Although the biaxial mesh array shown above does not appear to have lockup potential without further modifications and features, it at least possesses an excellent morphing shape for an ankle-enclosing manifold because it is capable of in-surface extension and compression, as well as out-of-surface bending. Thus, it seems the ideal platform for evaluating whether or not the HDM shape is truly ideal, or whether some modifications to its curvature might be in order (the top and bottom shapes probably should not be changed, since they correspond to the lower-leg's cross section and the profile of a ring bracing the eventual protective device on the shoe, respectively). Thus, two new surfaces were further derived from the Hyperboloid-Derived Manifold: a closed but nearly-singly-curved surface that resembles a frustrum of a cone (hereafter referred to as the "FOC") which effectively eliminates the mild inwards curvature of the HDM surface and is a straight loft between top and bottom, and, conversely, another surface

with exaggerated inwards curvature ("Extra-Concave Inwards HDM", ECIHDM) that would conform even more closely to the lower leg. The two surfaces are compared with the original HDM surface in Figure 204.

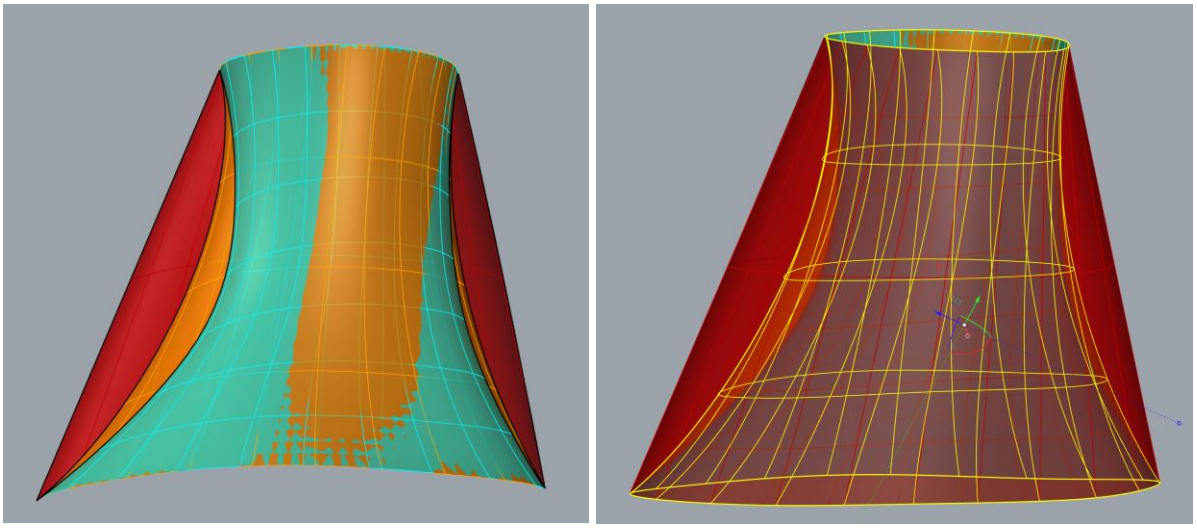

Figure 204: Comparing the Frustrum-of-Cone manifold (shown in red) with the original Hyperboloid-Derived Manifold (shown in marigold color) and the Extra-Concave-Inwards manifold (shown in teal). On the left, a section view is shown; on the right, there is no section.

Biaxial Mesh Array on Frustrum-of-Cone Manifold.

The FOC surface is nearly-singly-curved inasmuch as its peak Gaussian curvature magnitude is one order of magnitude smaller than that of the HDM, though of course it is closed with a single seam. Figure 205 compares the Gaussian curvature profiles of the HDM and FOC, illustrating how much smaller the FOC's Gaussian curvature levels are and how it is nearly singly-curved (like a true cone would be). Additionally, Figure 206 shows a comparison of mean curvature (i.e. the arithmetic mean of the principal curvatures, where the principal curvatures are the curvatures in the direction of highest and lowest curvature at any point on the surface) distributions on the FOCM and HDM, illustrating that both have similar mean-curvature intensity but that the FOCM has nearly straight-line gradients in its mean curvature (expected for a surface with weak double curvature that is in fact nearly singly-curved).

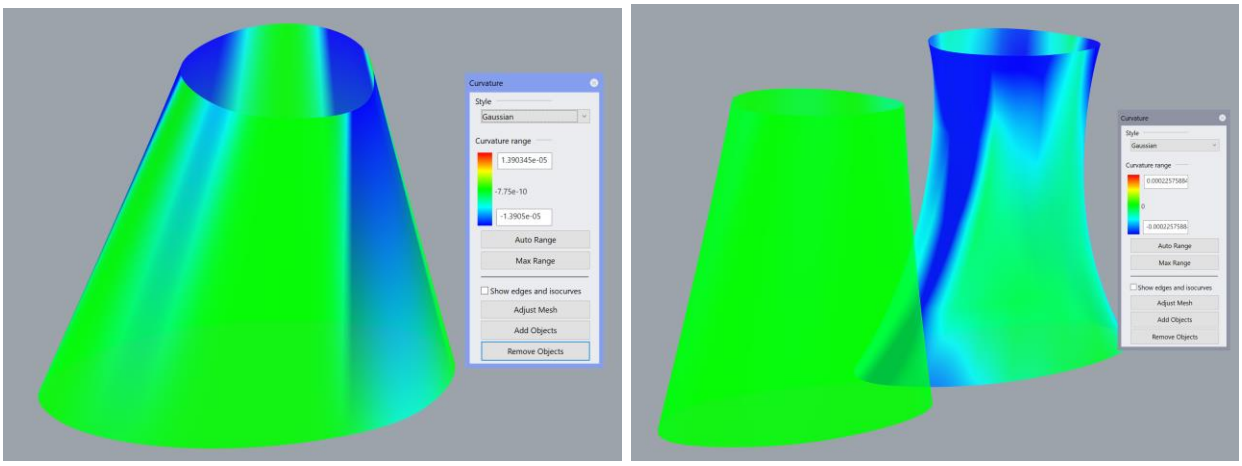

Figure 205: Comparing the curvature of the FOCM with the HDM. The left image shows Gaussian curvature contours plotted only on the FOCM, with an appropriate scale for that surface (ranging from -1.39e-5 to 1.39e-5); the right image shows Gaussian curvature plotted on both FOCM and HDM, but with a scale appropriate to the HDM (ranging from -2.22e-4 to 2.22e-4), at which scale the Gaussian curvature variations on the FOCM are small enough to appear nearly zero.

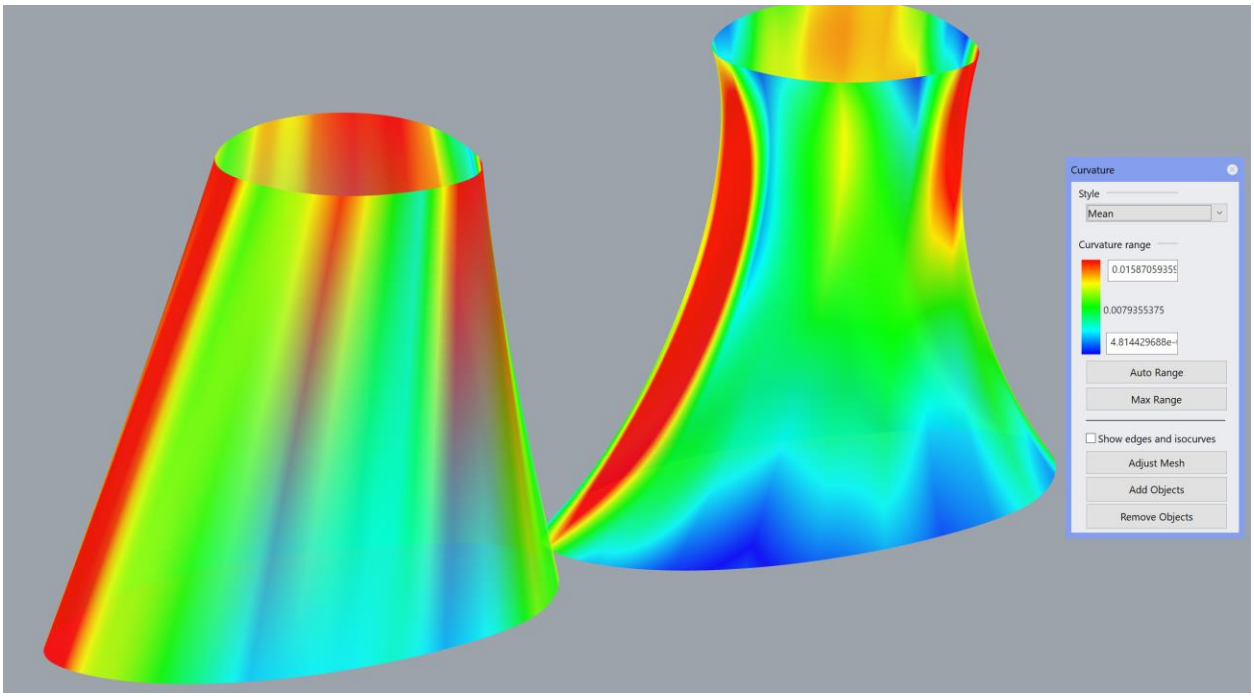

Figure 206: Comparing the mean curvature (arithmetic mean of principal curvatures) on the FOCM surface (left) and original HDM surface (right) highlights that the region around the front of the FOCM surface and regions around the rear-sides are still the areas of the highest mean-curvature intensity, roughly similar to that of the HDM. However, unlike the HDM, the FOCM has gradients of mean curvature that nearly follow straight lines, since it is nearly singly-curved as discussed earlier.

A biaxial mesh net with compliant joints was then generated on the FOCM surface, with a rendering of the CAD shown in Figure 207. Certainly it conforms less well to the leg than does the HDM, and arguably it is less graceful in aesthetic.

Figure 207: Rendering from CAD of the biaxial mesh on the FOCM, front view (left) and side view (right).

When manufactured and tested on the leg-simulating fixture (as shown in Figure 208, Figure 209, and Figure 210), the biaxial mesh on the FOCM was roughly comparable in behavior to the biaxial mesh array on the HDM, but of note, shell bending was far less present on the FOCM than on the HDM (global leg rotation resulted in much more extension and contraction onto its own footprint, with little change in the curvature of imaginary lines running vertically from the bottom ring to the top ring). The biaxial-mesh FOCM thus better resembles the ideal extension-contraction but no-bending morphing of a hypothetical joint protector shown in Figure 28 in Chapter 2 in the discussion on metamaterial modes and potential geometric embodiments, whereas the biaxial-mesh HDM features far more bending (though in-surface contraction and extension regions as well) and thus more closely resembles Figure 29 in Chapter 2.

Figure 208: Side view of biaxial mesh on frustrum-shaped manifold with leg rotating forwards (in this view, the leg is rotating counter-clockwise, in the direction indicated by the curved blue arrow, and about the axis shown with a green dotted line). Left: neutral position; right: leg rotated forwards.

Figure 209:Front view of biaxial mesh on frustrum-shaped manifold with leg rotating forwards (rotation direction shown with blue arrow and rotation axis shown with green dotted line; the leg is rotating out of the page). Left: neutral position; right: leg rotated forwards.

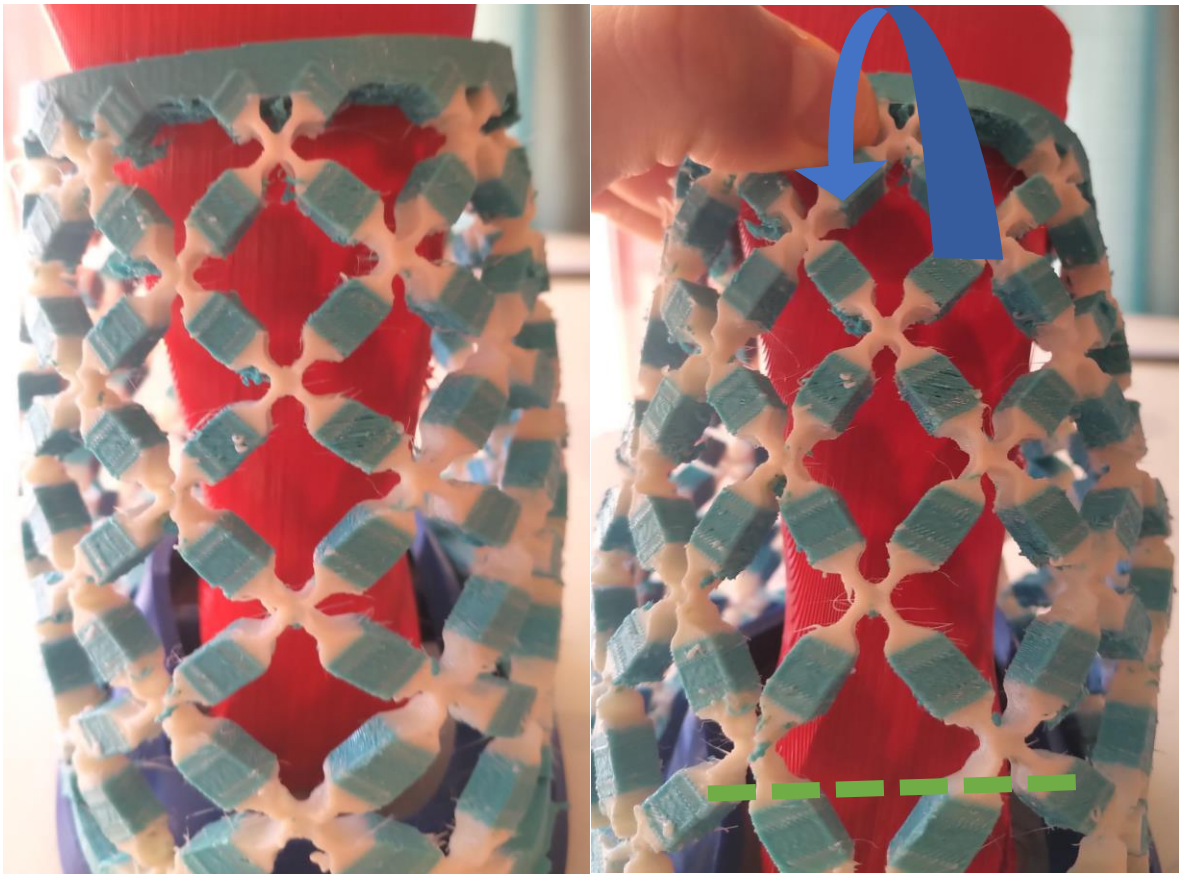

Figure 210: Rear view of biaxial mesh on frustrum-shaped manifold with leg rotating forwards (rotation direction shown with blue arrow and rotation axis shown with green dotted line; the leg is rotating into the page). Left: neutral position; right: leg rotated forwards.

Indeed, the only out-of-surface bending of elements the structure seemed to experience occurred from coupled radial-vertical behavior (Poisson phenomena, essentially): when the structure was compressed globally (or subject to local contraction from the rotating of the leg), the mesh elements became flattened and bulged outwards from the surface somewhat, as can be seen in Figure 211.

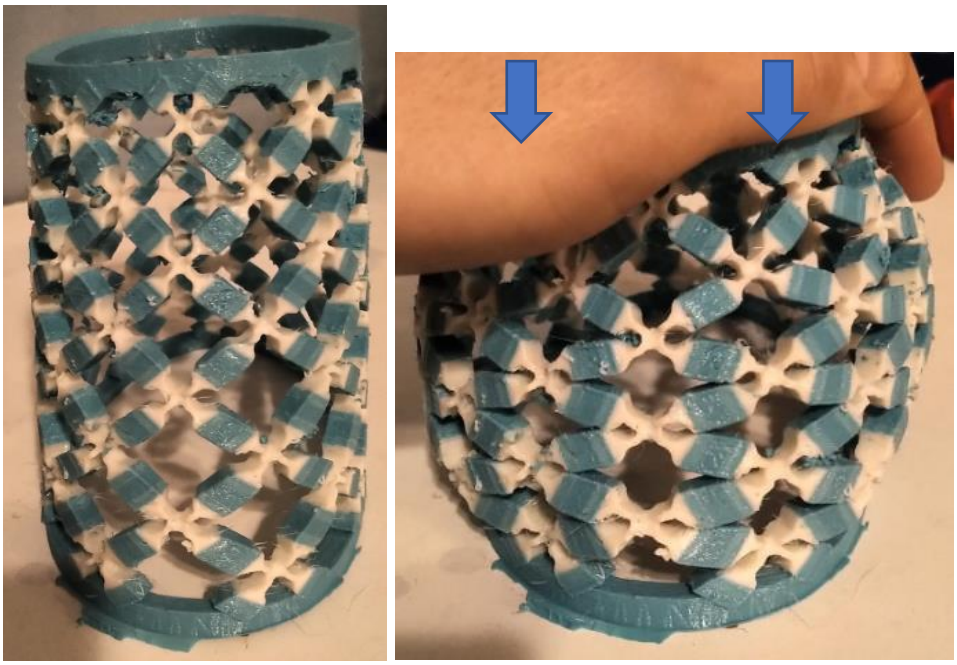

Figure 211: In global vertical compression, the mesh elements bulge outwards radially a bit as they contract vertically.

Finally, as illustrated in Figure 212, the structure was more resistant to localized shell buckling when loaded by a horizontal shearing point load than was the biaxial mesh on the HDM surface (which tended towards localized inwards shell buckling in apparently random regions, as can be seen earlier in Figure 203 for comparison purposes). Granted, testing equipment was not available to numerically compare the stiffness of the FOCM and HDM biaxial meshes in this mode.

Figure 212: When the base ring is fixed to the ground by tape (indicated schematically by red Xs) and the top ring is sheared forwards (to the left in this image, indicated by the orange arrow), the structure is quite stiff and additionally does not suffer obvious shell buckling, unlike the standard HDM-biaxial mesh.

Biaxial Mesh Array on Extra-Concave-Inward Manifold.

In an opposite vein to the FOCM (which reduces the double curvature of the HDM), the ECIHDM intensifies it and thus better conforms to the leg. Its Gaussian curvature distribution is compared with that of the HDM in Figure 213 and its mean-curvature distribution in Figure 214; overall, the surfaces are roughly similar in their topology, though the ECIHDM has more inwards curvature at both the front and the sides, especially in the middle strip (vertically-speaking).

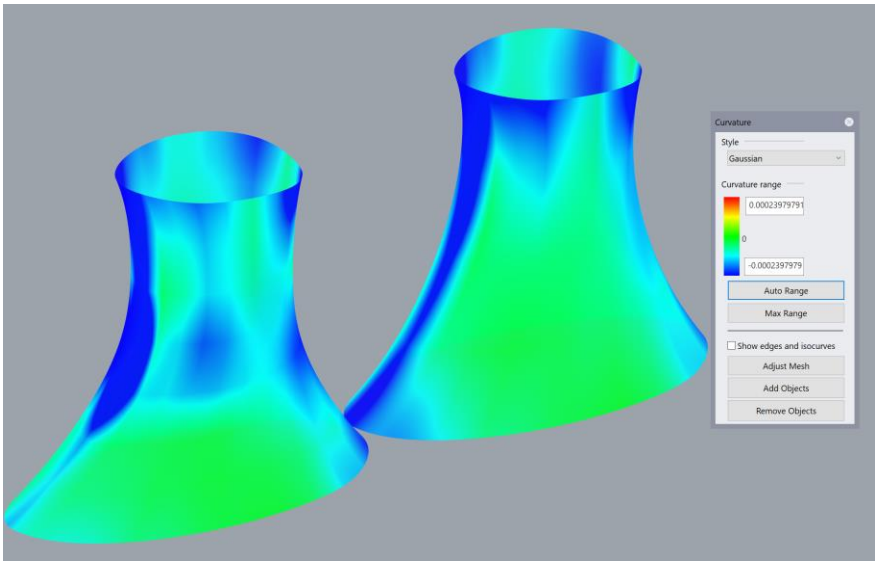

Figure 213: Comparing the Gaussian curvature intensity of the ECIHDM surface (left) with that of the original HDM surface (right); note that their Gaussian curvature distributions are most everywhere similar in magnitude and sign, though the ECIHDM has a more pronounced negative region in the front and also is more concave inwards in the middle strip (vertically speaking).

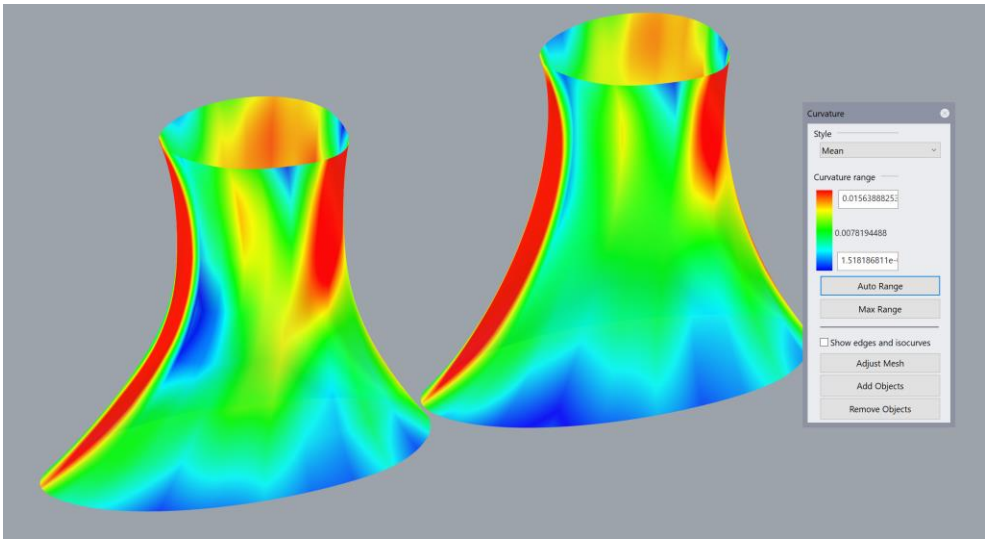

Figure 214: Comparing the mean curvature distributions between the ECIHDM surface (at left) and the original HDM surface (right) shows similar curvature as well, though the ECIDHM has more intense curvature along the sides.

Figure 215: CAD rendering of the biaxial mesh on the ECIHDM surface, side view (at left) and front view (at right).

When the ECIHDM biaxial mesh was placed on the leg-simulating fixture and the leg rotated forwards, immediate out-of-surface buckling of mesh elements on the starboard and port sides of the array was noted with surprise, as can be seen in Figure 216. When bent side-to-side (simulating inversion/eversion), the structure was especially prone to buckling, either inwards or outwards depending on the exact orientation of the loads (as an instability phenomenon, this is to be expected of buckling), as shown in Figure 217. Additionally the ECIHDM biaxial mesh was prone to immediate shell buckling (along strange, helix-like paths of mesh elements) when subjected to global shear in the form of a pure horizontal force (as shown in Figure 218), quite unlike the FOCM biaxial mesh which was noted to be quite resistant to shell buckling in this particular loading. Overall, the excessive inwards curvature of the structure seems to give it inferior kinematic properties and augments the role of out-of-surface bending relative to the FOCM and standard HDM, illustrating the importance of good manifold selection.

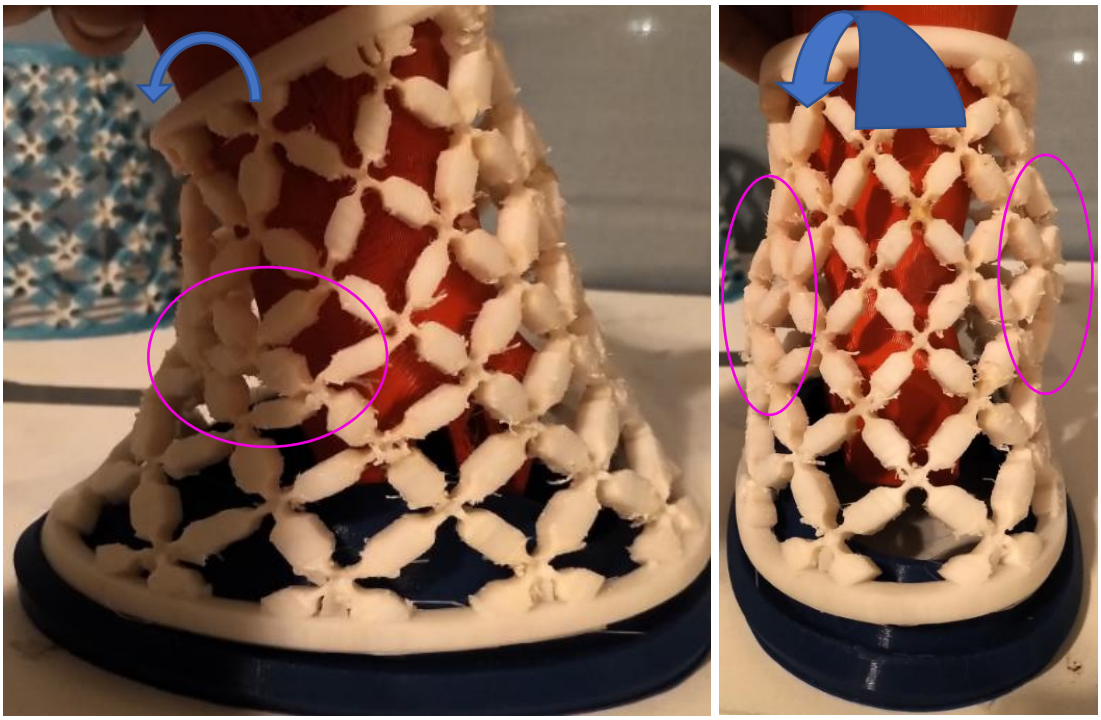

Figure 216: The ECIHDM biaxial mesh exhibited considerable out-of-surface bending, including in unexpected modes (e.g. in regions off to the sides when the leg was rotating forwards, as indicated with magenta circles). The left view is a side view of the leg rotating forwards, and the right view is a rear view of the same rotation.

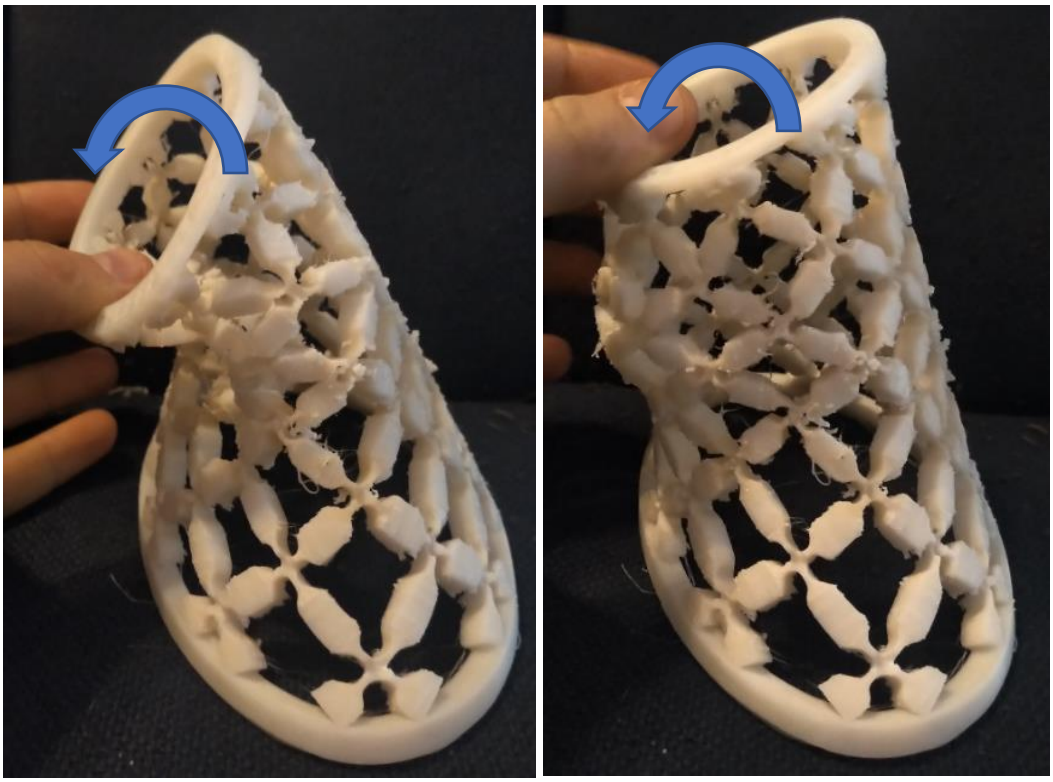

Figure 217: A modest bending moment applied to the structure (in this case, simulating leg inversion/eversion) readily produced out-of-plane bending that tended to reduce the structure's stiffness and could be classified as shell buckling. As an instability phenomenon, the buckling could either tend to be further into the surface (as at left) or out of the surface (at right), and the latter was less catastrophic than the former owing to increased effective cross-sectional area.

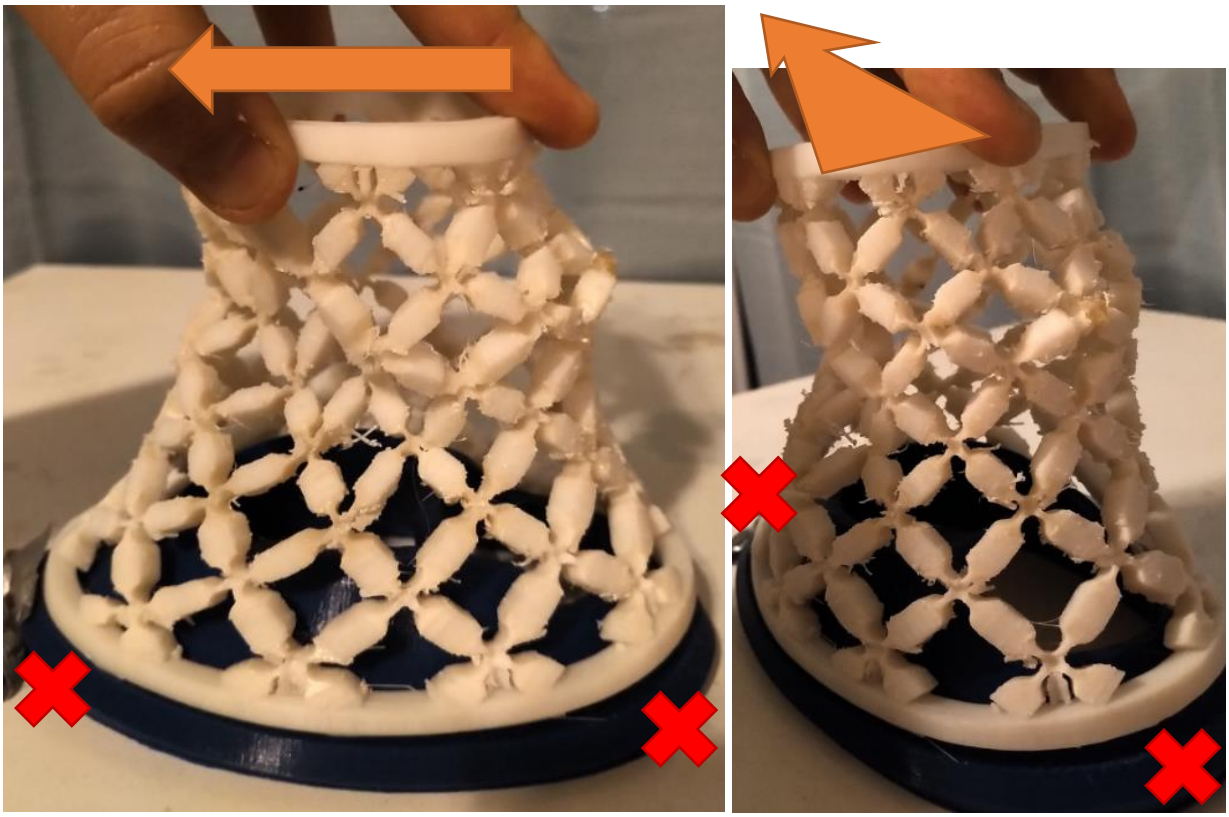

Figure 218: In pure shear (with the base fixed as indicated by the red Xs, and a horizontal force applied according to the orange arrow: leftwards in the left image, into the page in the right image), the ECIHDM biaxial mesh was also vulnerable to shell buckling (in regions circled in magenta) and generally not particularly resistant to shear, unlike the FOCM biaxial mesh.

Non-Jointed, Original Microstructured Cylinders in Bending.

In addition to the jointed mesh-network microstructures created by this author and tested in bending that are described in the preceding section, other classes of microstructured hyperboloids were tested in bending to compare with other potentially-promising classes of metamaterials that were not mesh networks, including a circular-hole metamaterial, bending-beam-based metamaterials, and origami.

Circular-Hole Auxetic Pattern on the Hyperboloid-Derived Manifold.

As discussed earlier in this chapter, hole-based auxetic cylinders (as a compliant-mechanism form of the jointed-square auxetic structure) showed promise as bending-tolerant cylinders in the research of Broeren et. al. [123]. Additionally, as mentioned in Chapter 2, Box

et. al. found [147] that “holey sheet” metamaterials (i.e. solid shells of medium thickness with cylindrical holes cut into them) made of a relatively-rigid bulk material experienced moderate stiffening in global compression loading simply from “pattern switching” (changes in load paths in the microstructure); because the bulk material was a low-strain-to-failure material, they did not test the structure in a fully-compressed state (as the beam-like joints between the squares would likely have broken from excess strain). Thus, it seemed worthwhile to investigate this metamaterial as tiled on the HDM surface. CAD geometry of this structure is shown in Figure 219.

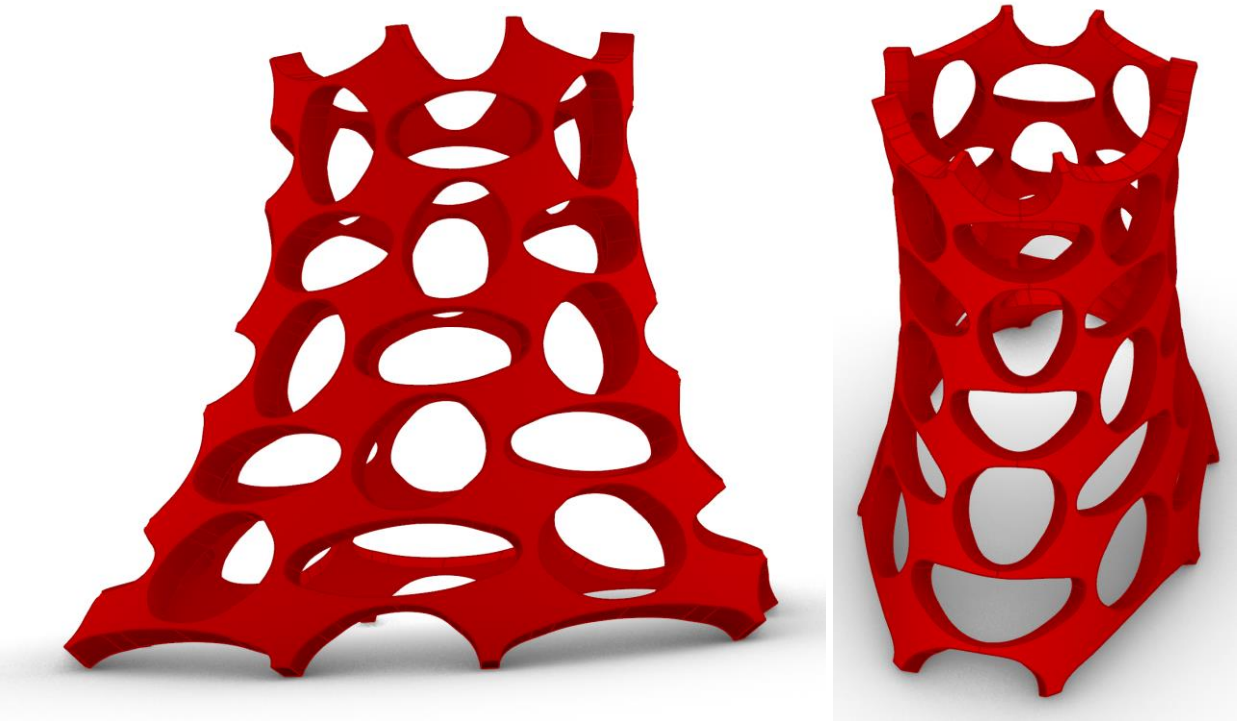

Figure 219: Rendering of a circular-hole auxetic pattern on the HDM surface.

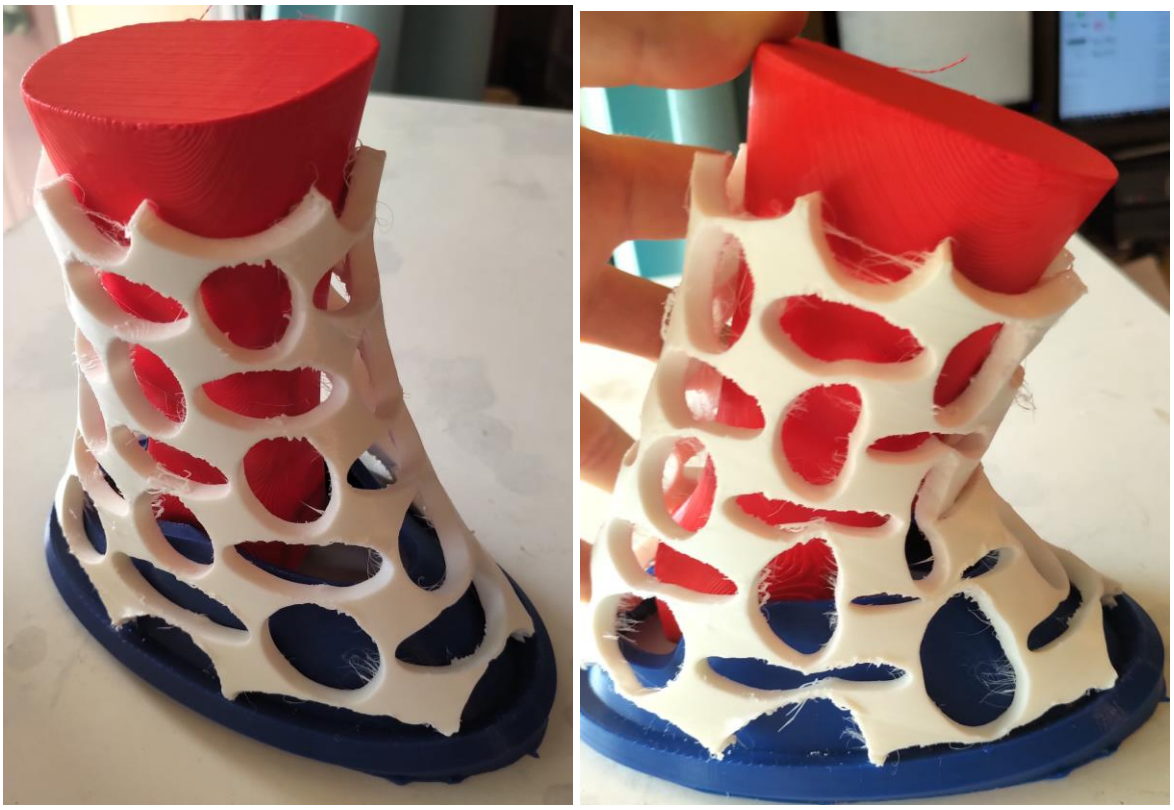

Figure 220: Circular-hole auxetic hyperboloid metamaterial on leg fixture in bending.

Figure 221: Vertical compression response of the "holey auxetic" hyperboloid. Note the radially-inward sympathetic contraction (in accordance with the auxetic behavior of the metamaterial).

Sinusoidal-Beam Planar Auxetic Pattern on the Hyperboloid-Derived Manifold.

The goal of this subsection was to build off of the work of Lei et. al. [124], which, as mentioned in the previous section of this chapter on auxetic cylinders in global bending, indicated that beam-based auxetic metamaterials with in-plane sinusoidal undulations had good tolerance of global compression and tension displacement (the authors unfortunately did not focus on global bending of these cylinders). Additionally, as mentioned in Chapter 2, Jang et. al. found that metamaterials with in-plane sinusoidal waviness or whorls even exhibited moderate stiffness increases after a certain amount of extensional displacement, owing to the deformation mode changing from bending of initially-undulating structures to tensioning of straightened structures (with the latter being a stiffer mode) [45], though strictly speaking this chapter is concerned purely with the more-basic question of ensuring conformity to a bending joint rather than lock-up per se.

Thus, a similar structure of beams having moderate in-plane thicknesses and higher out-of-plane thicknesses was patterned over the HDM surface, producing the geometry shown in Figure 199. It should be noted that the thickness by which the individual beams are extruded out of surface (indicated in Figure 199 with an orange line) is expected to have a significant impact on how much out-of-surface bending versus in-surface contraction and extension the structure experienced for the same prescribed leg rotation: increasing this parameter would increase the shell-bending stiffness of the overall structure far more (scaling with the cube of this thickness) than it affected the in-surface contractive and extensional properties (which would only scale with linearly with the thickness), as the in-surface extension and contraction depend on in-surface bending of the beams (which are relatively thin in this direction) whereas the overall surface bending depends on the extruded thickness.

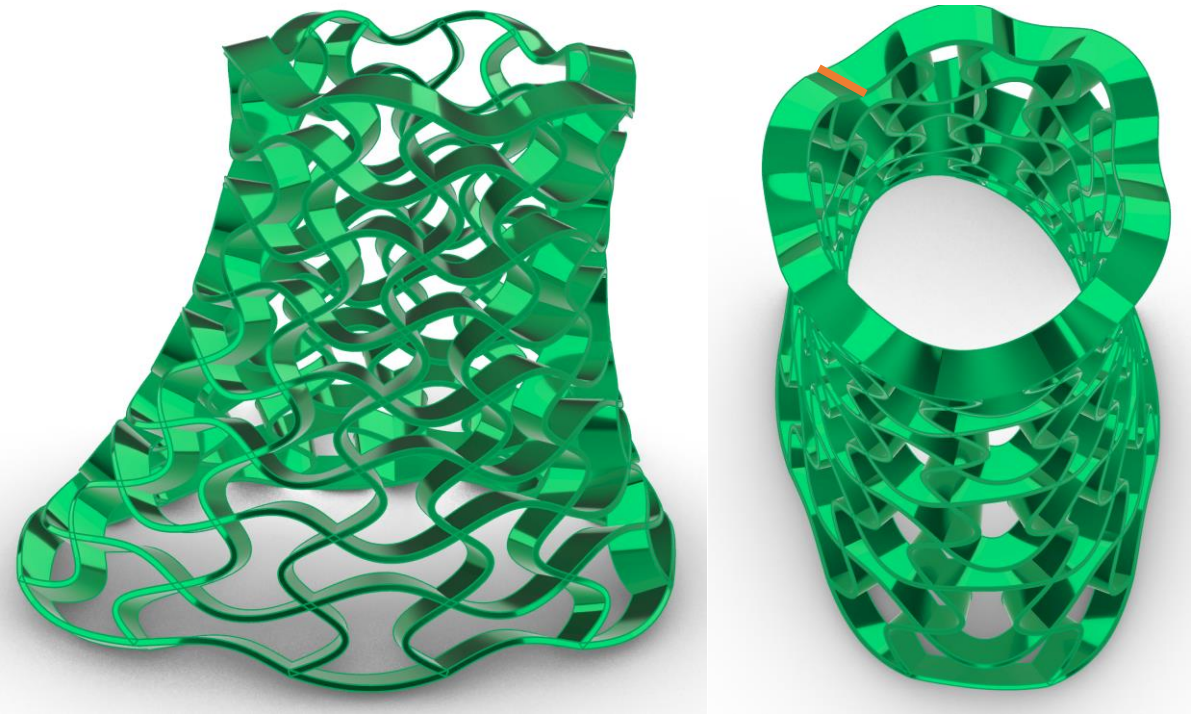

Figure 222: Two views showing renderings of the In-Plane Sinusoidally-Undulating Auxetic HDM array. The orange line indicates the extruded out-of-surface thickness of the beams, a quantity referenced above to have a far greater impact on the out-of-surface bending stiffness than in-surface contractile and extensional stiffness.

It was printed in Hytrel flexible thermoplastic elastomer (unlike multimaterial prints of previous sections, the part itself had no rigid inclusions; however, rigid PETg was used as a breakaway support material as its bond to TPC-TPE is weak once cooled), and then tested on the leg-simulating fixture, as shown in Figure 223 and Figure 224. Overall, at this offset-from-surface extruded thickness, the structure displayed excellent resistance to shell buckling (with its response dominated by in-surface contraction and extension), though curvature became somewhat concentrated (perhaps indicating the onset of some analogue of creasing) once the structure was deformed so much that the beams came into contact with each other vertically, as can be seen in Figure 225.

Figure 223: Sinusoidal-beam planar auxetic on HDM tested in bending on the leg fixture, side view shown. While there was some surface-bending contraction inwards, which could be reduced by further extruding the beams away from the surface, overall the shape was controlled.

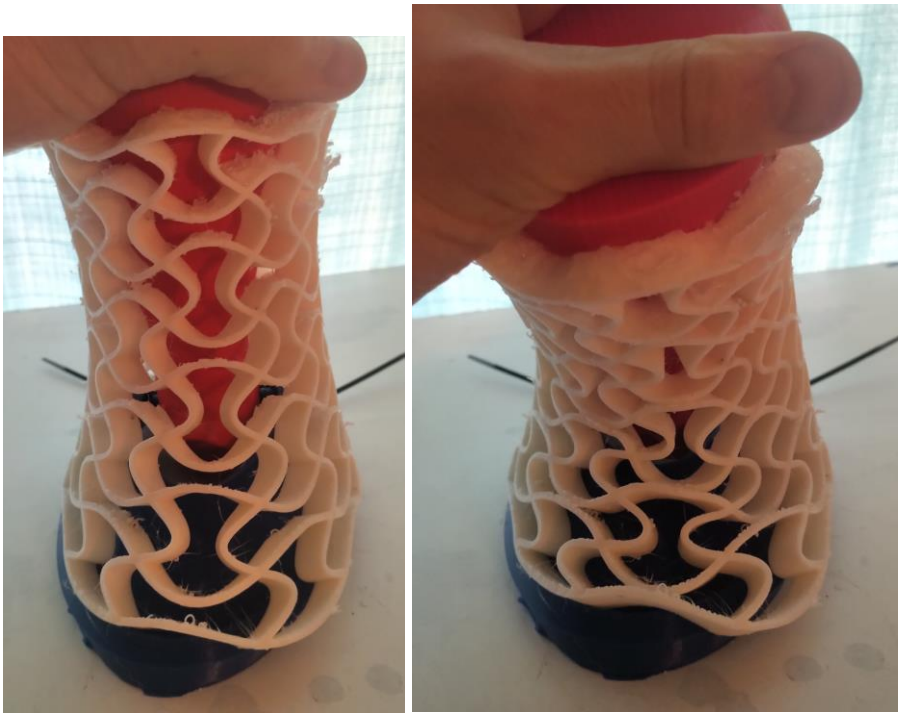

Figure 224: Front view of the array on the test fixture. The left view shows the leg in a neutral position, and the right view shows the leg rotating forwards (coming out of the plane). It should be noted that, after sufficient leg rotation, the beams tended to contact each other, but this did not produce palpably-strong stiffening-up.

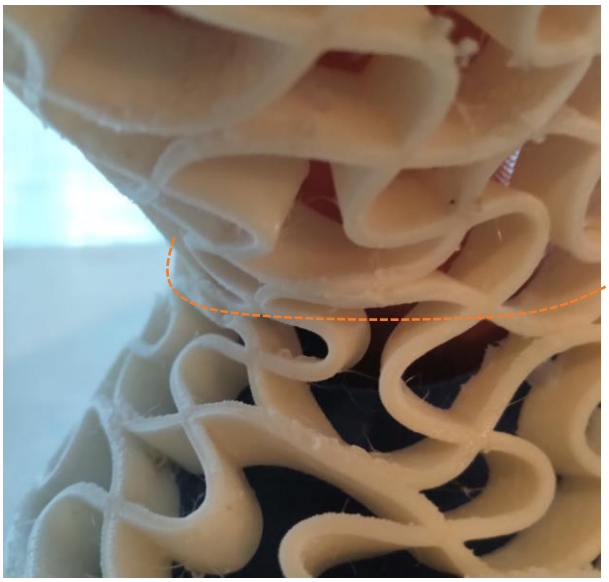

Figure 225: Closeup of the structure after especially high leg dorsiflexion, with many beams contacting each other vertically and potential onset of surface creasing as indicated by the dotted orange curve.

Vertically-Oriented, Undulating-Out-of-Plane Auxetic Metamaterial on the Hyperboloid-Derived Manifold.

As mentioned in Chapter 2's discussion of elastically-stiffening metamaterials, Li et. al. disclosed [46] a beam-based auxetic metamaterial that possessed the additional property of stiffening up after some elastic strain when the initially-out-of-plane undulations are fully stretched out, at which point further global tension gets converted into local tension inside the elements (prior to full elongation, the beam elements merely bend rather than stretching, and bending is necessarily more compliant than tension). (Li et. al. referred to their unit cell as a "3D planar auxetic metamaterial", but as "3D" and "planar" is something of an oxymoron, "undulating-out-of-plane" seems to be more apropos.) This is the same mechanism for stiffening as discussed in the immediately-previous section on the Sinusoidal-Beam Planar Auxetic pattern, with the main difference being the out-of-plane undulations that the unit cell in this case are out-of-plane rather than in-plane. The out-of-plane undulation also makes the structure more

difficult to visualize; several views of the unit cell are shown in Figure 226, Figure 227, and Figure 228.

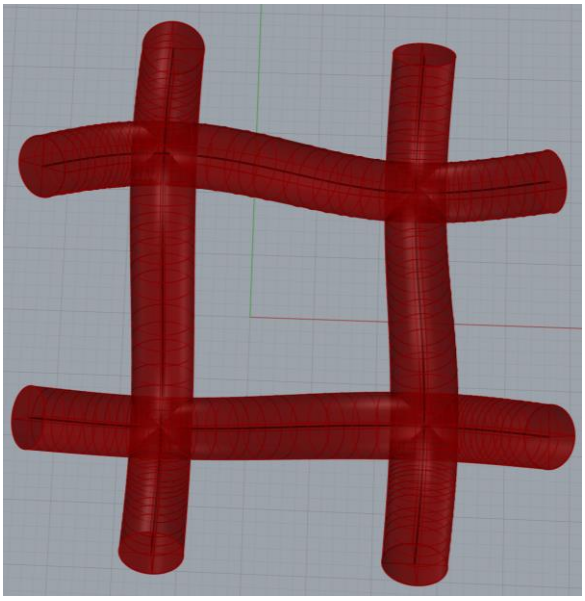

Figure 226: Top-down view of an undulating-out-of-plane auxetic metamaterial, semi-transparent with guide curves shown in black. From this angle, the out-of-plane undulations are not especially apparent. It attempts to replicate the work of Li et. al. [96], but the CAD itself is the creation of this author.

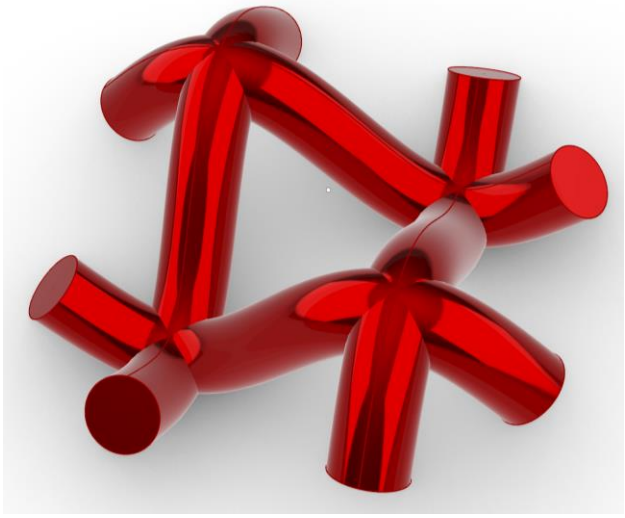

Figure 227: Isometric rendering of the unit cell of an undulating-out-of-plane auxetic metamaterial.

Figure 228: Side view of the unit cell of the undulating-out-of-plane auxetic metamaterial.

The repeating unit was tiled on the face of the HDM surface in preparation for being 3D printed in a continuous, elastomeric material with good interlayer adhesion (like TPU or CPE-TPC). Figure 229 shows two views of a rendering of the proposed metamaterial structure. It is henceforth referred to as the VOUP (Vertically-Oriented Undulating-out-of-Plane) metamaterial.

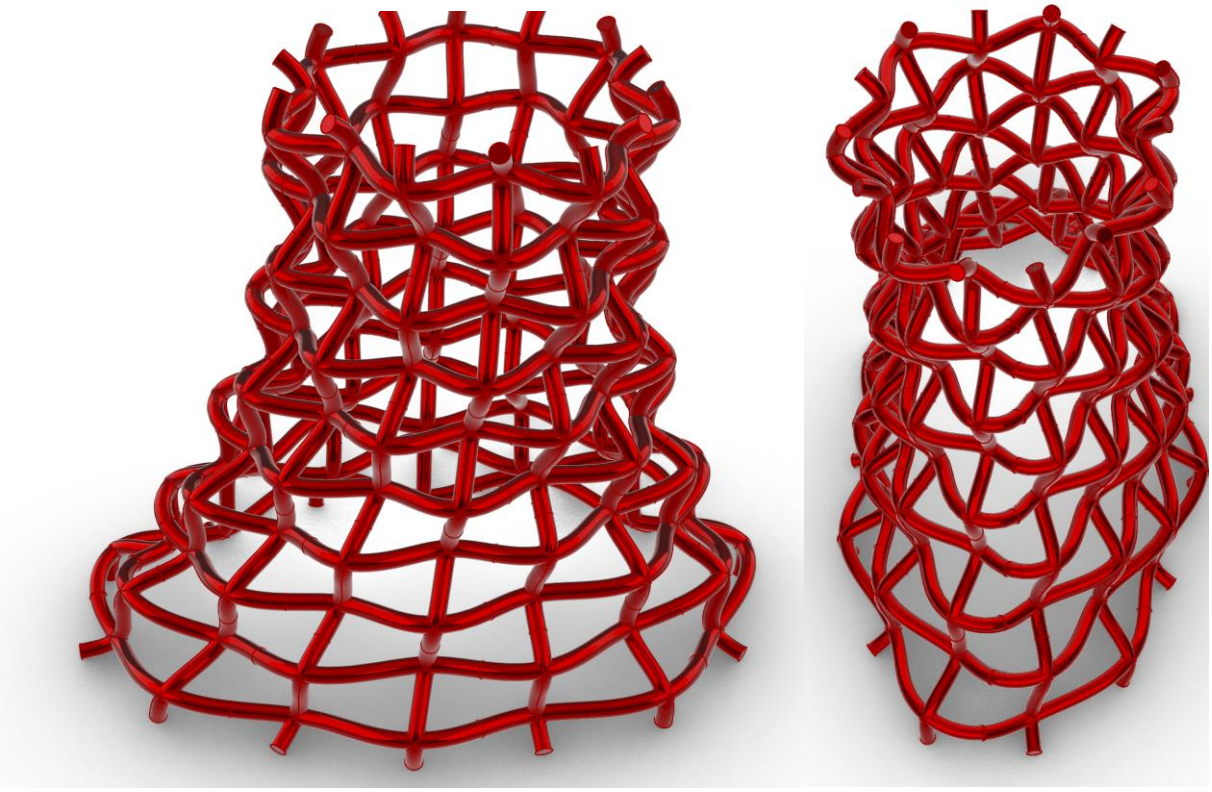

Figure 229: Two views of the undulating-out-of-plane auxetic metamaterial arrayed on the HDM surface with one axis oriented vertically (compare to the biaxially-oriented version in the next section).

When printed and processed (by breaking away support material), the structure had high initial stiffness and no perceptible lockup, and additionally tended to localize buckling inwards (see the circled region in Figure 230 and Figure 231); the microstructure did not appear to allow much local compression (shell buckling dominated). Similarly, the undulating microstructure gave the structure far more tensile compliance than a solid shell, it was still not enough to reduce initial stiffness.

Figure 230: Side view of the vertically-aligned, undulating-out-of-plane mesh. Right shows the leg in forward rotation, left in a neutral position.

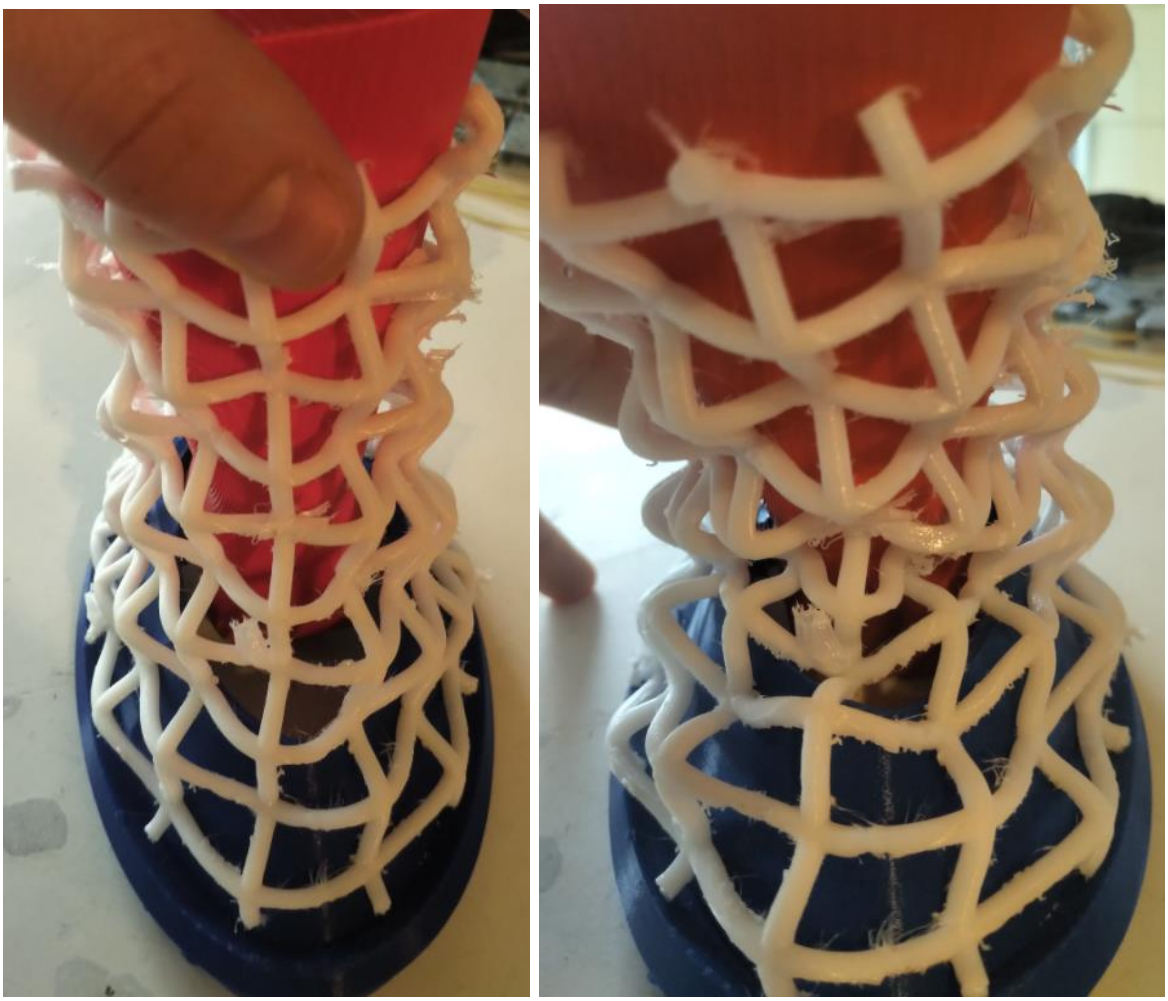

Figure 231: Front view of the vertically-aligned, undulating-out-of-plane mesh. Right shows the leg in forward rotation, left in a neutral position.

Biaxially-Oriented, Undulating-Out-of-Plane Auxetic Metamaterial on the Hyperboloid-Derived Manifold.

Owing to the poor properties (shell buckling and excessive stiffness) of the vertically-oriented undulating-out-of-plane flexible material, it seemed worthwhile to also study the same material structure arrayed at a 45° angle to the vertical axis on the HDM surface; just as the biaxially-oriented Cartesian mesh array proved far superior to the vertically-oriented Cartesian mesh array in the previous section, so too might the biaxial array be able to tolerate more local strain without shell buckling. The proposed CAD is rendered in Figure 232.

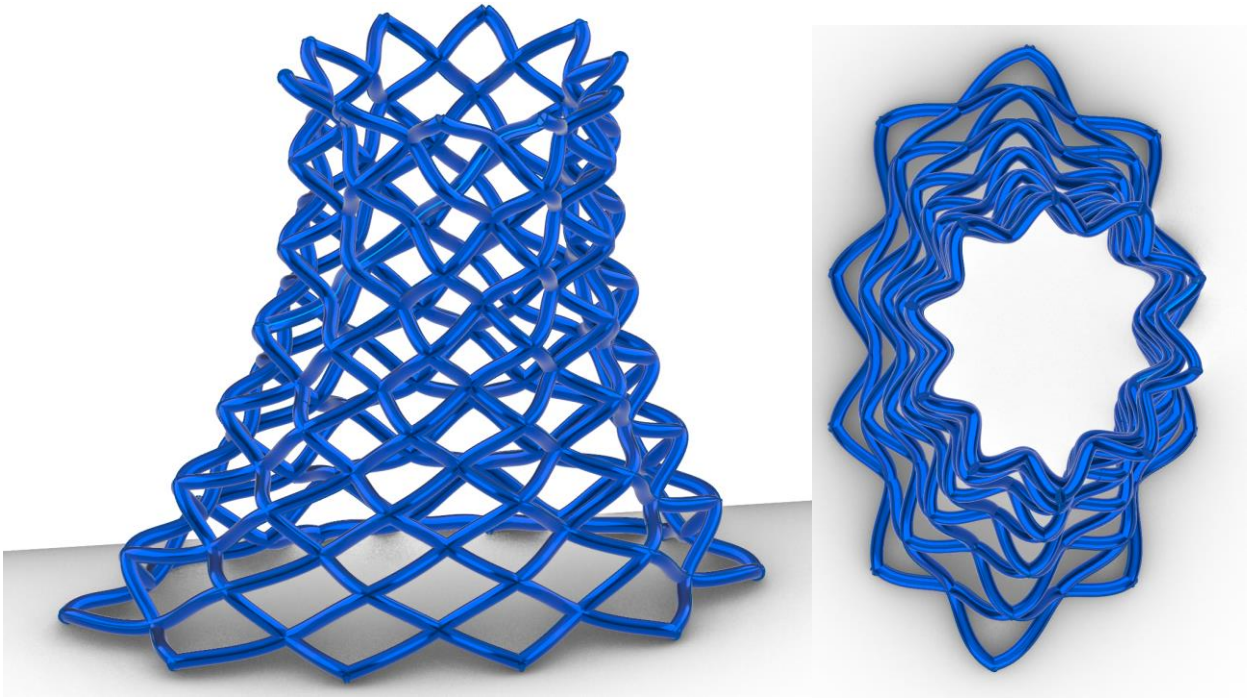

Figure 232: Side and top rendered views of the Biaxially-Oriented, Undulating-Out-of-Plane Auxetic Metamaterial.

When tested, the Biaxially-Oriented, Undulating-out-of-Plane (BOUP) metamaterial performed far better than the VOUP: the BOUP had much lower initial stiffness (despite both being printed in TPU with 95 Shore A hardness) owing to the trellis mechanism, and additionally the out-of-plane undulations created a secondary hinge mechanism that facilitated local compression, so inwards-directed shell buckling was much reduced relative to the VOUP. Figure 233 and Figure 234 show the mesh on the test fixture.

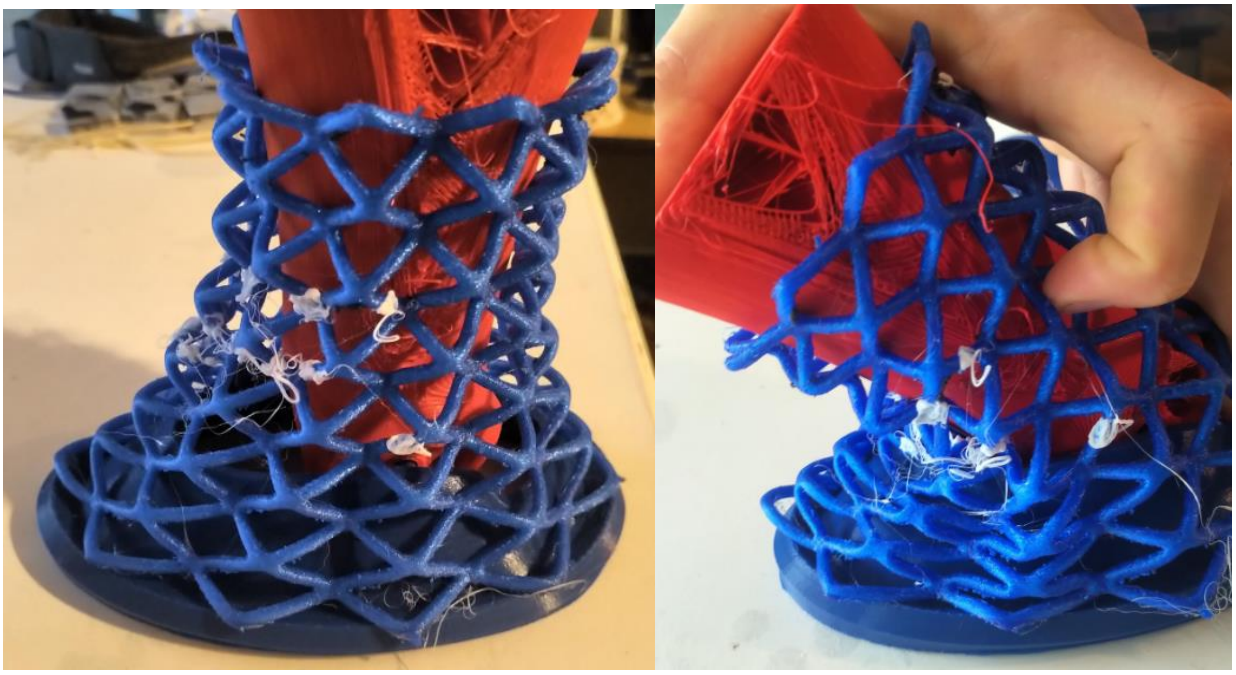

Figure 233: Biaxially-Oriented, Undulating-Out-of-Plane metamaterial structure on leg test fixture (right: leg rotated forwards). Note the flattening and opening of the diamond-shaped holes between beams (trellis mechanism), and the folding of unit cells in two at imaginary lines between the outwards-directed bulges of the undulating beams.

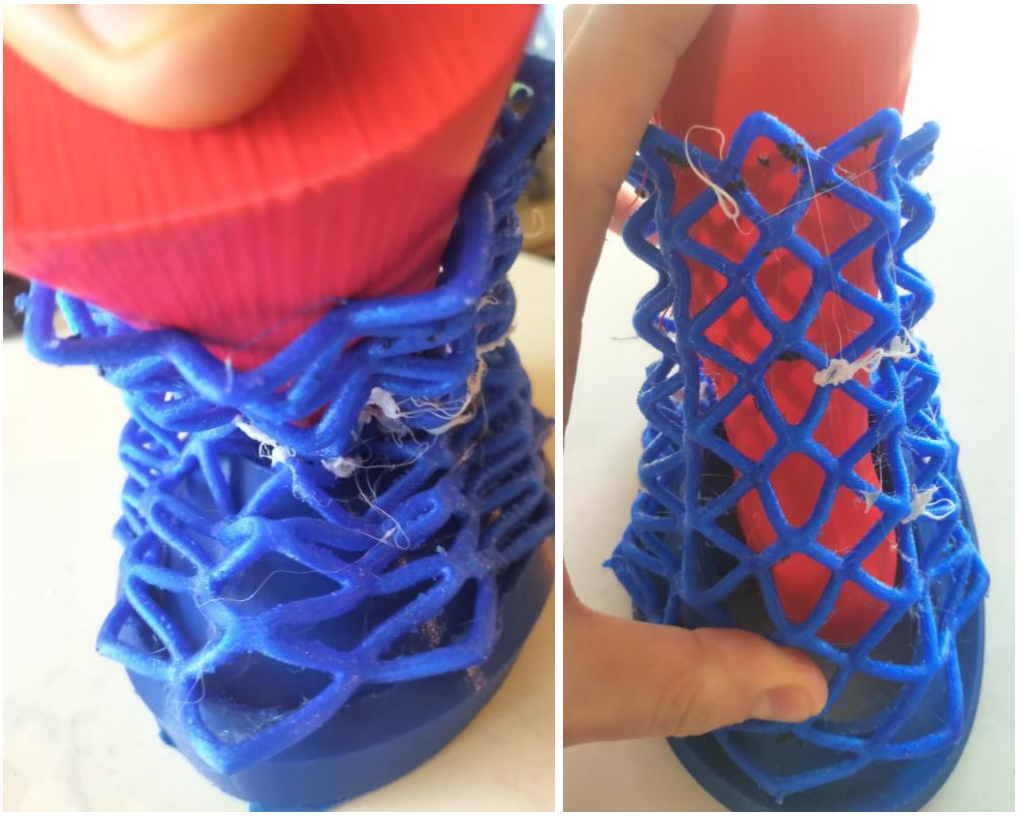

Figure 234: Front view (left) and rear view (right) of the metamaterial when the leg is rotated forwards (out of the page in the left image, into the page in the right image). Note the trellis-mechanism-like behavior of the beams.

Cylindrical Origami Structures.

In the preceding section of this chapter reviewing known cylindrical and other closed-surface folds of origami, it was tentatively concluded that the extant cylindrical origami structures would be unsuitable for this application because their mechanisms tend to only have one degree of freedom and because the structures are intrinsically low-stiffness. Admittedly, this hypothesis was simply the result of a survey of the literature rather than an exhaustive study of the underlying principles of origami, and it was mentioned that origami-like structures featuring rigid reinforcement in some regions might be more promising. To investigate how well cylindrical origami structures conform to bending joints (eliding the question of how to make them stiffen up after prescribed amounts of deformation), it was decided to 3D print a few

cylindrical origami structures, just in case researchers had mischaracterized the kinematic freedom of their structures.

Rectangular-Pattern-Origami Hyperboloid.

One origami pattern that seemed promising was obtained from user "peter120" on Thingiverse [148] and originally intended to act as a bellows as it compresses nearly-flat onto its footprint. The fold was also identified as being studied by Wickeler and Naguib, referred to by them as the "rectangular pattern" [149]. This behavior is illustrated in Figure 235. Whether this fold is known in the wider literature on origami is unclear.

Figure 235: Compression of the cylindrical origami bellows.

Next, the original geometry was deformed to follow the HDM shape instead of a cylinder, and then printed after this modification. A rendering of the structure (including a section view) is shown in Figure 236.

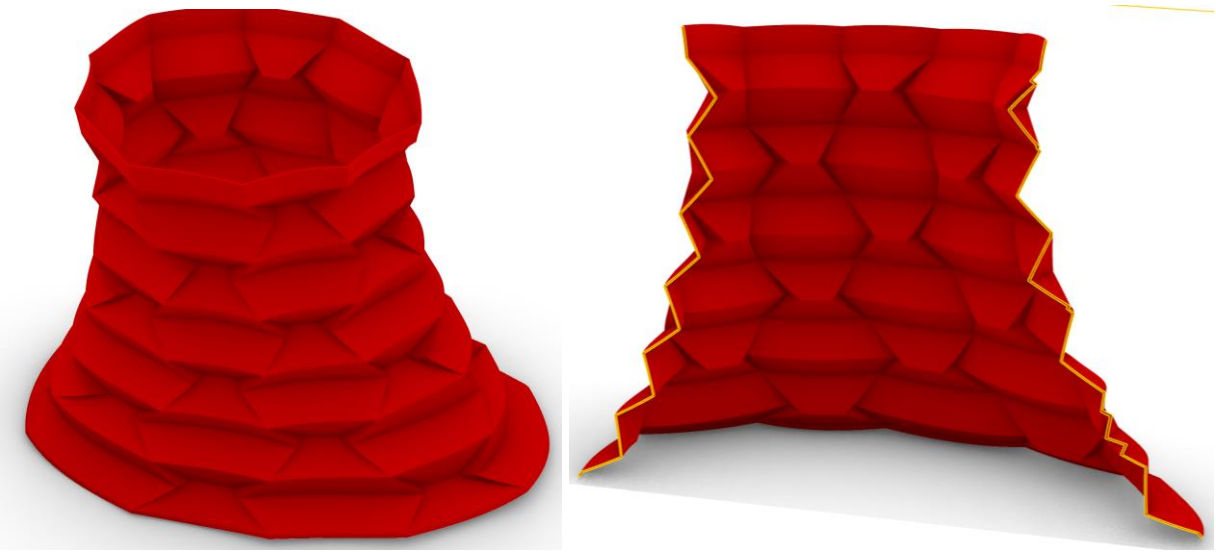

Figure 236: Rendering of the hyperboloid modification of the cylindrical origami structure shown in the previous Figure.

When tested on the leg-simulating bending test fixture, the structure unfortunately proved quite stiff if the bottom end was manually secured to the fixture, since this produced tension in the rear regions of the manifold, and, despite the origami microstructure, the structure was quite stiff in tension. Additionally, the origami pattern was not especially effective at preventing shell buckling by converting global compression into bending of individual faces at the creases; there thus was a significant region of localized shell buckling, whereas nearby regions were relatively

undeformed, as can be seen in Figure 237. The structure was, however, able to compress quite flat onto its own footprint, as shown in Figure 238.

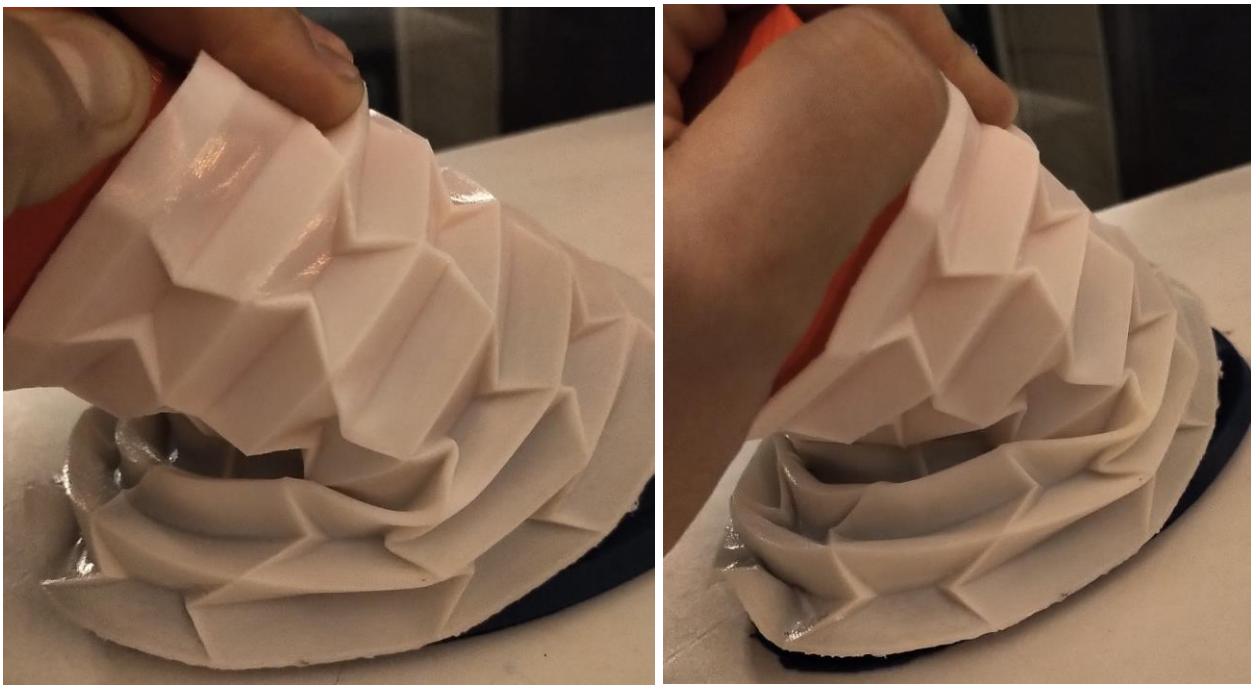

Figure 237: Two different views of the HDM-shaped origami structure on the leg-simulating bending fixture. Note the considerable shell buckling near the front of the manifold. Additionally,

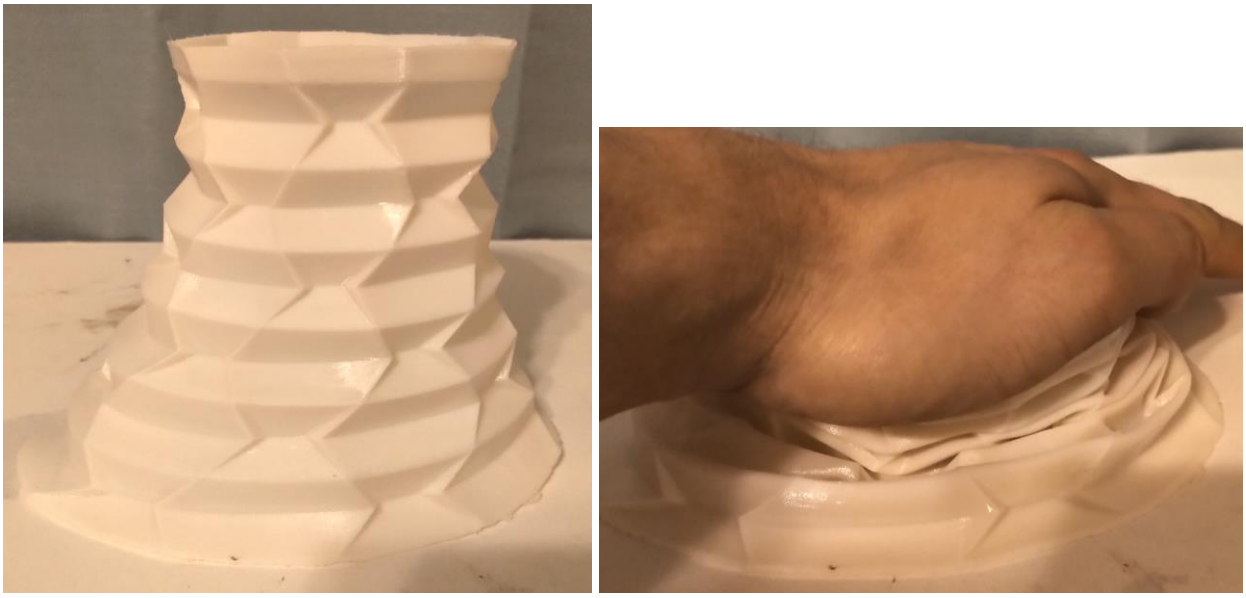

Figure 238: HDM version of the origami cylinder compressed nearly flat.

"Single-Collinear" Origami in Hyperboloid Form.

As discussed in Chapter 2, the "single-collinear" origami fold studied by Fang et. al. demonstrated reversible and considerable elastic stiffening after a prescribed amount of linear compression [38], and additionally, reorientation and flattening of the unit cell should also result in eventual tensile stiffening (although this aspect was not explicitly studied by Fang et. al.). Certainly, the unit cell was found by Fang et. al. to be capable of a considerable range of motion, findings that were confirmed by this researcher (as discussed in Chapter 2). The combination of elastic range of motion and eventual elastic lockup would seem to recommend this unit cell for study in closed-surface/hyperboloid form, though the fact that it only possesses one degree of freedom and has an auxetic property may not bode well.

Thus, based on the original unit cell of single-collinear origami (shown in Figure 10 in Chapter 2), a closed array of single-collinear rigid-flexible origami was tiled on the hyperboloid-derived surface, with flexible beam-like shells (to be printed in thermoplastic elastomer) connecting relatively-rigid facets (to be printed in PETg). Two views of the entire hyperboloid-shaped array are shown in Figure 239.

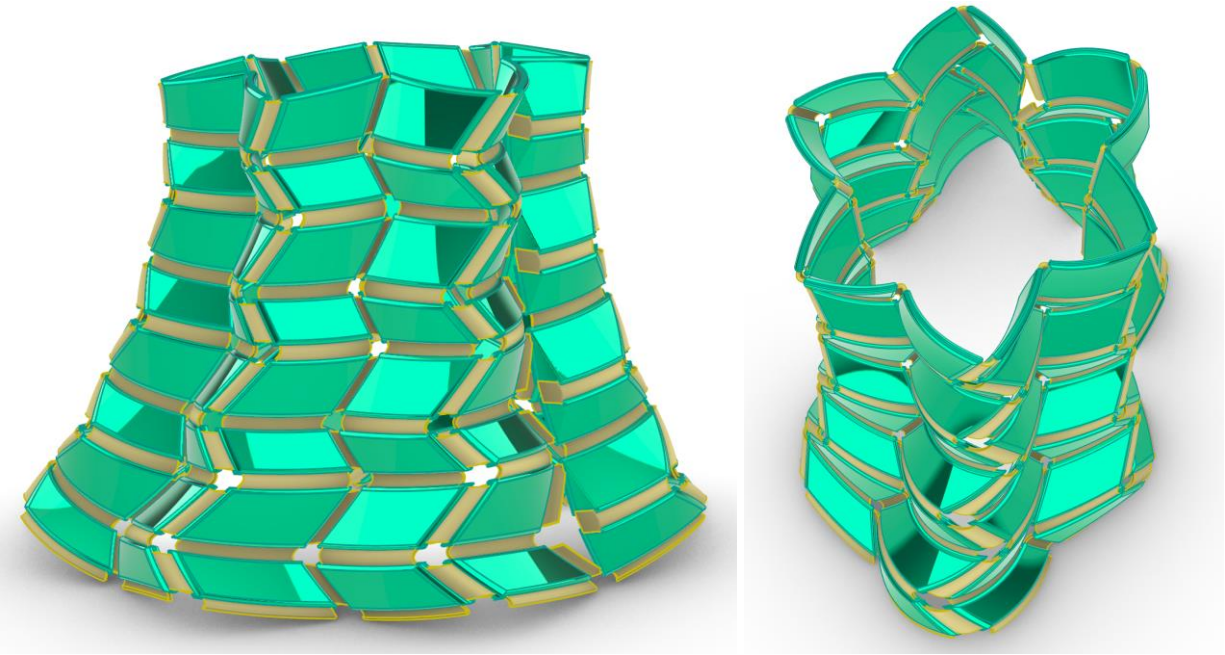

Figure 239: Renderings of the single-collinear origami pattern tiled on the hyperboloid-derived manifold, in two different views.

Unfortunately, as printed the structure was nearly rigid in point loading simulating leg movement, with only a very modest amount of point loading or compression possible, as Figure 240 illustrates. Since single unit cells and rectangular arrays of the rigid-compliant composite Single-Collinear origami were quite flexible (as studied in Chapter 2, e.g. see Figure 15), it is likely that the mapping or cylindrical configuration of the array was incompatible with the structure's natural kinematic behavior, making it nearly rigid. Of note, the structure had greater radial compliance than compressive or bending compliance, as can be seen in Figure 241.

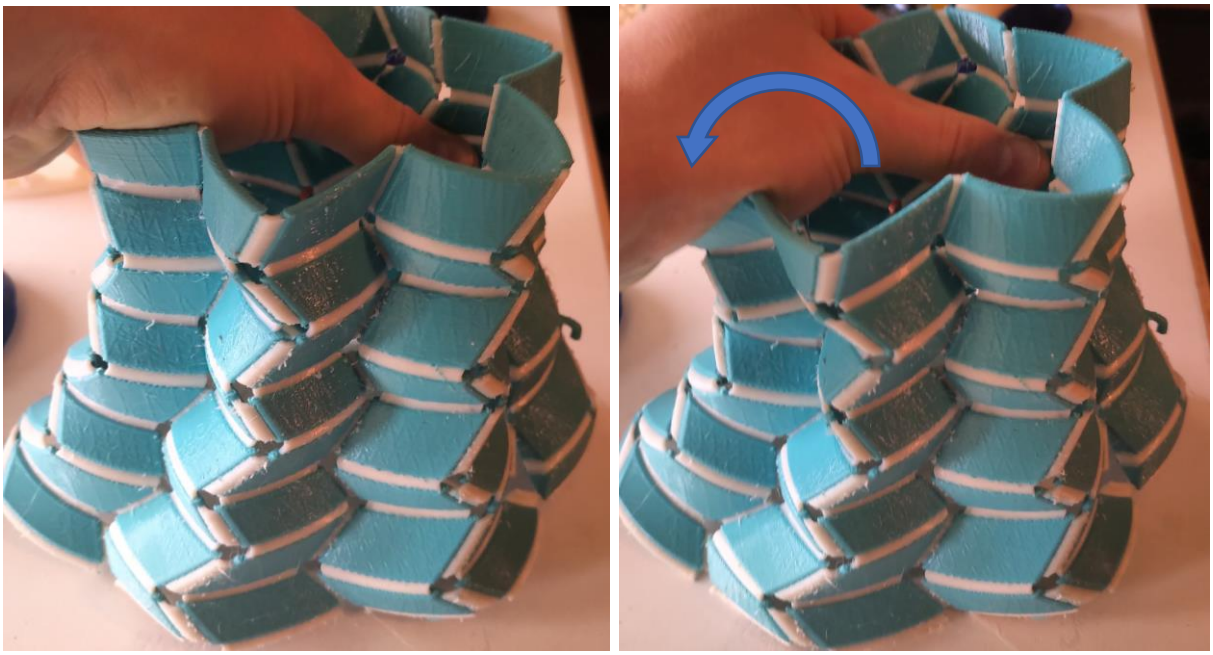

Figure 240: Undeformed (left) and barely-perceptibly-deformed (right) S-C origami on the HDM, illustrating how rigid the structure unfortunately is.

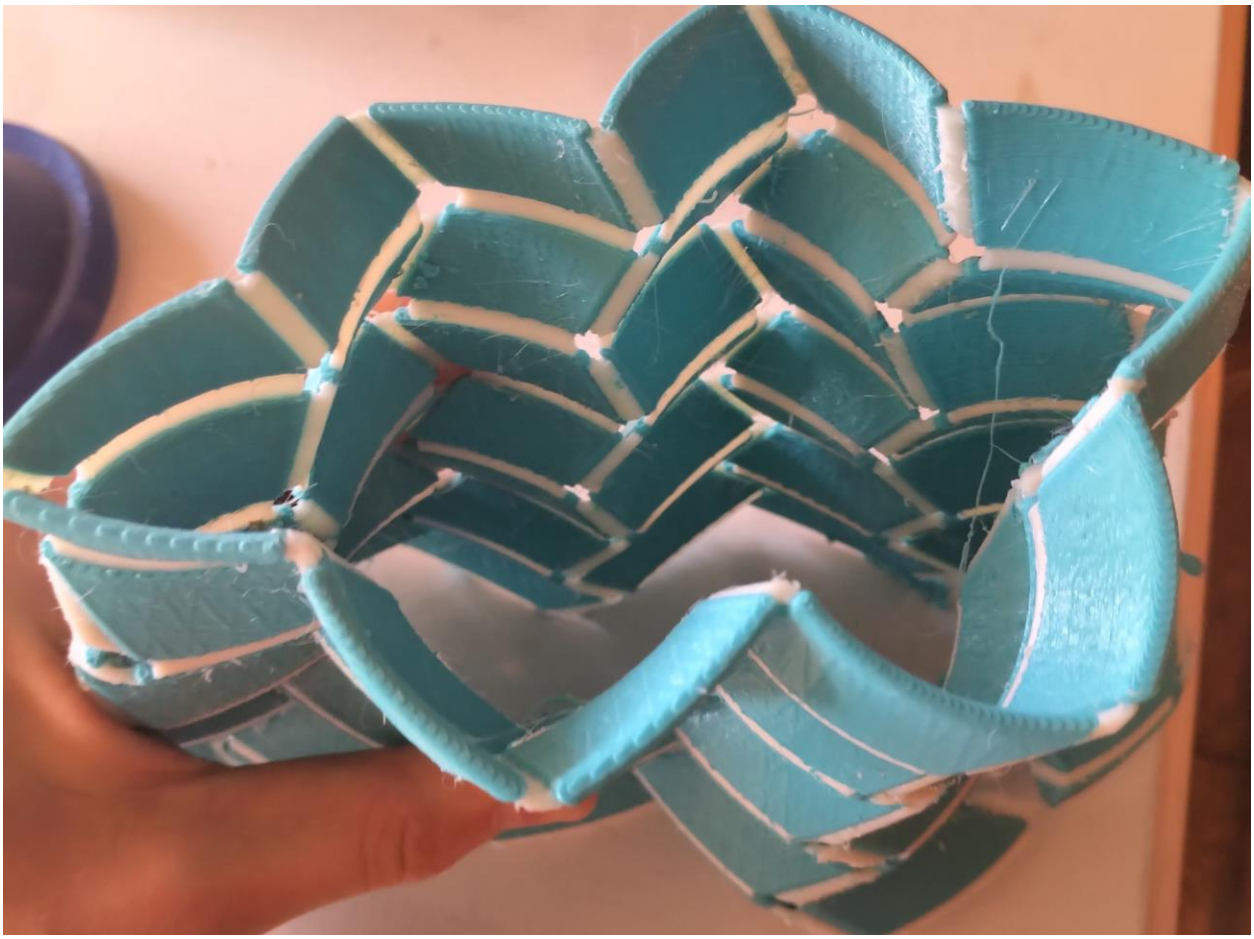

Figure 241: Vertical view showing the radial compliance (not useful) of the S-C origami arrayed onto an HDM.

Conclusions to Chapter 6.

This chapter first stressed the practical desirability of using a closed surface as the form to give a protective that encloses a joint and examined potential shapes for a closely-conforming ankle protector, with one original surface, referred to as the Hyperboloid-Derived Manifold (HDM) tentatively selected as promising for this application. Next, the problem of how such a surface should be allowed or designed to deform to continue to conform to a joint subjected to large rotation was reintroduced (having first been discussed in Chapter 2), with an eye towards acceptable boundary conditions and acceptable modes of deformation for the surface. This was augmented by a review of mathematical concepts relevant to the mechanical response of a

cylinder-like closed surface that encloses a bending joint were reviewed, with the necessity of preserving Gaussian curvature distributions and otherwise ensuring isometry stressed and the role of singularities of Gaussian curvature (in the form of creases) discussed; that said, it was noted that this discourse is binding only when the shell is a linear elastic one (metamaterials may offer more design freedom in this regard).

Next, a literature review of engineered cylinder-like surfaces designed to enclose a joint bending in large deflection without significant loss of stiffness (e.g. from shell buckling) was undertaken; the question is especially important to research into a joint protector that features a strain-stiffening metamaterial, since severe and globalized shell buckling would result in a loss of bending stiffness that would negate any lockup effects that some other aspects of microstructure could produce after the prescribed amount of free deflection. The review found no widely-accepted solution to the problem, and indeed it was not found to be of systematic interest to researchers. However, preliminary investigations, either on the part of this author or others, suggest potential mesostructuring (such as bellows-like waviness or patterning certain truss/beam patterns on a surface, or even using dry woven fabrics, which themselves effectively have a trellis-like mesostructure) may be a fruitful avenue of investigation for creating shell-buckling-resistant surfaces that can enclose jointed bodies that experience significant rotation. (Certainly, no design principle was found in this literature review that would cause a bending cylinder to experience a rapid increase in bending stiffness at a certain amount of large deflection, though in any event this chapter does not focus on methods of producing lockup, merely bending tolerance on the part of such closed surfaces.)

Occasional references to mesh-like metamaterials used for cylinder-bending applications thus motivated this author's original research into various patterns of compliant-jointed meshes

that were tiled on closed, cylinder-like surfaces. The results of these experimental creations indicated the microstructures indeed do give the overall structure resistance to buckling when the structure is loaded in global compression or bending, owing to their local kinematic freedom that lets them withstand large contractive (or extensional) deformations inside the surface that is described by the mesh (not requiring extreme out-of-plane bending in the form of shell buckling as an attempt to take up this load), though the degree to which such deformations are tolerated varies considerably based on aspects of the mesh geometry. The biaxially-oriented Cartesian arrays were found to be especially promising in terms of their in-surface contraction and extension tolerance as well as stiffness against global torsion and shear; however, the exact shape and curvature profile of the manifold on which these were tiled had a significant effect on their properties, with the Frustrum-of-Cone manifold producing the most robust resistance to shear as well as a response to leg rotation that was dominated by in-surface extension and contraction, with relatively little out-of-surface bending and curvature from leg rotation. Additionally, contra the preliminary research of Karnessis et. al., the effectiveness of mesh arrays in extending a cylindrical structure's toleration of applied bending displacement before buckling seems to have little to do with the effective Poisson's ratio of the structure, with positive effective Poisson ratio structures if anything having superior properties for this application.

In contrast to the metamaterial-inspired approach, bellows-like continuous shell structures (not having bending-dominated beam microstructures like those of the various mesh arrays studied) had an entirely different mechanism of deformation (but one that also gave them good global bending properties). The complexity of their response to simulated leg rotation is due to the combination of local, vertically-directed bending of their undulations being a compliant mode, combined with the fact that they localize shell bending deformation to the

regions of smallest offset from the neutral axis, often producing localized but limited shell creasing (limited by the high relative stiffness of the undulations that are furthest from the neutral axis, which are especially important for avoiding catastrophic losses of stiffness or severe cross-section distortions).

That said, this chapter has not proposed any design principles for causing such buckling-resistant, joint-enclosing surfaces to stiffen suddenly at a predetermined joint position, and indeed its preliminary investigations indicate that surfaces and meshes that have been microstructured to guard against shell buckling do not seem to acquire stiffening-up properties from those microstructures; thus, further features will be required to cause lockup, if it is even possible. The interrupted tile principle explored for singly-curved bending-lockup-capable surfaces may also be applicable to the more complicated case of cylinder-like surfaces that fully enclose jointed rotating bodies, though modifications will likely prove necessary. Building off of the ability of fabrics to shear (thanks to bias compliance) and compress locally (due to yarn microbuckling) and integrating the interrupted-tile principle, the next chapter will propose tiling the hyperboloid/cylinder-like shape with disjoint rigid tiles to produce a composite structure that may have the potential to lock up in bending, and then investigate the bending response of such an array with finite element simulations in LS-Dyna.

Chapter 7. CAD Geometry and Initial Simulation of Fabric-Backed Arrays with a Closed Initial Manifold in LS-Dyna with MAT_235.

Abstract.

This chapter describes the geometric modeling and subsequent simulation (as per the protocol described in the previous chapter) of multiple arrays of rigid tiles on a surface that is closed (like a cylinder) instead of open (a departure from the previous work described in this dissertation) and additionally has regions of negative Gaussian curvature, with the goal of producing a structure that encloses a joint (like the human ankle) and locks up after a specific amount of displacement of the enclosed joint. First, potential shapes for the enclosing manifold are investigated, including by printing prototypes without tiles in flexible material; a shape reminiscent of a hyperboloid of one sheet (though sculpted somewhat) proves to be the most promising for the manufacturing capabilities at this researcher's disposal. Then, tiles are generated on the surface to form the first array, with a fixed amount of offset between the tiles in the *u* direction plus a different offset in the *v* direction (allowing for some buckling inward that will hopefully be controlled and limited). Then, a rotating surface representative of a human leg is modeled inside the closed array, and the entire assembly is simulated in LS-Dyna with the methodology described in the previous chapter (with the addition of a rotating rigid-body leg). The results of this first simulation were inconclusive owing to simulation difficulties attributed to insufficient mesh elements between tiles (despite many attempted fixes by changing element type, hourglass settings, adding global damping, remeshing with triangular and quadrilateral-dominant meshes, etc.), so the array was regenerated with fewer tiles to produce larger areas of unbonded fabric between the bases of the tiles and simulation attempted again. Even with a high degree of mesh refinement, the simulations of the array still failed due to negative element

Jacobians prompting automatic erosion, indicating that the method of setting up simulations of fabric-backed tiled arrays disclosed in the previous chapter may not be valid for closed (cylindrical) surfaces, or alternatively that such cylindrical arrays may experience premature stiffening that renders them unable to bend significantly.

Introduction.

This chapter attempts to employ the techniques for FEA modeling of planar fabric-backed arrays described in Chapter 7 to study closed-surface fabric backed arrays in FEA. Ideally, researchers should be able to use LS-Dyna to rapidly simulate various patterns of tiles and lockup profiles without having to manufacture the arrays by hand, since manufacturing is presently quite time consuming, owing to the necessity of manufacturing tiles with unique shapes, organizing the tiles rather than confusing similar ones, precisely positioning each tile, and then bonding each tile to a fabric manifold with a complex shape. Indeed, the difficulty of manufacturing is compounded when applied to cylindrical arrays, or even arrays that are initially curved outwards (practically speaking, an array of this sort would likely be manufactured in two separate halves, both for ease of manufacture and to enable the user to put the protector on or take it off; the two halves could be jointed at tiles that would be rigidly locked to each other when the device is worn, then unlocked to remove it).

As discussed in the previous chapter, there are potential issues with closed surfaces in bending, whether backed by fabric or not, so an accurate prediction of the behavior of such a closed surface, when backed by fabric and tiled with rigid tiles and enclosing a bending surface, would be quite valuable for determining whether it is worth the effort to manufacture such an array, or whether it would either buckle so as to prevent lockup, or not permit the enclosed joint to rotate to the full extent desired. This is especially pressing considering the amount of work

required to manufacture the open, planar array of Chapter 4, and the fact that it is anticipated that a closed-surface array would be even more time-consuming than that array to produce. On the other hand, it is debatable whether a virtual (FEA) approach is superior to directly manufacturing arrays. While the research in Chapter 7 was successful in modeling the deflection at lockup of a planar fabric-backed array, the fidelity of a simulation of a closed surface may be inferior owing to the difficulty of predicting the exact orientations in yarns of the initial surface (since now the woven fabric must conform to a non-planar surface, which may result in local fabric shearing). That said, this is the approach that will be attempted first, both to build upon the author's FEA capabilities, and to save time on manufacturing.

Generating CAD Geometry of the Tiles for the Array.

Whether for manufacturing or FEA simulation, the first step must necessarily be the creation of a CAD model of the desired array and fabric backing. The general structure of the four types of tiles described in Chapter 4 will be repeated here (with a unit cell consisting of one of each of four types of tiles, color coded in the following figures, and flaring either inwards or outwards in the vertical and horizontal directions in order to prevent sliding of tiles relative to one another in the direction normal to the surface). That said, there are many remaining variables, such as spacing between tiles in the *u* and *v* (i.e. circumferential and vertical) directions on the manifold and the overall sizing and scale of the tiles.

Several different arrays with various proportions of tiles, gaps, etc. were generated, though owing to preliminary simulation difficulties (described in greater detail in Appendix IV), the size of the tiles (and, more importantly, the size of the regions of unbonded fabric between the tiles) was increased and their number decreased. Additionally, work in other chapters suggested that increased gaps in the vertical direction to accommodate both in-surface

compression (really fabric microbuckling) as well as out-of-surface bending displacement would be required. Thus, while Figure 242 shows preliminary array renderings, Figure 243 is what was used for the main simulation in this chapter.

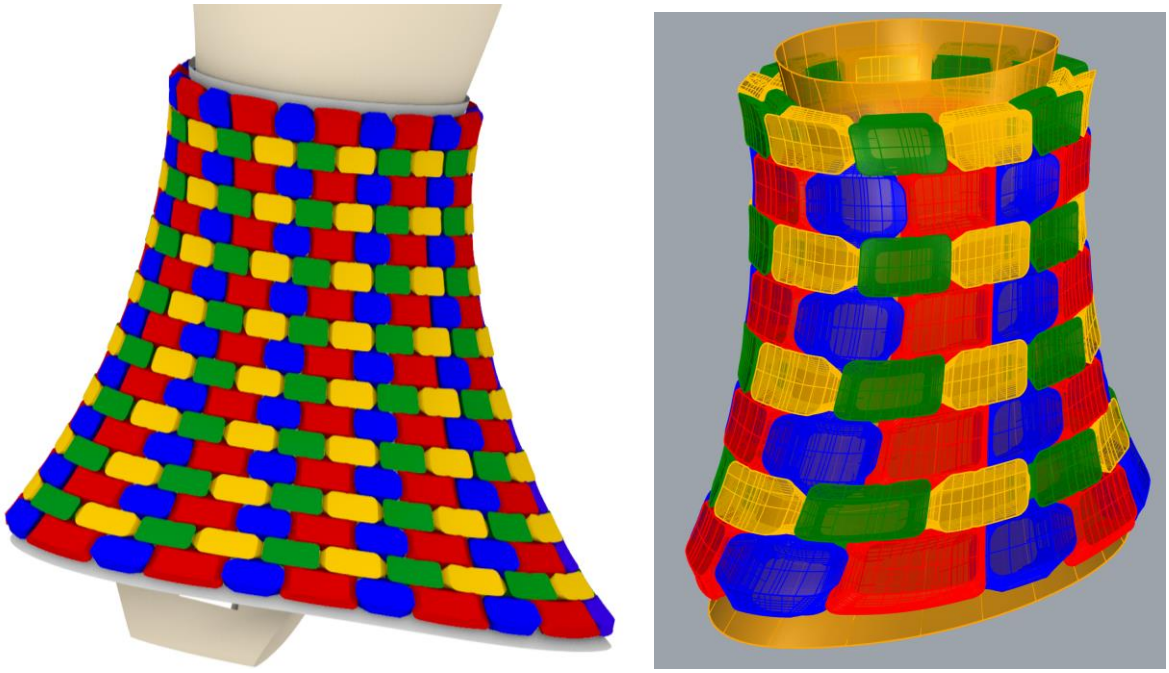

Figure 242: Preliminary tiled arrays generated for initial simulations that proved overcomplicated owing to the large number of tiles (as well as lacking in sufficient freedom).

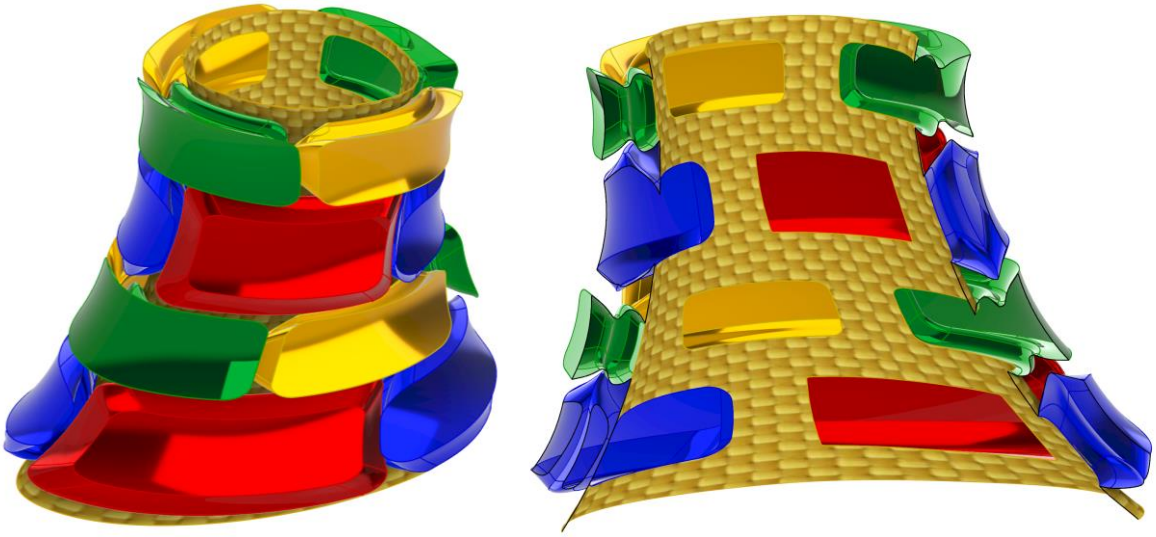

Figure 243: The array studied in this chapter (with a section view shown at right).

Testing Fabric Anisotropy Specification in LS-Dyna.

Prior to simulating the full array, however, it was necessary to check the behavior of the material model with closed-surface (cylinder-like) fabric shapes. The MAT_235 material model is necessarily anisotropic in that it attempts to simulate the warp and weft yarns with a continuum model. In the relatively-simple model of Chapter 5, the fiber directions could be expressed globally, but since LS-Dyna does not natively support cylindrical coordinate systems, a global specification is not directly possible for a cylinder (or hyperboloid that is similar to a cylinder in the sense of being a closed surface). Instead, each element must be given its own direction-vector specification (which all shell elements have, though for isotropic materials this functionality is ignored). By default, the element's intrinsic direction vector is directed from node 1 to node 2, which rarely gives the desired result unless the mesh is perfect. For instance, Figure 244 shows how the direction vectors are distributed semi-randomly over a meshed cylinder without modification.

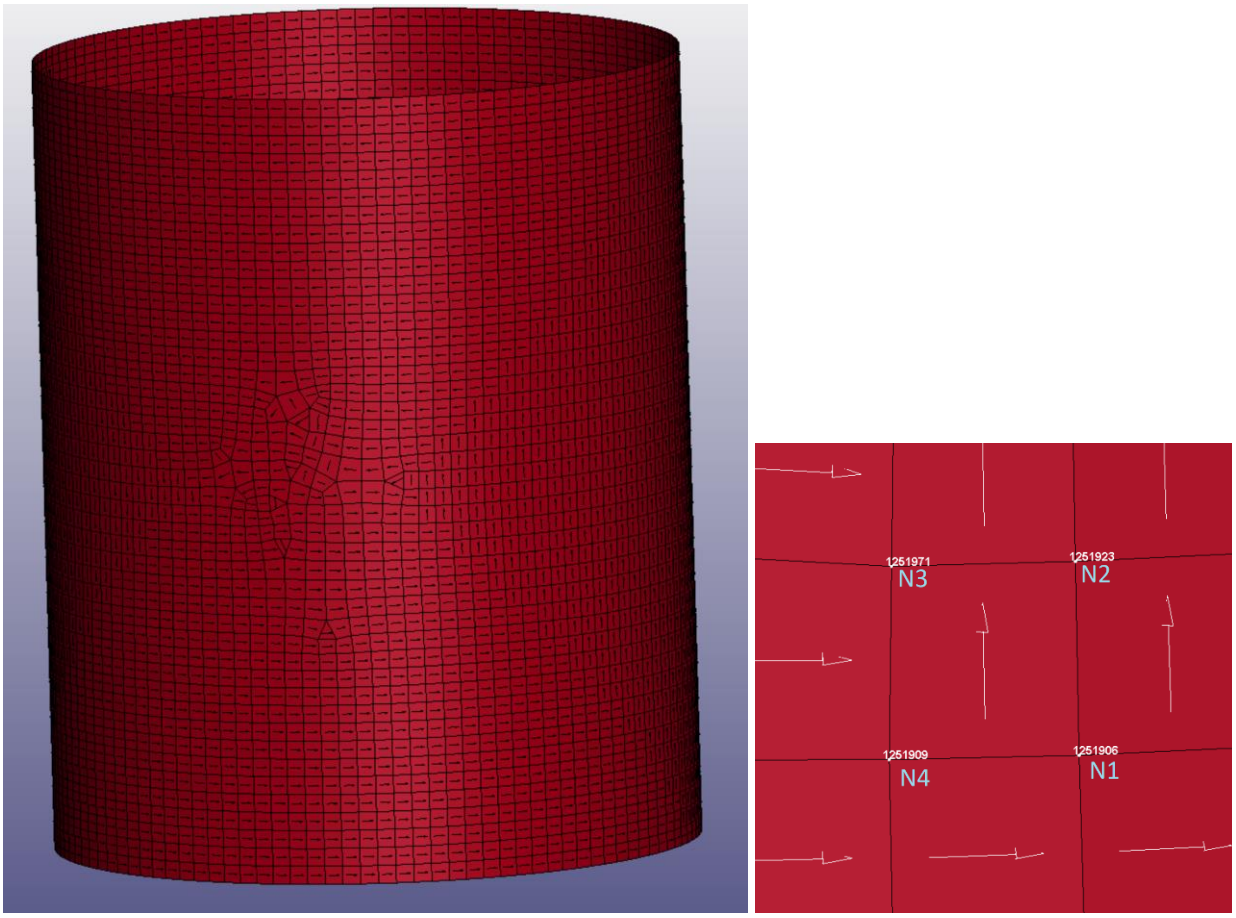

Figure 244: Unmodified cylindrical mesh with default element direction vectors indicated with arrows (left), and a closeup of one element with its direction vector directed as default from node 1 to node 2 (which happens to be vertically oriented, though surrounding elements are often horizontally oriented). These direction vectors are subject to the vagaries of meshing and must be modified for accurate simulation of anisotropic behavior.

Fortunately, the preprocessor for LS-Dyna, LS-PrePost, offers an interface for aligning the element direction vectors (referred to as "BETA" in the documentation and PrePost software) to correspond to the fiber directions of various anisotropic simulations. In fact, owing to the importance of accurately replicating fabric behavior, the following subsections will feature brief, preliminary simulations that simulate fabric cylinders with yarns oriented either vertically and circumferentially, or biaxially (at ±45° to the vertical).

Of note, when local element orientations are used to define the direction of anisotropy, the user must specify AOPT=0 on the material card for MAT_235. (Previously, AOPT=2 along with a global vector was used in Chapter 5).

Cylinder in Tension with Fibers Vertical and Circumferential (BETA at 45°).

To simulate fibers being aligned vertically and circumferentially on a cylinder, it is necessary for the element orientations/BETA values themselves to be at 45° to the vertical or horizontal, and then to specify the "braid angle" as 45° on the MAT_235 material properties card. Figure 245 illustrates how the element orientations will be aligned to simulate fibers being vertical and circumferential on a cylinder. Note that, perhaps confusingly, the BETA angle should not be oriented vertically or horizontally, because it will be further adjusted by the braid angle of MAT_235.

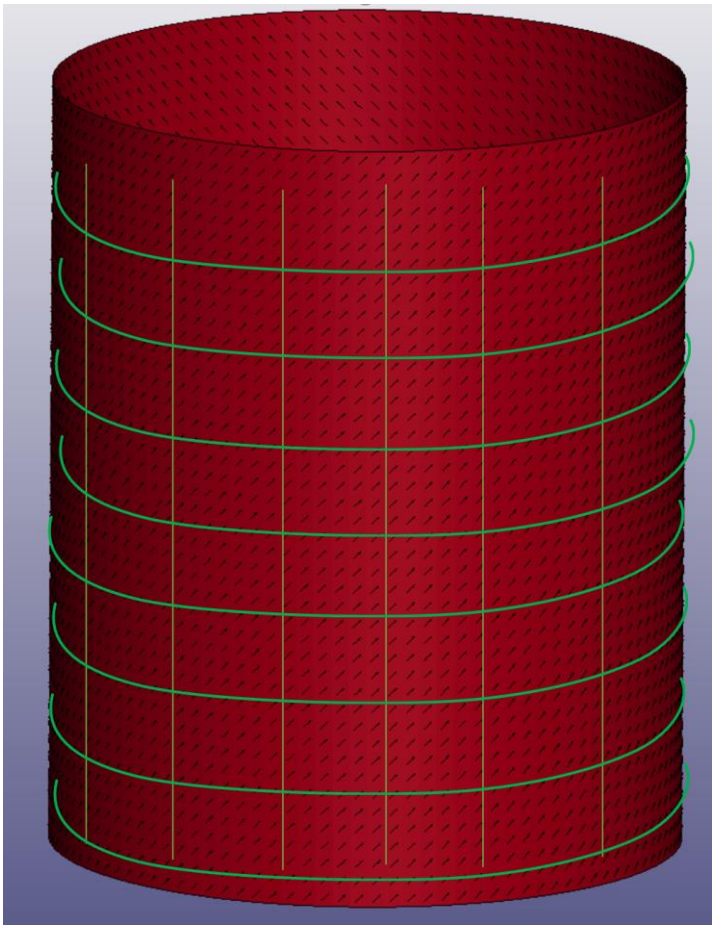

Figure 245: In this model, the parameter BETA is used to rotate the principal direction of each element by 45° from the vertical orientation (principal direction vectors are shown with small black arrows on each element). Since the principal direction corresponds to the braid angle axis of symmetry, and the braid angle is specified to be 45° in each direction from the axis of symmetry, this actually means that the model simulates yarns that are oriented vertically and radially, as shown in green.

When subjected to a moderate vertical tensile load, the cylindrical structure exhibited relatively little deformation (limited to light surface wrinkling, probably a numerical artifact from the simulated decrimping of the fabric), as can be seen in Figure 246. Overall, the structure was not expected to deform considerably since the vertical fibers would take up most tension (at least after decrimping was accomplished), so it appears this simulation was successful.

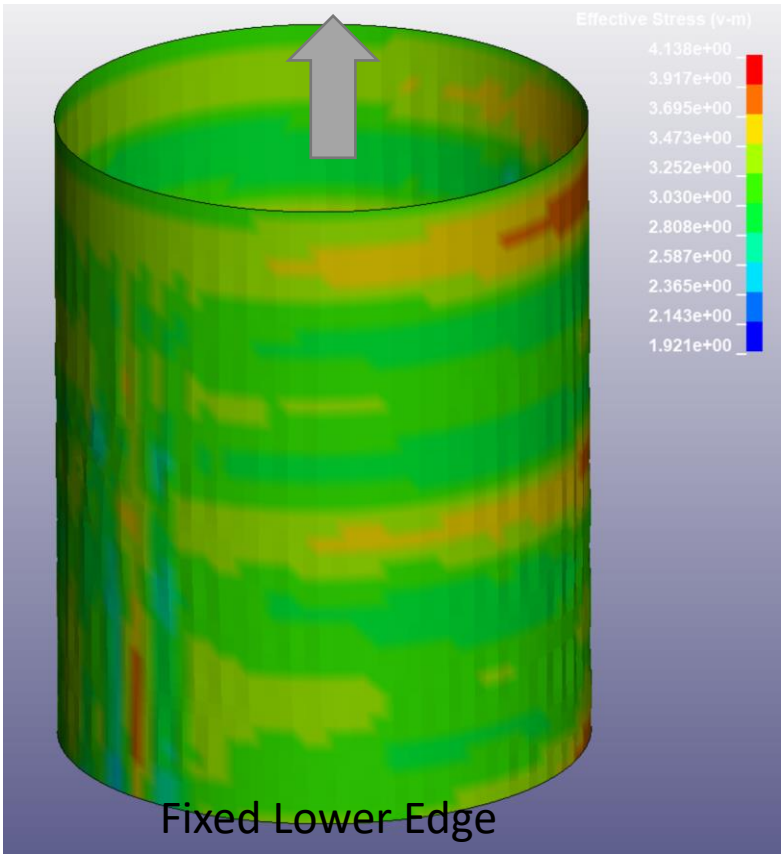

Figure 246: Contours of von Mises stress plotted on the cylindrical braid with BETA *oriented at a 45° to the vertical (resulting in fibers being oriented at 90° and 0° angles from the vertical). Note that there is negligible bias compliance engaged in this loading; however, there is some initial decrimping of the fabric, but afterwards deflection is quite minimal.*

Cylinder with Fibers at 45° (BETA Vertical).

In contrast, the same load was applied to the top ring of the cylinder after orienting the fibers biaxially instead of vertically and circumferentially; of course, to simulate biaxially-oriented fibers, it was necessary to specify BETA (element orientations) either vertically or horizontally, so that the braid angle (45°) would produce the proper offset. Figure 247 illustrates the simulated response of a biaxial braid in tension, which accurately replicates the inwards contraction that a "Chinese finger-trap" (biaxial braid) also demonstrates.

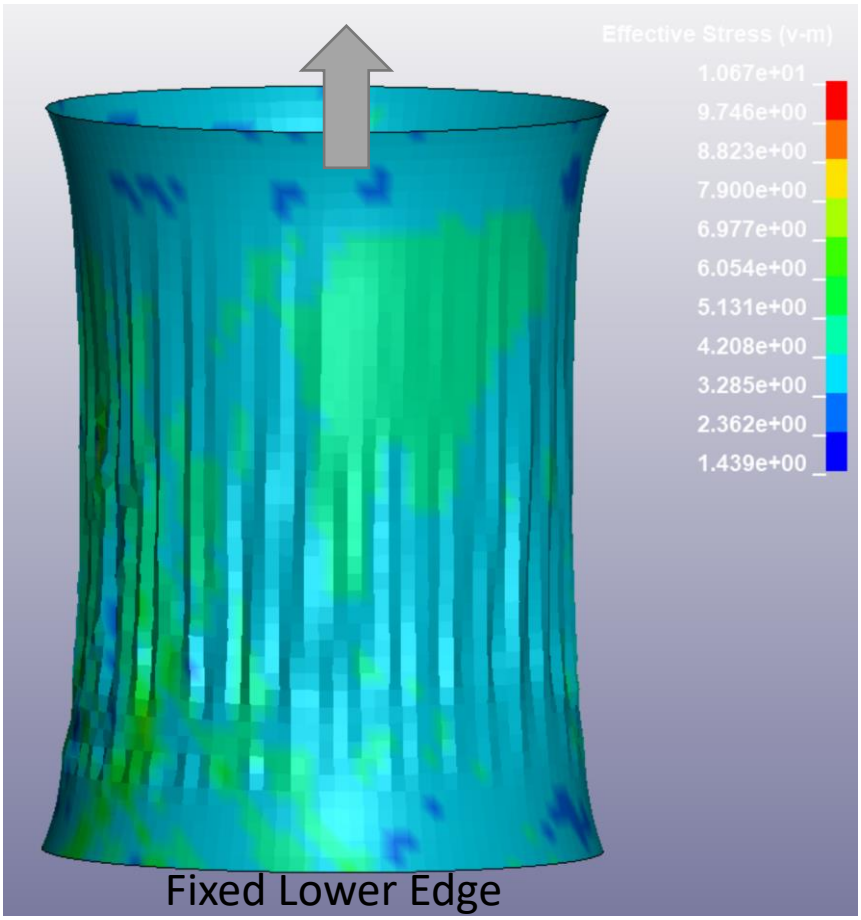

Figure 247: Contours of von Mises stress plotted on the cylindrical braid with BETA *oriented vertically (resulting in fibers being oriented at 45° angles from the vertical). Note that the bias compliance results in the braid "necking" inwards, much like a "Chinese Finger-Trap".*

Simple Simulations of Hyperboloid-Derived Manifolds in Tension.

In a similar vein to the above-described test simulations of cylindrical braids and weaves in tension, it seemed valuable to test fabric in the HDM shape subject to tension with weaves in either orientation. Of course, it should be noted that actually shaping a weave of fabric into even an approximation of this doubly-curved shape is a separate question (addressed in Chapter 10), with ensuring continuity of yarns especially difficult in actuality (but easy to simulate in FEA). The simple HDM surface manifold was imported into LS-PrePost and meshed with a quad-dominant mesh, producing the mesh and additionally the default element orientations shown in Figure 248; clearly, these need to be properly oriented.

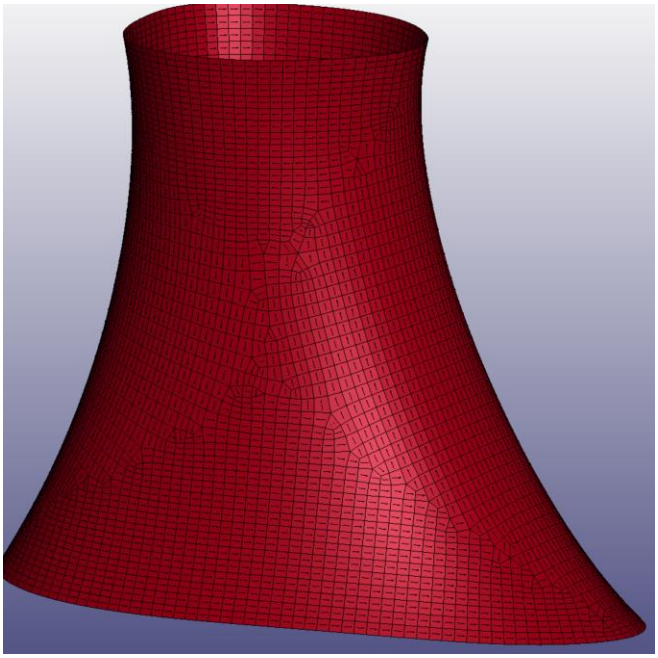

Figure 248: Default element orientations (based on the vector from N1 to N2 in each element) in the hyperboloid-based manifold, prior to elements being oriented properly.

Hyperboloid-Derived Manifold with Fibers Vertical and Circumferential (BETA at 45°).

As with the preceding cylindrical mesh, to simulate vertically/circumferentially-oriented yarns, the BETA element-direction vector must be set to 45° from the vertical, which is done as shown in Figure 249. The results of the tension simulation are shown in Figure 250; a few of the coarse mesh elements do bend slightly relative to the surface, which is unexpected, but overall the simulation appeared successful, and the tensile deformation was limited as was to be expected.

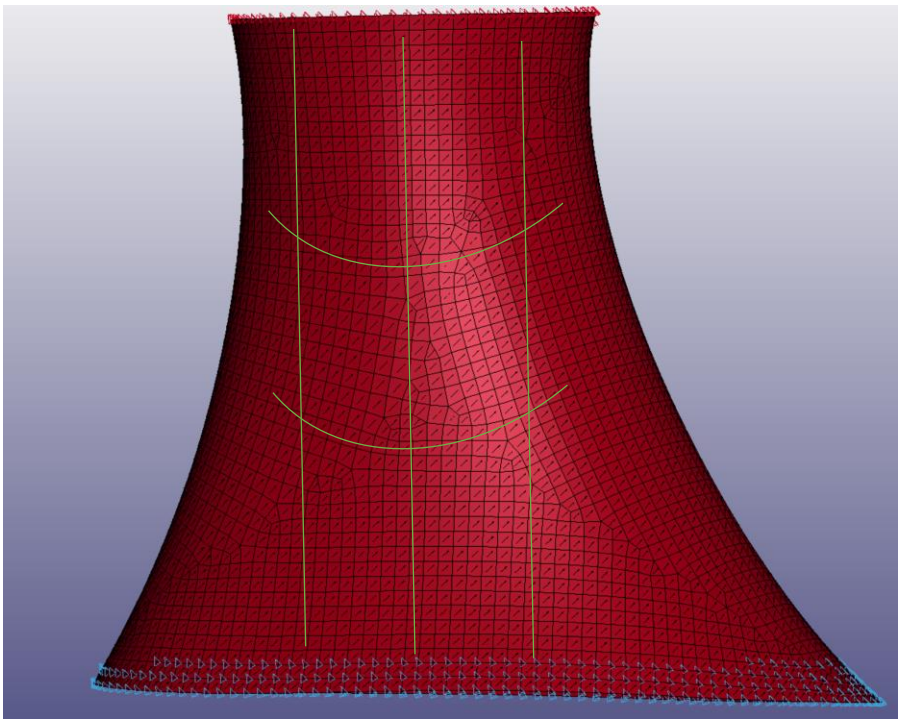

Figure 249: Hyperboloid-based manifold with element orientations at a 45° angle to the vertical (simulating yarns being oriented at 90° and 0° angles from the vertical—yarn orientations are shown roughly with green lines).

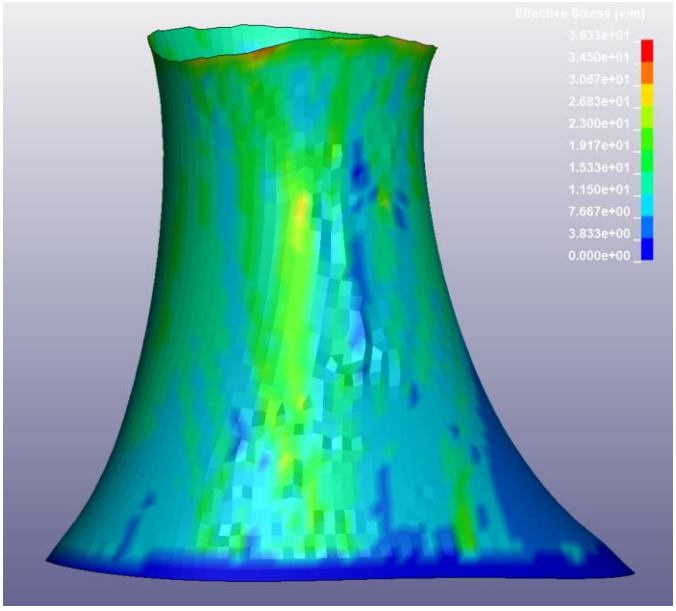

Figure 250: Contours of von Mises stress plotted on the hyperboloid-derived braid with BETA *oriented at 45° (resulting in fibers being oriented at 0/90° angles). There is limited extension of the structure (due to decrimping mainly) but little "necking" inwards.*

Hyperboloid-Derived Manifold with Fibers at 45° (BETA Vertical).

Similarly, simulating a biaxially-oriented braid on the HDM surface (leaving aside the question of how such a surface could actually be braided, without at the least causing conformity issues) was accomplished by setting the element direction vector BETA to the vertical, as the fibers would be oriented 45° from that, as can be seen in Figure 251. The response of the surface to the same amount of tension as the vertically/circumferentially-oriented surface was subjected to is shown in Figure 252; note that, on a conceptual level, the behavior was as expected for a biaxial-like orientation, with significant inwards contraction (though it is of course not easy to manufacture such a structure for testing purposes).

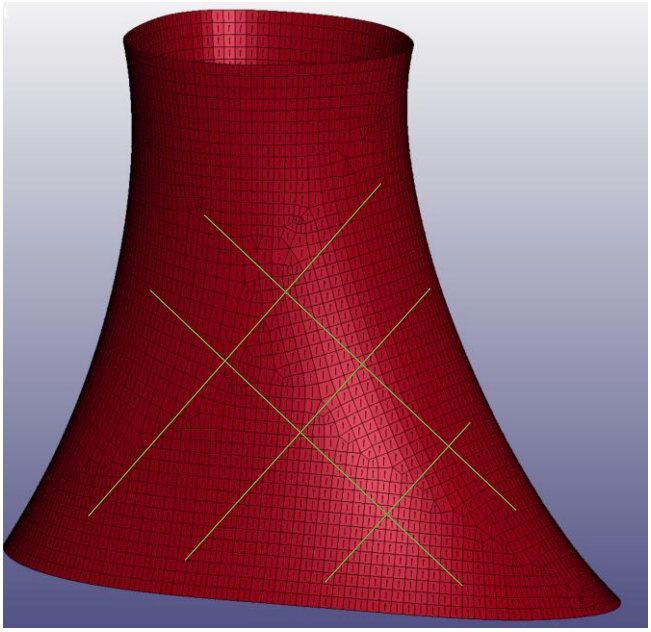

Figure 251: Hyperboloid-based manifold with element orientations made in the vertical direction (for the simulation with yarns being oriented at 45° angles from the vertical, as indicated with green lines).

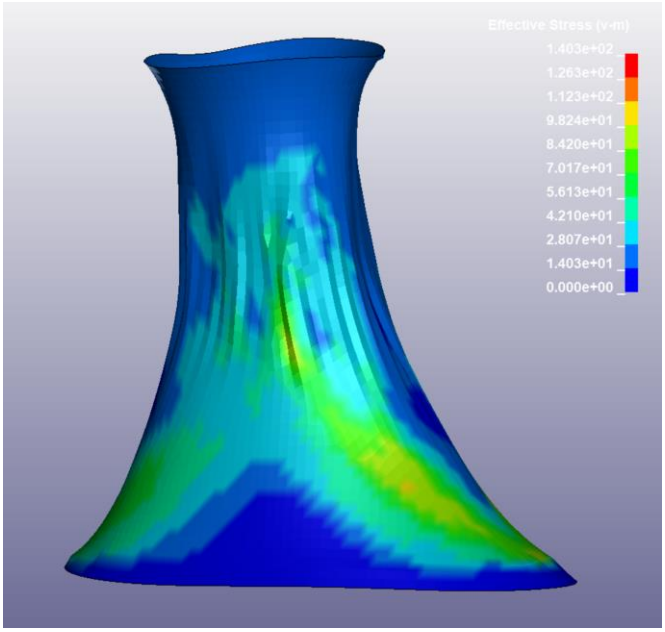

Figure 252: Contours of von Mises stress plotted on the hyperboloid-derived braid with BETA *oriented vertically (resulting in fibers being oriented at 45° angles from the vertical). Note that the bias compliance results in the braid "necking" inwards as the structure elongates, much like a "Chinese Finger-Trap".*

Simulation of An Entire Array.

Generating the Mesh.

Following the successful preliminary simulations of pure fabric structures in tension with accurately-captured anisotropy and orientations, it was necessary to mesh the selected CAD geometry. Again, as in Chapter 5, tiles were treated as rigid shells with open bottom surfaces (where they would be bonded to the fabric if actually manufactured), and node sharing was specified between fabric and tile elements in place of bonded contacts (which do not work with fabric material models in LS-Dyna). Figure 253 illustrates the mesh that was produced. Of note, an all-triangle mesh for the fabric was preferred to a mesh containing both quadrilaterals and triangles, owing to the tendency of quadrilateral elements to distort either in shearing or from spurious hourglassing modes. (Granted, LS-Dyna offers methods of controlling hourglassing, but they are imperfect, and triangular shells do not have hourglassing at all). Additionally, the

mesh of the fabric regions between tiles was extremely dense, both to ensure maximum mesh regularity (with elements being as close to equilateral triangles in shape as possible), and to enable maximum fidelity in the simulation. Figure 254 shows a close-up view of the quantity and quality of shell elements in the fabric region between two tiles, and Figure 255 shows the shared edge between a tile and the fabric, illustrating the sharing of nodes.

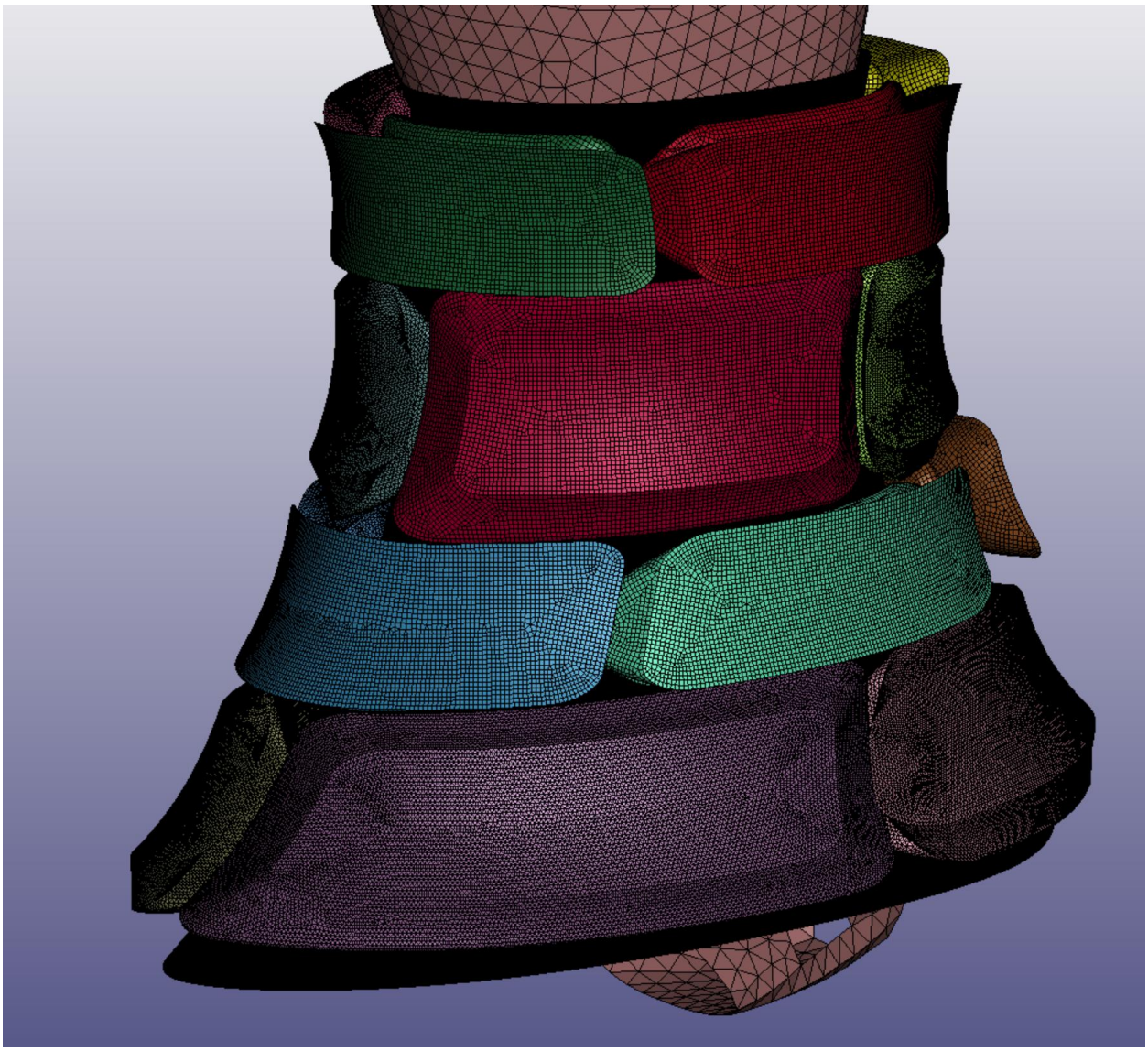

Figure 253: Overall view of the mesh used. The fabric is so densely-meshed that it appears black (in fact, it was colored brown, but this is only visible upon zooming in).

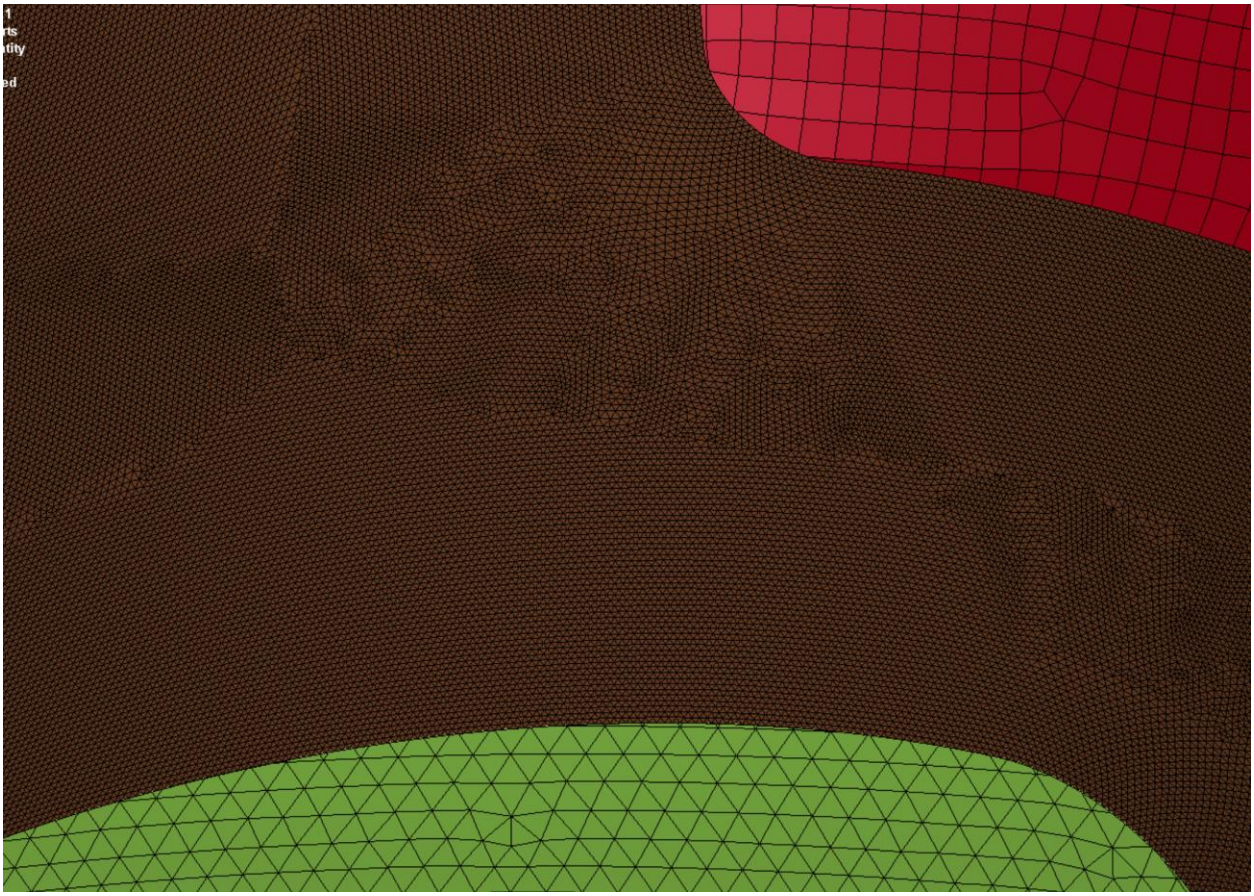

Figure 254: Closeup view of the fabric mesh (brown, with all triangular elements) and two tiles (green and red).

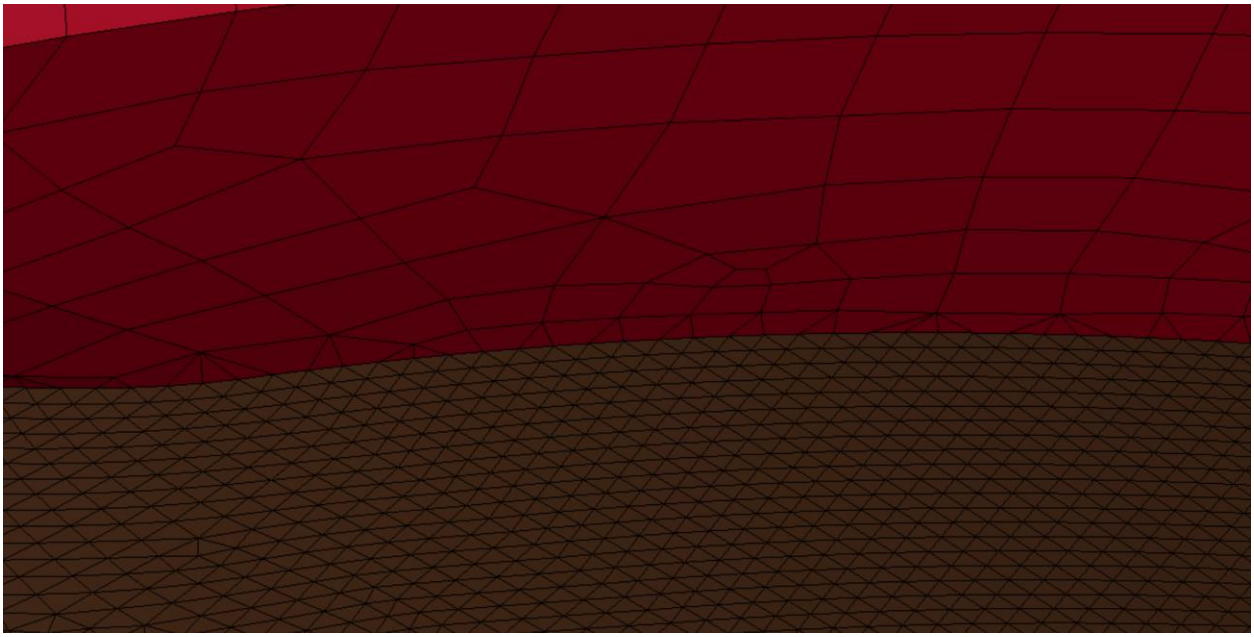

Figure 255: Node-sharing between one tile (red) and the fabric (brown)

Prescribing Fabric Fiber Orientations.

As with the simulations of cylindrical and hyperboloid-shaped fabric sections without teeth in earlier sections of the chapter, element directions were applied with the ELETOL interface in LS-PrePost, assigning the "BETA" shell quantity with a projected angle of 45° from the vertical angle, which, when combined with the braid angle of 45° in the specification of MAT_235 would treat fibers being oriented vertically and circumferentially. Figure 256 illustrates the element orientations of a small section of the fabric (because the elements are so small, it is necessary to zoom in to see the individual direction arrows).

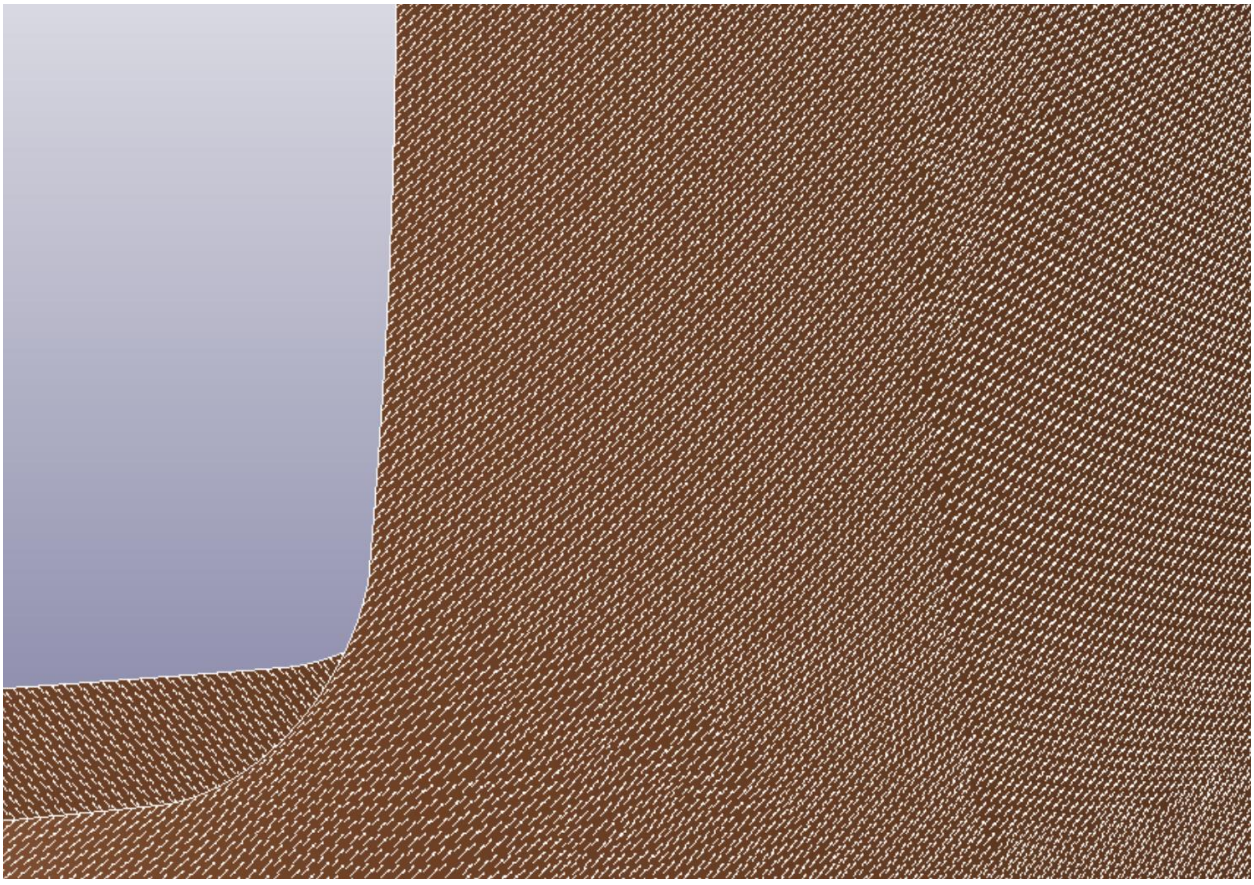

Figure 256: Element "BETA" directions indicated with tiny white arrows, at 45° to the vertical (corresponding to fiber directions oriented vertically and circumferentially).

Loads and Boundary Conditions for the LS-Dyna Simulation.

In order to model a revolute joint connecting the leg (through an axis at the ankle) to the ground, it was first necessary to create a rigid-body "dummy" part that was fixed in *xyz* in space and to which the leg was jointed, as shown in Figure 258. The leg was modelled as a rigid shell with a triangular extruded cut that identified the two nodes that would be fixed to simulate the revolute joint and give it its axis, with the tip nodes shown in Figure 257. The "dummy" part was fixed to the ground with a PRESCRIBED_MOTION_RIGID keyword, as shown in Figure 259. Then, a revolute joint was established between the "dummy" part and the leg at the shared nodes with the card CONSTRAINED_JOINT_REVOLUTE, as shown in Figure 260. Finally, a rotational motor was applied to the joint with CONSTRAINED_JOINT_ROTATIONAL_MOTOR, with the parameters shown in Figure 261.

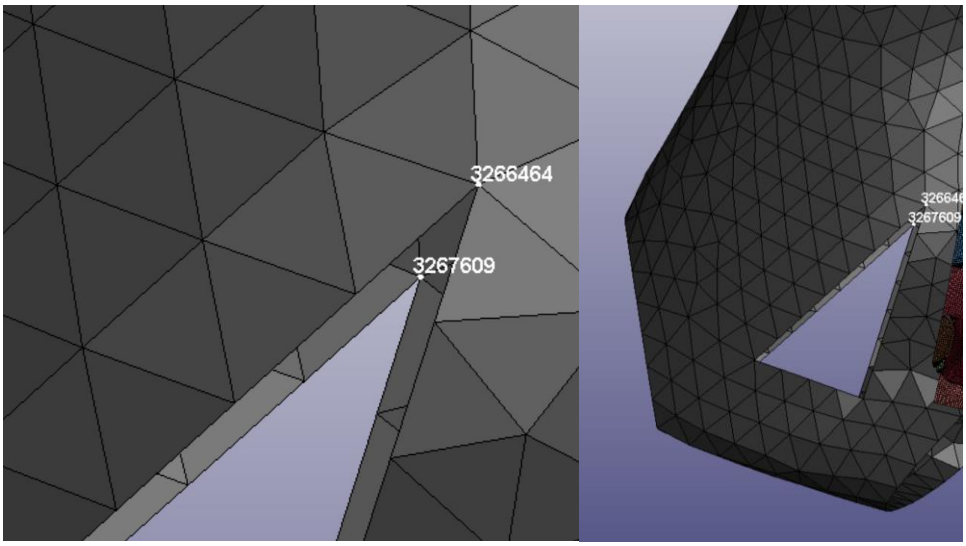

Figure 257: Selecting the two nodes on the rigid leg body that define the revolute-joint axis for the leg.

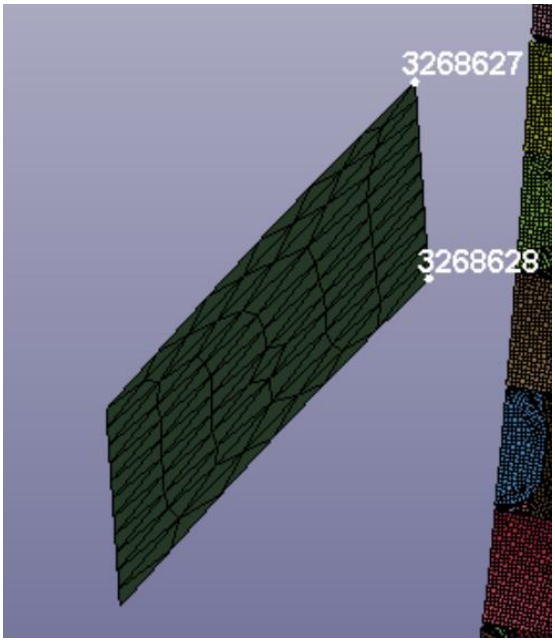

Figure 258: "Dummy" part with the two nodes that will be used for the revolute joint indicated.

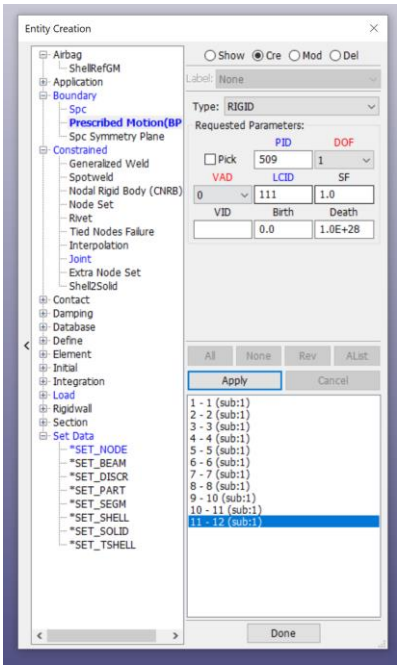

Figure 259: In order to fix the displacement of the "dummy" part, it is necessary to use PRESCRIBED_MOTION_RIGID as the boundary condition (namely, setting the velocity to a curve defined as zero throughout the simulation, in all three cardinal directions).

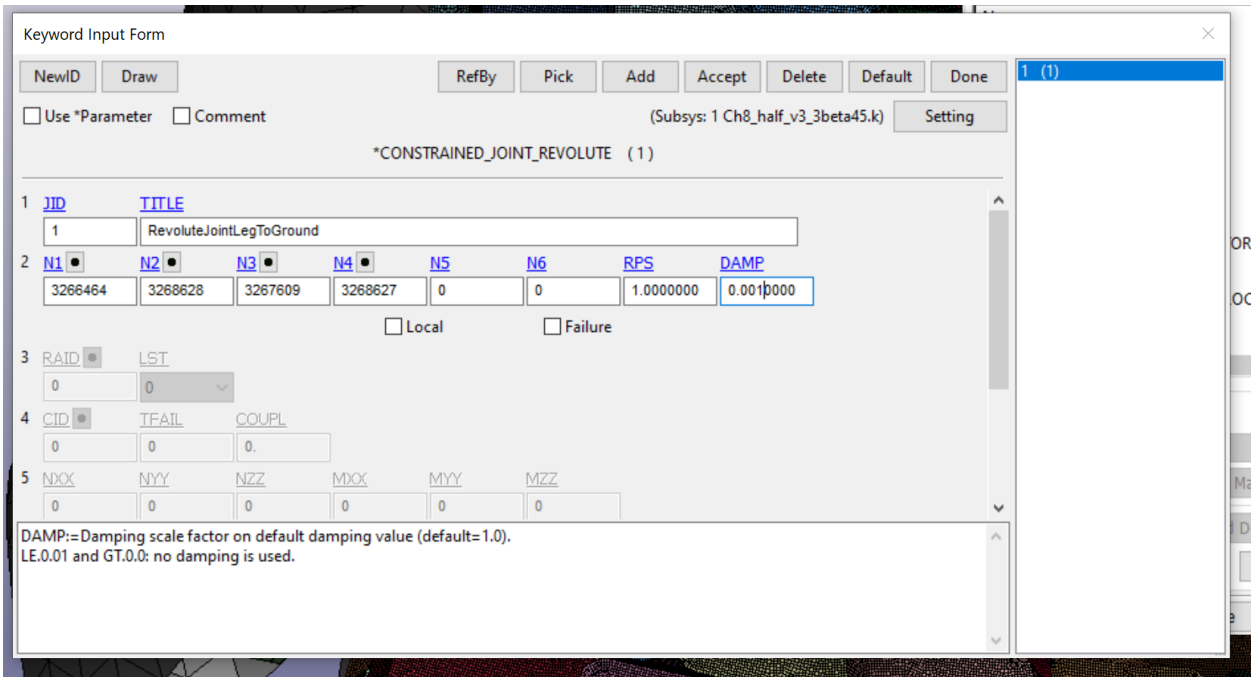

Figure 260: LS-Dyna card for the revolute joint.

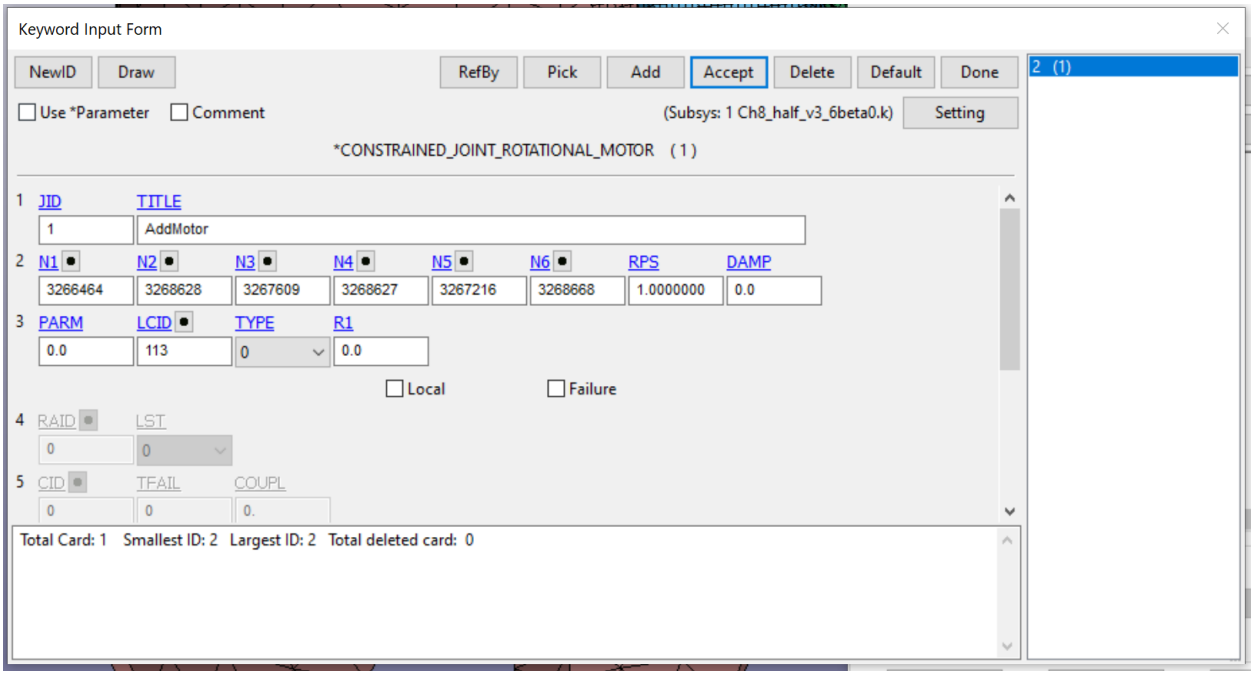

Figure 261: LS-Dyna card for the rotational motor.

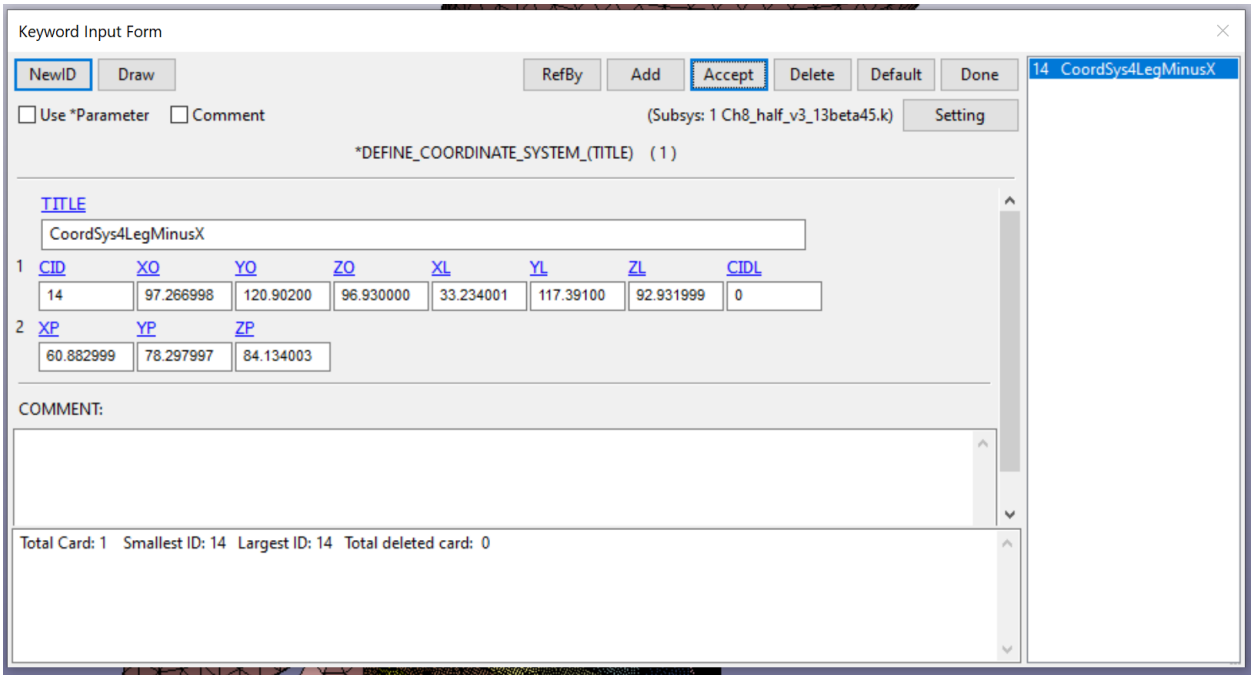

Figure 262: LS-Dyna card for the coordinate system for the leg's rotation.

Finally, the bottom-most four tiles were constrained against displacement and rotation in all directions. Additionally, contact was established only between the rigid leg and rigid tiles (there was intentionally no contact between the fabric and leg themselves, in order to save computation time by reducing the amount of time per timestep spent on the contact algorithm, and because the leg would generally only contact fabric if it was contacting the nearby tile). The full set of boundary conditions and loads, including fixed base tiles and revolute joint and motor on the leg are illustrated in Figure 263.

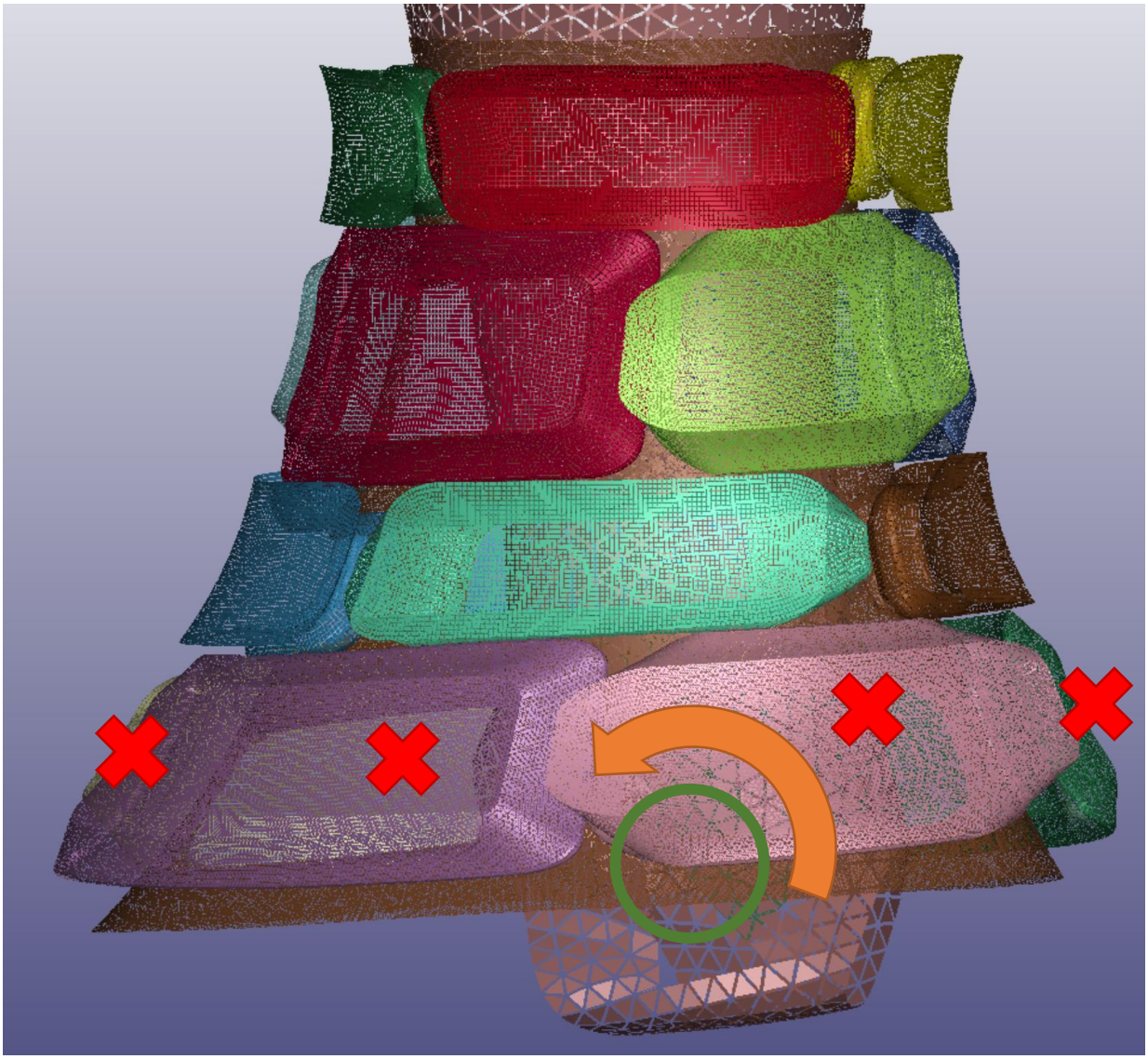

Figure 263: Full set of boundary conditions and loads on the array. The red Xs indicate tiles that are fixed in displacement and rotation; the green circle indicates the location of the revolute joint between the leg and "dummy part" (which is itself fixed rigidly to ground), and the orange arrow indicates the direction of rotation from the applied rotational motor on the leg.

Results of the LS-Dyna Simulation of the Closed-Surface Array.

Unfortunately, the simulation failed rather rapidly, resulting in "NaN" (not-a-number) nodal velocities causing the simulation to terminate at time 1.20e-4 seconds (corresponding to a leg rotation of just 0.54°). The maximum deformation reached is illustrated in Figure 264, and the von-Mises stresses that developed in the fabric from this displacement are shown in Figure 265. The cause of simulation failure appears to be a relatively small number of mesh elements

that became highly distorted, as illustrated in Figure 266, likely the result of non-shared nodes between tile and fabric meshes in that region in turn producing excessive fabric distortion from biaxial tension (combined circumferential and vertical tension). Various program errors in LS-PrePost (the program used to generate the mesh) made it difficult to ensure perfect node sharing, and the structure could not be successfully meshed in ANSYS Workbench, an alternative meshing application used in Chapter 5 with the simpler initially-planar array geometry. As is discussed in Chapter 8, MAT_235 appears ill-equipped to accurately simulate biaxial tension and produces similar "NaN" failures with even very simple tests in which biaxial tension dominates.

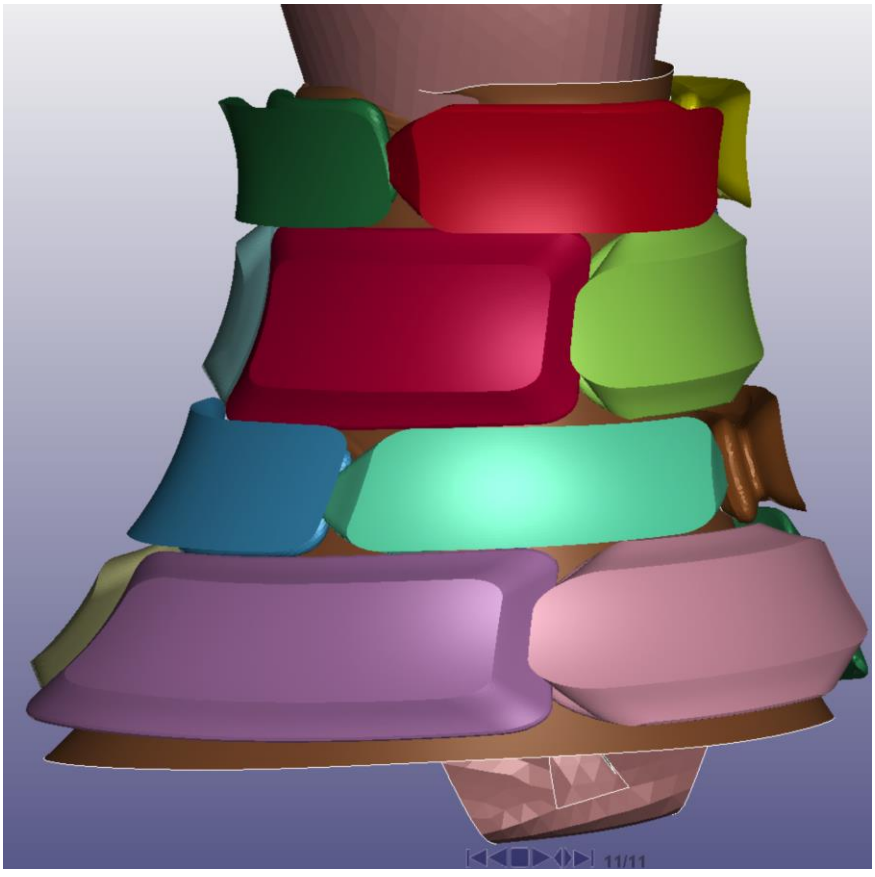

Figure 264: Maximum extent of leg rotation prior to simulation failure.

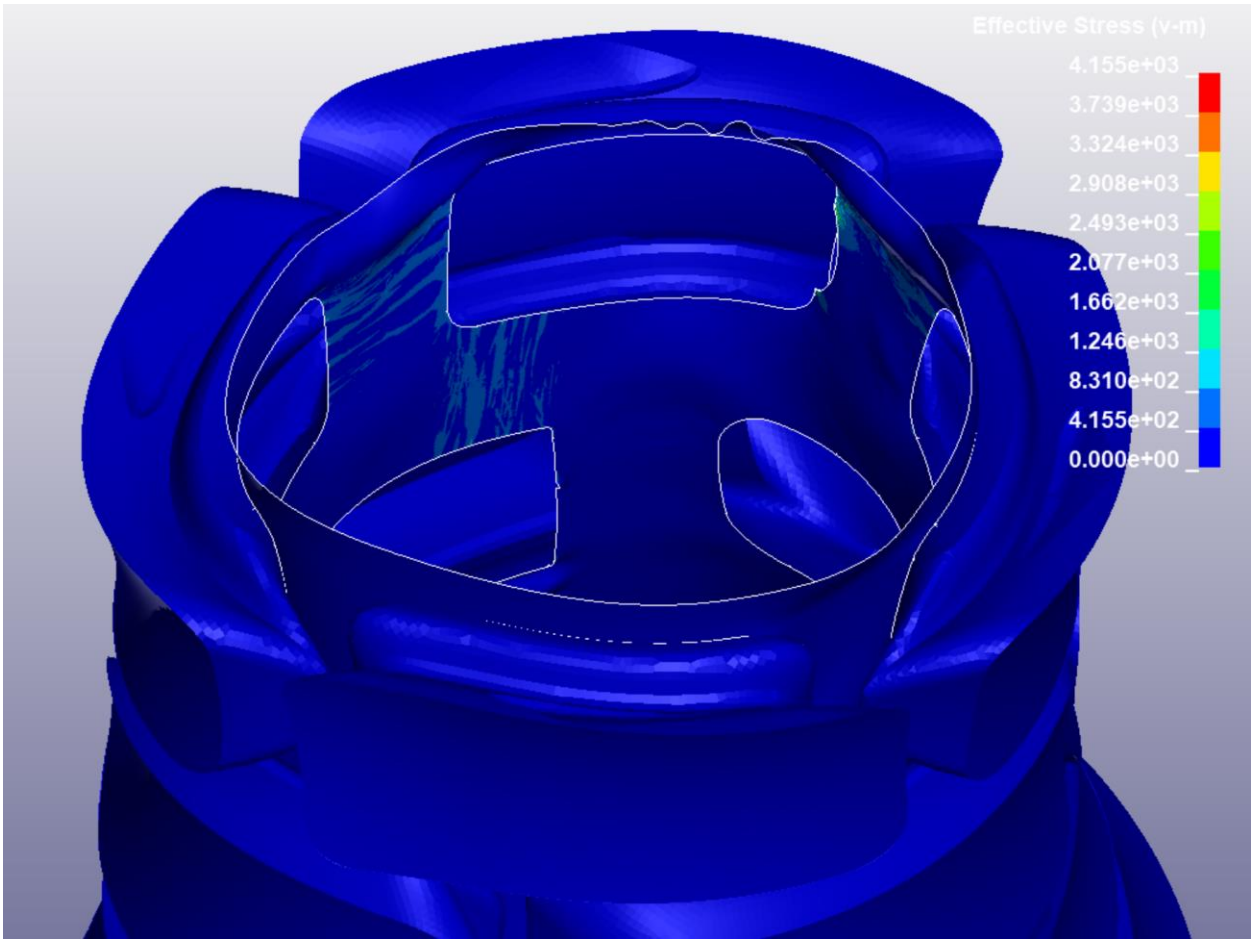

Figure 265: Fringes of von-Mises stress in the fabric (with the leg hidden from view for visibility), immediately prior to simulation failure.

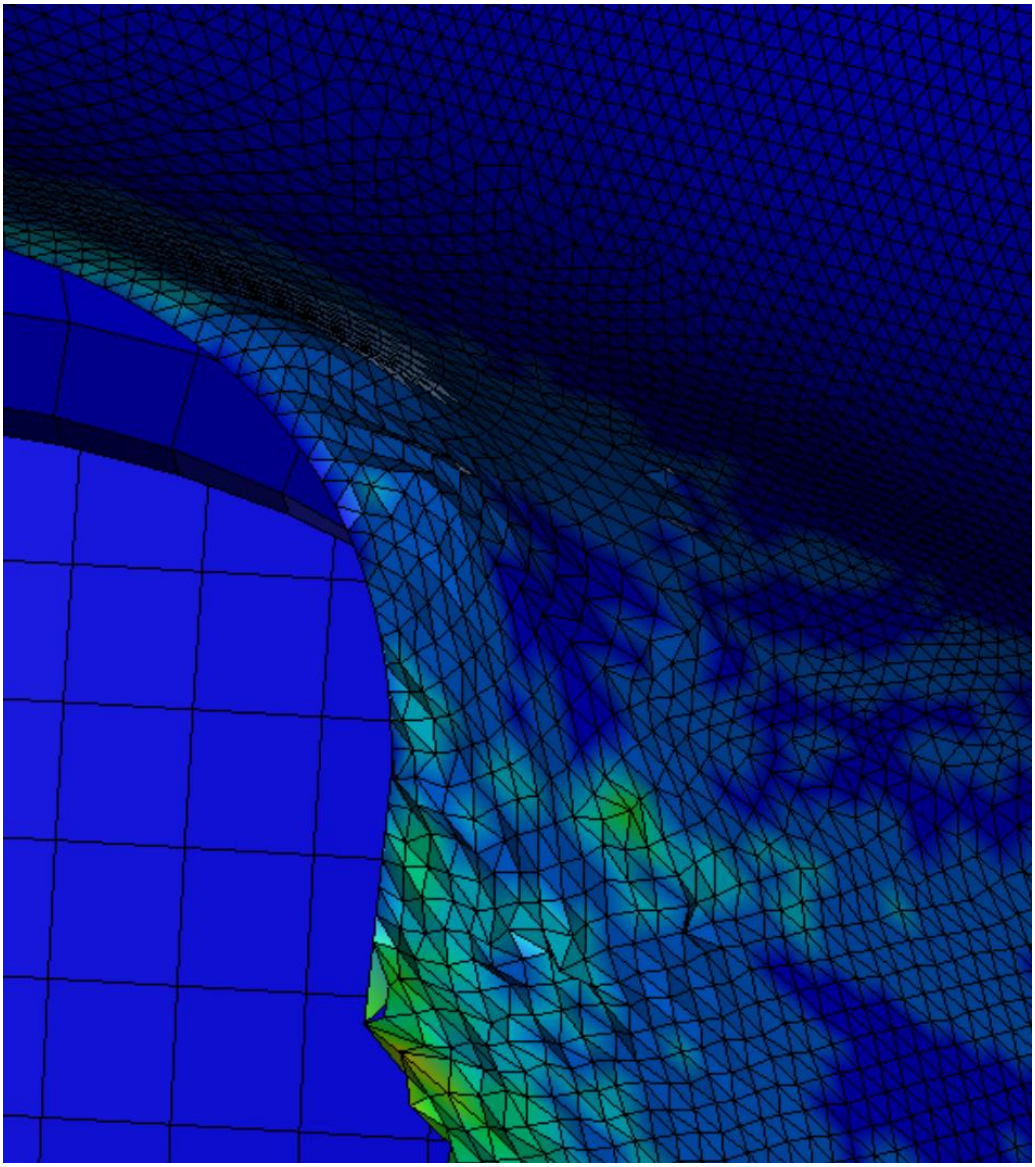

Figure 266: Closeup view of highly-distorted fabric elements. Note that the elements were initially nearly-perfectly-equilateral triangles, but some have since become highly elongated.

It should be noted that the simulation was repeated with a variety of changed parameters as well as many previous meshes (all documented in Appendix IV) in an attempt to correct this problem. For instance, various element formulations were used: in addition to the standard Belytschko-Tsay element (ELFORM=2 on the SECTION_SHELL card), the fast-fully-integrated element (ELFORM=16) and the fully-integrated element (ELFORM=-16) were also tried with poor results, as were the Hughes-Liu (ELFORM=1) and co-rotational Hughes-Liu

(ELFORM=11) shell elements. Membrane-type elements (which theoretically have zero bending stiffness and are effectively like origami in that they bend freely at shared edges), including ELFORM=5 (Belytschko-Tsay membrane) and ELFORM=9 (fully-integrated Belytschko-Tsay membrane) were also tried to little avail, though in any event using membrane elements is undesirable as they give the structure theoretically zero stiffness in shell bending (whereas even a fabric structure that is "soft" in bending does not have precisely zero bending stiffness). Additionally, a variety of through-thickness nodal integration points were used, including as many as five, with little benefit. Global mass damping (at 1% of critical) was also used with little apparent benefit. Fortunately, as described in Chapter 9, an alternative methodology proved successful for simulating the structure.

Conclusions.

Although MAT_235 gave good results when simulating an initially-planar array (as discussed in Chapter 5), it proved considerably more difficult for closed-surface arrays, as discussed briefly in this chapter, and documented more thoroughly in Appendix IV. As discussed in Chapter 8, the primary problem with MAT_235 appears to be difficulties in accurately simulating biaxial tension, although free (unshared) nodes in some areas between tiles and fabric may have contributed to the simulation failure. Thus, further research into accurate FEA of this type of structure is needed and will be conducted in the following chapters.

Chapter 8. Alternative Methods of Finite-Element Modeling of Woven Fabrics without MAT_235 in LS-Dyna.

Abstract.

This chapter considers various material models, element types, and overall strategies for modeling dry woven fabric in the LS-Dyna FEA package (version R8.1 for all files save for MAT_293, which required the newer R10.1). It first explores the apparent defect with MAT_235-MICROMECHANICS_DRY_FABRIC when placed into a biaxial tension state, resulting in unexpected simulation failure from apparently-random distortions of mesh Jacobians. Then, critical issues with MAT_234-VISCOELASTIC_LOOSE_FABRIC are disclosed for the first time, namely instant spurious element erosion when nodes are shared with rigid or elastic bodies of a different material or joined with tiebreak, welded, or similar constraints or contacts, stymieing this dissertation's goal of simulating composites consisting of dry fabric with rigid tiles permanently adhered thereto. Likewise, MAT_214-DRY_FABRIC is tested and found to have a similar critical issue as that for MAT_234, with the added problem of not accurately simulating a plain weave's trellis mechanism and having no way to specify fiber orientations. In turn, MAT_034-FABRIC is considered at length with various choices of the FORM parameter, including in its isotropic form, linear but orthotropic forms, and in multiple forms using tabulated data describing the weave's uniaxial, biaxial, and shear responses. Tabulated data is obtained from a direct FEA of a unit cell (with geometry generated via TexGen) for the target weave in question, and this data is then incorporated into MAT_034 with FORM=-14, in preparation for the FEA of the previous chapter to be redone with these material parameters. Additionally, the use of FEA at the yarn level to model woven fabrics, especially

those of unusual weave designs (such as woven Nitinol strips) is explored and adapted to the simulation of fabric-backed tiled arrays.

Introduction.

LS-Dyna stands out among all the commercially-available mechanical finite element codes for its wide array of continuum material models, with over 300 available in R12.0, the latest release as of this dissertation's publication. While simulating the mechanical behavior of dry fabrics does not attract nearly as much industrial or academic attention as simulating polymer-matrix composites reinforced with woven fabrics (or unidirectional tows), LS-Dyna nonetheless boasts several continuum material models that at least purport to accurately capture certain unique behaviors of woven fabrics. The most fundamental behavior of a single-layer woven fabric that must be accurately modeled with a material model is that its in-plane compressive stiffness should be orders of magnitude lower than its in-plane tensile stiffness, for in compression, the individual fibers that comprise the bundle that constitutes a warp or weft yarn easily buckle and are not bonded to each other in such a way as to augment the tow's bending stiffness. As a corollary, woven fabrics tend to have low though measurable bending stiffnesses. Next, the fabric's elastic stiffness should be quite high when tensioned along the warp or weft direction, at least once decrimping has occurred (i.e. initially-wavy yarns are tensioned to the point

Problems with MAT_235-MICROMECHANICS_DRY_FABRIC in LS-Dyna.

Since MAT_235 was highly effective in simulating planar arrays (as described in Chapter 7) but produced spurious simulation results (as described in the previous chapter) when applied to cylinder-like arrays, it was suspected that MAT_235 may have issues with accurately simulating the fabric when under biaxial tension; after all, the simple, planar arrays entailed

simple loadings (mostly bending and uniaxial tension). Indeed, MAT_235 is not widely used in the published literature, and when it is used, it is often for ballistic or jet-engine containment problems, though it is also sometimes informally recommended for fabric drape problems by technicians [150]. Additionally, extant literature describes checks on the accuracy of MAT_235 by simulating the "picture frame test" [150], which simulates fabric trellising under pure shear, and the uniaxial tension test, which simulates fiber decrimping in one direction [71], but no known mention of MAT_235 in the context of biaxial loading has been made in the public literature, let alone a more general loading consisting of biaxial tension plus shear. Consequently, it seemed wise to first simulate a basic biaxial tension test in LS-Dyna using MAT_235, to determine if the simulation would fail or result in excessive compliance. To this end, a 100x100mm flat shell was created in NURBS modeling software, and then some length of fabric was added to each edge, creating a plus-shaped fabric domain; four additional rectangular shells were then added, each sharing an edge with the fabric domain, so that node sharing could be enforced during the simulation. This CAD geometry is shown in Figure 267.

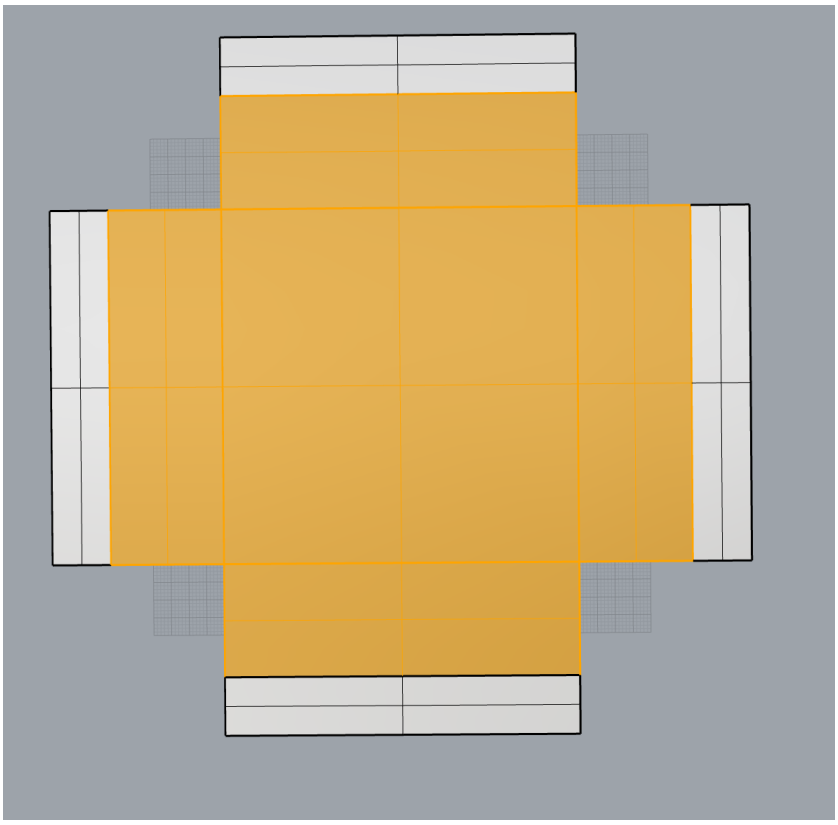

Figure 267: CAD geometry of a fabric sample to be tested in biaxial tension (yellow) and rigid bodies to apply the loads (light grey).

Once this geometry was created and exported in IGES format, it was meshed in LS-Dyna's PrePost preprocessor with a pure triangular mesh (as in the previous chapter it was determined that triangular meshes are more stable during such simulations, namely due to their resistance to hourglassing) with a characteristic element size of 0.6mm (roughly the size of elements in a coarse simulation from the previous chapter; fine simulations used a characteristic size closer to 0.15mm). Additionally, the four added rigid bodies were meshed in such a way that they shared nodes with the fabric. The resulting mesh is depicted in Figure 268. Note that its fineness is merely moderate, not exceptional.

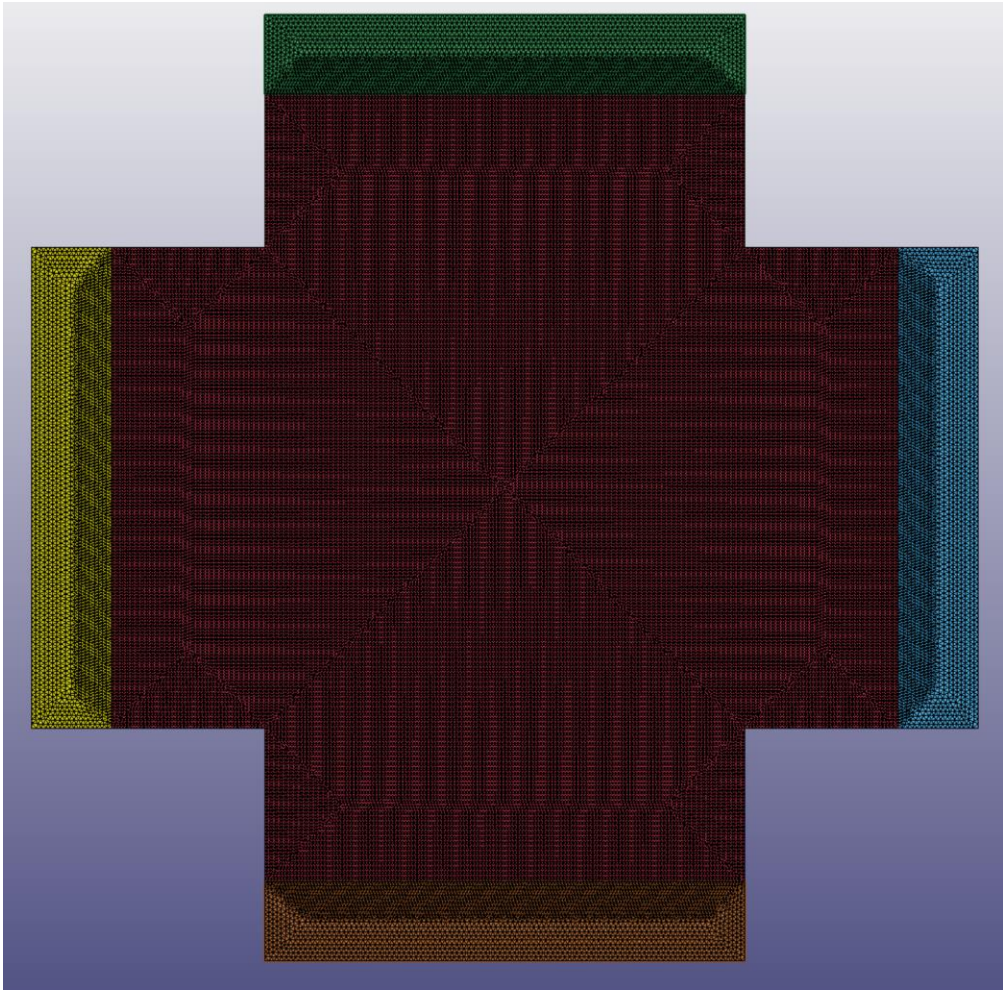

Figure 268: Mesh used for biaxial tension test of fabric sample with MAT_235 in LS-Dyna.

For boundary conditions, the bottom and left rigid bodies (colored brown and yellow, respectively, in Figure 268) had their displacements fixed to zero for the duration of the simulation, whereas the blue and green rigid bodies were merely constrained not to move out of plane and were loaded with a force. Strictly speaking, absolutely fixing both displacements on the left and bottom rigid bodies would result in a small amount of shear once the top and right rigid bodies were displaced appreciably form their initial positions, as well as of course biaxial tension, and this was seen as a positive feature since real loadings of the fabric in a cylinder-like protective array could involve both shear and biaxial tension.

The force with which the right and top bodies were loaded ramped from 0N to 10,000N in 0.01 seconds; certainly, this is a dynamic loading, but it was necessary to apply the load so fast in simulation time in order for the simulation to finish in a reasonable amount of "wall time" given the computing resources that were available at the time; since viscoelastic effects were disabled, the high strain rate that would result was not seen as especially inaccurate. Additionally, as described in the previous chapter, simulations of full arrays were also conducted at high speed in order to minimize the overall computation time. Of note, MAT_235 does not support implicit analyses as of this writing in LS-Dyna [84], so an implicit static analysis was out of the question.

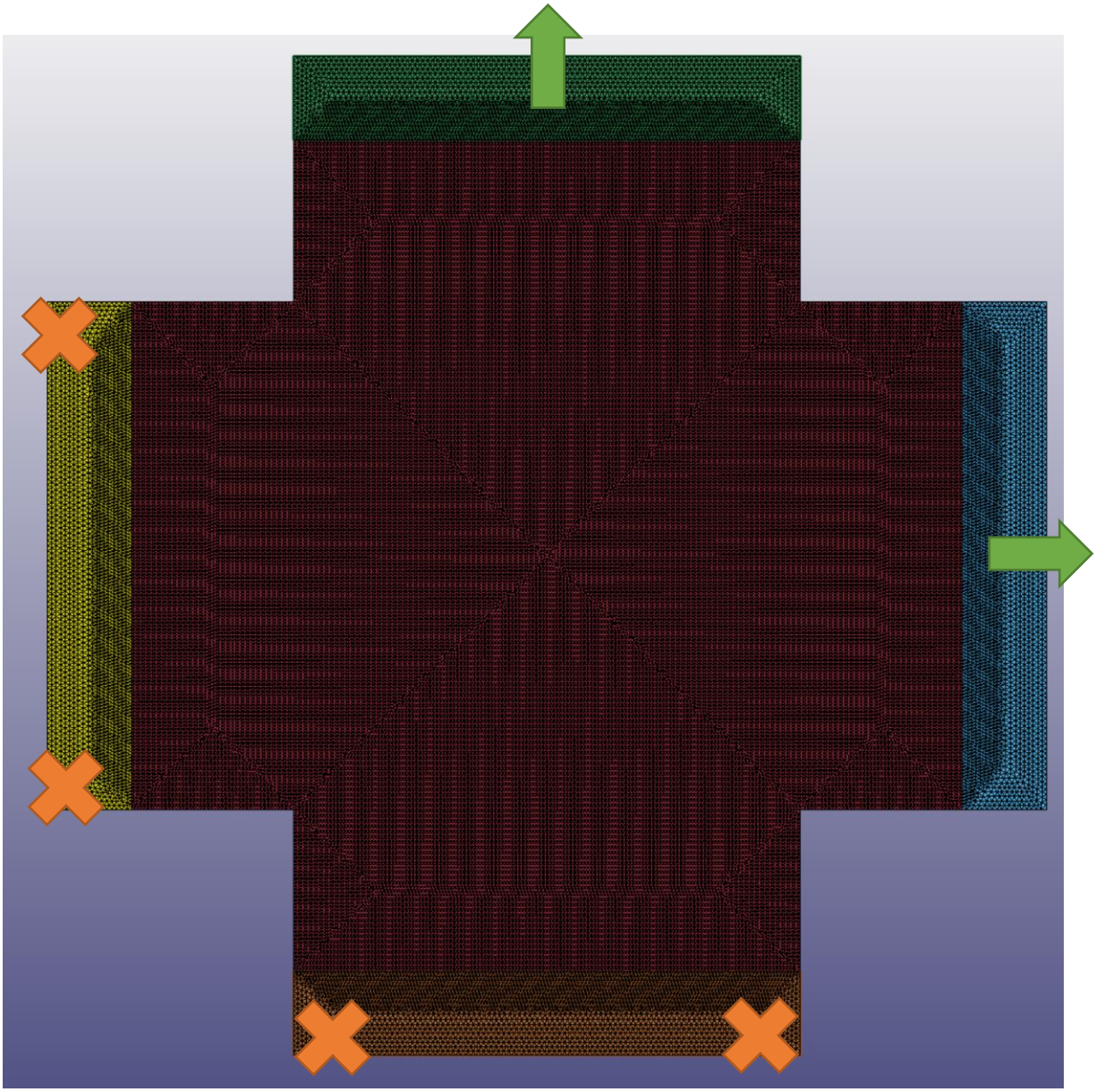

Figure 269: Undeformed mesh and boundary conditions. The green arrows indicate the direction in which ramped forces are applied; the orange Xs indicate the two rigid parts that are fixed in space. Only the maroon-colored body is assigned the fabric-micromechanics material model MAT_235; the other bodies are rigid bodies.

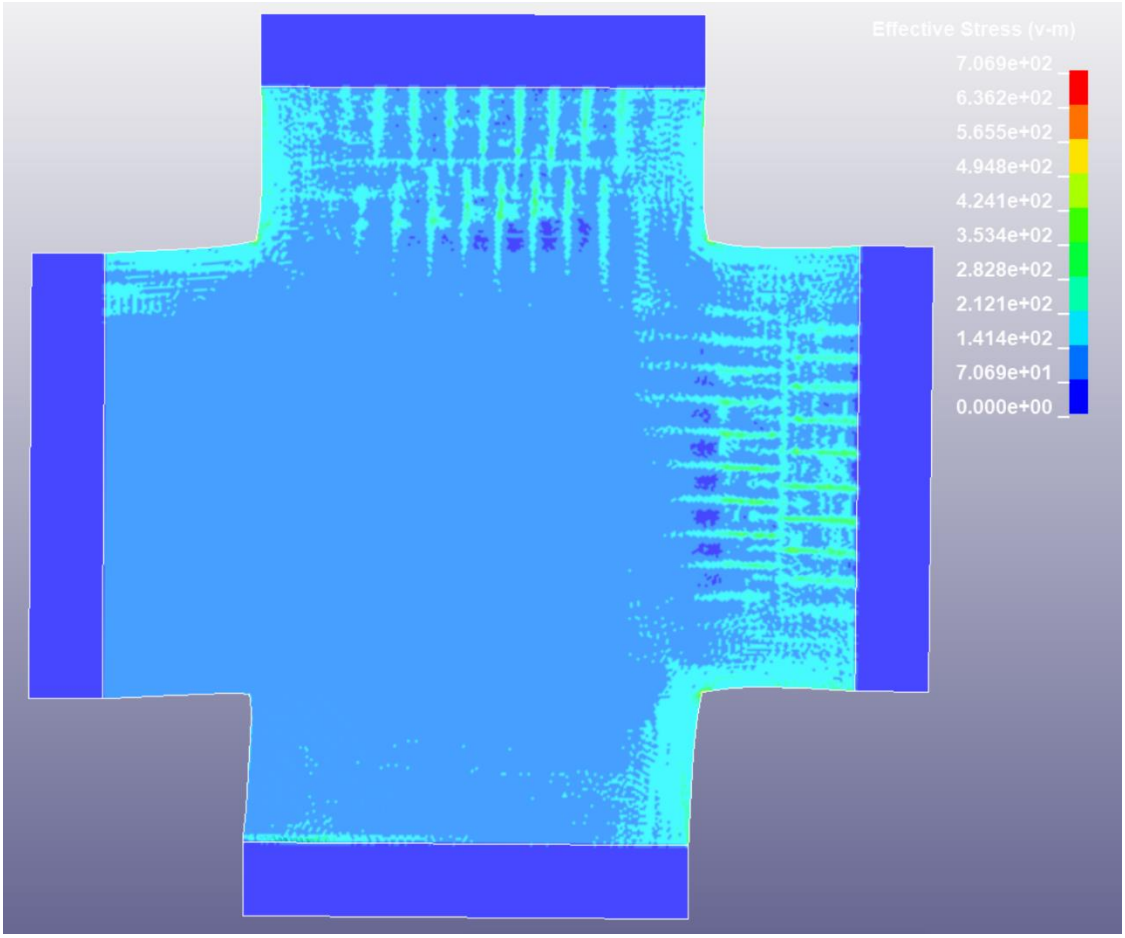

Figure 270: Simulation just prior to unexpected behavior, with right rigid body moving rightwards, top rigid body moving upwards, and left and bottom rigid bodies fixed. The contours of von Mises stresses are in MPa. While this figure does not show any unexpected behavior and is intended purely as a reference and proof that the simulation proceeded normally at least for some time, the next figure does show abnormal behavior.

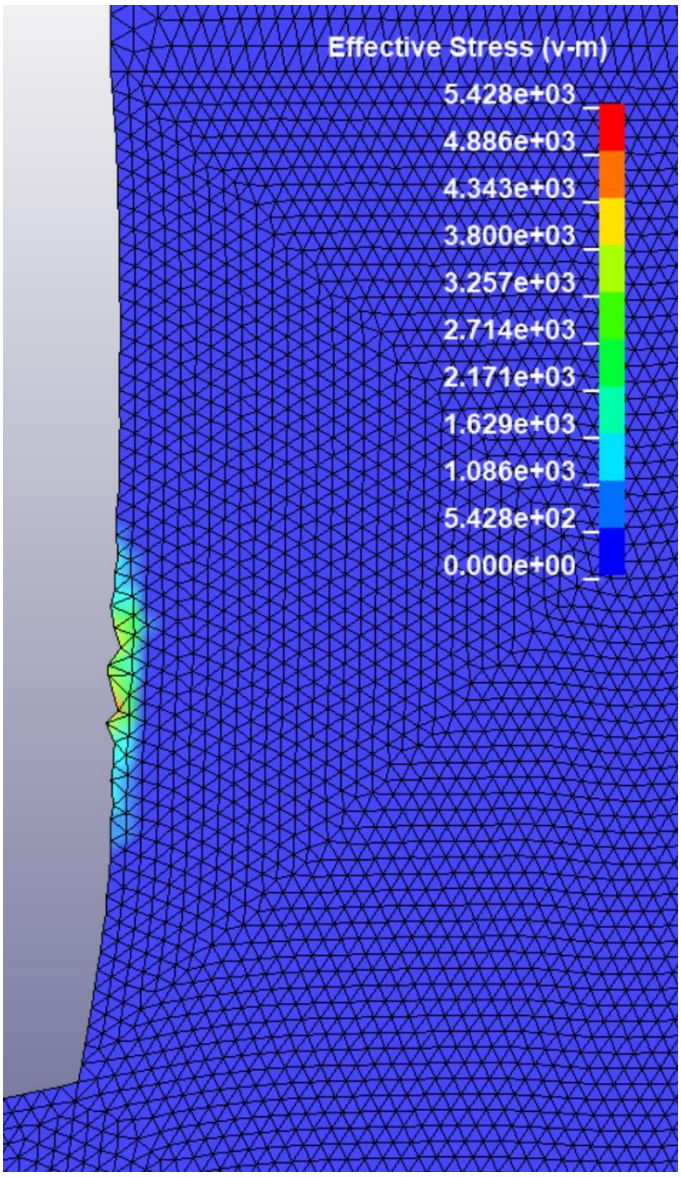

Figure 271: Several elements experienced a sudden and inexplicable rise in their stresses and distortions shortly after the position shown in Figure 270. Note that their von Mises stresses are now on the order of 3GPa compared with the more reasonable 200-500MPa of the previous figure, though the applied load is virtually unchanged from the previous snapshot. Moreover, these highly-stressed and distorted nodes are not even near a theoretical "stress concentration" such as a corner. This snapshot, at time 0.0037, was the result of a load only 1% higher than that shown in the previous figure.

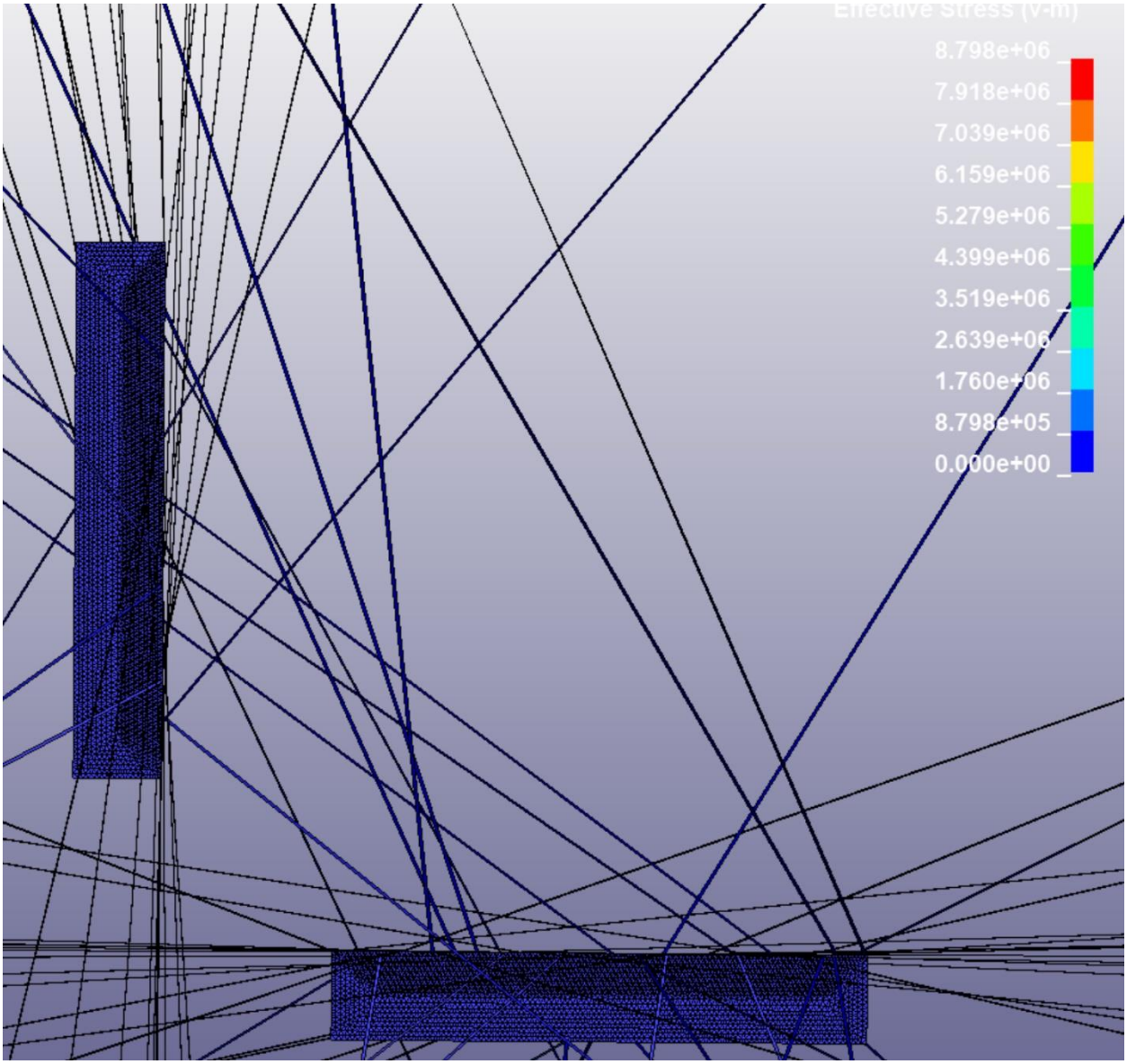

It should be noted that all analyses in this dissertation were performed with the double-precision executable of LS-Dyna R8.1: while the double-precision solver takes more computation time for the same timestep as compared with the single-precision solver, the double-precision solver is generally less vulnerable to simulation errors arising from undamped rounding errors magnifying. Certainly the double-precision solver is no panacea, nor is the use of the explicit FEA method (even though there are rarely convergence issues as such with explicit FEA, save when shockwave phenomena like high explosives are simulated; issues are usually of

another type, such as negative Jacobians in distorted meshes, programming errors in material models, etc.).

Velocity-Based Biaxial Tension Simulation.

The simulation was repeated with a constant velocity applied instead to each rigid body, producing biaxial extension. Although the precise stress distribution pattern prior to failure (shown in Figure 272) and the exact appearance of the "shooting nodes" differed from the previous case, the overall nature of failure was the same, as can be seen in Figure 273.

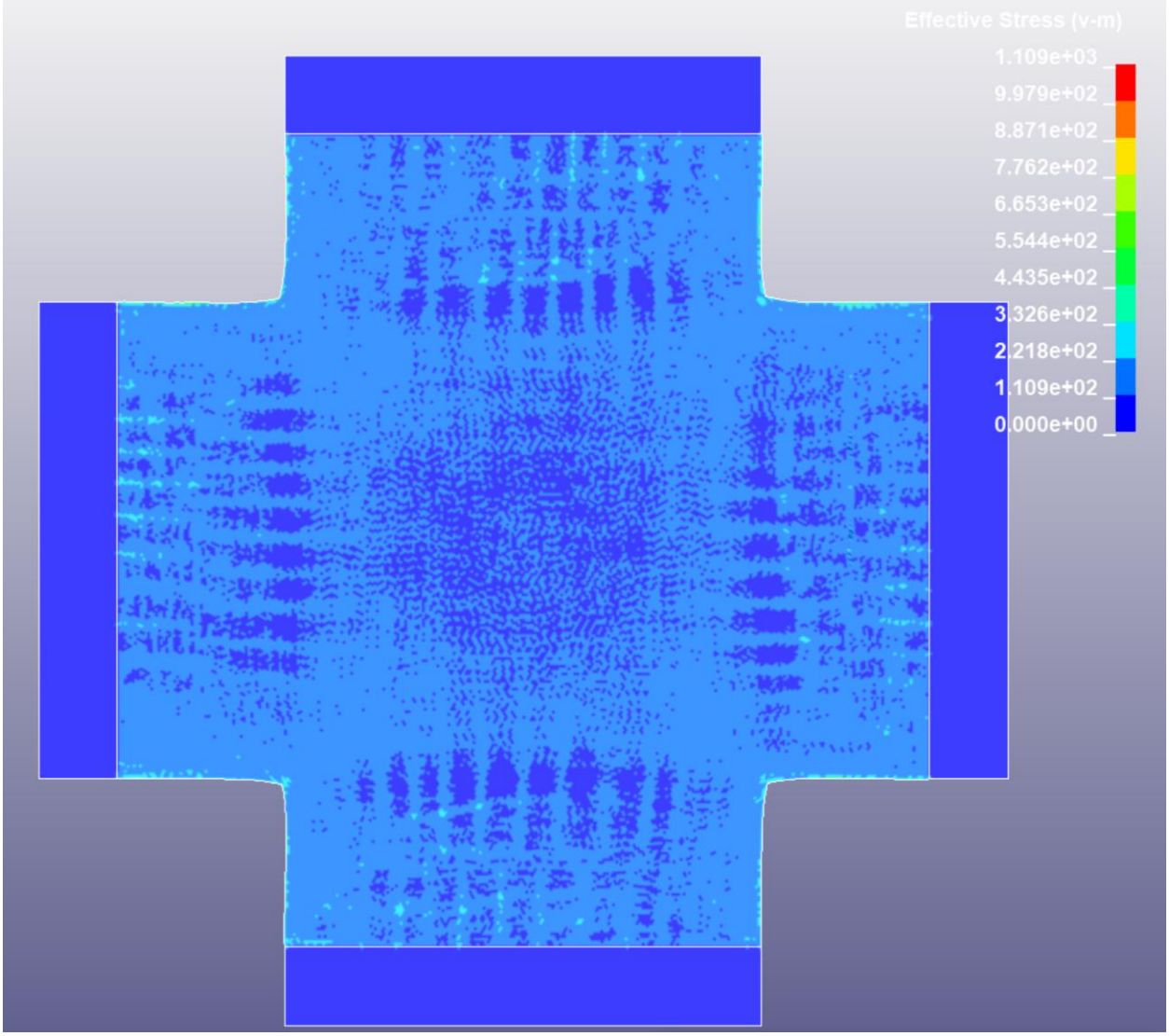

Figure 272: At simulation time 0.002s, immediately prior to the failure in the subsequent picture, there is little indication of stress concentrations or other sources of error. Since the contours of von Mises stresses plotted are in MPa, most regions of the fabric had stresses on the order of 200-400MPa, which is certainly not a non-physical amount of stress. Nonetheless, in the following timesteps, as can be seen in the next picture, the simulation failed catastrophically.

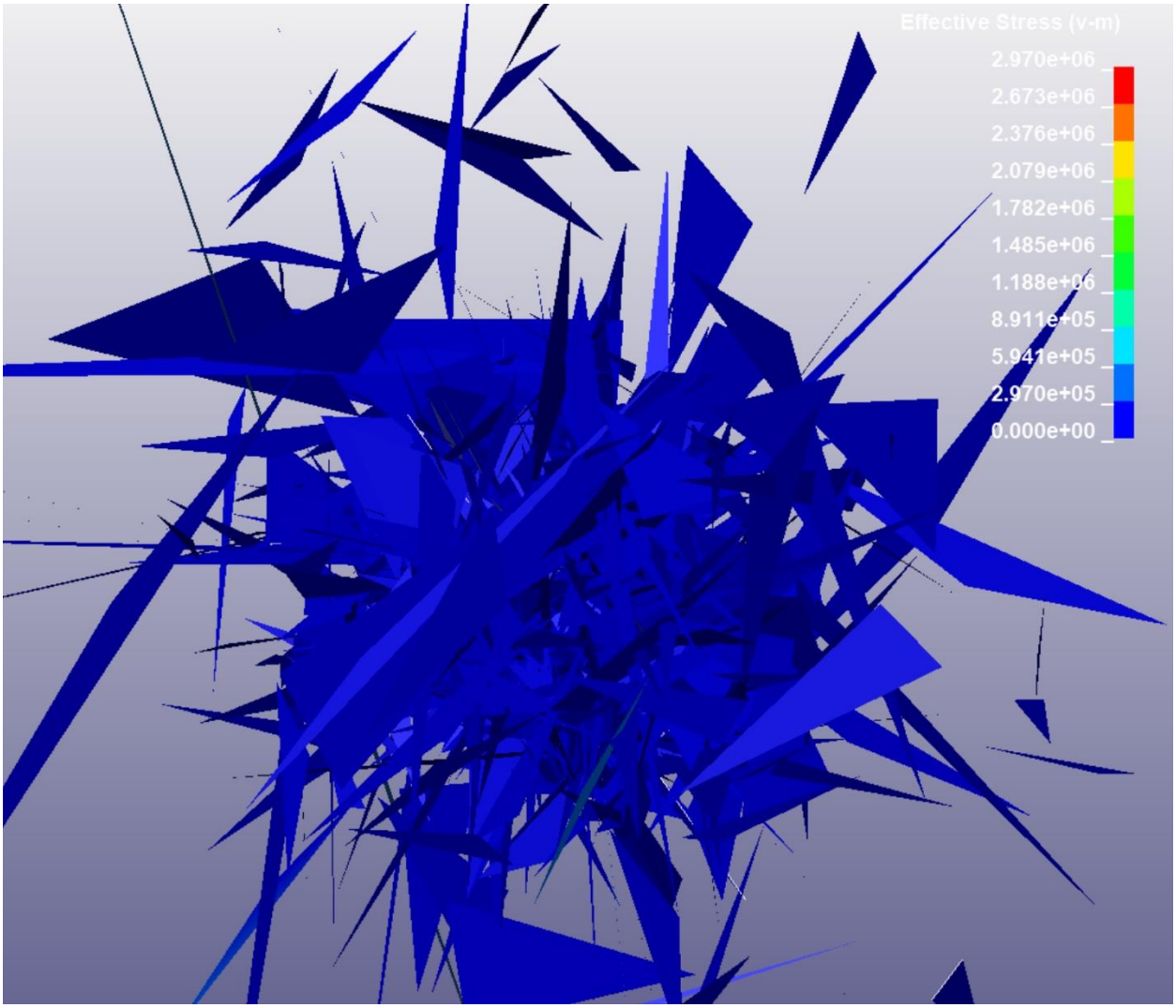

Figure 273: Immediately following the previous figure, this figure (at simulation time 0.0021) shows "shooting nodes" in the fabric and enormous stresses (on the order of 10^6 MPa, i.e. TPa, obviously non-physical in magnitude)

Simulations with MAT_234-VISCOELASTIC_LOOSE_FABRIC in LS-Dyna.

Comparison of MAT_234 and MAT_235.

Although its LS-Dyna ID precedes that of MAT_235, the paper disclosing MAT_234-VISCOELASTIC_LOOSE_FABRIC [151] was in fact published subsequently to that announcing MAT_235 [90], though both papers were written by the same authors (Tabiei et. al.). Interestingly, the 2004 paper disclosing MAT_234 does not cite the authors' earlier paper on

MAT_235, and indeed it makes no mention of MAT_235, to say nothing of contrasting the two or explaining when one is preferable over the other. Both material models can treat viscoelasticity (though MAT_234's designation in LS-Dyna as "VISCOELASTIC_LOOSE_FABRIC" in contrast to MAT_235's designation as "MICROMECHANICS_DRY_FABRIC" implies incorrectly that only MAT_234 supports viscoelasticity). Both are continuum models that attempt to treat the reorientation of yarns and micromechanic effects of fabric weaves. Certainly, MAT_234 offers the user far more parameters for specifying the nature of the weave: it allows the user to input the width of each yarn, the distance between yarns, the cross-sectional area of each yarn, and the real and effective thickness (where the effective thickness is determined by dividing the areal density of the particular weave by the mass density of the fabric overall [151]); in contrast, MAT_235 only allows the user to specify the undulation angle in the warp and weft and the angle at which the fabric/braid locks in shear (as well as the thickness assigned to the shell or membrane element). However, the specific yarn parameters that MAT_234 allows the user to input are in fact used mainly to calculate the undulation angle (for decrimping purposes) and braid locking angle that MAT_235 requires to be specified, so this difference is not as significant as it might appear. Likewise, an apparent difference that turns out to be semantic is the fact that the title for MAT_234 contains "loose" in the description but MAT_235's title does not; the user might be forgiven for errantly thinking that this means that only MAT_234 can simulate, although nonetheless the paper describing MAT_235 also shows a relatively loose weave with significant reorientation and trellising effects [86].

MAT_234 and MAT_235 in Academic Literature.

Ultimately, little formal literature is available on the proper uses of either MAT_234 or MAT_235. Fein's Master's thesis [91] explores the use of MAT_234 for simulating impact between a steel impactor (simulating an engine fragment) and dry woven Kevlar fabric acting as a jet engine protector; it makes no mention of the competing MAT_235 material model, and is not especially concerned with the micromechanical kinematic behavior of fabrics (trellising/shearing along the bias, etc.). Likewise, Fang et. al. employed MAT_234 for modeling the impact of a metal penetrator on Kevlar fabric [152], making no mention of MAT_235. Finally, Zhenhua et. al. also simulated Ti6Al4V and steel projectiles impacting on Kevlar 49 fabrics that acted as containment vessels with MAT_234, again not mentioning MAT_235 [153].

Morka et. al. used MAT_235 instead of MAT_234 to model the impact of a punch indenter on a layer of Twaron T750 fabric [154], with no mention of MAT_234 (let alone why MAT_235 was preferred), and similarly, Dotoli and Rizzo repeated the test on Twaron and Innegra fabric and compared a simulation of the test with MAT_235 [155], again making no mention of MAT_234. Finally, Hill's dissertation, mentioned previously, explores the use of MAT_235 to model Kevlar fabric in a hypersonic inflatable aerodynamic decelerator, and even compares experimental uniaxial testing of a fabric sample with the simulation of the same test, but makes no mention of MAT_234 as a competing material [71]. Beyond this, no journal or conference papers in which MAT_235 is employed for any purpose involving dry fabric are known, though a few other papers reference the material model or propose its combination with other material models to simulate laminated composites (a strange proposition since LS-Dyna already offers many material models for laminated composites).

Thus, it should be apparent that even using MAT_234 or MAT_235 in LS-Dyna is an advanced and rarely-performed undertaking, with little relevant public literature to guide the user even on using MAT_234 for its intended purpose (simulating the damage of high-strength fabrics), let alone for the more-exotic use of simulating the kinematic behavior of woven fabrics in complex loadings, on which no literature at all was found.

Parameters for MAT_234 for Simulations of Dry Kevlar Fabric.

Parameters for simulating woven Kevlar fabric with MAT_234 in LS-Dyna were conveniently shared with the public in Fein's Master's thesis [91], and they are repeated in LS-Dyna card form in Figure 274 in the N-mm-s consistent unit system.

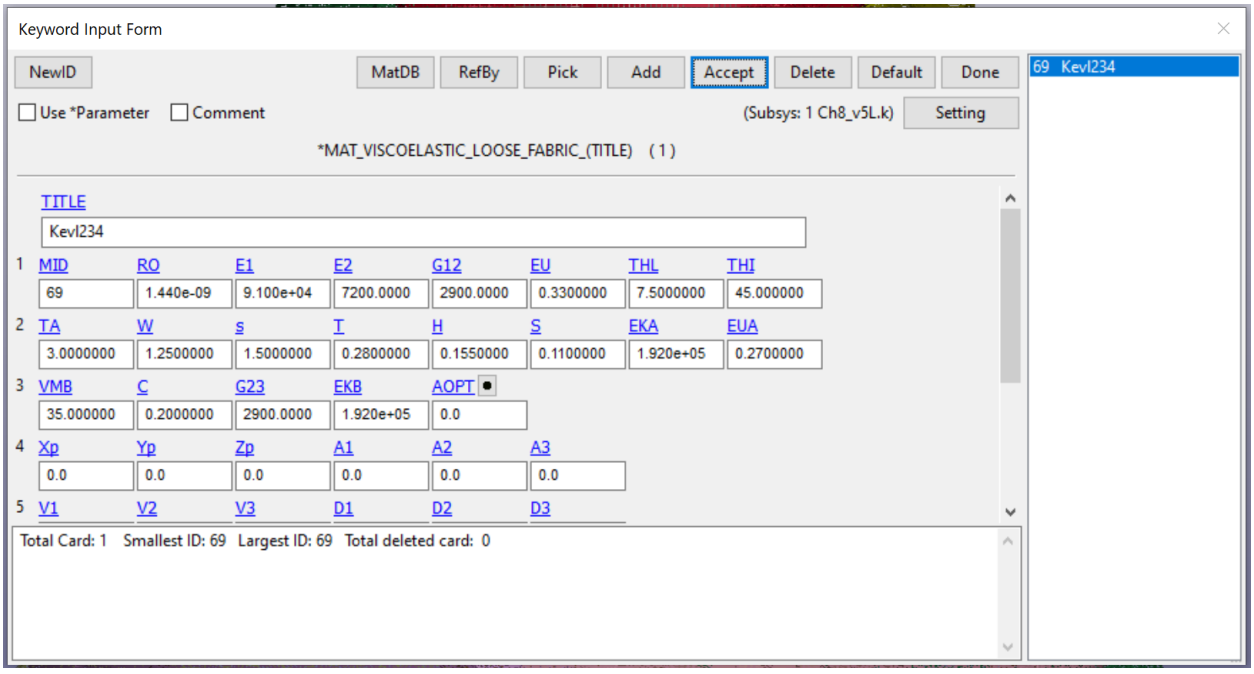

Figure 274: LS-Dyna card with properties for simulating Kevlar fabric with MAT_234 in the N-mm-s consistent unit system, taken from [91].

Simulations of Fabric-Backed Tiled Arrays with Node-Sharing to Connect Tiles to Fabric and with Fabric Modeled with MAT_234.

Immediately upon running the simulation with MAT_234 (which featured the same mesh as that used in Chapter 7 with MAT_235; see Figure 253 for instance), the solver began warning of failure in the yarns, with sample text output from the solver shown in Figure 275. Most remarkably, the solver predicted warp and fill yarn failures *even prior* to the first timestep and the d3plot being written at time 0 (with a screenshot of the error message shown in Figure 275), which is unheard of—usually a d3plot file is written at the first timestep prior to any mechanical initialization, etc. Additionally, when an attempt was made to evaluate von Mises stresses on the fabric part (with presumably all elements eroded), the post-processor indicated the range of von Mises stresses was from -1e20 (sic—von Mises stresses can never be negative as they are derived from a square-root relationship between the three principal stresses) to 1e20, though no elements were seen, as shown in Figure 276. Indeed, even in the first d3plot file at timestep 0 all fabric elements had been deleted, with the remainder of the mesh shown in Figure 277.

```
10957173 Element      3391652 failure:
10957174 secondary bond fill yarn, secondary bond warp yarn.
10957175  Element      3391742 failure:
10957176 secondary bond fill yarn, secondary bond warp yarn.
10957177  Element      3391785 failure:
10957178 secondary bond fill yarn, secondary bond warp yarn.
10957179  Element      3391864 failure:
10957180 secondary bond fill yarn, secondary bond warp yarn.
10957181        1 t 0.0000E+00 dt 1.38E-12 write d3plot file          02/15/21 13:51:10
10957182 secondary bond warp yarn.
10957183  Element      2347994 failure:
10957184 secondary bond fill yarn, secondary bond warp yarn.
10957185  Element      2347995 failure:
10957186 secondary bond fill yarn, secondary bond warp yarn.
10957187  Element      2347996 failure:
```

Figure 275: Solver output predicting fill and warp failures in MAT_234 even before the first timestep.

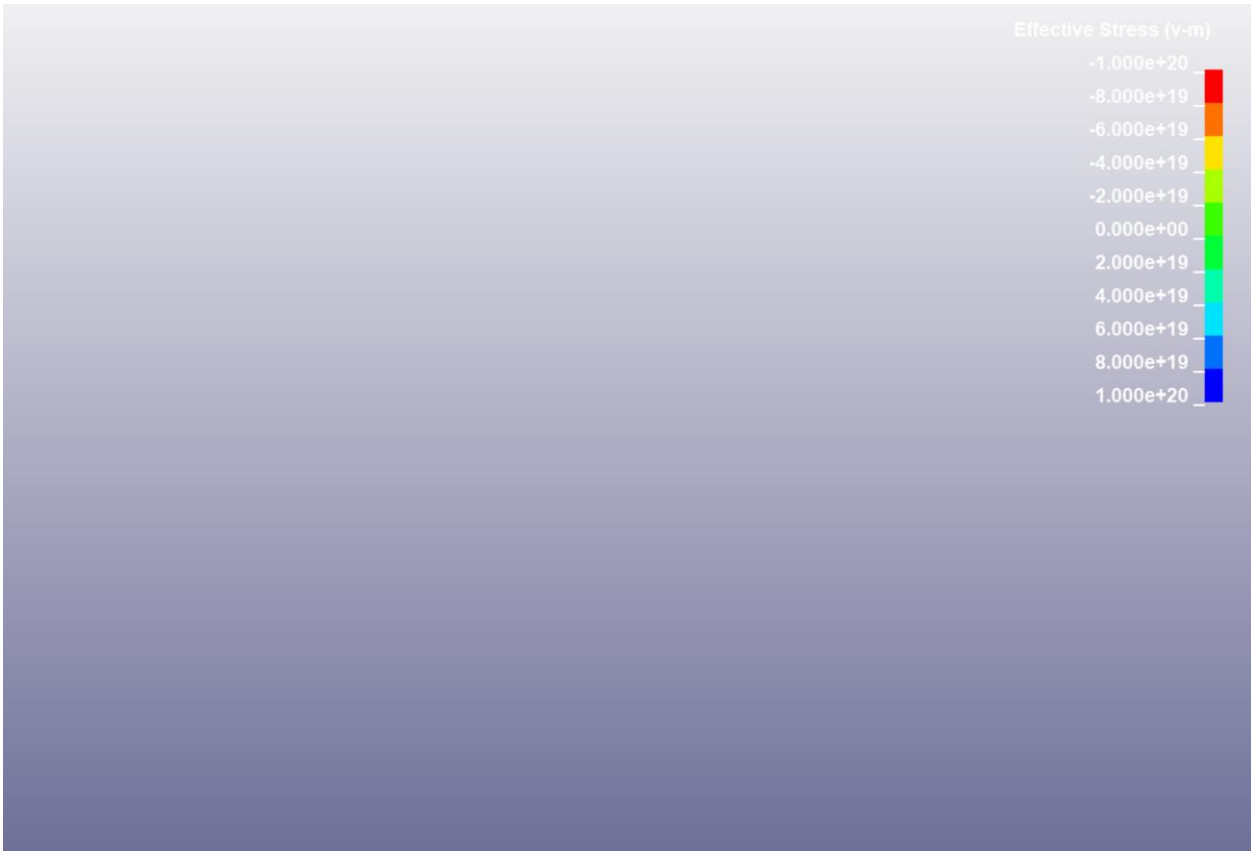

Figure 276: At the first timestep in the simulation, when the initial state is supposed to be output, the solver had already eroded all fabric elements, and claimed that the potential range of von Mises stresses in the fabric was between -1e20 and 1e20, which is obviously impossible (especially considering that von Mises stresses are magnitudes that must always be positive).

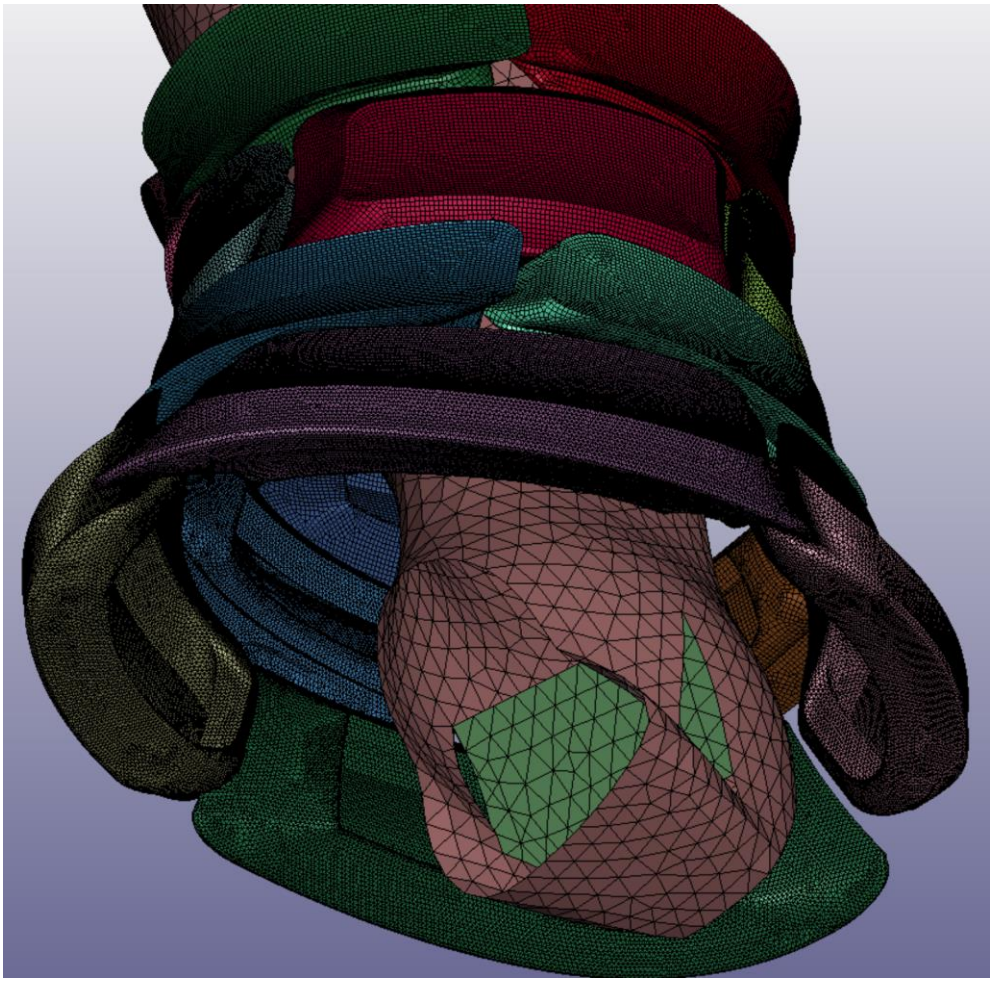

Figure 277: Even in the first timestep, the d3plot file was missing all fabric elements from erosion prior to the first timestep, so this is what remained of the mesh.

Simulations of Fabric-Backed Tiled Arrays with Various Bonded Contacts to Connect Tiles to Fabric and with Fabric Modeled with MAT_234.

The unexpected failure when using MAT_234 described in the previous section occurred when nodes were shared between tiles and fabric; thus, it seemed wise to try other simulation methods of joining tiles to the fabric, namely with generalized welds, spotwelds, tied and tiebreak contacts, etc. The mesh for these simulations that feature bonded contacts between tiles and fabric was necessarily quite different from the previous mesh wherein nodes were shared between tiles and fabric; in this case, the fabric mesh had no holes at all, and the rigid tiles were

likewise closed surfaces (though still modeled with shell elements, rather than meshing the interior with solid elements), with the surfaces roughly overlapping but nodes not necessarily coinciding. The mesh used is shown in Figure 278; note that the fabric mesh is coarser than that used for node-sharing simulations, because there are no complex hole edges to conform to, and because these simulations were intended simply as benchmark problems to determine how, if at all, it might be possible to simulate rigid tiles on flexible fabric using MAT_234.

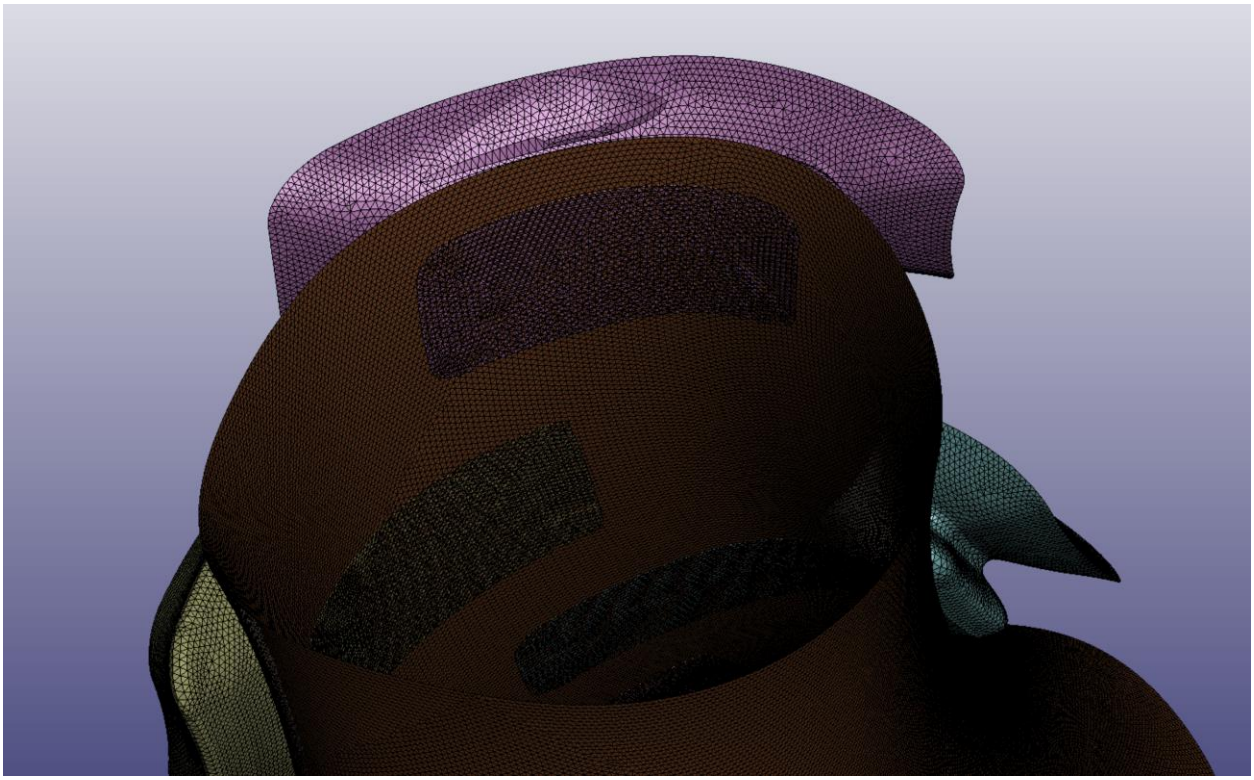

Figure 278: Mesh for simulations using general welds, spotwelds, tied/tiebreak contacts, etc. Note that the fabric mesh no longer has holes in it and instead roughly overlaps with the interior surfaces of the tiles, which are themselves also closed surfaces (unlike with node-sharing simulations, in which case the tiles were open surfaces).

Unfortunately, every possible method for simulating a bond between tiles and fabric caused the solver to instantly (usually literally at the third timestep, which was on the order of a nanosecond in simulation time) begin eroding MAT_234 elements after the bonding method caused enormous and non-physical stresses in the fabric: the keyword file was modified to output

d3plot files every timestep in order to observe this behavior in real-time, and a fringe plot of enormous, non-physical von Mises stresses is depicted in Figure 280. Additionally, a screenshot of the text output from LS-Dyna is printed in Figure 279 (when the user has specified MAT_234, the solver prints a message upon erosion of an element for failure of warp or weft yarns); the solver indicates that warp and weft yarns fail separately and then the elements are eroded.

```
 S t o r a g e   a l l o c a t i o n

 Memory required to begin solution      :      14M
 Additional dynamically allocated memory:     135M
                                Total:     148M
       1 t 0.0000E+00 dt 3.04E-06 flush i/o buffers          03/15/21 10:09:45
       1 t 0.0000E+00 dt 3.04E-06 write d3plot file          03/15/21 10:09:45
       2 t 3.0397E-06 dt 2.96E-06 write d3plot file          03/15/21 10:09:46
 Element      1606836
 failure: primary bond warp yarn, .
 Element      1606836
 failure: primary bond warp yarn, .
 Element      1606836
 failure: primary bond warp yarn, .
 Element      1606836
 failure: primary bond warp yarn, .
 Element      1609299
 failure: primary bond warp yarn, .
 Element      1609299
```

Figure 279: Text output from the LS-Dyna solver predicting yarn failure in MAT_234 elements on the second timestep.

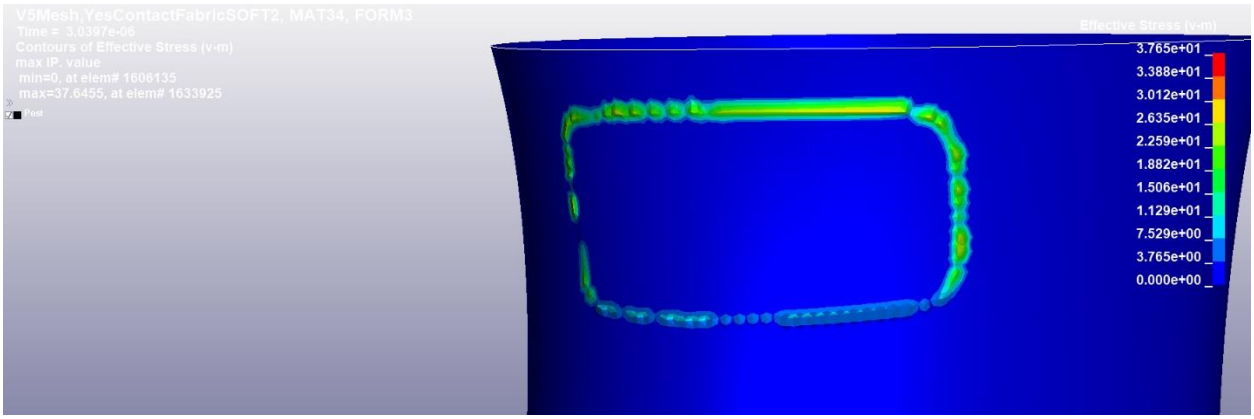

Figure 280: Von-Mises stresses in the fabric on the second timestep in the region of the bond between the tile and the fabric. Note that there is no contact yet between the leg and tile, so there should be no stress in the fabric whatsoever, but in fact there is already both stress and significant distortion of the fabric (with elements "dimpling" and being pulled normal to the fabric surface).

Problems with MAT_214-DRY_FABRIC in LS-Dyna when Simulating Fabric-Backed Tiled Arrays.

Introduction to MAT_214

Researchers at Arizona State University initially created a user-written material model in LS-Dyna that was then incorporated by LSTC into the program as MAT_214-DRY_FABRIC relatively recently in 2014 (a decade after MAT_234) [88]. Like the aforementioned MAT_234 and MAT_235 (as well as MAT_034, to be discussed below), MAT_214 is intended to simulate woven fabrics without any matrix constraining the fibers against bending, shear, or in-plane compression. Indeed, LSTC claims that MAT_214 is superior to MAT_234 and MAT_235 in that MAT_214 allegedly is more accurate in its handling of fabrics that have undergone significant shearing (resulting in yarn rotations according to the freedom allowed by the "trellis mechanism" of a weave), because MAT_214 tracks the two orthogonal fibers independently [156]. Indeed, this is the only extant acknowledgement in the literature that the previous dry fabric material models (MAT_234 and MAT_235) might have accuracy issues in shear, and this may explain some of the issues with MAT_235 disclosed in a previous section of this chapter (though MAT_235 was also found to produce fatal simulation errors when a fabric domain was simulated strictly in biaxial tension without significant shear). However, LSTC states that MAT_214 is most suited for simulating containment vessels and personal body armor made of high-strength fabrics, both of which do not involve significant global fabric shearing, which may thus constitute an acknowledgement that MAT_214 is still not especially accurate for simulations of fabrics whose behavior is dominated by the trellis mechanism of the weave. Finally, it should be noted that MAT_214 does not handle biaxial stiffening of woven fabrics (whereby the elastic tension response in one direction becomes stiffer if the fabric has already

been placed into tension in the orthogonal direction), though this stiffening property should be a second-order effect in and of itself; the greater concern with biaxial loadings is that the material model may exhibit spurious failure when loaded thusly (as did a fabric domain simulated with MAT_235, as discussed in a previous section of this chapter).

Proposed Material Properties for MAT_214.

Some properties required for MAT_214 to simulate woven Kevlar 49 fabric were straightforward, such as the warp and weft elastic moduli (assumed to be around 91GPa in accordance with previous simulations). However, without the equipment to perform testing on fabric specimens, it was necessary to find certain other measures demanded by the model from the extant literature. In particular, MAT_214 treats the curve relating in-plane shear strain to shear stress as a piecewise-linear curve with three different line segments and thus secant moduli, namely G_{AB1}, G_{AB2}, and G_{AB3}, as well as the two attendant shear strains at which the curve changes slope (γ_{B1} and γ_{B2}). Additionally, MAT_214 treats decrimping effects (as well as failure and post-failure effects) in the longitudinal and transverse directions with piecewise linear relations as well, requiring the appropriate moduli and strains at which decrimping is finished, etc. Fortunately, researcher Zekan He et. al. shared the material parameters they used to simulate a containment vessel wrapped with Kevlar 49 using MAT_214 for the fabric [157]. A screenshot containing these values, loaded into the card deck in LS-PrePost, is shown in Figure 281. A graph of the corresponding uniaxial tensile stress-strain response for the given values based on the interpretation given in the LS-Dyna User Manual for Material Models [84] is shown in Graph 24, and that for shear stress and strain is shown in Graph 25. Note that the User Manual indicates that MAT_214 has a hysteretic unloading profile, but this was not explored in the graphs as it is expected that the load in the fabric would be more or less monotonically

increasing and thus less important to explore here (in fact, as will be noted below, the material model immediately produced fatal errors when used, preventing the fabric even from being loaded appreciably, let alone unloaded).

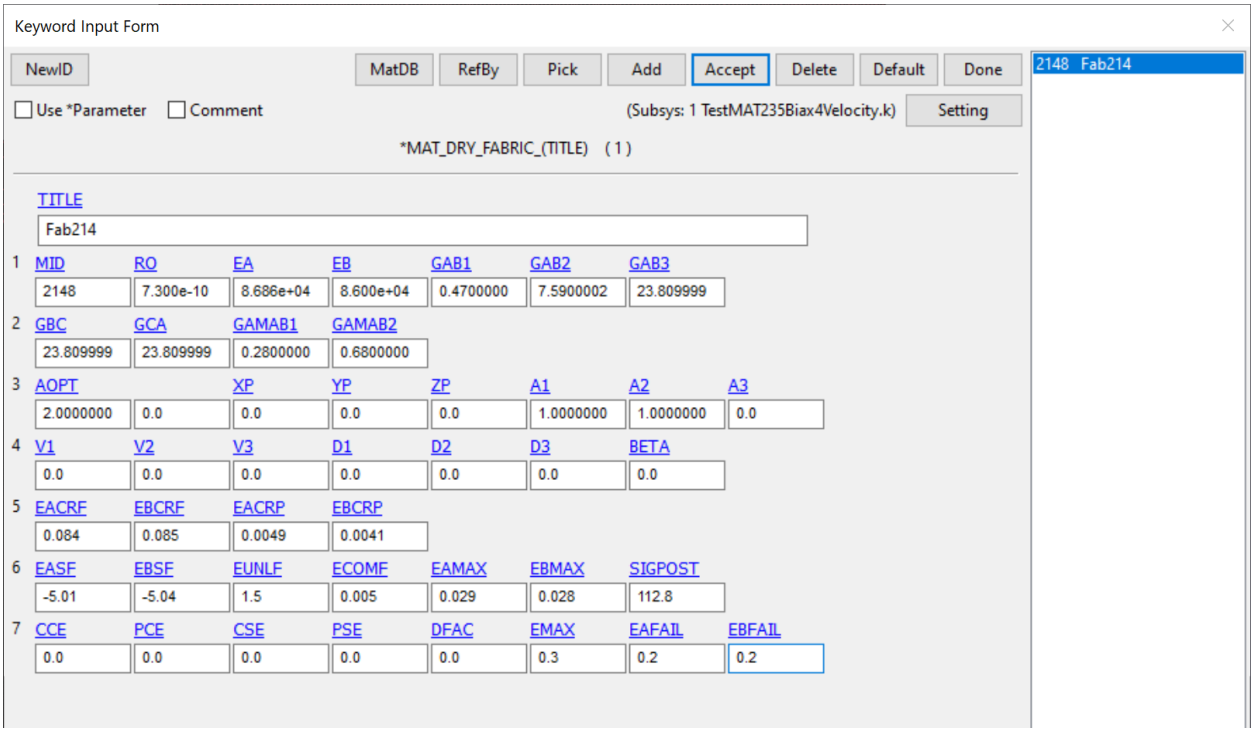

Figure 281: Proposed constants for MAT_214 in LS-Dyna, using the N-mm-s consistent unit system.

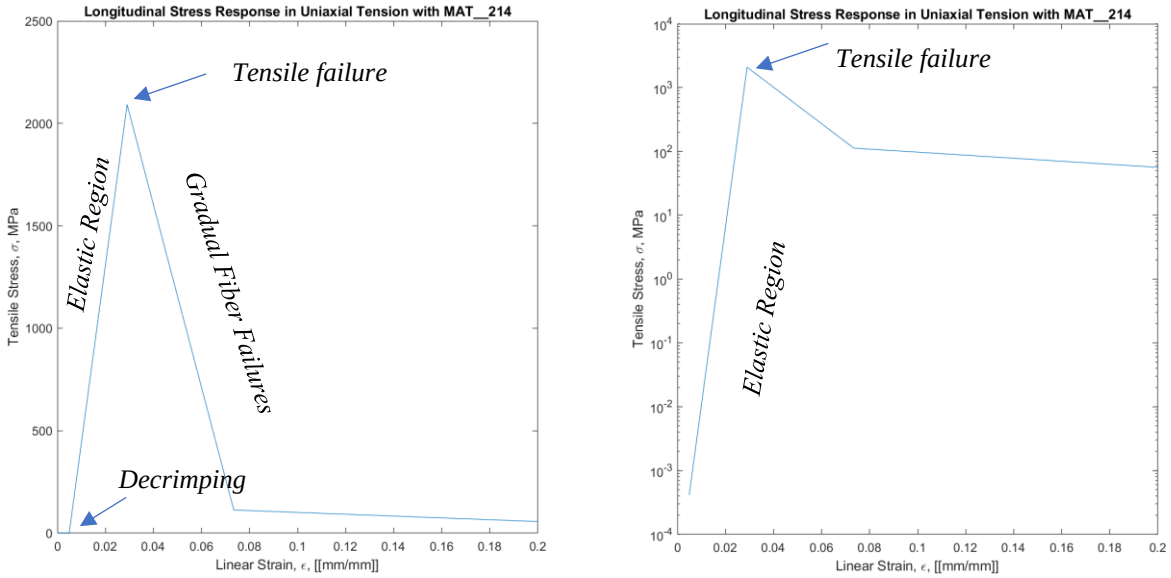

Graph 24: Tensile stress-strain response of MAT_214 using the proposed constants shown in the previous figure (the same graph is shown twice, in semilog scale on the right hand side to better illustrate that the decrimping region does not have precisely zero stiffness, merely very low stiffness).

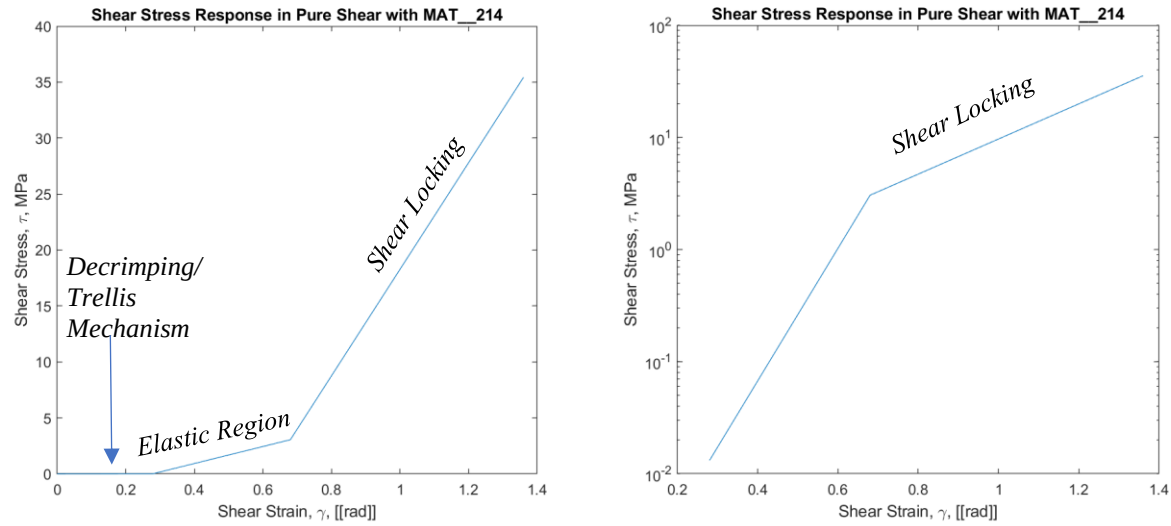

Graph 25: Shear stress-strain response of MAT_214 (the same graph is shown twice, in semilog scale on the right hand side to better illustrate that the decrimping region does not have precisely zero stiffness, merely very low stiffness).

Like MAT_234, MAT_235, and indeed many other anisotropic materials, MAT_214 allows the user to specify the principal material direction with the AOPT parameter (e.g. with ELEMENT_SHELL_BETA or with a global direction vector depending on which choice of

AOPT is made). However, unlike MAT_234 and MAT_235, the user may not specify a non-orthogonal initial weave pattern or multiple directions for fibers; thus, MAT_214 appears intended for use with fabrics that initially have the warp and weft perpendicular to each other and have not been sheared prior to the simulation, so the BETA direction should apparently correspond to either the warp or weft (unlike with MAT_234 and MAT_235, where the BETA direction corresponds to an offset by the amount of the braid angle from the warp or weft). On the other hand, the user has the option of specifying different tensile properties for the warp and weft yarns (in case it is a hybrid weave, e.g. Kevlar in one direction and carbon fiber in another, or merely in case the warp yarn is damaged during the weaving process to the point of having different elastic properties); this is not possible in MAT_234, nor in MAT_235.

Simulations of Fabric-Backed Tiled Arrays with Node-Sharing to Connect Tiles to Fabric and with Fabric Modeled with MAT_214.

Unfortunately, attempting to simulate the fabric-backed array using MAT_214 for the fabric material model and using node sharing between tiles and fabric as the means of adhering them in LS-Dyna produced an inexplicable error: nodes in the model were rapidly dragged towards the origin point of the entire model (i.e. <0,0,0> in model coordinates) and then eroded. Needless to say, there is no logical physical explanation for such behavior. This strange movement of nodes to the origin point and erosion had nearly finished by a simulation time of 1e-5 seconds, orders of magnitude faster than the onset of contact between the rotating leg and tiles, so it appears to be the result of a programming error or incompatibility with sharing nodes, not excessive leg rotation speed. (The error was repeated whether the tiles were given a rigid material or a linear elastic one). Screenshots of the progression of this inexplicable behavior are shown in Figure 283 and Figure 284. Of note, the simulation was attempted both with

membrane elements (either ELFORM 5 or its fully-integrated cousin ELFORM 9 on the SECTION_SHELL card) as recommended by the LS-Dyna Material Manual [84], and also non-membrane shell elements (either the fully-integrated ELFORM 16 or the simpler Belytschko-Tsay formulation with ELFORM 2), as recommended by Yeager et. al [158]; thus, there was no apparent easy solution to the problems involving MAT_214. Additionally, the tiles were made linear-elastic instead of rigid in case some tiny amount of compliance was needed, to no avail. If d3plot files are plotted at literally every timestep (on the order of 1e-9 seconds) just to observe the first few timesteps, it becomes apparent that massive stresses (even at the first timestep they are on the order of 1.5GPa) develop at some but not all of the shared nodes between fabric and tiles when the fabric is simulated with MAT_214, as shown in Figure 282. Why such stresses develop only at some fabric nodes (belonging to elements of excellent quality, nearly perfect equilateral triangles) is unclear; certainly, this behavior has not been reported in the small amount of extant literature on MAT_214.

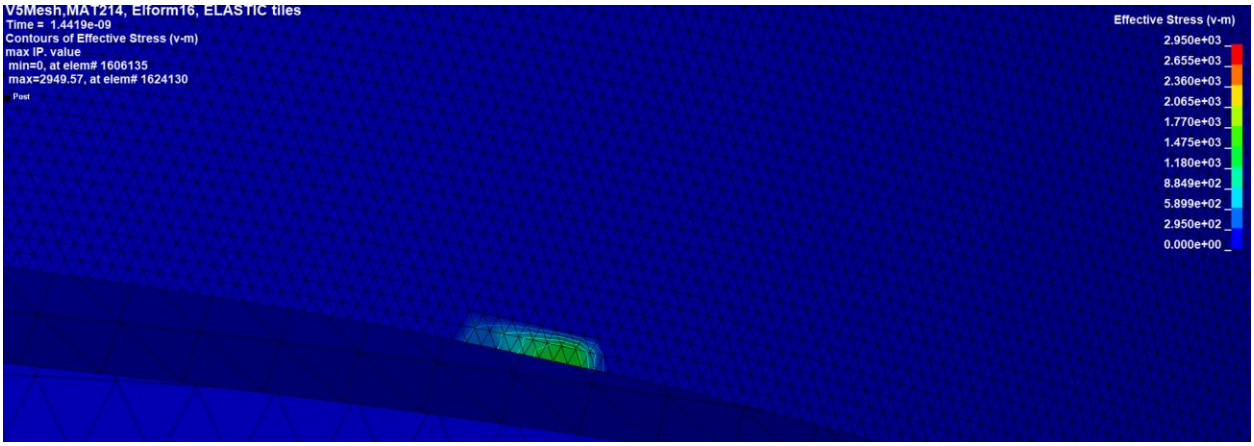

Figure 282: At time 1.441e-9, one of the very first timesteps in the simulation, spurious stresses (on the order of 1.5GPa) already develop at shared nodes between a tile and fabric, even if the tile is linear-elastic rather than rigid.

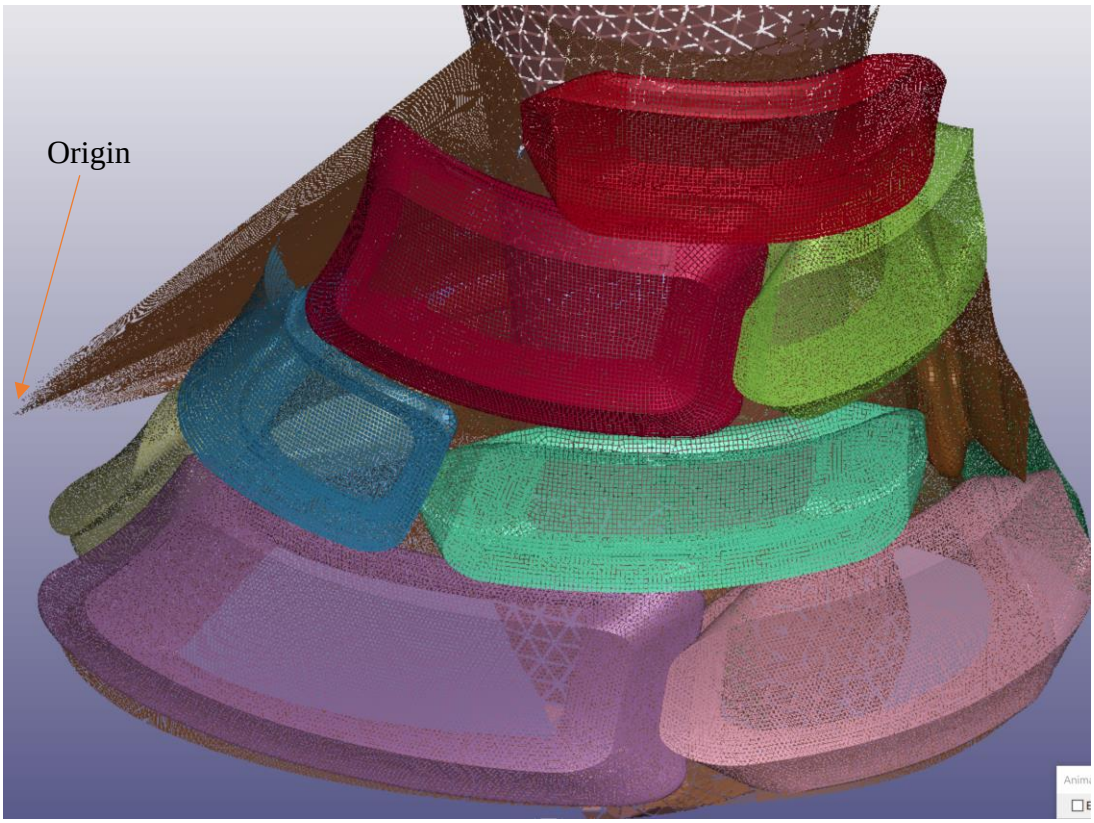

Figure 283: Unexpected and spurious gathering of nodes in fabric towards a distant point (namely, <0,0,0> in the simulation coordinates), along with random erosion of other nodes, at simulation time 9.6e-07 with MAT_214. Element edges are made transparent to better reveal the structure of the overall mesh.

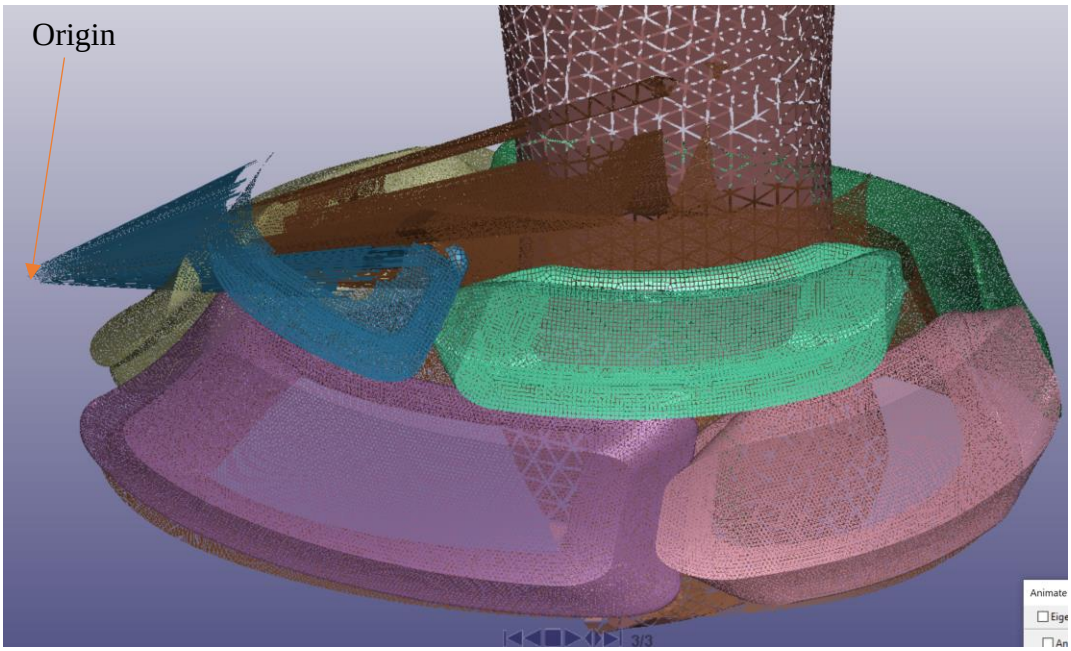

Figure 284: Continued gathering of some nodes towards the origin point in space along with the erosion of others, at simulation time 1.12e-05.

Simulations of Fabric-Backed Tiled Arrays with Bonded Contacts Between Tiles and with Fabric Modeled with MAT_214.

The strange behavior recounted above occurred when nodes were shared between tiles and fabric; this researcher thought that there might be a bug in the material model with regards to shared nodes, but that hopefully this bug would not extend to other methods of joining tiles to the fabric, e.g. with generalized welds, spotwelds, tiebreak contacts, etc. The same mesh (now featuring a fabric domain without holes, and separate rigid bodies for the tiles, with no nodes shared between fabric and rigid tiles, shown previously in Figure 278) as was used for the simulations with MAT_234 and bonded contacts or welds was used with MAT_234, and all of the same methods for welds or tiebreak contacts that were attempted with MAT_234 were again tried with MAT_214 in an attempt to enforce some sort of bond between tiles and fabric, but to no avail, as it resulted in "out-of-range moments" and "NaN" velocities within the first 500 timesteps.

MAT_293 for Simulating Woven Fabrics in LS-Dyna.

The newest micromechanics continuum model for woven fabrics in LS-Dyna is MAT_293_COMPRF (referring to composite-reinforced prepreg), introduced by Zhang et. al. [159] and implemented in LS-Dyna R10.1.0 and later [160]. This material model is intended to capture fabric draping features with woven prepreg sheets and is mainly used to simulate composite forming processes (e.g. to illustrate how the fibers will be oriented after forming and curing the prepreg into a stiff composite shell), rather than for the simulation of end-use parts. Unfortunately, no mention is made of biaxial tension properties (presumably because traditional prepreg forming methods do not entail biaxial tension loadings, only shear, local in-plane tension/compression, and through-thickness compression loadings), which may be problematic from the standpoint of convergence for simulating the fabric backing in the tiled-array stiffeners developed in this dissertation (considering how MAT_235 produced fatal simulation errors when loaded biaxially), to say nothing of accurately simulating second-order phenomena (such as how biaxially loading a woven fabric produces stiffening effects from decrimping), though granted such phenomena are not essential at this point to predicting the basic lockup shape of an array, which is the present focus.

Despite the lack of biaxial-specific properties, the model otherwise at first glance appears to be well-suited to modeling woven fabrics that may be significantly distorted, as its parameters nominally consider shear locking and bias compliance. Unfortunately, the LS-Dyna Material Manual contains the caveat that MAT_293 is not actually designed for simulating fabrics that undergo so much shear that they may reach shear locking, without indicating how severe the inaccuracies (or worse, simulation instabilities) that would result are [84]. The input deck for MAT_293 nonetheless requires the nominal locking angle of the weave, in addition to a 6th-

degree polynomial giving the engineering stress vs. stretch ratio for a uniaxial bias-extension tension test. While this researcher did not have access to the equipment required to conduct this test, literature introducing the test gives the following example polynomial (conveniently in the N-mm-s consistent unit system) for a representative weave of carbon fiber prepreg [161]:

$$\sigma = -0.29\gamma^6 + 1.09\gamma^5 - 1.68\gamma^4 + 1.37\gamma^3 - 0.56\gamma^2 + 0.12\gamma \quad (8.1)$$

where σ is the tensile stress in the fabric during the biaxial-extension test (for these coefficients, measured in MPa), and γ is the angle change (measured in radians). While this equation might not exactly be relevant for a non-prepreg, dry Kevlar weave (as opposed to a carbon fiber weave impregnated with tacky resin), it may be suitable as a first-order approximation of fabric behavior, and thus MAT_293 was used with these coefficients. The equation is graphed in Graph 26; note how the predicted tensile stress initially increases only moderately and gradually (corresponding to fiber decrimping perhaps and especially reorientation before trellis locking), before ramping up more rapidly once yarn jamming commences.

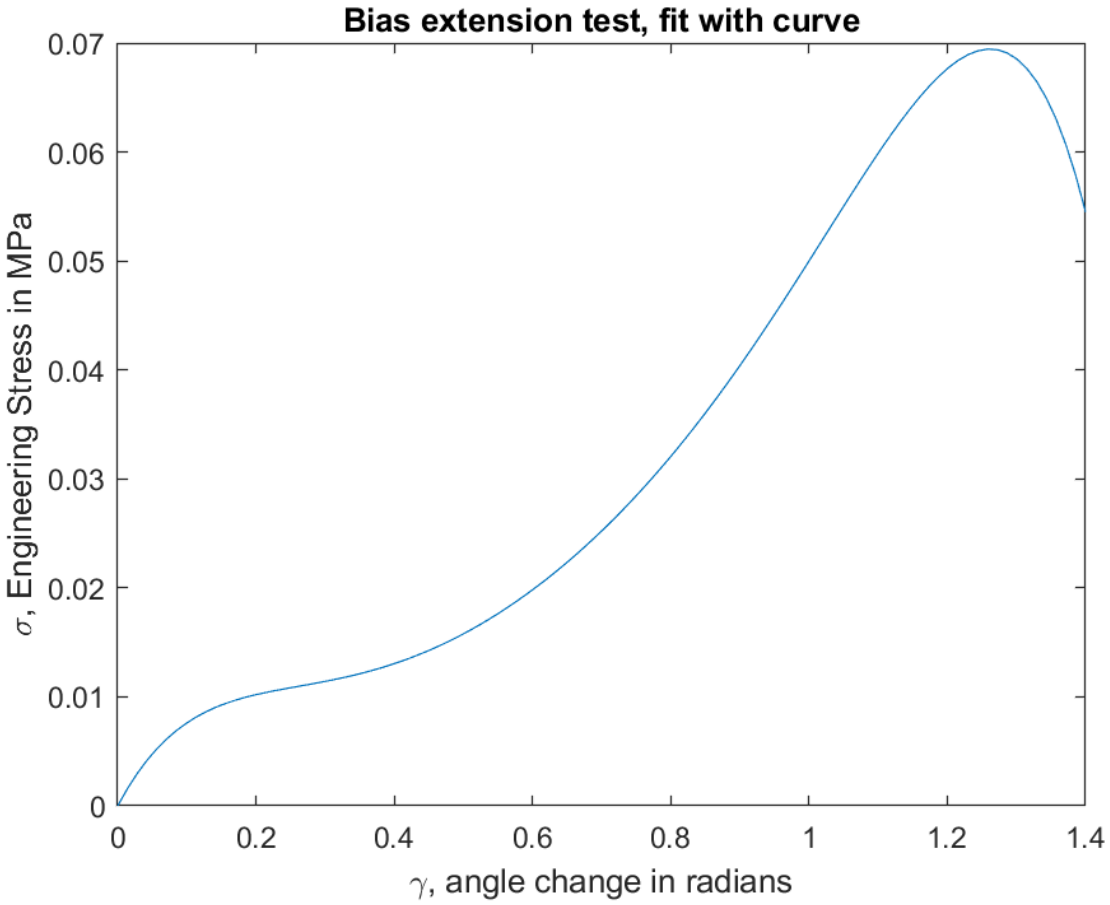

Graph 26: Sixth-degree polynomial to fit the results of the bias extension test, with coefficients taken from [161].

The model additionally incorporates uniaxial decrimping effects by requesting the "stretch ratio" (effectively engineering strain, on the order of 1%) at which decrimping is complete and the local tangent modulus becomes comparable to that at full decrimping. In simulations with this material, 1% was used, following the recommendations of Zhao [161], though the tensile modulus of 91GPa used with other simulations in this dissertation (for Kevlar 49) was used in place of Zhao's value for the specific grade of carbon fiber he studied. The entire card deck of material properties proposed for simulating dry woven Kevlar with MAT_293 is shown in Figure 285. Note that on card 2 of the deck, it requests "EM", the Young's modulus of the post-cured matrix (a confusing parameter considering that the material

is simulated when uncured); 100MPa was chosen for this just in case it was employed in the simulation.

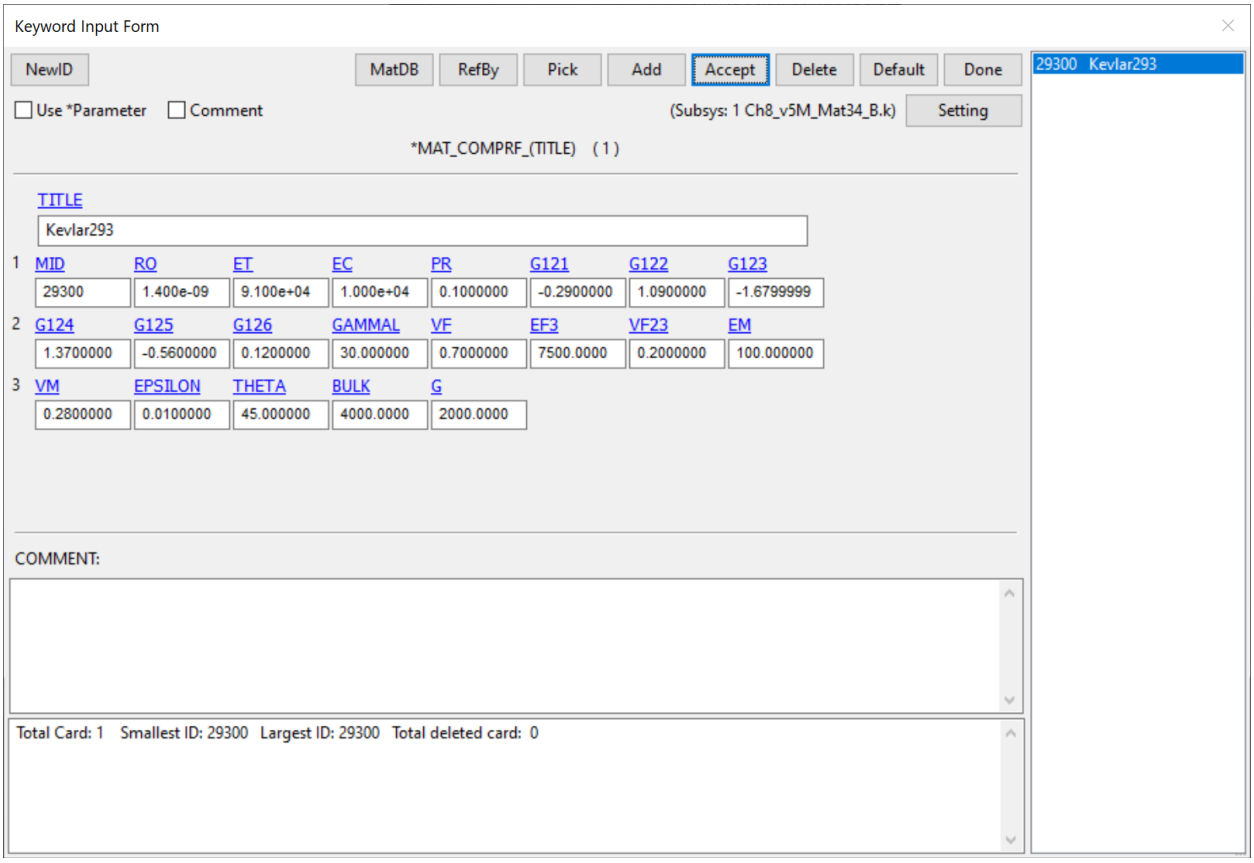

Figure 285: Material constants proposed for use in simulating woven Kevlar fabric using MAT_293.

Zhao recommends [161] that MAT_293 be used with fully-integrated shell elements, e.g. ELFORM=16 or ELFORM=-16 on the SECTION_SHELL card (+16 is faster, but -16 is more accurate), without stating whether fully-integrated elements are strictly speaking required, or whether faster formulations such as the Belytschko-Tsay (ELFORM=2) may be used. At the very least, it bodes well for the use of MAT_293 for this application that shell elements are preferred over membrane elements, since membrane elements have only tensile and shear stiffness, not bending stiffness (and thus their edges effectively turn into zero-stiffness hinges),

and thus tend to fare poorly in simulations where fabric bending modes dominate over tensile modes.

Problems with MAT_293 in LS-Dyna for Simulating Fabric-Backed Tiled Arrays.

As with MAT_214 and MAT_234, MAT_293 produced inexplicable stress concentrations when either node-sharing between tiles and fabric, or some form of bonded contacts (tiebreak contacts, genwelds, spotwelds, etc.) were employed. In this case, the response was marked by random loadings apparently being applied to single nodes eventually producing distortions in all adjacent elements; of note, the random distortions generally occurred at elements that were far away from any kind of interaction with rigid tiles, which was especially inexplicable. For instance, the progression of apparently-random mesh distortions at one of several loci of instability is shown in Figure 286. These distortions appear to arise from the solver trying to bring fabric nodes towards the origin (i.e. <0,0,0> in the simulation space) as shown in Figure 287, which is certainly not correct solver behavior. Thus, MAT_293 also proved incapable of simulating these structures correctly.

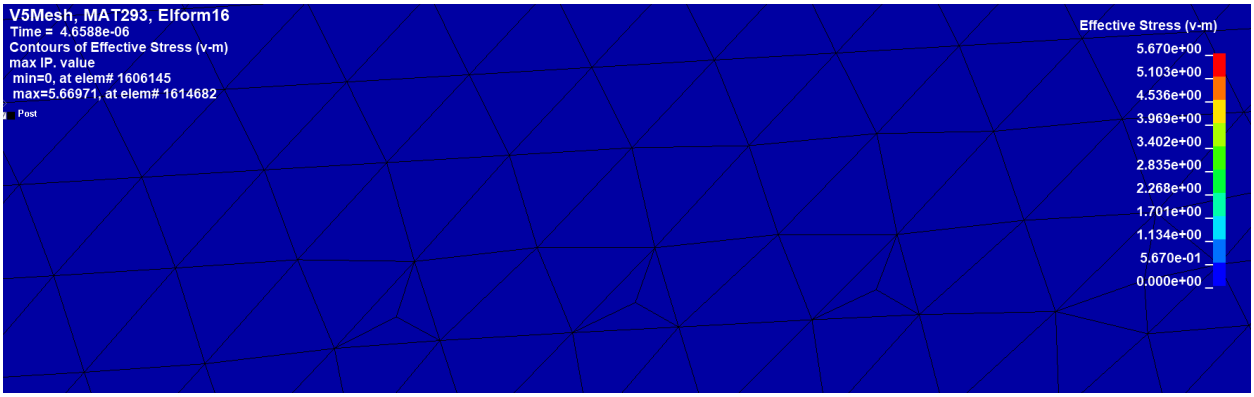

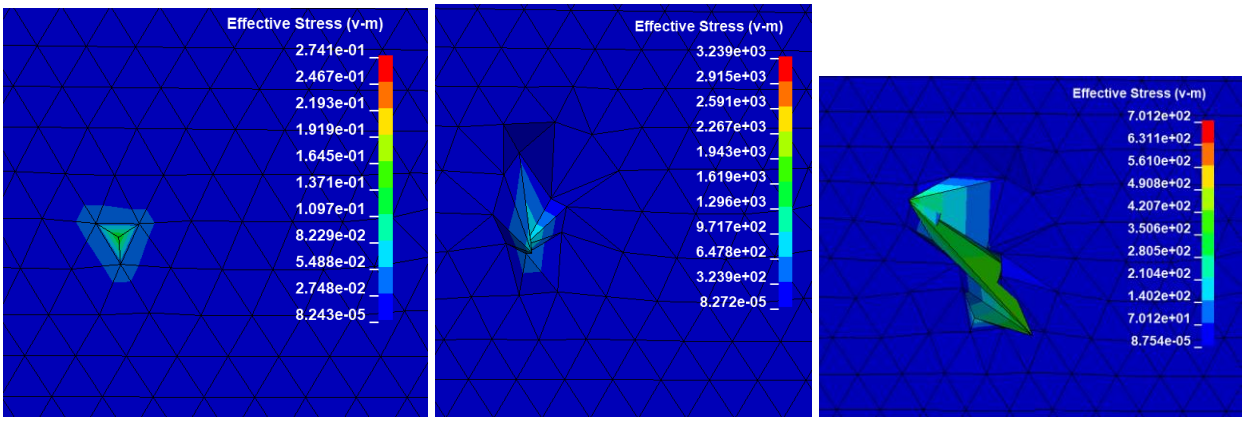

Figure 286: Progression of instability at one of the loci of mesh distortion over time. The top image shows the mesh at the first timestep, zooming in on a region that will soon demonstrate instability. Then the following three images, from left to right, show contours of von-Mises stress as the nodes begin to travel in a direction normal to the surface. This behavior is inexplicable and occurs in the first few timesteps of the simulation.

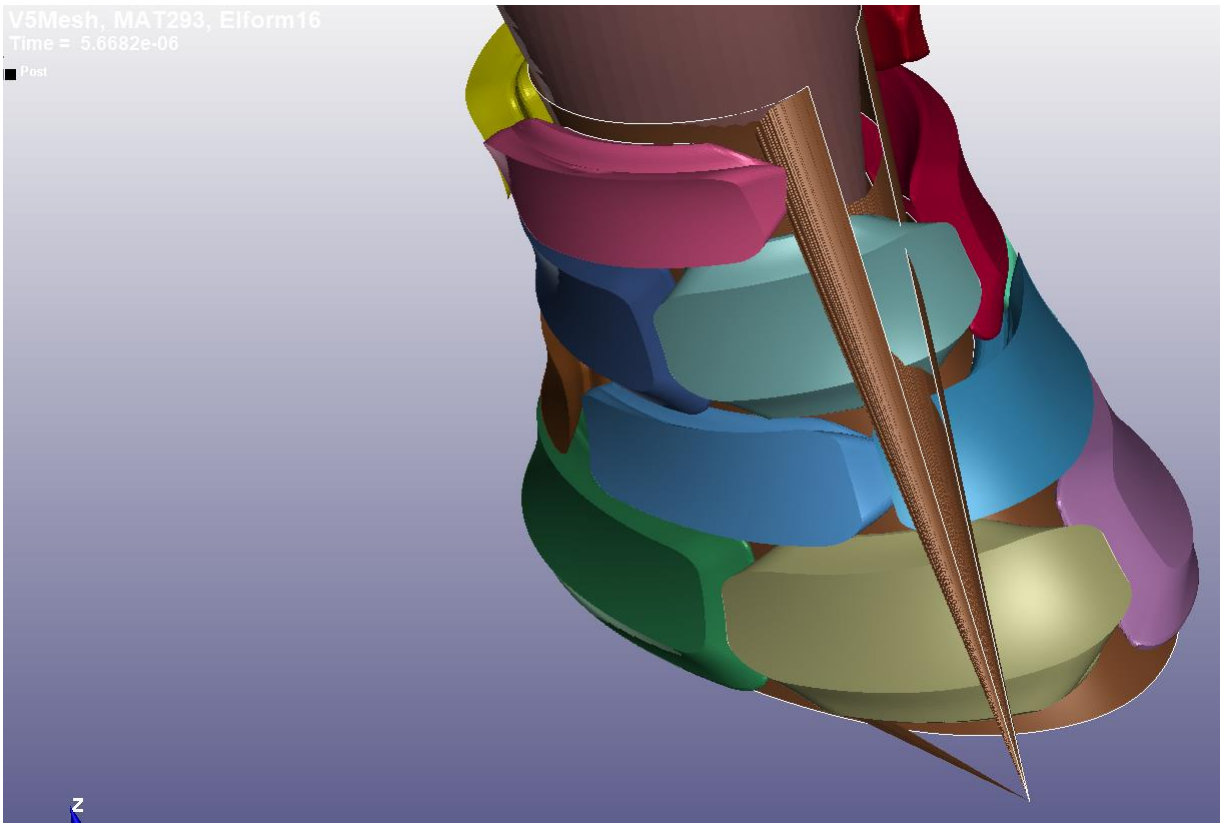

Figure 287: Fabric nodes modeled with MAT_293 inexplicably and erroneously "gravitate" towards the origin, starting with random loci of instability on the mesh (e.g. see the previous figure for a depiction of the progression of the material's stress).

Direct Modeling of Yarns in LS-Dyna.

If the aforementioned continuum models are unsatisfactory or non-functional for certain fabric-simulation applications, the user has the option of modeling and simulating the individual yarns of the fabric. Certainly this entails more setup work as well as computational power, but it should be more robust than the continuum models, and additionally it should give a clear visual indication of how the weave distorts/shears, decrimps, buckles, etc. Additionally, the technique would be amenable to static-implicit simulations (though large deflections and post-buckling phenomena would require appropriate treatment), whereas most of the continuum models for woven fabrics in LS-Dyna currently are only compatible with the explicit solver.

The easiest approach to direct modeling of fabrics at the yarn level is to treat each yarn/bundle of filaments as a unitary body (either as a beam of the desired cross-section or as a solid body that is meshed with solid elements); however, even-more-elaborate methods (in which the yarns are modeled as tows of many individual fibers, with the fibers treated themselves as beams) are known [162].

Direct Modeling of NiTi Fabric Strips in FEA.

This technique (specifically, modeling each yarn as a single beam of circular cross-section) was used by this author to simulate the behavior of a novel fabric strip weave pattern (with a rendering of a single unit cell depicted in Figure 288 and several unit cells combined lengthwise shown in Figure 289) made of nickel-titanium (NiTi, “Nitinol”) shape memory alloy, using the beam-FEA capability of MSC.Adams software (published by a team containing this author in [163]); it was particularly useful as no continuum micromechanics fabric model was available for a weave of this pattern, and interrupted contacts between the wires could treat decrimping, shear-stiffening, and bending effects.

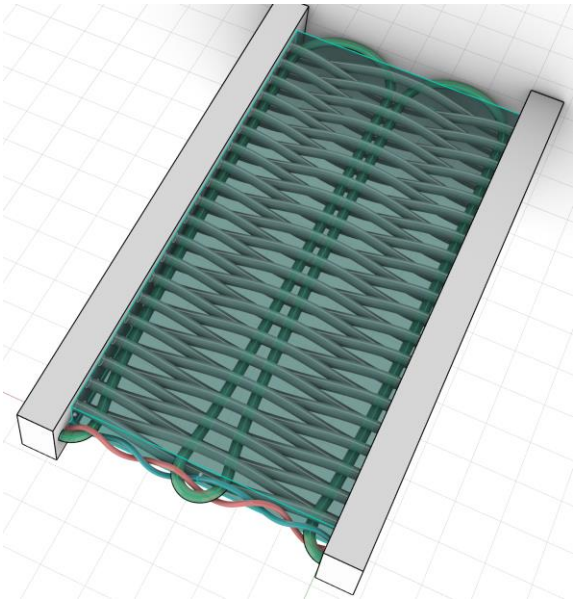

Figure 288: A single unit cell of a strip of NiTi-wire fabric, with warp yarns indicated in grey, weft yarns in green, and binder yarns in cyan and salmon-color.

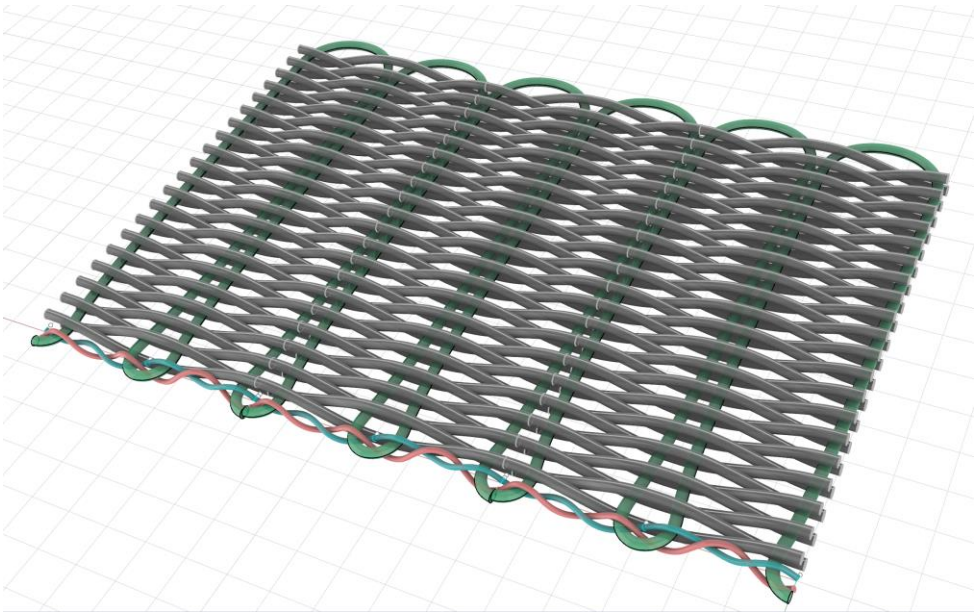

Figure 289: Multiple unit cells in the fabric strip combined lengthwise.

Additionally, further investigations (as-yet unpublished) of the NiTi fabric strips were conducted in LS-Dyna, with an eye towards determining their response to vibrational excitation. Figure 290 and Figure 291 depict beam-based meshes of such fabric strips; the beam elements

follow spline curves and are then assigned the appropriate sectional properties to give them thickness, which can trigger radial contacts in LS-Dyna.

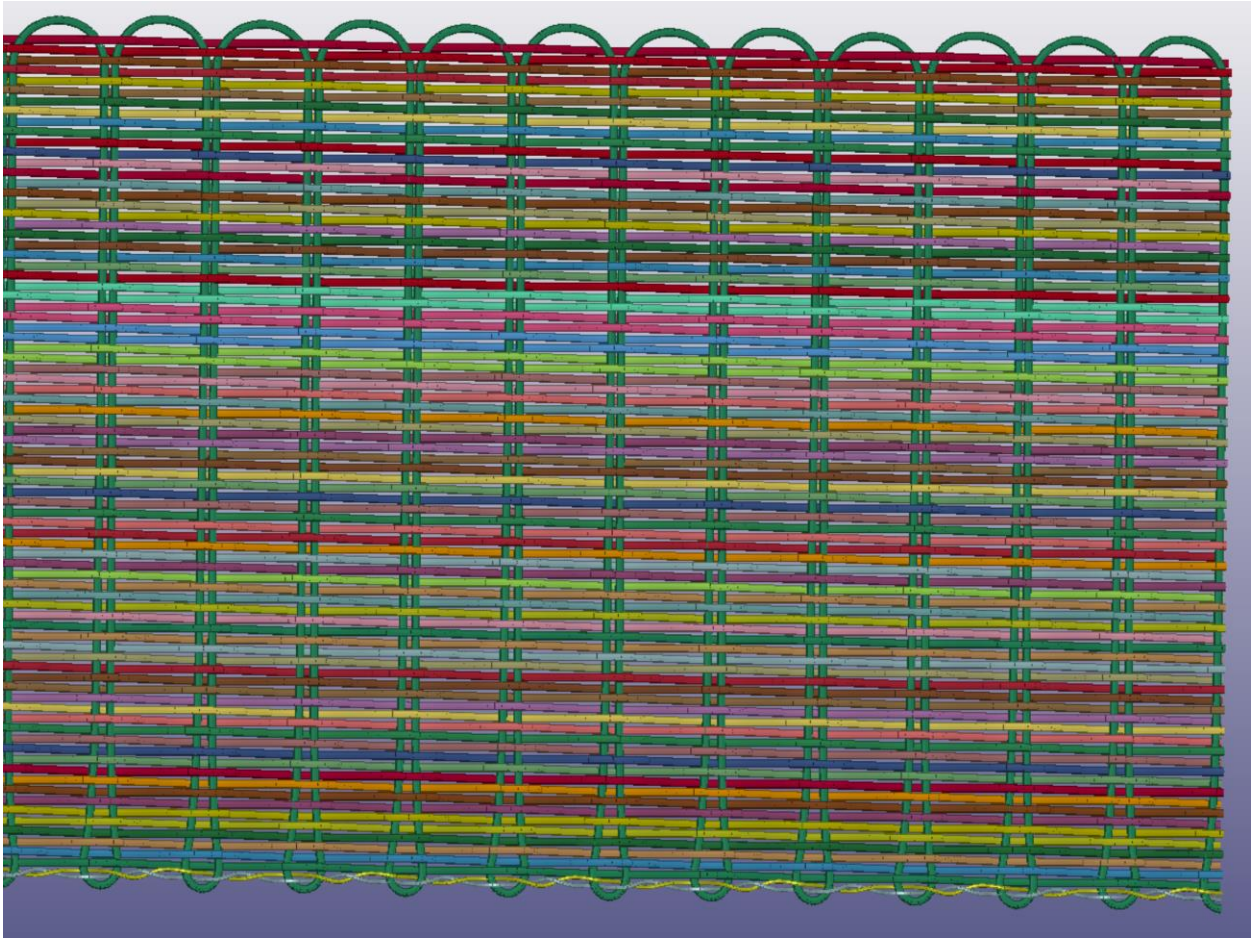

Figure 290: Top view of a NiTi woven fabric strip with the wires modeled with beam elements of circular cross-sections.

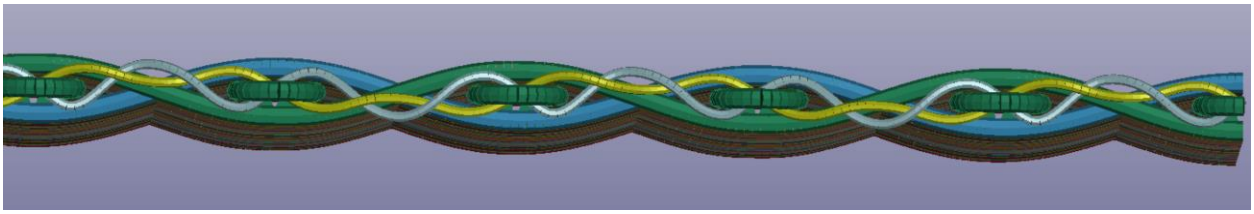

Figure 291: Side view of a NiTi woven fabric strip with the wires modeled with beam elements of circular cross-sections.

It is anticipated that it would prove far more difficult to even create the geometry for the fabric backing of the tiled arrays on the HDM using beams for each tow. Moreover, plain fabric weaves do not lend themselves so easily to modeling with beam elements, as the cross-sections

of yarns tend to become rather ovalized (like the intersection of sine curves) and thus are quite deviated from the circular cross-sections that the NiTi wires used in the fabric strips above do indeed possess (and LS-Dyna does not support complicated beam cross sections for contact purposes). Thus, solid elements would be required to capture the shape of woven Kevlar yarns than would beam elements, but unfortunately they would be very computationally-demanding, especially when one considers that it is not just a single unit cell that would need to be simulated, but many thousands. For instance, if the unit cell of the weave used in this research is 3.4mm x 3.4mm, then on the order of 100 unit cells would be required for the height of the ankle protector, and perhaps 150 in the circumference. For comparison, an array of just 5x5 unit cells (having $1/600^{th}$ the required number of unit cells) is depicted in Figure 292, and just modeling this 5x5 cell was computationally demanding, so simulating 100x150 cells is expected to be hopeless with current computing power. To add complexity, the designer would need to figure out how the fabric would drape on the hyperboloid-derived shape and model how the seams would be joined.

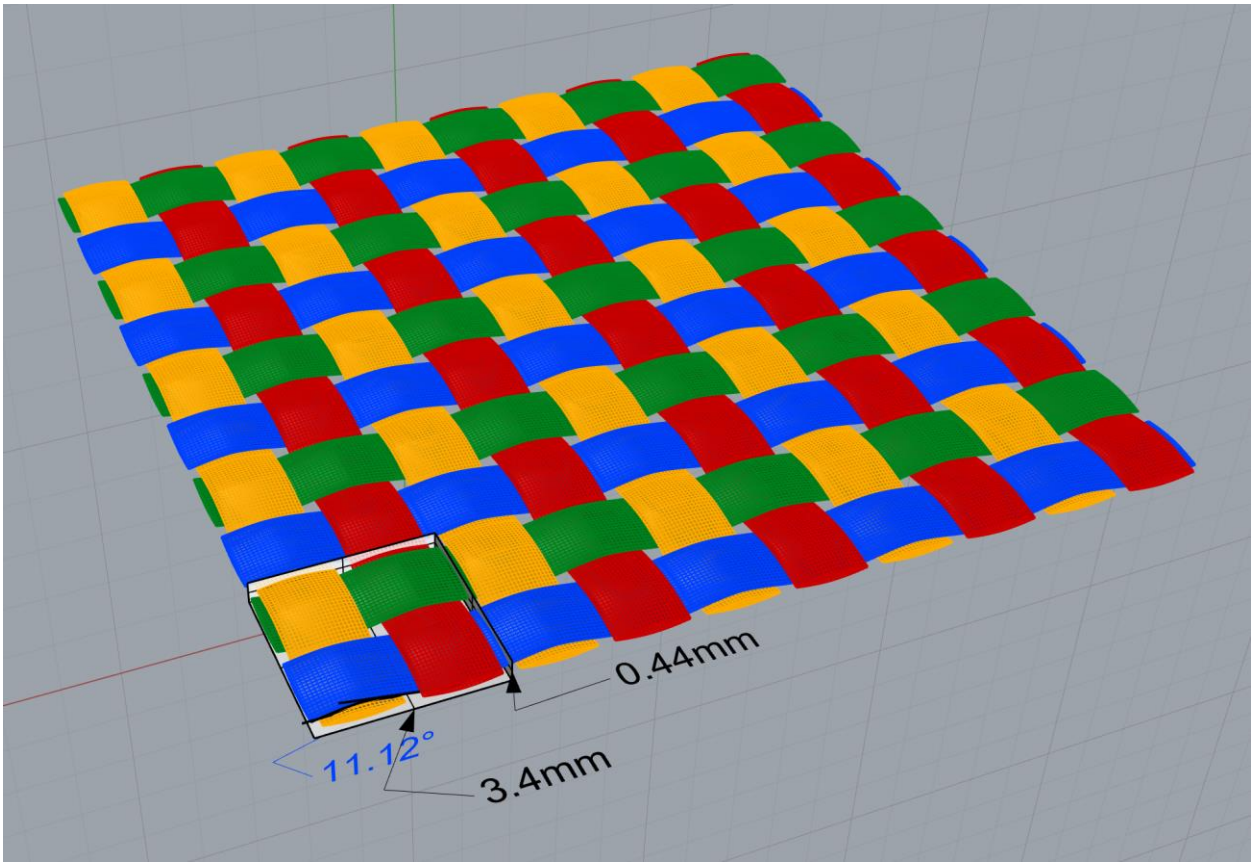

Figure 292: A 5x5 grid of unit cells in the fabric weave used in this dissertation.

Conclusion.

This chapter disclosed apparent flaws with several micromechanics-based continuum material models for dry fabrics in LS-Dyna, including the venerable MAT_235 and MAT_234, plus the newer MAT_214 and MAT_293. In particular, when MAT_234, MAT_214, and MAT_293 are set to share nodes with rigid or linear-elastic shells, spurious stresses develop that often cause the nodes to be dragged towards the origin point in space in the simulation. Additionally, attempting to secure tiles to the fabric in the model using techniques like spotwelds, genwelds, and tiebreak contacts was equally fruitless. It is theoretically possible to model the entire fabric body at the tow level with either beams or solid elements (as was done for relatively-simple strip weaves of NiTi wires), but this is likely to entail significant design work

as well as computational time. However, there is one non-micromechanics continuum fabric material model that may be more promising, MAT_034, which will be explored in Chapter 9.

Chapter 9. Advanced Simulation of Fabric-Backed Array in LS-Dyna with Modified Formulation of MAT_034.

Abstract.

This chapter investigates the use of LS-Dyna's MAT_034 fabric material model for use in simulating the kinematic behavior of woven fabric in a hyperboloid-shaped fabric-backed tiled array composite metamaterial, having the geometry selected in Chapter 7. The simplest formulation of MAT_034, tolerant only of small strains and with anisotropic properties, displayed disappointing results in terms of robustness. However, when a combination of a large-strain formulation and an artificially-reduced shear modulus (to simulate fabric trellising) were used, along with the appropriate specification of fiber directions, MAT_034 was found to be more robust computationally than the other material models referenced in previous chapters, allowing far more kinematically-accurate results to be obtained.

Introduction.

In addition to the material models MAT_235, MAT_234, MAT_214, and MAT_293 discussed in the preceding chapters, LS-Dyna has one more continuum fabric model, MAT_034 [84], with many sub-formulations depending on the parameter chosen for the quantity FORM in on the third card of the deck as well as whether orthotropic parameters are included. In particular, with FORM=0, MAT_034 can simulate a "fabric" that is either isotropic or orthotropic in-plane, with or without any out-of-plane bending stiffness; with FORM=4 or FORM=14, MAT_034 gains a nonlinear membrane formulation for larger displacements, plus the ability to treat a nonlinear stress-strain relationship for uniaxial tension as well as shear; with FORM=-14, it gains the abilities of FORM=4 or 14 plus the added ability to treat a nonlinear

relationship between stress and strain in biaxial tension; and finally, MAT_034_MAP enables special stress-map functionality, where tensile stresses can be made a general function of strains [164].

MAT_034 with Isotropic Properties.

The original, isotropic version of MAT_034 (the oldest continuum fabric material model in LS-Dyna) is a rather poor-fidelity material model for woven fabric: it treats the fabric as a membrane (thus having zero bending stiffness, which facilitates correct simulation of microbuckling under compression) unless dummy elements from an elastic liner are added at an offset, and additionally does not treat trellising behavior, decrimping behavior, or anisotropy from the orientation of warp and weft. In effect, MAT_034 in its isotropic formulation is best suited for non-wovens and far from ideal for modelling the woven fabric structures of this dissertation, where shearing is especially important. Figure 293 depicts the material properties that might be used for an isotropic fabric model roughly approximating woven Kevlar 49 with MAT_034.

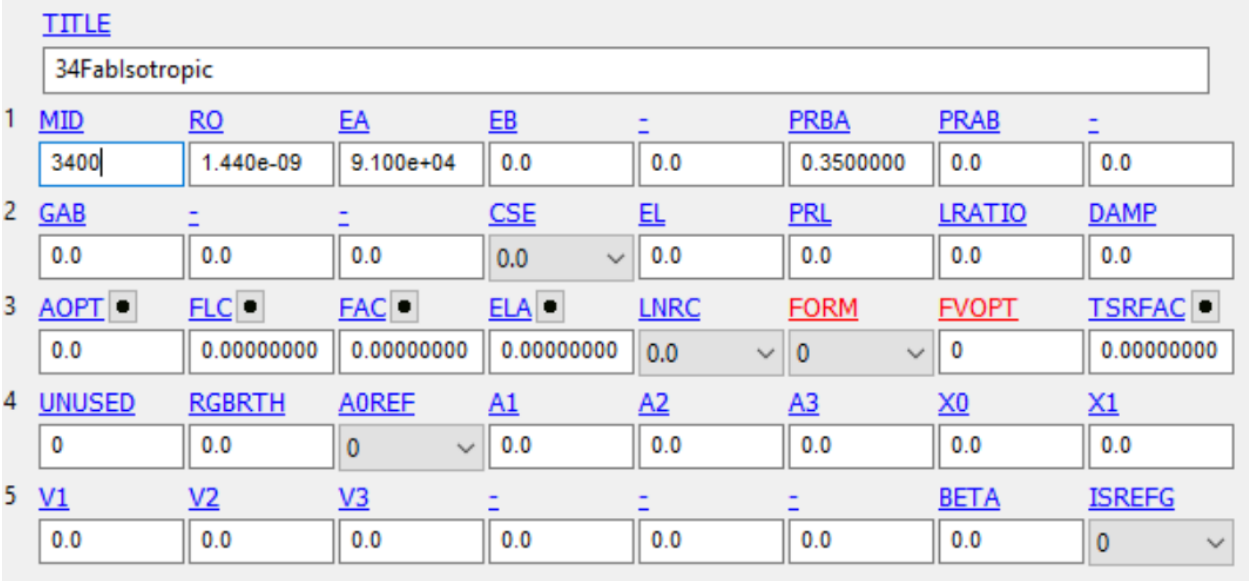

Figure 293: Standard version of MAT_034 with isotropic properties (owing to EB, PRAB, and GAB being set to 0 and FORM set to 0).

When the mesh of a hyperboloid-based array (introduced in Chapter 7, see Figure 253 therein) was simulated with this isotropic formulation of MAT_034, shooting nodes quickly appeared in one region of fabric, as illustrated in Figure 294 and Figure 295. Indeed, MAT_034 was less robust than MAT_235 (inasmuch as the simulation failed earlier with MAT_034 in the isotropic, small-strain formulation), despite using simple membrane elements with MAT_034 (which should be more robust than Belytschko-Tsay shells). However, as will be discussed in the next section, an improved formulation of MAT_034 gave both superior physical fidelity and simulation robustness.

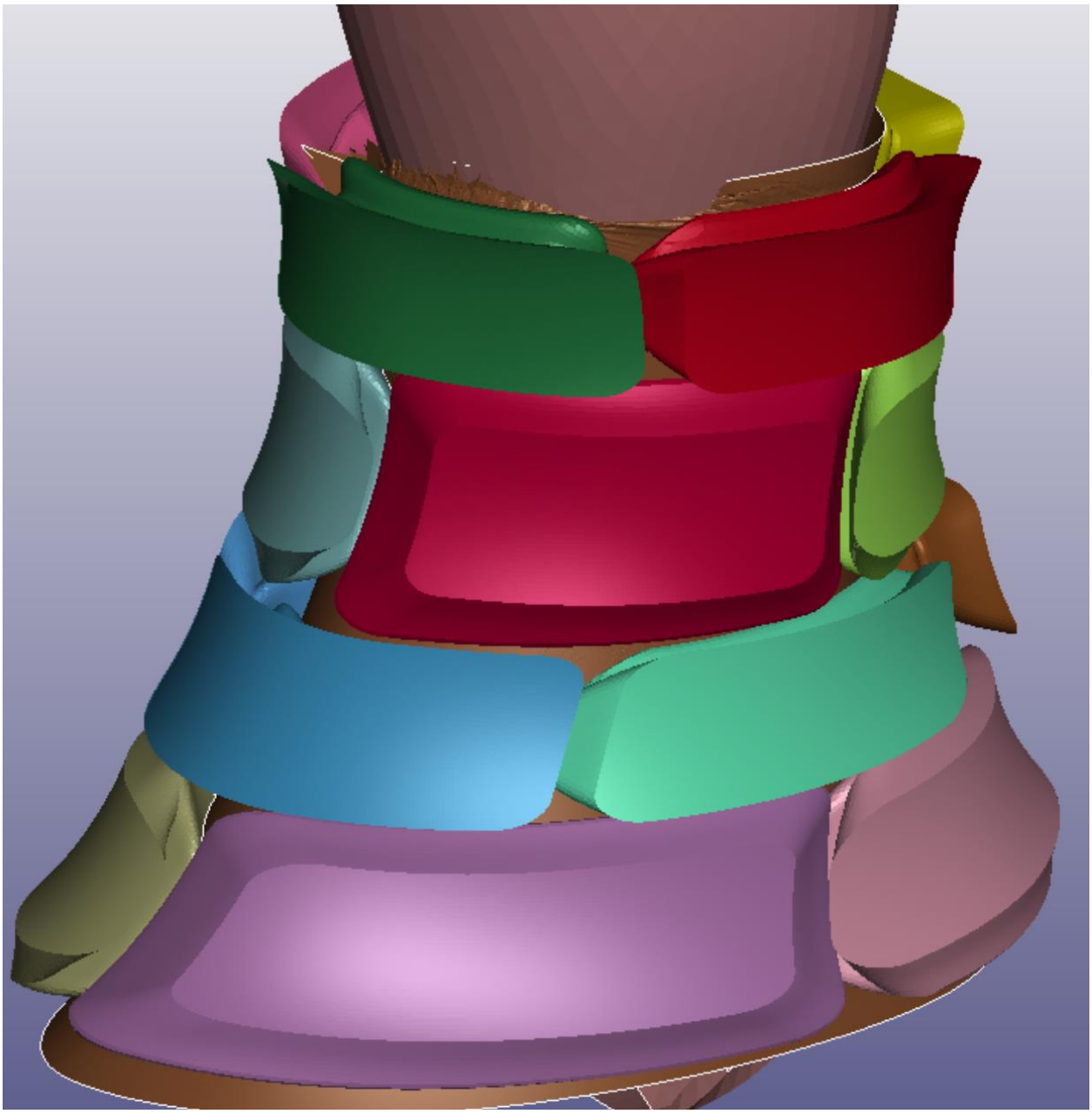

Figure 294: Shooting nodes already apparent with 0.21° of leg rotation using MAT_034 in the linear-elastic, isotropic, small-strain formulation.

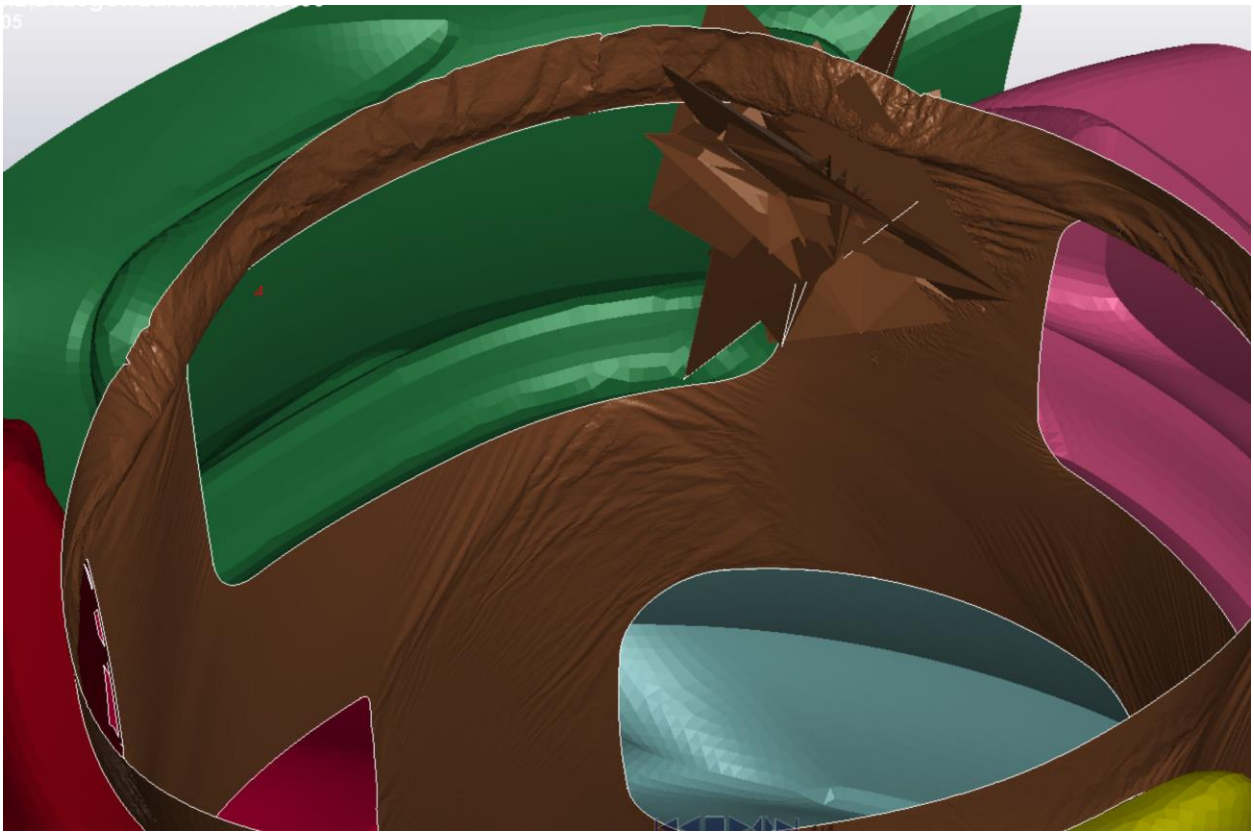

Figure 295: Interior view of the shooting nodes at simulation time 4.76e-5 seconds.

MAT_034 with Form -14 and Modified Shear.

In contrast, other formulations of MAT_034 offer far superior performance. Changing the parameter FORM to +3, +4, +14 or -14, for instance, invokes a different element formulation automatically that tolerates large strains and nonorthogonal angles in the fiber orientations from reorientation under shear. Additionally, the use of +4, +14 or -14 for the FORM parameter enables card 6, whereon the user can specify an arbitrary (i.e. from tabulated data) stress-strain relationship for uniaxial tension along the warp and weft fibers (the parameters can be specified independently in case the warp and weft are different materials) as well as tabulated data relating shear stress and strain, in the event that the user has access to testing equipment for uniaxial testing and the "picture frame" test which is commonly used to determine fabric shear properties. In particular, if such tabulated data were readily available, it would contain the pre-lockup as

well as post-lockup trellising behavior. Finally, FORM=-14 enables further functionality in that card 7, which allows the input of stress-strain data from a biaxial test, becomes active. Card 7 also allows simple hysteresis behavior to be activated with the parameter H, which is a simple, non-dimensional hysteresis ratio between 0 and 1 (0.05 seemed appropriate, though in any event this simulation does not entail both loading and unloading).

Unfortunately, this author did not have access either to test data for a comparable weave, nor to testing equipment. Fortunately, while this formulation of MAT_034 can employ such test data, in the absence of the data, linear (but anisotropic) relations can be used as well. Thus, as a first-order approximation of the initial freedom that a plain weave of fabric has in shear, it seemed wise to reduce the shear modulus of the fabric to one-tenth its actual value, though as this was a constant value, it would hardly treat shear locking after trellising was complete. Additionally, to compensate for the fact that the membrane elements used have zero bending stiffness and thus may be more vulnerable to dynamic instabilities, the "liner" option was employed to surround the fabric with a thin, elastic-plastic liner (with a Young's modulus of 100MPa, a yield stress of 30MPa, and a thickness of 0.01mm) for enough bending stiffness to prevent numerical issues. Moderate hysteresis was engaged with H=5% (input as 0.05). Incidentally, Borrvall also recommended [85] using a Poisson's ratio of 0.75 (PRBA) in one direction and 0.30 in the orthogonal direction (PRAB) to simulate fabrics with MAT_034 on the basis of comparisons with uniaxial extension tests. Finally, the compressive stress elimination option (CSE=1) was employed (though this only eliminates compressive stresses, to avoid numerical errors, in the fabric and not in the surrounding elastic liner). Figure 296 includes the material parameters used for this superior version of MAT_034.

TITLE

34FabOrthoCSE14

1	MID	RO	EA	EB	-	PRBA	PRAB	-
	9916	1.440e-09	9.100e+04	7200.0000	0.0	0.7500000	0.3000000	0.0
2	GAB	-	-	CSE	EL	PRL	LRATIO	DAMP
	290.00000	0.0	0.0	1.0	0.0	0.0	0.0	0.0
3	AOPT	FLC	FAC	ELA	LNRC	FORM	FVOPT	TSRFAC
	0.0	0.00000000	0.00000000	0.00000000	0.0	-14	0	0.00000000
4	UNUSED	RGBRTH	A0REF	A1	A2	A3	X0	X1
	0	0.0	0	0.0	0.0	0.0	0.0	0.0
5	V1	V2	V3	-	-	-	BETA	ISREFG
	0.0	0.0	0.0	0.0	0.0	0.0	0.0	0
6	LCA	LCB	LCAB	LCUA	LCUB	LCUAB	RL	
	0	0	0	0	0	0	0.0	
7	LCAA	LCBB	H	DT	_	ECOAT	SCOAT	TCOAT
	0	0	0.0500000	0	0	100.000000	30.000000	0.0100000

Figure 296: Material properties card for MAT_034 with nonlinear strain formulation, reduced shear modulus, elastic-plastic coating, and special Poisson's ratio.

Additionally, it was necessary to specify the anisotropy in the form of the fiber orientations separately on the SHELL card (unlike with MAT_234 and MAT_235, which require element direction specifications with ELEMENT_SHELL_BETA), as shown in Figure 297. Note the B_i angles that are added on card 3 (not used with other fabric formulations), which specify the angles of the fibers relative to the element direction vector. Since the same mesh as that used in previous chapters was used (with element direction vectors oriented at 45° from the vertical), it was necessary to set the fiber orientations to 45° and 135° relative to the element directions; had the element directions been oriented vertically, instead, for instance, the B_i quantities on card 3 should have been set to 0° and 90° for this formulation of MAT_034 instead.

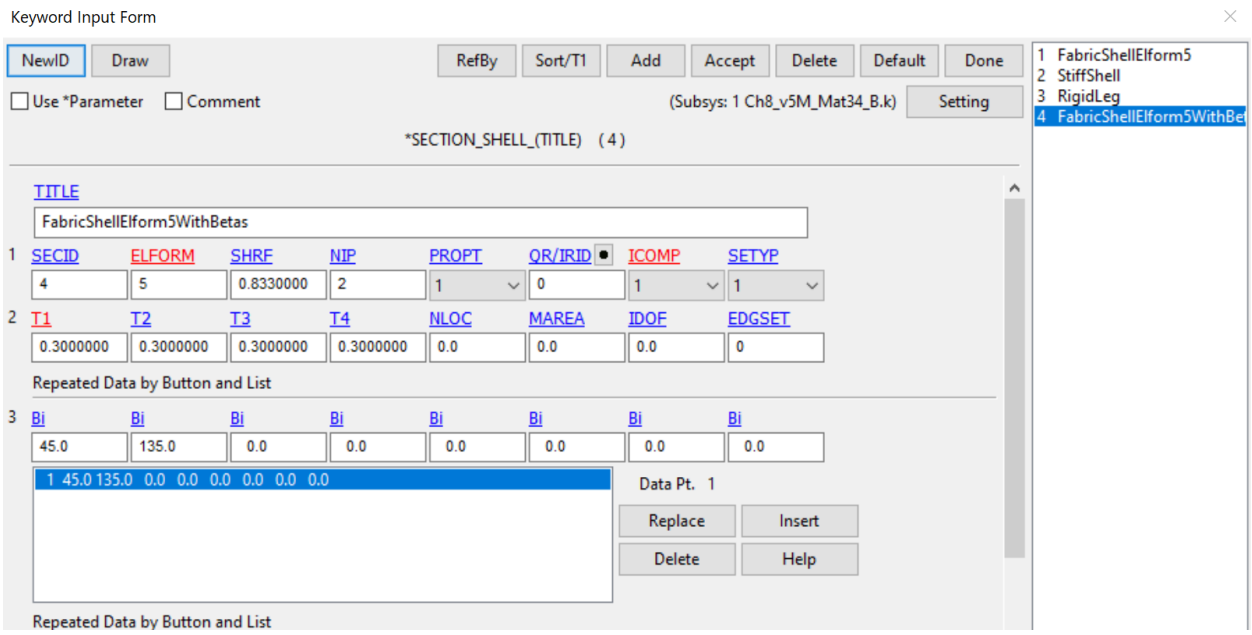

Figure 297: Shell section data required for this formulation of MAT_034. Note the Bi's added on card 3, which correspond to angle offsets of fibers from the element vector.

Fortunately, this modified formulation of MAT_034 proved quite robust, with the simulation proving successful and apparently accurate up to 16°, as shown in Figure 298. The simulation did not fail at this point, but the simulation was ended at this point as it became apparent that the tiles were becoming misaligned, and manual manufacturing of the same array (discussed in Chapter 10) indicated that the design was lacking. A future iteration of the simulation might benefit from a further reduction in the shear modulus, though a tabulated relation of fabric shear stress to shear strain (as well as uniaxial and biaxial relations) would be even better if access to the needed equipment could be obtained.

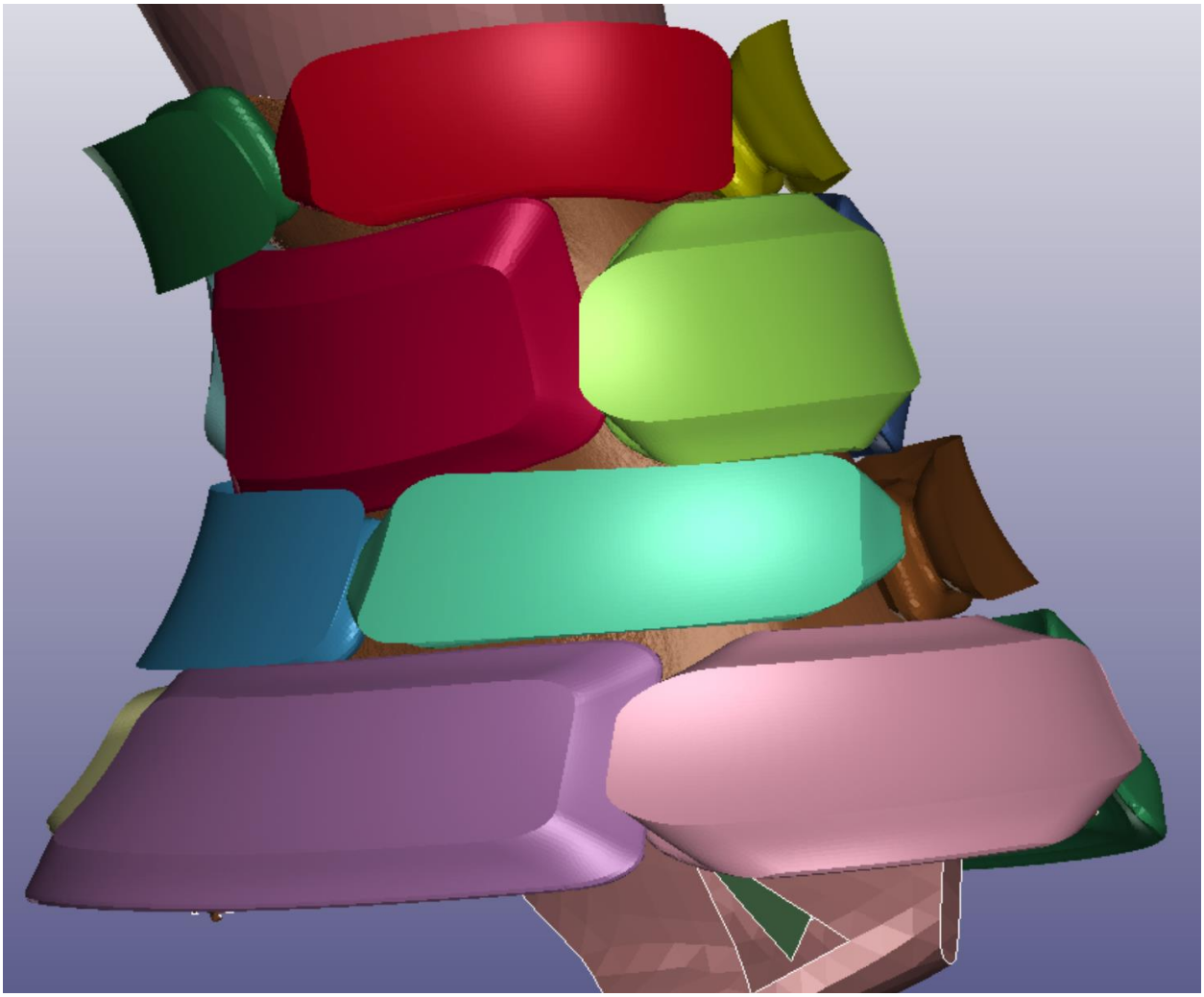

Figure 298: The array after 16.18° of leg rotation. Certainly this simulation does indicate that tiles may slide past each other instead of locking up at the surfaces where they were supposed to.

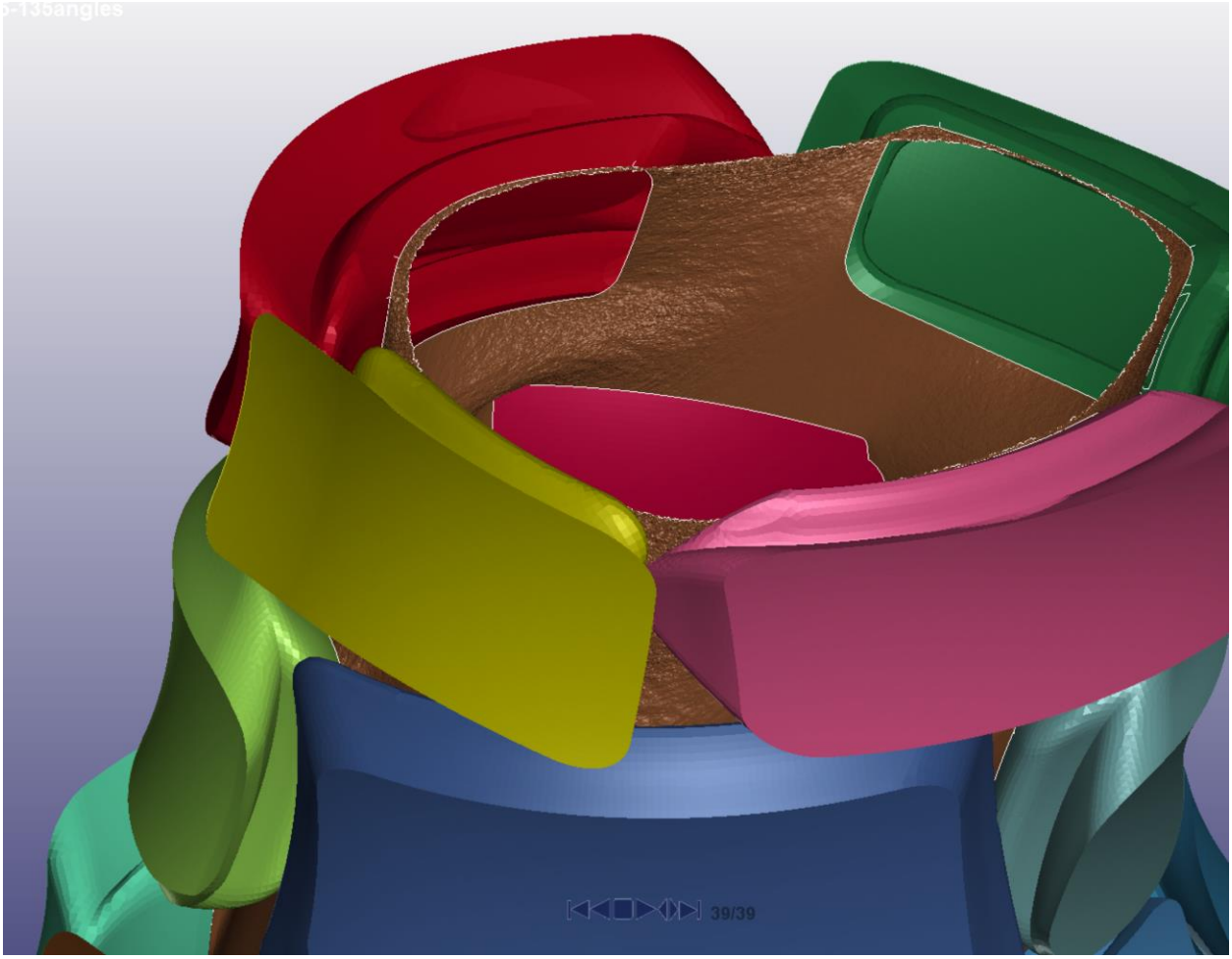

Figure 299: Interior view of the simulation at 16.18° of leg rotation.

The purpose of FEA simulations of tiled arrays on the HDM surface was that of form-finding (rather than, for instance, determining, post lock-up stiffness or evaluating strength or fatigue concerns): determining if the structure would lock up from tile contacts, or whether they would be displaced normally relative to the surface so much that they would not engage, or alternatively if the fabric would be unable to conform to the needed shape for lockup. As can be seen earlier on in Figure 298, the top tiles (including the green one) easily slide past features that were specifically intended to engage them relative to one another in bending at around 16° of leg rotation forwards, which is undesirable and will require a complex investigation into needed alterations into the relative initial angles of lockup surfaces prior to contact that is beyond the

scope of this dissertation. Additionally, it should be noted that the displaced shape of the structure (best observed with the tiles hidden, e.g. in Figure 301 below) greatly resembles the shear-dominated behavior of the vertically-oriented Cartesian mesh array studied in Chapter 6 (see Figure 195 for instance) in forwards-directed shear, suggesting that fabric-backed tiled arrays in cylinder form may be quite reliant on shearing of the fabric for pre-lockup flexibility (note that the vertically-oriented Cartesian mesh array was noteworthy for its reliance on shear rather than in-surface contraction or extension or out-of-surface bending, though certainly a fabric should at the very least be much more compliant in in-surface contraction owing to the ability of a woven fabric to undergo microbuckling). This may suggest designing the structure to lock up purely in shear behavior (with a radical reshaping of tiles towards this end), or alternatively may recommend orienting the fabric biaxially (so that the bias is roughly vertically-oriented).

Thus, as evaluating stress gradients and checking for material overstress are not especially germane to form-finding, stress in the fabric was a secondary concern. However, contour plots of von Mises stress were plotted in Figure 300 and Figure 301 in order to verify that excessive stresses were not present, and unfortunately the figures do indicate that the material model predicts that most regions of the fabric will be stressed over 1.8GPa, approximately half the 3.6GPa strength of Kevlar 49 [165] (though additionally the use of the rule of mixtures and an understanding that the transverse strength of the fibers is minimal suggests that even a dense weave with minimal decrimping effects would likely fail at around 1.8GPa). Of course, these stress values are not likely especially accurate owing to the lack of stress-strain relationships for fabric shear in particular, so this should serve only as a preliminary warning. Indeed, if contours of von-Mises strain are plotted instead of stress, a few relatively-

isolated shear bands between tiles become apparent as the main loci of strain, as shown in Figure 302.

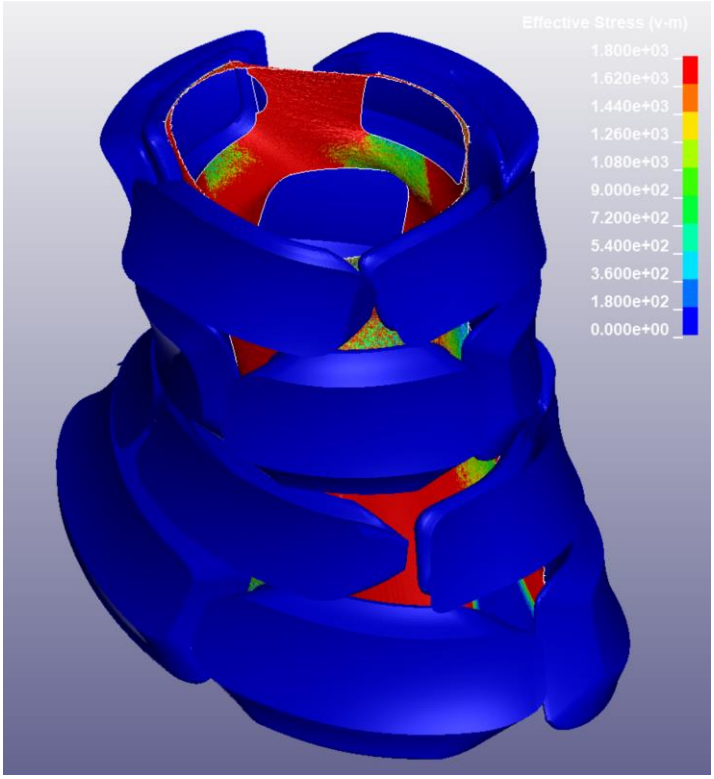

Figure 300: Contour plot of von Mises stress in the fabric, with the scale limited to 1800MPa (probable failure of Kevlar 49).

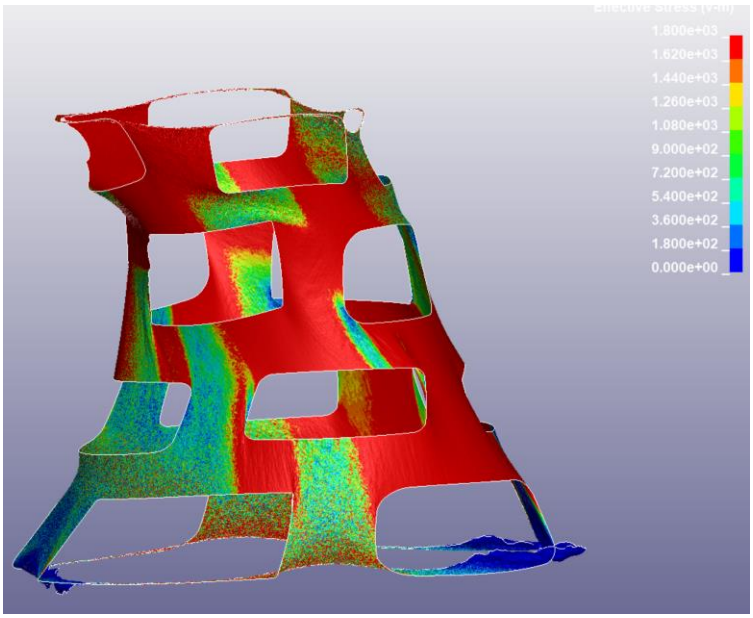

Figure 301: Contour plot of von-Mises stress on the fabric, with tiles hidden for visibility.

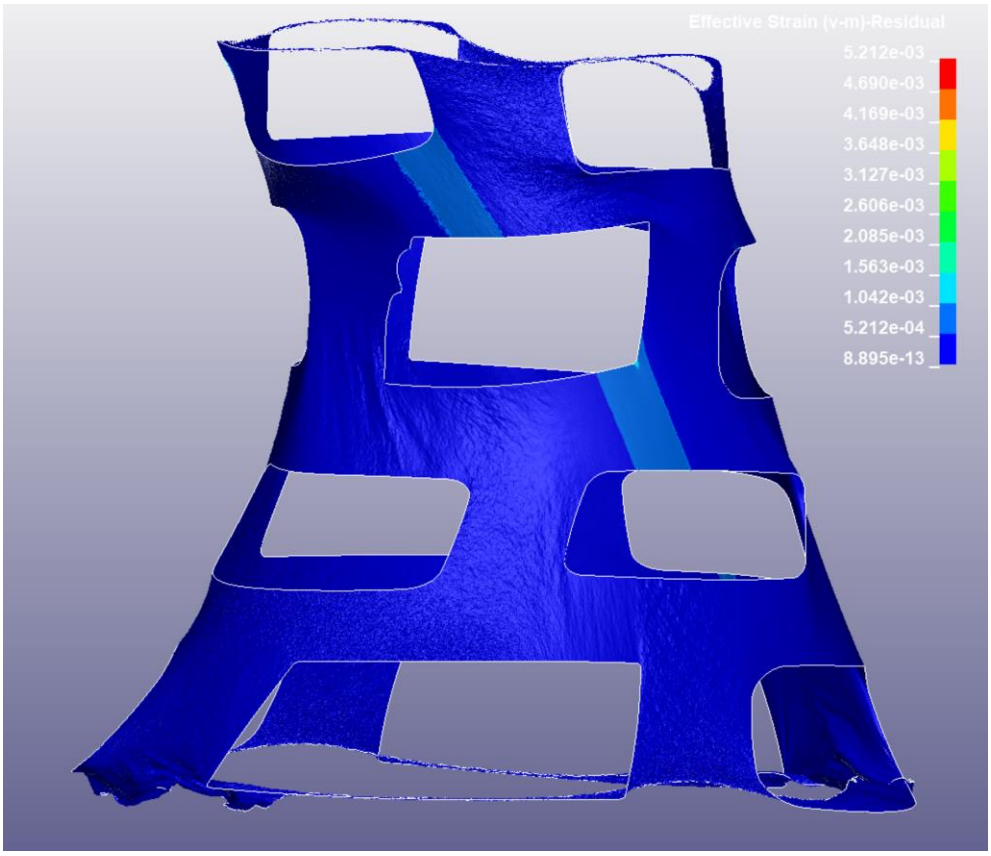

Figure 302: The plot of von-Mises strains shows distinct banding (albeit of relatively low strain magnitude on the order of 0.0015, save at corners where some concentrations exist). The tiles were hidden for greater visibility of the fabric's strain distribution.

Conclusions and Future Research.

Although theory would suggest that MAT_034 is far less sophisticated than true micromechanics fabric continuum material models like MAT_234 and MAT_235 (in that the latter are billed as able to predict weave shearing and trellising behavior without stress-strain data from tests), practice indicates that judicious modification of linear properties in MAT_034 can give acceptable results, and moreover MAT_034 is far more robust in handling large fabric strains and bonds (or shared nodes) between fabric and rigid parts. Furthermore, MAT_034 should be quite accurate indeed when coupled with appropriate uniaxial, biaxial, and shear test data. Indeed, acquiring and employing such data should be the first form that future research into FEA of fabric-backed tiled composite metamaterial arrays should take, provided that the necessary test equipment can be secured. Additionally, the FEA results suggest several potential changes to the mechanism of the structure and its target lockup shape, as discussed above, including changing the tile profiles radically (further reducing contact area and reducing tile curvature) to cause them to engage based on underlying fabric shear rather than out-of-surface bending. Alternatively, it might be wise to experiment with fabric oriented with the bias in the vertical direction (approximating a biaxial braid, though due to manufacturing constraints, a true biaxial braid with the shape of the HDM cannot be made), as the research into the biaxially-oriented Cartesian mesh array suggests that such surfaces are more tolerant of in-surface extension while also tolerating out-of-surface bending depending on the manifold geometry. Certainly, the potential merits of experimenting along these lines can also be confirmed by manufacturing the original prototype and determining if its actual mechanical behavior is as deficient as the FEA of this chapter suggests; manufacturing will thus be undertaken in the next chapter.

Chapter 10. Manufacturing and Testing of Closed-Surface Tiled Arrays.

Abstract.

In this chapter, variations of the closed-surface tiled arrays from the previous chapter are manufactured in a few different ways, and the resulting samples are tested and compared with FEA results where applicable. For the first embodiment of the concept, the array is split into two halves and then manufactured by printing all tiles in rigid polymer and then precisely positioning them with workholding devices in order to glue them at the appropriate locations to fabric pieces (with the pieces derived from an approximate flattening of the doubly-curved surface that is used in CAD). The two halves of the array can then be attached to one another at tiles to form a complete array. The next embodiment consists of 3D printing the entire assembly in two materials, namely a rigid polymer for the tiles and a thermoplastic elastomer for the thin shell that replaces the fabric. The final embodiment entails a slightly different concept, again featuring interrupted rigid tiles, but using a bellows-like wavy manifold instead of a simple shell without undulations. This version showed the greatest promise owing to the local tension and compression freedom as well as local bending freedom translating most successfully into global bending freedom followed by lockup, although the concept was very much a preliminary one in need of perfection.

Introduction.

In the course of the simulation work detailed in Chapter 7, this researcher encountered considerable difficulty in simulating closed-surface, cylindrical/hyperboloidal arrays with LS-Dyna, apparently due to a deficiency in MAT_235 producing spurious stress responses in the presence of combined biaxial and shear stresses in the fabric. Consequently, the theoretical

advantage that FEA should offer—rapidity of iteration and testing without the need to manufacture a physical sample—failed to materialize, making direct manufacture of arrays the most time-efficient method for determining the viability of the general concept for joint protection as well as the ideal manifold shape, tile gap distance, etc. As such, two different methods were undertaken to manufacture cylindrical arrays: firstly, the tiles were manufactured separately and then assembled in workholding devices to precisely locate them relative to each other (in a neutral position), then joined to the fabric; and secondly, multimaterial 3D prints were performed, using a flexible thermoplastic elastomer for a thin shell constituting the backbone (replacing the woven fabric) and relatively rigid polymer for the tiles. The latter method did not have perfect fidelity to the original design concept of a fabric-backed array: an elastomeric shell has far greater shell bending stiffness than a closed fabric surface of the same area, yet the elastomeric shell is at the same time vastly inferior in tensile stiffness compared with the fabric. Thus, an elastomeric shell structure should have higher pre-lockup stiffness and lower post-lockup stiffness than a comparable fabric-backed array. Nonetheless, elastomeric-shell structures are far easier both to design and to manufacture than fabric-backed arrays of the same size, because elastomeric shell multimaterial prints do not require manual assembly of the elastomeric shell to the tiles (this is effectively performed by the 3D printer), nor does the manufacturer need to create a separate workholding device, nor does the manufacturer need to cut out shapes out of Kevlar woven fabric (a difficult process even with specialty Kevlar shears), etc. Consequently, provided that free machine-hours are available on a suitable, high-quality, multimaterial-capable 3D printer, the multimaterial 3D printing method is preferable at least for prototyping.

Manufacturing the Fabric-Backed Tiled Array.

The first array to be produced on fabric (and additionally on an elastomeric shell) was to have the same lockup surface profiles as the final fabric-backed tiled array that was simulated in Chapters 7 and 9 (i.e. the one with the largest tiles and greatest amount of area of unbonded fabric). While this particular array had enormous tiles relative to the expected final size, it would provide easy comparison between the FEA results and results from physical manufacture and testing, and additionally, since each tile was unique, it would be far easier to work with large-size tiles (namely because there would be fewer in number of them, as well as larger features for gluing, etc.). A generic CAD rendering of this array is shown in Figure 303, devoid of any added features (such as workholding-positioning features or splitting features).

Figure 303: CAD rendering of the goal shape to produce, with rigid tiles shown in dark blue, and fabric shown in yellow. This is a generic rendering and does not contain workholding features if required to precisely position the tiles, nor splitting features, etc.

Splitting the Device into Two Halves.

For actual manufacture (as opposed to simulation), it was necessary first to determine how it could be removed and put on the body. Given that the tiles are rigid and the fabric very stiff in tension, the wearer's foot cannot be inserted through the top of the device; instead, it proved necessary to split the device into two sections which could be joined in a clamshell around the wearer's leg, namely by joining the rigid ring-halves with joints that are also rigid. Splitting the closed-surface array into two halves that were (of course) each open surfaces also facilitated manufacture by giving easier access to the inner surfaces of the tiles, which were to be glued to the fabric.

The choice of splitting curve was more or less arbitrary, and in this case the designer chose to split the part into fore and aft parts with a plane running from left to right, as shown in Figure 304 (though later on and for a different array, an undulating splitting curve was used). Both the tiles (at least those that lie roughly evenly on the two halves of the fabric) and the underlying fabric manifold had to be split in order to allow the device to be taken off and put on. Additionally, a mechanical means of joining the halves of each ring of the front and rear halves was required; the simplest method was simply to cut holes for machine screws and nuts and screw/unscrew all screws to break the two halves apart or reassemble them, and additionally tabs were added to half of the split tiles (with corresponding slots for the other half) for initial alignment before the screws were tightened. These features are shown in Figure 305. There was no need to join the two halves of fabric; it was sufficient that the fabric of each half was bonded to the rings and that the ring halves were rigidly secured to each other when the two halves were joined by four machine screws per set of ring halves.

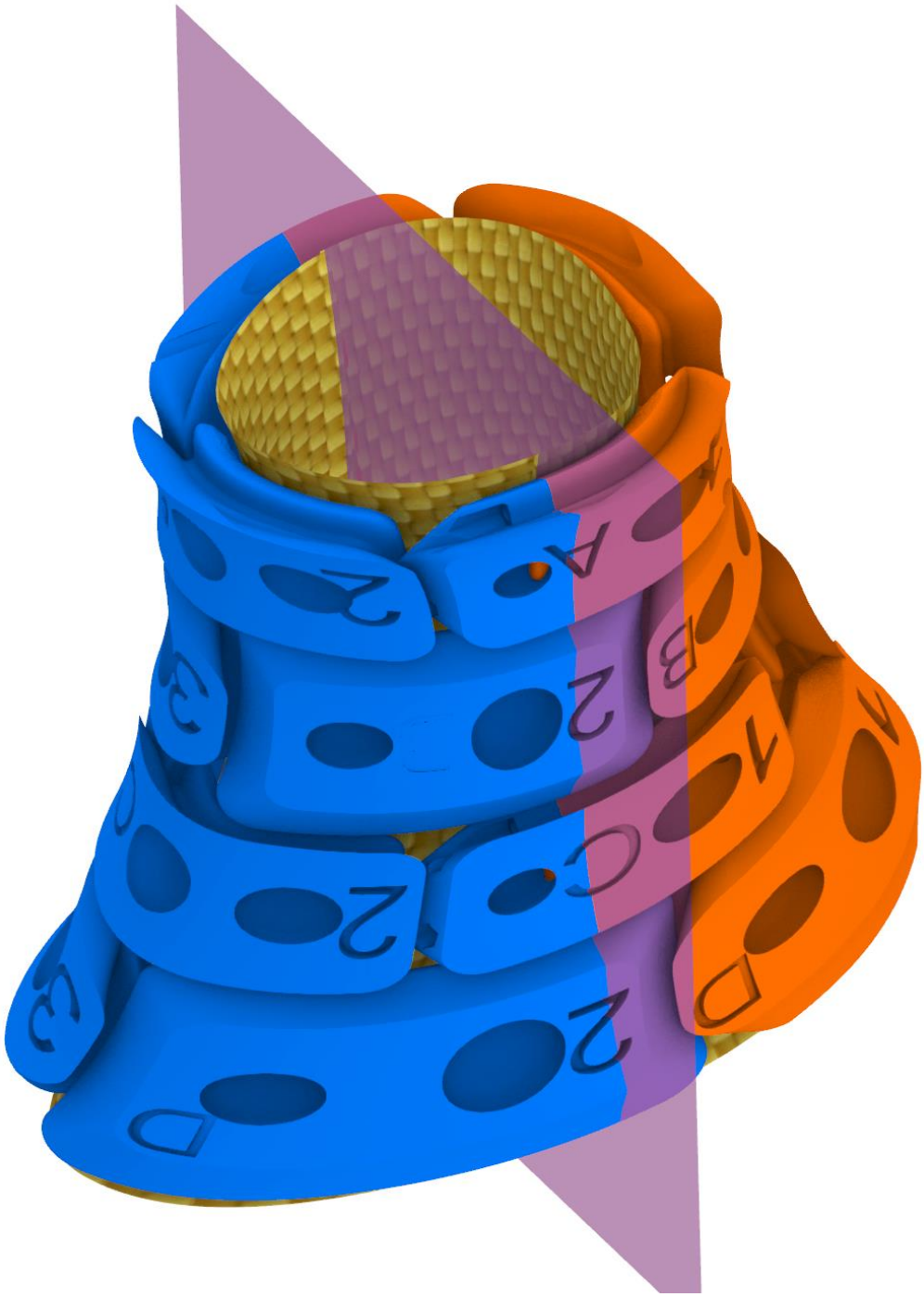

Figure 304: The entire domain split in two (by the splitting plane colored with transparent purple color), with tiles colored blue in the front half and orange in the back half. The fabric is depicted as Kevlar fabric with a yellow-colored weave.

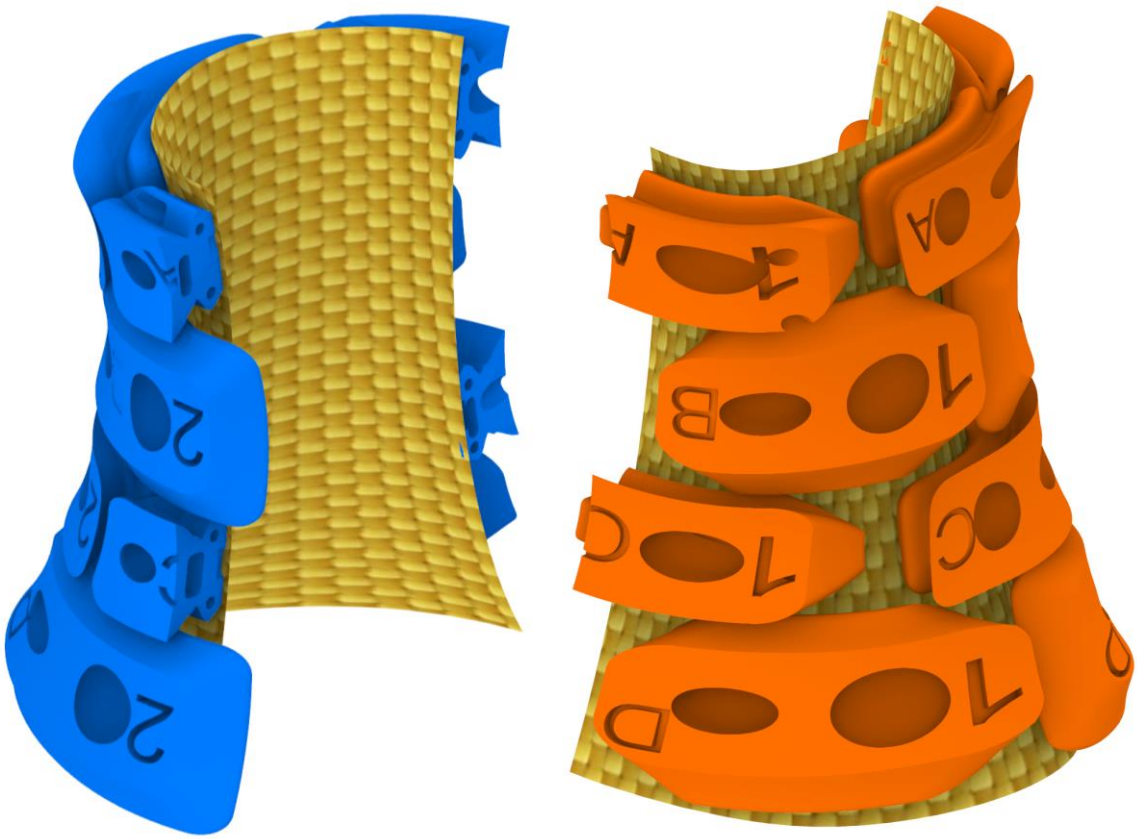

Figure 305: Proposed method of arranging the two halves of the ultimate array. The tiles in the front half are rendered in blue, the tiles in the rear half are rendered in orange, with the fabric in both being depicted in yellow. The tiles marked 1A and 1C are split in half, with tabs (or holes, depending on the tile) and holes for threaded fasteners visible.

Manufacturing the Tiles and Workholders.

The tiles were manufactured individually and separately by additive manufacturing for this embodiment (in a subsequent embodiment, they were printed simultaneously in a multimaterial print). No special material properties were needed, simply rigidity (relative to fabric), so PLA was selected due to its general ease of printing and low cost; print settings were also unremarkable, with a modest infill percentage of 30% for moderate interior strength but light weight. Each tile has a unique geometry, and thus they were assigned numbers and letters to keep track of them (with these identifiers cut into the tile for easy visibility). Additionally, each tile was given two bulb-shaped cuts to precisely index it; the bulb-shaped cuts were designed so that the corresponding bulb-shaped mandrel could snap into the cut and hold it

securely, yet be removed with light force once the tiles were fully assembled and glued to the fabric. A section view and a full view of one representative tile with offset cuts for the bulbous locating features is shown in Figure 306. All of the 3D printed tiles (printed but not yet assembled) are shown in Figure 307.

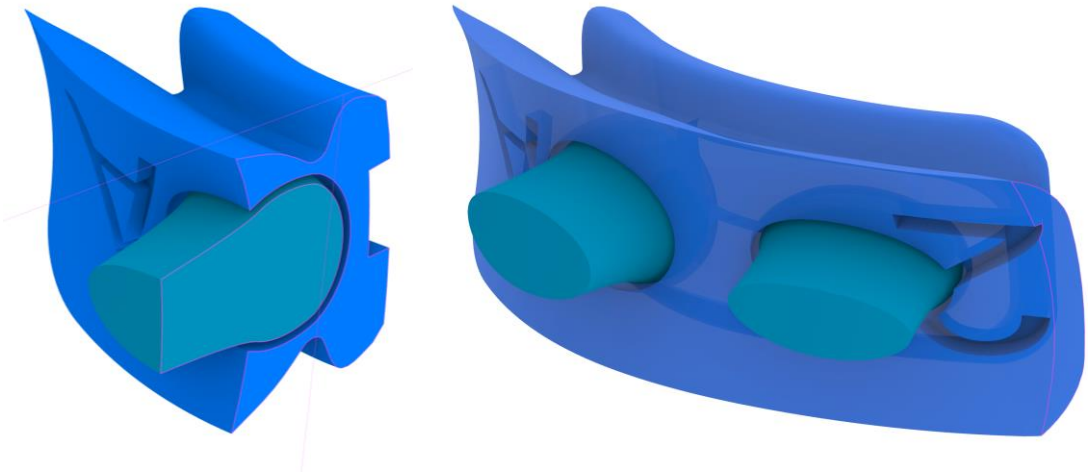

Figure 306: Section view (left) and full view (right) of tile 2A depicted in blue, with the bulbous locating extrusions colored in teal.

Figure 307: Entire set of tiles (including split tiles) after printing and prior to assembly. The colors used are random and have no correspondence to tile geometry.

After manufacturing the individual tiles, it was also necessary to design and manufacture workholding devices to precisely index and position each tile relative to the others and relative to the fabric. At the same time, access to the interior surface of each tile needed to remain open so that the fabric could be glued there. Then, once the composite was manufactured, it needed to be possible to pull the structure off the workholding device so that it would assume its kinematic freedom. As such, a workholding device with many splits that could be easily disassembled was designed. A rendering of the entire set of workholding pieces, assembled along with the tiles and fabric, is shown in Figure 308. Furthermore, renderings of the front and back subassemblies with the attendant workholding pieces are shown in Figure 309 and Figure 310. The workholding device needed to be relatively rigid so as not to bend during assembly and was thus

manufactured by 3D printing out of PLA; a photograph of the workholding pieces as printed is shown in Figure 311.

Figure 308: CAD rendering of the entire set of seven workholding devices (shown in magenta) precisely positioning the tiles (shown in orange and blue).

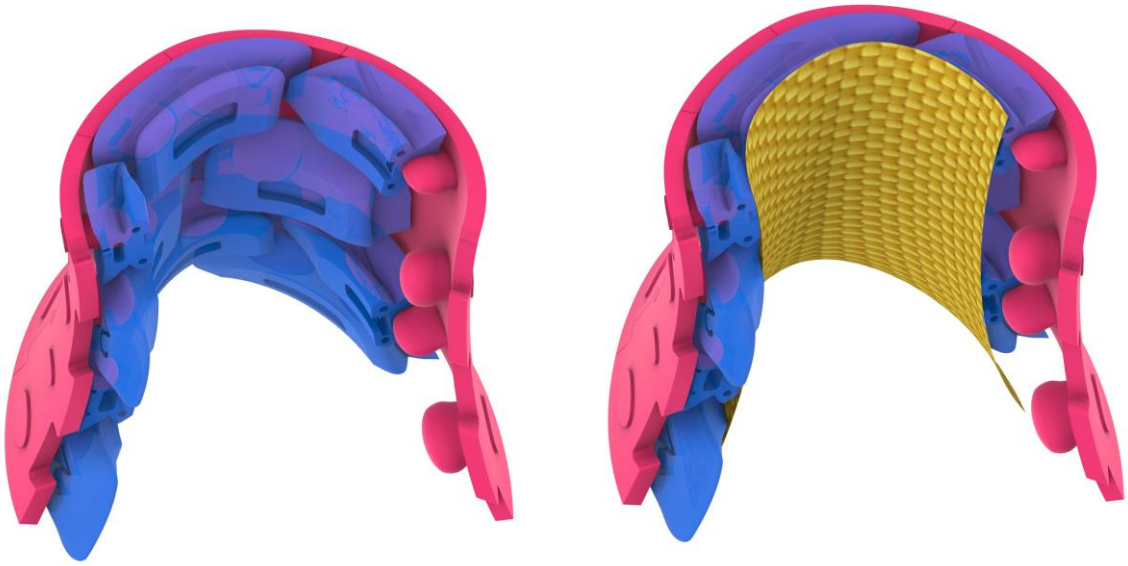

Figure 309: Left, workholding devices precisely positioning the front set of tiles before front fabric shell is glued; right: after shell is glued to tiles.

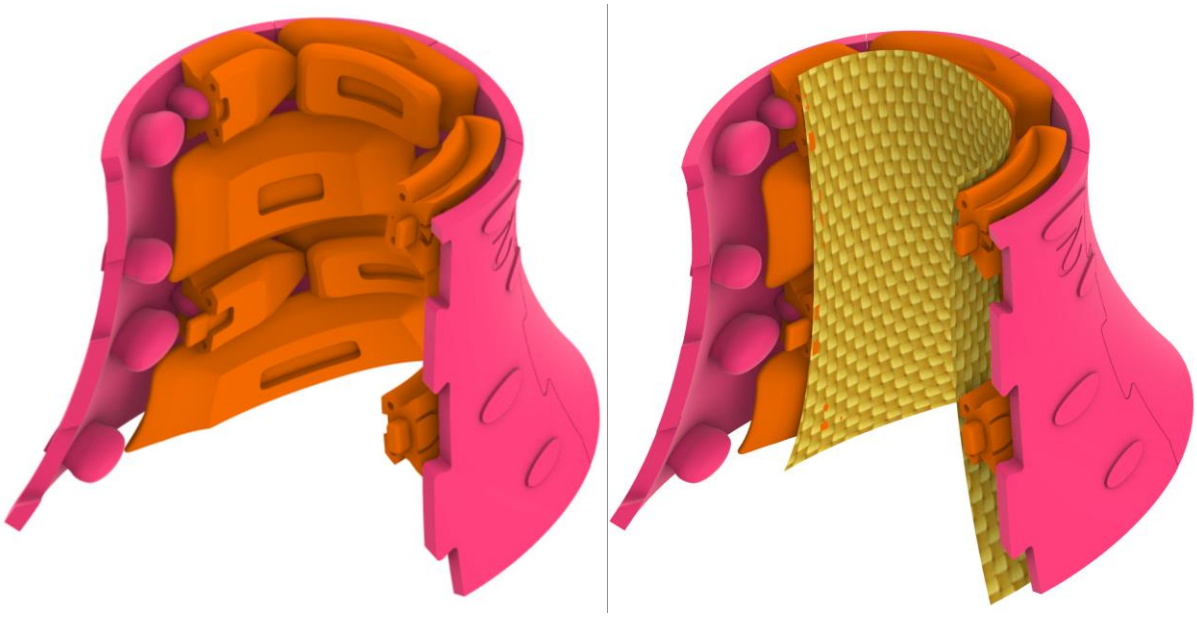

Figure 310: Left, workholding devices precisely positioning the rear set of tiles before rear fabric shell is glued; right: after shell is glued to tiles. Note that workholder #6 is used in both the front and rear halves.

Figure 311: All seven subparts of the workholding device shown after being 3D printed and mostly slotted together. Each one is unique and is numbered; however, the color (yellow vs. black) has no significance.

Creating the Fabric Shells.

The fabric surface (used in both CAD and computer simulations) in most arrays proposed in the second part of this dissertation has been the doubly-curved "hyperboloid-derived manifold", i.e. with Gaussian curvature somewhat deviating from zero over most of the surface, as discussed in Chapter 8. Thus, a surface made of an isotropic material in this shape cannot be unrolled and flattened (even allowing for a finite number of splits) perfectly; flattening it would

necessarily require areas of significant tension and compression in smashing such a surface. Likewise, a thin, isotropic flat surface cannot be rolled exactly into such a doubly-curved shape. At most, initially-flat surfaces of materials could approximate doubly-curved surfaces with significant tensile or compressive stresses (with compressive stresses usually resulting in local shell buckling that manifests as creasing, etc.). With this being said, woven fabrics are considerably more successful at approximating doubly curved surfaces by draping thanks to their bias compliance (allowing shear and attendant contraction) and local microbuckling facilitating compression. Thus, it is reasonable to hope that a woven fabric will be able to conform relatively well to the target shape ("hyperboloid-derived manifold").

While there are many potential approaches to approximating the doubly-curved shell shapes with a flat surface, the CAD package Rhinoceros 3D offers a simple, non-FEA feature in the form of the "Squish" command that appears promising [166]. This command allows the user to select a doubly-curved NURBS surface (or even a triangle mesh), select curves on the surface, and pick a few different modes of mechanical response for the material that is to be thus flattened, and then it produces a flattened approximation and even indicates areas on the flattened surface that are most compressed or tensioned to achieve the flattening (of course, any doubly-curved surface that is forced flat will necessarily develop in-plane internal stresses and strains, whereas theoretically an infinitely-thin singly-curved surface can be flattened without such in-surface stresses and strains). The mode of mechanical response is selected with the "Deformation" type command line option, and the user may pick "Free", "StretchMostly", "StretchOnly", "CompressMostly", "CompressOnly", or "Custom". The "StretchMostly" mode prefers to achieve flattening by stretching the material more than compressing it; the "StretchOnly" mode totally avoids compression; the "CompressMostly" mode prefers

compression; the “CompressOnly” mode totally avoids tension; the “Free” mode is unbiased between tension and compression; and the “Custom” mode allows the user to input a relative ratio of boundary and internal tension and compression preference.

Additionally, the “Squish” command gives the user the choice of “Material” type, either “Rigid” or “Floppy”, where the “Rigid” mode (somewhat of a misnomer) prefers to minimize stresses (though of course it cannot eliminate them considering that a doubly-curved surface will necessarily be stressed when flattened; thus, there is no “rigid” mode in a mechanical sense) and the “Floppy” mode prefers to minimize geometric distortions and changes in final surface area.

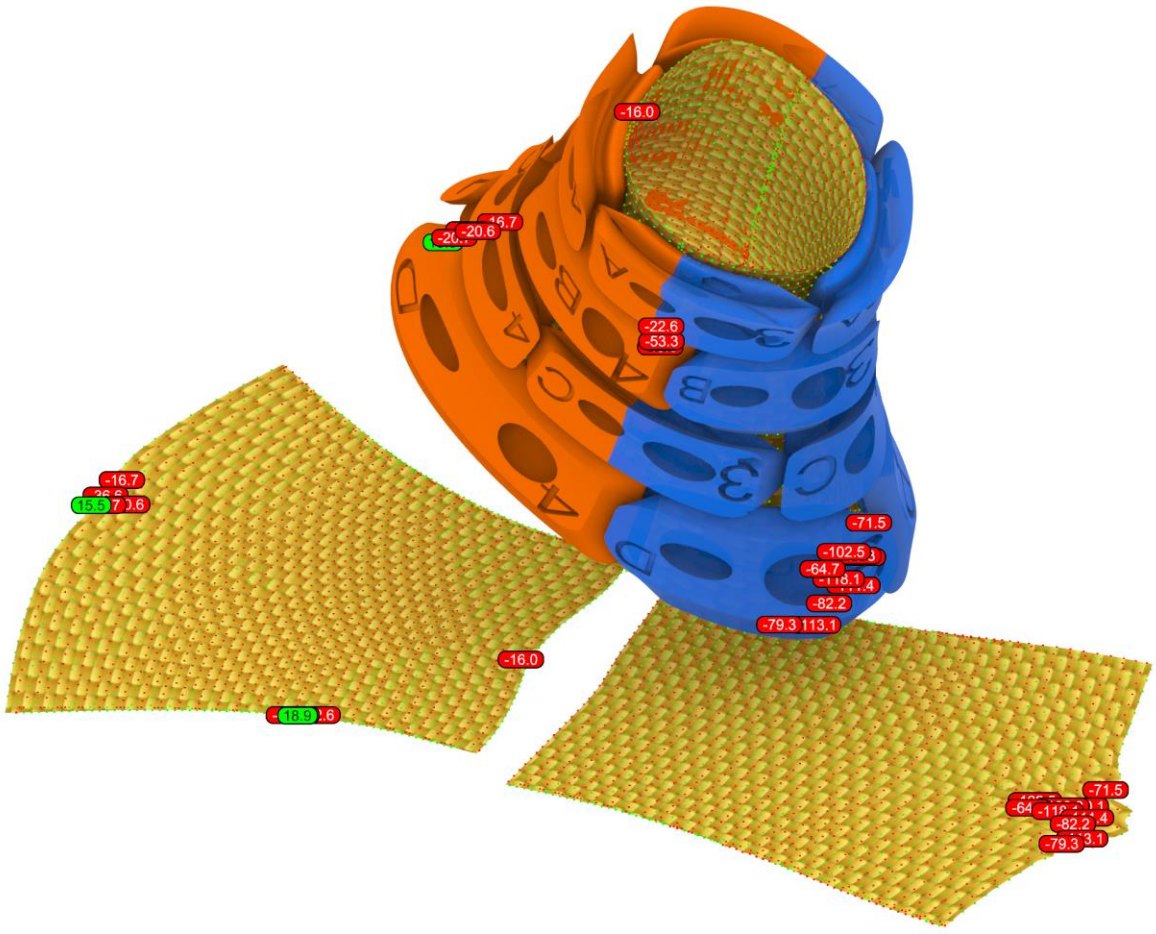

Figure 312: Using the “Squish” command in Rhino to approximate the unrolling of the two halves of the fabric manifold. Note that, because the surface to be “unrolled” is doubly curved, this is only an approximation; “compress mostly” was used to limit the amount of tensile deformation expected (since the fabric can tolerate compression due to local microbuckling), and “floppy”

was used instead of "rigid" to prefer better conformation to the surface at the cost of imposing greater stress. The flattened piece on the left is for the rear half (corresponds to orange tiles); the flattened piece on the right is for the front half (corresponds to blue tiles).

Considering that woven Kevlar fabrics are far more compliant in compression (wherein yarns can respond by localized microbuckling and folding) than in tension, it seemed wise to choose either the "CompressMostly" or "CompressOnly" setting for "Deformation" type. However, it was not clear which of these two to use, and additionally the choice between "Rigid" (a misnomer) and "Floppy" for "Material" was also unclear. Thus, the surface was flattened with all possible combinations of these parameters, and the lengths of the four edge curves on the approximately-flattened surface with each setting and the original doubly-curved surface were compared, with an eye towards minimizing the Root-Mean-Square (RMS) difference between them; the lengths of the four edge curves for the original front half-sheet of fabric and different attempts at flattened versions are shown in Table 3. The best combination, in terms of the RMS average of errors, to be the "Compress Mostly/Floppy" set: it minimized the RMS average and the peak difference between one of the four edge curves on the flattened surface and the corresponding edge curve on the doubly-curved surface (with "Compress Mostly Rigid" being the next-best approach, but unfortunately producing one very large peak difference and additionally creating a "flattened" surface with self-intersecting edges that suggested folding the surface on top of itself locally). Thus, the "Compress Mostly/Floppy" surface was used, and additionally scaled linearly after "Squishing" by a factor of 103.66% in every direction to accommodate the average discrepancy between edge lengths.

Table 3: Edge lengths on the original (doubly-curved surface) and on flattened versions produced with the Squish command with various settings. Percentage differences are also shown. The "Compress Mostly/Floppy" combination was preferred. Lengths are in mm.

Curve	Compress Mostly Floppy	Percentage Difference CMF	Scale Factor	Compress Only Floppy	Percentage Difference COF	Compress Mostly Rigid	Percentage Difference CMR	Compress Only Rigid	Percentage Difference COR	True Length (Target)
Right	179.581	-1.94%	101.98%	205.557	12.25%	183.257	0.07%	199.636	9.01%	183.131

Left	180.107	-1.82%	101.86%	205.816	12.19%	181.702	-0.95%	198.008	7.93%	183.453
Top	144.129	-4.52%	104.73%	165.675	9.76%	139.986	-7.26%	162.781	7.84%	150.947
Bottom	262.02	-5.71%	106.06%	302.893	8.99%	268.298	-3.45%	295.166	6.21%	277.899
RMS Average % Difference		**3.88%**	**103.66%**		**10.89%**		**4.05%**		**7.81%**	

Once the appropriate flattened surfaces to approximate the target (doubly-curved) fabric surfaces were obtained via the Squish command, 2D drawings for stencils for the front and back fabric shells were created (see Figure 313) and then printed on cardstock on a standard inkjet printer, whereupon they were taped to woven Kevlar fabric (after it was stretched biaxially and sheared in order to ensure that the warp yarns were as close to the desired orientation to make them "vertical" when the fabric was glued to the tiles; otherwise, bias compliance might be engaged in the vertical direction, preventing lockup even after the tiles touched); taping them to the fabric (rather than just tracing out the pattern with permanent marker on the fabric) helped prevent the fabric from being accidentally sheared during cutting, and it also facilitated cutting by making it easier to exert tension between fabric on both sides of the cut. This was non-trivial as, even with sharp and specially-designed Kevlar shears, Kevlar is very difficult to cut by hand. The fabric pieces that were produced by this are shown in Figure 314.

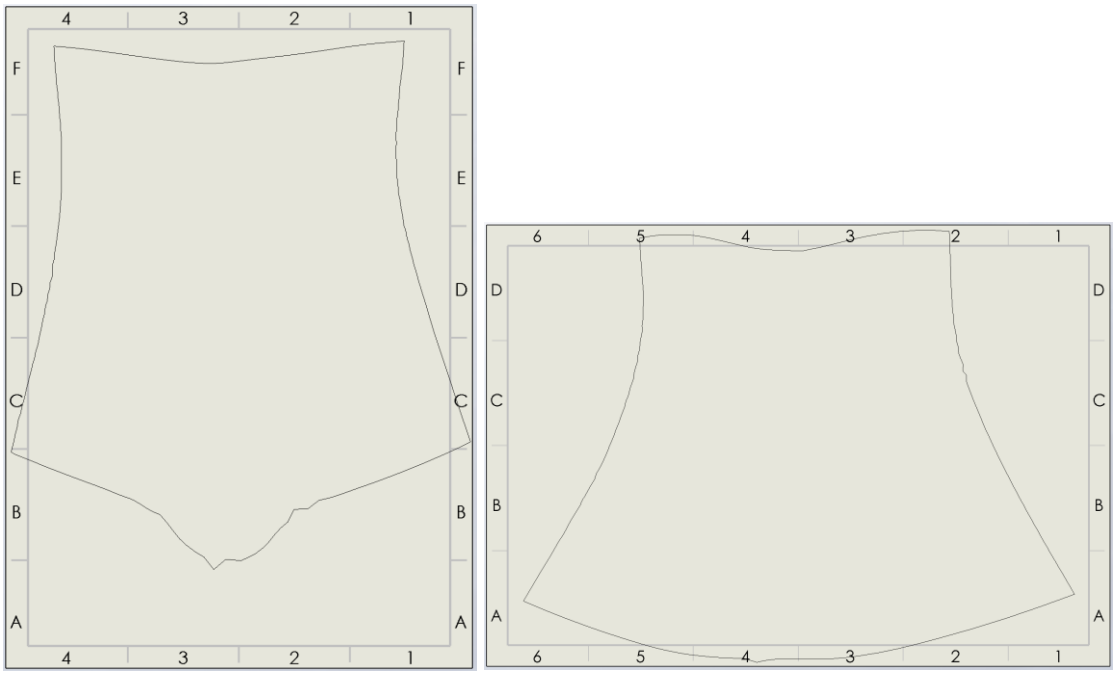

Figure 313: Two-dimensional drawings of the flattened approximations of the front (left) and rear (right) halves of fabric, used to create stencils.

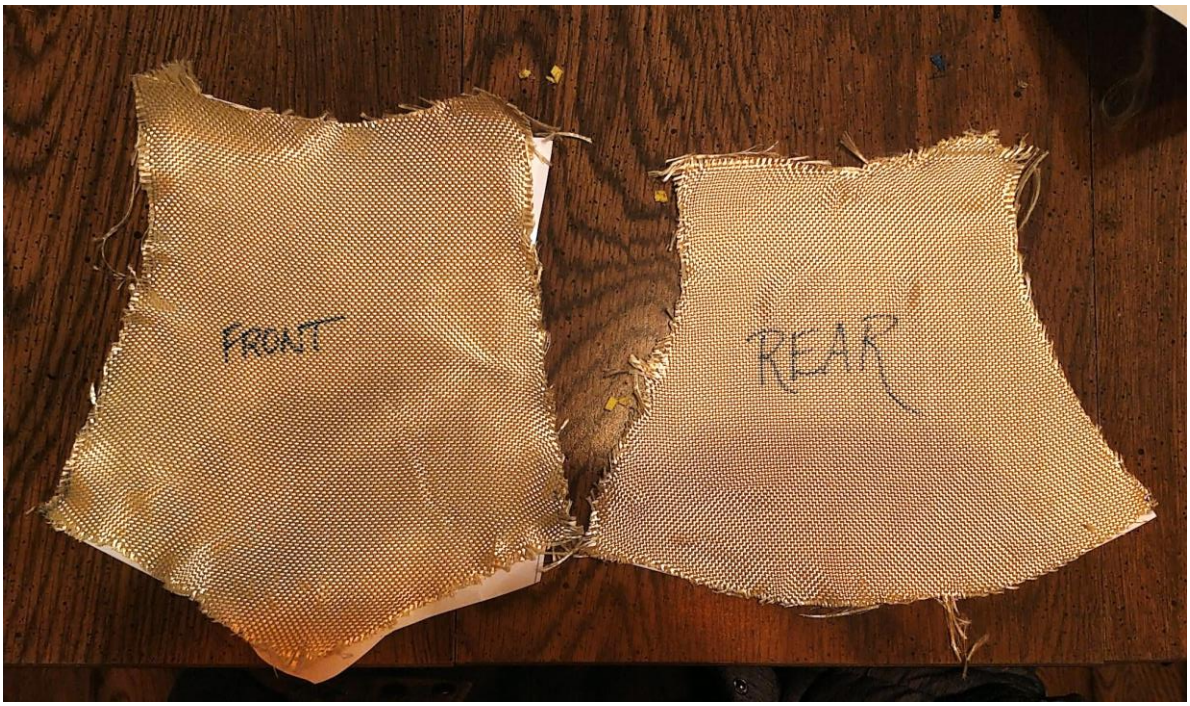

Figure 314: Fabric pieces cut out after tracing along the lines produced by the stencils from the previous figure. Note the orientation of the weave, with warp yarns roughly vertical in this picture (corresponding to a roughly-vertical projection once the fabric is adhered to the tiles).

Final Assembly of the Fabric-Backed Array.

Once all needed tiles, fabric pieces, and workholders were manufactured separately, the two halves of the experimental protective device were assembled accordingly. The tiles were assembled in the proper order inside the workholding shells, and then they were bonded to the Kevlar fabric using simple thermoplastic hot melt adhesive. While this adhesive was not expected to be a good choice for service due to relatively low peel strength and low maximum service temperature, it was appropriate for prototype experimentation due to the ease of deployment. Figure 315 depicts the front set of tiles in the workholder shells once glued to the front piece of fabric, and Figure 316 shows the resulting front half of the entire array as viewed from the interior or exterior. The rear half was manufactured in a similar fashion, and then the two halves were joined and tested in the next section.

Figure 315: Adhering the front half of fabric to the front set of tiles while they are held in the assembled front workholding device.

Figure 316: Interior (left) and exterior (right) view of the assembled front half of the fabric-backed tiled array.

Testing the Fabric-Backed Tiled Array on the Hyperboloid-Derived Manifold.

Once the fabric-backed tiled array halves were manufactured and then assembled together, several concerning aspects were noticeable. First, the array was vulnerable to tiles drooping significantly (tending pull the fabric in folds until the tiles touched each other, and additionally often rotating away from the planned neutral orientation owing to the center of mass of each tile being offset from the fabric). Figure 317 shows the magnitude of this drooping—it is most problematic because it facilitates misalignment between tiles, which is discussed next.

Figure 317: Once fully assembled, this fabric-backed tiled array was vulnerable to drooping under gravitational loading. The left image depicts the array being suspended by the top tiles (more or less eliminating drooping and producing the initial geometry designed on the computer); the right image shows the array unsupported and drooping.

Unfortunately, the tiles were quite prone to misalignment (usually from displacing one tile in the direction roughly normal to the surrounding fabric) with respect to their neighbors. This will likely prove to be a fatal flaw with this concept, mainly because such misalignment between tiles generally results in far more local bending freedom between a given pair of tiles than was intended. Figure 318 depicts one of the nearly infinite configurations of tile misalignment, and Figure 319 compares a properly-aligned pair of tiles with the same pair of tiles in a misaligned configuration.

Figure 318: Many tiles have gotten out of alignment and will not properly engage and lock up with leg rotation. In particular, tile 3,D (black in color) is displaced normally with respect to tile 2,C (also black), meaning that the convex feature on tile 3,D that is supposed to engage with the corresponding concave feature on tile 2,D in fact does not. Likewise, tile 3,B (also black) is displaced angularly with respect to tile 2,A (also black in color). This is just one of the nearly infinite possible combinations of tile misalignments.

Figure 319: Comparing proper alignment (left) between tile 4,B and tile 2,C, and improper alignment (right) between the same tiles after displacing tile 4,B and the region of fabric surrounding it in the positive normal direction.

At first glance, the severity of tile misalignment from normal displacement was surprising, considering that this phenomenon was nearly unknown with the singly-curved arrays studied in Chapter 4 and Chapter 5. However, the arrays that targeted singly-curved lockup shapes tended to have far less free (unbonded) fabric between bond locations relative to the length of the tiles themselves than does this cylindrical/hyperboloidal closed-surface array, and indeed, the singly-curved-lockup arrays had even most of the unbonded fabric directly under one of the two tiles. In contrast, this cylindrical/hyperboloidal closed-surface array had a very significant increase in the amount of free fabric between tiles in an attempt to allow the compressive freedom required on the side of the array towards which the leg is rotating, as well as to allow shear freedom to the sides when the leg is rotating forwards. A section view illustrating the comparison of the amount of unbonded (kinematically free) fabric in the singly-curved-lockup array and in this chapter's array is shown in Figure 320.

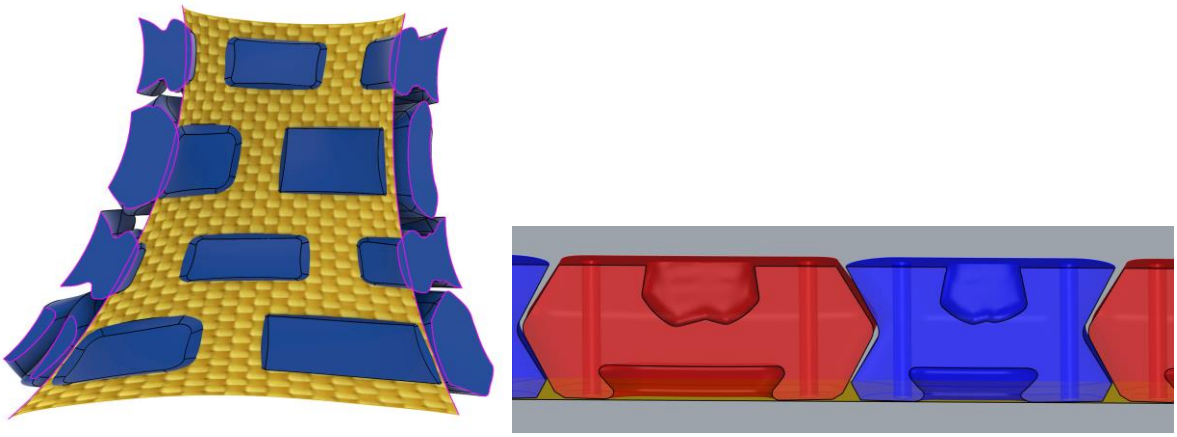

Figure 320: Section views of the tiled HDM manifold of this chapter (left) versus the planar manifold studied in Chapters 4 and 5 (right).

Indeed, estimating whether the array could tolerate an amount of leg rotation before lockup even within an order of magnitude of what would be required was a fraught question as the tiles often had to be manually rearranged relative to each other (each locally with respect to the fabric normal) to ensure a semblance of proper behavior and limited sliding and the resulting disengagement. Figure 321 shows the array in a point loading condition applied to the front and top-most tiles until effective lockup, after manually aligning the tiles to ensure they would properly engage instead of sliding past each other in a direction normal to the fabric. Clearly, this is not sufficient freedom for the full range of safe dorsiflexion for a healthy subject.

Figure 321: Point loading the fabric-backed tiled array to lockup to simulate a leg rotating in dorsiflexion (leftwards in this image). Unfortunately, the array had far less freedom than desired.

Multimaterial Elastomer-Backed Tiled Array, Revision 1.

The entire process of creating a fabric-backed tiled array on the hyperboloid manifold was quite involved, owing to the print time and design time required to create the workholding devices and the manual work to glue the tiles to the fabric; consequently, to rapidly iterate different tile (and perhaps manifold) shapes, it would be preferable to have a manufacturing technique that required less manual assembly and no workholding devices. It would be acceptable if the resulting prototype merely had a similar lockup shape, even if its pre-lockup

stiffness were different. Thus, it seemed wise to investigate replacing the fabric backing with a thin elastomeric shell, at least for the purposes of prototyping. Certainly, even a thin elastomeric shell would result in higher pre-lockup stiffness as compared with a fabric-backed array (for the same tile size) owing to the much greater bending stiffness contribution of the elastomeric shell (which would have to be considerably thicker than the fabric, and would not have the micromechanical properties of fabric like bias compliance and yarn microbuckling that greatly reduce the effective bending and shear stiffness of fabric). Likewise, an array backed with a thin elastomeric shell would have lower post-lockup stiffness than the same array backed with a high-stiffness fabric like Kevlar due to the far lower tensile stiffness of the elastomer.

The primary concern with using an elastomer-backed array to simulate a fabric-backed array would be whether or not the absence of micromechanical features specific to fabrics, especially trellising (enabling a degree of in-plane shear with little resistance as well as extension along the bias) but perhaps also yarn and filament microbuckling, would give the elastomer-backed array qualitatively-different kinematic properties from the fabric-backed array. Thus, for comparison purposes, the first elastomer-backed array to be printed had the same tile configuration as the fabric-backed array produced in the previous section, though future elastomer-backed arrays could be given different tile configurations to determine which is optimal. The primary difference as regards the tiles was the absence of features that facilitated workholding (such features were unnecessary considering the entire array was printed in one piece).

Manufacturing the Elastomer-Backed Tiled Array, Revision 1.

The thickness of the elastomeric shell was chosen to be 1.2mm based on previous experiments with shells (discussed in greater detail in Chapter 8), as this was felt to not be

excessively thick (which would have resulted in excessive pre-lockup stiffness), nor excessively thin as this would have resulted in manufacturing difficulties: for additive manufacturing of shell structures, it is wise to assign them a thickness of at least two nozzle widths, and the parts were to be printed on a printer with 0.4mm-diameter nozzles. Using only one diameter width for the shell (i.e. 0.4mm thick) would have made the shell quite vulnerable to tearing, especially at minor printing defects (e.g. underextruded areas).

The array was 3D printed on an Ultimaker S5 multimaterial-capable Fused-Deposition Modeling (FDM) 3D printer using two materials, DuPont Hytrel 4100FL (a thermoplastic ether-ester elastomer) for the elastomer, and either acrylonitrile butadiene styrene (ABS) or PETg (glycol-modified polyethylene-terephthalate) filament for the rigid tiles, since DuPont literature [144] indicated that the Hytrel elastomer would blend most effectively with either PET(g) or ABS (or additionally polyvinyl chloride-PVC, but PVC is not safe to print on FDM 3D printers owing to the evolution of chlorine gas during melt processing). A visualization of the "G-code" (toolpath instructions showing printed lines) for this print is shown in Figure 322. The two materials are shown in different colors in the G-code visualizer for ease of distinguishing them. Note that this manufacturing technique was also used in Chapter 7 to create a compliant-mechanism auxetic array on the hyperboloid-derived manifold.

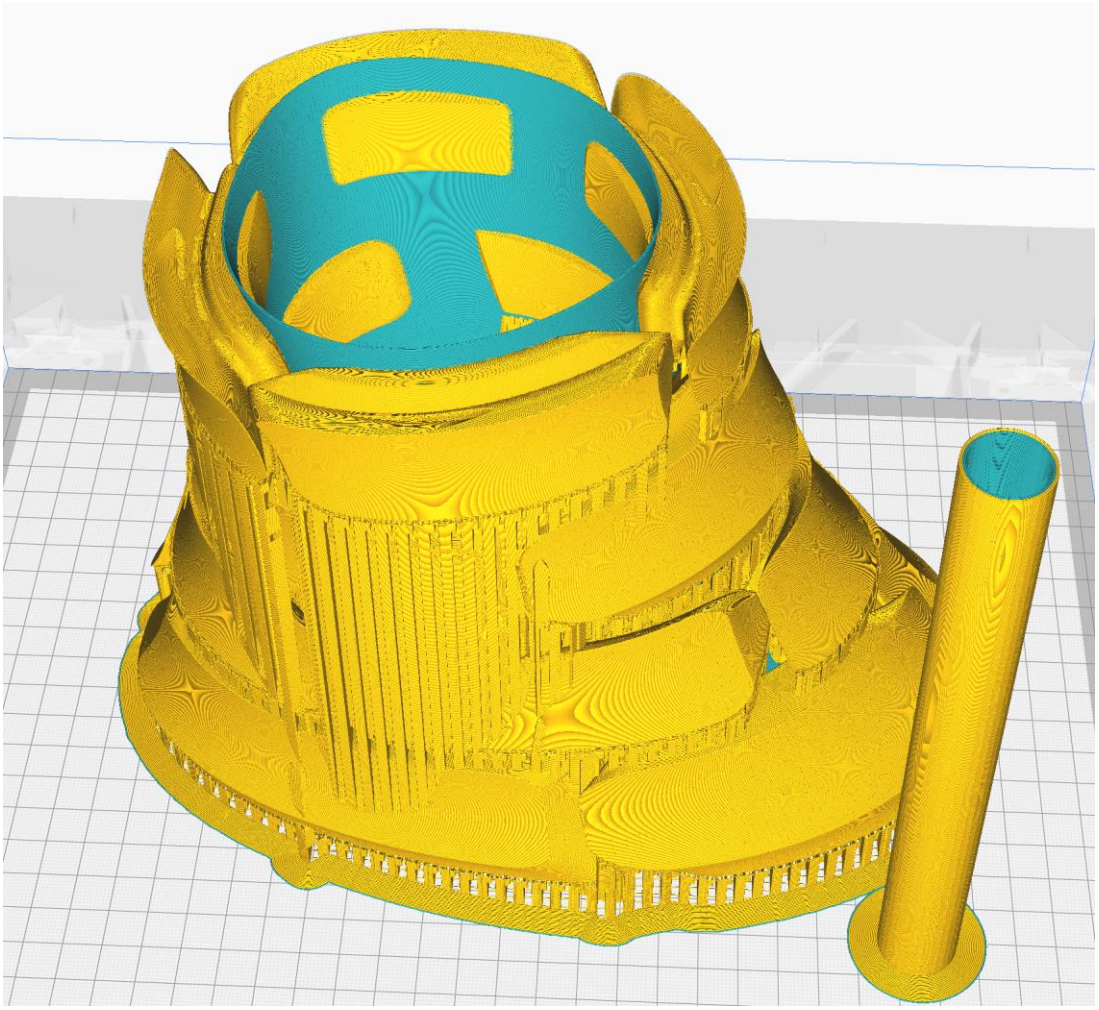

Figure 322: Preview of the Gcode toolpaths for the multimaterial print on the Ultimaker S5, shown in Ultimaker's Cura slicing program. Yellow lines indicate printing in PETg, and teal lines indicate printing in TPE. Breakaway support for overhangs is used and printed in PETg (due to its higher brittleness, which facilitates breaking the material away). Additionally, in the lower right-hand corner, a "prime tower" consisting of both materials was generated to improve the print surface finish. (Like the breakaway material, this is discarded once the print is finished).

While PETg (a polyester) and Hytrel 4100FL (a polyether-ester) are chemically compatible and thus should bond fairly well, the bond strength between the elastomeric shell backbone and the rigid tiles was further maximized by causing the slicing program (which generates G-code toolpaths for the 3D printer) to alternate the material used to print areas of overlap with each layer, and additionally ensuring that lines between the two materials overlapped slightly (on the order of 0.2mm—too much would cause overextrusion, but too little could cause voids between the two materials, especially in the case of nozzles that were

imperfectly aligned in the *x*, *y*, or *z* directions). The effect of these adhesion-promotion settings on the toolpaths is depicted in Figure 323.

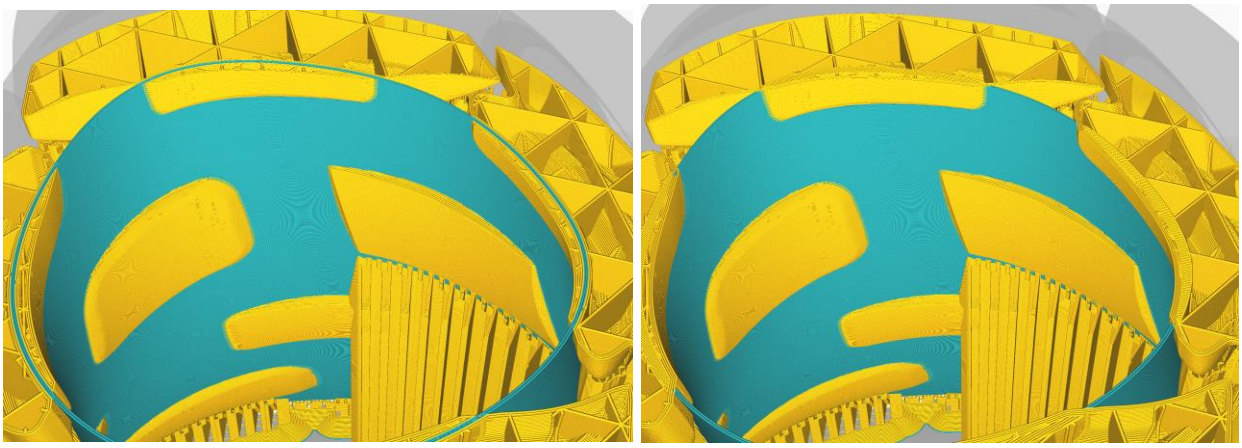

Figure 323: Close up of the extrusion paths (visualizing the Gcode) for the multimaterial print. Two sequential layers are shown (layers 790 and 791) in order to illustrate the effect of using the "alternate mesh removal" setting in Ultimaker's Cura slicer: note how, in the left image (layer 790), the TPE shell (shown in teal) is continuous, but in the right image (layer 791), it is interrupted by the PETg shells. Additionally, because the "merged mesh overlap" setting was set to 0.2mm instead of the default 0.0mm, the teal lines of the TPE extrusions overlap by 0.2mm with the yellow lines of the PETg extrusions when they occupy the same space in the CAD file; this ensures even better adhesion between the two materials. Granted, this setting cannot be too high, or there may be overextrusion resulting in warpage or dimensional inaccuracy. Also note the relatively hollow, infilled structure of the tiles (whereas the TPE shell that simulates the fabric is solid but only consists of a couple of lines).

Testing the Multimaterial Elastomer-Backed Tiled Array.

After the multimaterial array was printed and support removed, it was tested in point loading, just as the fabric-backed array was in its corresponding section. Certainly, point loading the top region of the array forward while constraining the bottom tiles is not precisely the same as the load/boundary condition of a leg rotating about an axis and contacting the interior at a sliding contact patch of moderate area; however, it was a first-order test sufficient to determine if the array had even within an order of magnitude of the freedom before lockup required. Figure 324 shows a comparison between the array in an unloaded state and when it is point-loaded forward until lockup. Unfortunately, the array had perhaps an eighth of the requisite freedom in the dorsiflexion direction, owing both to contact between tiles in the front and sides and to the tensioning of the rear area of the elastic manifold (though the TPE certainly had an effective

Young's Modulus orders of magnitude lower than that of woven Kevlar fabric, it was nonetheless sufficiently stiff, especially at this thickness, to produce some lockup).

Figure 324: Left: multimaterial (TPE-PETg) array, not loaded but after removing breakaway support material. Right: the array is loaded to lockup. Note that the array is quite deficient in freedom, and a user wearing this particular array would have sorely limited freedom. The yellow tiles are rigid (PETg) and the shell is Hytrel 4100FL TPE.

While the rear region of the TPE shell was quite stiff in the tension loading it received when the structure was placed into global bending, the TPE shell readily buckled under compressive stresses that developed in the front region of the manifold. Indeed, as discussed in Chapter 7 in the section titled "Intended Deformation Behavior, Lockup Shape, and Boundary Conditions," it was fully anticipated in the design of the original fabric-backed tiled arrays that, when the leg experiences dorsiflexion (rotating forwards), the rear region of the shell (opposite the leg's direction of rotation) would go into tension and be nearly length-invariant, whereas the region nearest the front of the manifold would go into compression and shell buckling; specifically, the unbonded regions of fabric between tiles would compress and crease inwards, though the areas bonded to the tiles would of course be stiffened against shell buckling.

Additionally, once the tiles in the front regions came into compressive vertical contact, the structure should lock up. As can be seen in Figure 325, the regions of the TPE shell that were not bonded to the rigid tiles indeed compressed somewhat vertically and creased under forwards point loading.

Figure 325: Bending the array forward with a point loading, viewed from the inside/underside of the array. Left: unloaded, right: loaded until lockup. Note the "wrinkling" (just a form of localized shell buckling) in the elastomer regions between the tiles.

Additionally, the structure was resistant to ovalization, i.e. a significant change in the cross-sectional profile (becoming fatter in one direction and thinner in the orthogonal direction), owing to the circumferential contacts between tiles being engaged as gaps closed up. Certainly, it was anticipated (as described in Chapter 7, section "Intended Deformation Behavior, Lockup Shape, and Boundary Conditions") that some cross-sectional changes would be required to allow the front regions of the array to compress without requiring significant tensile strain in the side

regions of fabric; however, it seemed wise to limit the amount of circumferential bending since there could be a positive feedback loop effect from excessive ovalization (inasmuch as it further reduces the structure's stiffness against bending and indeed is associated with shell buckling; e.g. see the tests conducted on the hyperboloid-derived manifold without any tiles, discussed in Chapter 6). Figure 326 illustrates the range of circumferential freedom before lockup that this array possesses.

Figure 326: The structure's bending freedom was tested in different directions out of curiosity. Left: unloaded; right: loaded. It is not clear how much freedom against point loading in the radial direction is required of such arrays.

Overall, as mentioned above, this array was severely deficient in terms of the magnitude of the pre-lockup rotational freedom that it would allow the wearer. However, it was vastly superior to the fabric-backed array with the same tile configuration in that it was impossible to misalign the tiles and cause jamming, probably owing to the far greater pre-lockup stiffness that the elastomer offers over fabric. Additionally, there was practically no drooping under self-weight on the part of the tiles (thanks again to the intrinsic stiffness of the shell at least being able to comfortably bear the moments imparted by gravity acting at the offset centers of mass of the tiles). While there were other potential issues with the solid elastomeric shell backing

(ranging from ventilation and reliability of manufacture owing to weak interlayer strength with 3D printing, to excessive pre-lockup stiffness and damping), the principle seemed promising enough to conduct several more iterations on the elastomer-backed array focused on increasing the pre-lockup freedom, discussed in the following sections. If an appropriate lockup shape were discovered, it might also be worthwhile to investigate the same array of tiles with a fabric backing instead of an elastomeric shell, or alternatively, a composite consisting of high-strength fabric coated with a thin layer of elastomer for moderate intrinsic bending stiffness against drooping and misalignment.

Elastomer-Backed Tiled Array, Revision 2-4.

The next approach to determining a suitable set of tile geometries for a protective array with sufficient pre-lockup freedom was to progressively bend each individual tile about an axis running through its center of mass, in the hopes that, by increasing the distance between tiles and targeting a sharper local curvature for tile engagement, the entire structure would allow more curvature at lockup. Indeed, it seemed wise to err on the side of "overshooting" the lockup freedom. Other than repeatedly applying this bending transformation, the three arrays that constituted Revisions 2 through 4 of the elastomer-backed tiled arrays were identical. Figure 327 compares these three revisions together, portraying their respective tiles in different colors and superimposing them on the same manifold.

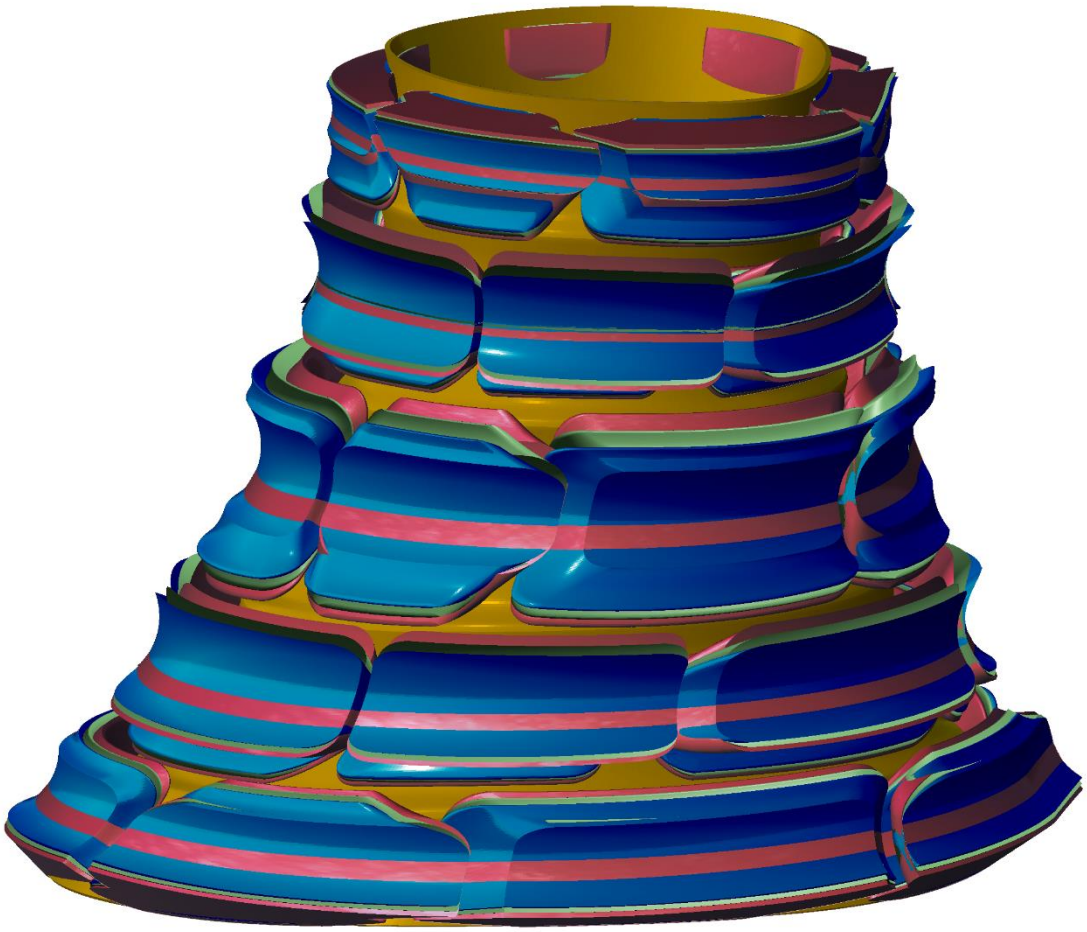

Figure 327: Revisions 2 (red color tiles), 3 (green color tiles), and 4 (blue color tiles), all on the same shared elastomeric backbone (colored yellow). Each revision added curvature to the tiles in the vertical-bending direction with the intention of increasing the amount of freedom the array was capable of before lockup.

Testing Revisions 2-4 of the Elastomer-Backed Tiled Array on a Special Test Fixture.

While simply applying a point load to the first array to manually bend it forward was acceptable to roughly estimate the freedom of the array prior to lockup, it seemed preferable to create a test fixture featuring a rotating "leg" in order to accurately simulate the sliding contact as well as the leg's own radial stiffness potentially preventing cross-sectional ovalization or other buckling phenomena. The "leg" was given a simple revolute joint through an axis corresponding roughly to the axis of dorsiflexion/plantarflexion (as this is the mode that requires the most freedom). Further test fixtures could use axes oriented in different directions, e.g. for pure

inversion/eversion or for coupled behavior (or simply use ball joints). Owing to the flared shape of the calf muscle and the flared shape of the foot interface, it was necessary to be able to remove the arrays by moving the leg up through the array rather than downwards; thus, an extruded cut through the bottom half of the revolute joint surface on the leg was created in order that it could be removed through the top of the array (alternatively, the array could have been designed with a split and with fasteners to connect the two halves, as the fabric-backed array was designed, though this added both design and manufacturing time and was thus seen as an undesirable expenditure of time when the alternative principle of removing and inserting the "leg" through the top of the array was understood). A section view of the "leg" and "shoe" assembly, inside the array, is visible in Figure 328. The assembly is shown in a disassembled state after printing in Figure 329 and fully assembled in Figure 330.

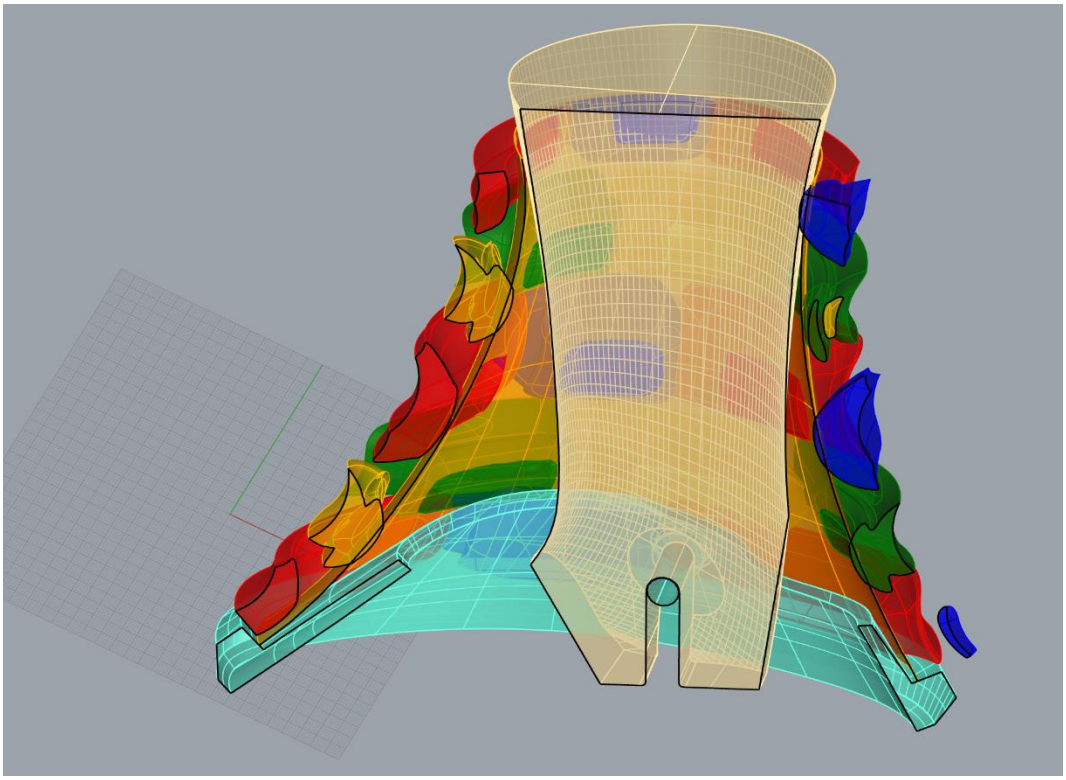

Figure 328: Section view showing the two-part test fixture, consisting of a base part (colored cyan) with a cylindrical beam for a revolute joint, and a rigid "leg" (colored pale yellow) with a mating surface for the revolute joint, as well as an extruded cut allowing the simulated leg to be removed upwards through the top of the cylinder-like protective surface or placed back on the joint through the surface (thus, the protective surface did not have to be split into two parts and assembled on the "leg", which would have made manufacturing the protective surface much more difficult).

Figure 329: Test fixture, 3D printed and disassembled. The "leg" is printed in red polymer, and the base fixture in blue polymer. The base piece has a conical surface that is intended to hold the bottom part of a protective array.

Figure 330: Test fixture, assembled after 3D printing. The red "leg" can rotate quite freely about its revolute joint with the blue base piece.

After printing and breaking away the support material, each array was tested on the fixture, manually loading it until moderate lockup was subjectively felt through the leg.

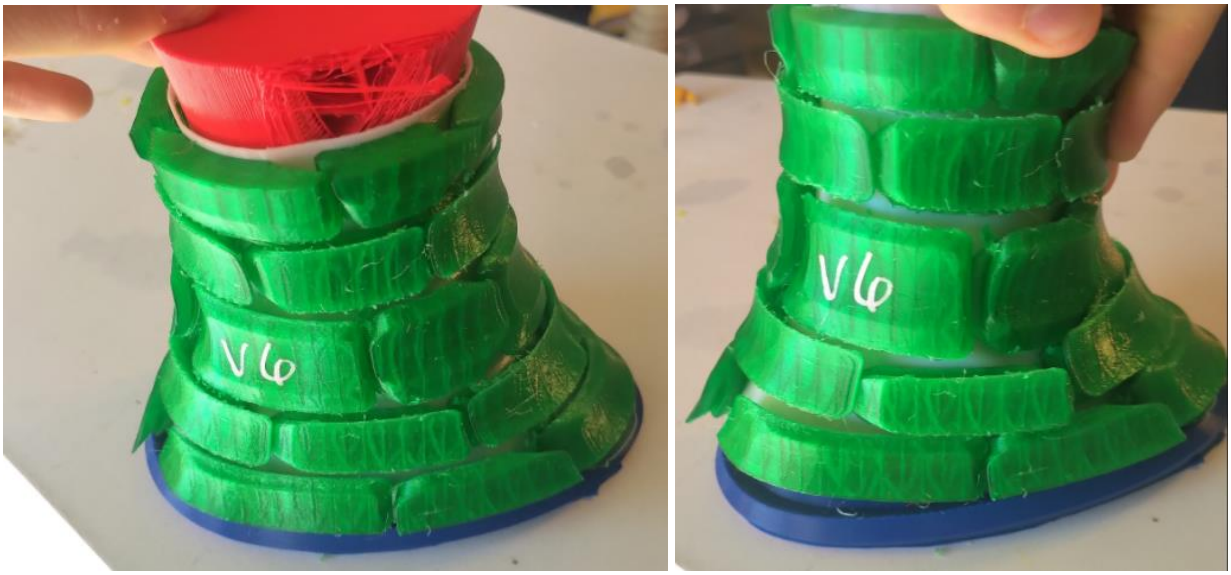

Figure 331: Revision 2 of the elastomer-backed array (left: unloaded; right: loaded until stiffness was prohibitive).

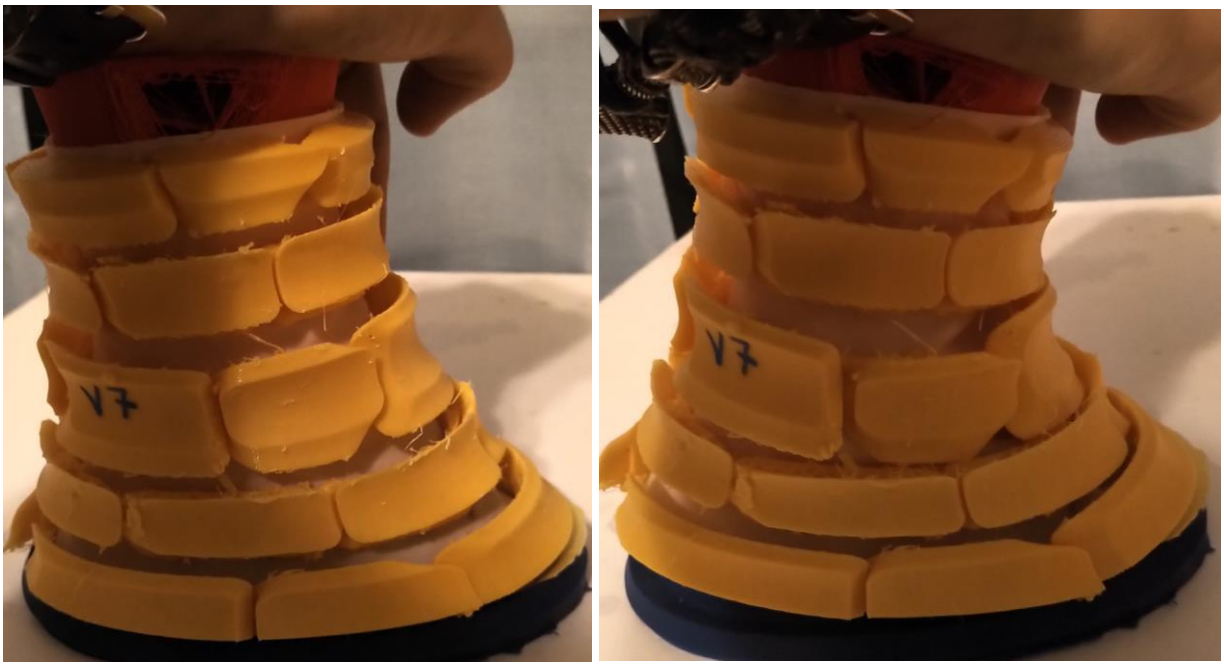

Figure 332: Revision 3 of the elastomer-backed array (left: unloaded; right: loaded until stiffness was prohibitive).

Figure 333: Revision 4 of the elastomer-backed array (left: unloaded; right: loaded until significant stiffening).

Figure 334: Closeup view of the Revision 4 elastomer-backed array, focusing on two different areas of local tile misalignment.

Bellows-Elastomer-Backed Tiled Array.

Indeed, this approach would be somewhat reminiscent of the bellows-like surfaces studied in Chapter 6, which were found to have considerable tolerance for the joint they enclose bending (though at the time it was unclear how to make them lock up after a prescribed amount of bending). Specifically, the original bellows-like surface consists of a repeating pattern of wave crests that are offset from the initial surface (the hyperboloid-derived surface that this researcher sculpted to conform to his foot and leg) tangent to areas that replicate the original surface. Just as the wave crests stiffened the elastomeric surface of the bellows surface circumferentially against local radial indentation (resulting in localized buckling and torsion about instantaneous circumferential axes in the non-wavy area), so too would rigid rings circumferentially stiffen the surrounding strips of fabric and force deformation to instead occur in vertical bending, circumferential torsion, etc.

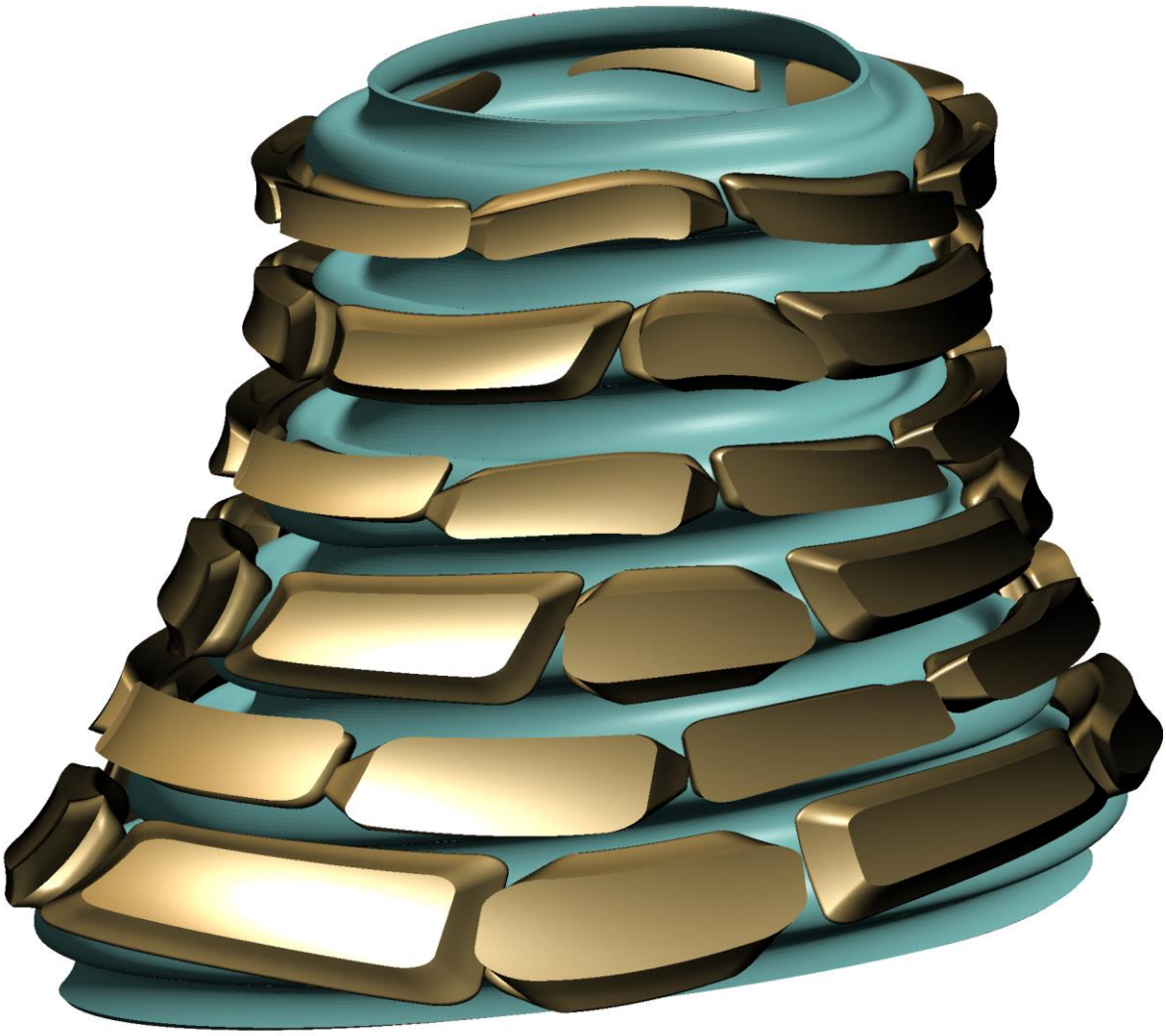

Figure 335: Overall CAD geometry of the bellows-backed tiled array, with the elastomeric portion of the multimaterial print depicted in teal color, and the rigid portion depicted in gold.

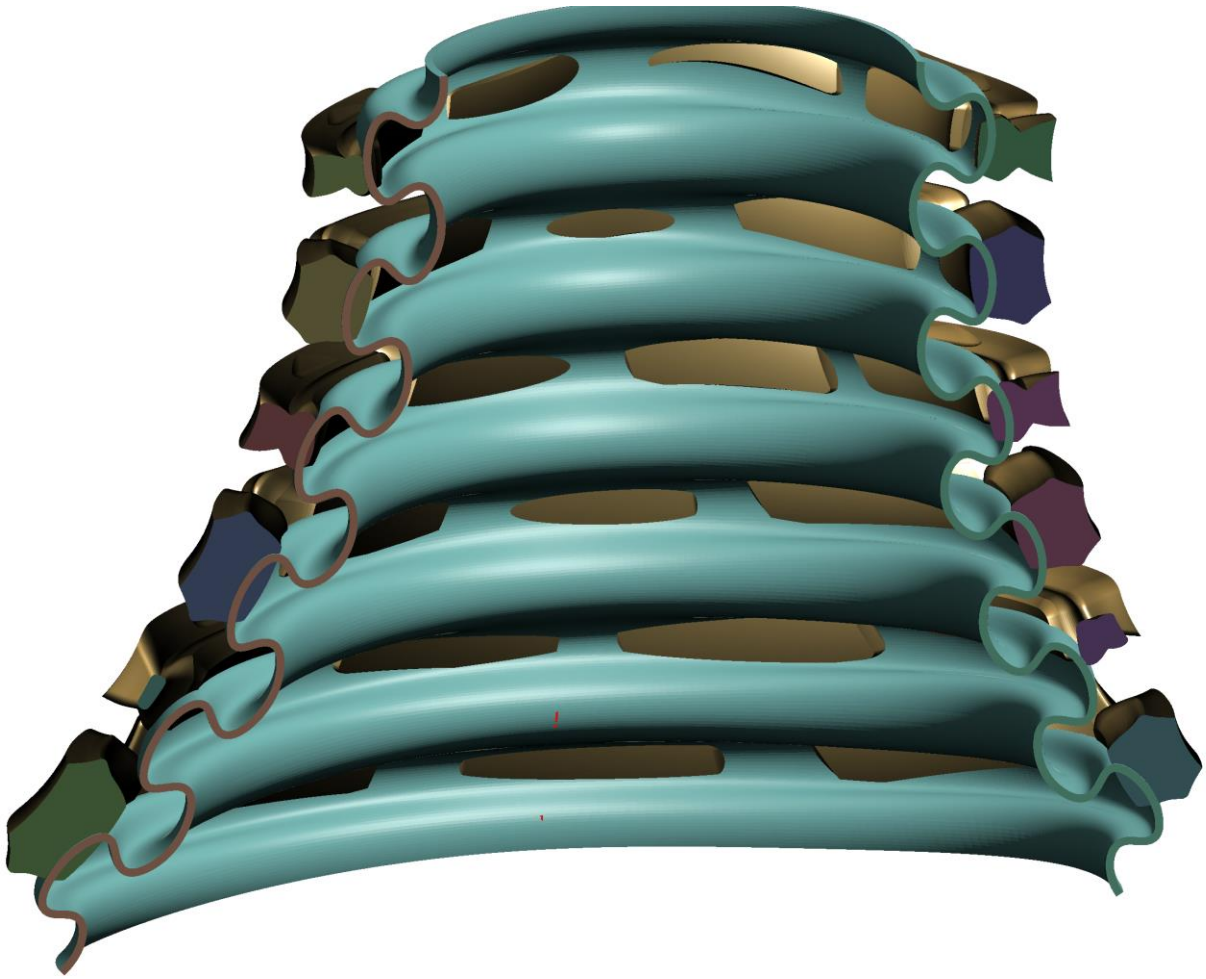

Figure 336: Sectioned view of the same multimaterial composite shown in Figure 335, showing the reentrant waviness of the bellows surface. The surfaces cut by the sectioned plane are colored variously in purple, green, etc.; otherwise, teal represents the elastomeric portion, and gold represents the rigid portion.

Figure 337: Prototype bellows-backed tiled array on the test fixture. Left: neutral position; right: leg bent forward (to the right in this picture) until stiffening.

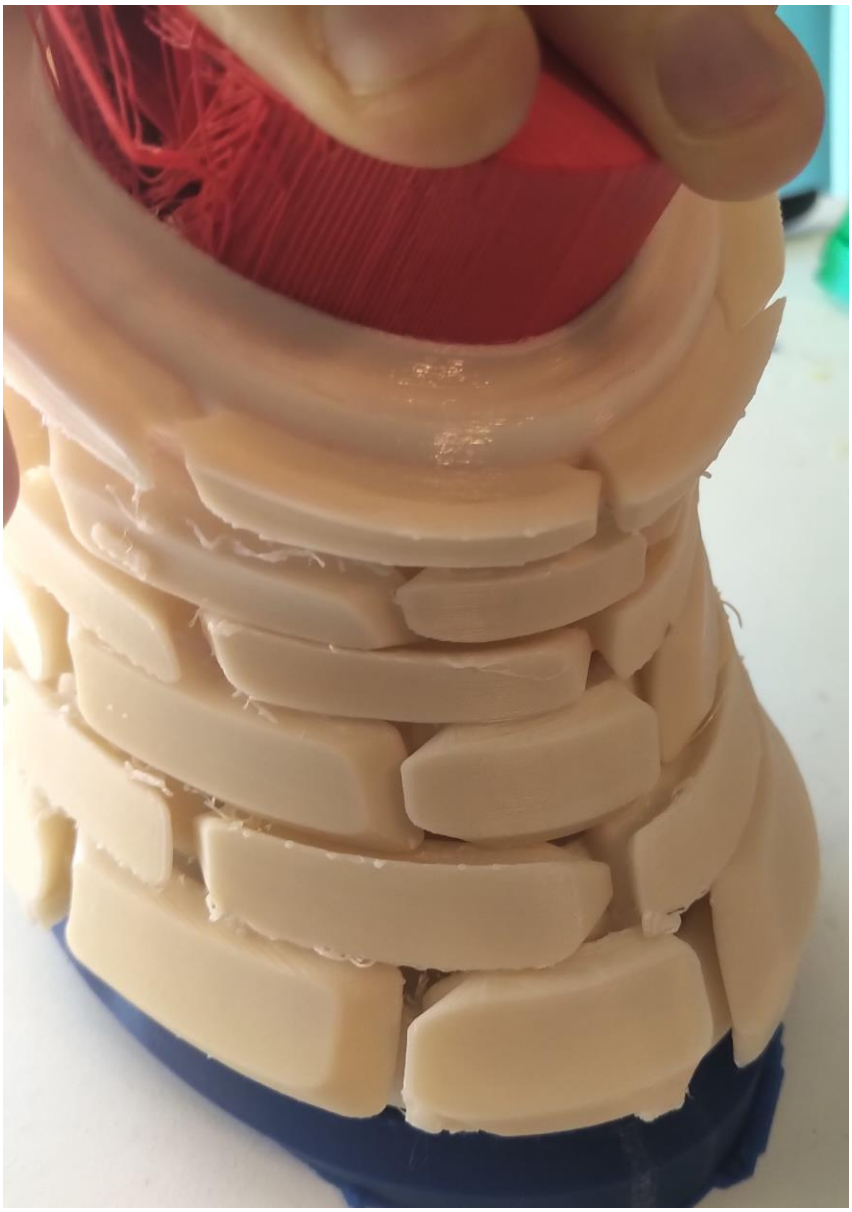

Figure 338: View of the bellows-backed tiled array on the test fixture with the leg rotated forwards (roughly out of the page). Same position as the right view in the previous figure, but this time from the front instead of from the right. Note that the vertical gaps between the rigid tiles have mostly closed up at the same time to produce effective compressive stiffening in the front.

Full-Size Bellows-Elastomer-Backed Tiled Array for Human Testing.

The bellows-backed tiled array examined in the previous section seemed promising enough to create a full-scale version, with several practical alterations, that could be tested on a human subject. First, in order to don and remove the protective device, it must be capable of splitting and then rejoining around the lower leg (since, owing to the close conformity between

the structure and leg, the wearer's foot cannot pass through the top opening unless it is split and temporarily enlarged). The splits were made through rigid tiles, so that the tiles themselves would communicate forces and moments between each other (rather than relying upon the softer elastomeric membrane to communicate such forces, which would be excessively compliant). Owing to the offset nature of the unit cell, the splitting curves had to be wavy rather than monotonically curved. The entire array, consisting of rigid tiles and elastomeric membrane, is rendered in Figure 339. Note that the membrane halves also have rounded-square holes cut into them, primarily for purposes of ventilation for the wearer (they are not expected to have significant mechanical effects). It would also be reasonable to cut additional ventilation holes directly into the centers of the tiles (though the outer faces of the tiles, which are involved in lockup, should not be altered), though this was not done owing to the extra work it entailed.

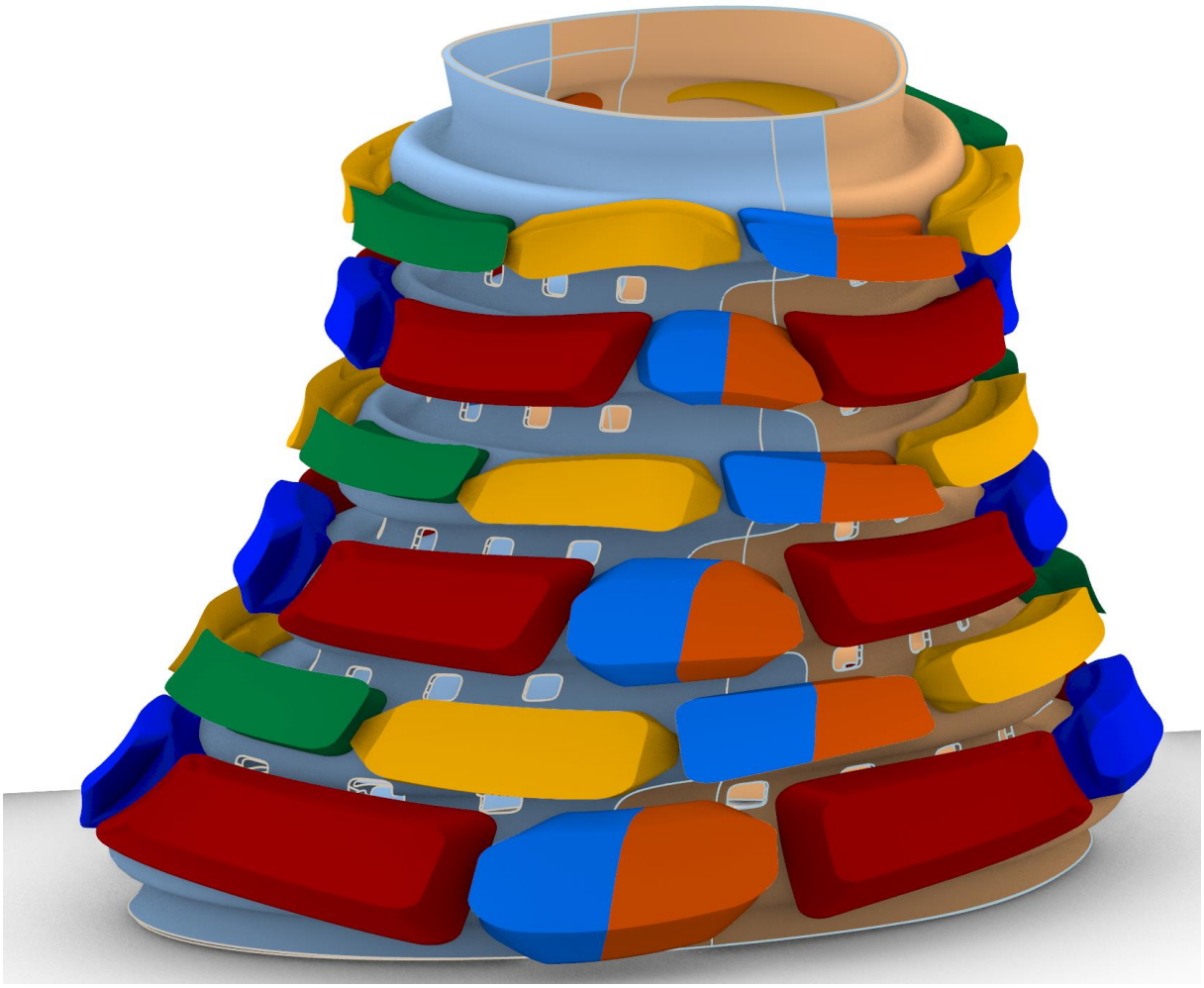

Figure 339: CAD rendering of the entire array, with splits producing color changes. The rear membrane is light orange and the front membrane half is light blue; the tiles that are split are dark orange and dark cerulean, respectively. The colors of the tiles that were not split correspond to the same four repeating tiles (variously concave and convex) used in previous chapters. There are additionally rounded holes in the membrane for ventilation.

In addition to splitting both the membrane and the central tiles, it was necessary to add indexing features (variously male and female) to the tiles to enable them to be aligned and secured to each other once around the wearer's leg. Holes for long, M3x30mm threaded fasteners were also drilled, which were to fully secure the unit around the leg. Admittedly, it would be exceedingly cumbersome to unscrew such fasteners to remove the unit, and a better means of taking the unit off and putting it on should be devised if it shows promise in terms of

basic kinematic properties; however, this method of joining was relatively simple to design. Figure 340 shows the two halves of the array with joining features.

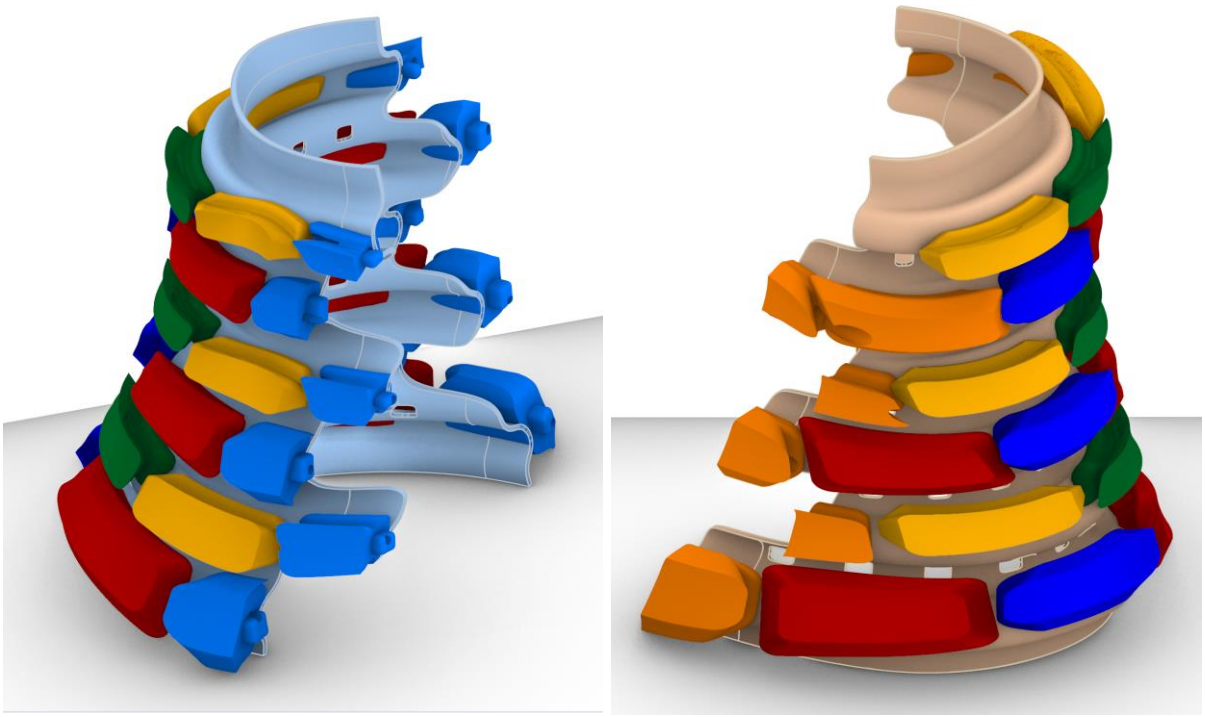

Figure 340: Separated halves of this array, featuring holes for threaded fasteners and additionally tabs (on the front set of tiles) and corresponding cavities (on the rear set of tiles) to align and secure all split tiles to their mates once the protective device is to be worn by a user.

Building on the experience of the previous section's inquiry into the first bellows-backed tiled array, in which the elastomeric bellows portion delaminated at several planes from weak interlayer adhesion during the printing process, it seemed prudent to print the array in a different orientation, so that the relatively-weak interlayer bonds would be reinforced by the rigid tiles, and so that vertically-oriented tensile loads would be orthogonal to the *z* direction of the print. A rendering of the G-code used to print one half-array is shown in Figure 341, with layer lines visible.

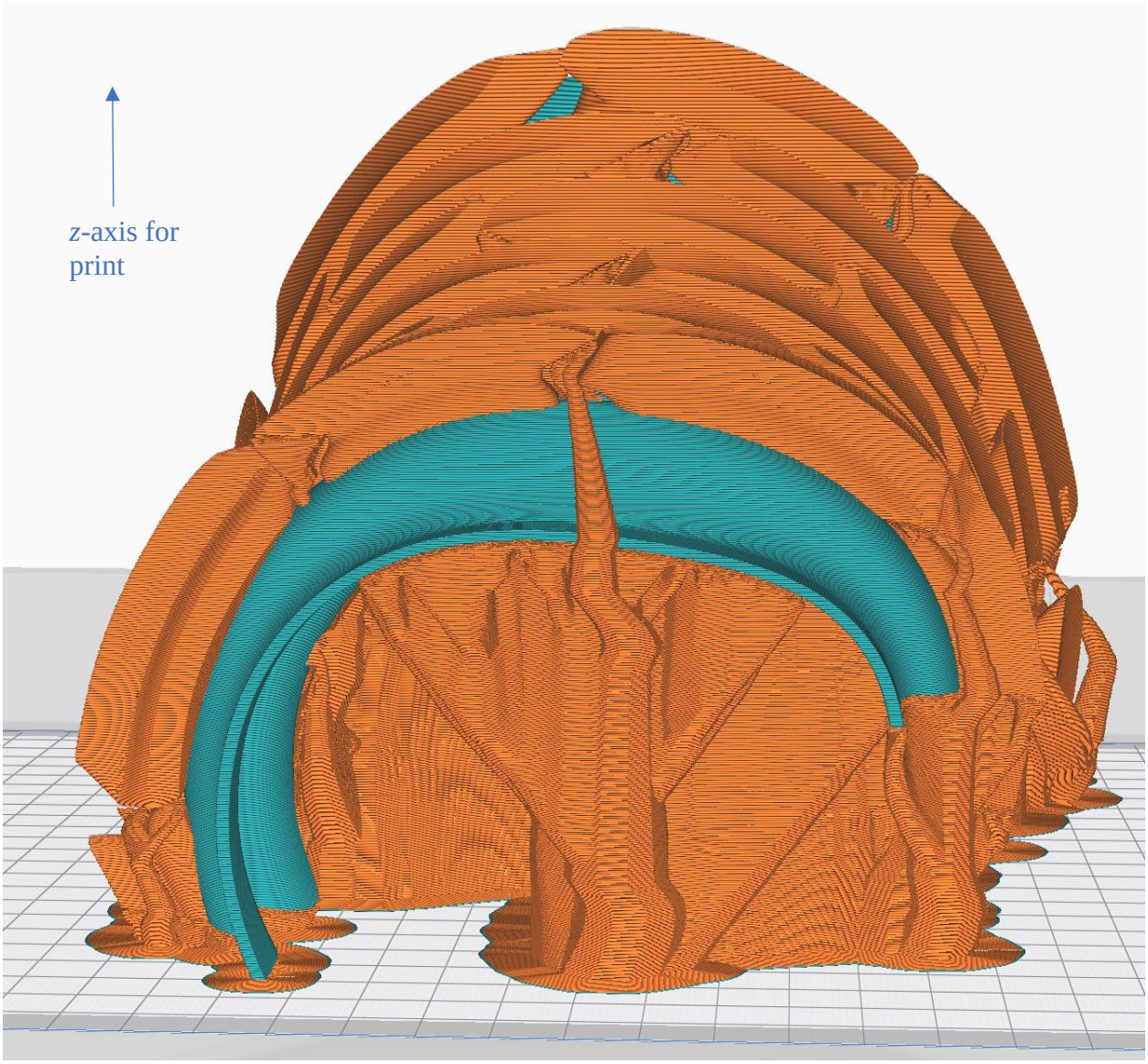

Figure 341: Rendering of G-code to print one half-array on the Ultimaker S5 3D printer. Note the orientation in which the array is printed (preventing the layer lines from being oriented in the direction that will be vertical once the structure is worn).

After both half-arrays were printed and support manually broken away, print quality was found to be overall excellent and more than serviceable. It should be noted that the areas that were overhangs in this orientation (though supported by breakaway support material) had some partially-unfused lines and general surface roughness, as can be seen in Figure 342, but, in the

course of testing, these minor defects never proved mechanically problematic. Figure 343 contains photographs of both halves of the array, separated and ready to be joined.

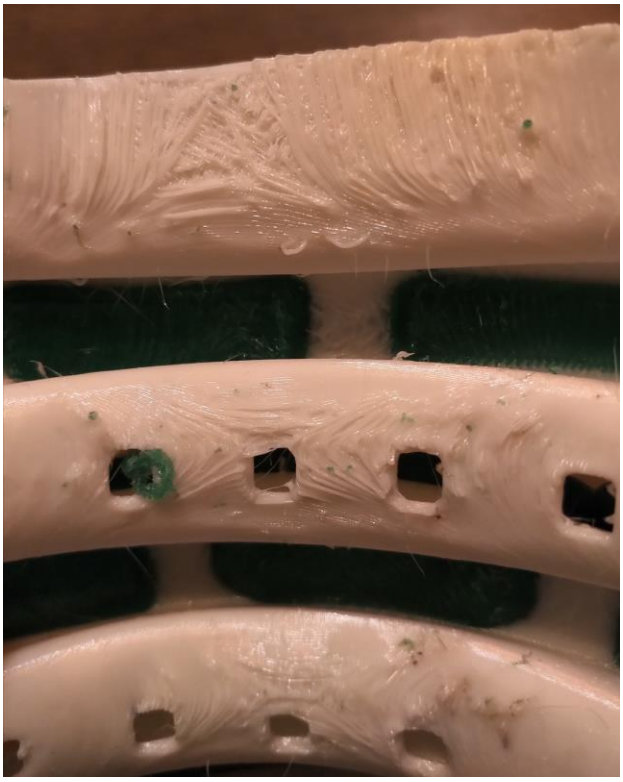

Figure 342: Closeup of the interior of one of the half-arrays, focusing on some minor surface roughness and incompletely-fused print lines.

Figure 343: Both halves of the array, separated and ready to be joined.

Once manufactured and processed (support removed, etc.), the two halves of the array were joined together around the right leg of this researcher, for whom the array had been designed (in terms of initial position and fit, primarily, for there is as yet no known forward method of directly designing the lockup properties of a closed and doubly-curved surface, and thus this author has had to resort to trial and error). As regards boundary conditions, the top edge of the structure contacts the wearer's shin lightly; the bottom edge of the structure currently merely rests on the wearer's shoe owing to the difficulty of engineering a more rigid interface between shoe and protective brace. If the protective device proves effective, future iterations should directly bind the structure to the shoe at points both front and back, else the structure may slip relative to the foot and thus give more effective freedom than it would give when properly

positioned. For the purposes of this dissertation, the structure was manually held in place to the shoe and not allowed to slip by this added force.

Figure 344 portrays the protective device in both neutral configuration and with the leg bent forwards as much as the structure will permit. Much to the delight of this researcher, the structure does indeed prevent forward motion after a point, while at the same time tolerating significant forward rotation.

Figure 344: Left: protective brace around the leg in neutral configuration; right: leg bent forward as much as the brace allows.

Unfortunately, the initial (pre-lockup) stiffness of the protective array is considerable, to the point that it is in fact impossible for this researcher to fully dorsiflect his leg (i.e. raising toes to the sky) with only his calf muscle (i.e. without using his bodyweight or hands) against the stiffness of the structure, which is present even when no tiles are touching. This is no doubt in large part due to the thickness of the elastomeric backing, which was 1.6mm at full scale, a large thickness to be sure that gives the structure considerable bending stiffness even without the effects of the rigid tiles; however, reducing the thickness of the shell makes it vulnerable to voids

that act as stress concentrations and provoke tears, so the 1.6mm thickness chosen to ensure that there would be at least four nozzle thicknesses when extruding the shell and that any local voids during one track of printing would be filled in by the other three tracks of printing each layer. This thickness can theoretically be reduced to an extent while still maintaining the four-nozzle-widths thickness by using a smaller-diameter nozzle during the printing process (for instance, 0.25mm diameter, instead of the 0.4mm nozzle used in this research), but Bowden-drive printers like the Ultimaker S5 often cannot extrude flexible filament through such a small orifice size owing to small amounts of filament buckling inside the Bowden tube (even with precision-extruded tubes that conform to the filament very closely), and indeed this researcher was unable to print Hytrel 4100FL through a 0.25mm nozzle on the Ultimaker S5. A direct-drive printer (especially using 2.85mm-diameter filament) might very well prove capable of extruding flexible materials like Hytrel 4100FL through a 0.25mm nozzle, but this researcher did not own such a direct-drive, multi-extruder printer at the time of writing.

Conclusions to Chapter 10.

This chapter discloses manufacturing methods that were used to successfully create the tiled arrays modeled on the computer, whether backed by woven fabric or an elastomeric shell. Additionally, the arrays demonstrated a small amount of freedom before significant stiffening and indeed stiffened significantly, though nowhere near as much as was designed for and desired. Nonetheless, this constitutes an advance inasmuch as there is no other metamaterial or material known to have this property. Future research could employ the elastomer-backed multimaterial-additive-manufacturing technique to rapidly iterate on tile configurations until an effective one is found, whereupon the tile configuration could be manufactured with a fabric-backed array for maximum initial compliance and post-lockup stiffness.

Chapter 11. Final Conclusions.

Recapitulation of the Dissertation.

The foregoing chapters combine an investigation into shell-based metamaterials that stiffen at a prescribed amount of strain (either in the form of in-shell tension or compression, or out-of-shell bending) with a form-finding inquiry into what initial and final shapes a closed-surface (cylinder-like) ankle protector should take on to avoid stiffness-reducing shell buckling and indeed lock up. The first major contribution to the field is found in Chapter 2, wherein a review is presented of the limited existing literature on those mechanical metamaterials that feature strain-stiffening or outright lockup (a small subset of the overall literature on mechanical metamaterials); no prior review of stiffening metamaterials is known, and indeed there has been limited academic interest in the subject overall. Additionally, Chapter 2 proposes a novel composite metamaterial that stiffens in shell bending, referred to as the fabric-backed tiled array.

In Chapter 3, the fabric-backed tiled array composite metamaterial concept is compared with previously-existing structures found in the literature (including a patented composite armor and some works from hobbyists, but significant differences in basic properties and intended function are noted). Additionally, basic principles of the array are stressed, including the importance of using a fabric weave that offers high tensile stiffness but low effective bending stiffness in order to maximize the "figure of merit" of lockup.

Although many tiling patterns and face shapes for the sides of tiles were investigated (and some are documented in Appendix III), one particular pattern was found to be especially meritorious for its relative resistance to normal-to-surface jamming, and this unit cell is introduced in Chapter 4. Next, Chapter 4 demonstrates how to program the gap distance and side

shapes of tiles to produce an array that locks up in bending at a specific target singly-curved surface having a chosen curvature profile (which need not be constant over the length of the surface), subject to certain constraints on the initial and final surface shape (namely that it must be possible to obtain the final surface from an isometric transformation of the initial surface that preserves Gaussian curvature distributions as well as curve lengths and angles). It includes MATLAB code for this calculation in Appendix I. In turn, after the CAD geometry is generated, the array is manufactured by 3D printing all tiles separately, arranging them precisely relative to one another with a precision workholder specially designed for the task, and then bonding them to the fabric (either by gluing or sewing and with the aid of specially-designed "buttons"). Finally, the manufactured surface's actual lockup profile is evaluated and compared with the ideal profile (with the aid of further MATLAB code for comparing the curvature profiles of the ideal curve and the estimated elastic curve of the actual structure); errors of moderate magnitude are identified, and further refinements for future manufacturing precision are proposed. It should be noted that the design techniques (including MATLAB code) and manufacturing methods are new additions to the scientific literature.

Chapter 5 seeks to develop a Finite-Element Analysis methodology for simulating fabric-backed tiled composite metamaterial arrays in bending, starting with the same relatively-simple initially-planar array used in Chapter 4 in order to enable comparison of the manufactured structure, the CAD-design technique, and the FEA results. Chapter 5 first introduces the MAT_235 micromechanics woven fabric model offered in the LS-Dyna code, explaining the basic functionality of this novel material model (including its ability to treat bias deformation and fabric decrimping) and including material parameters derived from an outside source for the same plain-weave Kevlar fabric used in this simulation. Other parameters are included,

including a node-sharing scheme for causing tiles to be effectively bonded to the fabric without the use of bonded contacts (which present issues with MAT_235), contact parameters that were needed to avoid incorrect contact behavior, and a mass-scaling to speed computation. The results of the simulation are analyzed and compared with the predicted lockup profile, with the decrimping behavior of the simulated fabric being responsible for modest errors. Chapter 5 concludes Part I of the dissertation, which is primarily focused with open surfaces.

Chapter 6 begins Part II of the dissertation, which is concerned almost exclusively with surfaces that are closed in the sense of having seams like cylinders. Chapter 6 first investigates practical requirements for the overall shape of an ankle protector, indicating that ideally such a device should constitute a closed surface and proposing one specific surface shape, referred to as the Hyperboloid-Derived Manifold (HDM) owing to its resemblance to a hyperboloid of one sheet. This surface is 3D printed after being tailored to fit around the lower leg and foot of the researcher, and a thin-shell version is printed in a soft elastomer for preliminary insight into the behavior of such structures when they enclose a rotating joint (such as the leg rotating about the ankle); its shell buckling and creasing motivate both a look at the mathematics of bending of closed surfaces (with the tendency towards preserving Gaussian curvature save at creases discussed) and then a literature review of extant techniques and geometries for enabling closed surfaces to enclose large-deflection-rotating joints. This literature review focuses both on modifications to shell shapes (such as bellows-like displacements) and on the use of metamaterial structures patterned on the surfaces. Of note, no other literature review of how closed surfaces may be modified to maintain their stiffness against severe shell buckling is known.

Chapter 6 also contains another contribution in the form of original experimental investigations into the effects of modifying the HDM shape with either bellows-like features on the solid surface, or alternatively by patterning unique microstructures on the surface. Several bellows-like modifications are studied, with one particular curvature profile proving especially promising in shell bending though complex to manufacture owing to its reentrant geometry. On the other hand, the microstructured-meshes tend to reduce shell bending modes in favor of in-surface extension and contraction, with the biaxially-oriented Cartesian arrays proving especially promising. The kinematic-mesh structures do feature a novel repeating unit with compliant-mechanism-inspired compliant joints approximating ball joints (in that they allow torsion and rotation but are relatively stiff against shear, tension, and compression) as well as a novel method of manufacturing structures with compliance localized to their joints through the use of multiple FDM-compatible materials. Additional classes of structures (dominated by non-localized beam bending), generally based on those metamaterials from Chapter 2 that were noted to offer some stiffening-up potential, are also modelled on the HDM surface and tested with a fixture designed by this author. These metamaterial structures highlight the various modes of deformation that are possible for a closed surface containing a rotating joint, including in-surface shear, compression, and tension, and out-of-surface bending: some speculation is made as to the relative amounts of each mode that are desired, and variations on the HDM surface are compared with the standard HDM surface using the biaxially-oriented Cartesian mesh array.

Chapter 7 extends the fabric-backed tiled array metamaterial concept from the domain of open and singly-curved surfaces to the HDM surface, which is both closed and anticlastically curved. It draws on the insights of Chapter 6 to recommend added vertical gaps between tiles to enable the structure to effectively contract vertically in this direction, which (along with shear)

will produce a transformation that is not a strict isometry but will hopefully prove tolerable to the metamaterial. From this insight, an array on the surface is proposed first for simulation in LS-Dyna using the guidelines and techniques developed in Chapter 5. However, the simulation is persistently hampered by unexpected negative Jacobians of elements even in a very high-quality mesh, and further research reveals that MAT_235 has spurious instability that produces shooting nodes and negative Jacobians when subjected to biaxial tension; this disclosure adds important practical information to the limited literature on the effective simulation of dry woven fabrics in LS-Dyna.

Chapter 8 investigates other potential material models that might be used to simulate dry woven fabrics in LS-Dyna with greater success, but unfortunately problems with MAT_214, MAT_234, and the new MAT_293 are discovered and disclosed; these problems are not acknowledged in any extant literature and thus their discovery is important to users of LS-Dyna. Flaws are also identified with the simplest formulation of MAT_034, though more advanced formulations appear to have promise. Finally, the existing technique of modeling woven fabrics by simulating individual tows as beams is reviewed with examples from this author of simulating both woven Kevlar and woven Nitinol shape memory fabric presented.

Chapter 9 concludes the FEA work by simulating the mesh originally developed in Chapter 7 with a more-accurate formulation of MAT_034 informed by the nonlinear and anisotropic properties of the weave under question. The results do indicate that the kinematic behavior of this proposed ankle protector may not be as desired.

Finally, Chapter 10 is dedicated to the manufacture of several different arrays. It first demonstrates a method for manufacturing fabric-backed tiled arrays that is analogous to the method of Chapter 4 for initially-planar arrays in that it features a workholder to position the tiles

exactly as desired (though it must be possible to disassemble and reassemble this one around the surface); it also discusses how to split the array into two parts and how to approximately flatten the underlying doubly-curved surface for construction in fabric. Once the structure is manufactured, it is tested and found wanting in performance; further iteration with this method is discouraged though given the considerable amount of time required to manufacture the array. Instead, another manufacturing technique involving multimaterial 3D printing of a thin elastomeric shell with connected rigid tiles (whose layers are interleaved for a strong bond) is used to rapidly prototype several variations on the original array, each time increasing vertical gaps between tiles to little avail. Finally, the concept of a bellows-like added waviness is reused from Chapter 6 and combined with rigid tiles, and found promising in a scale model, so it is produced in full size, with a unique wavy-split profile allowing it to be split in half and joined at the tiles around the leg. It is tested briefly on the leg of the author of this dissertation and recommendations for future modifications are made. Certainly, all the geometries in this chapter are unique and unprecedented contributions, and the combination of polyethylene-terephthalate and polyester-ether elastomer for manufacturing is itself likely to prove useful to many other researchers.

Overall, this work contains several novel achievements that have not been seen in the field, including a review of published strain-stiffening mechanical metamaterials and the systematic development of a mechanical metamaterial, in either planar or cylindrical/hyperboloidal embodiment, that displays low initial bending stiffness followed by lockup at a programmable shape. The development spans several disciplines, including finite element analysis, surface curvature analysis, a unique unit cell of rigid tiles, a numerical algorithm, and additive manufacturing techniques to bring it to physical realization.

Future Research.

There are many potential avenues for future research, both towards the development of a product and towards the more-basic questions of how to ensure precise lockup and comprehend the pseudo-bending behavior of closed surfaces. The creation of a functional product was this researcher's primary focus, but of note, no final product has been created out of this investigation, though there are several promising metamaterial principles that can be employed in further development of a future product. As explained in Chapter 6, practically speaking, any saleable protector of a multi-DoF joint (e.g. ankle, neck, wrist, etc.) should embody a closed-surface (cylinder-like) shape rather than a flat plane (though, owing to the engineering difficulties of making a closed surface tolerate a bending joint, most existing research efforts have indeed focused on simple, open strips around a joint), so either the tiled arrays on cylinders or perhaps the microstructured metamaterial cylinders should be the basis for future research.

Of the tiled arrays, the elastomeric-bellows-backed tiled array appeared to be the most promising and indeed thus far it is the most-developed concept, though it was marred by excessive pre-lockup stiffness as well as imperfect tile contact at lockup. Further research into this concept should thus first and foremost entail practical manufacturing improvements that would allow the use of a much thinner elastomeric shell while retaining the reentrant bellows geometry and avoiding unfused regions. For instance, finer nozzles with FDM of the elastomeric material could be employed (though a direct-drive extruder will likely be required to produce the needed extrusion pressure with an elastomer), or alternatively the SLS process could be investigated with TPU as the feedstock. (Of course, SLS processes cannot use multiple materials, but even if the tiles are made of an elastomer like TPU, as long as they are sufficiently thick and solidly-infilled, they should have sufficient bending and compressive stiffness that

multiple materials are not required). Alternatively, it might be feasible to produce the bellows-like backing in a high-stiffness woven fabric as it will need to be split anyways for the purposes of enabling the wearer to doff and don the protector. (Of note, it would not be theoretically feasible to make a bellows-like closed surface with one piece of woven fabric, so it is convenient indeed that splitting is required for other reasons). In either case, a bellows-like shape (either of a thin elastomeric shell or a thin woven fabric) might prove amenable to fixing the top tiles to the leg, which is a preferred boundary condition (as compared with merely letting the leg slide inside the surface), provided that global tensile compliance in the backing (prior to lockup) can also be achieved; this may require optimizations and modifications to the design of the array curvature as even the reentrant bellows profile proved stiffer in tension than in compression (and the non-reentrant, sinusoidal bellows profile was notably quite stiff in tension relative to its compressive stiffness). A higher-resolution manufacturing process would likely enable smaller physical wavelengths in the bellows backing shape as well as thinner tiles, enabling weight and volumetric-footprint reductions.

Beyond these product improvements stemming from improved manufacturing capabilities, tailoring the tile lockup profile to ensure proper behavior in other ankle modes than just plantarflexion (the only one engineered for in Chapter 10), namely dorsiflexion, inversion, eversion, and combined modes, would also be essential. Next, adequate ventilation should be ensured, perhaps by adding through-all holes all the way through the rigid tiles (which should not be appreciably weakened by such holes) for adequate airflow; since a future product would be targeted at active individuals such as athletes and soldiers, ventilation would be essential. Finally, a new method of adhering the two halves to each other that is both more robust and more

convenient to lock or unlock should be developed; the catches found on ski boots may be particularly promising in this regard.

Alternatively, the hyperboloid-like mesh arrays might be deemed to be more promising. In particular, the biaxial mesh array pattern appears to be the most interesting of those studied in this dissertation, owing to its excellent in-surface extension and contraction properties and its resistance to horizontal shearing (which may be important for ankle protection on top of kinematic control of the joint). Of the manifold shapes studied with the biaxially-oriented Cartesian compliant multimaterial mesh arrays, the frustrum-of-cone shape seemed to recommend itself above the other shapes owing to its virtually-zero Gaussian curvature inhibiting out-of-surface bending, even when the rotation of the individual links was kinematically constrained from self-contacts after a certain amount of displacement: indeed, this produced moderate stiffening-up, though other features should certainly be added to augment the magnitude of stiffening up (including tile-like extrusions in the direction normal to the surface in order to guard against out-of-surface bending, and perhaps initially-slack cables that are tensioned after a prescribed amount of rotation to augment the lockup).

That said, it should be acknowledged that the mesh-based multimaterial arrays, while convenient for rapid iteration and high-level qualitative evaluation of manifold shapes and kinematic profiles, may not be suited for a final product, principally because the compliant flexures may be deficient both in tensile strength and in fatigue life (especially if random printing defects occur). In fact, as regards fatigue life, usually flexures must be made of polypropylene that has been specifically oriented by the manufacturing process (usually injection molding across a narrow flexure that orients polymer chains) for “living hinge” properties, though then the hinge is only long-lived in bending about its principal axis, not in tension,

tearing, etc. Thus, it might be preferable to replace them with true ball joints, though this would likely only be practical if the ball-jointed members can be 3D printed as one piece (else they would need to be manufactured in sandwich form and manually assembled, a myopic and difficult task). Strictly speaking, the ball-joint-approximating flexures could likely be replaced with revolute-joint-approximating flexures (or revolute joints themselves), though the kinematics of this question should be evaluated; if feasible, it would facilitate manufacture.

As with all other proposed ankle protectors, it would be necessary to split a biaxially-oriented jointed or mesh array into at least two pieces, which in this case would likely entail splitting each individual link; the features required to join each link could be rather weak, and additionally connecting the two pieces (as required each time the user wishes to put it on) or disconnecting them to take it off could be time-consuming and myopic in and of itself. Certainly, experimentation with different densities of unit cells of the trellis mechanism could be employed to determine how many are truly required; the array might be quite functional with just a 4x3 grid, for instance, which might make splitting more feasible.

At a more basic level, there are important biomechanical questions that were outside the scope of this dissertation that should be addressed in future work, including the mode-coupling of the ankle joint (which would affect lockup freedom in one direction when rotation in another direction has perhaps reduced the wearer's safe zone in the first direction), the role of shear forces versus the role of excursions outside the safe range of motion in provoking injury, and the desired initial, transition, and post-lockup stiffnesses. As regards this latter question, there may be some merit to very slight initial stiffness (whether from preventing misalignment of moving members, or even in the sense of altering the wearer's gait in a favorable direction; for instance, Shao et. al. proposed [167] a passive ankle-enclosing exoskeleton that purportedly increases the

wearer's ambulatory efficiency with the activation of elastic springs that store and release kinetic energy at appropriate points in the wearer's gait cycle. Therefore, the conceit that safe-zone stiffness should be as low as achievable in the metamaterial design may prove incorrect, especially for patients with preexisting injuries. Similarly, the strain range over which the stiffness changes from low to high may also need to be larger than appreciated in this dissertation in order to prevent injury from excessively-abrupt deceleration of the wearer, especially since injuries are most likely to be sustained during highly-dynamic events.

Finally, this dissertation has raised other questions that are more basic inasmuch as they pertain globally to the mechanics of soft bodies in high deflection; in particular, the nature of how bellows-like elastic shells tolerate pseudo-bending by transforming the global load into shell bending, potentially with localized creasing, should be explored in great detail with the use of FEA software as well as additively-manufactured shells. Indeed, the concept should be researched in light of an understanding of origami folds (including those along curved folds, rather than exclusively-straight-folded origami).

Additionally, the original fabric-backed tiled array composite metamaterial could be refined by employing more precise techniques to calculate the gaps for lockup at a prescribed target surface shape, and the concept might benefit from expansion to double-sided tilings of fabric to produce lockup in upwards and downwards bending directions. Additionally, arrays capable of some bending freedom along multiple in-plane (assuming a flat initial surface) bending axes should be investigated; this would likely require a fabric weave with quasi-isotropic in-plane properties (such as a nonwoven or a triaxially-braided fabric) to ensure that the bias mechanism is not activated, or alternatively, lockup could be engineered in light of this kinematic behavior. The concept might also be extended to the precise bending/morphing of

doubly-curved surfaces (especially open ones, as open and doubly-curved surfaces were not used for the fabric-backed tiled arrays in this dissertation). Direct 3D printing to fabric could greatly facilitate manufacture of this concept, but only if the gaps between tiles were sufficiently large to ensure that they would not be fused together during printing (which would generally be the case only if bending in multiple directions were tolerated, which was not explored in this dissertation). Finally, practically speaking, the fabric-backed tiled arrays would benefit greatly from an improved method of bonding the tiles to the fabric (rather than the "buttons" with concave features that interlock with features on the tiles once forced in), as this greatly distorts the fabric; instead, a flat button that is sewn and glued to the tile may supply sufficient bond strength while not distorting the fabric appreciably.

References

[1] C. Petersen, *Variable-Stiffness Protective Material,* Auburn, AL: Auburn University, 2016.

[2] R. L. J.B. Choi, "Nonlinear properties of polymer cellular materials with a negative Poisson's ratio," *Journal of Materials Science,* vol. 27, pp. 4678-4684, 1992.

[3] H. Sönnerlind, "Obtaining Material Data for Structural Mechanics from Measurements," COMSOL, 23 02 2015. [Online]. Available: https://www.comsol.com/blogs/obtaining-material-data-for-structural-mechanics-from-measurements/.

[4] J. H. B. Geoffrey N Maksym, "A distributed nonlinear model of lung tissue elasticity," *Journal of Applied Physiology,* vol. 82, no. 1, pp. 32-41, 1997.

[5] MSC.Software, "MSC.Software Whitepaper: Nonlinear Finite Element Analysis of Elastomers," [Online]. Available: http://www.mscsoftware.com/Submitted-Content/Resources/WP_Nonlinear_FEA-Elastomers.pdf.

[6] J. J. C. A. W. J. A. T. B. D. W. B. J. T. G. Richard M Greenwald, "Dynamic Body Protector". US Patent US20080146981A1, 19 07 2007.

[7] C. E. Murray, "Auxetic crystals under stress: Peering into their mechanics using x-rays," *Journal of Applied Physics,* vol. 125, 2019.

[8] C. H. A. G. Prateek Verma, "Implications for Auxetic Response in Liquid Crystalline Polymers: X-Ray Scattering and Space-Filling Molecular Modeling," *Basic Solid State Physics,* vol. 257, no. 10, 2020.

[9] S. D. C. S. L. M. P. B. M. J. H. C. &. H. F. G. D. Mistry, "Coincident molecular auxeticity and negative order parameter in a liquid crystal elastomer," *Nature Communications,* vol. 9, no. 5095, 2018.

[10] C. L. G. L. J. L. X. Y. J. F. Zhenwei Wang, "Progress in Auxetic Mechanical Metamaterials: Structures, Characteristics, Manufacturing Methods, and Applications," *Advanced Engineering Materials,* 2020.

[11] R. D. P. T. T. D. N. Y. M. X. Xin Ren, "Auxetic metamaterials and structures: a review," *Smart Materials and Structures,* vol. 27, no. 023001, 2018.

[12] M. H. Sadd, Elasticity: Theory, Applications, and Numerics, 3rd Edition, Academic Press, 2014.

[13] K. Muamer, T. Buckmann, N. Stenger, M. Thiel and M. Wegener, "On the feasibility of pentamode mechanical metamaterials," *Applied Physics Letters,* vol. 100, no. 19, 2012.

[14] X. Yu, J. Zhou, H. Liang, Z. Jiang and L. Wu, "Mechanical metamaterials associated with stiffness, rigidity and compressibility: A brief review," *Progress in Materials Scienc,* vol. 94, pp. 114-173, 2018.

[15] J. Y. Yichao Tang, "Design of cut unit geometry in hierarchical kirigami-based auxetic metamaterials for high stretchability and compressibility," *Extreme Mechanics Letters,* vol. 12, pp. 77-85, 2017.

[16] Z. Z. R. S. F. S. Weinjia Zhang, "In-Plane Mechanical Behavior of a New Star-Re- Entrant Hierarchical Metamaterial," *Materials,* vol. 11, no. 7, 2019.

[17] L. W. Zian Jia, "Instability-Triggered Triply Negative Mechanical Metamaterial," *Physical Review Applied,* vol. 12, 2019.

[18] D. Y. H. Q. Chenhui Ren, "Mechanical Performance of Multidirectional Buckling-Based Negative Stiffness Metamaterials: An Analytical and Numerical Study," *Materials (Basel),* vol. 11, no. 7, 2018.

[19] W. D. R.S. Lakes, "Dramatically stiffer elastic composite materials due to a negative stiffness phase?," *Journal of the Mechanics and Physics of Solids,* vol. 50, no. 5, pp. 979-1009, 2002.

[20] H. M. A. K. A. A. Z. Christa P de Jonge, "Non-auxetic mechanical metamaterials," *MDPI Materials,* vol. 12, no. 4, 2019.

[21] V. V. J. C. M. v. H. Katia Bertoldi, "Flexible mechanical metamaterials," *Nature Reviews: Materials,* vol. 2, 2017.

[22] F. L. X. J. L. W. Zian Jian, "Engineering lattice metamaterials for extreme property, programmability, and multifunctionality," *Journal of Applied Physics,* vol. 127, no. 150901, 2020.

[23] Y. Tummala, M. I. Frecker, A. A. Wissa and J. J. Hubbard, "Design and optimization of a bend-and-sweep compliant mechanism," *Smart Materials and Structures,* vol. 22, no. 094019, 2013.

[24] T.-C. Lim, "Analogies across auxetic models based on deformation mechanism," *Physica Status Solidi: Rapid Research Letters,* 2017.

[25] D. S. D.-N. K. Hyeonho Cho, "Mechanics of Auxetic Materials," in *Handbook of Mechanics of Materials*, Singapore, Springer, 2019.

[26] T. S. C. M. L. F. P. D. V. K. W. T. A. A. A. Olly Duncan, "Review of Auxetic Materials for Sports Applications: Expanding Options in Comfort and Protection," *MDPI Applied Sciences*, vol. 8, no. 6, 2018.

[27] Y. Wang, L. Wang, Z.-d. Ma and T. Wang, "Parametric analysis of a cylindrical negative Piosson's ratio structure," *Smart Materials and Structures*, vol. 25, 2016.

[28] L. K.-O. Z. R. M. V. N. Novak, "Mechanical properties of hybrid metamaterial with auxetic chiral cellular structure and silicon filler," *Composite Structures*, vol. 234, 2020.

[29] A. J. N. Warner, "Relative tensile strengths of chainmail weaves," Massachusetts Institute of Technology. Department of Mechanical Engineering., [Online]. Available: http://dspace.mit.edu/handle/1721.1/7582.

[30] M. K. a. M. W. Christian Kern, "Experimental Evidence for Sign Reversal of the Hall Coefficient in Three-Dimensional Metamaterials," *Physical Review Letters*, vol. 118, 2017.

[31] R. J. M. R. M. M. Anna R. Ploszajski, "4D Printing of Magnetically Functionalized Chainmail for Exoskeletal Biomedical Applications," *Materials Research Society Advances*, 2019.

[32] P. S. M. M. Mark Ransley, "Active Chainmail Fabrics for Soft Robotic Applications," *Smart Materials and Structures*, 2017.

[33] D. M. H. E. R. G. &. A. V. Soroush Kamrava, "Origami-based cellular metamaterial with auxetic, bistable, and self-locking properties," *Nature Scientific Reports,* vol. 7, no. 46046, 2017.

[34] C. Lv, D. Krishnaraju, G. Konjevod, H. Yu and H. Jiang, "Origami based Mechanical Metamaterials," *Nature Scientific Reports,* vol. 4, no. 5979, 2014.

[35] J. J. Park, P. Won and S. H. Ko, "A Review on Hierarchical Origami and Kirigami Structure for Engineering Applications," *International Journal of Precision Engineering and Manufacturing-Green Technology,* vol. 6, pp. 147-161, 2019.

[36] A. D. J. Z. Ning An, "Programmable Hierarchical Kirigami," *Advanced Functional Materials,* vol. 30, no. 6, 2019.

[37] Y. Tang, G. Lin, Y. K. Yi, R. Kamien and J. Yin, "Programmable kirigami metamaterials," *Advanced Materials,* vol. 29, no. 10, 2016.

[38] S. L. K. W. Hongbin Fang, "Self-Locking Degree-4 Vertex Origami Structures," *Proceedings of the Royal Society A,* vol. 472, no. 20160682, 2016.

[39] S.-C. A. C. Y. X. K.-W. W. Hongbin Fang, "Programmable Self-Locking Origami Mechanical Metamaterials," *Wiley Advanced Materials,* 2018.

[40] S. D. G. Mark Schenk, "Geometry of Miura-folded metamaterials," *Proceedings of the National Academy of Sciences of the United States of America,* vol. 110, no. 9, pp. 3276-3281, 2013.

[41] I.-S. C. R. D. K. Shu Yang, "Design of super-conformable, foldable materials via fractal cuts and lattice kirigami," *MRS Bulletin,* vol. 41, pp. 130-138, 2016.

[42] D. M. H. E. R. G. &. A. V. Soroush Kamrava, "Origami-based cellular metamaterial with auxetic, bistable, and self-locking properties," *Nature Scientific Reports,* vol. 7, 2017.

[43] J. M. H. F. D. H. J. G. Y. C. Z. Y. Tanmoy Mukhopadhyay, "Programmable stiffness and shape modulation in origami materials: Emergenceof a distant actuation feature," *Applied Materials Today,* 2019.

[44] S. P. Yang Li, "A Theory for the Design of Multi-Stable Morphing Structures," *Journal of the Mechanics of Physics and Solids,* vol. 136, 2020.

[45] H. U. C. S. X. C. H. L. H. L. J. J. H. C. G.-T. K. S. Y. H. J. W. L. J. K. M. C. F. M. Y. Y. H. N. J. M. F. H. L. G. W. K. e. a. Kyung-In Jang, "Soft network composite materials with deterministic and bio-inspired designs," *Nature Communications,* vol. 6, 2015.

[46] T. Li, X. Hu, Y. Chen and L. Wang, "Harnessing out-of-plane deformation to design 3D architected lattice metamaterials with tunable Poisson's ratio," *Nature Scientific Reports,* vol. 7, no. 8949, 2017.

[47] A. A. D. P. A. Rafsanjani, "Snapping mechanical metamaterials under tension," *Advanced Materials,* vol. 27, no. 39, pp. 5931-5935, 2015.

[48] J. J. Zhiming Cui, "Topologically reconfigurable mechanical metamaterials with motion structures," *Mechanics of Materials,* vol. 143, 2020.

[49] Y. C. Xiao Zhang, "Mobile assemblies of Bennett linkages from four-crease origami patterns," *Proceedings of the Royal Society A,* vol. 474, no. 2210, 2018.

[50] T. A. d. J. Y. S. S. A. B. G. M. W. J. C. W. C. H. &. K. B. Johannes T.B. Overvelde, "A three-dimensional actuated origami-inspired transformable metamaterial with multiple degrees of freedom," *Nature Communications,* vol. 7, no. 10929, 2016.

[51] X. K. C. D. H. J. Q. S. Macrae Montgomery, "Recent advances in additive manufacturing of active mechanical metamaterials," *Current Opinion in Solid State and Materials Science,* vol. 24, no. 5, 2020.

[52] K. K. Dudek, "Negative and positive stiffness in auxetic magneto-mechanical metamaterials," *Proceedings of the Royal Society A*, 2018.

[53] V. Slesarenko, "Planar Mechanical Metamaterials with Embedded Permanent Magnets," *MDPI Materials,* vol. 13, no. 6, 2020.

[54] J. B. S. Rimma Uysal, "A New Method of Printing Multi-Material Textiles by Fused Deposition Modelling (FDM)," *Tekstilec,* vol. 62, no. 4, pp. 248-257, 2019.

[55] J. S. C. M. J. C. David Jauffres, "Discrete mesoscopic modeling for the simulation of woven-fabric reinforcement forming," *International Journal of Material Forming,* vol. 3, pp. 1205-1216, 2010.

[56] S. A. T. Zheng Ming Huang, "Modeling the stress/strain behavior of a knitted fabric-reinforced elastomer composite," *Composites Science and Technology,* vol. 60, no. 5, pp. 671-691, 2000.

[57] N. N. M. B. M. V. Z. R. Polona Dobnik Dubrovski, "In-Plane Behavior of Auxetic Non-Woven Fabric Based on Rotating Square Unit Geometry under Tensile Load," *Materials,* vol. 11, no. 6, 2019.

[58] C. K. M. v. H. Corentin Coulais, "A characteristic length scale causes anomalous size effects and boundary programmability in mechanical metamaterials," *Nature Physics,* vol. 14, pp. 40-44, 2018.

[59] T. H. R. L. C. S. M. M. K. D. P. M. Itai Cohen, "Abstract: H40.00015 : Q: How many folded angels can we fit on the head of pin? A: 22+/-5," March 2016. [Online]. Available: http://meetings.aps.org/link/BAPS.2016.MAR.H40.15.

[60] M. F. Bryant, "Myoelectric Hand Orthosis". US Patent US9387112B2, 28 02 2013.

[61] G. V. André Schiele, "Exoskeleton for a human arm, especially for spatial applications". European Union Patent EP1364755B1, 04 11 2009.

[62] G. S. F. Donald G. Mortensen, "Pneumatic variable resistance rehabilitation/therapy apparatus". US Patent US5312315A, 21 12 1990.

[63] C. Ortiz, M. C. Boyce, J. Song and S. H. Reichert, "Articulating protective system for resisting mechanical loads". US Patent US8978535B2, 11 08 2011.

[64] K. Z. L. M.-S. S. V. N. O. M. C. B. C. O. Jorge Duro-Royoa, "MetaMesh: A hierarchical computational model for design and fabrication of biomimetic armored surfaces," *Computer-Aided Design,* vol. 50, pp. 14-27, 2015.

[65] C. O. M. B. Stephan Rudykh, "Flexibility and Protection by Design: Imbricated Hybrid Microstructures of Bio-Inspired Armor," *Soft Matter,* vol. 11, pp. 2547-2554, 2015.

[66] D. A. K. A. K. K. Dereje Berihun Sitotaw, "Additive Manufacturing and Textiles—State-of-the-Art," *Applied Sciences (MDPI),* vol. 10, no. 15, p. 5033, 2020.

[67] T. Koslow, "3D Systems Textiles: 3D Printed Fashion Out-of-the-Box & into the Cube," 3D Printing Industry, [Online]. Available: https://3dprintingindustry.com/news/3d-systems-textiles-fashion-out-of-the-box-into-the-cube-3d-printer-57075/.

[68] Richa, "3D Printing on fabric is easier than you think!," Geeetech Blog, [Online]. Available: https://www.geeetech.com/blog/2018/02/3d-printing-on-fabric-is-easier-than-you-think/. [Accessed 26 02 2018].

[69] K. Sierzputowski, "Conductive Origami by Yael Akirav Unites 3-D Printing and Textiles to Create Foldable Modern Light Fixtures," 8 8 2019. [Online]. Available: https://www.thisiscolossal.com/2019/08/conductive-origami-by-yael-akirav/.

[70] G. Fields, "Self Forming Structures: An Exploration into 3D Printing on Pre-stretched Fabric," 24 04 2018. [Online]. Available: https://n-e-r-v-o-u-s.com/blog/?p=8011.

[71] J. L. Hill, "Mechanical Property Determination for Flexible Material Systems," Georgia Institute of Technology (Daniel Guggenheim School of Aerospace Engineering), Atlanta, GA, 2016.

[72] DuPont, "DuPont Hytrel 3D4100FL NC010," 30 03 2017. [Online]. Available: https://www.matterhackers.com/r/NM1c7M.

[73] Jacobs & Thomson, "Technical Data Sheet: Foam | EVA | VA35," 2017. [Online]. Available: https://www.foamparts.com/wp-content/uploads/2018/10/va35.pdf.

[74] K. Larson, "Can You Estimate Modulus From Durometer Hardness for Silicones," 2019. [Online]. Available: https://www.dow.com/content/dam/dcc/documents/en-us/tech-art/11/11-37/11-3716-01-durometer-hardness-for-silicones.pdf.

[75] A. Treibergs, "Geometry of Bending Surfaces," University of Utah, 6 November 2012. [Online]. Available: www.math.utah.edu/~treiberg/BendingSlides.pdf.

[76] B. N. S. A. K. L. T. L. Z. B. S. L. Stephen Hyde, "Chapter 1 - The Mathematics of Curvature," in *The Language of Shape: The Role of Curvature in Condensed Matter: Physics, Chemistry, and Biology*, 1997, pp. 1-42.

[77] Encyclopedia of Mathematics, "Gaussian Curvature," 27 September 2012. [Online]. Available: https://www.encyclopediaofmath.org/index.php/Gaussian_curvature. [Accessed 23 December 2019].

[78] "Surfaces of Gaussian curvature zero," in *Map Projections*, Berlin, Springer, 2006, pp. 153-159.

[79] Triaxial Structures, Inc., "The Story of Triaxial Fabrics," [Online]. Available: http://www.triaxial.us/Triaxial%20Fabric%20History%201.php.

[80] F. K. Frank Scardino, "Triaxial Woven Fabrics, Part I: Behavior under Tensile, Shear, and Burst Deformation," *Textile Research Journal,* vol. 51, no. 2, pp. 80-89, 1981.

[81] J. K. Hodgins, "Lecture 08: Curves and Splines, Part 2," Carnegie Mellon University Computer Science, [Online]. Available: http://www.cs.cmu.edu/~jkh/462_s07/08_curves_splines_part2.pdf.

[82] FlashForge 3D Printer, "Creator Pro," [Online]. Available: https://www.flashforge.com/product-detail/4.

[83] Livermore Software Technology Corp., *LS-Dyna R10.1*, Livermore, CA, 2019.

[84] Livermore Software Technology Corporation, LS-DYNA Keyword User's Manual: Volume II: Material Models, Livermore, CA: LSTC, 2014.

[85] C. E. T. S. Thomas Borrvall, "A Fabric Material Model with Stress Map Functionality in LS-DYNA," in *10th European LS-DYNA Conference*, Wurzburg, Germany, 2015.

[86] I. I. Ala Tabiei, "Computational micro-mechanical model of flexible woven fabric for finite element impact simulation," *International Journal for Numerical Methods in Engineering,* vol. 53, pp. 1259-1276, 2002.

[87] A. T. Ivelin Ivanov, "Loosely woven fabric model with viscoelastic crimped fibres for ballistic impact simulations.," *International Journal for Numerical Methods in Engineering,* vol. 61, pp. 1565-1583, 2004.

[88] William J. Hughes Technical Center, "Explicit Finite Element Modeling of Multilayer Composite Fabric for Gas Turbine Engine Containment Systems, Phase IV," US Department of Transportation Federal Aviation Administration, Atlantic City International Airport, NJ, 2014.

[89] A. K. V. K. S. Kilimtzidis, "Blast Reinforcing of Unit Load Device Using High Modulus Polypropylene Plain Weave Fabrics," *International Journal of Astronautics and Aeronautical Engineering*, vol. 2, no. 006, pp. 1-20, 2017.

[90] A. Tabiei and I. Ivanov, "Computational micro-mechanical model of flexible woven fabric for finite element impact simulation," *International Journal for Numerical Methods in Engineering,* vol. 53, no. 6, pp. 1259-1276, 2002.

[91] J. Fein, "Improvements in Numerical Modeling Methodology of Dry Woven Fabrics for Aircraft Engine Containment Systems," Tempe, AZ, 2012.

[92] "High Performance and Parallel Computing: Hopper Cluster (2016)," Auburn University Office of Information Technology, 2016. [Online]. Available: https://hpcportal.auburn.edu/hpc/2016_cluster.php. [Accessed 6 6 2020].

[93] E. W. Weisstein, "Courant-Friedrichs-Lewy Condition," MathWorld, [Online]. Available: https://mathworld.wolfram.com/Courant-Friedrichs-LewyCondition.html. [Accessed 6 6 2020].

[94] L. P. B. a. A. C. Long, "Chapter 8: Modelling the geometry of textile reinforcements for composites: TexGen," in *Composite reinforcements for optimum performance (Second Edition)*, Woodhead Publishing, 2021, pp. 237-265.

[95] M. E. H. S. K. ,. J. L. S. G. R. R. G. D. C. M. L. L. N. H. A. J. H. Sebastian W. Pattinson, "Additive Manufacturing of Biomechanically Tailored Meshes for Compliant Wearable and Implantable Devices," *Advanced Functional Materials*, 2019.

[96] E. W. Weisstein, "Hyperbolic Paraboloid," MathWorld--A Wolfram Web Resource, [Online]. Available: http://mathworld.wolfram.com/HyperbolicParaboloid.html.

[97] E. Weisstein, "One-Sheeted Hyperboloid," Mathworld--A Wolfram Web Resource, 1999. [Online]. Available: http://mathworld.wolfram.com/One-SheetedHyperboloid.html.

[98] R. Issa, Essential Mathematics for Computational Design - Third Edition, Robert McNeel & Associates, 2013.

[99] E. W. Weisstein, ""Ruled Surface"," MathWorld--A Wolfram Web Resource, [Online]. Available: https://mathworld.wolfram.com/RuledSurface.html.

[100] N. S. X. J. D. P. H. Matteo Pezzulla, "Curvature-driven morphing of non-Euclidean shells," *Proceedings of the Royal Society A,* vol. 473, no. 2201, 2017.

[101] T. A. Witten, "Stress focusing in elastic sheets," *Reviews of Modern Physics,* vol. 79, no. 643, 2007.

[102] A. A. E. S. I.-G. L. A. M. I. C. R. C. H. C. D. S. Nakul Prabhakar Bende, "Geometrically controlled snapping transitions in shells with curved creases," *Proceedings of the National Academy of Sciences,* vol. 112, no. 36, pp. 11175-11180, September 2015.

[103] L. Braizer, "On the Flexure of Thin Cylindrical Sections and other "Thin" Sections," *Proceedings of the Royal Society of London, Series A. Containing Papers of a Mathematical and Physical Character.,* vol. 116, no. 773, pp. 104-114, 1927.

[104 J. Yao, "Large-Deflection Analysis of Buckling of a Cylinder Under Bending," *Journal of*
] *Applied Mechanics,* vol. 29, no. 4, pp. 708-714, 1962.

[105 "The Large-Deflection Pure Bending Properties of a Square Thin-Walled Tube,"
] *Cimpoeru, S.J.; Murray, N.W.,* vol. 35, no. 3/4, pp. 247-256, 1993.

[106 S. K. Sotiria Houliara, "Buckling of Thin-Walled Long Steel Cylinders Subjected to
] Bending," *ASME Journal of Pressure Vessel Technology,* vol. 133, 2011.

[107 J. Wilson, "Mechanics of bellows: A critical survey," *International Journal of Mechanical*
] *Sciences,* vol. 26, no. 11-12, pp. 593-605, 1984.

[108 D. Ubido, *Analysis and Design of Multi-Ply Metallic Bellows.*
]

[109 B. Sun, "Closed-Form Solution of Axisymmetric Slender Elastic Toroidal Shells," *ASCE*
] *Journal of Engineering Mechanics,* vol. 136, no. 10, pp. 1281-1288, 2010.

[110 J. Park, J. Jung, H.-W. Kang, Y. Joo, J.-S. Lee and D.-W. Cho, "Development of a 3D
] bellows tracheal graft: mechanical behavior analysis, fabrication and an in vivo feasibility study," *Biofabrication,* vol. 4, no. 3, September 2012.

[111 E. V. T. T. L. M. Levi H Dudte, "Programming Curvature using Origami Tessellations.,"
] *Nature Materials,* vol. 15, pp. 583-588, 2016.

[112 A. Z. S.J.P Callens, "From flat sheets to curved geometries: Origami and kirigami
] approaches," *Materials Today,* 2017.

[113] G. P. T. T. E.T. Filipov, "Origami tubes with reconfigurable polygonal cross-sections," *Proceedings of the Royal Society A*, vol. 472, no. 2185, 2016.

[114] S. M. Y. G. Y.-J. L. D. K. S. Y. a. C. R. S. Wei-Hsi Chen, "A Programmably Compliant Origami Mechanism for Dynamically Dextrous Robots," *IEEE Robotics and Automation Letters*, 2020.

[115] W. L. J. L. Z. Y. Yan Chen, "An Extended Family of Rigidly Foldable Origami Tubes," *Journal of Mechanisms and Robotics*, vol. 9, no. 2, 2016.

[116] T. Tachi, "Rigid-Foldable Thick Origami," *(Unknown)*, 2011.

[117] F. C. W. T. M. A. S. T. C. D. O. Siamak G. Faal, "Hierarchical Kinematic Design of Foldable Hexapedal Locomotion Platforms," *ASME Journal of Mechanisms and Robotics*, vol. 8, no. 1, 2016.

[118] A. R. K. Dustin Ahrendt, "Development of a computer-aided engineering–supported process for the manufacturing of customized orthopaedic devices by three-dimensional printing onto textile surfaces," *Journal of Engineered Fibers and Fabrics*, vol. 15, pp. 1-11, 2020.

[119] "Uniaxial and Buckling Mechanical Response of Auxetic Cellular Tubes," *Smart Materials and Structures*, vol. 22, no. 8, p. 084008, 2013.

[120] A. F. M. B.-M. J. W. A. &. K. S. Sedal, "Auxetic Sleeves for Soft Actuators with Kinematically Varied Surfaces," *IEEE/RSJ International Conference on Intelligent Robots and Systems (IROS),* pp. 464-471, 2018.

[121] M. Panico, C. Langella and C. Santulli, "Development of a Biomedical Neckbrace through Tailored Auxetic Shapes," *Italian Journal of Science & Engineering,* vol. 1, no. 3, 2017.

[122] V. v. d. W. J. L. H. Freek G Broeren, "Spatial pseudo-rigid body model for the analysis of a tubular mechanical metamaterial," *Mathematics and Mechanics of Solids,* vol. 25, no. 2, pp. 305-316, 2020.

[123] P. M. R. Arnaud Lazarus, "Soft Actuation of Structured Cylinders through Auxetic Behavior," *Advanced Engineering Materials,* vol. 17, no. 6, 2015.

[124] W. H. Z. Z. C. H. M. C. H. L. H. J. Q. Ming Lei, "3D Printing of Auxetic Metamaterials with Digitally-Reprogrammable Shape," *ACS Applied Materials and Interfaces,* vol. 11, pp. 22768-22776, 2019.

[125] H. Yang and L. Ma, "Design and characterization of axisymmetric auxetic metamaterials," *Composite Structures,* vol. 249, 2020.

[126] D. B. R. B. D. B. Austin Gurley, "The Design of Optimal Lattice Structures Manufactured by Maypole Braiding," *Journal of Mechanical Design,* vol. 147, pp. 101417-1 to 7, 2015.

[127] R. M. Z. M. L. C. D. C. D. R. Jeffrey Ian Lipton, "Handedness in shearing auxetics creates rigid and compliant structures," *Science,* vol. 360, no. 6389, pp. 632-635, 2018.

[128 A. L. N. T. T. F. M. W. G. D. B. André Hemmler, "Customized stent-grafts for
] endovascular aneurysm repair with challenging necks: A numerical proof of concept," *Numerical Methods in Biomedical Engineering,* 2020.

[129 J. P. K. C. M. P. MINA KONAKOVIĆ-LUKOVIĆ, "Rapid Deployment of Curved
] Surfaces via Programmable Auxetics," *ACM Transactions on Graphics,* 2018.

[130 H. P. V. Carneiro, "Modeling and elastic simulation of auxetic magnesium stents," in *IEEE
] 4th Portuguese Meeting on Bioengineering (ENBENG)*, 2015.

[131 W. L. Yafeng Han, "Optimizing the deformation behavior of stent with nonuniform
] Poisson's ratio distribution for curved artery," *Journal of the Mechanical Behavior of Biomedical Materials*, vol. 88, no. December, pp. 442-452, 2018.

[132 L. M. J. I. A. K. M. A. D. A. A. C. J. B. J. N. G. Ruben Gatt, "Hierarchical Auxetic
] Mechanical Metamaterials," *Scientific Reports,* vol. 5, no. 8395, 2014.

[133 B. A. F. B. R. B. William Jacob S. Dolla, "Structural and Drug-Diffusion Models of
] Conventional and Auxetic Drug-Eluting Stents," *ASME Journal of Medical Devices,* vol. 1, no. 1, pp. 47-55, 2007.

[134 B. E. Jenett, "Discrete Mechanical Metamaterials," Cambridge, MA, 2020.
]

[135 Y. J. &. Q. Wang, "Highly-stretchable 3D-architected Mechanical Metamaterials," *Nature
] Scientific Reports*, vol. 6, 2016.

[136] Z. M. J. P. S. D. N. V. H. I. Jifei Ou, "KinetiX - designing auxetic-inspired deformable material structures," *Computers & Graphics,* vol. 75, pp. 72-81, 2018.

[137] Y. C. R. K. R. a. P. M. Andrews Boakye, "A Review on Auxetic Textile Structures, Their Mechanism and Properties," *Journal of Textile Science and Fashion Technology,* vol. 2, no. 1, 2019.

[138] P. T. Boon, "Origami Magic Ball," Boon's Origami Blog, 14 August 2012. [Online]. Available: https://singaporeorigamiguy.wordpress.com/2012/08/14/origami-magic-ball/.

[139] H. F. J. M. R. P. a. Z. Y. Yan Chen, "Symmetric waterbomb origami," *Proceedings of the Royal Society A,* 2016.

[140] A. B. K. N. T. e. a. Takakura, "Strength of carbon nanotubes depends on their chemical structures," *Nature Communications,* vol. 10, no. 3040, 2019.

[141] Y. T. X. C. Guoxin Cao, "Elastic Properties of Carbon Nanotubes in the Radial Direction," *Proceedings of the Institution of Mechanical Engineers, Part N: Journal of Nanomaterials, Nanoengineering and Nanosystems,* vol. 219, no. 2, 2005.

[142] K. Jensen, W. Mickelson, A. Kis and A. Zettl, "Buckling and kinking force measurements on individual multiwalled carbon nanotubes," *Physical Review B,* vol. 76, no. 19, 2007.

[143] Hawk's Perch Technical Writing, LLC, "Electrical properties of nanotubes," [Online]. Available: https://www.understandingnano.com/electrical-properties-carbon-nanotubes.html.

[144 DuPont, "DuPont Hytrel Thermoplastic Polyester Elastomer," [Online].
]

[145 J. F. L. W. R. K. M. A. J. L. P. L. H.-T. C. a. P. B. Alexandra Ion, "Metamaterial
] Mechanisms," in *UIST '16: Proceedings of the 29th Annual Symposium on User Interface Software and Technology*, October 2016.

[146 S. S. S. M. H. V. Nazanin Ezazshahabi, "Effect of Fabric Structure and Weft Density on
] the Poisson's Ratio of Worsted Fabric," *Journal of Engineered Fibers and Fabric*, vol. 8, no. 2, pp. 63-71, 2013.

[147 C. J. D. P.-P. Finn Box, "Hard auxetic metamaterials," *Extreme Mechanics Letters*, vol. 40,
] no. 100980, 2020.

[148 peter120, "Air Bellows origami structure," MakerBot Thingiverse, 6 April 2020. [Online].
] Available: https://www.thingiverse.com/thing:4266259.

[149 H. E. N. Anastasia L. Wickeler, "Novel origami-inspired metamaterials: Design,
] mechanical testing and finite element modelling," *Materials & Design*, vol. 186, no. 108242, 2020.

[150 C. Liebold, "Workshop ENVYO: Mapping and Data Management along the Simulation
] Process Chain," DYNAmore GmbH, Stuttgart, 2016.

[151 A. Tabiei, "Loosly Woven Fabric Model with Viscoelastic Crimped Fibers for Ballistic
] Impact Simulations," *International Journal for Numerical Methods in Engineering*, vol. 61, pp. 1565-1583, 2004.

[152] E. P. M. G. Howie Fang, "Numerical Simulation of High-Speed Impacts Involving Metallic and Non-Metallic Materials," *International Journal of Computational Methods and Experimental Measurements,* vol. 6, no. 3, pp. 463-475, 2018.

[153] Z. Zhenhua, L. Lulu, C. Wei and L. Gang, "Numerical simulation methodology of multi-layer Kevlar 49 woven fabrics in aircraft engine containment application," *International Journal of Crashworthiness,* vol. 24, no. 1, pp. 86-99, 2019.

[154] P. K. P. B. T. N. Andrzej Morka, "A Punch Test as a Simple Verification Method of the Fabric Material Model," in *4th International Conference on Integrity, Reliability, and Failure*, Funchal/Madeira, 2013.

[155] M. R. Rosario Totoli, "Fabric impact drop tests: numerical simulations using the Ls-Dyna micromechanical approach and experimental characterization," in *International CAE Conference*, Pacengo del Garda, 2014.

[156] Y. H. I. C. J. W. John Hallquist, "LS-DYNA: Status and Development Plan," in *13th International LS-DYNA User's Conference*, 2014.

[157] Z. He, H. Xuan, C. Bai, M. Song and Z. Zhu, "Containment of soft wall casing wrapped with Kevlar Fabric," *Chinese Journal of Aeronautics,* vol. 32, no. 4, pp. 954-966, 2019.

[158] J. C. K. W. T. B. J. S. Michael Yeager, "Characterization and Modeling of the In-Plane Shear Deformation in Ultra-High Molecular Weight Polyethylene (UHMWPE) Composites," DEVCOM Army Research Laboratory, September 2019. [Online]. Available: https://apps.dtic.mil/sti/pdfs/AD1080467.pdf.

[159] W. Zhang, H. Ren, B. Liang, D. Zeng, X. Su, J. Dahl, M. Mirdamadi, Q. ZHao and J. Co, "A Non-Orthogonal Material Model of Woven Composites in the Preforming Process," in *15th International LS-DYNA Users' Conference*, 2018.

[160] DynaSupport, "LS-DYNA R10.1.0 (R10.123355) released," LSTC, [Online]. Available: https://www.dynasupport.com/news/ls-dyna-r10.1.0-r10.123355-released.

[161] J. Zhao, "An Overview of Carbon Fiber Modeling in LS-DYNA," 23 October 2017. [Online]. Available: http://lsdyna.com.cn/2017conf/document/2017_Session_Zhaoqiangsheng.pdf.

[162] I. Ciesielska-Wrobel, Finite Element Modeling of Textiles in Abaqus CAE, CRC Press, 2019.

[163] C. P. A. G. D. B. Amanda Skalitzky, "Woven Nitinol Fabric Strips Characterized in Tension via Finite Element Analysis and Geometric Modeling," in *ASME 2019 Conference on Smart Materials, Adaptive Structures and Intelligent Systems*, Louisville, KY, 2019.

[164] C. E. T. S. Thomas Borrvall, "A Fabric Material Model with Stress Map Functionality in LS-Dyna," in *10th European LS-DYNA Conference 2015*, Wurzburg, Germany, 2015.

[165] MatWeb, "DuPont™ Kevlar® 49 Aramid Fiber," [Online]. Available: http://www.matweb.com/search/datasheet.aspx?MatGUID=77b5205f0dcc43bb8cbe6fee7d36cbb5&ckck=1.

[166] McNeel Associates, "Squish - Rhino 3D Modeling," Rhinoceros 3D, [Online]. Available: http://docs.mcneel.com/rhino/7/help/en-us/commands/squish.htm.

[167] W. Z. K. X. X. D. Yixin Shao, "Design of a Novel Compact Adaptive Ankle Exoskeleton for Walking Assistance," in *Advances in Mechanism and Machine Science*, Springer, 2019, pp. 2159-2168.

[168] BASF, "Innofil3D PRO1 Technical Data Sheet," Innofil3D, 17 06 2019. [Online]. Available: https://www.matterhackers.com/r/hZqqHl. [Accessed 10 02 2020].

[169] PolyMaker, Inc., "PolyMax PC Technical Data Sheet," 11 2018. [Online]. Available: https://polymaker.com/Downloads/TDS/PolyMax_PC_TDS_V4.pdf. [Accessed 10 02 2020].

[170] DSM, "Novamid ID1030-CF10," [Online]. Available: https://www.dsm.com/content/dam/dsm/additive-manufacturing/en_US/documents/novamid-id1030-cf10-leaflet.pdf. [Accessed 10 02 2020].

[171] Mitsubishi, "KyronMAX™ S-4230," Mitsubishi Chemical Advanced Materials, [Online]. Available: https://media.mcam.com/fileadmin/quadrant/documents/ES/DataSheets/KyronMAXS-4230_DataSheet_5_16.pdf. [Accessed 10 02 2020].

[172] McNeel, Inc., "Rhino - Rhinoceros 3D," [Online]. Available: https://www.rhino3d.com/.

[173] H. Z. W. C. M. W. B. Z. W. S. Jianwen Chen, "Full-strain range characteristics of the Poisson’s ratio for coated biaxial warp-knitted fabrics under bias tensile loading," *Textile Research Journal,* vol. 89, no. 10, pp. 1997-2009, 2018.

[174] geeko_team, "Tachi Miura Compressible Origami," MakerBot Thingiverse, 17 March 2019. [Online]. Available: https://www.thingiverse.com/thing:3497763.

[175] L. J. Y. L. Z. W. W. H. W. W. B. L. L. M. D. F. Ran Tao, "4D printed origami metamaterials with tunable compression twist behavior and stress-strain curves," *Composites Part B,* vol. 201, p. 108344, 2020.

Appendix I. MATLAB Code for Calculating Gaps between Tiles (from Chapter 4).

```
%Bezier spline matrix
clc
clear all
length_of_array=402.236; %mm
Bez_control_matrix=[0,0,0;
                    202.583,0,0.358;
                    261.126,0,23.368;
                    371.802,0,117.762];
Bez_basis_matrix=[-1,3,-3,1;
                  3,-6,3,0;
                  -3,3,0,0;
                  1,0,0,0];

syms u
xyz=[u^3,u^2,u,1]*Bez_basis_matrix*Bez_control_matrix;
x=xyz(1);
z=xyz(3);

uvector=linspace(0,1,1000);
xvector=196.2*uvector.^3-432.1*uvector.^2+607.7*uvector;
zvector=48.73*uvector.^3+67.96*uvector.^2+1.074*uvector;
kappa=abs(-10.26*uvector.^3+206350*uvector.^2-176400*uvector-
83522)./(367700*uvector.^4-977400*uvector.^3+1481000*uvector.^2-
1050000*uvector+369300).^(3/2);
figure(1)
plot(uvector,kappa)
xlabel('Parameter u, dimensionless parameter along curve. NOT x
position!')
ylabel('Curvature intensity \kappa, units [1/mm]')
title('Curvature vs. curve parameter u (NOT vs. x position!)')
figure(2)
yyaxis left
plot(xvector,zvector)
title('Z vs. X Coordinates of Base Curve, and Curvature vs. X-
Coordinate on Curve')
ylabel('Z coordinate on Base Curve [mm]')
yyaxis right
kappafofx=0;

plot(xvector,kappa)
ylabel('Magnitude of \kappa, Curvature [1/mm] at Given X-
Coordinate')
xlabel('X-coordinate on Curve, [mm]')
```

```
%%%% Calculate curvature
width_red=30.858;
width_blue=24.198;
width_green=24.09;
width_yellow=31.004;
num_unit_cells=8;
% theta=w_old/rho;
% s_new=theta*(rho-h);
% width_top_new=sqrt(2*(rho-h)^2-2*(rho-h)^2*cos(theta));
list_of_xs=[16.662, 28.72, 41.138, 53.284, 65.832, 77.888,
90.303, 102.46, 114.932, 126.988,...

139.403,151.56,164.032,176.088,188.503,200.66,213.132,225.188,23
7.603,249.76,262.232,274.288,...

286.703,298.86,311.332,323.388,335.803,347.96,360.432,372.488,38
4.903];
list_of_us=list_of_xs/length_of_array; %Each u must vary from 0
to 1

%Sort them into green, red, yellow, blue:
greenus=0;
redus=0;
yellowus=0;
blueus=0;
height=11.86;
i=1;
while(1)
    greenus(i)=list_of_us(4*i-3);
    redus(i)=list_of_us(4*i-2);
    yellowus(i)=list_of_us(4*i-1);
    if i<=num_unit_cells-1
        blueus(i)=list_of_us(4*i); %One fewer blue than others
    end
    i=i+1;
    if i>=num_unit_cells
        break
    end
end
kappa_centroids=abs(-10.26*list_of_us.^3+206350*list_of_us.^2-
176400*list_of_us-83522)./(367700*list_of_us.^4-
977400*list_of_us.^3+1481000*list_of_us.^2-
1050000*list_of_us+369300).^(3/2);
list_of_ROCs=1./kappa_centroids;
i=1;
```

```
greenROCs=[];
redROCs=[];
blueROCs=[];
yellowROCs=[];
while(1)
    greenROCs(i)=list_of_ROCs(4*i-3);
    redROCs(i)=list_of_ROCs(4*i-2);
    yellowROCs(i)=list_of_ROCs(4*i-1);
    if i<=num_unit_cells-1
        blueROCs(i)=list_of_ROCs(4*i); %One fewer blue than
others
    end
    i=i+1;
    if i>=num_unit_cells
        break
    end
end

figure(20)
plot(length_of_array*redus,redROCs,'r*',length_of_array*greenus,
greenROCs,'g*',length_of_array*blueus,blueROCs,'b*',length_of_ar
ray*yellowus,yellowROCs ,'y*')
%     'LineWidth',2,...
%     'MarkerSize',4,...
%     'MarkerEdgeColor','y',...
%     'MarkerFaceColor',[238/256,190/256,0])
xlabel('x-position of centroid from left edge, mm')
ylabel('Average radius of curvature at lockup at each centroid,
mm')
title('Radii of curvature at centroids of different tiles at
lockup')
legend('Red tile', 'Green tile', 'Blue tile', 'Yellow tile')
heightssaboveplane=linspace(0,height,10);
kappa_at_greenpoints=abs(-10.26*greenus.^3+206350*greenus.^2-
176400*greenus-83522)./(367700*greenus.^4-
977400*greenus.^3+1481000*greenus.^2-
1050000*greenus+369300).^(3/2);
radii_of_curvature_at_greenpoints=kappa_at_greenpoints.^-1; %mm
thetasgreen=width_green./radii_of_curvature_at_greenpoints;
width_top_greens=sqrt(2*(radii_of_curvature_at_greenpoints-
height).^2.*(1-cos(thetasgreen))); %Use Law of Cosines
halfdelta_greens=(width_green-width_top_greens)/2;
x_greens=greenus*length_of_array;
half_delta_matrix_greens=[];
for i=1:length(x_greens)
    for j=1:length(heightssaboveplane)
```

```
half_delta_matrix_greens(i,j)=halfdelta_greens(i)*(heightssabove
plane(j)/height);
    end
end
%Create green colormap:
greenmap=[3/256,222/256,135/256; 0/256,102/256,40/256];
greenmapcol1int=interp1([1,2],greenmap(:,1),linspace(1,2,20));
greenmapcol2int=interp1([1,2],greenmap(:,2),linspace(1,2,20));
greenmapcol3int=interp1([1,2],greenmap(:,3),linspace(1,2,20));
greenmapbig=[greenmapcol1int',greenmapcol2int',greenmapcol3int']
;
figure(3)
surf(x_greens',heightssaboveplane',half_delta_matrix_greens')
xlabel('Distance along x, in mm')
ylabel('Height above ground plane, in mm')
zlabel('Half-delta (half total gap between teeth) at height and
x position, in mm')
title('Magnitude of half-delta gap only for green tiles')
colormap(greenmapbig)
% figure(4)
% surf(x_all',heightssaboveplane',half_delta_matrix_all')
% xlabel('Distance along x')
% ylabel('Height above ground plane')
% zlabel('Half-delta (half total gap between teeth) at height
and x position')
% title('Magnitude of half-delta gap, for all tiles')
%
kappa_at_redpoints=abs(-10.26*redus.^3+206350*redus.^2-
176400*redus-83522)./(367700*redus.^4-
977400*redus.^3+1481000*redus.^2-1050000*redus+369300).^(3/2);
radii_of_curvature_at_redpoints=kappa_at_redpoints.^-1; %mm
thetasred=width_red./radii_of_curvature_at_redpoints;
width_top_reds=sqrt(2*(radii_of_curvature_at_redpoints-
height).^2.*(1-cos(thetasred))); %Use Law of Cosines
halfdelta_reds=(width_red-width_top_reds)/2;
x_reds=redus*length_of_array;
half_delta_matrix_reds=[];
for i=1:length(x_reds)
    for j=1:length(heightssaboveplane)

half_delta_matrix_reds(i,j)=halfdelta_reds(i)*(heightssaboveplan
e(j)/height);
    end
end
%Create red colormap:
```

```
redmap=[245/256,52/256,62/256; 172/256,0/256,0/256];
redmapcol1int=interp1([1,2],redmap(:,1),linspace(1,2,20));
redmapcol2int=interp1([1,2],redmap(:,2),linspace(1,2,20));
redmapcol3int=interp1([1,2],redmap(:,3),linspace(1,2,20));
redmapbig=[redmapcol1int',redmapcol2int',redmapcol3int'];
figure(5)
surf(x_reds',heightssaboveplane',half_delta_matrix_reds')
xlabel('Distance along x, in mm')
ylabel('Height above ground plane, in mm')
zlabel('Half-delta (half total gap between teeth) at height and
x position, in mm')
title('Magnitude of half-delta gap only for red tiles')
colormap(redmapbig)
kappa_at_bluepoints=abs(-10.26*blueus.^3+206350*blueus.^2-
176400*blueus-83522)./(367700*blueus.^4-
977400*blueus.^3+1481000*blueus.^2-
1050000*blueus+369300).^(3/2);
radii_of_curvature_at_bluepoints=kappa_at_bluepoints.^-1; %mm
thetasblue=width_blue./radii_of_curvature_at_bluepoints;
width_top_blues=sqrt(2*(radii_of_curvature_at_bluepoints-
height).^2.*(1-cos(thetasblue))); %Use Law of Cosines
halfdelta_blues=(width_blue-width_top_blues)/2;
x_blues=blueus*length_of_array;
half_delta_matrix_blues=[];
for i=1:length(x_blues)
    for j=1:length(heightssaboveplane)

half_delta_matrix_blues(i,j)=halfdelta_blues(i)*(heightssabovepl
ane(j)/height);
    end
end
%Create blue colormap:
bluemap=[0/256,177/256,253/256; 13/256,44/256,89/256];
bluemapcol1int=interp1([1,2],bluemap(:,1),linspace(1,2,20));
bluemapcol2int=interp1([1,2],bluemap(:,2),linspace(1,2,20));
bluemapcol3int=interp1([1,2],bluemap(:,3),linspace(1,2,20));
bluemapbig=[bluemapcol1int',bluemapcol2int',bluemapcol3int'];
figure(4)
surf(x_blues',heightssaboveplane',half_delta_matrix_blues')
xlabel('Distance along x, in mm')
ylabel('Height above ground plane, in mm')
zlabel('Half-delta (half total gap between teeth) at height and
x position, in mm')
title('Magnitude of half-delta gap only for blue tiles')
colormap(bluemapbig)
```

```
kappa_at_yellowpoints=abs(-10.26*yellowus.^3+206350*yellowus.^2-
176400*yellowus-83522)./(367700*yellowus.^4-
977400*yellowus.^3+1481000*yellowus.^2-
1050000*yellowus+369300).^(3/2);
radii_of_curvature_at_yellowpoints=kappa_at_yellowpoints.^-1;
%mm
thetasyellow=width_yellow./radii_of_curvature_at_yellowpoints;
width_top_yellows=sqrt(2*(radii_of_curvature_at_yellowpoints-
height).^2.*(1-cos(thetasyellow))); %Use Law of Cosines
halfdelta_yellows=(width_yellow-width_top_yellows)/2;

x_yellows=yellowus*length_of_array;
half_delta_matrix_yellows=[];
for i=1:length(x_yellows)
    for j=1:length(heightssaboveplane)

half_delta_matrix_yellows(i,j)=halfdelta_yellows(i)*(heightssabo
veplane(j)/height);
    end
end
%Create yellow colormap:
yellowmap=[255/256,230/256,83/256; 205/256,150/256,20/256];
yellowmapcol1int=interp1([1,2],yellowmap(:,1),linspace(1,2,20));

yellowmapcol2int=interp1([1,2],yellowmap(:,2),linspace(1,2,20));
yellowmapcol3int=interp1([1,2],yellowmap(:,3),linspace(1,2,20));
yellowmapbig=[yellowmapcol1int',yellowmapcol2int',yellowmapcol3i
nt'];

figure(6)
surf(x_yellows',heightssaboveplane',half_delta_matrix_yellows')
xlabel('Distance along x, in mm')
ylabel('Height above ground plane, in mm')
zlabel('Half-delta (half total gap between teeth) at height and
x position, in mm')
title('Magnitude of half-delta gap only for yellow tiles')
colormap(yellowmapbig)

figure(8)
clf(8)
hold on
surf(x_yellows',heightssaboveplane',half_delta_matrix_yellows','
FaceLighting','gouraud',...
    'MeshStyle','column',...
    'SpecularColorReflectance',0.1,...
    'SpecularExponent',5,...
    'SpecularStrength',0.2,...
    'DiffuseStrength',0.3,...
    'AmbientStrength',0.4,...
    'AlignVertexCenters','on',...
```

```
    'LineWidth',1,...
    'FaceAlpha',0.9,...
    'FaceColor',[255/256,230/256,83/256],...
    'EdgeColor',[205/256,150/256,20/256],...
    'EdgeAlpha',1)
% colormap(yellowmapbig)
surf(x_blues',heightssaboveplane',half_delta_matrix_blues','Face
Lighting','gouraud',...
    'MeshStyle','column',...
    'SpecularColorReflectance',0,...
    'SpecularExponent',5,...
    'SpecularStrength',0.2,...
    'DiffuseStrength',0.3,...
    'AmbientStrength',0.4,...
    'AlignVertexCenters','on',...
    'LineWidth',1,...
    'FaceAlpha',0.9,...
    'FaceColor',[0/256,177/256,253/256],...
    'EdgeColor',[13/256,44/256,89/256],...
    'EdgeAlpha',1)
% colormap(bluemapbig)
surf(x_reds',heightssaboveplane',half_delta_matrix_reds','FaceLi
ghting','gouraud',...
    'MeshStyle','column',...
    'SpecularColorReflectance',0,...
    'SpecularExponent',5,...
    'SpecularStrength',0.2,...
    'DiffuseStrength',0.3,...
    'AmbientStrength',0.4,...
    'AlignVertexCenters','on',...
    'LineWidth',1,...
    'FaceAlpha',0.9,...
    'FaceColor',[170/256,0/256,0/256],...
    'EdgeColor',[245/256,52/256,62/256],...
    'EdgeAlpha',1)
surf(x_greens',heightssaboveplane',half_delta_matrix_greens','Fa
ceLighting','gouraud',...
    'MeshStyle','column',...
    'SpecularColorReflectance',0,...
    'SpecularExponent',5,...
    'SpecularStrength',0.2,...
    'DiffuseStrength',0.3,...
    'AmbientStrength',0.4,...
    'AlignVertexCenters','on',...
    'LineWidth',1,...
    'FaceAlpha',0.9,...
    'FaceColor',[3/256,222/256,135/256],...
```

```
    'EdgeColor',[0/256,102/256,40/256],...
    'EdgeAlpha',1)
xlabel('Distance along x, in mm')
ylabel('Height above ground plane, in mm')
zlabel('Half-delta (half total gap between teeth) at height and
x position, in mm')
title('Magnitude of half-delta gap for all tiles')
hold off
```

Appendix II. MATLAB Code for Comparing the Actual Elastic Curve and Desired Lockup Curve for Chapter 4.

```
%Elastic curve for actual bent array with 38.44mm tip deflection.
%Bezier spline matrix
clc
clear all
length_of_array=402.236; %mm
Bez_control_matrix=[0,0,0;
                    202.583,0,0.358;
                    261.126,0,23.368;
                    371.802,0,117.762];
Bez_basis_matrix=[-1,3,-3,1;
                  3,-6,3,0;
                  -3,3,0,0;
                  1,0,0,0];
syms u
xyz=[u^3,u^2,u,1]*Bez_basis_matrix*Bez_control_matrix;
x=xyz(1);
z=xyz(3);
uvector=linspace(0,1,1000);
xvector=196.2*uvector.^3-432.1*uvector.^2+607.7*uvector;
zvector=48.73*uvector.^3+67.96*uvector.^2+1.074*uvector;
kappa=abs(-10.26*uvector.^3+206350*uvector.^2-176400*uvector-
83522)./(367700*uvector.^4-977400*uvector.^3+1481000*uvector.^2-
1050000*uvector+369300).^(3/2);
%%%%%%%%%%ACTUAL ARRAY
length_of_array=402.236; %mm
Bez_control_matrix_actual=[0,0,0;
                    159.454,0,1.463;
                    273.828,0,40.745;
                    351.846,0,154.684];
Bez_basis_matrix=[-1,3,-3,1;
                  3,-6,3,0;
                  -3,3,0,0;
                  1,0,0,0];
syms u
xyz_actual=[u^3,u^2,u,1]*Bez_basis_matrix*Bez_control_matrix_actual;
x=xyz_actual(1);
z=xyz_actual(3);
rprimevector=diff(xyz_actual,u)
rdblprimevector=diff(rprimevector,u)
syms kappa_actual(u)
kappa_actual(u)=norm(cross(rprimevector,rdblprimevector)./norm(rprimev
ector).^3)
kappa_actual_vector=eval(kappa_actual(uvector));
uvector=linspace(0,1,1000);
```

```
xvector_actual=-69.59*uvector.^3+20.832*uvector.^2+401.21*uvector;
zvector_actual=16.55*uvector.^3+155.184*uvector.^2-16.17*uvector;
u=uvector;
figure(1)
plot(uvector,kappa_actual_vector,uvector,kappa)
xlabel('Parameter u, dimensionless parameter along curve. NOT x
position!')
ylabel('Curvature intensity \kappa, for actual and ideal curves, with
units [1/mm]')
title('Curvature for actual and ideal curves')
legend('Actual \kappa','Ideal \kappa')
figure(88)
plot(uvector,1./kappa_actual_vector,uvector,1./kappa)
xlabel('Parameter u, dimensionless parameter along curve. NOT x
position!')
ylabel('Instantaneouls Radius of Curvature \rho, units [mm]')
title('Radius of Curvature for actual and ideal curves')
legend('Actual \rho','Ideal \rho')
figure(110)
plot(uvector,1./kappa)
xlabel('Parameter u, dimensionless parameter along curve. NOT x
position!')
ylabel('Instantaneous Radius of Curvature \rho, units [mm]')
title('Radius of Curvature vs. curve parameter u (NOT vs. x
position!)')
RMSKappaerror=sqrt(1/length(kappa_actual)*sum((kappa_actual_vector-
kappa).^2))
```

Appendix III. Additional Fabric-Backed Arrays of Interest.

This appendix will contain some conceptual discussion and images of other arrays that were investigated, differing in tile geometry or manifold topology from those of the array introduced in Chapter 4. The appendix will give further demonstration of the author's ability with CAD, 3D printing, conceptual understanding of the concept of fabric-backed interrupted-tile arrays, and, in some cases, tailoring the lockup of such arrays (though, as illustrated in Chapter 7, arrays with closed manifolds or that target doubly-curved surfaces behave substantially differently from arrays whose initial and target manifolds are only singly-curved or flat).

A pentagonal tiling of tiles on a plane intended to give near-isotropic lockup properties.

A cylindrical array with tiles that also could tolerate some rotation (to increase shear tolerance)

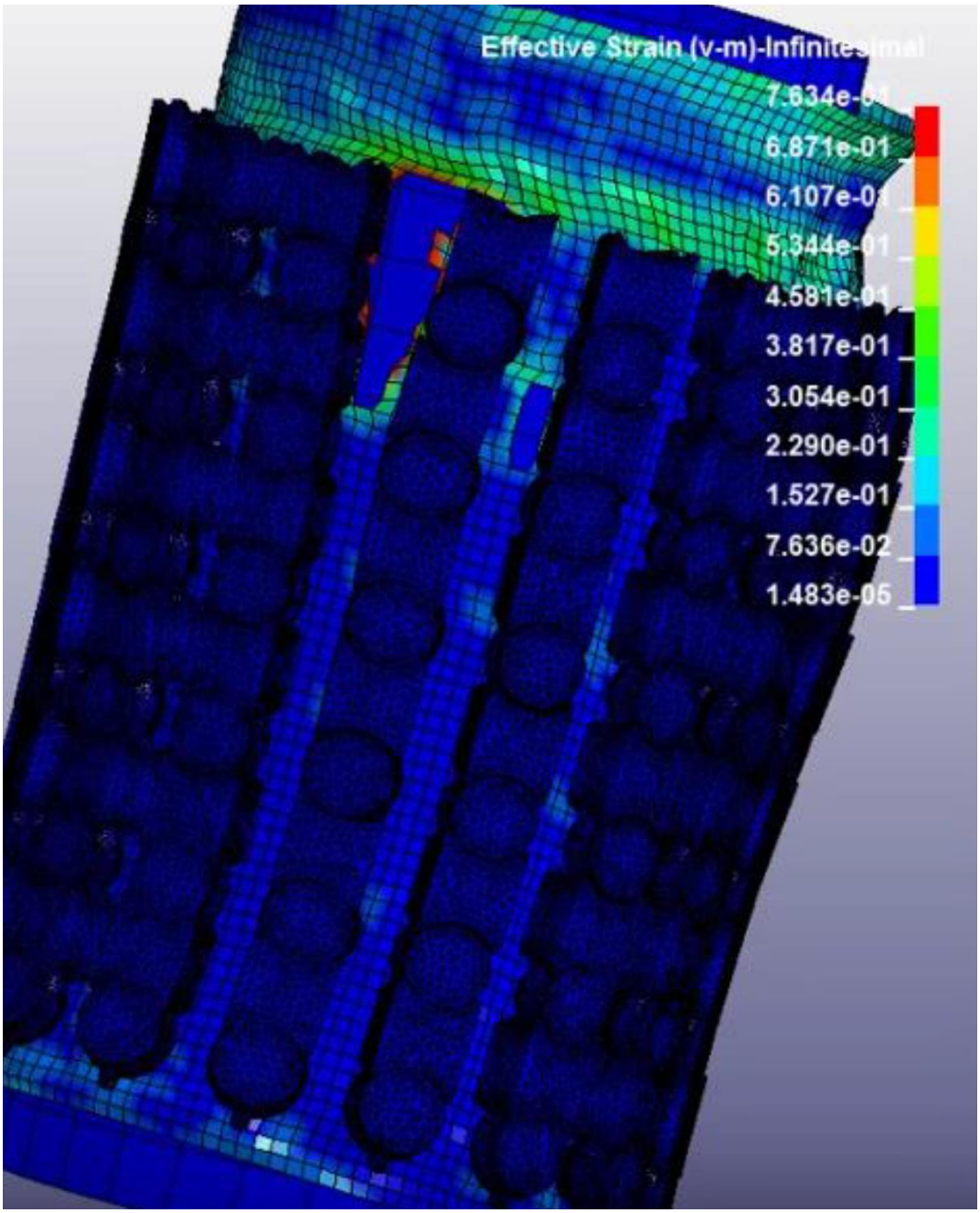

A preliminary FEA simulation of one array.

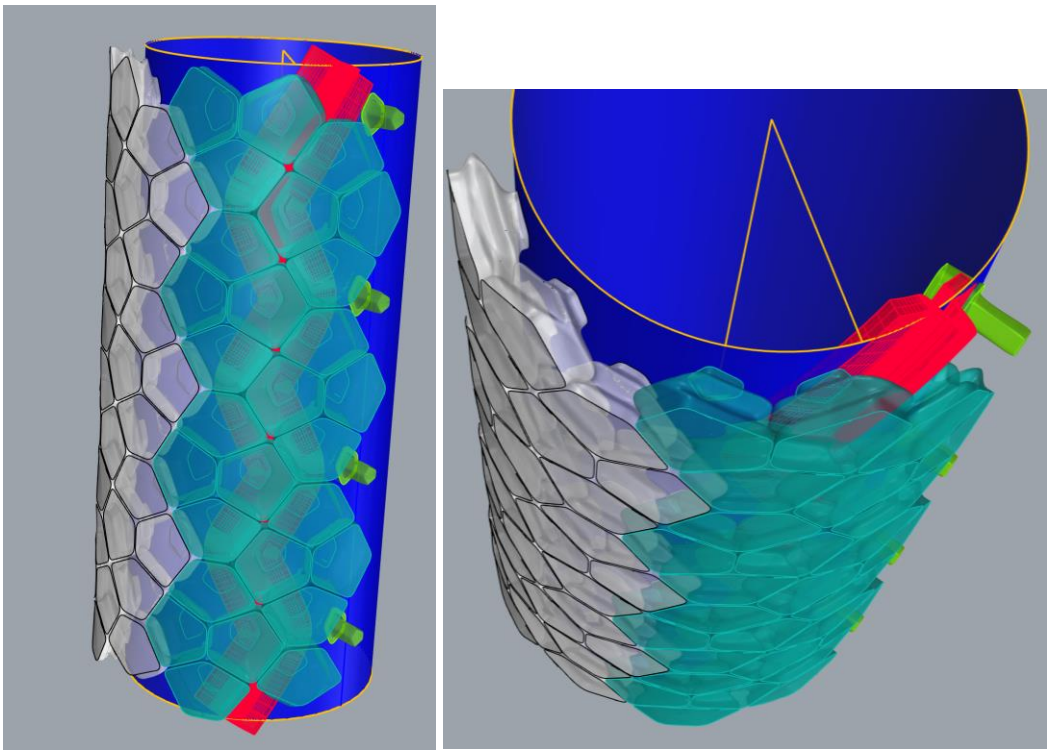

An array of tiles shaped like the Cairo pentagonal tiling on a cylinder. The red tool was designed to force the fabric to take on extra waviness around the bases of the tiles.

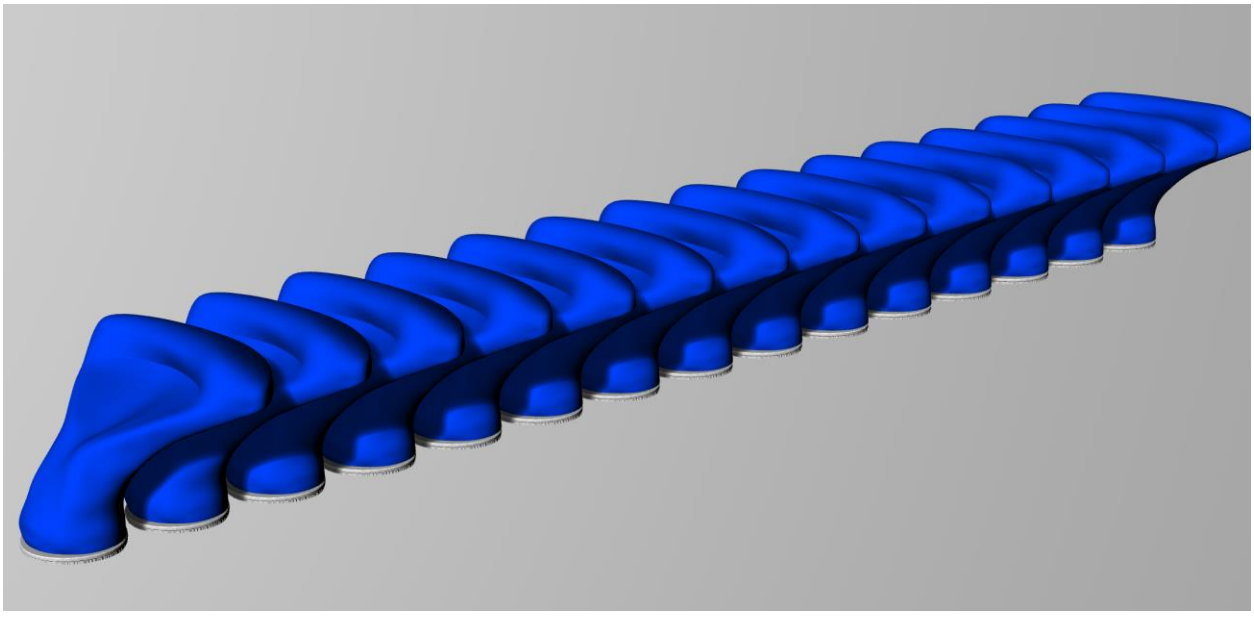

An array of scale-like (“imbricated”) tiles with rotational freedom about the axis normal to the fabric as well as bending freedom prior to lockup.

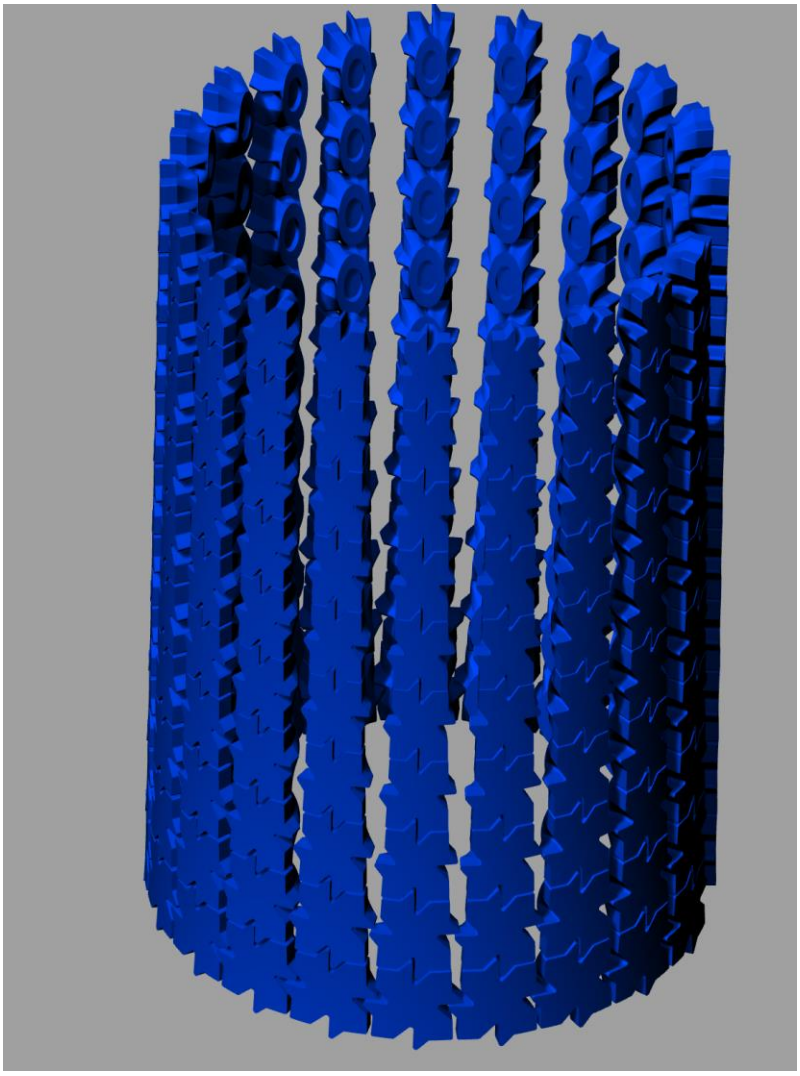

An array with increasing radial freedom at the top of the cylinder and with anti-sliding/shearing features.

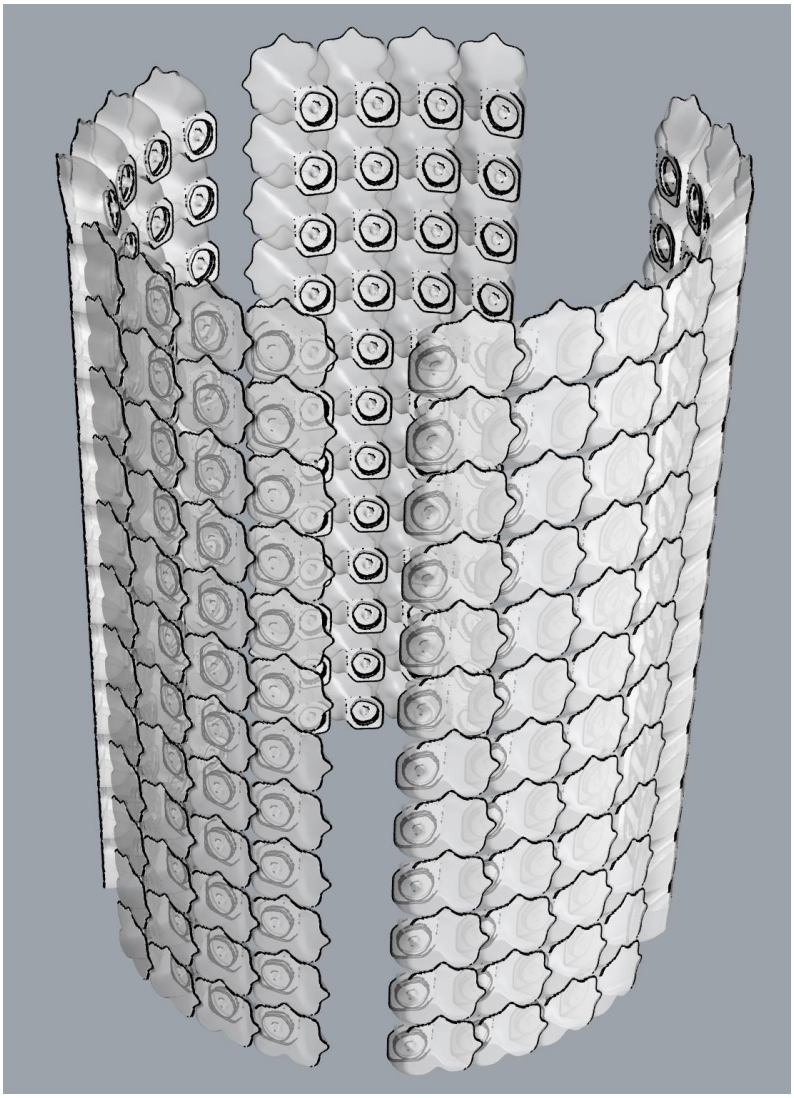

An array of imbricated tiles on a cylindrical surface.

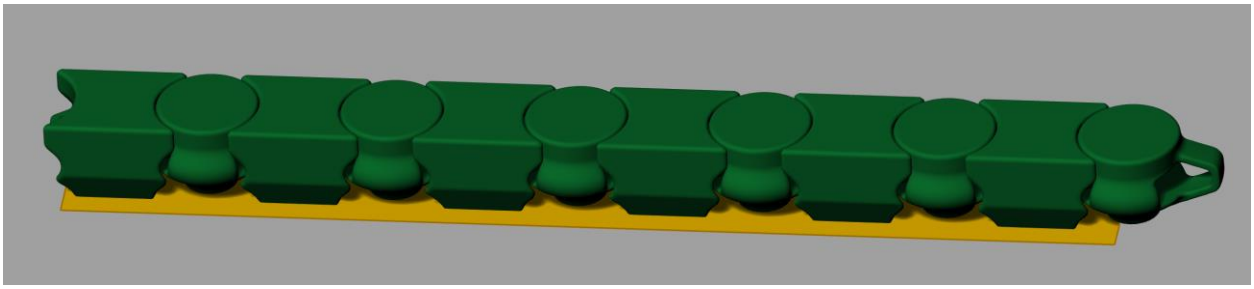

Tiles with interlocking chain-link features as well as rotation capability.

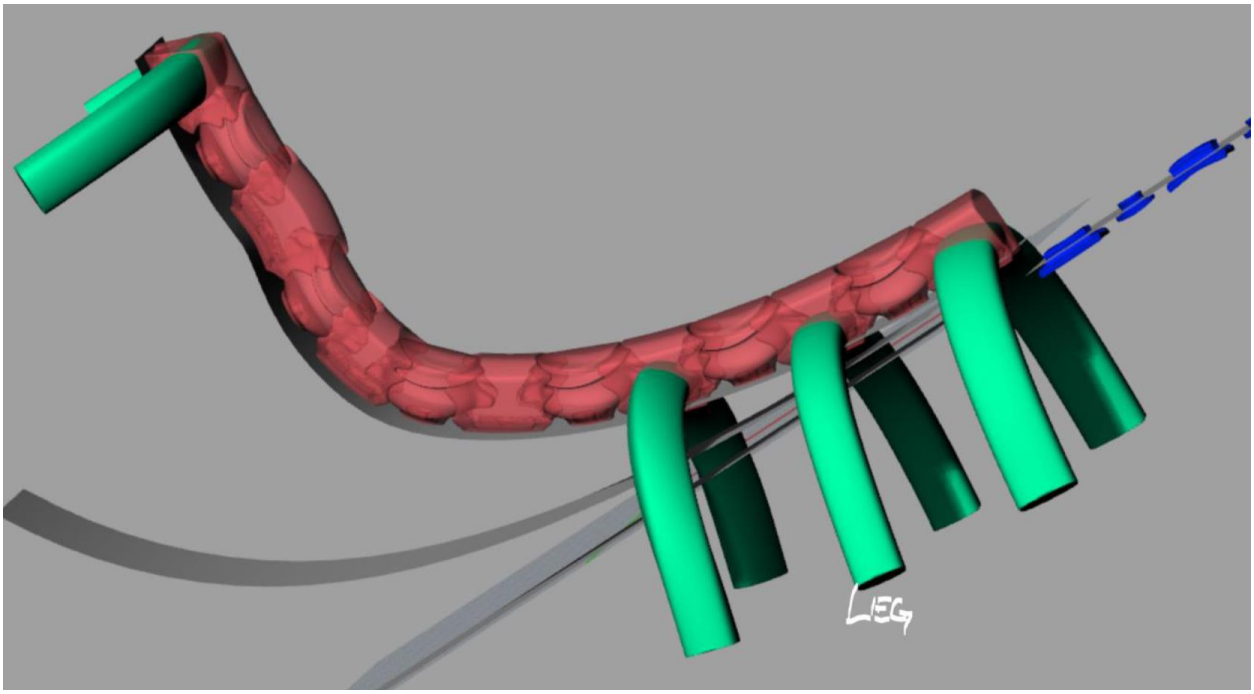

Tiles with rings to constrain the leg to them. The tiles were arrayed on a thin strip of fabric that could tolerate some rotation about axes normal to the fabric, as well as bending.

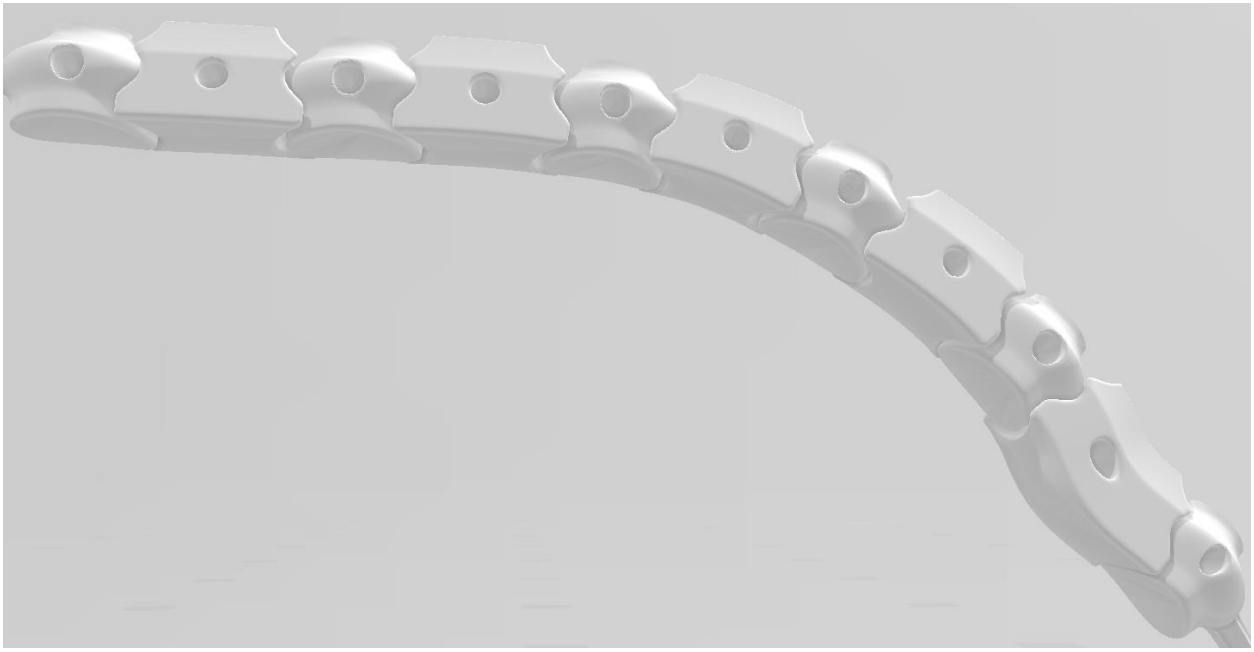

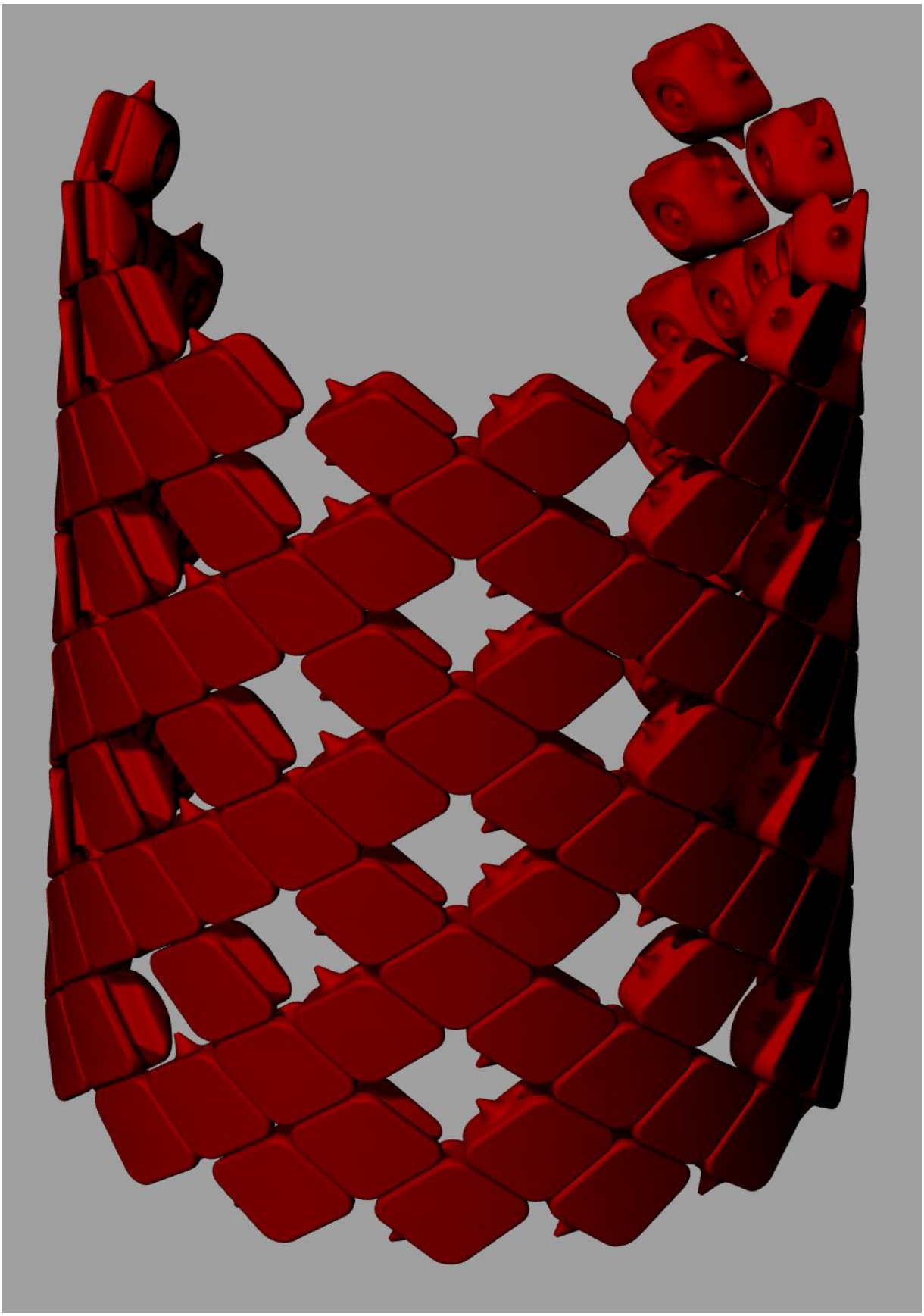

Tiles with contact surfaces oriented biaxially and with anti-sliding features in a cylindrical array.

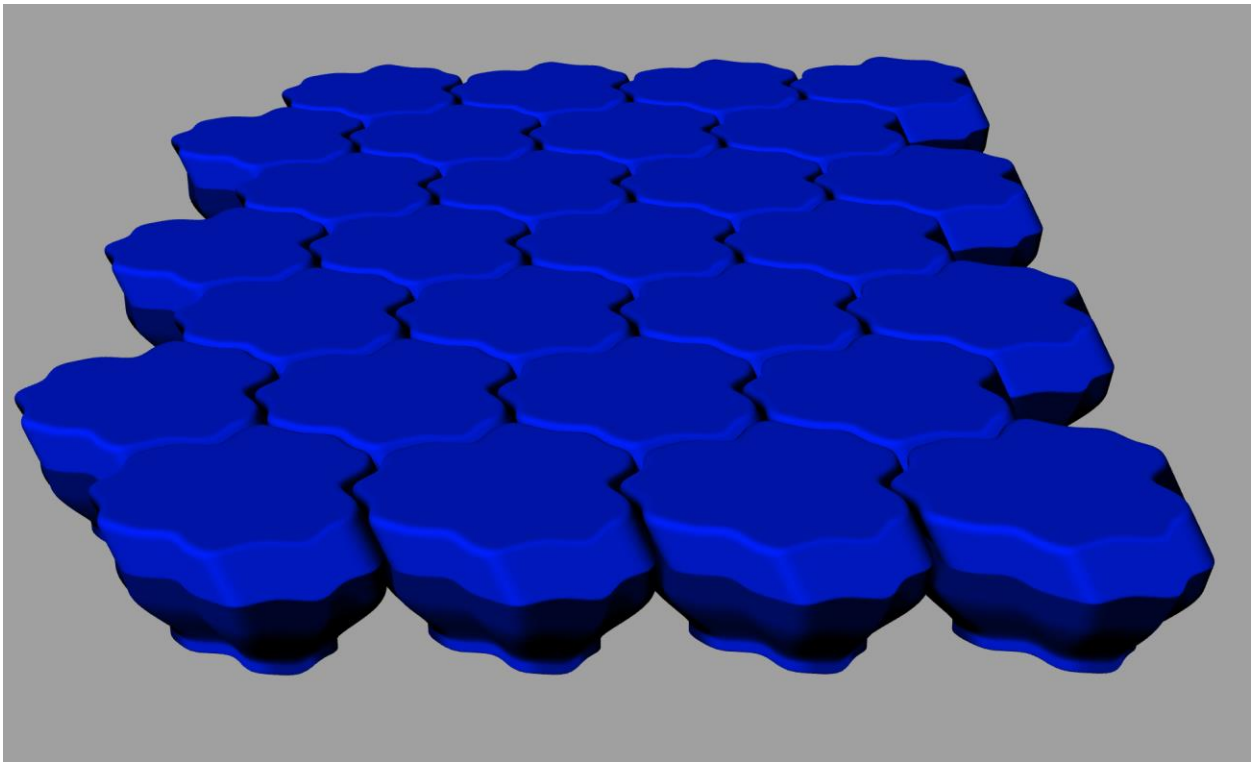

Planar tile array with anti-sliding features and imbricated profile.

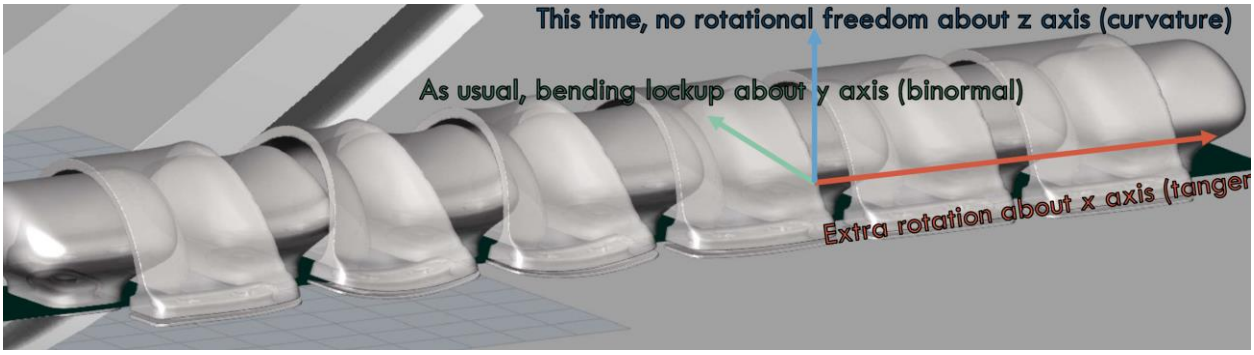

An array on a fabric strip with bending freedom until lockup plus limited rotation about the tangent axis.

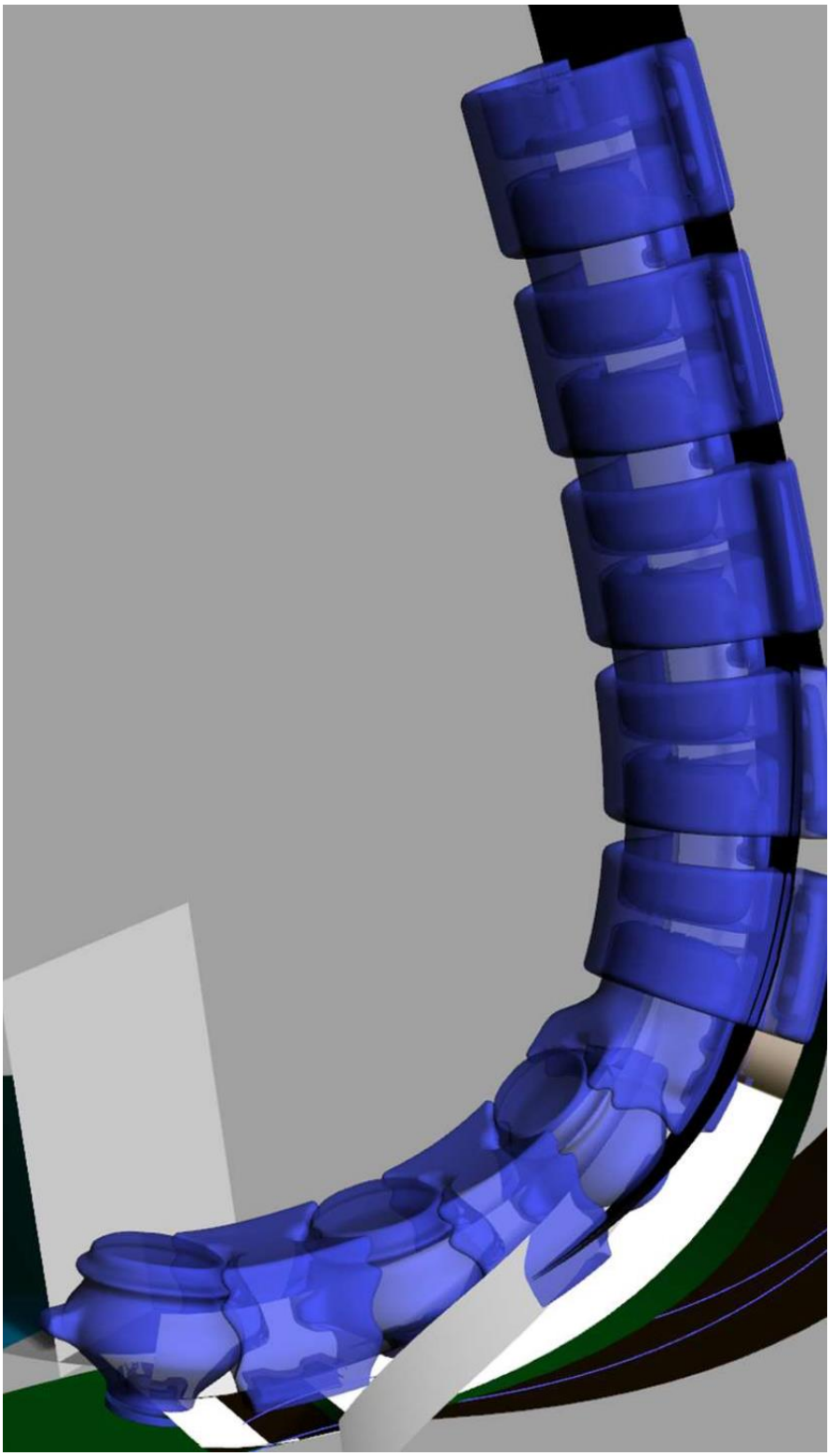

Spine-like 1D array with rotation tolerated either tangent to the fabric or normal to it.

A tile design featuring toothed gears and imbricated structures to prevent sliding.

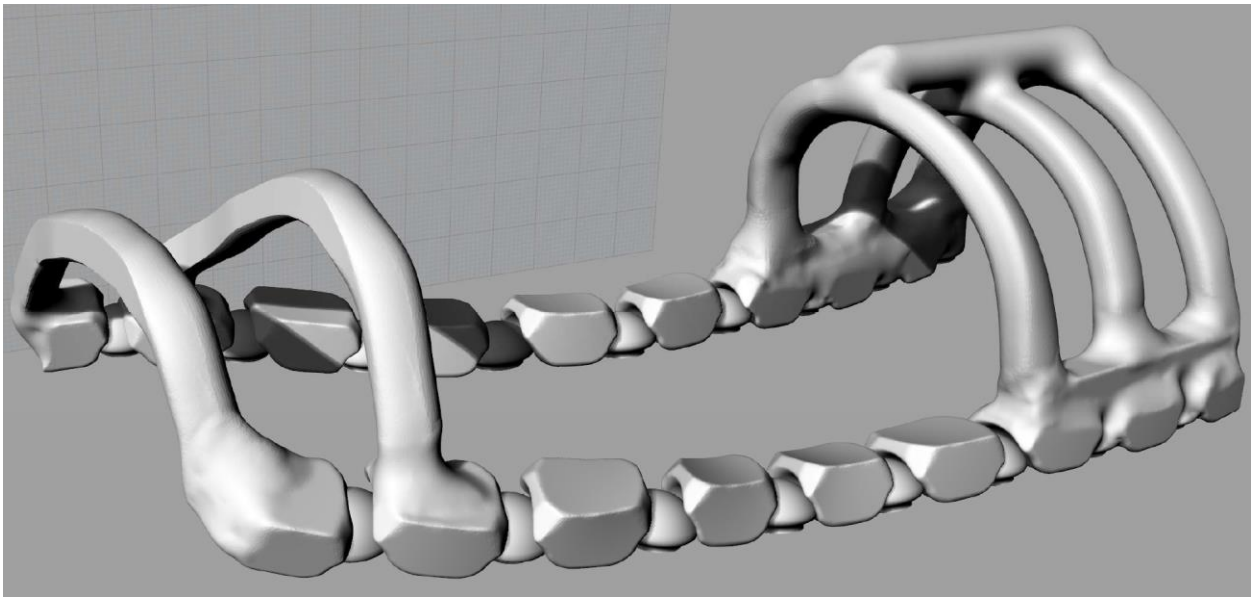

An array with tiles shaped like spheres to allow rotation in various directions, as well as rings to interact with the leg and shoe.

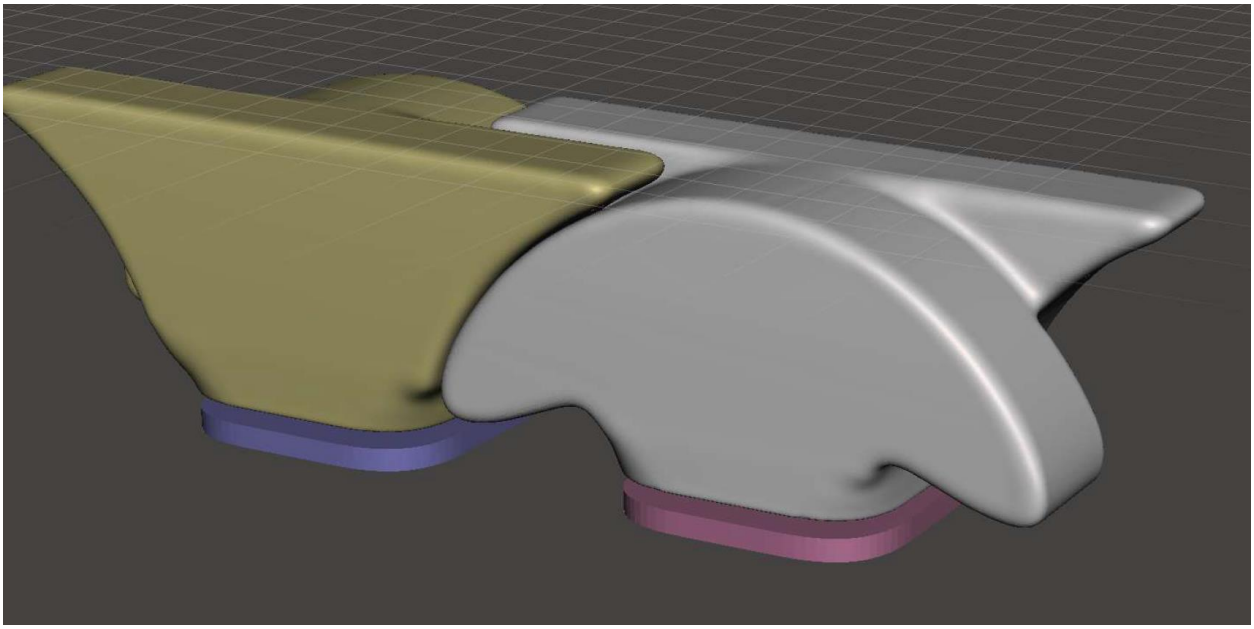

A unit cell allowing twist along the tangent axis as well as bending before lockup, with rivets.

Appendix IV. Additional LS-Dyna Simulations of Fabric-Backed Arrays.

Half-Array, Version 3

V3_16_sub1 (NIP=3, Shell 2, VDC=40)

Hourglassing was quite strong, partly owing to the significant mass-scaling required and the speed at which the load was applied in the simulation (to speed computation).

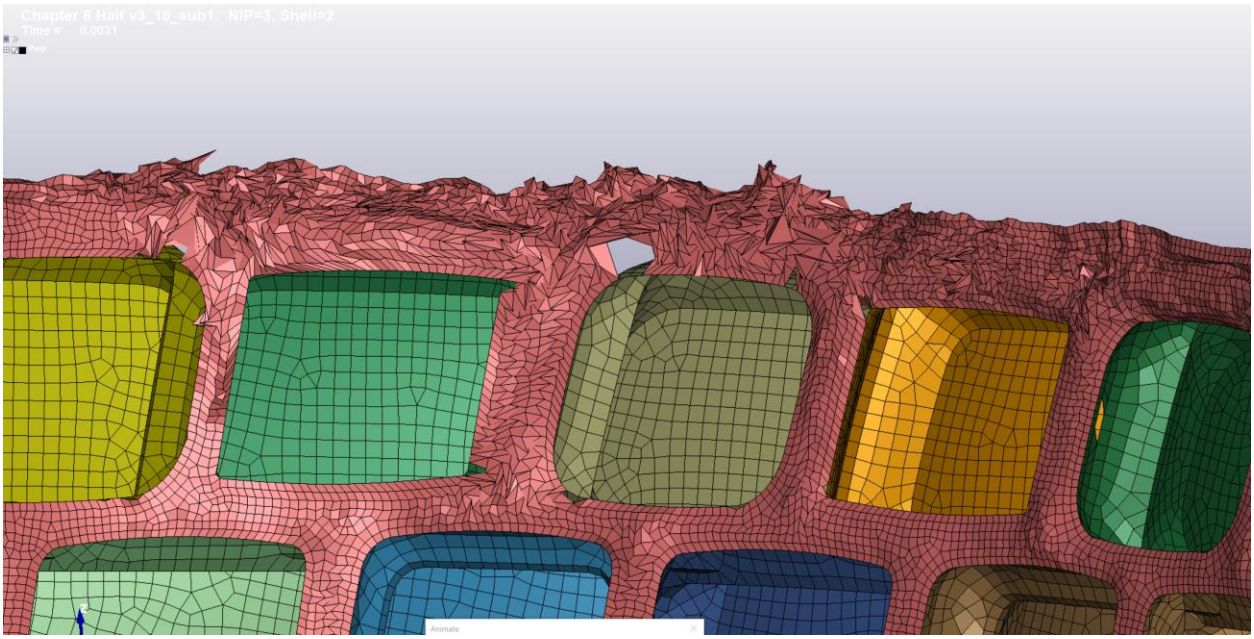

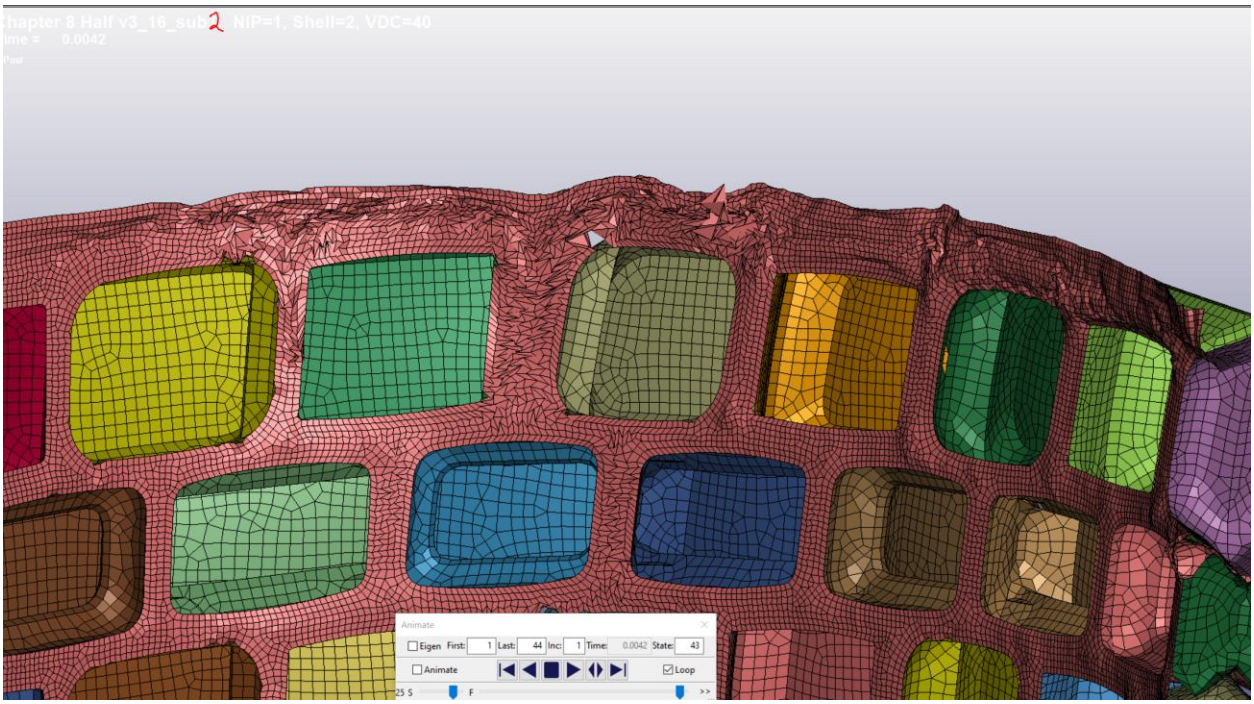

Half-Array, Version 5

The mesh was refined considerably and only used triangles in order to avoid hourglassing.

V5a: Triangular remesh (size 0.2mm)

Other changes made include: VDC=50 on the contact card and fabric was excluded from contact. Shell element formulation 2, NIP=3, and no damping were used.

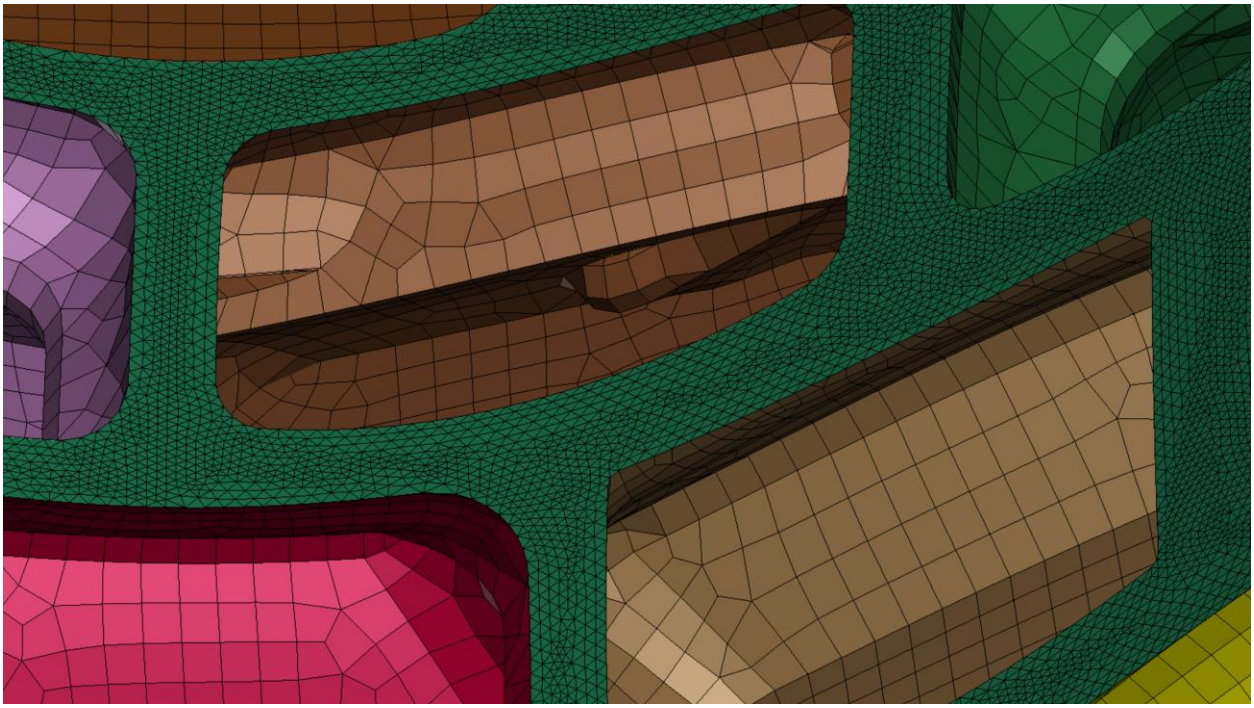

v5b: added Frequency Damping (Deformable) to Fabric, otherwise v5a

Frequency-based damping based on an estimate of the min and max frequencies of relevant eigenmodes was used.

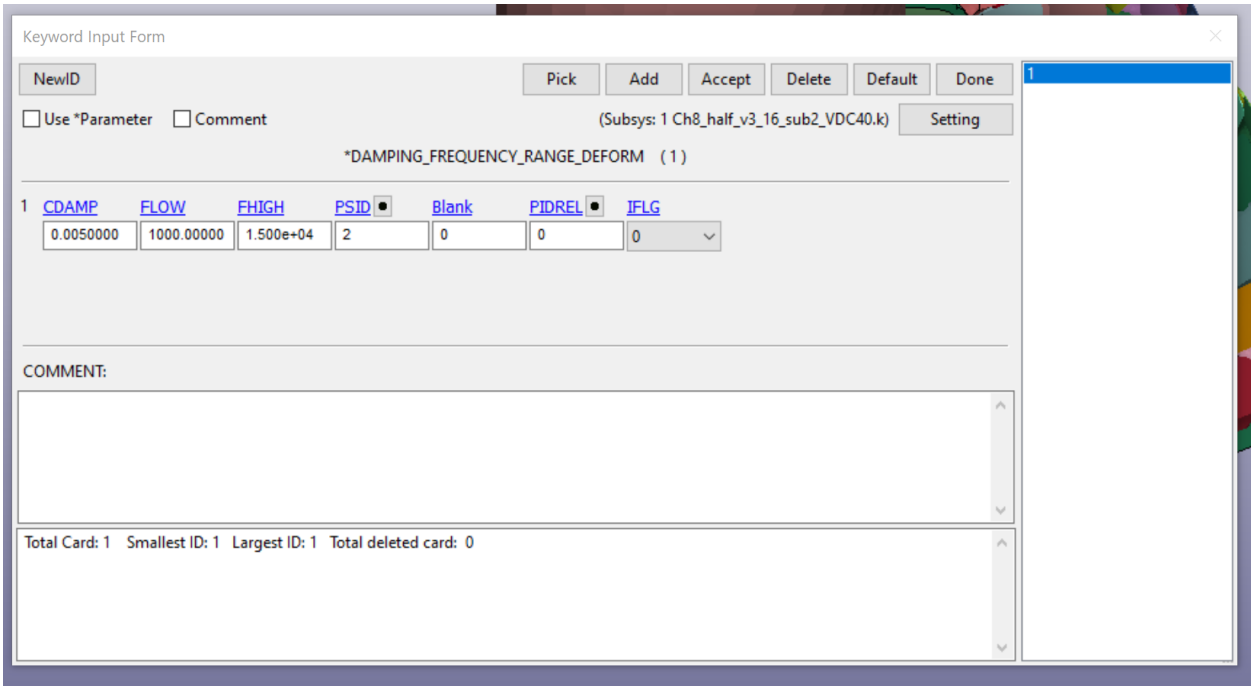

Half v6: EFG Added

Attempts were made to use the EFG method with adaptive remeshing against larger deflections. The solver refused to conduct even one timestep with the following settings though:

V6A:

Using H-adaptive because shell (not R-adaptive as examples use)

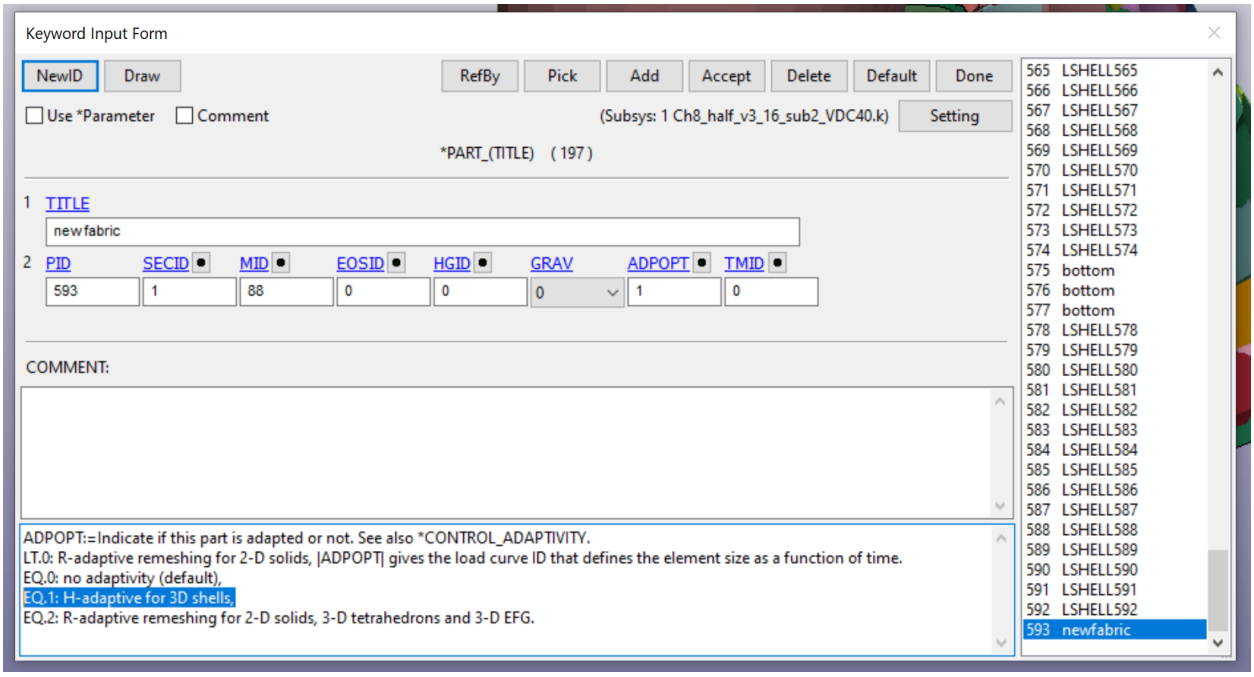

Various EFG settings:

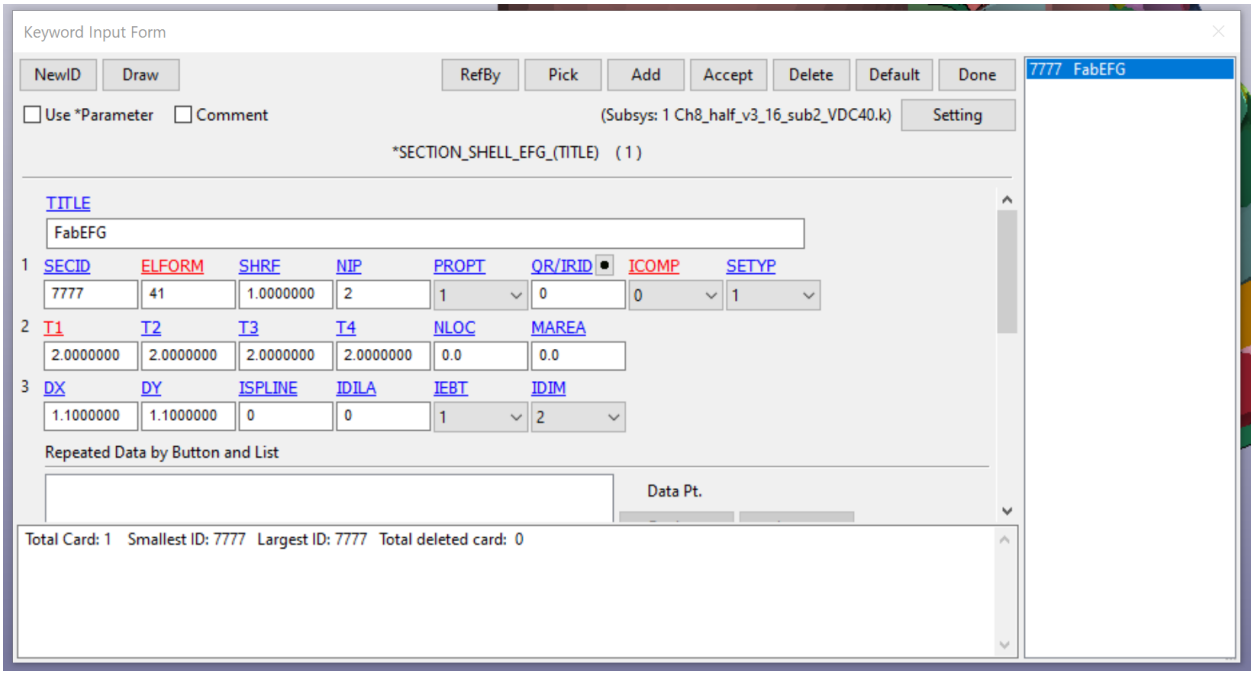

Ch8_full_v4C

By 0.0015 sec, when part of the fabric bursts, the distance between the yellow and green tiles was up about 13%. This using 2deg undulation angles

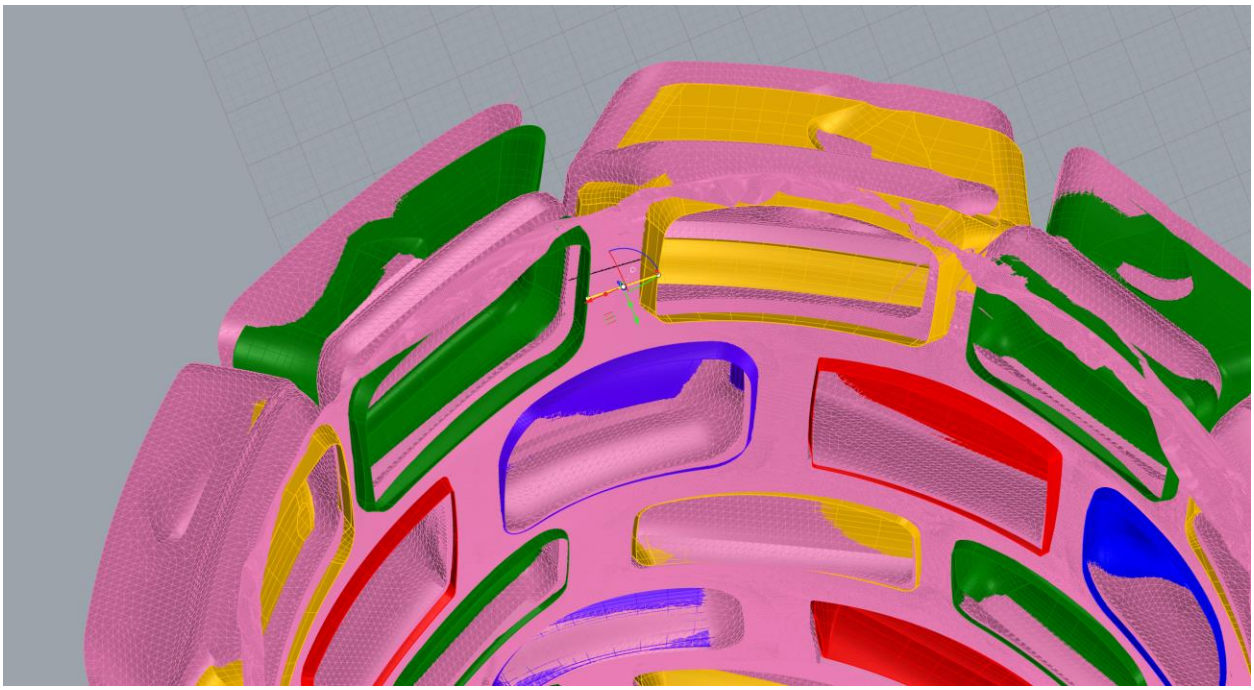

Ch8_Full_V4C3_5BF

Changed undulation angles to 5deg—resulted in earlier failure and more significant between-tile stretch at less leg rotation. (Also, thetalock was 30deg, thought this restricted it but it does the opposite)

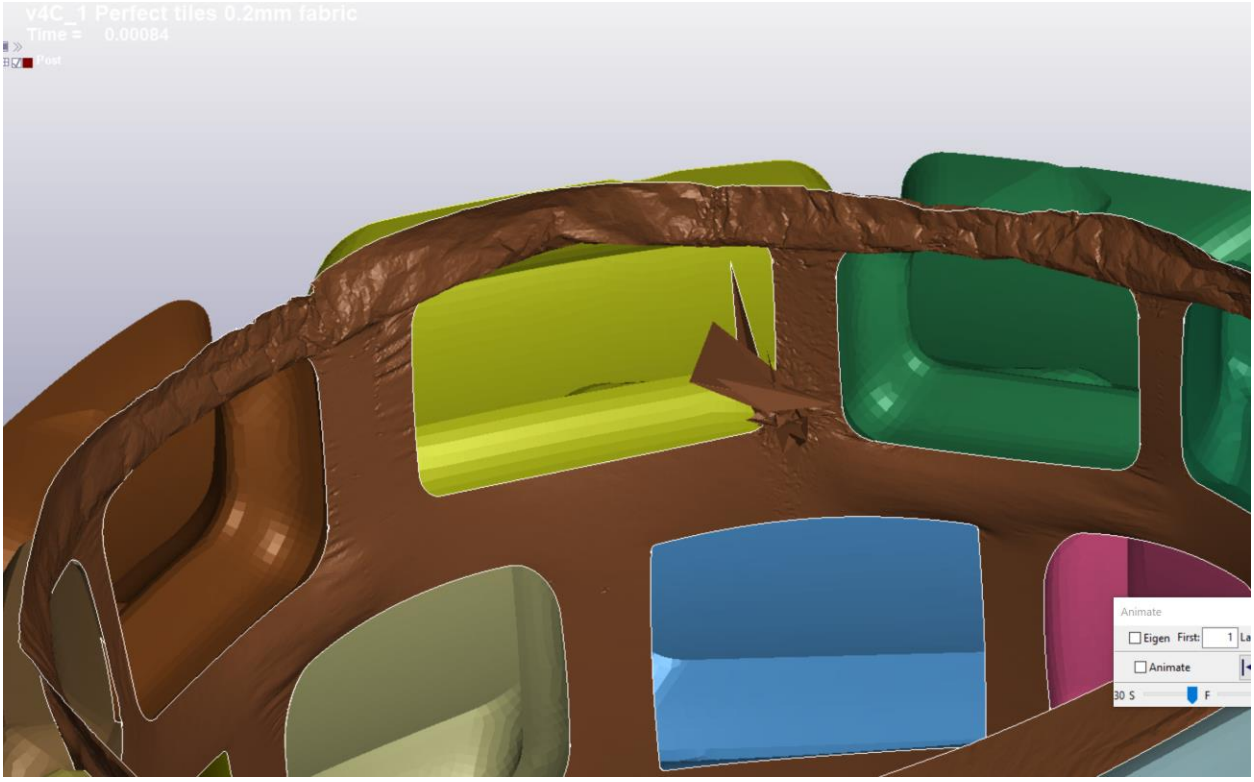

Ch8_Full_V4C3

Many elements failed at time 0.00098sec (not shown on d3plot):

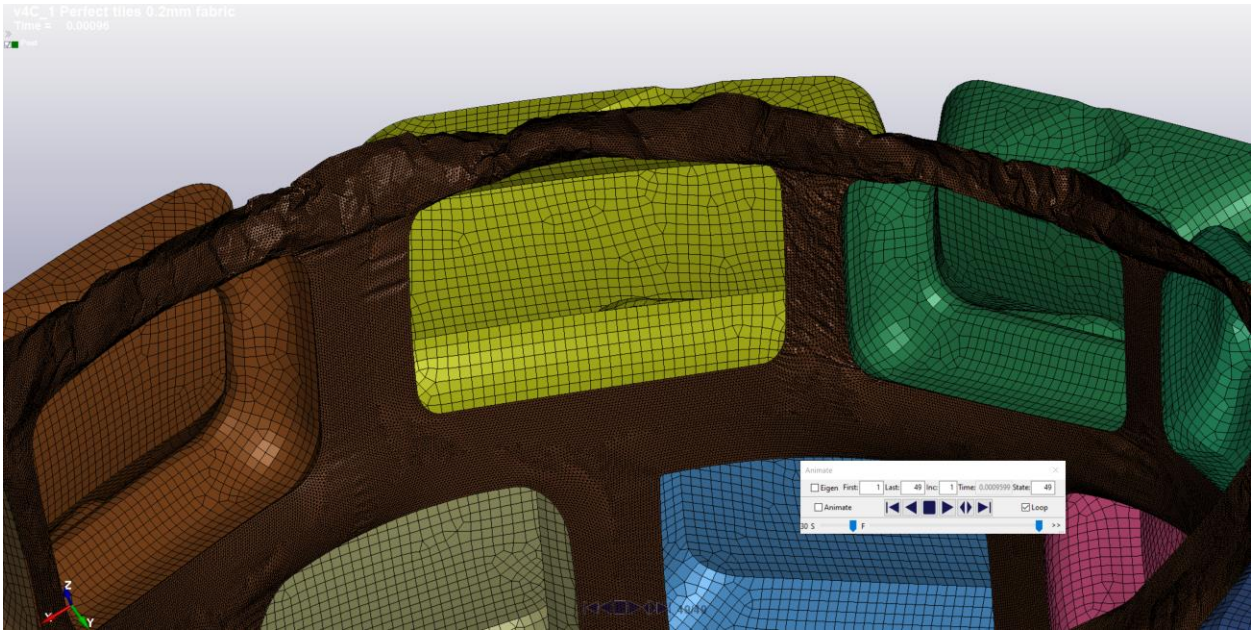

Ch8_Full_V4C4

Failure happens EARLIER (t=6.8e-4), not later!

There were strain/stress concentrations at a couple of corners. Perhaps those cause catastrophic failure.

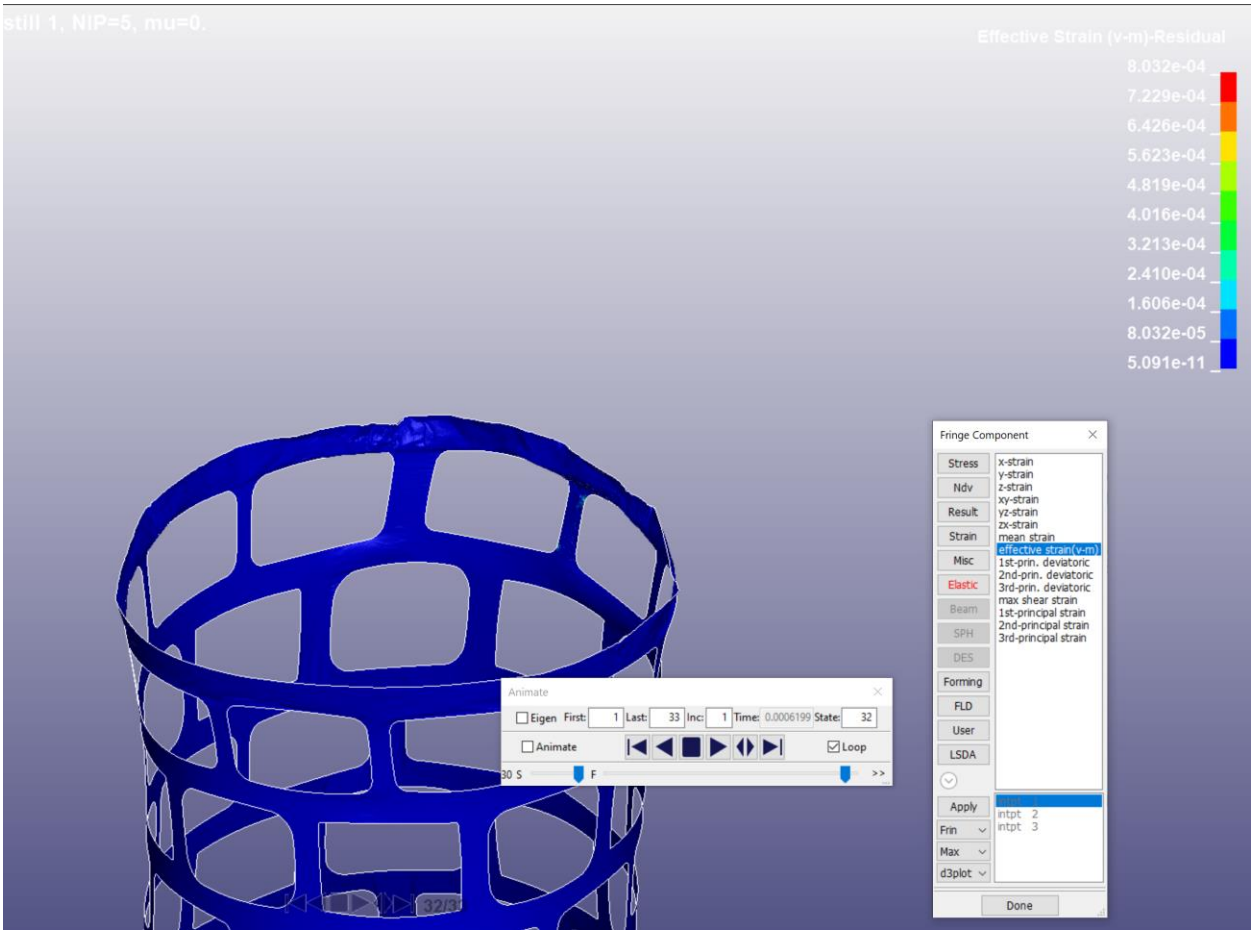

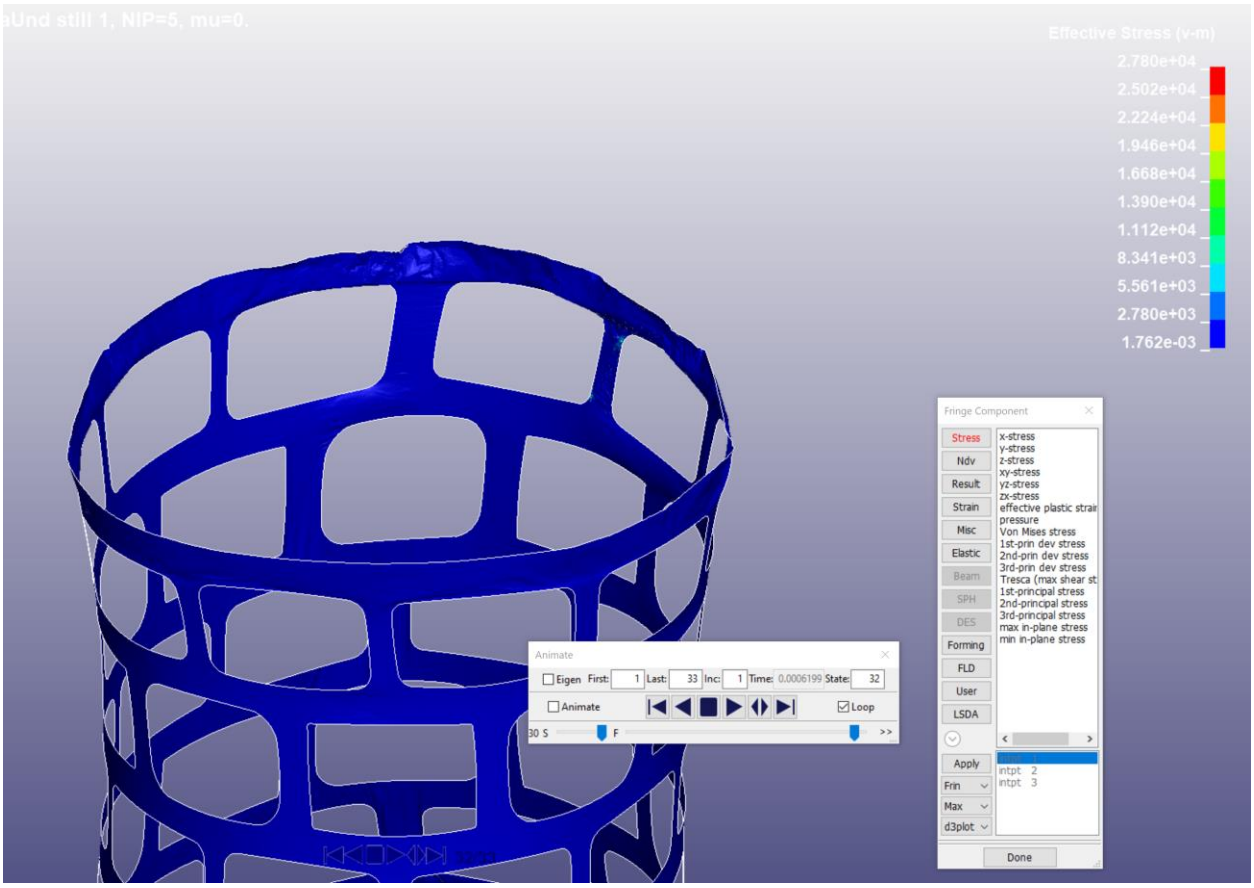
Effective Stress (v-m)
2.780e+04
2.502e+04
2.224e+04
1.946e+04
1.668e+04
1.390e+04
1.112e+04
8.341e+03
5.561e+03
2.780e+03
1.762e-03
Animate
Eigen First: 1 Last: 33 Inc: 1 Time: 0.0006199 State: 32
Animate
Loop
Fringe Component
Stress
Ndv
Result
Strain
Misc
Elastic
Beam
SPH
DES
Forming
FLD
User
LSDA
x-stress
y-stress
z-stress
xy-stress
yz-stress
zx-stress
effective plastic strain
pressure
Von Mises stress
1st-prin dev stress
2nd-prin dev stress
3rd-prin dev stress
Tresca (max shear st
1st-principal stress
2nd-principal stress
3rd-principal stress
max in-plane stress
min in-plane stress
Apply
Frin
Max
d3plot
intpt 2
intpt 3
Done

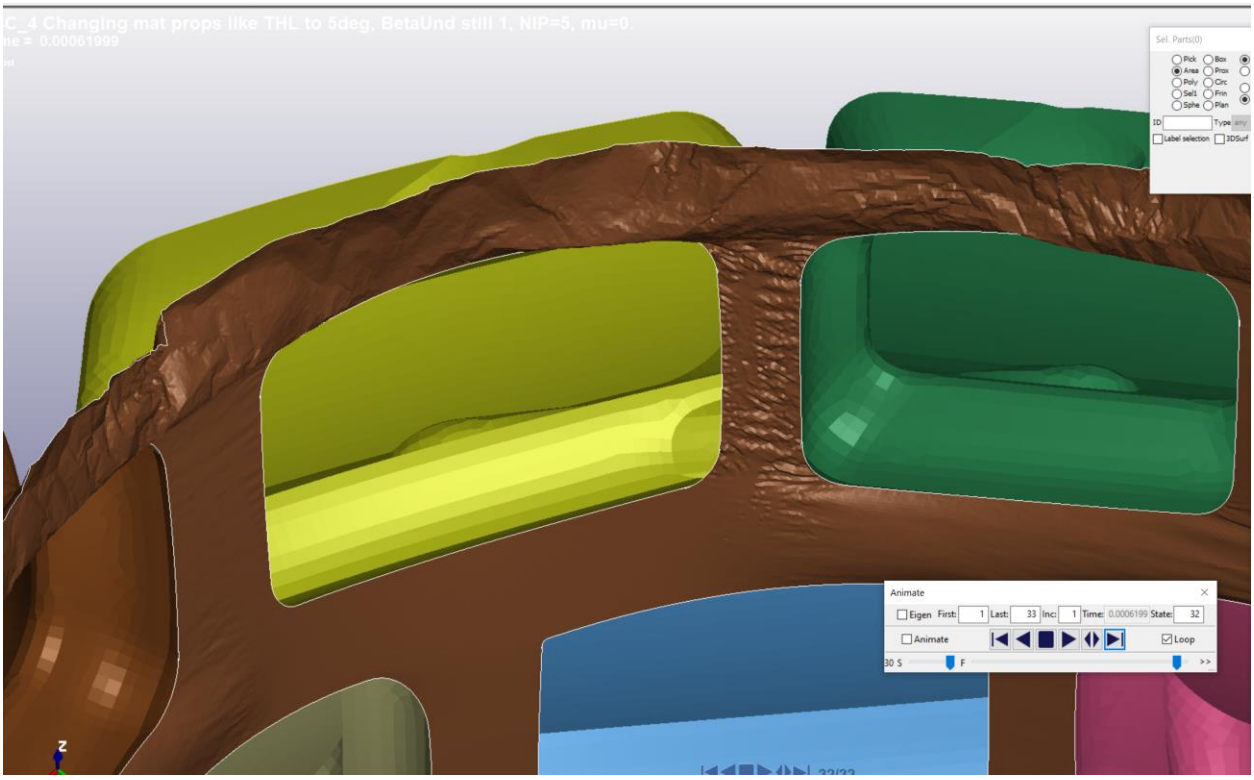
Animate
Eigen First: 1 Last: 33 Inc: 1 Time: 0.0006199 State: 32
Animate
Loop